

INSTITUT DE CIÈNCIA MOL·LECULAR

Bax $\alpha$ 5 AT LIPID MEMBRANES: STRUCTURE, ASSEMBLY  
AND PORE FORMATION.

GUSTAVO FUERTES VIVES

UNIVERSITAT DE VALÈNCIA  
Servei de Publicacions  
2011

Aquesta Tesi Doctoral va ser presentada a València el dia 29 d'abril de 2011 davant un tribunal format per:

- Dr. Javier Sancho Sanz
- Dr. Gorka Basáñez Asua
- Dr. Erik Strandberg
- Dr. Isaiah Arkin
- Dra. Ana J. García Sáez

Va ser dirigida per:  
Dr. Jesús Salgado Benito

©Copyright: Servei de Publicacions  
Gustavo Fuertes Vives

---

I.S.B.N.: 978-84-370-8226-4

Edita: Universitat de València  
Servei de Publicacions  
C/ Arts Gràfiques, 13 baix  
46010 València  
Spain  
Telèfon:(0034)963864115

# **Bax $\alpha$ 5 at lipid membranes: structure, assembly and pore formation**

Gustavo Fuertes Vives

Ph.D. Thesis 2011

Instituto de Ciencia Molecular (ICMOL)  
Universitat de València





UNIVERSITAT DE VALÈNCIA

**Jesús Salgado Benito**, Doctor en Ciències Químiques y Profesor Titular del Departament de Bioquímica y Biología Molecular de la Universitat de València,

CERTIFICA:

Que Don Gustavo Fuertes Vives, Licenciado en Bioquímica, ha realizado bajo su dirección el trabajo que con el título: *Bax $\alpha$ 5 at lipid membranes: structure, assembly and pore formation*, presenta para optar al grado de Doctor por la Universitat de València.

Y para que así conste y produzca los efectos oportunos, firmo la presente en Paterna a 11 de marzo de 2011

Fdo: Jesús Salgado Benito



Elsewhere you die and disintegrate. Here [*in Jerusalem*] you die and mingle

SAUL BELLOW in *To Jerusalem and back: a personal account*

Dresden: “Florence of the Elbe”

La investigación que corresponde a esta Tesis se realizó principalmente en el *Instituto de Ciencia Molecular de la Universitat de València*, en parte gracias al disfrute de una ayuda para la formación de personal investigador de carácter predoctoral en el marco del programa “V Segles” (de la propia Universitat). La fase inicial de la investigación se llevó a cabo en el *Departamento de Bioquímica y Biología Molecular*. Así mismo, parte del trabajo aquí descrito se realizó en el *Alexander Silberman Institute of Life Sciences, The Hebrew University of Jerusalem* y en el *Biotechnologisches Zentrum der TU Dresden*, gracias al disfrute de sendas ayudas para la realización de estancias cortas en el extranjero dentro del marco del programa “V Segles”.



*A mi familia*



Muchas gracias a todos los que habéis participado directa o indirectamente en esta tesis. Especialmente a Jesús, Santi, Diana, Orlando, Ismael, Cucha, Ana García, Ana Saurí, Dunja, María, Cristina, Luis, Marçal, M<sup>a</sup> Carmen, Mar, Alexa, Vasko, Kim, Claudine, Alberto, Shy, Josh, Petra y Erik.



# Contents

<b>Abbreviations</b>	<b>xvii</b>
<b>Glossary</b>	<b>xxi</b>
<b>I Introduction</b>	<b>1</b>
<b>1 Biological membranes</b>	<b>3</b>
1.1 The lipid component . . . . .	3
1.1.1 Types of lipids . . . . .	3
1.1.2 Self-assembly of lipids in water . . . . .	5
1.1.3 Lipid polymorphism . . . . .	7
1.1.4 Phase transitions of lipids . . . . .	8
1.2 The proteic component . . . . .	9
1.2.1 Protein insertion in biological membranes . . . . .	10
1.2.2 Structure and folding of membrane proteins . . . . .	10
1.2.3 Helix-helix packing in tertiary and quaternary structures . . . . .	12
1.3 Reductionism for studying biomembranes . . . . .	14
1.3.1 Peptides as models for studying membrane proteins . . . . .	14
1.3.2 Model membranes . . . . .	14
1.4 Models of biomembrane organization . . . . .	14
1.5 Summary of the state-of-the-art . . . . .	15
<b>2 Pores in Membranes</b>	<b>17</b>
2.1 The (w)hole story: ways of crossing the membrane . . . . .	17
2.1.1 Pore-forming toxins . . . . .	18
2.1.2 Antimicrobial peptides . . . . .	18
2.1.3 Cell-penetrating peptides . . . . .	18
2.1.4 Fusion proteins . . . . .	18
2.1.5 Membrane channels . . . . .	19
2.1.6 Carriers and transporters . . . . .	19
2.2 A lipocentric view to pores induced by peptides and proteins . . . . .	20
2.2.1 Lipids as receptors for pore-forming polypeptides . . . . .	21
2.2.2 Lipids as chaperones for pore-forming polypeptides . . . . .	23
2.2.3 Lipids as protagonists in the formation and stabilization of pores . . . . .	26
2.2.4 Physical properties of polypeptide-induced pores . . . . .	31
2.3 Summary of the state-of-the-art . . . . .	34

<b>3</b>	<b>Pores in mitochondria-mediated cell death</b>	<b>37</b>
3.1	An overview of apoptosis . . . . .	37
3.2	Bcl-2 proteins and the permeabilization of the mitochondrial outer membrane . . . . .	39
3.2.1	Structure of Bcl-2 proteins . . . . .	40
3.2.2	Pore-forming properties . . . . .	44
3.2.3	The complex regulatory network of Bcl-2 proteins . . . . .	47
3.3	Physiological and medical importance of apoptosis . . . . .	50
3.3.1	Mitochondrial membrane permeabilization in major human diseases . . . . .	50
3.3.2	Pharmacological manipulation of mitochondrial permeabilization . . . . .	51
3.4	Summary of the state-of-the-art . . . . .	51
<b>4</b>	<b>Aim of this work</b>	<b>53</b>
<b>II</b>	<b>Methodology</b>	<b>55</b>
<b>5</b>	<b>Methods</b>	<b>57</b>
5.1	Sample preparation . . . . .	57
5.1.1	Model membrane systems . . . . .	57
5.1.2	Peptide synthesis and purification . . . . .	62
5.1.3	Protein expression and purification . . . . .	64
5.2	Structural studies . . . . .	65
5.2.1	Circular dichroism spectroscopy . . . . .	66
5.2.2	Infrared spectroscopy . . . . .	69
5.2.3	X-ray scattering . . . . .	83
5.3	Peptide-peptide interactions in membrane environments . . . . .	85
5.3.1	Electrophoretic methods: Tricine SDS-PAGE . . . . .	85
5.3.2	Resonance energy transfer . . . . .	86
5.4	Thermodynamic studies . . . . .	91
5.4.1	Peptide-lipid interactions . . . . .	91
5.4.2	Peptide-peptide interactions . . . . .	93
5.5	Activity studies . . . . .	95
5.5.1	Leakage experiments in ensembles of LUVs . . . . .	95
5.5.2	Quenching of fluorescent lipids in ensembles of LUVs . . . . .	96
5.5.3	Single vesicle experiments . . . . .	97
<b>6</b>	<b>Protocols</b>	<b>101</b>
6.1	Sample preparation . . . . .	101
6.1.1	Model membrane systems . . . . .	101
6.1.2	Peptide synthesis and purification . . . . .	104
6.1.3	Protein expression and purification . . . . .	111
6.2	Structural studies . . . . .	117
6.2.1	Circular dichroism spectroscopy . . . . .	117

6.2.2	Infrared spectroscopy	118
6.2.3	X-ray scattering	121
6.3	Peptide-peptide interactions in membrane environments	121
6.4	Thermodynamic studies	122
6.4.1	Peptide-lipid interactions	122
6.4.2	Peptide-peptide interactions	122
6.5	Activity studies	123
6.5.1	Leakage experiments in ensembles of LUVs	123
6.5.2	Quenching of fluorescent lipids in ensembles of LUVs	125
6.5.3	Single GUV experiments	126
6.6	Miscellaneous reagents	129
6.6.1	Common buffer systems	129
6.6.2	Electrophoresis buffers	129
<b>III</b>	<b>Results, Discussion and Conclusions</b>	<b>133</b>
<b>7</b>	<b>Binding of Bax<math>\alpha</math>5 to membranes</b>	<b>135</b>
7.1	Introduction	135
7.2	Secondary structure of Bax $\alpha$ 5 in vesicle membranes	136
7.2.1	CD spectra	136
7.2.2	FTIR spectra	138
7.3	Energetics of Bax $\alpha$ 5-membrane interactions	141
7.4	Binding and pore-forming activity	142
7.5	Conclusions	143
<b>8</b>	<b>Homo- and hetero-oligomers of Bax<math>\alpha</math>5 in membranes</b>	<b>145</b>
8.1	Introduction	145
8.2	Oligomerization potential of Bax $\alpha$ 5 by SDS-PAGE	147
8.3	FRET of labeled Bax $\alpha$ 5 in lipid membranes	149
8.3.1	Design and synthesis of labeled Bax $\alpha$ 5 peptides	149
8.3.2	Effect of labeling on the structure and activity of Bax $\alpha$ 5	150
8.3.3	Calculation of the Förster distance	150
8.3.4	Measurements of FRET efficiency	152
8.4	Energetics of Bax $\alpha$ 5 oligomerization in membranes	161
8.5	Effect of mitochondrial lipids in Bax $\alpha$ 5 oligomerization	163
8.6	Bax $\alpha$ 5-Bcl-xL $\alpha$ 5 and Bax $\alpha$ 5-Bcl-xL $\Delta$ Ct interactions	167
8.6.1	Detection of Bax $\alpha$ 5 hetero-interactions	167
8.6.2	Effect of Bax $\alpha$ 5 heterointeractions on membrane activity	168
8.7	Discussion	169
8.7.1	Sequence determinants of Bax $\alpha$ 5 dimerization	169
8.7.2	Functional importance of Bax $\alpha$ 5/Bax $\alpha$ 5 interactions	171
8.7.3	Functional importance of Bax $\alpha$ 5/Bcl-xL $\alpha$ 5 interactions	173
8.8	Conclusions	174

<b>9</b>	<b>Structure of complexes of Bax<math>\alpha</math>5 with membranes</b>	<b>175</b>
9.1	Introduction . . . . .	175
9.1.1	Objectives . . . . .	176
9.2	Molecular orientation within the peptide-membrane complexes . . . . .	176
9.2.1	Determining peptide orientations from dichroic ratios . . . . .	178
9.2.2	Calculations using order parameters . . . . .	183
9.2.3	Including distributions of the orientation angles . . . . .	184
9.2.4	Orientation refinement assisted by rigid body modeling . . . . .	189
9.2.5	Monomers <i>vs</i> dimers. . . . .	192
9.3	Effect of the peptide on the membrane phase properties . . . . .	193
9.3.1	Insights from ATR-FTIR . . . . .	196
9.3.2	Insights from X-ray scattering . . . . .	197
9.4	Orientation and pore-forming activity . . . . .	201
9.5	Conclusions . . . . .	204
<b>10</b>	<b>Pore formation by Bax<math>\alpha</math>5</b>	<b>205</b>
10.1	Introduction . . . . .	205
10.2	Experiments in ensembles of LUVs . . . . .	207
10.2.1	Bax $\alpha$ 5-dependent dye efflux in LUVs . . . . .	207
10.2.2	Capturing long-term and equilibrium pores in ensembles of LUVs . . . . .	208
10.3	Single vesicle experiments with GUVs . . . . .	212
10.3.1	Successive leakage events in single GUVs . . . . .	212
10.3.2	Pores in reconstituted GUVs . . . . .	217
10.4	The two types of pores differ at least in their size . . . . .	218
10.4.1	Leak-in kinetics of pre-equilibrium pores . . . . .	218
10.4.2	Leak-in kinetics of equilibrium pores . . . . .	225
10.4.3	Estimating the size of individual pores . . . . .	227
10.4.4	Non-equilibrium <i>vs</i> equilibrium pores . . . . .	230
10.5	Membrane binding and leakage . . . . .	231
10.5.1	The lag time of vesicle poration depends on $P/L$ . . . . .	231
10.5.2	Peptide binding and pre-equilibrium GUV leakage . . . . .	231
10.5.3	Peptide binding and pores at equilibrium . . . . .	234
10.6	Comparing leakage in GUVs and LUVs . . . . .	237
10.7	Conclusions . . . . .	237
<b>11</b>	<b>General discussion, perspectives and conclusions</b>	<b>239</b>
11.1	General discussion . . . . .	239
11.1.1	Energetics of Bax $\alpha$ 5-membrane interactions . . . . .	239
11.1.2	Kinetics of Bax $\alpha$ 5-membrane interactions . . . . .	241
11.1.3	Structure of Bax $\alpha$ 5/membrane complexes . . . . .	243
11.1.4	The Bax $\alpha$ 5 code . . . . .	246
11.1.5	Bax $\alpha$ 5 as a minimal active domain of Bax . . . . .	247
11.2	Perspectives . . . . .	247
11.3	Conclusions . . . . .	248

<b>IV Versión Resumida en Español</b>	<b>251</b>
<b>12 Introducción</b>	<b>253</b>
12.1 Membranas biológicas	253
12.1.1 Composición de las biomembranas	253
12.1.2 Modelos estructurales de biomembranas	255
12.1.3 Estudio de las biomembranas bajo una aproximación reduccionista	255
12.2 Poros inducidos por polipéptidos: una visión lipocéntrica	256
12.2.1 Las membranas lipídicas como receptores de PFPPs	256
12.2.2 Las membranas lipídicas como carabinas de los PFPPs	257
12.2.3 Las membranas lipídicas controlan la asociación entre PFPPs	258
12.2.4 Las membranas lipídicas tienen un papel activo en la formación y estabilización de poros	258
12.3 Papel de los poros en mecanismos de muerte celular mediada por mitocondrias	260
12.3.1 MMP en apoptosis	260
12.3.2 Proteínas de la familia Bcl-2	261
12.3.3 Importancia de la apoptosis	262
12.4 Objetivo de este trabajo	262
<b>13 Materiales y métodos</b>	<b>265</b>
13.1 Preparación de muestras	265
13.1.1 Membranas modelo	265
13.1.2 Síntesis y purificación de péptidos	265
13.2 Estudios estructurales	266
13.2.1 Dicroísmo circular (CD)	266
13.2.2 Espectroscopia infrarroja (IR)	266
13.3 Interacciones péptido-péptido	268
13.3.1 Método electroforético: Tricina SDS-PAGE	268
13.3.2 Transferencia de energía por resonancia	268
13.4 Estudios termodinámicos	269
13.4.1 Interacciones péptido-lípido	269
13.4.2 Interacciones péptido-péptido	269
13.5 Estudios de actividad	270
13.5.1 Experimentos con poblaciones de vesículas lipídicas	270
13.5.2 Experimentos con vesículas lipídicas individuales	270
<b>14 Resultados, discusión y conclusiones</b>	<b>271</b>
14.1 Unión de Bax $\alpha$ 5 a membranas	271
14.1.1 Estructura secundaria de Bax $\alpha$ 5 en membranas	271
14.1.2 Energética de las interacciones Bax $\alpha$ 5-membrana	271
14.2 Auto-ensamblaje de Bax $\alpha$ 5 en membranas	271
14.2.1 Oligomerización de Bax $\alpha$ 5 usando micelas de SDS	271
14.2.2 Oligomerización de Bax $\alpha$ 5 en membranas por FRET	273

## Contents

14.2.3	Energética de la interacción Bax $\alpha$ 5-Bax $\alpha$ 5 . . . . .	275
14.2.4	Interacciones Bax $\alpha$ 5 y otros polipéptidos derivados de Bcl-xL . . . . .	275
14.3	Estructura de complejos Bax $\alpha$ 5-membranas . . . . .	276
14.3.1	Orientación de Bax $\alpha$ 5 en la membrana . . . . .	276
14.4	Formación de poros por Bax $\alpha$ 5 . . . . .	278
14.4.1	Experimentos en LUVs . . . . .	278
14.4.2	Experimentos con GUVs . . . . .	279
14.5	Discusión general . . . . .	283
14.5.1	Energética de las interacciones Bax $\alpha$ 5-Bax $\alpha$ 5 y Bax $\alpha$ 5-membrana . . . . .	283
14.5.2	Cinética de las interacciones Bax $\alpha$ 5-membrana . . . . .	285
14.5.3	Estructura de complejos Bax $\alpha$ 5-membrana y formación de poros . . . . .	285
14.5.4	El código de Bax $\alpha$ 5 . . . . .	285
14.5.5	Bax $\alpha$ 5 es un dominio activo mínimo de Bax . . . . .	286
14.6	Conclusiones . . . . .	286
	<b>Bibliografía</b> . . . . .	<b>289</b>

# Abbreviations

ACN	acetonitrile
AGV	average gray value
ANTS	8-Aminonaphtalene-1,3,6-trisulfonic acid
ATR-FTIR	attenuated total reflection Fourier transform infrared
Bak	Bcl-2 homologous antagonist killer
Bax	Bcl-2 associated protein X
Bcl-2	B-cell lymphoma 2
Bcl-xL	B-cell lymphoma extra large
BH	Bcl-2 homology domain
Bid	BH3 interacting domain death agonist
Bim	Bcl-2 interacting mediator of cell death
BSA	bovine serum albumin
CDC	cholesterol-dependent cytolysin
CD	circular dichroism
Cho	cholesterol
CL	cardiolipin
CTD	C-terminal domain
cyt c	cytochrome c
Dabcy1	4-((4-(dimethylamino)phenyl)azo)benzoic acid
DCM	dicloromethane
DiD	1,1'-dioctadecyl-3,3,3',3'-tetramethylindodicarbocyanine, 4-chlorobenzenesulfonate salt
DIEA	N,N-diisopropylethylamine
DLPC	1,2-dilauroyl-3- <i>sn</i> -phosphocholine
DLS	dynamic light scattering
DMPC	1,2-dimiristoyl-3- <i>sn</i> -phosphocholine
DOPC	1,2-dioleoyl-3- <i>sn</i> -phosphocholine
DPPC	1,2-dipalmitoyl-3- <i>sn</i> -phosphocholine

## Abbreviations

DPX	p-xylene-byspiridinium bromide
EDANS	5-((2-aminoethyl)amino)naphthalene-1-sulfonic acid
EPR	electron paramagnetic resonance
ESI-Q	electrospray mass ionization quadrupole
FD	fluorescein-labeled dextran
Fmoc	fluorenylmethyloxycarbonyl
FRET	Förster resonance energy transfer
GPI	glycosylphosphatidylinositol
GUV	giant unilamellar vesicle
HBTU	O-benzotriazole-N,N,N',N'-tetramethyl-uronium-hexafluoro-phosphate
HFIP	1,1,1,3,3,3-hexafluoro-2-propanol
HOBT	hydroxybenzotriazole
IMAC	immobilized metal affinity chromatography
IMS	inter-membrane space
IRE	internal reflection element
LUV	large unilamellar vesicle
MALDI-TOF	matrix assisted laser desorption ionization time of flight
MD	molecular dynamics
MIM	mitochondrial inner membrane
MLV	multilamellar vesicle
MMP	mitochondrial membrane permeabilization
MOM	mitochondrial outer membrane
MOMP	mitochondrial outer membrane permeabilization
NBD	N-(7-nitrobenz-2-oxa-1,3-diazol-4-yl)
NMP	N-methyl-2-pyrrolidone
NMR	nuclear magnetic resonance
OCD	oriented circular dichroism
PAGE	polyacrylamide gel electrophoresis
PBS	phosphate buffered saline
PC	phosphatidylcholine
PE	phosphatidylethanolamine
PG	phosphatidylglycerol
PI	phosphatidylinositol

PFPP	pore-forming polypeptide
P/L	peptide-to-lipid molar ratio
POPC	1-palmitoyl-2-oleyl- <i>sn</i> -glycero-3-phosphocholine
PTPC	permeability transition pore complex
RMSD	root mean square deviation
RP-HPLC	reversed phase high performance liquid chromatography
SD	standard deviation
SDS	sodium dodecyl sulphate
SE	succinimidyl ester
SFCS	scanning fluorescence correlation spectroscopy
SM	sphingomyelin
SSID	site-specific infrared dichroism
SUV	small unilamellar vesicle
TDM	transition dipole moment
TFA	trifluoroacetic acid
TLC	thin-layer chromatography
TM	transmembrane
VDAC	voltage-dependent anion channel
XS	X-ray scattering

## *Abbreviations*

# Glossary

$A$	acceptor in FRET or absorbance
$A_0$	total pore area at short-term
$A_\infty$	total pore area at long-term/equilibrium
$C$	concentration
$C_{open}$	peptide amount at the onset of pore opening
$\overline{C}_{open}$	mean peptide amount at the onset of pore opening
$D$	donor in FRET or diffusion coefficient
$Di$	dimer
$d$	lamellar repeat distance in supported multibilayers
$E_a$	activation energy of pore formation in a lipid membrane
$E_a^*$	activation energy of pore formation in a membrane in the presence of a pore-forming peptide
$E$	efficiency of energy transfer
$E_{dimer}^{ss}$	$E$ in steady-state due to dimerization only
$E_{proximity}^{ss}$	$E$ in steady-state due to proximity effects
$E^{ss}$	$E$ in steady-state (total)
$E_{dynamic}^{tr}$	$E$ in time-resolved experiments due to dynamic contributions
$E_{static}^{tr}$	$E$ in time-resolved experiments due to static contributions
$E^{tr}$	$E$ in time-resolved experiments
$F$	fluorescence intensity
$F_D$	fluorescence intensity of donor only samples
$F_{DA}$	fluorescence intensity of donor-acceptor samples
$F_{DAU}$	fluorescence intensity of donor-acceptor-unlabeled samples
$F_A$	fluorescence intensity of acceptor samples
$f_A$	fraction of acceptors
$f_{Di}$	fraction of dimers
$f_{Mo}$	fraction of monomers
$f_x$	fraction of peptide partitioned to the membrane

## Glossary

$f_\beta$	fraction of peptides with tilt $\beta$
$G(\tau)$	autocorrelation function of intensity fluctuations
$h$	hill coefficient
$I$	intensity
$J(\lambda)$	spectral overlap integral in FRET
$K_A$	equilibrium association constant
$K_{dimer}$	equilibrium constant of dimerization
$K_x$	water-membrane partition coefficient
$k$	kinetic constant of external dye diffusion
$k_{flux}$	kinetic constant of dye flux accross a pore
$k_{off}$	kinetic constant of peptide dissociation from the membrane
$k_{on}$	kinetic constant of peptide association to the membrane
$k_{open}$	kinetic constant of pore opening
$k_{relax}$	kinetic constant of pores size relaxation
$Mo$	monomer
$N$	number of observed molecules in FCS
$m$	membrane thickness
$n$	refractive index or number
$P$	pore permeability coefficient
$P(x)$	probability function of variable $x$
$Q$	quantum yield
$Q_D$	quantum yield of the donor
$Q(t)$	quenching at time $t$
$q$	scattering vector
$R$	dichroic ratio in FTIR or D-A distance between neighbouring subunits in FRET
$R(t)$	Content release (leakage) at time $t$
$R_H$	hydrodynamic radius
$R_0$	Förster distance
$r$	donor-acceptor distance
$r_{max}$	equivalent radius of pre-equilibrium pores
$r_{min}$	equivalent radius of equilibrium pores
$r_v$	vesicle radius
$S$	orientational order parameter in ATR-FTIR or

	aspect ratio of the elliptical Gaussian detector area in FCS
$T$	absolute temperature
$T_m$	phase transition temperature
$t$	time
$V$	volume
$\Delta G_{dimer}$	Gibbs free energy of dimerization
$\Delta G_{if}$	Gibbs free energy of partitioning to the membrane interphase
$\Delta G_{if}^{helix}$	Gibbs free energy of partitioning and folding as $\alpha$ -helix in the membrane interphase
$\Delta G^{ins}$	Gibbs free energy of insertion in the membrane hydrocarbon core
$\Delta G_{oct}^{helix}$	Gibbs free energy of partitioning and folding as $\alpha$ -helix in the membrane hydrocarbon core
$\Delta G_{pore}$	Gibbs free energy of pore formation
$\Delta G_x$	Gibbs free energy of water-membrane partition
$\alpha$	angle between the TDM and the polymer director in FTIR or angle between the X-ray and the plane of the bilayer in XS
$\beta$	tilt or angle between the polymer director and the $z$ axis
$\bar{\beta}$	mean of the Gaussian distribution of tilt angles
$\delta_{on}$	delay time for the onset of peptide binding to the membrane
$\epsilon$	molar extinction coefficient
$\epsilon_i$	electric field component of axis $i$
$\theta_i$	angle between the TDM and the $z$ axis for residue $i$
$[\theta]_{MR}$	mean residue ellipticity
$\kappa_i$	integrated absorption coefficient of axis $i$
$\kappa^2$	orientation factor
$\lambda$	wavelength
$\rho(z)$	electron density profile in the $z$ axis
$\eta$	viscosity
$\sigma$	mosaicity
$\sigma_\beta$	standard deviation of the tilt angle distribution
$\sigma_\omega$	standard deviation of the rotational pitch angle distribution
$\tau$	lifetime in time-resolved FRET experiments or delay time in a correlation function
$\tau_{D,n}$	donor lifetime of component $n$

## Glossary

$\tau_{DA,n}$	donor lifetime in the presence of acceptor of component $n$
$\tau_{on}^{app}$	apparent time constant of peptide binding to the membrane
$\tau_{flux}$	time constant of dye flux across a pore
$\tau_{relax}$	time constant of pore relaxation
$\bar{\tau}$	amplitude-averaged lifetime
$\langle \tau \rangle$	amplitude-weighted lifetime
$\chi^2$	chi-squared error function
$\omega_i$	rotational pitch angle around the helix director for residue $i$
$\bar{\omega}$	mean of the Gaussian distribution of rotational pitch angles
$\omega_0$	waist radius of the detector laser

# List of Figures

1.1	Examples of lipids found in membranes. . . . .	5
1.2	Schematic illustration of supramolecular aggregates formed by the self-organization of lipids in water environments. . . . .	6
1.3	Lipids speak the language of curvature . . . . .	8
1.4	Schematic view of lipid bilayer structures in various crystalline phases . . . . .	9
1.5	The two known structural classes of membrane proteins. . . . .	11
1.6	The two major structural motifs of interacting TM pairs. . . . .	12
2.1	The membrane as a docking surface . . . . .	22
2.2	Chaperon-like foldase activity of membranes . . . . .	25
2.3	Comparison of flip-flop assisting, stress induced and peptide induced pores . . . . .	27
2.4	Bilayer structure at the edge of peptide-induced pores. . . . .	29
2.5	Cartoons of kinetic, two-state ( $B_{ex}/P_i$ ), and equilibrium two-phase ( $S/I$ ) pore models . . . . .	30
2.6	Classical and non-classical lipid curvature effects in pores formed by polypeptides . . . . .	33
3.1	Release of intermembrane space proteins during the intrinsic pathway of apoptosis . . . . .	38
3.2	Classification of Bcl-2 proteins . . . . .	40
3.3	Structure of Bcl-2 proteins . . . . .	42
3.4	Helical-wheel representations of the helices $\alpha 5$ from Bax and Bcl-xL . . . . .	45
3.5	Permeabilization of the outer mitochondrial membrane by proteins of the Bcl-2 family . . . . .	49
5.1	Dynamic light scattering for liposome size determination . . . . .	59
5.2	Determination of mosaicity of oriented multibilayers . . . . .	61
5.3	Solid phase peptide synthesis . . . . .	63
5.4	The circular dichroism phenomenon . . . . .	67
5.5	ATR-FTIR infrared spectrum of phospholipid bilayers supported on a Ge crystal with reconstituted proteins . . . . .	70
5.6	Geometrical configuration of ATR-FTIR . . . . .	72
5.7	Geometrical definitions in ATR-FTIR . . . . .	73
5.8	Theoretical dependence of $R_{helix}$ on the value of the tilt angle . . . . .	76

5.9	Theoretical dependence of $R_{site}$ on the angular position of the labeled residue . . . . .	79
5.10	Geometrical definitions in a peptide dimer . . . . .	83
5.11	Sketch of a X-ray scattering geometry . . . . .	84
5.12	Dependence of the energy transfer efficiency on distance between donor and acceptor . . . . .	88
5.13	Schematic illustration of the FRET-based analysis of dimer formation in membranes using lifetime measurements . . . . .	89
5.14	Calculated efficiencies of energy transfer for donor-acceptor pairs localized in the membrane . . . . .	90
5.15	Thermodynamic cycle for the transfer of a peptide from water to the bilayer interior . . . . .	94
5.16	Schematic representation of an experiment of contents release . . . . .	95
5.17	NBD quenching by sodium dithionite . . . . .	96
5.18	The principle of two-foci scanning fluorescence correlation spectroscopy . . . . .	99
6.1	Size distribution of LUVs by intensity of scattered light . . . . .	103
6.2	Examples of mass spectra of purified Bax $\alpha$ 5 . . . . .	112
6.3	Example of a HPLC chromatogram of purified Bax $\alpha$ 5 . . . . .	112
6.4	Monitoring the purification of Bcl-xL $\Delta$ Ct by SDS-PAGE . . . . .	116
6.5	Example of a UV-Vis spectrum of Bax $\alpha$ 5 . . . . .	117
7.1	Titration of Bax $\alpha$ 5 with LUVs monitored by circular dichroism spectroscopy . . . . .	137
7.2	Representative Amide regions in ATR-FTIR spectra of Bax $\alpha$ 5 in different environments . . . . .	139
8.1	Bax $\alpha$ 5 dimerization in SDS micelles . . . . .	147
8.2	Effect of mutations on the leakage activity of Bax $\alpha$ 5 . . . . .	148
8.3	Effect of conjugation with fluorescence dyes on the secondary structure and pore-forming activity of Bax $\alpha$ 5 . . . . .	151
8.4	Excitation and emission spectra of fluorescence labeled Bax $\alpha$ 5 peptides in various combinations . . . . .	153
8.5	Control experiments for FRET measurements in membranes . . . . .	156
8.6	Steady-state FRET of Bax $\alpha$ 5 in POPC vesicles . . . . .	157
8.7	Time-resolved FRET of Bax $\alpha$ 5 in POPC vesicles . . . . .	161
8.8	Energetics of Bax $\alpha$ 5 oligomerization in vesicles . . . . .	164
8.9	Effect of lipid composition on Bax $\alpha$ 5 oligomerization . . . . .	166
8.10	Hetero-interactions between Bax $\alpha$ 5 and Bcl-xL polypeptides . . . . .	168
8.11	Effect of Bcl-xL polypeptides on the membrane activity of Bax $\alpha$ 5 . . . . .	169
9.1	Representative ATR-FTIR spectra of the amide I region of unlabeled groups of Bax $\alpha$ 5 in lipid membranes . . . . .	177

9.2	Representative isotope-shifted amide I bands of 1- <sup>13</sup> C= <sup>18</sup> O labeled Baxα5 in lipid membranes . . . . .	179
9.3	Helical wave plots of $R_{site,i}^{exp}$ and $R_{site}^{theo}$ as a function of the residue angular position around the helix . . . . .	182
9.4	Visualization of the best-fit orientational distribution for the four proposed models . . . . .	184
9.5	Estimating the mosaicity of the bilayer stack by a $\chi$ -scan on the first Bragg peak . . . . .	186
9.6	$\chi^2$ error analysis for different combinations of parameters in fits of IR data considering distributions of $\beta$ and $\omega$ . . . . .	188
9.7	Rigid body modeling of the orientation of Baxα5 . . . . .	196
9.8	Effect of Baxα5 on the lipid order as determined from ATR-FTIR spectra . . . . .	197
9.9	Effect of Baxα5 on the bilayer thickness determined from XS . . . . .	199
9.10	Electron density profiles of oriented lipid multilayers in presence of Baxα5 . . . . .	199
9.11	Dependence of Baxα5 tilt angle on several parameters . . . . .	203
10.1	Vesicle leakage as a function of peptide-to-lipid molar ratio . . . . .	209
10.2	Short-term, long-term and equilibrium pore activities in ensembles of LUVs . . . . .	211
10.3	Successive leak-in of serially added dyes for individual GUVs showing all-or-none release . . . . .	213
10.4	Successive leak-in kinetics of serially added dyes, showing partial refilling of GUVs and eventually pore closure . . . . .	215
10.5	Effect of the relative amount of Baxα5 on GUV poration . . . . .	216
10.6	Baxα5 binding and activity in reconstituted vesicles . . . . .	217
10.7	Kinetic analysis of short-term pores . . . . .	219
10.8	Distributions of total pore area per vesicle for pre-equilibrium and equilibrium pores . . . . .	223
10.9	Kinetic analysis of long-term pores . . . . .	226
10.10	Pores shrink with equilibration . . . . .	229
10.11	Simultaneous monitoring of binding of Baxα5 and permeabilization on single GUVs . . . . .	232
10.12	Effect of the amount of Baxα5 bound to the GUV membrane on vesicle poration . . . . .	234
10.13	Vesicle poration at equilibrium depending on Baxα5 bound to the membrane . . . . .	236
10.14	Single GUV vs ensemble LUV . . . . .	238
11.1	The action of Baxα5 understood as a catalysis-like effect . . . . .	240
11.2	Kinetic model for pore induction by amphipathic cationic peptides . . . . .	242
11.3	Molecular models of Baxα5 oriented in lipid bilayers . . . . .	245

*List of Figures*

12.1 Principales lípidos usados en esta Tesis . . . . .	254
12.2 El papel activo de las membranas en la formación de poros mediada por PFPPs . . . . .	257
12.3 Modelos de formación de poros . . . . .	259
12.4 Permeabilización de la membrana mitocondrial externa por proteínas de la familia Bcl-2 . . . . .	260
14.1 Estructura secundaria de Bax $\alpha$ 5 analizada mediante espectroscopia de dicroísmo circular . . . . .	272
14.2 Dimerización de Bax $\alpha$ 5 en micelas de SDS . . . . .	273
14.3 Dimerización de Bax $\alpha$ 5 en membranas usando FRET en estado estacionario . . . . .	274
14.4 Interacción entre Bax $\alpha$ 5 y otros polipéptidos derivados de Bcl-xL . . . . .	275
14.5 Estudio de la liberación de contenidos encapsulados en LUVs en función de la relación molar Bax $\alpha$ 5/lípido . . . . .	278
14.6 Efecto de las mutación de residuos de Bax $\alpha$ 5 en la liberación de contenidos encapsulados en LUVs . . . . .	279
14.7 Entrada sucesiva de sondas fluorescentes en GUVs individuales mostrando el comportamiento “todo o nada” . . . . .	281
14.8 Los poros formados por Bax $\alpha$ 5 encogen con el tiempo . . . . .	282
14.9 Efecto de la concentración de Alexa647-Bax $\alpha$ 5 en GUVs sobre la formación de poros . . . . .	283
14.10 Modelos que se derivan de los resultados obtenidos en esta Tesis . . . . .	284

# List of Tables

5.1	Principal IR absorption bands from membrane protein samples.	71
5.2	Correlations between common protein secondary structures and amide I frequency . . . . .	71
6.1	Aminoacid sequences of unlabeled peptides . . . . .	106
6.2	Extinction coefficients of polypeptides and dyes used in this Thesis	110
6.3	Steady-state fluorescence parameters . . . . .	124
6.4	Lifetime fluorescence parameters . . . . .	124
6.5	Glycine SDS-PAGE set up . . . . .	130
6.6	Tricine SDS-PAGE set up . . . . .	131
7.1	Secondary structure of Bax $\alpha$ 5 as estimated from CD spectra . .	138
7.2	Secondary structure content of Bax $\alpha$ 5 in estimated from FTIR-ATR spectra . . . . .	139
7.3	Position of 1- $^{13}\text{C}=\text{O}$ absorption bands of Bax $\alpha$ 5 in membranes	140
7.4	Energetics of Bax $\alpha$ 5 binding to LUV membranes . . . . .	142
8.1	Peptides used for the oligomerization studies . . . . .	146
8.2	Fluorescence parameters. . . . .	154
8.3	<i>Förster distances</i> ( $R_0$ ) . . . . .	154
8.4	Distance between labels for the different D/A pairs in POPC membranes . . . . .	158
8.5	Toward the relative orientation of the monomers in the Bax $\alpha$ 5 dimer. . . . .	160
8.6	Time-resolved fluorescence of Alexa350-Bax $\alpha$ 5/K(Dabcyl)-Bax $\alpha$ 5 in POPC membranes. . . . .	162
8.7	Energetics of Bax $\alpha$ 5 dimerization in membranes . . . . .	163
8.8	Steady-state FRET of Bax $\alpha$ 5 in different lipid membranes . . . .	165
9.1	Peptides used for the structural study . . . . .	177
9.2	Dichroic ratios of Bax $\alpha$ 5 in DMPC . . . . .	180
9.3	Dichroic ratios of Bax $\alpha$ 5 in POPC . . . . .	181
9.4	Tilt angle of Bax $\alpha$ 5 in different lipid membranes . . . . .	183
9.5	Best-fit parameters describing the orientation of Bax $\alpha$ 5 in multi-bilayer stacks. . . . .	185
9.6	Values of $\theta_i^{exp}$ for Bax $\alpha$ 5 in DMPC . . . . .	190
9.7	Values of $\theta_i^{exp}$ for Bax $\alpha$ 5 in POPC . . . . .	191

List of Tables

9.8	<b>Bax<math>\alpha</math>5 helix geometry in the <i>explicit</i> model used for rigid body refinement</b>	194
9.10	<b>Results from the rigid body modeling</b>	195
9.11	<b>Structural characterization of multilamellar membrane stacks by XS</b>	200
10.1	<b>Effect of the bulk <math>P/L</math> ratio on the size of pores induced by Bax<math>\alpha</math>5.</b>	224
10.2	<b>Effect of the <math>P/L</math> on the kinetics of peptide binding and pore formation.</b>	233
10.3	<b>Parameters derived from the SFCS analysis of Alexa647-Bax<math>\alpha</math>5 in single GUVs</b>	237
14.1	<b>Estructura secundaria de Bax<math>\alpha</math>5 estimada a partir de los espectros de CD</b>	272
14.2	<b>Resultados del modelado mediante cuerpo r�gido</b>	277

**Part I**

**Introduction**



# 1 Biological membranes

Biological membranes, or biomembranes, are separating layers around or within cells which define enclosed spaces necessary to maintain specific biochemical environments<sup>1</sup>. The control of physicochemical conditions in such compartments, within acceptable ranges and in a regulated way, is vital for the existence of life. Thus, biomembranes are not just physical barriers, but have evolved to act as dynamic structures capable of a variety of complex functions, like selective permeability, electrical excitability, reception and transduction of signals, electron transfer and physical anchoring for shape control and movement [1]. A dramatic demonstration of the importance of membranes for the maintenance of life is the role of membrane integrity in mechanisms of cell death used by organisms at multiple levels, from simple strategies of defense and attack to sophisticated physiological cell suicide<sup>2</sup>. Coherent with the complexity and variety of their functions, natural biomembranes have a varied and heterogeneous composition where lipids of multiple types appear together with proteins, and to a smaller extent sugars. In the following Sections we will present the lipid and protein components, first separated (SEC. 1.1 and 1.2), but continuing with an integrated view for the discussion of the membrane structure and its main characteristics (SEC. 1.4). Finally, we will show how reductionism, which is the strategy employed in this Thesis, has help in getting new insights into biomembrane structure and function. Pores in membranes, which are the main topic of this Thesis, will be introduced in separate Chapters dedicated to their general properties (CHAP. 2 on page 17) and to specific aspects of Bax-induced mitochondrial pores (CHAP. 3 on page 37).

## 1.1 The lipid component

### 1.1.1 Types of lipids

Lipids are a large and varied group of molecules characterized by being markedly amphipathic. Because their hydrophobic part is typically big and elongated, compared to their polar groups, lipids do not readily dissolve in water, but instead self organize

---

1 [http://en.wikipedia.org/wiki/Biological\\_membrane](http://en.wikipedia.org/wiki/Biological_membrane)

2 To defend themselves from infections, animals have evolved to develop a battery of membrane-active antibiotics, able to kill microbes by porating their membranes. In turn, the attack systems of pathogenic microorganisms include strategies to drive toxins across the cell membrane of animal cells, and in a number of cases toxins may act directly by increasing the membrane permeability to destroy the cell homeostasis. This simple cell death systems share striking similarities with steps of a much more sophisticated mechanism used for self-control of cell fate in animal tissues, where intracellular membranes are porated to deliver molecules specialized in orchestrating cell suicide. The latter example refers to the function of Bcl-2 proteins, like Bax, in apoptosis, which is of main interest for this Thesis.

## 1 Biological membranes

forming complex structures, like micelles and vesicles. In the cells, lipids are responsible of important functions, like energy storage and signaling, but the main interest for this work relates to their structural role as dynamic building blocks in membranes. The major groups of membrane lipids are *glycerophospholipids*, *sphingolipids*, *glycolipids* and *sterols*.

### Glycerophospholipids

Phospholipids contain a phosphate group esterified with an alcohol in a core or backbone moiety, which is in turn linked to one or more alkyl chains (FIG. 1.1 B-C). They are the principal structural components of membranes in all kinds of cells, from bacteria to eukaryotic cells, but not in the very primitive microorganisms known as Archaea<sup>1</sup>. Most common phospholipids, known as *glycerophospholipids*, have glycerol (a trialcohol) as the backbone moiety, which apart from the phosphate group makes ester bonds with two long-chain fatty acids, thus forming *amphipathic* molecules with *hydrophobic tails*, the hydrocarbon chains, and a *hydrophilic head*, the glycerol and phosphoryl groups (depicted schematically in FIG. 1.1 A). The phosphorus group is normally further derivatized to give different types of glycerophospholipids, mainly phosphatidylcholine (PC), phosphatidylethanolamine (PE), phosphatidylglycerol (PG), phosphatidylserine (PS) and phosphatidylinositol (PI). Of particular interest for this Thesis is the lipid *cardiolipin* (CL), found in the mitochondria inner membrane (MIM) [2] as well as in chloroplast membranes and some bacterial membranes, which is basically a dimer lipid that has four fatty-acid chains and two PG head groups. Examples of glycerophospholipids are shown in FIG. 1.1 B-C.

While PC and PE are neutral (zwitterions), PG, CL, PS and PI can be anionic at normal pH conditions. This difference has important consequences for the properties of membranes depending on the lipid composition, as it influences, for example, the type of interactions with proteins and peptides.

### Sphingolipids

As an alternative to glycerol, Nature also constructs lipids by linking the fatty acids to *sphingosine*, a long-chain amino alcohol. The simplest version of the resulting *sphingolipid* is *ceramide*, a rather hydrophobic molecule which is an important component of the skin and is also involved in programmed cell death (see CHAP. 3 on page 37). A head group can be attached to ceramide, like PC, leading to *sphingomyelin* (SM) which is shown in FIG. 1.1 D.

### Glycolipids

Lipids can have in their head groups sugars of varying complexity. Such lipids are called *glycolipids* (for an example see FIG. 1.1 E). Glycolipids are usually placed asymmetrically

---

<sup>1</sup> The major polar lipids in Archaea are ether lipids of different types. Although some ether lipids are also phospholipids, in this case the alkyl chains are bound via ether linkage, instead of ester linkage as it is the case in normal phospholipids.

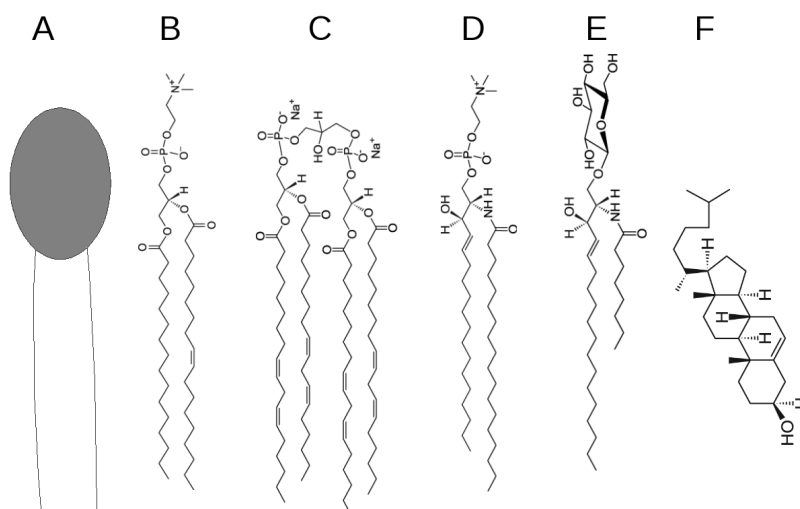


**Fig. 1.1 : Examples of lipids found in membranes.**(A) Schematic representation of a polar lipid with a hydrophilic head group and a hydrophobic tail consisting of two hydrocarbon chains. (B) Palmitoyloleoylphosphatidylcholine (POPC). (C) Cardiolipin (CL). (D) Sphingomyelin (SM). (E) A glycolipid. (F) Cholesterol (Cho). POPC and CL are particularly relevant for this Thesis. Lipid structures were downloaded from <http://avantlipids.com/>.

in the membrane, as they appear typically in the extracellular monolayer, where they may be involved in specific functions like protein sorting and cellular signaling [3].

## Sterols

Sterols are ubiquitous in the plasma membrane of eukaryotic cells, but are generally excluded from bacterial membranes. *Cholesterol* (Cho) is an abundant component in the membrane of mammalian cells, where it has an important role modulating permeability and fluidity [4]. In other types of organisms Cho is substituted by other sterols, like *ergosterol* in fungi and *sitosterol* in plants. The structure and physicochemical characteristics of Cho are quite different from those of phospholipids and sphingolipids. Its polar head is made simply of a hydroxyl group, and instead of fatty-acids Cho has a steroid ring as its hydrophobic part, with a small hydrocarbon chain at the end (FIG. 1.1 F). Hence, Cho can be defined as a lipid molecule with a bulky and stiff tail and a small head .

### 1.1.2 Self-assembly of lipids in water

The stability of the hydrogen bonding network in water makes it difficult to dissolve hydrophobic compounds into this solvent. This is referred to as the *hydrophobic effect*. Hydrophobic molecules, as well as hydrophobic parts of amphipathic molecules, cannot relate with water through dipole-dipole interactions or hydrogen bonds. This reduces

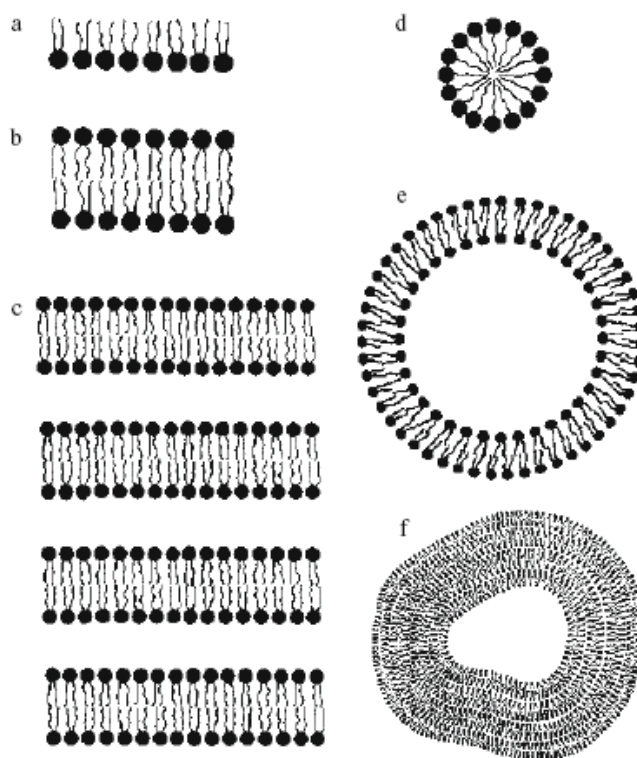


**Fig. 1.2 : Schematic illustration of supramolecular aggregates formed by the self-organization of lipids in water environments.** (a) Lipid monolayer. (b) Lipid bilayer. (c) Multi-lamellar lipid bilayers in a stack. (d) Micelle. (e) Uni-lamellar vesicle or liposome (closed lipid bilayer). (f) Multi-lamellar vesicle or liposome. With kind permission from Springer Science+Business Media: Chapter Oil and Water in Life as a matter of fat [5] ©2004.

the freedom of water in the vicinity of the hydrophobic group and decreases its entropy. Therefore the exposition of hydrocarbons to water is thermodynamically unfavorable, which forces them to group together in order to minimize their accessible surface. Hence, when lipids are placed in water, the hydrophobic effect makes sure that their oily chains are screened as much as possible from water, while the head groups keep exposed to the polar solvent. This leads to a whole family of supramolecular aggregates that are formed spontaneously. Such a *self-assembly* of lipids is a many-molecule effect as it requires that many lipid molecules act together. The family of common lipid aggregates is illustrated in FIG. 1.2. In all of them the polar head of the lipids is hydrated by water and the fatty-acid chains are screened from this solvent.

The simplest lipid aggregates in water are *micelles*, which are relatively small globular assemblies where polar groups are exposed in the surface while all acyl chains are packed and hidden in the core. Micelles are very curved structures and require that the cross sectional area of the hydrophobic tails of the lipids is smaller than that of the polar headgroups, which corresponds to a cone shape. However, most lipids have cylindrical

shapes and tend to form layer-like lamellar assemblies (SUB. 1.1.3). Lipid *monolayers* can self-organize at the air-water interface, where they form planar monomolecular films with the polar heads immersed in the water solvent and the hydrophobic tails sticking out into the air. In order to bathe completely into water, lipid *bilayers* are formed, with two lipid monolayers associated back to back and excluding water from the hydrophobic interior. To avoid the appearance of borders, which are highly unfavorable, bilayers close onto themselves forming continuous surfaces known as *liposomes* or *lipid vesicles*, which may be constituted by one (unilamellar) or several (multilamellar) bilayers (FIG. 1.2 E-F). *Unilamellar* liposomes constitute simple and useful models of cell membranes.

### 1.1.3 Lipid polymorphism

The effective shape of lipid molecules relates to their ability to form a stable bilayer. Such an effective shape depends on the compatibility between the size of the head group and the size of the hydrophobic tail which can be expressed in terms of a geometric *packing parameter*  $P \equiv V/(A * l)$ , where  $V$  is the volume of the entire lipid molecule,  $l$  is its length, and  $A$  is the area of the lipid headgroup at the lipid-water interface. Full compatibility implies an effective cylindrical form,  $P = 1$ , which is the most favorable for a stable bilayer giving rise to a lamellar arrangement. On the contrary, for non-cylindrical shapes (i.e. non-lamellar lipids with  $P > 1$  or  $P < 1$ ) the monolayers will have a tendency to elastically relax toward a state of finite curvature (FIG. 1.3), and are thus said to display *spontaneous curvature* [6, 7]. When the spontaneous curvature is different for the two monolayers, the bilayer becomes asymmetrically stressed. In such a case, and if the cohesion of the bilayer cannot sustain the curvature stress, non-lamellar structures will be forced into appearance. The variety of lipid structures with different morphology is referred to as *lipid polymorphism* [8]. Because the lipid morphology has direct implications for the curvature of monolayers, the lipids are often also said to have *intrinsic* (or *spontaneous*) *curvature*, which can affect membrane protein structure and function [9]. The specific effects of lipid spontaneous curvature on the action mechanism of pore-forming polypeptides will be reviewed in SUB. 2.2.4.

The self-assembly process of lipid molecules into aggregates of different structure involves a subtle competition between forces of different origin. Since many of those forces are of a colloidal and entropic nature, the relative stability of the resulting structures is intimately dependent on temperature, composition, and environmental conditions. In particular, incorporation of amphiphilic solutes, such as pore-forming peptides, can shift the equilibrium from one structure to another [10, 11].

In summary, the most important lesson from the observation of lipid self-assembly is that lipid aggregates and water are inextricably connected. i.e., lipid bilayers and hence biological membranes, owe their existence to water as the biological solvent. Moreover, the fact that lipid aggregates are formed and stabilized by self-assembly processes implies that they possess *self-healing* properties. If they are subject to damage, like lipidic pores, they can be repaired automatically by filling in holes and by annealing defects. As we discuss later in CHAP. 2, this has a consequence for the action mechanism of pore-forming agents, which will have to develop strategies to cope with the hydrophobic effect

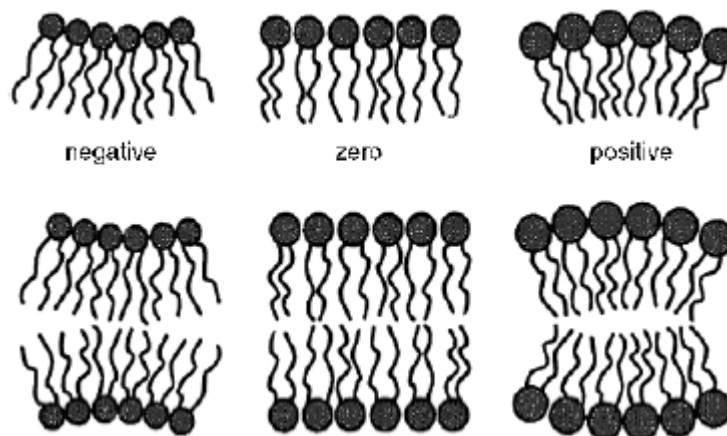


**Fig. 1.3 : Lipids speak the language of curvature.** Illustration of the destabilization of a lipid bilayer composed of lipids with conical shapes that introduce a tendency for the two monolayers to curve. With a packing parameter  $P = 1$ , planar structures having zero curvature are obtained. The intrinsic or spontaneous curvature is defined as positive for inverted cone shapes of lipids ( $P > 1$ ) and negative for normal cone shape ( $P < 1$ ). With kind permission from Springer Science+Business Media: Chapter Lipids Speak the language of curvature in *Life as a matter of fat* [5] ©2004 .

and the self-repair phenomena.

### 1.1.4 Phase transitions of lipids

The different phases available for a particular molecule, or mixture of molecules, are typically connected by *phase transitions*. Transitions that can be triggered by changes of temperature are said to be *thermotropic*. Increasing the temperature will lead to transitions towards more disordered phases.

As described in SUB. 1.1.2, lipids in water form a number of different supramolecular aggregates. Such molecular arrangements can be considered phases and states of matter. Because lipid phases depend on the degree of hydration, phase transitions between the different lipid aggregates can in many cases be triggered by changing the proportion of water in the sample under isothermal conditions. Such phase transitions are called *lyotropic*.

In addition, lipid aggregates undergo a number of *internal* phase transitions without changing morphology. At sufficiently low temperature the lipid molecules adopt a solid-like, 3D *crystalline* lamellar structure termed  $L_c$  phase (FIG. 1.4 A). In this state, the lipids show short and long range order with little translational motion, and their acyl chains adopt an extended trans conformation. Such an state is also favored at low water content. At increasing hydration and/or temperature, lipids form a *gel* phase,  $L_\beta$ , where disorder increases, specially in the acyl chain region, and molecules can rotate about their long axis (FIG. 1.4 B). At even higher temperatures, well hydrated bilayers become more fluid and form liquid crystal phases,  $L_\alpha$ , characterized by high disorder

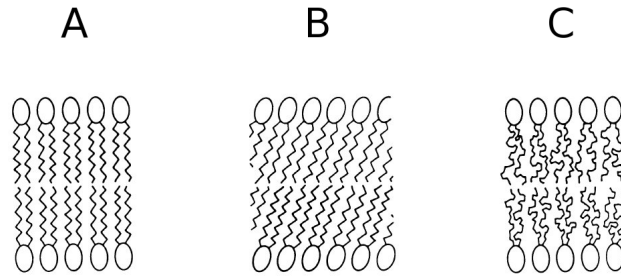


**Fig. 1.4 : Schematic view of lipid bilayer structures in various crystalline phases.** A) Crystalline lamellar structure ( $L_c$ ). B) Gel phase ( $L_\beta$ ). C) Liquid crystal or fluid lamellar phase ( $L_\alpha$ ). Reprinted from Chapter 5 Physical basis of self-organization and function of membranes: Physics of vesicles in Handbook of Biological Physics [15] ©1995 with permission from Elsevier.

(liquid-like) of the acyl chains and rapid whole-lipid translational and rotational motions, although still conserving the positional order proper of a *smectic* phase<sup>1</sup> (FIG. 1.4 C). The temperature for this latter phase transition is characteristic for each type of lipid and is usually known as the *main transition temperature* (or melting temperature,  $T_m$ ). Lipid phase transitions are known to be affected by composition. Thus, they vary for different lipid mixtures and depending on the presence of membrane bound proteins or peptides [12–14].

## 1.2 The proteic component

Proteins may associate with membranes to different extents. Membrane proteins are classified as *integral* or *peripheral*, depending on how easy they can be dissociated from the lipids. Integral membrane proteins usually span the lipid bilayer and interact extensively with its hydrophobic core. Only reagents that can compete efficiently for these nonpolar interactions, such as detergents or organic solvents, can be able to release them. In contrast, peripheral membrane proteins bind to the membrane mainly through electrostatic and hydrogen-bond interactions established with the polar head group. In this case dissociation can be accomplished by adding high salt concentrations, the presence of a denaturing agent, or pH changes. Some peripheral membrane proteins associate to the membrane through interactions with the surface of integral membrane proteins, on either the cytosolic or the extracellular side of the membrane. Others can be anchored through a covalent bond with a fatty acid, such as a palmitoyl group attached to a cysteine, or a glycosylphosphatidylinositol (GPI) group bound to the carboxyl terminus.

Membrane proteins can also be classified depending on their topology and the number of regions spanning the bilayer. *Monotopic* proteins bind strongly to the bilayer but do

<sup>1</sup> A lipid bilayer is an example of liquid crystal of the smectic type in which individual molecules have orientational order (their long axis have a preferred direction) and, in addition, they exhibit positional order since they are localized in a set of parallel planes which are separated by a fixed distance, as in a crystal. However, within each of these planes, the molecular positions are disordered, like in a two-dimensional liquid.

not span it. *Bitopic* proteins span the membrane once, and *polytopic* proteins span the membrane several times.

### 1.2.1 Protein insertion in biological membranes

The majority of membrane proteins are incorporated to the cellular membranes during their synthesis. Nascent membrane proteins of this type, as well as secreted proteins, typically contain an N-terminal *signal sequence* with hydrophobic character. As soon as the signal sequence is synthesized and exposed in the cytosol, it will be recognized by the *signal recognition particle* (SRP). Binding of the signal sequence to the SRP pauses the translation process, causing the ribosomal complex to target to the endoplasmic reticulum (ER). There, the SRP recognizes a membrane bound SRP receptor (SR), which is dynamically associated with the *translocon*. The translocon is a large protein complex in the ER membrane which is responsible for insertion and assembly of the nascent polypeptides in the bilayer [16, 17].

However, some proteins insert in the membrane after they have been synthesized and independently of the machinery of the translocon. In this case, two types of proteins can be distinguished: *amphitropic* proteins and *tail-anchored* proteins (TA). Amphitropic proteins are those whose activity is regulated by reversible membrane interaction [18]. Toxins have the built-in capacity to adopt two generally incompatible states: water-soluble and transmembrane and can thus be considered as amphitropic [19]. Similarly to amphitropic proteins, amphipathic membrane-active peptides bypass the translocon machinery and insert autonomously into lipid bilayers. On the other hand, TA proteins are integral membrane proteins that span the lipidic bilayer through a single hydrophobic domain located in the C-terminal region, while the remaining polypeptide chain is folded into a soluble domain oriented to the cytosol [20]. Some proteins of the Bcl-2 family, which is the subject of this Thesis (discussed in SUB. 3.2.1), regulate apoptosis after translocating from the cytosol to mitochondrial membranes, and can thus be considered amphitropic. Other Bcl-2 proteins are constitutively anchored to intracellular membranes and thus belong to the TA category (SUB. 3.2.1).

### 1.2.2 Structure and folding of membrane proteins

The lipid bilayer provides a complex environment where membrane proteins can acquire their active conformation. Membrane proteins usually aggregate in aqueous environments, thus making difficult the processes of purification and handling. This has been so far the major handicap for the structural studies of membrane proteins and the main reason for the slower progress in this field, compared to water soluble proteins (see also SEC. 5.2). As of December 2010 there are ~714 high resolution structures solved of membrane proteins<sup>1</sup>. Among them, only ~219 are unique, including proteins of the same type from different species. This number represents a very small fraction of the

---

<sup>1</sup> According to the following membrane protein databases: <http://blanco.biomol.uci.edu/> and <http://www.mpd.b.tcd.ie/>





measurements [27, 28]. Although there are up to 7 residues in the putative dimerization sequence of glycoporphin A [29], the core *minimal* sequence comprises Gly residues spaced four amino acids apart, and is thus designated GxxxG or GG4. Importantly, the Gly residues can be substituted by Ala and Ser without large effects in the dimerization propensity [30, 31]. It is interesting to notice that such *Small-xxx-Small* motifs can be found also in packing  $\alpha$ -helical segments of other TM proteins [32–34] and in many water-soluble proteins [35], both for intra- and inter-molecular dimeric and trimeric interactions. Thus, it may be considered a “universal” helix-packing motif with an intrinsic “stickiness”<sup>1</sup>, suitable for the tight association of hydrophobic and amphipathic helices, within the core of hydrosoluble proteins and for protein fragments crossing the membrane.

On the other hand,  $GAS_{Left}$  motifs have been found for instance in the  $\zeta\zeta$ -T cell receptor [38]. These left-handed-parallel helix packing motifs bear similarities with water-soluble coiled coils, showing a crossing angle of  $\sim 20^\circ$  and a consensus sequence displaying Gly (replaceable by Ala and Ser) at position “a” of the heptad repeat Gxxxxxx [38].

For both,  $GAS_{Right}$  and  $GAS_{Left}$  motifs, a close packing of helices facilitates stabilization through van der Waals interactions. An uncommon type of hydrogen bonding, involving  $C^\alpha H$  groups as donors and amide carbonyl groups of peptide bonds as acceptors, has also been described [39]. Additionally, hydrogen bonding between appropriate polar side-chains, the so-called *polar motifs*, can also play an important role in the stabilization of helix-helix associations [40, 41]. On the other hand, despite the similarities in the helix-helix interaction motifs of water-soluble and TM proteins, the energetic basis for the oligomerization in each of these cases seems to be quite different. For water-soluble helical bundles, the driving force for association derives mainly from the *hydrophobic effect* (SUB. 1.1.2), i.e. the solvent entropy contribution that pushes hydrophobic residues to be hidden from the aqueous environment [42, 43]. However, for TM helical bundles, placed within the membrane core, the opposite force i.e. the *lipophobic effect* or screening of polar groups from the hydrophobic acyl chains of lipids, seems a weakly specific contribution [44]. In membranes, the main contributions arise from side-chain rotamer entropy, van der Waals contacts, steric clashes and polar interactions [45]. TM helices have also been reported to have an intrinsic potential to form antiparallel dimers [46, 47]. The reason for that is the  $\alpha$ -helix macrodipole which associates favorably the C-terminus of one helix, with excess of negative charge, with the N-terminus of a partner helix, with defect negative charge, thus facilitating unspecific, sequence-independent, electrostatic interactions in antiparallel fashion.

Finally, the hybrid nature of amphipathic helices and the heterogeneity of the environment where they reside, raises the question of which forces play a leading role. In water soluble proteins, such amphipathic segments form water-exposed parts which pack their hydrophobic side toward the protein core, so that the balance of interactions will in principle depend on the balance of water-exposed against water-occluded area. In membrane proteins, amphipathic parts may be in water exposed domains, and will then be similar to the case of water soluble proteins, or may be associated with membrane

<sup>1</sup> In most cases, only one of the interacting helices need to have the small-xxx-small motif [26, 36, 37]

interfaces. They may also form the wall of membrane spanning pores or channels. For either of the two latter cases, the characteristics of helix-helix association have not been investigated in detail. The formation of homo- and hetero-dimers involving the  $\alpha 5$  fragment of Bax, the study of which is one of the objectives of this Thesis, connects directly with this problem (see CHAP. 8).

### 1.3 Reductionism for studying biomembranes

#### 1.3.1 Peptides as models for studying membrane proteins

As already mentioned, membrane proteins are usually both difficult to obtain in sufficient amounts for structural/functional studies and difficult to reconstitute in a functional form. An increasingly recognized strategy to circumvent these difficulties is studying their membrane-interacting regions [48, 49]. These sequences are in general short enough to be chemically obtained in a peptide synthesizer although due to their hydrophobicity special care must be taken during the synthesis and purification steps (SUB. 5.1.2). A plethora of unnatural amino acids can be easily introduced with high yields in order to obtain valuable information about the peptide structure, dynamics and activity. Such a site-specific peptide labeling and engineering capacity is usually not attainable with conventional protein expression methods. For example amino acids labeled with the infrared-sensitive probe  $1\text{-}^{13}\text{C}=^{18}\text{O}$  can be incorporated at almost any desired position in the peptide sequence to study its orientation relative to the bilayer. In general, membrane-interacting peptides are able to fold and function independently of the rest of the parent full-length protein and as a consequence they can be regarded as true domains [50].

#### 1.3.2 Model membranes

The complexity of isolating and measuring biological membranes has led to the use of model membrane systems mimicking at least partially the properties of biomembranes. Such models include the family of lipid aggregates discussed in SUB. 1.1.2: micelles, monolayers and lipid vesicles or liposomes of different sizes and lamellarities. Importantly, their composition can be easily varied and their phase properties can be controlled through changes in the temperature and water content. Except for lipid monolayers all these lipid assemblies are used in this Thesis. The preparation of such model membrane systems is described in SUB. 5.1.1.

### 1.4 Models of biomembrane organization

In 1972 SINGER and NICOLSON proposed the *fluid mosaic* model to explain membrane structure [51], and this has since constituted a central paradigm in membrane science. The simple, yet powerful, conceptual framework that it provided continues to have an enormous impact on the field of biomembranes. *Fluidity* was a key property of the SINGER-NICOLSON model, which was meant to characterize the lipid bilayer as a kind of

pseudo two-dimensional liquid in which both lipids and membrane-associated proteins display lateral mobility. The overall random appearance of this lipid-protein fluid composite made the membrane look like a *mosaic*. In summary this model conceives that “proteins float in a fluid sea of lipids” [51]. The notion of membrane fluidity emphasized the dynamic character of membranes, but unfortunately it was assumed that fluidity implies randomness. However, from a wealth of new experimental results it is now recognized that far from being random, the lateral distribution of molecular components in membranes is heterogeneous, both statistically and dynamically, corresponding to an organization into compositionally distinct *domains*, *rafts* and *compartments* [52, 53].

An alternative view regards biomembranes as *supra-molecular complexes* where both lipids and proteins determine the structure, dynamics and physicochemical properties necessary for their function [54]. The lipids impose liquid-crystal order within the membrane complex, including embedded proteins or peptides, and may affect their structure, orientation, dynamics and aggregation state [55–57]. The bound polypeptides, in turn, change the composition and the physicochemical context of the membrane where they are hosted and can end up affecting its molecular organization [12, 58]. Such bilayer perturbations or deformations, which can also be related to the membrane material properties, are important to define the stability and functional structure of the polypeptide-bilayer complex [59, 60]. Thus, many dynamic processes occurring in biological membranes result from the mutual adaptation between lipids and polypeptides. Pore formation is an example of such processes (explained in detail in CHAP. 2 from a global perspective and in CHAP. 3 for the specific case of pores involved in apoptotic cell death).

## 1.5 Summary of the state-of-the-art

1. Phospholipids in general and phosphatidylcholines in particular are the most abundant lipids found in natural membranes. Specific membranes contain particular phospholipids. Of particular relevance for this Thesis is CL which is found in the MIM.
2. A lipid bilayer with a hydrophobic core and a hydrophilic interface is the most simple model of a biological membrane. Amphipathic lipids assemble spontaneously in water, due to the hydrophobic effect, giving rise to different structures (micelles, lipid vesicles, etc) depending on their intrinsic curvature.
3. Biomembranes contain also embedded proteins which can be dissected into its constituent membrane-interacting peptides. Membrane proteins contain a high ratio of hydrophobic residues, fold into  $\alpha$ -helices or  $\beta$ -sheets, which arrange into bundles and barrels respectively, and associate through interactions involving mostly van der Waals-based packing motifs.
4. Biomembranes can be viewed as supramolecular protein-lipid complexes where both proteins and lipids contribute to their structure, dynamics and function.

*1 Biological membranes*

## 2 Pores in Membranes

In the functional studies of biomolecules, proteins and peptides (polypeptides in general) take usually the starring role. This is due to various reasons, like the wide range of properties encoded by the side-chains of amino acid residues, which gives polypeptides an extraordinary potential for structure and function, and the direct link between the polypeptide sequence and genetic information. In the case of biological membranes, polypeptides occupy also a predominant position in terms of function. Thus lipids (or the lipid bilayer) are generally relegated to a secondary role or merely considered as a *solvent*. Much of this conception connects to the predominant view after SINGER & NICOLSON's *fluid mosaic* model [51], where the lipidic part of the membrane is depicted as a two-dimensional liquid. An alternative view, however, regards biological membranes as dynamic supramolecular complexes, where lipids are active components even in functions usually assigned to proteins.

Following SCHWARZ we define a *pore* as any local membrane perturbation that allows the passive flow of ions or molecules up to a certain size [61]. Importantly, this does not assume any special arrangement of molecules, i.e. regular and ordered structures as well as disorganized (membrane defects) structures fit with the definition. For the pore forming function assigned to amphipathic peptides, the lipids put also their peculiar physicochemical characteristics into action. We will first discuss that, from the point of view of peptides, pores are weakly specific phenomena, loosely codified at the level of sequence. We will then see that pores are natural phenomena in lipid membranes, where they may exist even in the absence of proteins or peptides. We believe that this lipo-centric view is useful and complementary to the usual peptido/proteo-centric perspectives and helps understanding critical aspects of pore formation, structure and stability. We argue that purely lipidic pores and peptide induced pores are mechanistically related, and similar arguments may indeed be extended to protein induced pores.

### 2.1 The (w)hole story: ways of crossing the membrane

Different protein and peptide molecules are known to transport ions, molecules or even themselves across the membrane via pore formation. Thus, there is a number of cases where pores are formed at some stage, although not always being stable, functional or final structures. The large number and diversity of polypeptide molecules exhibiting similar pore activities over multiple types of membranes shows that it is a weakly specific phenomenon, loosely codified at the level of the primary structure. In fact, structure-function relationships in these cases appear to follow special rules, based on *interfacial activity* and modulated by physicochemical balances of properties like hydrophobicity and amphipathicity [62, 63]. In an attempt to make our discussion as general as possible

we are going to describe now these type of peptides/proteins and we will show how all of them are intimately related.

### 2.1.1 Pore-forming toxins

Pore-forming toxins (PFTs) are one of Nature's most potent biological weapons that function as part of the defense and attack mechanisms of cells by way of increasing the permeability of membranes. Notice that from all known protein toxins, at least a third of them act by disrupting membranes. They can be classified according to the prevalence of  $\alpha$ -helical or  $\beta$ -sheet secondary structure elements into  $\alpha$ - and  $\beta$ -PFTs. Thus, despite their low sequence similarity their active membrane-bound conformations usually display similar structural motifs: a bundle of  $\alpha$ -helices or a  $\beta$ -barrel. Some examples include colicins, equinatoxins and Cho-dependent cytolysins (CDC). Proteins of the Bcl-2 family, which function as regulators of apoptosis (CHAP. 3) are also structurally and mechanistically related to PFTs.

### 2.1.2 Antimicrobial peptides

Membrane active antimicrobial peptides (AMP) are able to kill bacteria thanks to their ability to perturb the membrane integrity via pore formation. They tend to be short and highly cationic, binding readily to lipid membranes and usually folding as an amphipathic  $\alpha$ -helix. The two most well studied AMP are melittin and magainin-2. Since pores can be induced or enhanced by both *AMP and PFT*, hereafter they are named collectively *pore-forming polypeptides* (PFPPs) and will be described extensively in SEC. 2.2 with an special emphasis on the role of lipids.

### 2.1.3 Cell-penetrating peptides

Cell-penetrating peptides (CPP) are able to translocate themselves, as well as cargo molecules as big as proteins and DNA, across the membrane [64]. Although the exact mechanism that they follow is not completely understood, it is likely to involve a transient pore, i.e., a pore with a very short lifetime. This would explain why there is no, or incomplete, leakage of dyes initially encapsulated into vesicles. Very recently, ALMEIDA proposed that whether a peptide will form long-lived pores (the so-called "all-or-none" mechanism) or short-lived pores (the so-called "graded" mechanism) depends on its free energy of insertion into the bilayer core [65]. Indeed, it is possible to switch from long-lived to short-lived pores by point mutations as demonstrated with magainin where the introduction of an additional charged residue drastically reduced the lifetime of the induced pores [66]. The control of pore lifetime is of fundamental biotechnological importance since it could allow the "silent" incorporation of molecules into cells.

### 2.1.4 Fusion proteins

Membrane fusion constitutes a pivotal process in eukaryotic cell physiology. Both specialized proteins and membrane lipids play key roles in fusion. Recent observations sug-

gest that viral fusion proteins use packed conformational energy and bilayer-destabilizing domains to (i) bring participating membranes into intimate contact, (ii) merge proximal lipid monolayers through highly curved stalk/hemifusion intermediates, and (iii) generate a lipid-containing fusion pore, thereby terminating the fusion process [67]. However, fusion proteins and peptides thereof are also able to cause leakage of encapsulated dyes [68]. On the other hand, PFPPs are also known to enhance fusion rates.

### 2.1.5 Membrane channels

Channels are transmembrane proteins controlling the influx and outflux of materials across cellular membranes. They usually exhibit high selectivity, combined with high conductivity, and gating that is sensitive to essential environmental factors. Although channels furnish optimal performance, they do not use energy to advance motion across a membrane since that occurs *downhill* in the electrochemical gradient. Membrane channels typically transport small molecules, like ions (e.g potassium channels) or water (e.g aquaporins). Therefore *channels* can be considered as a special type of pores which are distinguished by their selectivity for particular ions/molecules and their ability to gate (i.e. open and close) in response to ligands or voltage.

Since ion channel recording may be equally applied to PFPPs as well, it is difficult to trace a clear separation line between membrane channels and PFPPs with electrophysiological measurements only. However, while all PFPPs will display ion channel activity, the opposite is not necessarily true. PFPPs are usually not (or weakly) selective and they would transport anything across the membrane as long as it is smaller than the pore size. As a matter of fact, pore forming peptides are believed to form transient pores (that would behave like ion channels allowing the passage of ions but not larger molecules) at very low concentrations through which they can translocate across the bilayer, while at higher concentrations they would form “true” pores [69].

### 2.1.6 Carriers and transporters

In contrast to membrane channels that provide a passive permeation pathway for their substrates, transport in membrane transporters is mediated by close interaction and engagement of the protein and the substrate. This is necessary owing to the active (energy-dependent) nature of the transport process, during which the energy provided by various sources, for example, ATP hydrolysis or an ionic gradient across the membrane, is used to actively *pump* the substrate across the membrane against its electrochemical gradient. Membrane transporters are structurally much more diverse than membrane channels, as they need to harvest various sources of energy in the cell and efficiently couple them to substrate transport. Interestingly, mutations in these proteins may alter their transport selectivity transforming them into “true” pore-forming proteins. In this sense, a pore allows the passage of anything that fits into it: the size-discrimination or molecular sieve effect is generally the only limiting factor. For instance, the mitochondrial ADP/ATP carrier can switch from a vital function (stoichiometric ADP/ATP exchange on MIM) to a lethal one, corresponding to its pore-forming activity [70]. Another example is

the uncoupling protein from brown fat which can be converted from a carrier into an unspecific pore by a small deletion [71].

### 2.2 A lipocentric view to pores induced by peptides and proteins

Although with a very low probability, or associated with stress conditions pores can exist in lipid membranes in the absence of peptides or proteins [72–75]. It is thus natural to relate polypeptide induced pores and tension-induced lipidic pores as closely connected phenomena [76]. Even for the cases where polypeptides are clear protagonists, lipids are more than just a passive barrier transversed by the pore [58, 77, 78]. However, the mechanisms and structures associated to pore formation have most often been studied using peptidocentric or proteocentric views. Pores can be induced or enhanced by *pore-forming polypeptides* (PFPPs). Whenever possible, we will use a general, integrated view for these two types of molecules, supported among other things by the fact that the essentials of the membrane activity of pore-forming proteins can be reproduced by individual peptide fragments [50, 79, 80]. We will extract the main consensus ideas of previous models by MATSUZAKI, HUANG and SHAI [81], complemented with recent interpretations from molecular dynamics simulations (MD) [82, 83], kinetics and single-vesicle studies [69, 84–86].

The complete pathway of a PFPP towards the “pore state” involves at least three steps: membrane binding, structure rearrangement and pore formation itself. Therefore, the role of lipids can be envisioned at three different levels.

1. First, lipids can be regarded as dynamic docking surfaces for the binding of PFPPs to membrane from the external water milieu.
2. Second, the lipids may condition the structure adopted by PFPPs upon membrane binding. Additionally, lipids may influence association between membrane-bound PFPPs.
3. And third, lipids can participate in the molecular reorganization of the polypeptide-membrane complex, to end up with the formation of a pore.

Depending of the particular mechanism and the type of pore structure which is finally formed, the lipids can be more or less directly involved. For example, lipids play a very direct role for the so called toroidal pores [87, 88], where they form part of the pore wall. Once pores are induced, the lipids may exert a further active role cooperating with polypeptides in the stabilization of the pore [76]. We should bear in mind that the first three steps (binding, folding and association) apply in general to any membrane peptide/protein. The fourth step, pore-formation is, however, specific to PFPPs and related polypeptides. As we have just seen, fusion peptides may induce vesicle perturbations defined as pore-like structures [68, 89, 90]; it is also known that cargo peptides work through transient transmembrane pores [91, 92].

### 2.2.1 Lipids as receptors for pore-forming polypeptides

Most natural and synthetic pore-forming peptides as well as membrane-active parts of pore-forming proteins are composed of hydrophobic and hydrophilic residues which arrange into amphipathic structures [81, 93]. The lipid bilayer interface provides an optimal region where physicochemical properties complement the amphipathicity of PFPPs for an effective binding (FIG. 2.1) [24, 94–97]. The charged and polar residues will prefer to reside in the hydrated headgroup region, where they may participate in a variety of stabilizing electrostatic forces [95, 98]. With most PFPPs being cationic, the positively charged residues (of Lys and Arg residues) interact closely with the phosphate group of phospholipids [58, 99–101]. This binding mode allows simultaneous immersion of the hydrophobic side-chains into the membrane hydrophobic core, facilitated by the fact the charges in Lys and Arg are at the end of long and flexible aliphatic chains and can thus snorkel toward the interface from relatively deep positions [99]. For amphipathic  $\alpha$ -helices, the binding depth is expected to depend on the helix polar angle, which determines the size of the hydrophobic sector of the helix relative to the polar sector [93, 102]. Such an adaptation of amphipathic polypeptides for binding at membrane interfaces has been termed partition-folding coupling [94] and is explained with more detail in the next section. It implies that the stability of the membrane-polypeptide complex increases as the secondary structure is formed, as it is indeed observed for a number of different systems [94, 95, 103–106]. Thus, phospholipid membrane interfaces can be envisioned as ideal binding sites for docking amphipathic PFPPs (see FIG. 2.2) [24, 95]. Supporting a direct targeting role of phospholipid membranes, with no intervention of receptor proteins, are the facts that PFPPs are active against pure lipid vesicle and at least in the case of the peptides, independent of chirality (all D-amino acid peptides are as active as natural L-amino acid versions) [107].

One consequence of the direct lipid-based membrane targeting is a relatively low specificity. For example, scrambled sequences of pore forming peptides tend to have similar activity [62, 108], and in general hundreds of different peptides and proteins, differing in size, secondary, tertiary and quaternary structure, share a similar model of binding [81, 109–111]. Moreover, the similarity extends outside the PFPPs to cell penetrating peptides [112, 113], fusion peptides [68] and with striking relationships to membrane active proteins of different types and across disparate organisms [110]. Nevertheless, lipid-based targeting can be also the source of complex binding schemes, including high affinity, cooperativity and lipid-dependent protein assembly [114, 115]. The general non specific interfacial binding can in some cases superimpose to additional interactions with a different degree of specificity, from electrostatic effects, to sophisticated and efficient control mechanisms through specific interactions with receptor lipids or lipid-anchored proteins.

**General effects of negatively charged lipids.** Because most PFPPs are cationic, a way to increase their binding from solution is by presence of negatively charged lipids. In neutral membranes, binding of PFPPs depends mainly on their hydrophobicity, which accentuates the importance of structural parameters like hydrophobic moment and he-

## 2 Pores in Membranes

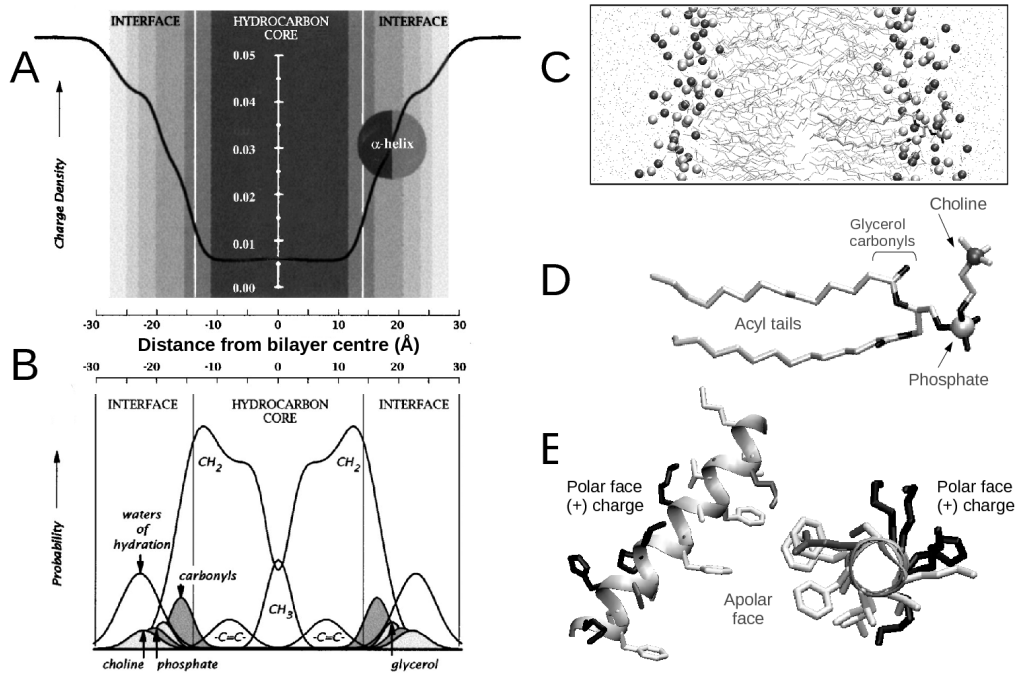


**Fig. 2.1 : The membrane as a docking surface.** A and B show representations of the polarity gradient and structure, respectively, of a fluid liquid-crystalline bilayer. The interfaces are the regions defined by the distribution of head group's water of hydration and the hydrocarbon core is the center slab where the presence of water drops to zero. The experimental membrane structure can be appropriately modeled at atomic detail by MD simulations, as is shown in C for a simulated self-assembled dimiristoylphosphatidylcholine (DMPC) bilayer. A DMPC lipid highlighted in C with thick lines is shown enlarged in more detail in D. In E we represent lateral and top views (left and right, respectively) of the amphipathic  $\alpha$ -helix structure of magainin, solved in detergent micelles (PDB:2MAG). Panels A and B are reprinted with permission from the Annual Review of Biophysics, Volume 28 [24], © 1999 by Annual Reviews, www.annualreviews.org.

licity [93]. Partitioning of cationic peptides into zwitterionic lipids is generally weak. However, the presence of negatively charged lipids, like those with PG, PS and PI head groups, pose an electrostatic attraction over the peptides which increases the strength of their binding. A careful kinetic analysis shows that the stronger binding of cecropin and magainin to acidic lipids is due mainly to a reduced desorption rate [84, 116]. It is also seen that the main contribution of electrostatic interactions is increasing the concentration of interfacially adsorbed peptides. Thus, discounting this effect on the basis of GOUY-CHAPMAN theory [117] i.e. replacing bulk concentrations by surface concentrations, yields similar binding constants and pore activities regardless of the membrane surface-charge density [86, 103, 118, 119].

The electrostatic contribution is the main basis for the selective binding of peptide antimicrobials to bacteria [81], since the outer membrane of these microorganisms is abundant in negatively charged lipids, in contrast to the plasma membrane of eukaryotic cells, abundant in neutral lipids [120]. However, this alone cannot explain the selective killing of peptide antibiotics against bacteria, compared to host cells. Such a selectivity can be understood considering the characteristic strong membrane-mediated cooperativity of these systems, observed as a nonlinear concentration dependence with a rapid rise of activity when a threshold concentration value is passed [114]. Thus, the different affinity for neutral compared to acidic membranes places normal extracellular peptide concentrations well above the threshold for bacteria, but below the threshold for eukaryotic cells. The cooperativity originates from the effect of peptide binding on the bilayer material properties and is discussed in SEC. 2.2.4 with more detail in connection to the mechanism of pore formation [114, 121]. An additional factor explaining cell-type selectivity of antimicrobial peptides is the presence of Cho in eukaryotic cells, which in general reduces peptide and protein binding to the membrane but it has effects also at other levels. For example it affects the oligomeric assembly of PFPPs, their membrane insertion pattern and their pore activity [121–123].

A preferential binding to negatively charged membranes is also observed for some pore forming colicins [124] and for active fragments of the Bcl-2 family [50]. However, in these cases, electrostatic attraction may have also an inhibitory effect on activity, since the strong interfacial binding appears to hinder pore formation. In addition, it is not always easy to separate the effects arising from the electrostatic properties of lipids from those deriving from other physical properties, like intrinsic curvature [125].

### 2.2.2 Lipids as chaperones for pore-forming polypeptides

PFPPs can be found in alternative water soluble and membrane bound species with different corresponding structures (FIG. 2.2). Because their function is performed in the membrane, the change of structure associated to membrane binding is an important step for their activation. The question of how membrane-mediated activation takes place is connected to the more general question of how the water solvent influences protein folding [24]. Pore-forming peptides change from an unfolded state in the high dielectric medium to an organized structure, in most cases  $\alpha$ -helical, in the more hydrophobic membrane environment. Pore-forming proteins have globular compact structures in wa-

ter, which largely reorganize in the membrane-bound state. In both cases the structural re-adaptation follows a multi-step process which typically involves deeper insertion in the membrane and in some instances membrane oligomerization. Interestingly, most of these secondary, tertiary and quaternary structural changes occur spontaneously upon membrane binding without the aid of extra proteins. Thus, this role of the lipid membrane in promoting polypeptide activation through a control of their folding can be described as a chaperon-like foldase activity. How these conformational changes take place can be very different depending on the case, especially for the pore forming proteins [126].

**Structure remodeling at the membrane interface.** As we have discussed in SEC. 2.2.1, the membrane interface is the receiving surface for PFPPs reaching the lipid bilayer. This chemically heterogeneous region, where physicochemical properties vary dramatically with depth (FIG. 2.1), is ideal for stabilizing polypeptides in different conformations and thus facilitating their molecular re-adaptation. Because partitioning of free backbone-peptide groups to this environment is very unfavorable, compared to H-bonded groups, there is a strong tendency to form secondary structures [24, 96, 127]. Moreover, folding is accompanied by the accentuation of amphipathicity, which then increases the stability of the polypeptide in the interface and, following the hydrophobic gradient, favors a deeper binding [95, 103]. The membrane-dependent coil-to-helix transition of peptides has been described as *partitioning-folding coupling* (FIG. 2.2 A) [24]. It has been characterized experimentally [103, 128, 129] and also studied in detail by MD simulations [100, 101, 130, 131]. Membrane-induced  $\alpha$ -helix formation is exothermic and energetically favorable, with reported free energy changes for folding in the range of -0.14 to -0.4 kcal/mol per amino acid residue [96, 103, 118, 128]. Although with more modest thermodynamic consequences,  $\beta$ -structure is also favored by membranes [96, 105, 127, 132, 133]. Thus, for pore-forming peptides, interfacial binding involves a large increase of their secondary structure with respect to their state in water where they are largely unfolded [93, 103, 104, 118, 119, 134–136]. Nevertheless, MD simulations of pores formed by magainin and melittin suggest that well structured  $\alpha$ -helices are not a prerequisite for pore formation [82, 83]. In line with that conclusion a D-amino acid synthetic analog of melittin, having predominant  $\beta$ -structure, has been found to be active, although membrane binding in this case is largely decreased compared to that of the native  $\alpha$ -helix peptide [103].

Pore-forming proteins also reorganize their structure due to membrane binding, which we can name *partitioning-refolding* (FIG. 2.2 B) since they already possess a stable fold in the aqueous environment. For  $\alpha$ -pore forming proteins such a structural reorganization is in some cases preceded by a pH-dependent molten-globule intermediate [137] and may include the detachment of a single preformed  $\alpha$ -helix from the protein core, a general increase of the proportion and average length of various  $\alpha$ -helices (case of colicin E1 channel domain) [138] and several pH-dependent refolding states (case of Diphtheria toxin T-domain) [106, 139].

Another important characteristic of the membrane interface is anisotropy, which constrains the possible molecular organizations in the membrane complex to a small num-

## 2.2 A lipocentric view to pores induced by peptides and proteins

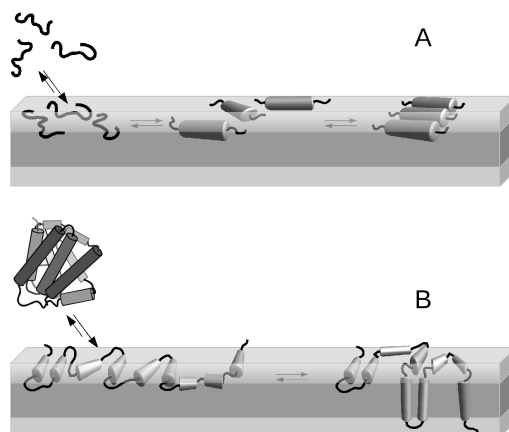


**Fig. 2.2 : Chaperon-like foldase activity of membranes.** Lipid membranes control refolding of polypeptides partitioning into them. A) Partitioning-folding coupling of amphipathic peptides at the membrane interface. The peptides are mostly unstructured in water. Immediately after binding to the membrane surface, the interface promotes the appearance of secondary structure. B) Partitioning-refolding of globular water-soluble pore-forming proteins as they bind to the membrane. The structure change can be dramatic upon adsorbing into the interface like in the case of  $\alpha$ -helix bundle proteins. In both cases successive molecular reorganizations give rise to transmembrane pores (not shown), which depending on the case may also involve protein oligomerization.

ber. This selects a flat arrangement of amphipathic polypeptides, with the main axis of peptide segments running near parallel to the membrane plane in such a way that the hydrophobic face is immersed into the hydrocarbon tail slab while the hydrophilic face resides in the hydrated head group region. This is the configuration most often found experimentally for pore-forming peptides [140]. In these cases, changes into a perpendicular alignment have been seen accompanying pore formation over a threshold peptide concentration [141] (see SEC. 2.2.3) or associated to a change of phase of the lipids [142]. For helix-bundle  $\alpha$ -pore forming proteins, this corresponds to extended two-dimensional arrays of helices, which have been characterized as membrane-dependent refolding intermediates for some colicins [138, 143, 144] and members of the Bcl-2 family [145–147].

**The lipid membrane controls inter-protein interactions.** As another way to reshape peptides and proteins, membrane interfaces can promote protein-protein homo-associations. Oligomerization is in many cases a characteristic step for the activation of PFPPs. However, with a few exceptions, the water soluble states are monomeric and oligomers form prepore structures which are strictly dependent on membrane binding [148]. In general the membrane controls oligomerization at the level of protein or peptide folding, by reconfiguring the structure to shape the binding sites and/or by making such binding sites accessible. In the case of pore forming peptides the presence and possible role of oligomers is not always clear. In MD simulations of pore formation by magainin and melittin the appearance of interfacially adsorbed aggregates is a prerequisite for pore induction [82, 83]. A characteristic endothermic step in the calorimetric titration of

melittin has been assigned as a reversible peptide aggregation (coupled to pore formation), occurring after membrane binding and  $\alpha$ -helix formation [103]. In that study, peptide aggregation is described with a phase diagram depending on the total peptide and lipid concentrations, with three phases corresponding to monomers, aggregates and coexistence of monomers and aggregates and phase boundaries defined by threshold values of the peptide-to-lipid molar fractions (P/L). Such boundaries correspond to the threshold peptide-to-lipid mole fraction (P/L\*) in the two-state model of HUANG and colleagues [141], which has been recently reformulated also as a two-phase model [114].

Another powerful mechanism for promoting inter-protein oligomerization is by two-dimensional clustering [149]. Some toxins bind selectively to lipid rafts, which may act as protein concentration platforms and enhance oligomeric assembly. Reduction of dimensionality, as corresponding to binding to a two dimensional membrane surface, can lead to an effective increase of concentration by a factor of about  $10^3$ . Additionally, recruitment of proteins into membrane microdomains can largely increment the concentration factor. This has been described for aerolysin, whose GPI-anchored receptor associates transiently with lipid rafts, and can also be the case for other toxins which bind to SM-Cho microdomains, like CDCs and actinoporins among others.

### 2.2.3 Lipids as protagonists in the formation and stabilization of pores

**The latent membrane pores: relatives of pores induce by polypeptides?** Although rare, spontaneous pores are inherent to lipid bilayer membranes. They occur independently of the presence of peptides or proteins, although with very low frequency. In pure lipid membranes pore formation is kinetically hindered by a large energy barrier, which cannot be easily overcome by thermal energy (FIG. 2.3) [73–75, 150–155]. However, thermal fluctuations of the bilayer lipids gives a chance for stochastic disruptions of the equilibrium bilayer structure, explaining, among other things, the spontaneous formation of pores [73, 126, 150]. For example, the transbilayer movement of lipids, known as *flip-flop*, which in cell membranes is accelerated by a number of specialized catalytic proteins [156], can occur in pure lipid vesicles in time scales from hours to days, depending on the type of lipids and experimental conditions [157–160]. Such unassisted flip-flop has been proposed to be mediated by lipid-packing defects [159, 161]. MD simulations have shown recently that this process may occur via transient water-pores (FIG. 2.3 A) which allow passage of the hydrated charged groups of the lipids across the membrane hydrophobic slab [75]. The pores are structurally similar to the ones simulated under mechanical and electrical stress (FIG. 2.3 B) [74, 151], a type of bilayer disruption which is well known experimentally [72, 73, 162, 163]. These flip-flop coupled pores might also be responsible for the passive ion permeation through membranes, although they represent a negligible contribution to water permeation [75].

The background spontaneous flip-flop and pore formation can be largely affected by the phase state and composition of the membrane. For example, the passive permeability of lipid bilayers exhibits a maximum at conditions of coexistence of gel domains and fluid domains [159, 164, 165]. On the other hand, the presence of Cho increases the free energy barrier for water pore formation [53, 166] and on the contrary, the presence

## 2.2 A lipocentric view to pores induced by peptides and proteins

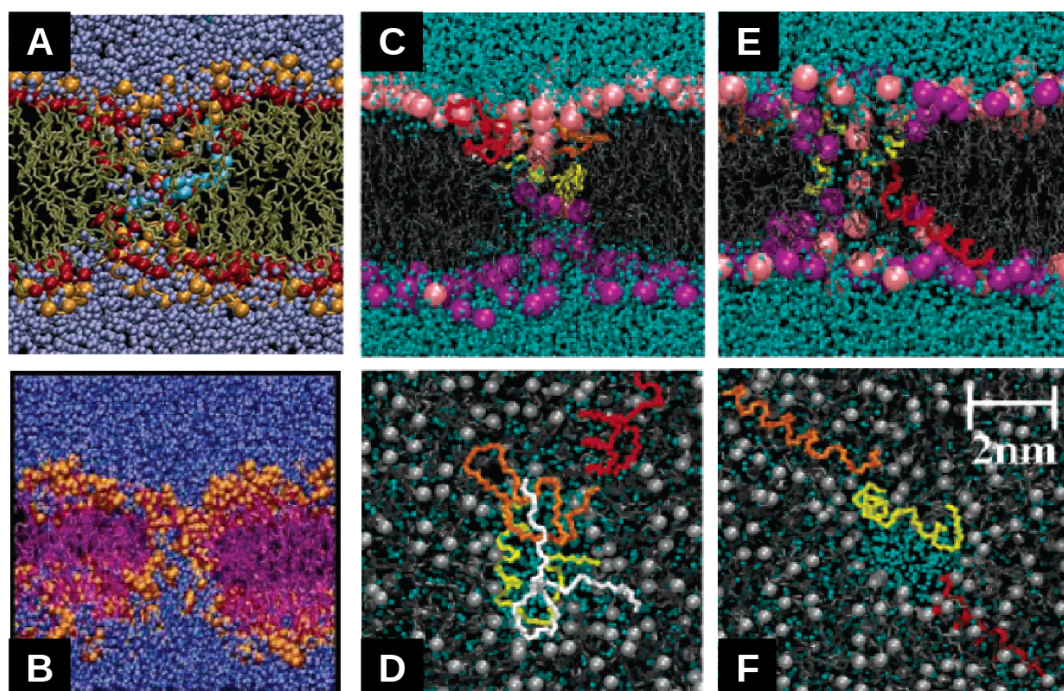


**Fig. 2.3 : Comparison of flip-flop assisting, stress induced and peptide induced pores.** All structure models are from MD simulations. Flip-flop assisting pores (A) are transient water-permeable defects which form as the charged groups of a phospholipid traverse the low dielectric membrane interior. Similar structures can be seen in pores induced by electrical stress, shown in panel B. Lipidic pores are also observed in simulations of membranes containing magainin peptides, when they are placed either initially near the membrane in the bulk water (C, top view in D) or self-assembled with the lipids from initial random configurations (E, top view in F). These peptide induced pores are largely disorganized, with variable positions of the peptides with respect to the rim of the pore. Figures reprinted from the *Journal of the American Chemical Society*, Volume 128 (A, [75]; C-F, [82]), © 2006 and Volume 125 (B, [74]), © 2003 with permission from the American Chemical Society.

of ceramide facilitates flip-flop and the formation of large and stable lipidic channels [167–171]. Including proteins in the membrane composition has also been observed to affect lipid flip-flop, like in presence of  $\alpha$ -helical proteins, in principle not related to pore formation, from the plasma membrane of bacteria [172]. This latter effect appears weakly specific, since it is also found for other polypeptides, like glycophorin and synthetic model transmembrane peptides [172, 173]. It has been speculated that this type of protein-facilitated flip-flop is due to a much lower barrier for defect (water-pore) formation as a consequence of the protein-membrane interaction [75]. Induction of lipid flip-flop is also a common phenomenon associated to the activity of many PFPPs [87, 174–177]. The large increase of transbilayer movement observed in these cases is often explained as due to lateral diffusion of lipids at points of monolayer fusion existing at the edge of the pore and it is one of the preferred test to distinguish different types of pores [175–178]. Additionally, similar to intrinsic lipid flip-flop, pore formation by peptides and proteins is in many cases described as a stochastic process related to membrane disruption and nucleation of defects [69, 82, 85, 116, 179].

The basic action of specialized pore-forming peptides and proteins may then overlap with the intrinsic pore-formation capacity of membranes. A number of specific examples support this idea. Osmotic tension and class L amphipathic peptides act synergistically as they induce pores in vesicles [180]. The general attenuation of membrane permeability exerted by Cho affects also the activity of pore forming peptides [121, 123]. In some cases pore formation is favored by defect-rich domain boundaries [179] and at the phase transition temperature [181]. The lipopeptide syringomycin E, which forms a characteristic lipidic pore, provides an interesting example linking intrinsic membrane pores and polypeptide induced pores [182]. The charge and dipolar moment of host membrane lipids modifies the effective gating charge of the syringomycin E ionic channel. Additionally the channel is inhibited in the presence of non-lamellar lipids with negative spontaneous curvature. Similarly, effects of lipid charge and intrinsic curvature have been observed for channels formed by other peptides or proteins [50, 177].

Can we establish mechanistic connections between intrinsic membrane pores and pores induced by peptides and proteins? In an attempt to do that, we will make an overview of different proposed models and will extract from them a minimum general consensus.

**A consensus view of pore formation.** There have been a number of different classical (general) models of pore formation by membrane active polypeptides. Previous work has often stressed the difference between particular models, amplified by detailed (not always justified) drawings. Instead, we want to underline here their common points, as many of their apparent contradictions can be regarded as either superficial or arising from the use of different experimental conditions. Although mostly developed for membranolytic peptides, many of these ideas can be extended to pore-forming toxins [77, 111]; they essentially leave a prominent role for lipids around the postulate of more or less stable and more or less organized, lipid-based pores.

MATSUZAKI proposed a *supramolecular peptide-lipid dynamic complex* in order to explain the simultaneous transbilayer diffusion of magainin and membrane lipids, coupled

## 2.2 A lipocentric view to pores induced by peptides and proteins

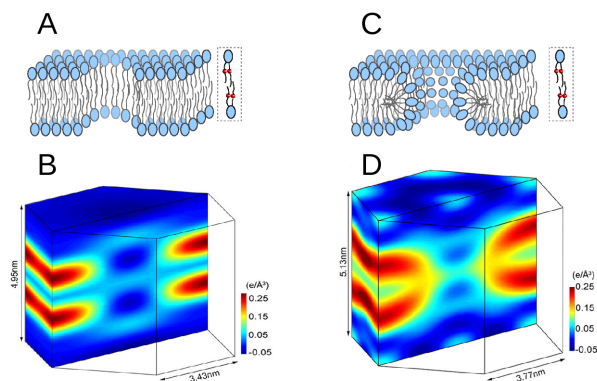


**Fig. 2.4 : Bilayer structure at the edge of peptide-induced pores.** The two paradigmatic types of pore, for long time postulated as alternative models (here illustrated with drawings A and C) are viewed from the electron density of brominated lipids resolved by X-ray diffraction (B and D). The alamethicin induced pores leave bilayer holes with no contact of electron density between the two monolayers (B). In contrast, the structure induced by the  $\alpha 5$  active fragment of the protein Bax shows continuous electron density between the two monolayers at the pore edge (D), as expected for the case of toroidal pores with a wall lined (at least partially) by lipids, drawn schematically in C. Figures B and D are reprinted with permission from PNAS, Volume 105 [183] ©2008 National Academy of Sciences, USA.

to leakage of vesicles [87]. In this model both, lipids and peptides form the pore wall, where the presence of acidic phospholipids may counteract repulsion between the positively charged peptides and explain the cation selectivity of the channel [184]. This is basically the same as the *toroidal wormhole* model, proposed almost simultaneously by HUANG's group on the basis of neutron in-plane scattering and oriented circular dichroism (OCD) data [88]. HUANG's view is sustained on the membrane thinning that accompanies peptide embedding in the head-group region (*S*-phase). Above a certain threshold  $P/L^*$  this triggers a molecular reorganization which involves the reorientation of some peptide molecules (*I*-phase) and formation of a pore [185, 186] (FIG. 2.5 B). Noteworthy, from a similar *S*-phase the model postulates different *I*-phases for alamethicin-type peptides: a *barrel-stave* pore of interacting transmembrane peptides forming a relatively small pore, than for magainin-type peptides: a larger pore where the two monolayers fuse like in a torus and the curvature strain is alleviated by peptides bound across the membrane, in the interface of lipids making the pore wall [141]. From the membrane side, these two alternative pore states correspond to the two possible lipid structures at the edge of a pore, which have been experimentally observed by reconstructing the lipid electron density profiles from X-ray diffraction [183, 187] (FIG. 2.4). This thermodynamic model [76, 114, 188], derived from equilibrium measurements, has been complemented by kinetic experiments performed with single giant unilamellar vesicles (GUVs) in the presence of melittin [69]. The kinetic analysis presents pore formation as a probabilistic phenomenon dependent on the nucleation of defects on the lipid bilayer, which occurs after area expansion, due to interfacial binding of the peptides, reaches a limiting value. Thus, the pore is the response of a bilayer to a polypeptide-induced internal tension,

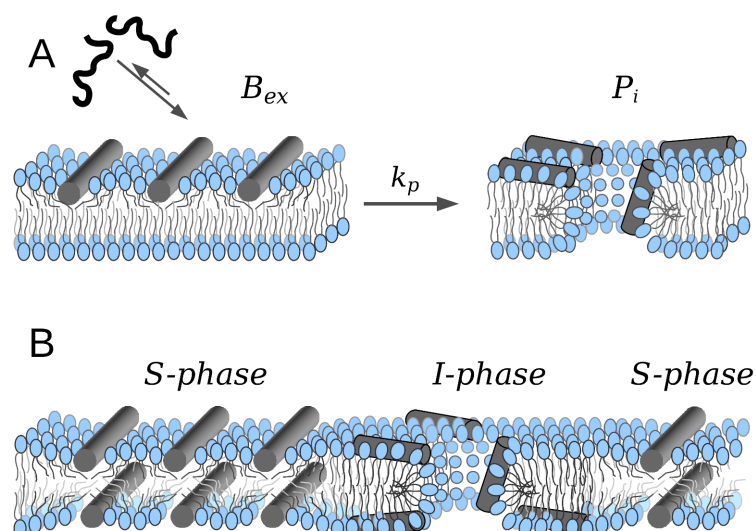


**Fig. 2.5 : Cartoons of kinetic, two-state ( $B_{ex}/P_i$ ), and equilibrium two-phase ( $S/I$ ) pore models.**

(A) The initial asymmetric binding-refolding of active peptides at the membrane interface ( $B_{ex}$  state) drives the transition to a pore  $P_i$  state. (B) At equilibrium the peptide is bound interfacially to both monolayers, causing area expansion and membrane thinning ( $S$ -phase). Above a threshold P/L ratio, it coexists with a different molecular organization ( $I$ -phase) corresponding to observable toroidal pores. The particular organization of peptides is unknown (the one chosen for this model is arbitrary).

which in turn helps to maintain a stable pore with a defined size [69, 76, 88]. Direct evidence and a low resolution structure for such a lipid-based arrangement, in this case induced by an active fragment from the protein Bax [50, 176], have been provided by X-ray diffraction [183].

Disruption of the bilayer is also the main ingredient of the *carpet* model proposed by SHAI et al [109], which is similar to so called *sinking raft* [189], the *chaotic pore* of ALMEIDA [116], or more generally the *detergent-like* activity [190, 191]. It essentially consists on an extensive surface coverage at the level of the head group of phospholipids by cationic peptides, up to the point of yielding the disintegration of the membrane. In this case the toroidal pore is adopted as a disordered early transient stage, before membrane rupture occurs through micellization. Leaving this latter complete disruption aside, as it is observed only at very high peptide concentrations [190, 192], both MATSUZAKI and SHAI/ALMEIDA coincide on proposing pore formation as due to asymmetric membrane disturbance or mass imbalance over the external (accessible) monolayer, where the peptide primarily binds. It follows that pores are necessarily *transient*, because they will close at equilibrium as soon as mass imbalance dissipates through the pore. This is supported by recent kinetic interpretations of content release experiments from LUV suspensions by ALMEIDA's group [84, 116], as well as kinetic studies with single GUVs by TAMBA and YAMAZAKI [85, 86], which also introduce the idea of stochastic pores (or pores opening at random after a threshold stress). The latter authors propose a two state  $B_{ex}$ -to- $P_i$  transition model, where the  $B_{ex}$  state corresponds to the peptide

## 2.2 A lipocentric view to pores induced by peptides and proteins

bound only to the external monolayer, and the rate-limiting step is the insertion of the peptide across the membrane, and  $P_i$  is the metastable transient pore (FIG. 2.5 A). Although these ideas have some resemblance with HUANG’s two state model (FIG. 2.5 B), there are two main contrasting points: (i) in the  $S$ -state the peptides are assumed to equilibrate fast across the membrane through small *transient* pores occurring even at low concentration, meaning that the stress responsible for pore induction is exerted symmetrically in the two monolayers [193]; and (ii) the pores in  $I$ -state correspond to a minimum energy structure and are thus *stable* once they are formed [88, 114, 187, 188].

The toroidal “pores in action” reported by MD simulations also form stochastically and after the asymmetric attack to the bilayer [82, 83]. In this case the interesting feature is the low level of molecular organization within the pore, both for lipids and peptides (FIG. 2.3 C-F), which is put in contrast to HUANG’s view. However, the disagreement may be illusory. Thus, on the lipid side the regular torus derived from X-ray diffraction data is an averaged structure [187] which cannot be directly compared with single pores in non-equilibrium, relatively short MD trajectories. On the peptide side, there is no precise experimental information about the number of peptides involved per pore, or their position and orientation with respect to the pore [103, 114]. It should also be noted that measurements of peptide reorientation upon pore formation performed by OCD, do not give accurate orientation values, but rather inform of a change of tilt. Thus, the OCD results, normally interpreted as a transition between two extreme states, parallel and perpendicular to the membrane, might as well be compatible with other linear combinations of extreme tilts, or even a distribution of peptide orientations, perhaps similar to that seen in simulations (FIG. 2.3 E,F).

Thus, the three main classical models of pore formation have important elements in common, recognized by ZASLOFF, who has termed them collectively as the *Shai-Matsuzaki-Huang (SMH) mechanism* [81]. Considering the new ingredients from MD simulations and kinetic and single vesicle studies, the emerging main consensus ideas are as follows: membrane disruption due to interfacial binding is the basic mechanism of polypeptide-induced pore formation. It proceeds through a stochastic cooperative transition, assisted by bilayer defects, in a two-state process modulated by the membrane elastic properties (see SEC. 2.2.4). This, depending on the type of protein or peptide, may form barrel-like pores (stable cylindrical peptide or protein aggregates) or disordered mixed lipidic-protein or peptidic pores. These ideas are valid for most (if not all) membranolytic peptides. Among the pore-forming proteins, the  $\beta$ -type form preferentially barrels of interacting  $\beta$ -strands [111, 126], while  $\alpha$ -type seem to prefer toroidal pores, so far described for colicins [177], actinoporins [194] and Bcl-2 apoptotic regulators [175, 195, 196] as well as their active fragments [50, 176, 183, 197]. In any case, the importance of membrane disturbance and nucleation of defects to facilitate protein insertion and pore formation should be of general validity.

### 2.2.4 Physical properties of polypeptide-induced pores

**Surface tension, line tension and the stability of membrane pores.** As we have discussed in SEC. 2.2.3, the lytic pores induced by polypeptides have many ingredients of

general lipidic pores, like those formed under tension (mechanical or electrical tension or osmotic swelling). According to proposed mechanisms [74, 198], pores form after a build up of a critical surface tension, which increases the probability of appearance of nucleation sites of packing defects. Theoretical models describe these pores as meta-stable arrangements, with free energy of formation being a function of the pore radius,  $r$ , as

$$E(r) = 2\pi r\gamma - \pi r^2\sigma \quad (2.1)$$

The first term is the energy needed to expand the rim of the pore and  $\gamma$  is the *line tension*, opposing the pore. The second term, proportional to the pore area, represents the work done by the membrane to open the pore,  $\sigma$  being the *membrane tension* or *surface tension*, which favors pore opening and expansion [162, 199]. This model predicts an intrinsically unstable pore which tends to close for  $r < \gamma/\sigma$  and expands indefinitely for  $r > \gamma/\sigma$ . Thus, while external tension effects increase the pore lifetime and can lead to vesicle rupture, different lipids as well as non lipid inclusions, like detergents, may affect the pore stability by changes in the line tension [162].

In a generalization of this model to polypeptide-induced toroidal pores, it has been proposed that pore forming peptides (we may extend it to PFPPs) act by affecting both, the line tension and membrane tension terms and making the open-pore state energetically more favorable [76]. This can occur through an effect of the PFPPs on the membrane elastic properties. The membrane thinning (area expansion) accompanying the interfacial binding of PFPPs is a source of (internal) surface tension which above a threshold value overcomes the energy barrier to open the pore. Additionally, the binding of PFPPs at or near the pore rim may act by reducing the line tension [113, 195, 197]. Evidence of this latter effect has been obtained as shape changes and coalescence of liquid-ordered ( $L_o$ ) domains in phase-separated lipid bilayers in presence of the Bax $\alpha$ 5 fragment and the reduction of line tension was quantified using AFM-firm rupture experiments [197]. An extensive AFM study of membrane remodeling for a variety of pore-forming and cell-penetrating peptides suggests that line tension may be a common ingredient of the mechanism of these systems [113].

**Lipid-driven cooperativity: a many-body effect triggering pore formation.** Kinetic, structural and thermodynamic studies agree on describing pore formation by active peptides as a cooperative process. It is manifested as a nonlinear concentration dependence of activity and a rapid rise to saturation as the concentration exceeds a threshold value and it consists of a steep transition between two main structural states of the peptide-membrane complex [185, 186, 200]. The interfacial binding of the peptide in the S-state (below a threshold P/L\*) expands the membrane area and causes a local thinning. This corresponds to a positive energy of elastic deformation, proportional to the number of peptides bound per lipid. The consequence is an increase of the energy of the S-state which reaching a threshold value (corresponding to a limit tension) triggers a molecular

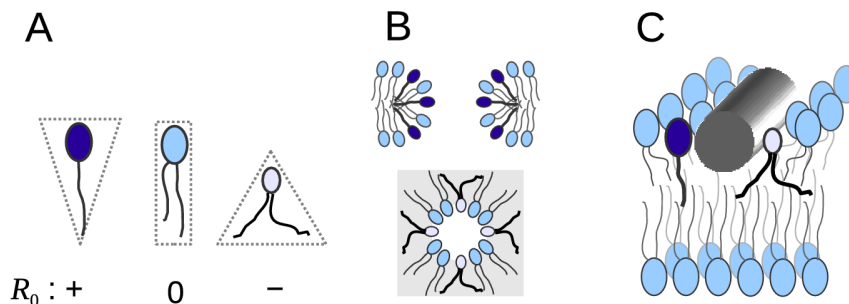


**Fig. 2.6 : Classical and non-classical lipid curvature effects in pores formed by polypeptides.** The tendency of lipids to bend the monolayer can be measured by the radius of spontaneous curvature,  $R_0$ . This depends on the lipid morphology (A) and can be near zero (cylindrical shape like PC lipids), positive (inverted cone-shape, like lysolipids) or negative (cone-shape, like PE lipids). The classical interpretation arises from the fact that toroidal pores are highly curved structures (B). The curvature strain in the plane perpendicular to the membrane (B, top) is alleviated by lipids with positive curvature. On the contrary, negatively curved lipids would destabilize the pores. The opposite is expected for the lipid arrangement in the bilayer plane (B, bottom). The spontaneous curvature of lipids can also affect the strain produced by polypeptides adsorbed at the interface (C, non-classical effects). The polypeptide inclusion can be viewed as introducing positive curvature strain, which can be compensated by negatively curved lipids.

reorganization (I-state) with the opening of lipidic pores and a change of peptide orientation. This has been recently interpreted as similar to a micellization process and the two states have been renamed phases [114].

Interestingly, the membrane-mediated cooperativity of pore-forming peptides suggest a model for the activity of  $\alpha$ -helical pore-forming proteins, e.g. pro apoptotic Bax [114]. The prepore state of these proteins is thought to consist on an extended two-dimensional array of helices, which has been characterized for some colicins [138, 143, 144] and members of the Bcl-2 family [145–147]. Such a configuration would correspond to the S-state, where each helical segment of the array contributes to membrane thinning. Moreover, because the different segments are linked within the same polypeptide chain, they keep confined in a small membrane area, which corresponds to a high effective density of amphipathic  $\alpha$ -helices. This should facilitate the transition to the pore (I-) state which can be expected to occur at a low threshold protein-to-lipid ratio. In fact, these proteins are known to be active at nanomolar concentrations [175]. A similar effect may be valid for the pore formation by protein toxins from other families.

**The elusive role of spontaneous curvature: classical and non-classical effects.** Because pores imply bilayer deformations, they are also related to bilayer elastic (mechanical) properties, namely the isothermal area compressibility modulus, the bending modulus and the monolayer spontaneous radius of curvature [121, 201, 202]. These three parameters depend on bilayer composition [202]. It is proposed that the interfacial adsorption of the peptide induces a bending moment in the bilayer causing deformations which act as nucleation sites for pore opening. The opening probability, stability and

size of the pores is then determined by the deformation energy of the lipids and it thus depends on the intrinsic lipid curvature [121]. These observations are in line with the characteristic high curvature strain of lipidic and proteo-lipidic toroidal pores (FIG. 2.6).

Strong positive curvature arises from the bending/fusion of the two monolayers at the pore edge, forming a structure with a radius approximately half of the membrane width as it can be visualized in a plane perpendicular to the bilayer traversing the pore (FIG. 2.6 B). Thus, the pore rim would be stabilized by lipids with wedge or inverted-cone shape, which are said to have positive spontaneous curvature (most generally lysolipids, FIG. 2.6 A). This concept predicts also that cone-shaped negatively curved lipids, which are those that induce the hexagonal  $H_{II}$  phase [203], should have an opposite effect, i.e. destabilize the pore. For the case of PFPPs the activating/stabilizing effect of positively curved lipids has been shown to be valid in a number of instances [121, 176, 196, 204, 205]. However, the effect of negatively curved lipids seems to be less general and they have been reported to both inhibit [121, 176, 196, 204, 205] and facilitate [50, 125, 176, 177] pore formation. This heterodox role of negative curvature has been related to the fact that a toroidal arrangement of lipids in the pore edge possess also regions of negative curvature strain in a plane parallel to the membrane (FIG. 2.4). Such an effect is predicted to be strictly dependent on the pore size, being comparable to the positive curvature effect for a pore radius of  $\sim 2$  nm (approximately half of membrane thickness) and vanishing small as the pores increase in size [206]. However, conflicting examples can be found in the literature which have been explained by additional properties of lipids complementing or compensating the curvature effects. Additionally, the existence of distorted toroidal pores [75] might also explain the heterogeneity of negative curvature effects, since they are related to the local pore radius which will be variable in a complex manner for non-cylindrical pores.

Based on structural measurements (membrane thinning), HUANG *et al* have described a different effect of lipid spontaneous curvature, which we term *nonclassical curvature effect* (FIG. 2.6 C). In agreement with leakage experiments, negatively and positively curved lipids increase and reduce, respectively, the P/L\* value for the S-state to I-state transition. However, the observed correlations are similar for barrel-stave pores (alamethicin) and toroidal pores (melittin) and in either case the relative stability of the S and I states appear weakly dependent on lipid curvature [200]. Instead, the major effect of varying the spontaneous curvature of lipids is a change of the degree of membrane thinning that accompanies the interfacial adsorption of the peptide [200].

### 2.3 Summary of the state-of-the-art

1. Lipids participate at all stages of the formation of pores by providing the binding site for proteins and peptides, conditioning their active structure and modulating the molecular reorganization of the membrane complex.
2. Lipids are able to self organize as pores in peptide- and protein-free membranes, with increased probability under conditions like phase coexistence, external stress

### 2.3 Summary of the state-of-the-art

or perturbation associated to binding of non lipidic molecules. Pore formation is thus an intrinsic property of lipid bilayers.

3. PFPPs bind, (re)fold and often oligomerize prior to pore formation. PFPPs bound to membranes can be understood as a source of internal surface tension which facilitates pore formation by diminishing the activation energy barrier.
4. Pores formed or induced by PFPPs are typically studied by examining the kinetics of vesicle leakage after peptide addition or obtaining structural measurements, related to the peptide orientation and the membrane thickness, in reconstituted peptide-lipid systems. In the first case, the pores have been considered transient phenomena that allow the relaxation of the peptide-membrane system. In the second, they correspond to equilibrium structures at minimum free energy.



## 3 Pores in mitochondria-mediated cell death

Independently of the morphological features eventually displayed by dying cells, *mitochondrial membrane permeabilization* (MMP) is frequently the key event that delimits the frontier between life and death. Thus mitochondrial membranes constitute the “court” where the “final judgment” takes place and the cell’s fate is decided: either life is passed and death revoked or *vice versa*. The lawyers that determine the propensity to MMP include the Bcl-2 family proteins as key regulators, as well and a myriad of interacting partners including mitochondrial lipids. Signals of opposing nature, pro-life and pro-death, emanating from distinct cellular compartments are finally integrated in the mitochondria. Once the MMP has been induced, it causes the release to the cytoplasm of proteases and activators of such enzymes. The action of final “executioner” catabolic enzymes, together with the fact that mitochondrial bioenergetic function comes to a standstill, lead to cellular demise. In this chapter we will give first a brief introduction to apoptosis followed by a tour through the structure and function of Bcl-2 family proteins. Finally, the physiological importance of MMP and the biomedical importance of Bcl-2 proteins will be discussed.

### 3.1 An overview of apoptosis

*Apoptosis* is a type of *programmed cell death* characterized morphologically by cell shrinkage, nuclear pyknosis (chromatin condensation) and karyorrhexis (nuclear fragmentation), and biochemically by phosphatidylserine exposure on the surface of the plasma membrane [207, 208]. It is an essential and natural process that removes superfluous, ectopic, damaged or mutated cells according to the rule “better death than wrong” [209, 210]. The mechanism of apoptosis is finely orchestrated and carefully controlled. After this process there are no material losses since apoptotic cells end up forming small round bodies which are finally engulfed by phagocytic cells.

The apoptotic program may be elicited by several molecular pathways. The best characterized and most prominent ones are called the *extrinsic* and *intrinsic* pathways, yet there is some cross-talk between them. In the extrinsic pathway, ligand-induced activation of death receptors located on the plasma membrane induces the assembly of the death-inducing signaling complex (DISC) in the cytosol. This promotes the activation of caspase-8, and possibly other caspases, which in turn is able to cleave “effector” or “executioner” caspases (caspases-3, -6 and -7). Caspases (“cysteine proteases cleaving after Asp”) are a family of proteases that cleave specific substrates in the cell leading to its complete dismantling and the apoptotic phenotype. In the intrinsic pathway, several

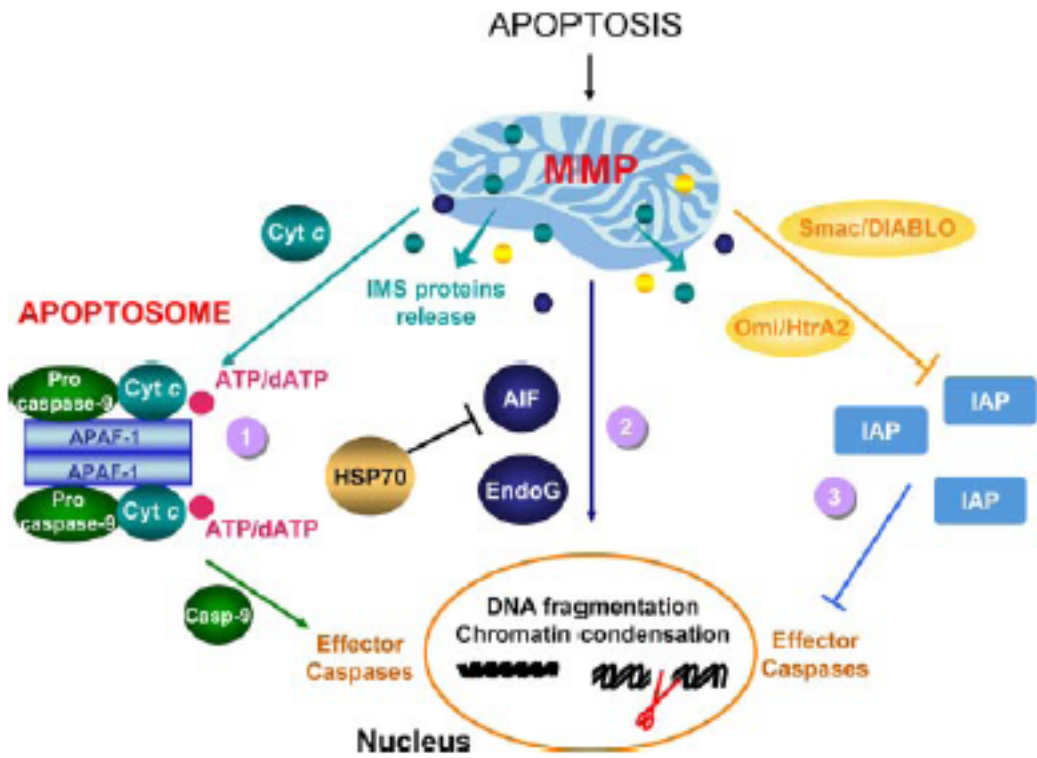


**Fig. 3.1 :** Release of intermembrane space proteins during the intrinsic pathway of apoptosis.

Pro-apoptotic signals resulting in MMP provide IMS proteins with a route for release. Once in the cytosol, IMS follow different fates: 1) Cytochrome c (Cyt c) participates in the formation of apoptosomes, a molecular platform for the activation of caspase-9 (Casp-9) including also APAF-1 and ATP/dATP. 2) AIF and endonuclease G (Endo G) translocate from the cytosol to the nucleus where they favor DNA fragmentation and chromatin condensation. 3) Smac/DIABLO and Omi/HtraA2 promote apoptosis indirectly, by binding to and antagonizing members of the IAP family. Reprinted with permission from *Physiological Reviews*, Volume 87 [211] ©2007 American Physiological Society, USA.

### 3.2 Bcl-2 proteins and the permeabilization of the mitochondrial outer membrane

intracellular signals, including DNA damage and ER stress, converge on mitochondria to induce MMP, which causes the release of apoptogenic factors from the intermembrane space (IMS) into the cytosol. Among these, cytochrome c, in the presence of ATP, is essential for the apoptosis protease-activating factor 1 (APAF-1) to assemble the apoptosome complex, a molecular platform which promotes the proteolytic maturation of caspase-9 (FIG. 3.1). Active caspase-9 or the APAF-1\*procaspase-9 complex [212], in turn, cleaves and activates the effector caspases. Caspase-8 can also proteolytically activate Bid, a BH3-only member of the Bcl-2 family (see SEC. 3.2), which promotes MMP and represents the mayor link between the extrinsic and intrinsic pathways. Although cytochrome c is the paradigm of death effectors released from mitochondria, several other proteins residing in this organelle have important proapoptotic functions (FIG. 3.1):

- Smac/DIABLO and Omi/HtrA2 which are inhibitors of IAPs (inhibitor of apoptosis), endogenous inhibitors of caspases.
- AIF (Apoptosis Inducing Factor) that is a redox protein required for optimal detoxification of reactive oxygen species (ROS) and for the assembly and maintenance of respiratory chain complex I; however, after apoptosis induction, it translocates to the nucleus where it triggers chromatin condensation and DNA fragmentation.
- Endonuclease G, which cleaves chromatin DNA into nucleosomal fragments.

For vertebrates, cell death proceeds in most cases via the intrinsic or mitochondrial pathway of apoptosis [213]. MMP is the critical event responsible for caspase activation in the intrinsic pathway, and can commit a cell to die even when caspases are not activated. This latter “caspase-independent death” [214, 215] can occur because of an irreversible loss of mitochondrial function or because of release of caspase-independent death factors like the aforementioned AIF, endonuclease G, and others. The consequences of MMP are thus many-fold: (i) apoptogenic proteins released from mitochondria; (ii) metabolic alterations, like cessation of ATP synthesis,  $\text{Ca}^{2+}$  release and reactive oxygen species generation; and (iii) morphological alterations in mitochondria. Defects in initial signal transduction (initiation phase) or in the integration/decision phase of apoptosis can arrest the lethal process. On the contrary, defects in the execution/degradation phase will not affect the final outcome, yet change the phenotypic manifestation of cell death, shifting it to a necrosis of autophagic appearance. Accordingly, MMP is considered the “point of no return” [213, 216].

MMP involves at least the permeabilization of the mitochondria outer membrane (MOMP). The involvement of MIM permeabilization is still controversial.

### 3.2 Bcl-2 proteins and the permeabilization of the mitochondrial outer membrane

Proteins of the Bcl-2 family are key regulators of apoptosis via MMP control. The ability of some members of this family to form pores *in vitro* is unquestionable. However, the exact mechanism by which these proteins control the permeability of MOM *in vivo* and

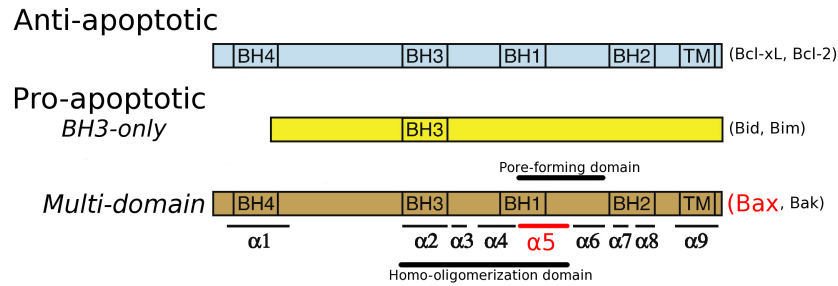


**Fig. 3.2 : Classification of Bcl-2 proteins.** Bcl-2 homology (BH) domains and the C-terminal transmembrane (TM) domain are indicated. The position of the nine helices of Bax is shown together with important functional regions.

the relative importance of Bcl-2's *vs* other pore complexes is a matter of controversy [217]. Bcl-2 (B-cell lymphoma 2), that gives name to the family was first discovered because of its involvement in follicular lymphoma [218]. Since then, several dozen proteins have been assigned to the family and their importance in cancer has become clear. First, we will discuss our current structural knowledge of the Bcl-2 family proteins. Then we will focus on their pore-forming activity and finally we will describe how membrane permeabilization is regulated through a complex interaction network of Bcl-2 family members.

### 3.2.1 Structure of Bcl-2 proteins

Bcl-2 proteins are conserved in evolution and show a high level of sequence and structure similarity [219]. Despite this, proteins of this family have opposing roles in cell death. Depending on their function and on the presence of one or up to four *Bcl-2* homology (BH) domains they can be further classified in three subgroups (FIG. 3.2): 1) anti-apoptotic or pro-survival Bcl-2 proteins (prototypes: Bcl-2 and Bcl-xL), that contain all four BH domains and inhibit apoptosis; 2) proapoptotic or pro-death Bcl-2 proteins, (prototypes: Bax and Bak), that contain BH domains 1 to 3 and are the main executioners of MOMP; and 3) BH3-only Bcl-2 proteins (prototypes: Bid and Bim), that share similarity only in the BH3 domain and are “receptors” that sense different apoptotic stimuli and initiate apoptosis. A comprehensive database of Bcl-2 proteins can be found at <http://bcl2db.ibcp.fr/site/>[220]

Proteins of the Bcl-2 family, like pore-forming toxins, can be found in at least two stable conformations, one in aqueous environments and the other in the membrane milieu. Thus, refolding in the lipid bilayer is an important step in the activation of these proteins, which can then be classified as amphitropic [18]. This holds true even though some members of the family, like Bcl-2 and Bak, are constitutively bound to the MOM via an anchor C-terminal domain (CTD) [221]. In this case, the full-length protein is considered to be tethered to the membrane via the CTD, while most of the protein retains a globular fold outside the membrane. Other members, like Bax and Bid, reside

### 3.2 Bcl-2 proteins and the permeabilization of the mitochondrial outer membrane

in the cytosol of healthy cells and translocate to the MOM in response to an apoptotic stimulus [222–225].

Most three-dimensional structures of Bcl-2's correspond to that of water soluble structures [226–234]. Indeed, to date only one high-resolution structure of a Bcl-2 protein, namely the BH3-only Bnip3, in a membrane media has been achieved [235, 236]. Nonetheless there is indirect evidence about the structural changes accompanying membrane translocation and insertion.

**Water-soluble structures.** Almost all members of the Bcl-2 family display a similar fold in aqueous environment consisting of a central  $\alpha$ -helical hairpin surrounded by several amphipathic  $\alpha$ -helices [237] (FIG. 3.3). The central antiparallel hairpin is often described as being hydrophobic. However, a careful sequence analysis shows that, although hydrophobic residues predominate in that region, there are also many ionizable residues placed in positions that render the two central helices as clearly amphipathic. The other helices also possess amphipathic character. Thus, *a priori* all the helices could be well accommodated in the bilayer interface. Another important feature of these structures is that the BH1, BH2 and BH3 domains are in close proximity and shape a hydrophobic cleft carved in the protein surface, which has been shown to be the site for docking BH3 domains of other Bcl-2's [238, 239]. Interestingly, the helix 9 of Bax, which resembles the C-terminal hydrophobic domain of Bcl-xL, is buried in the hydrophobic cleft, which has been proposed to have implications for the regulation of membrane binding through BH3-dependent interactions. Hence, current models of Bcl-2's translocation suggest that the hydrophobic C-terminus is normally sequestered in the cleft rendering the protein hydrosoluble. Importantly, a recent structure of Bax complexed with a BH3 peptide, suggest that apart from that groove, there may be other regions involved in BH3-dependent protein-protein interactions [240]. Overall, the water soluble structures of Bcl-2 family members correspond to the fold class of membrane translocation channel formation domains in the SCOP classification. Specifically, it resembles the pore-forming domain of colicins and diphtheria toxin. The striking similarity between these proteins with very divergent and even opposite functions remains a major mystery [241] yet some clues are being unveiled. We will return later to this issue.

It should be pointed out that not all Bcl-2 proteins display a defined fold in water. Except for the case of Bid, most BH3-only proteins seem to be *intrinsically disordered proteins* (IDP) and fold only when they engage appropriate Bcl-2 partners [242]. Promiscuous binding and multifaceted regulation, essential features of BH3-only proteins, suggest that a disordered state would be advantageous. Additionally, although Bcl-2 proteins form mostly a compact core in water, with well defined secondary structure elements, they also possess *intrinsically disordered regions* (IDRs). For instance, disordered residues are found in the long inter-helical loop connecting helices  $\alpha 1$  and  $\alpha 2$  of Bcl-xL. Phosphorylation, deamidation and proteolytic cleavage in this region have all been associated with down regulation of pro-survival activity [243, 244]. Whether this loop remains unstructured in the membrane-bound state of Bcl-xL remains unknown. As a result, there is a novel view emphasizing the fact that Bcl-2 proteins are either in-

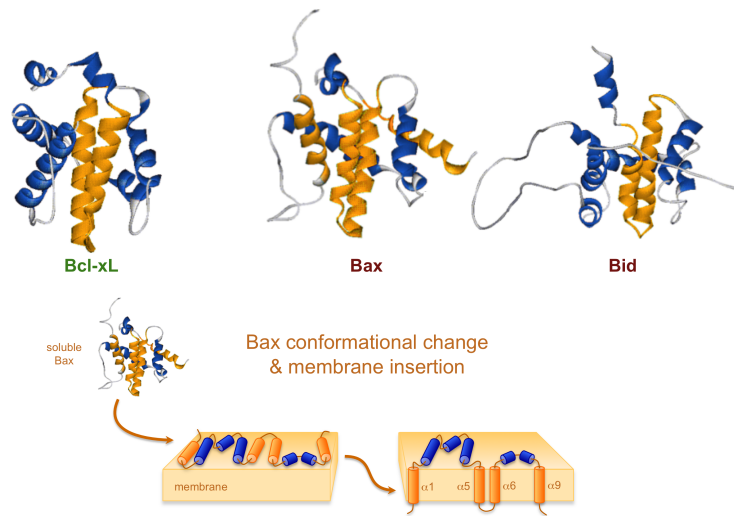


**Fig. 3.3 : Structure of Bcl-2 proteins.** Top, structures of the soluble forms of Bcl-xL [226] (PDB:1MAZ), Bax [229] (PDB:1F16) and Bid [228] (PDB:1DDB). The membrane-interacting fragments are shown in yellow and intrinsically disordered regions in gray. Bottom, model for Bax structural reorganization associated to membrane insertion and prior to oligomerization and pore formation. The detailed structure of the membrane-inserted conformations is still unclear. Taken from [246] .

trinsically disordered or contain intrinsically disordered regions/domains that are critical to their function [245].

**Membrane-associated conformations.** Since the pore-forming domain, i.e. the central hairpin, is normally hidden in the interior of the hydrosoluble structure, extensive conformational changes must occur in order to render this region accessible for membrane interactions (FIG. 3.3). We will discuss now the proposed structural rearrangements for representative family members.

The helix  $\alpha 9$  has a leading targeting function directing Bax toward the MOM, where it adopts a TM orientation [247–251]. Upon interaction with the MOM, Bax unfolds exposing N-terminal epitopes but without major structural rearrangements and conserving the BH3 domain fold [249, 252–254]. However, the sequence of events leading to extensive insertion of the protein is unknown. Currently, it is widely accepted that helix 9 will be in a transmembrane configuration while the insertion depth of helices 1, 5 and 6 is more controversial. The “TM-only” model suggests that only the hydrophobic helix  $\alpha 9$  is able to insert TM while the rest of the protein will be located near the membrane surface [255]. This hypothesis has its basis on the fact that Bax oligomerization depends on the BH1-3 groove (see below) which in principle is not compatible with the central helices being TM. In fact, the hydrophobic length of the central  $\alpha 5$ - $\alpha 6$  helices is too short to span the bilayer and the only way for the hairpin to avoid the energetically

### 3.2 Bcl-2 proteins and the permeabilization of the mitochondrial outer membrane

unfavorable exposure of charged residues to the lipid acyl chain would be to reside in the membrane interface, including at the edge of a pore. In the first case the tilt angle with respect to the membrane normal is expected to decrease compared to the transmembrane configuration. The orientation of the isolated helix  $\alpha 5$  has been studied by oriented circular dichroism suggesting that 30% of the helical components were oriented perpendicular to the plane of the bilayer [183]. Under different conditions, this peptide showed two orientations with tilt angles of 80 and 30 degrees [50]. Alternatively, the  $\alpha 5$ - $\alpha 6$  hairpin has also been proposed to insert in a transmembrane configuration [256–258]. Additionally, helices 1 and 6 have been involved in MOM targeting [250, 259] and their corresponding peptides insert deeply in MOM-mimicking membranes [176, 260].

*In vivo*, membrane insertion and oligomerization of Bax and Bak are triggered by Bid, Bim and perhaps other BH3-only proteins [261–264]. *In vitro*, Bax activation can be induced by incubating the protein with non-ionic detergents [265] or at increasing temperature [266]. Importantly, once Bax is bound to the membrane it can auto-activate by recruiting other soluble Bax molecules [267]. A number of experimental techniques, including size-exclusion chromatography, chemical cross-linking and FRET, have shown that Bax, as well as Bak, is able to form oligomers with variable number of subunits both in mitochondria and in model membrane systems and this seems intimately connected to the formation of pores and the induction of apoptosis [268–277]. However, in a few instances oligomeric Bax was found to release only a minor fraction of cytochrome c [276, 278]. Very recently, the interaction interface between adjacent Bax molecules has been mapped. The first surface overlaps with the groove formed by BH1-3 domains [258, 279, 280]; the second surface is a rear pocket located on the opposite side of the protein from the BH1-3 groove [280]. New insights suggest that massive oligomerization might not be essential for pore formation. While Bax activation may end up in the formation of large aggregates, pore induction is believed to occur early when the Bax membrane concentration and oligomerization is still at low levels [281].

The proposed model for antiapoptotic proteins suggests that these proteins are initially anchored to the MOM through the CTD while the rest of the protein would be folded as in the globular structure. It is not clear whether the membrane-anchored structure is a competent apoptosis inhibitor, but recent pieces of evidence suggest that during apoptosis antiapoptotic Bcl-2 proteins insert extensively into the membrane to inhibit apoptosis [282, 283]. *In vitro*, acidic pH and negatively charged lipids were found to be essential for membrane binding of a Bcl-xL version lacking the C-terminal anchor [284–286]. Pioneering studies in micelles showed that helices 1, 6 and possibly 5 were partially buried in the hydrophobic interior [287]. Glycosylation mapping experiments suggested that helix 5, the hairpin of helices 5 and 6 and the C-terminus of Bcl-xL are able to insert into the membrane while helix 6 alone cannot [256]. Surprisingly, a solid-state NMR study showed no evidence for deep insertion of any helix excluding helix 9 and proposed instead a surface location of the protein with a TM anchor like in the “TM-only” model [145]. For the related protein Bcl-2, cysteine labeling showed that helices 5, 6 and 9 inserted deeply in the MOM and that this structural rearrangement was required to inhibit Bax oligomerization [282, 283].

Bcl-xL homodimerizes in water via interactions between the CTD and the BH3 binding

### 3 Pores in mitochondria-mediated cell death

groove [288], and by three dimensional domain swapping either at alkaline pH [289] or after heat induction [290]. Bcl-xL can also dimerize in non-ionic detergent micelles, forming two different types of dimers distinguishable by the presence or absence of BH3 binding activity [291]. Similarly, Bcl-2 can homodimerize through two distinct surfaces [292]. Both Bcl-xL and Bcl-2 can heterodimerize with Bax in the membrane partly explaining the ability of antiapoptotic proteins to block Bax pore formation [269, 282]. Very recently, it has been shown that Bcl-2/Bax heterodimers in micelles are held together via interactions through two interdependent surfaces: one involves the BH3 regions of Bax and the BH1-3 groove of Bcl-2 and the other involves the helix 6 of Bax and the BH4 domain of Bcl-2 [293]. Antiapoptotic Bcl-2 members have been found in dimeric or trimeric complexes but never engage into higher-order oligomerization states. This fact may explain the inability of these proteins to create big membrane pores and thus may be one reason explaining their inefficient permeabilization of the MOM [294, 295].

Regarding BH3-only proteins, various approaches agree in a shallow insertion of Bid into the membrane [146, 147], though glycosylation mapping assays showed that the hairpin of helices 6 and 7 (the equivalent of helices 5 and 6 in Bax and Bcl-xL) inserts into lipid membranes via hydrophobic interactions [256]. Importantly, the only known high-resolution membrane structure comes from the BH3-only protein Bnip3. It forms a right-handed parallel dimer with a unique dimerization motif [235, 236]. The structure displays a flexible network of hydrogen bonds and water accessibility up to the middle of the membrane that has been proposed to enable the protein to form an ion-conducting pathway across the membrane. However, due to the particular evolutionary history of Bnip3-like proteins it is difficult to extrapolate these results to other Bcl-2's [219].

The mitochondrial permeability by proteins of the Bcl-2 family during apoptosis is regulated by specific lipids and membrane properties [296, 297]. CL is a characteristic lipid of the MIM and has been related to the apoptotic release of cytochrome c [296, 298, 299]. This negatively charged lipid provides specific targeting for tBid at mitochondria through a high affinity binding domain [298]. The protein gets access to CL at the contact sites between inner and outer mitochondrial membranes [299]. This, in turn, causes membrane remodeling and reordering of lipids, specially CL, which is mobilized to the MOM. Experiments with vesicles reconstituted with mitochondrial lipids show that CL is also necessary for Bax action [296], participating in the recruitment and activation of the protein [300]. Other lipids present in the mitochondria may have specific effects on Bcl-2's as well. For example, PE is known to inhibit Bax oligomerization at high concentrations [300]. Cho does not seem to affect Bax membrane binding, but impairs deep insertion and oligomerization of the protein thereby reducing pore formation [301, 302].

#### 3.2.2 Pore-forming properties

When the first 3D structure of a Bcl-2 family member became available, its similarity with the pore-forming domains of bacterial toxins, like colicins and diphtheria toxin, was obvious [226]. This prompted researchers to study the ion channel activity of Bcl-2

### 3.2 Bcl-2 proteins and the permeabilization of the mitochondrial outer membrane

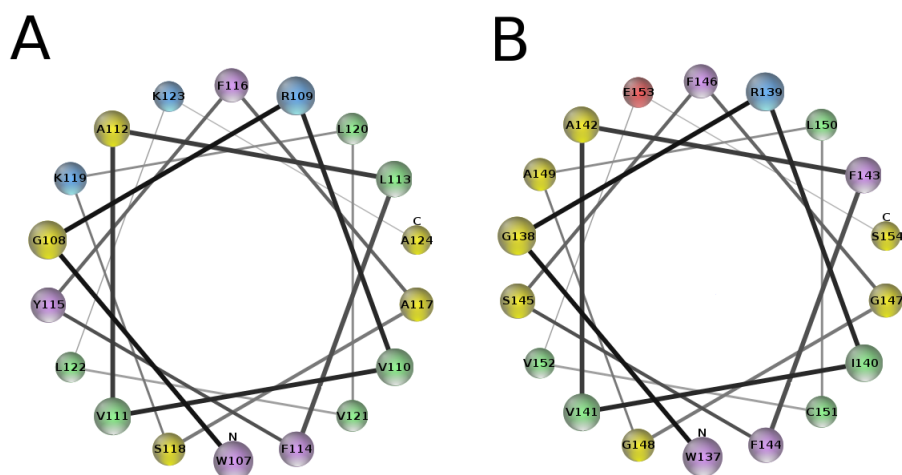


**Fig. 3.4 : Helical-wheel representations of the helices  $\alpha 5$  from Bax (A) and Bcl-xL (B).** The residue color code is as follows: hydrophilic (yellow), hydrophobic (green), aromatic (violet), acidic (red) and basic (blue). The figure was generated with MPEX [303].

proteins [304]. Initially, ion channel recordings of Bax were performed with truncated versions lacking the C-terminus. Bax first formed small anion-selective channels, followed by multiple conductance levels of moderate anion selectivity and, finally, stable ohmic pores [305]. Further work with full-length Bax showed arbitrary and variable changes in membrane permeability with a marked decrease in membrane stability [195]. This study suggested for the first time the implication of lipids in pores induced by Bax. The dependence of Bax-induced pores on lipid spontaneous curvature and the increase in lipid flip-flop were taken as signatures of proteolipidic toroidal pores being formed [175, 176, 196, 306]. However, other evidences suggested pore assembly by a barrel-stave model [307]. Besides, cardiolipin has been shown to be necessary for the formation of large pores induced by a mixture of tBid and Bax [296]. Although Bax alone can induce the opening of pores in pure lipid bilayers, MOMP is believed to depend on the collaborative action of Bax, mitochondrial lipids and possibly other MOM proteins [296, 308, 309].

Accumulating evidence indicates that the central hairpin is the main part responsible for the pore-forming activity of the Bcl-2 proteins: (i) deletion of the C-terminus does not affect Bax functionality [310], but deletion of the central hairpin of Bax abrogates the release of cytochrome c from mitochondria [311], and (ii) small peptide fragments corresponding to either helix of the hairpin can form pores essentially identical to that of full-length proteins [50, 176]. Compared to Bcl-xL, Bax-derived fragments possess a better “design” for pore formation since positively charged residues are located preferentially in one face of the helix (FIG. 3.4). Moreover, the Bcl-xL central hairpin possesses a greater proportion of negatively charged residues which may reduce membrane insertion through electrostatic repulsion [285]. However, pore formation may not be the

only function associated with the central hairpin. For example, the mitochondrial localization of Bax, the antiapoptotic effect of Bcl-xL, and homo- and hetero-interactions between Bax and other members are thought to be mediated by the pore-forming domain [259, 279, 293, 312–315].

The expression of at least one of the two proapoptotic proteins, Bax or Bak, is required for MMP induction [264]. Accordingly, cells lacking both Bax and Bak (but not cells deficient solely for Bax or Bak) are highly resistant against MMP induction and against the activation of cell death by the intrinsic pathway. However, Bax/Bak double knocked-out cells are not completely resistant to MMP and such mitochondria can be permeabilized by alternative mechanisms such as high calcium concentrations, which can induce the phenomenon known as “permeability transition”<sup>1</sup> [316, 317] (PT), or by a VDAC-dependent mechanism [317].

Bax pores were first observed at low resolution by AFM [318]. A more recent X-ray study of a membrane in the presence of a peptide derived from the helix  $\alpha 5$  of Bax showed that the two monolayers bend continuously in the rim of the pore, demonstrating that this peptide forms lipidic pores [183]. However, the location of the peptide molecules with respect to the pore is unknown. This model of pore satisfactorily explains both the lipid dependence of leakage caused by Bax and the fast lipid transbilayer diffusion. The toroidal lipid pore has also been proposed to explain the mode of action of structurally similar proteins like colicins [177, 205]. Membrane binding of amphipathic fragments stretches the membrane surface (and simultaneously reduces the membrane thickness) so that when a threshold value of area expansion (or decrease in hydrophobic thickness) is reached, a pore opens to alleviate the generated tension. In this context, the confinement of the amphipathic helical segments of pore-forming proteins, like Bcl-2 family proteins, in a reduced area may provoke the same effect as several individual pore-forming peptides, thus explaining the apparent higher activity of the former with respect to the latter [114]. Protein and peptide induced pores are supposed to be stable and of a well defined size [319], which could be explained in terms of Bax-induced decrease of line tension [195, 197].

The case of antiapoptotic proteins is somewhat confusing. As discussed above, their soluble structure is similar to that of proapoptotic members while their biological function is just the opposite. Furthermore, both Bcl-xL and Bcl-2 can form ion channels in planar lipid membranes and in liposomes. As with Bax, these channels are pH-sensitive and display different conductance states. But they differ from those of Bax in that they are cation selective, show no decrease in membrane lifetime and have a small opening probability at physiological pH [320]. In the case of Bcl-xL lacking the CTD, the pH

---

<sup>1</sup> Permeability transition (PT) is a sudden increase of MIM permeability to solutes with molecular mass up to 1.5 kDa. This phenomenon is caused by the opening of a voltage-dependent, high-conductance channel located in the MIM that is known as the *permeability transition pore complex* (PTPC). The exact molecular nature of the PTPC is still a matter of debate, although an emerging consensus considers the PTPC as a multi-component protein complex as being responsible for the opening of PTP. It is believed that PTPC is assembled at the contact sites of the mitochondrial membranes and that its scaffold structure is based on the dynamic interaction between VDAC, ANT (adenine nucleotide translocase) and Cyclophilin D. Both anti- and proapoptotic members of the Bcl-2 family modulate the activity of PTPC, through direct interactions with ANT or VDAC

### 3.2 *Bcl-2* proteins and the permeabilization of the mitochondrial outer membrane

sensitivity was demonstrated to correlate with protein binding [284–286]. Poor leakage activity at neutral pH is thus just a consequence of low membrane affinity in the absence of the CTD. Accordingly, it seems that full-length Bcl-xL is able to form pores at pH 7 although with low efficiency [321]. Similarly, Bcl-2 was found to induce the formation of small pores, which are not cytochrome c permeable, either at physiological pH through tBid induced conformation changes [295] or at acidic pH in the absence of Bid [294]. Low pH changes the protonation state of residues located in the loop connecting helices 5 and 6 thus allowing membrane binding via an electrostatic mechanism even in the absence of a CTD [285]. Interestingly, proteolytic cleavage releasing the N-terminal part of the protein can transform antiapoptotic members into proapoptotic partners with pore-forming properties essentially identical to those of Bax [244, 322, 323]. It is tentative to speculate that the intrinsic pore-forming ability of antiapoptotic Bcl-2's is similar to that of proapoptotic ones but they are normally unmanifested due to the fact that the initial conformational changes in the N-terminal region upon membrane binding are blocked. In line with this hypothesis exposures similar to the N-terminal epitope of Bax have never been found in Bcl-xL or Bcl-2.

The pore-forming capacity of Bid has been studied less than that of other Bcl-2 proteins, since in general it is not able to induce apoptosis on its own [324, 325]. Both Bid and tBid are able to destabilize planar lipid membranes and to induce leakage from, and lipid mixing in, liposomes [326–328]. It has been hypothesized that the membrane destabilization by Bid is related to the induction of negative curvature [329], but its lipid transfer activity between membranes could also be involved [330].

#### 3.2.3 The complex regulatory network of Bcl-2 proteins

**Activation.** Under normal conditions, many of the proteins of the Bcl-2 family remain in an apoptosis-inactive form within cells. While the expression levels of some anti-apoptotic members of the family can be regulated transcriptionally [331], Bax and Bak levels are constitutively expressed in cells and their activity is mainly regulated by other Bcl-2 proteins especially involving relocalization to the MOM [332]. Post-translational modifications may also alter Bax binding to the MOM [333–335]. Another way for the cell to control the levels of the different Bcl-2 proteins is by ubiquitination and proteosomal degradation [336]. Increase of the degradation activity has been shown to have a proapoptotic effect on pro-survival members, like Bcl-2, while it reduced cell death in the case of proapoptotic proteins, like Bax, Bid and Bak [337].

In the presence of an apoptotic stimuli, the BH3-only proteins are activated first (FIG. 3.5). They are considered the initial sensors that recognize the diverse apoptotic signals in the cell. The levels of some of them, like Bim, are increased in response to transcription factor signaling [338]. Others are activated by post-translational modifications. For example, Bid is activated via proteolytic cleavage by caspase-8 [339]. Once induced or activated, these proteins translocate spontaneously to the MOM, where they engage with other Bcl-2 proteins to induce apoptosis. Based on their ability to activate Bax and Bak, the BH3-only proteins are classified as “direct activators” or “sensitizer/derepressors”. The latter are unable to directly induce Bax/ Bak activation. Instead, they bind to the

antiapoptotic proteins with high affinity leading to the release of the “direct activators”, which in turn activate Bax and Bak membrane permeabilizing activity.

Translocation to the MOM is also experienced by other family members when activated for apoptosis induction. Except for a minor fraction weakly associated to mitochondria, Bax exists mostly in monomeric form in the cytosol of healthy cells [252]. During apoptosis, tBid and Bim have been shown to trigger Bax to translocate to the MOM and to potently induce cytochrome c release [224, 261, 340]. Based on experiments with model membranes, it has been suggested that tBid and Bim cooperate with Bax to induce membrane permeabilization [296]. Bax translocation to the mitochondria is accompanied by conformational changes that lead to extensive insertion into the lipid bilayer (see above). *In vitro* experiments have shown that interaction with lipid membranes is enough to initiate Bax conformational rearrangements [341]. Once in the mitochondria, Bax oligomerizes and induces the release of cytochrome c and other apoptotic factors, which usually correlates with the commitment of cells to die [265, 342]. Relocalization of Bax is required for its proapoptotic function since when it is retained in the cytosol mitochondrial damage and apoptosis are efficiently prevented [343].

However, the molecular mechanism by which tBid and Bim activate Bax and Bak remains elusive. It seems to be dependent on interactions with the BH3 domains of the direct activators, though difficulties in observing direct binding between them [344] have led to the proposal of a “kiss-and-run” hypothesis. In an elegant study, ANDREWS and coworkers have shed light on the Bax activation pathway showing that it follows a set of ordered steps that culminate with membrane permeabilization [272]. Using a reconstituted *in vitro* system, they found that the presence of membranes was necessary for tBid to activate Bax. The temporal analysis of their data suggested that tBid/Bax interactions occurred prior to Bax insertion into the lipid bilayer, which was then rapidly followed by Bax/Bax oligomerization (FIG. 3.3) Then, once a threshold concentration of Bax was inserted into the bilayer, membrane permeabilization happened very quickly.

**Inhibition.** The antiapoptotic members of the Bcl-2 family inhibit apoptosis by blocking the MMP and the subsequent activation of caspases. The first hypothesis to explain their mechanism of action was the *rheostat* model, in which the relative levels of pro- and antiapoptotic proteins determine the cell’s fate [345, 346]. This was supported by the observation that over-expression of antiapoptotic Bcl-2 proteins promoted cell survival in tumor cells, while their genetic deletion resulted in an increase in apoptosis [347, 348]. Also supporting this vision, deletion of the pro-apoptotic members increases resistance to apoptosis [349]. However, the rheostat model was insufficient to explain the complex regulation of MOM permeabilization by the Bcl-2 proteins. During the last years alternative models have been proposed to describe this process.

The antiapoptotic Bcl-2 proteins are believed to inhibit the apoptotic members by direct complex formation. Available structures show that the hydrophobic cleft formed by the BH1, -2 and -3 domains of Bcl-xL can accommodate peptides corresponding to the BH3 regions of Bak, Bad and Bim [238, 239]. This suggests that the hydrophobic pocket is involved in the heterodimerization with other family members via their BH3 domain.

### 3.2 Bcl-2 proteins and the permeabilization of the mitochondrial outer membrane

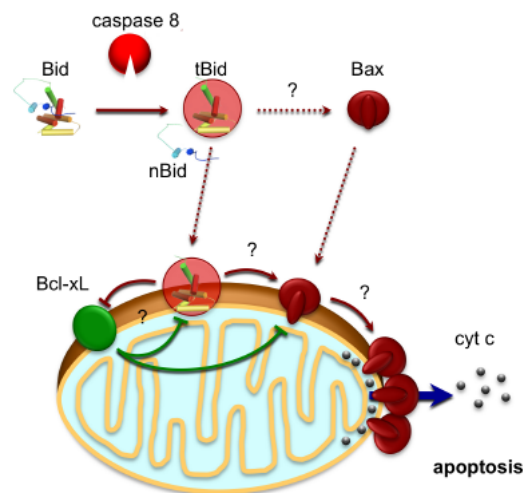


**Fig. 3.5 : Permeabilization of the outer mitochondrial membrane by proteins of the Bcl-2 family.**

The proteolytic cleavage of Bid by caspase-8 at the onset of apoptosis yields the active form tBid. tBid translocates to the outer mitochondrial membrane, where it activates Bax, which inserts into the membrane, oligomerizes and forms pores releasing pro-apoptotic factors like cytochrome c (cyt c). Bcl-xL is an anti-apoptotic member of the family that inhibits tBid and Bax.

Supporting this idea, BH3 peptides of proapoptotic Bcl-2 proteins bind to proapoptotic members with different affinities [350]. Also, mutations in the BH3 domain of tBid abrogate their interactions with multi-domain Bcl-2 proteins.

Interestingly, Bcl-xL, among other antiapoptotic proteins, reside partially in the cytosol and translocate to the MOM during apoptosis. Once there, tBid has been shown to induce conformational changes in Bcl-2 that are associated with its extensive insertion into the membrane [351]. Although the physiological implications are not completely clear, these observations lead to the idea that antiapoptotic Bcl-2 could be “activated” for inhibition of apoptosis at the MOM in a similar way to Bax [352]. This hypothesis is also based on the structural similarities between the multi-domain Bcl-2 proteins and on the fact that both pro- and antiapoptotic members display pore-forming activity. Indeed, Bcl-xL has been shown to compete with soluble Bax for membrane binding induced by tBid [269]. Once in the membrane, Bcl-xL is able to interact with and inhibit both tBid and Bax [269]. As a consequence, tBid is sequestered, Bax oligomerization is impaired and cytochrome c release is inhibited.

From these experiments, Bcl-xL was proposed to behave as a dominant negative version of Bax [269]. This very interesting concept assumes that the antiapoptotic Bcl-2 proteins are incapable of forming high-order oligomers. As a result, they would form small pores after membrane insertion, yet being unable to produce the giant protein-permeable pores necessary for MOMP. In addition, Bcl-xL binding to Bax would result in small oligomerization-defective complexes, unproductive for cytochrome c release.

The role of the lipid membrane in the regulation of MOMP is thus being increasingly

recognized. The recently proposed “embedded together” model [353] assumes that the final regulation of MOMP takes place in the lipid membrane and is associated with an extensively inserted conformation of the Bcl-2 proteins. As a consequence, multiple parallel equilibria between the different Bcl-2 proteins happen in solution and within membranes. The relative strength of the interactions in both environments would then shift the equilibrium towards Bax and/or Bak oligomerization and MOMP, or towards the formation of unproductive complexes associated to maintenance of MOM integrity [272].

## 3.3 Physiological and medical importance of apoptosis

### 3.3.1 Mitochondrial membrane permeabilization in major human diseases

Altered MMP, either enhanced or inhibited, has been described as a feature of many human diseases such as ischemia/reperfusion, intoxication with xenobiotics, viral infection, or neurodegeneration.

Apoptotic cell death pathways have been implicated in acute brain injury, including cerebral ischemia/reperfusion damage [354, 355]. The importance of mitochondria and the release of cytochrome c after pro-apoptotic protein Bax translocation has been revealed [356].

Mitochondrial dysfunction has also been implicated in several different models of neuronal death [357]. Interestingly, MMP modulators that block mitochondrial apoptosis like anti-apoptotic Bcl-2 members are able to efficiently prevent neuronal cell death following a stroke or a hypoglycemic insult [358] and are active in models of traumatic brain and spinal cord injury as well [359, 360].

Viruses have evolved multiple strategies to modulate apoptosis to their own benefit, including some that act specifically at the mitochondrial level [361, 362]. Antiapoptotic viral proteins contain mitochondrial targeting sequences in their C-terminus that are homologous to tail-anchoring domains. These domains are similar to the C-terminal domain of some members of the Bcl-2 family and are responsible for inserting the protein into the MOM. Viral proapoptotic proteins translocate to mitochondrial membranes and induce MMP. From a structural point of view, all the viral propapoptotic proteins discovered so far contain amphipathic helices that are necessary for their proapoptotic effects and seem to have pore-forming properties.

Impaired MMP may lead to the invalidation of the apoptotic response that is found in cancer [363]. Several independent mechanisms may cause MMP including: 1) alterations of gene expression resulting from genetic or epigenetic events; 2) loss-of-function mutations; or 3) defects in the post-translational regulation of activity resulting from intracellular localization/trafficking (e.g. inhibition of Bax translocation to mitochondria). The up-regulation of Bcl-2 (and of other antiapoptotic members of the Bcl-2 family) and/or the down-regulation of Bax have been reported in several clinical studies of cancer patients and, notably, in a high proportion of hematopoietic and lymphoid neoplasm [364, 365]. These changes may be directly related to MMP regulation.

### 3.3.2 Pharmacological manipulation of mitochondrial permeabilization

MMP control by Bcl-2 proteins is crucial not only for physiological but also for pathological cell death, and its manipulation constitutes a clear target for the pharmaceutical industry [366]. We will discuss briefly two current strategies: BH3 mimetics and mitochondriotoxic compounds for cancer therapy.

Bcl-2, as the prototype of antiapoptotic proteins, stabilizes mitochondrial membranes and inhibits cell death via multiple and complex processes (see SUB. 3.2.3). Bcl-2 antagonists can trigger MMP through a variety of mechanisms, namely: 1) by increasing the bioavailability of BH3-only proteins [367, 368]; 2) by disrupting MMP-inhibitory protein-protein interactions with Bax and Bak [226, 230]; and 3) by disrupting interactions between Bcl-2 and PTPC constituents [369, 370]. Structure-based computer screens have been exploited to identify natural or synthetic Bcl-2 or Bcl-xL antagonists [371, 372]. Subsequent NMR analysis have revealed that such inhibitors target the BH3-binding pocket of Bcl-2 or Bcl-xL, blocking the BH3-mediated heterodimerization between Bcl-2 family members *in vitro* and *in vivo*, and inducing apoptosis. Recent highlights in the field include the development of ABT-737, a small molecule which occupies the BH3 binding domains of Bcl-xL and Bcl-2 [373] and that of synthetic BH3 peptides that have been stabilized and rendered cell-permeable by hydrocarbon stapling [374]. These reagents may be employed either to sensitize tumor cells to conventional chemotherapy or as single agents. All these works corroborate the notion that BH3-dependent heterodimerization between pro- and anti-apoptotic species is required for the stabilization of mitochondrial membranes. However, most protein-protein and protein-lipid interactions take place at the mitochondrial locus, where protein structure changes possibly including BH3 impairment. Thus, other regions may have unprecedented effectiveness in allowing pharmacological manipulation of MMP.

Indeed peptides derived from Vpr and ANT [375], as well as synthetic peptides such as (KLAKKLAK)<sub>2</sub> [376], demonstrated the ability to kill cancer cells, both *in vitro* and in mouse models, by triggering MMP. Their specific effects on mitochondria can be demonstrated by their capacity to induce MMP also when added to the purified organelles. Very recently it has been shown that small membrane-active fragments derived from the pore-forming domain of Bax (and to a minor extent fragments derived from Bid) can directly target the mitochondria and effectively induce cytochrome c release, thus bypassing all the complex Bcl-2 regulatory network [377].

## 3.4 Summary of the state-of-the-art

1. The proteins of the Bcl-2 family regulate the release of apoptotic factors, like cytochrome c, from mitochondria during apoptosis, a key event in physiological cell death
2. The proapoptotic protein Bax is one of the key executioners of MMP. To this end, Bax must bind first to the MOM, followed by deep insertion and massive oligomerization, like other PFPPs. However, the molecular mechanisms are largely

### *3 Pores in mitochondria-mediated cell death*

unknown. Importantly, the helix  $\alpha 5$  is part of both the pore-forming domain and the homo-oligomerization domain.

3. Bcl-xL inhibits MOMP by blocking Bax binding, refolding and oligomerization via hetero-associations mediated at least by the BH3 domain. However, membrane-dependent hetero-interactions are largely unknown.

## 4 Aim of this work

Because individual membrane-inserting  $\alpha$ -helices can be considered as true protein domains, i.e. independently folded units with specific functions, in the process of membrane protein functional assembly, the challenge of over-expressing and purifying full-length membrane proteins can be circumvented by a “divide-and-conquer” approach; individual peptides derived from single membrane-insertion sequences can be used to evaluate experimentally the fundamentals of binding-folding-poration processes. Moreover, the relative simplicity of peptides makes it easier to test the sequence requirements involved in homo- and hetero-interactions and pore formation. Thus, several membrane active peptides derived from prototypical Bcl-2 proteins, Bax, Bcl-xL and Bid, are currently being studied in our lab.

In this Thesis we focused specifically on one fragment of proapoptotic Bax, Bax $\alpha$ 5, as a minimal active version. However, proteins or peptides are far from being the only participants in pore formation: the role of lipids is critical as well and will also be taken into account. Such a study will be performed at two levels: from a fundamental biophysics point of view, we wished to gain deep insight into the general mechanism of pore formation common to Bax, an  $\alpha$ -helical pore-forming toxin, and to some extent also to other PFPPs. On the other hand, from a more specific physiological perspective, we wished to contribute to the knowledge of the function of Bax at a molecular level by describing the basis of homo and hetero molecular interactions involving Bax $\alpha$ 5 in membranes. The following specific objectives were proposed:

1. Characterizing of Bax $\alpha$ 5 binding-folding into membranes (CHAP. 7 on page 135).
2. Studying the structure of Bax $\alpha$ 5-membranes complexes, including the orientation of Bax $\alpha$ 5, its oligomerization state and its effect on the membrane phase properties (CHAP. 8 on page 145 and 9 on page 175).
3. Characterizing the pore-forming activity of Bax $\alpha$ 5 by combining classical ensemble experiments with single vesicle approaches (CHAP. 10 on page 205).
4. Investigating the interactions between Bax $\alpha$ 5 and Bcl-xL-derived polypeptides and their possible pore-forming inhibitory role (CHAP. 8 on page 145).

#### *4 Aim of this work*

**Part II**

**Methodology**



# 5 Methods

## 5.1 Sample preparation

### 5.1.1 Model membrane systems

Natural biological membranes are very complex and diverse in their composition. Thus, the study of the structure and function of membrane peptides and proteins often needs to be done in simplified systems, with controlled and well defined properties. Throughout decades of research a number of well known model systems have been developed (discussed in SEC. 1.3). This section describes briefly the preparation and characterization of the model membrane systems used for this work.

#### **Types and preparation.**

**Micelles.** Due to the hydrophobic effect, amphipathic molecules tend to self-associate in aqueous environments, excluding their hydrophobic parts from water, whereas polar and charged groups are exposed to and interact with the polar solvent. Depending on the shape of the amphiphile, this type of self-association leads to different structures (see SUB. 1.1.3). Fatty acids, detergents and lysophospholipids have an inverted cone-like shape, which makes them organize forming relatively small spherical structures, known as micelles. Micelles are very often employed to stabilize membrane proteins in water and are useful also to handle denatured proteins, like in the widely used SDS-PAGE method for the electrophoretic analysis of proteins.

**Liposomes.** Most phospholipids, however, have nearly a cylindrical shape, and form growing bilayers when they pack in water. Because bilayer edges are very unfavorable, membranes appear as continuous surfaces forming enclosed water-filled compartments, known as liposomes or lipid vesicles (FIG. 1.2 E and F). The LAPLACE pressure maintains liposomes with an spherical shape. These structures constitute very useful model systems, easy to prepare with variable and controllable composition and size, which enables the modulation of membrane properties such as fluidity, phase state, charge and intrinsic curvature. In addition, membrane proteins and peptides can be reconstituted into vesicle membranes, which can also be doped with fluorescent dyes, or be manipulated to encapsulate substances inside the vesicle lumen. This allows the study of important processes, such as different types of transport across the membrane, lateral and transbilayer diffusion phenomena, domain segregation, binding, folding and assembly of membrane proteins, etc.

## 5 Methods

We used POPC liposomes as the basic phospholipid composition since most biological membranes are composed of unsaturated phosphatidylcholines. In most cases we also incorporated CL because of the suggested significance of this lipid for the activity of Bcl-2 proteins [378, 379]. Additionally, depending on the particular experiments, liposomes were doped with small amounts of fluorescent labeled lipids.

Depending on the number of lamellae and the vesicle size, liposomes can be classified as follows:

**Multilamellar Large Vesicles (MLV)**, with more than one lamellae and a heterogeneous size varying from  $\sim 100$  nm to more than  $1 \mu\text{m}$  diameter. They are prepared by directly resuspending a dried film of lipids in an aqueous solution. Their homogeneity can be enhanced and their size diminished with several cycles of freezing and thawing. Thus, freeze-thawed MLVs may be used for experiments in which neither a fixed size nor a single bilayer is needed.

**Large Unilamellar Vesicles (LUVs)** have only one lamella and dimensions ranging from  $\sim 50$  nm to  $\sim 600$  nm diameter. They are prepared from a suspension of MLVs which is subjected to a number of freezing-thawing cycles and extruded through polycarbonate membranes with pores of a size similar to that required for the vesicles [380]. The homogeneity, unilamellarity and stability of LUVs makes them the most appropriate model membrane system for functional studies.

**Small Unilamellar Vesicles (SUVs)**, which contain also a single lamella but have a smaller size than LUVs, ranging from  $\sim 25$  to  $\sim 50$  nm diameter. Thus, there is not a clear threshold size to distinguish between SUVs and LUVs. SUVs can be easily prepared by sonication of a suspension of MLVs. In general, it is not recommended to work with SUVs because of the high curvature associated to their small size, which reduces the membrane stability and may affect the properties of peptide- or protein-membrane complexes under study. Nevertheless, their small size is of great advantage for optical spectroscopy since they minimize light scattering artifacts.

**Giant Unilamellar Vesicles (GUVs)**, which contain a single lamella and can range in diameter from a few microns to a few hundreds of  $\mu\text{m}$ . GUVs can be prepared using a variety of methods, including electroformation and controlled hydration [381]. Due to their large size they can be easily observed using phase-contrast optical microscopy, and the use of fluorescent dyes, either through specific types of fluorescent lipids or labeled peptides/proteins bound to the membrane, allows access to a wealth of information.

**Supported multibilayers.** When liposomes are deposited on a flat surface and gently dried, capillary forces flatten the membranes, which spontaneously organize into oriented multibilayer stacks. Typically, several thousands of highly ordered membranes can be piled up using this method, with a mosaicity (distribution of bilayer normal vectors) of a few degrees. These systems are useful to study the orientation of peptides and proteins in membranes by solid state NMR or ATR-FTIR [382, 383].

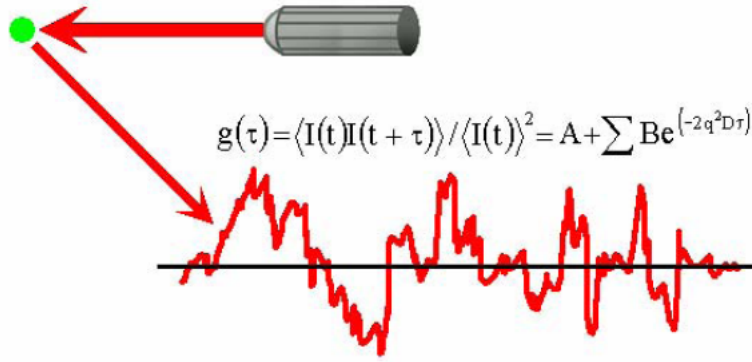


**Fig. 5.1 : Dynamic light scattering for liposome size determination.** Incident photons induce an oscillating dipole in the electron cloud. As the dipole changes, energy is radiated or scattered in all directions. Fluctuations in the detected light are a result of Brownian motion and can be used to extract the diffusion coefficient and size of particles via the auto-correlation function.

### Characterization of model membrane systems.

**Vesicle size distributions from dynamic light scattering.** *Dynamic Light Scattering* (DLS), also named *Quasielastic Light Scattering* (QELS) or *Photon Correlation Spectroscopy* (PCS) is a technique used to characterize the Brownian motion (diffusion) and size distribution of an ensemble of particles in solution [384, 385]. For a collection of particles illuminated by a monochromatic light source, such as a laser, the scattered intensity measured by a detector located at some point in space will be dependent upon the relative positions of the particles within the scattering volume (FIG. 5.1). Such a dependence of the scattering intensity arises from constructive and destructive interference of the scattered light waves. Since particles are diffusing according to Brownian motion, the scattering intensity fluctuates about an average value equivalent to the static intensity. These fluctuations are known as the dynamic intensity. Across a long time interval, the dynamic signal appears to be representative of random fluctuations about a mean value. When viewed on a much smaller time scale, however, it is evident that the intensity trace is in fact not random, but rather composed of a series of continuous data points. This absence of discontinuity is a consequence of the physical confinement of the particles to be in a position very near to the position occupied a very short time earlier.

Correlation is a second order statistical technique for measuring the degree of non-randomness in an apparently random data set. When applied to a time dependent intensity trace, as measured with a dynamic light scattering instrument, the correlation coefficients are calculated as shown below, where  $\tau$  is the delay time:

$$G(\tau) = \int_0^{\infty} I(t)I(t + \tau)dt \quad (5.1)$$

## 5 Methods

Typically, the correlation coefficients are normalized such that  $G(\infty) = 1$ . For monochromatic laser light, this normalization imposes an upper correlation limit of 2 for  $G(t_0)$  and a lower baseline limit of 1 for  $G(\infty)$ . In dynamic light scattering instruments, a digital correlate adds and multiplies continuously short time fluctuations in the measured scattering intensity, to generate the correlation curve for the sample. All information regarding the motion or diffusion of particles in the solution is embodied within the measured correlation curve. For monodisperse samples, consisting of a single particle-size group, the correlation curve can be fit to a single exponential, as given in the following expression:

$$I(t)I(t + \tau)dt = A + Be^{-2q^2D\tau} \quad (5.2)$$

where  $A$  is the baseline,  $B$  is the amplitude, and  $D$  is the diffusion coefficient. The scattering vector,  $q$ , is defined by:

$$q = \frac{4\pi n}{\lambda_0} \sin\left(\frac{\theta}{2}\right) \quad (5.3)$$

where  $n$  is the solvent refractive index,  $\lambda_0$  is the vacuum wavelength of the laser (633 nm), and  $\theta$  is the scattering angle ( $173^\circ$ , i.e. back-scattering conditions). The hydrodynamic radius of a particle is defined as the radius of a hard sphere that diffuses at the same rate as the particle under examination. Such a radius is calculated using the particle diffusion coefficient,  $D$ , and the well known STOKES-EINSTEIN equation.

$$R_H = \frac{kT}{6\pi\eta D} \quad (5.4)$$

where  $k$  is the BOLTZMANN constant,  $T$  is the absolute temperature and  $\eta$  is the dispersant viscosity. A single exponential or Cumulant fit of the correlation curve is the usual fitting procedure. The hydrodynamic size extracted using this method corresponds to an intensity weighted average called the *Z average*. The width of the particle size distribution is described by the *polydispersity*, which is derived from the *polydispersity index*, which in turn is calculated from a Cumulants analysis of the DLS measured intensity auto-correlation function. It is important to note that the Cumulants analysis algorithm does not yield a distribution: it gives only the intensity weighted Z average and the polydispersity index. If one were to assume a single size population following a Gaussian distribution, then the polydispersity index would be related to the standard deviation ( $\sigma$ ) of the hypothetical Gaussian.

While the Cumulant algorithm and the Z average are useful for describing general solution characteristics, for multimodal solutions consisting of multiple particle size groups, the Z average can be misleading. For multimodal solutions, it is more appropriate to fit the correlation curve to a multi-exponential function.

**Lipid concentration.** The concentration of lipids in the sample is an important parameter for the analysis of the activity of membrane peptides. It was determined with

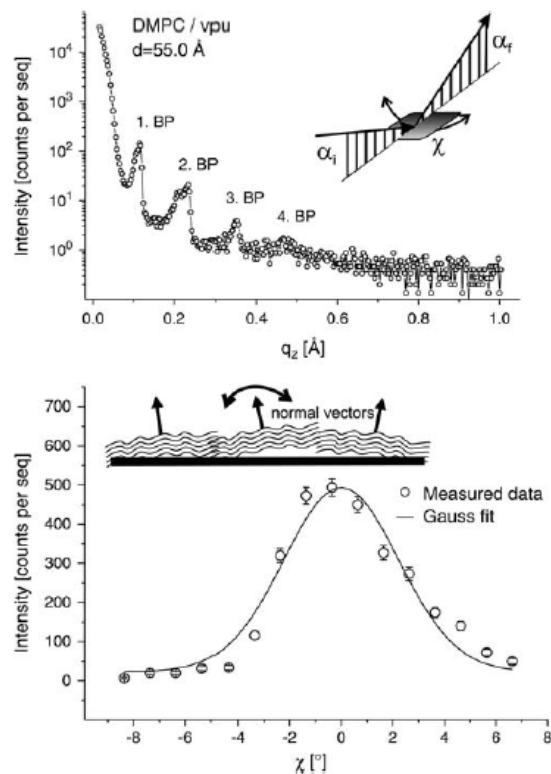


**Fig. 5.2 : Determination of mosaicity of oriented multibilayers.** Bilayer stacks are formed over the surface of a flat substrate. For example a Ge glass plate is commonly used in ATR-FTIR spectroscopy (see SEC. 5.2.2). *Top*: X-ray reflectivity curve of the multilamellar membranes under specular conditions (see FIG. 5.11) showing different BRAGG peaks (BP). The scattering geometry is shown in the inset. *Bottom*: The  $\chi$  scan on the first Bragg peak (labeled 1 BP in the figure) is fit to a Gaussian mosaicity function with standard deviation  $\sigma$ , being a measure for the probability distribution of local membrane normal vectors (see sketch in inset). Reprinted from Biophysical Journal, Volume 89 [386] ©2005 with permission from the Biophysical Society.

the help of a commercial kit (Phospholipids-B, from Wako), consisting of an enzymatic-colorimetric assay based on the hydrolysis of choline-containing phospholipids. Free choline is then coupled to a series of reactions ending up with the formation of a colored product which can be easily quantified with spectrophotometry. Choline solutions of known concentration are used to build a reference curve, where the measured sample absorbance is interpolated to get the phospholipid concentration.

**Mosaicity.** The orientational distribution of aligned membrane stacks, or mosaicity,  $\sigma$ , can be measured by a  $\chi$  scan where the sample is rocked around an axis in the plane of incidence of X-rays, symmetrically around the specular position [386] (see FIG. 5.2). First, a scattering profile of the peptide, reconstituted in lipid bilayers, was obtained in order to determine the location of the first BRAGG peak (see SEC. 5.2.3). Subsequently,

the angle of the X-ray source and detector are set according to the first Bragg reflection. The sample is then gradually tilted ( $\chi$ -scanned) around an axis perpendicular to the X-ray beam. The maximal reflectivity intensity,  $I$ , is plotted as a function of the  $\chi$  angle and fit with a Gaussian distribution function with mean,  $\mu$ , and standard deviation,  $\sigma$ :

$$I(\chi) = b + \frac{C}{\sqrt{2\pi}\sigma} e^{-\frac{(\chi-\mu)^2}{2\sigma^2}} \quad (5.5)$$

where  $b$  is the baseline and  $C$  is a correction factor.  $\sigma$  constitutes the orientational distribution (mosaicity) of the bilayer.

### 5.1.2 Peptide synthesis and purification

**Solid phase peptide synthesis.** Peptides derived from human (*Homo sapiens*) Bax<sup>1</sup> and mouse (*Mus musculus*) Bcl-xL<sup>2</sup> were prepared using automatic *solid-phase peptide synthesis* (SPPS) with Fmoc (fluorenylmethyloxycarbonyl) chemistry [387] (see SUB. 6.1.2 for details). We chose the ChemMatrix resin, which is specially useful for difficult sequences [388]. Peptides are assembled by coupling amino acids one by one while the peptide chain grows in the “unnatural” sense, from C-terminus to N-terminus (see FIG. 5.3). Each cycle consists on the following steps: (i) The Fmoc in the protected  $\alpha$ -amino group of the growing chain is removed in basic media (piperidine). (ii) The amino acid that follows in the sequence is *activated* with HBTU/DIEA at its  $\alpha$ -carboxyl group, while kept Fmoc-protected at the  $\alpha$ -amino, to enhance the coupling efficiency and subsequently transferred to the reaction vessel [389]. (iii) Any unprotected growing peptide that failed coupling with the new amino acid is *capped* at the N-terminus with an acetyl group so as to prevent reactions for these free sites in subsequent coupling cycles. The combination of Fmoc protection with HBTU activation is often called FastMoc chemistry, due to the speedy nature of the reaction. At the end of all cycles peptides are N-terminal acetylated. After synthesis, peptides are cleaved off the resin and deprotected in order to remove the side chain protecting groups, usually with a mixture of scavengers in presence of trifluoroacetic acid (TFA) [390]. The nature of the C-terminus depends on the type of resin and cleavage conditions. All our peptides are C-terminal amidated. Cleaved peptides are precipitated and washed with several centrifugation steps. The crude powder is then dried and ready to be purified.

**Peptide purification.** Crude peptides were purified by preparative *reversed-phase high performance liquid chromatography* (RP-HPLC). Chromatographic techniques separate the components of a mixture according to the differential velocity of each component through a stationary phase when they are moved through a mobile phase. In the particular case of HPLC, the stationary phase is composed of small silica particles tightly packed inside a column. The high area-to-surface ratio results in a strong resolution power, but due to the tight packing of gel particles, high pressure must be applied in order to obtain an appropriate flow. The most commonly used modality of HPLC for the

1 <http://www.uniprot.org/uniprot/Q07812>

2 <http://www.uniprot.org/uniprot/Q64373>

## 5.1 Sample preparation

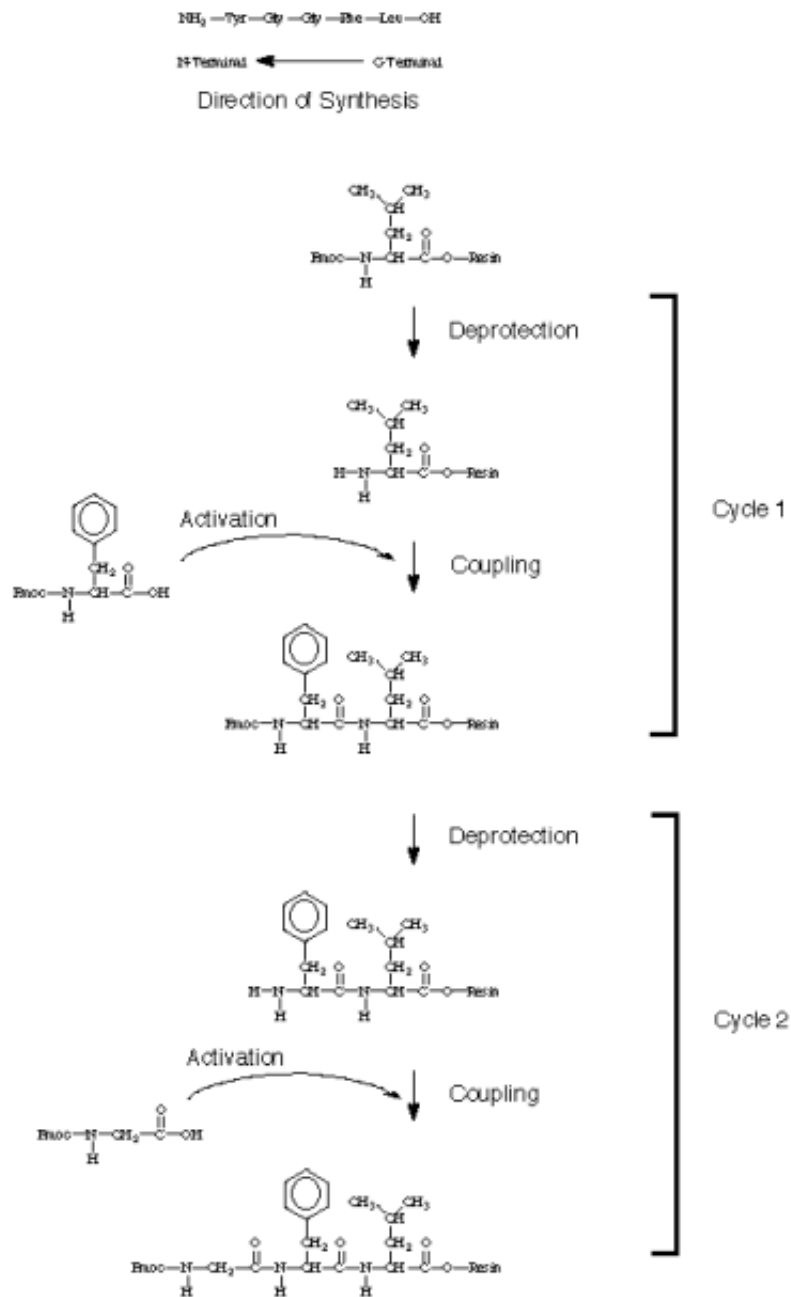


**Fig. 5.3 : Solid phase peptide synthesis.** The first step in chain assembly is deprotection, or removal of the Fmoc group by piperidine. A new amino acid is then coupled to the deprotected amino end of the growing peptide, forming a peptide bond and a *capping* step is performed to block non reactive sites (not shown in the figure). These steps are cyclically repeated to yield the desired sequence.

separation and analysis of peptide mixtures is the reversed-phase technique in which the silica beads are derivatized with hydrophobic hydrocarbon chains (usually with eighteen carbon atoms, so they are called C18 columns) while the eluent most often is a mixture of water, acetonitrile (ACN) and TFA [391, 392]. Reversed-phase chromatography separates the solutes on the basis on their hydrophobicity: hydrophilic compounds interact better with the polar mobile phase and elute first from the column, while hydrophobic compounds are retarded in the stationary phase and elute later. Peptides eluting from the column are detected by UV absorption. From a crude peptide sample usually several peaks are observed in the resulting chromatograms, although one of them is typically dominant. The elution samples corresponding to these peaks are collected and analyzed by mass spectrometry to determine which fractions contain the desired peptide sequence. The MALDI-TOF technique determines the mass-to-charge ratio of the different species within the sample although the peak intensities are not easily related to the amount of the corresponding compound [393]. A quantitative assessment of peptide purity is usually made by RP-HPLC, where the area of elution peaks is directly proportional to the amount of product. Fractions with more than 90% purity, assessed by the relative area of elution peaks, are pooled and lyophilized. For long-term storage, lyophilized peptides can be kept at  $-20^{\circ}\text{C}$ .

**Peptide quantification.** All peptide concentrations were determined by UV-Vis absorbance spectroscopy using the BEER-LAMBERT's law:

$$A(\lambda) = \epsilon(\lambda) C l \quad (5.6)$$

where  $A(\lambda)$  is the absorbance of the sample at a particular wavelength  $\lambda$  where the peptide is a chromophore,  $\epsilon(\lambda)$  is the molar extinction coefficient of the chromophore at the same wavelength and  $l$  is the path-length of the cuvette used for the measurement. In general we use  $\lambda = 280 \text{ nm}$  to make it coincide with the maximum absorption of the aromatic side chains (specially tryptophan and tyrosine) present in the sequence.  $\epsilon(280 \text{ nm})$  was estimated from the extinction coefficient of tryptophan and tyrosine amino acids in water (TAB. 6.2). For the peptides labeled with specific dyes,  $\lambda$  values within the visible region of the spectrum were also used and the corresponding extinction coefficients were assumed to be those of the free dyes (TAB. 6.2).

### 5.1.3 Protein expression and purification

**Cell culture and protein expression.** Mouse (*Mus musculus*) Bcl-xL<sup>1</sup>, with a histidine-tag (HHHHHH) in the N-terminus and a tobacco-etched virus (TEV) cleavage site (ENLYFQ/G) was cloned in the p11 plasmid (a pET11 derivative). Gene expression in the p11 vector is under the control of the *T7lac* promoter, which contains a *lac* operator sequence just downstream of the T7 promoter. For maintenance of the constructs, the *Escherichia coli* DH5 $\alpha$  host was used, but for expression purposes the plasmids were

---

<sup>1</sup> <http://www.uniprot.org/uniprot/Q64373>

transformed into *E. coli* BL21(DE3). This latter strain lacks several proteases and contains the lysogen  $\lambda$ DE3, which codifies for the RNA polymerase of the phage T7, under the control of the *lacUV5* promoter. Such a polymerase transcribes selectively genes regulated by the T7 promoter. Under normal conditions the expression of the protein of interest is not induced because of the constitutive repression of gene expression by the lac repressor *lacI*, which acts over both, the T7*lac* promoter (in the plasmid construct) and the *lacUV5* promoter (in the host chromosome).

Transformed BL21(DE3) cells are allowed to grow up to the exponential phase. Cell density monitoring can be easily done by measuring the optical density at 600 nm. When isopropyl  $\beta$ -D-1-thiogalactopyranoside (IPTG), a non-metabolizable analogue of lactose, is added to the culture medium, the *lacUV5* and T7*lac* promoters are unblocked. The first one initiates the expression of the T7 RNA polymerase, which in turn transcribes the target gene in the plasmid under the control of T7*lac*. Culture growing continues for several hours after induction to allow for sufficient protein production.

**Protein purification.** *E. coli* cells were collected by centrifugation and subsequently lysed in order to release the cytoplasmic proteins. This was accomplished with a combination of three procedures: (i) several rounds of freeze-thawing, (ii) addition of lysozyme, which is an enzyme that breaks the peptidoglycan layer of the bacterial cell wall, and (iii) sonication. Nucleases were also added to remove nucleic acids. The resulting protein extract was clarified by centrifugation and purified by *immobilized metal affinity chromatography* (IMAC). This chromatographic technique makes use of stationary phases with immobilized metal ions (usually  $\text{Ni}^{2+}$ ) which show high affinity for sequences with a few consecutive histidine residues. Since Bcl-xL has an engineered tag of six histidines, it is strongly bound to the column. Elution was achieved by addition of a large excess of imidazol that competes with the protein for binding to the  $\text{Ni}^{2+}$ . Eluted fractions were analyzed by SDS-PAGE, which separates proteins according to their size, and stained with Coomassie Blue for band visualization. The fractions with Bcl-xL were pooled and dialyzed in order to adjust the buffer to the desired composition. Dialysis allows the flow of low molecular weight solutes, but not proteins, which are retained inside by the dialysis membrane. In order to cleave off the poly-histidine tag, the TEV protease was incubated together with Bcl-xL at a 1/40 w/w protease/protein ratio. Cleavage mixtures were passed again through the  $\text{Ni}^{2+}$  column. Now, however, the Bcl-xL molecules lacking the histidine tag eluted in the flow-through. Protein purity was judged by SDS-PAGE and the Bcl-xL concentration was quantified by UV absorption spectroscopy using Eq. 5.6, as described for the case of peptides (SUB. 5.1.2). Pure fractions (>95%) were stored at -20 °C for use within a few days.

## 5.2 Structural studies

Membrane proteins constitute roughly one-third of all gene products and play key roles in cell function. However, they are poorly represented among the proteins of known structure at atomic-resolution, mainly because both, crystallography and NMR, encounter

strong difficulties when dealing with this type of proteins. In the case of X-ray diffraction, the limit lays in the conditions needed to grow crystals of membrane proteins. This involves the use of detergents for protein isolation, handling and crystallization, and although there is a good number of successful examples of structures of membrane proteins solved by this method<sup>1</sup>, the strategies required are still not easily generalizable as it is the case with water soluble proteins. On the other hand, modern high-resolution NMR is applied to isotropically, fast-rotating molecules in solution, which for the case of macromolecules is usually restricted to moderate sizes. For membrane proteins, this limits strongly the applicability of *liquid-state* NMR, because it prohibits the use of lipid vesicles, which tumble slowly in solution and where proteins move anisotropically, and forces investigators to work with either organic solvents or detergent micelles to mimic the membrane environment.

Thus, the media conventionally used for crystallography and NMR is very different from the membrane-water interface, which is the native environment of membrane proteins and is an important determinant of their structure and function. Therefore, the development of special biophysical techniques for studying the structure of membrane proteins under conditions closer to their native environment (bound to lipid membranes) is one of the most demanding problems of modern structural biology. Some such techniques are circular dichroism spectroscopy (CD) [394, 395], attenuated total reflection Fourier transform infrared spectroscopy [382, 396, 397] (ATR-FTIR), electron paramagnetic resonance spectroscopy (EPR) [398] and *solid-state* NMR spectroscopy (ssNMR) [383]. On the lipid side, structural information can be obtained by X-ray scattering (XS), ATR-FTIR and ssNMR, providing important insights about lipid conformation, orientation and dynamics [399–401].

In the following we introduce CD, ATR-FTIR and XS with more detail, since they were the structural methods employed for this Thesis.

### 5.2.1 Circular dichroism spectroscopy

CD allows the structural characterization of peptides and proteins at low resolution, both in simple water solutions and in model membrane systems, like detergents and lipid vesicles. This method provides information mainly about the secondary structure content of the polypeptide chain and is also useful for monitoring conformational changes, such as those that occur upon peptide or protein binding to membranes.

**Physics of CD.** Linearly polarized light can be described as a superposition of two circularly polarized light beams of equal phase and amplitude but opposite directions (FIG. 5.4). A projection of the combined amplitudes in a plane perpendicular to the propagation direction results in a vector of oscillating magnitude describing a *line*. When this light passes through a sample containing *optically active chiral* molecules, with a difference in absorbance for each of the two circularly polarized components, the amplitude

---

<sup>1</sup> Most of the 219 unique structures of membrane proteins or peptides known so far have been solved by X-ray diffraction. See databases at <http://www.mpdb.tcd.ie/> and <http://blanco.biomol.uci.edu/>.

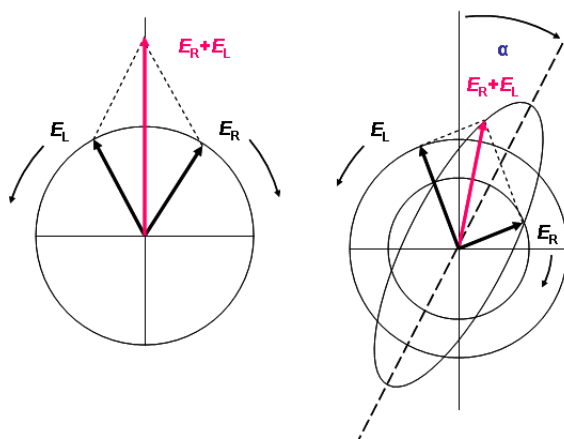


**Fig. 5.4 : The circular dichroism phenomenon.** The two components of linear polarized light, left circularly polarized light  $E_L$  and right circularly polarized light  $E_R$ , possess the same magnitude, and a projection of their combined amplitudes yields a line. If, however,  $E_L$  and  $E_R$  have different values, due to their differential absorption by a chiral compound, the resulting transmitted radiation is elliptically polarized. In practice, the observed effect is numerically very small and the ellipse would still approximate to a line. This corresponds to a very small ellipticity ( $\theta$ ) angle.

of the component absorbed more strongly will be smaller than that of the other component. The consequence is that, while the polarization direction does not change, the projection of the resulting amplitude now yields a vector for which both, amplitude and direction change, describing an *ellipse* instead of a line. Such a differential absorbance of the two circularly polarized components of incident linearly polarized light, to yield elliptically polarized light, is called *circular dichroism*.

CD is measured as the difference of absorbance of left ( $A_L$ ) and right ( $A_R$ ) circularly polarized light:

$$\Delta A = A_L - A_R \quad (5.7)$$

Considering the cell path-length and the concentration of the chromophore (Eq. 5.6), we arrive to an expression for the *molar circular dichroism*:

$$\Delta \epsilon = \epsilon_L - \epsilon_R = \Delta A / (Cl) \quad (5.8)$$

where  $\epsilon_L$  and  $\epsilon_R$  are *molar extinction coefficients* of  $L$  and  $R$  light respectively,  $C$  is the molar concentration and  $l$  is the path-length in cm.

$\Delta A$  and  $\Delta \epsilon$  are intuitive magnitudes, as they are derived from the familiar concepts used for UV/Vis absorbance spectroscopy, and this is also how modern CD instruments actually work. CD can also be expressed as *degree of ellipticity* ( $\theta$ ), which is defined as the tangent of the ratio of the minor to the major optical axes. It is very easy to inter-convert between  $\theta$  and  $\Delta A$  using:

$$\theta = 32.982 \Delta A \quad (5.9)$$

Thus,  $\theta$  can be manipulated in the same way as  $\Delta A$ . For instance, taking into account concentration and path-length according to BEER-LAMBERT's law, we can derive a measure of molar ellipticity ( $[\theta]$ ). Following polarimetric conventions,  $[\theta]$  is reported in degrees  $\text{cm}^2\text{dmol}^{-1}$ . Molar ellipticity can be calculated using the following equation:

$$[\theta] = 100 \Delta A / (C l) \quad (5.10)$$

However, in Polymer Science a useful unit is the *mean residue ellipticity*  $[\theta]_{MR}$ , which reports the molar ellipticity per residue, instead of that corresponding to the whole molecule. This, for example, allows easy comparison of CD spectra from different proteins, even if they have different molecular weights.  $[\theta]_{MR}$  can be calculated as follows:

$$[\theta]_{MR} = 100 \Delta A / (C_{MR} l) \quad (5.11)$$

where  $C_{MR}$  is the mean residue concentration, which is the protein concentration multiplied by its number of amino acid residues.

**CD in protein science.** Because chiral molecules are common in biological systems, there are a number of interesting applications for CD spectroscopy in Biological Sciences [394]. A very common use of this method is the identification and relative quantification of the secondary structure components in a protein or a peptide. Polypeptides present at least three types of chromophore in the UV-Vis region: (i) the side chains of aromatic residues, which absorb light in the range 260-320 nm; disulphide bridges, which absorb below 240 nm; and peptide bonds, which absorb also below 240 nm. The latter is the only type of chromophore present in all polypeptides. In its region of absorption there are two electronic transitions, one corresponding to a weak and broad band centered around 220 nm and a second one of stronger intensity around 190 nm. These transitions depend on the local chemical environment of the chromophore, and hence they are sensitive to the secondary structure of the protein. In practice different secondary structure elements display characteristic CD spectra.

Prediction algorithms allow estimating the secondary structure content using far-UV CD spectra [402]. Most prediction programs are based on databases containing CD spectra of proteins whose structure has been solved crystallographically. A very convenient resource for CD spectra analysis is DichroWeb<sup>1</sup>, which is an on-line interface for the use of several open source algorithms (including CONTINLL, SELCON3, CDSSTR, VARSLC and K2D) [403]. Importantly, all of these programs, except K2D, rely upon reference data-sets of proteins, but unfortunately, most databases do not include structures of peptides. Moreover, the structure of these molecules tends to be highly dependent on solution conditions, and particularly it varies in lipidic with respect to aqueous environments. K2D is also different from other algorithms as it is based on a neural network.

---

<sup>1</sup> <http://dichroweb.cryst.bbk.ac.uk/html/home.shtml>

In any case, one must be very cautious when applying such algorithms for secondary structure predictions of peptides [404], especially in a membrane bound state.

Another source of uncertainty is due to the absence of information corresponding to the far-UV region (down to 180 nm) in CD spectra, or to the low quality of the band registered in this region by conventional CD instruments. This part of the spectrum contains the most intense and sensitive band regarding secondary structure information. However, scattering artifacts occur also at these short wavelengths, which makes it difficult obtaining reliable spectra. This limitation is stronger when using dense media and especially in samples made of suspensions of large lipid vesicles, which is required for the study of membrane peptides and proteins. The aforementioned prediction algorithms, usually require CD data starting at least at 195 nm, which might not be achievable in samples with liposomes. In order to circumvent these problems most studies with membrane-active polypeptides are performed either in organic solvents or in detergent micelles. As an alternative, small unilamellar vesicles may be employed. Again, care must be taken in order not to over-interpret the results, since the number of predicted secondary elements will depend on the wavelength range used.

### 5.2.2 Infrared spectroscopy

The spectrum of the electromagnetic radiation between visible light and microwaves is known as infrared light. Its wavelength range (750 nm-1 mm) covers energy values corresponding to the vibrational transitions in molecules. The discrete energy levels of a harmonic oscillator are separated by  $h\nu$ ,  $h$  being the Planck constant and  $\nu$  the oscillation frequency. An IR photon with  $h\nu$  energy can be absorbed by the oscillator, which then goes from the ground-energy state to an excited state. The transition probability between the two vibrational levels is proportional to the square of the *transition dipole moment* (TDM). For simplicity, the vibration frequency can be approximated by the bond strength and the atom mass and can be therefore associated with particular bond types and isotopes. Thus, the absorption frequency,  $\nu$ , of a single bond between two atoms of masses  $m_1$  and  $m_2$  can be approximated to that of a *two-atomic oscillator*:

$$\nu = \frac{1}{2\pi} \sqrt{\frac{\kappa}{\mu}} \quad (5.12)$$

$$\mu = \frac{m_1 m_2}{m_1 + m_2} \quad (5.13)$$

where  $\kappa$  is the spring constant of the bond and  $\mu$  is the reduced mass of the atoms. A direct consequence of EQ. 5.12 and 5.13 is that the absorption frequency will differ when the mass of at least one atom is varied while maintaining the chemical nature of the bond, i.e., with different isotope versions of the atoms involved.

**Group vibrations in membrane spectroscopy.** As a result of the large number of vibrations and of the intrinsic width of vibrational absorption bands, IR spectra of large molecules are generally very complex and not well resolved in many regions. However, IR

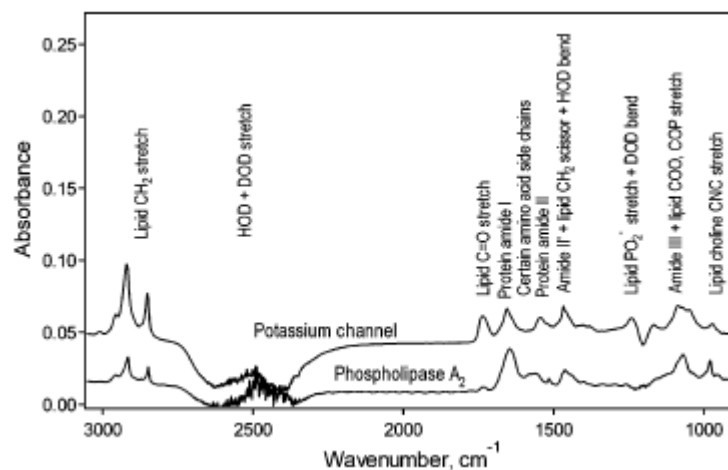


**Fig. 5.5** : ATR-FTIR infrared spectrum of phospholipid bilayers supported on a Ge crystal with reconstituted proteins. The position of lipid, protein and water absorption bands is clearly indicated. Reprinted with permission from [405] ©2003 American Chemical Society.

absorption bands at distinct group frequencies can still be assigned to various functional groups of protein, lipid and water molecules (see TAB. 5.1 and FIG. 5.5).

The infrared absorption frequencies of H<sub>2</sub>O, HOD, and D<sub>2</sub>O are listed in TAB. 5.1. Particularly important is the fact that the H<sub>2</sub>O bending mode at 1645 cm<sup>-1</sup> overlaps with the *amide I* mode of proteins. Thus, a relatively low water content in the samples is essential for measuring IR of proteins. Lipids absorb in many different regions of the IR spectrum (TAB. 5.1). The exact frequencies of the absorption bands associated with methylene vibrations of the fatty acyl chains depend on the physical state of these chains. Therefore, precise measurements of band progressions corresponding to CH<sub>2</sub> stretchings can be used to probe the physical state of lipids under various conditions.

Proteins give rise to backbone and side-chain vibrations. The approximate frequencies for the backbone amide vibrations are listed in TAB. 5.1. All amide frequencies are conformation-sensitive, but the *amide I* is by far the most widely used vibrational mode to characterize conformations of proteins. Several studies have proposed empirical correlations between amide I frequencies and the secondary structures of proteins, using as a reference proteins of known structure from X-ray crystallography studies. These correlations may be considered only as guidelines. Furthermore, there are proteins and peptides that absorb outside the frequency range given in the TAB. 5.2. It should also be noted that amide I frequencies decrease by 10 cm<sup>-1</sup> upon complete H/D exchange of the amide protons. Since unordered structures undergo H/D exchange at much higher rates than regular secondary structures, this effect is often used to distinguish between  $\alpha$ -helical and random structures which overlap in H<sub>2</sub>O, but are well separated after a relatively short time of exposure to D<sub>2</sub>O. The frequency of the *amide II* band decreases by about 100 cm<sup>-1</sup> upon H/D exchange of the amide protons. Therefore, this band has been frequently used to measure the extent of amide-proton exchange in proteins and

Tab. 5.1 : Principal IR absorption bands from membrane protein samples [397].

Assignment	Frequency (cm <sup>-1</sup> )
<i>H<sub>2</sub>O bending</i>	1645
<i>OH stretching</i>	3500-3200
<i>OD stretching</i>	2600-2400
<i>CH<sub>2</sub> antisymmetric stretching</i>	2920
<i>CH<sub>2</sub> symmetric stretching</i>	2850
<i>C=O stretching</i>	1730
<i>Amide A</i>	3300
<i>Amide I</i>	1700-1600
<i>Amide II</i>	1580-1500

Tab. 5.2 : Correlations between common protein secondary structures and amide I frequency [397].

Secondary structure	Amide I frequency (cm <sup>-1</sup> )
<i>Antiparallel <math>\beta</math>-sheet/ aggregated strands</i>	1675-1695
<i>Turn</i>	1660-1685
<i><math>3_{10}</math>-helix</i>	1660-1670
<i><math>\alpha</math>-helix</i>	1648-1660
<i>Unordered</i>	1652-1660
<i><math>\beta</math>-sheet</i>	1625-1640
<i>Aggregated strands</i>	1610-1628

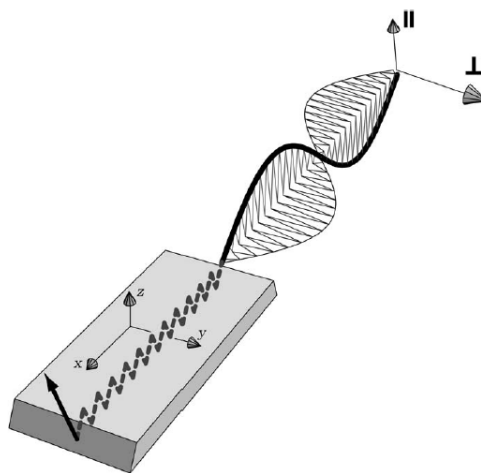


**Fig. 5.6 : Geometrical configuration of ATR-FTIR.** Supported bilayers are formed over a trapezoidal Ge crystal so that the membrane normal approximately coincides with the z axis. Two polarizations of light, parallel (||) and perpendicular ( $\perp$ ), are used to get the molecular orientation of the sample. The light beam is reflected several times within the Ge crystal and the resulting evanescent wave is used to probe the sample. Reprinted from Biophysical Journal, Volume 89 [386] ©2005 with permission from the Biophysical Society.

peptides. When measured in  $D_2O$ , the amide modes are referred to as amide I', II', etc.

**Transmission vs attenuated total reflection spectroscopy.** The most common experimental configuration in absorbance spectroscopy is a transmission experiment in which light passes through the sample and the absorbance is calculated from the intensities of transmitted and incident light. Although it is possible to extract structural information of membrane proteins, like orientation, from IR transmission experiments, they are of very little use because of their low sensitivity [406].

In *internal reflection* spectroscopy the sample is deposited on the surface of an IR-transparent crystal, named *internal reflection element* (IRE). For the analysis of lipid bilayer samples an IRE made of Germanium crystal is used. The IR beam is reflected within the internal reflection element and an *evanescent wave* of the same frequency as the incoming IR light is set up in the optically rarer medium which is immediately in contact with the IRE (FIG. 5.6). The amplitude of the electric field falls off exponentially with the distance from the interface of the two media, with a characteristic decay length or *depth of penetration*. Because in many typical applications the penetration depth is only in the order of a few hundred nm, internal reflection spectroscopy is a surface-sensitive technique. Samples, such as lipid membranes, that are deposited at the solid-liquid (or solid-gas) interface forming stacks of aligned multibilayers, absorb electromagnetic radiation of the evanescent wave, and thereby reduce the intensity of the reflected light. Hence, the technique is referred to as *attenuated total reflection spectroscopy*, or ATR. A major advantage of ATR spectroscopy is that absorption due to water and other molecules in the bulk solution is greatly reduced. Another advantage is

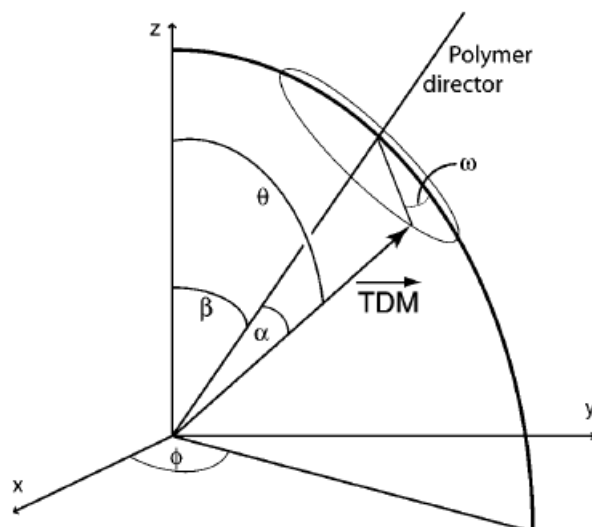


**Fig. 5.7 : Geometrical definitions in ATR-FTIR.** Schematic diagram of the angles that define the orientation of a chromophore TDM which is located in a rod-like polymer. See text for detailed definitions. Reprinted from Biophysical Journal, Volume 89 [386] ©2005 with permission from the Biophysical Society.

that molecular orientations can be easily determined in oriented samples using polarized light.

**Molecular orientation by IR: Geometrical definitions.** In order to retrieve spatial information from chromophores when using different polarizations of light, a set of axes must be defined. As the polarization of light is defined according to the IRE, in which the  $x,y$  plane is defined as its surface and  $z$  axis as the *normal*, one must make sure that the sample dispersed on the IRE (on the  $x,y$  plane) maintains the same coordinate system, which in practice means that it must be perfectly oriented on its surface. In order to achieve this, small vesicles are deposited over the IRE so that upon dehydration they fuse and spread forming multibilayer stacks corresponding to a smectic phase. This means that the normal of the supported bilayers is approximately also normal to the IRE (i.e., along the  $z$  axis) .

Any transition dipole moment (TDM) in a membrane peptide (we will use specifically the amide I) can be located in 3D space with respect to the smectic phase principal axis using a set of five angles (FIG. 5.7). These are defined as follows:

- $\alpha$  : the angle between the TDM and the helix director. In the case of the amide I mode,  $\alpha_{amide\ I}$  is measured to be  $39^\circ$  [407, 408]. This angle must be known in order to calculate  $\beta$  and  $\omega$  (defined next). For methylene stretching vibrations of lipid hydrocarbon chains in all-trans conformation  $\alpha_{CH_2} = 90^\circ$ .
- $\beta$ : the *tilt* angle of the peptide director axis with respect to the smectic phase principal axis ( $z$ ).  $\alpha$ -helical peptides can be modeled as rigid rods, so that the

## 5 Methods

peptide director would be a vector going from the middle bottom base of the cylinder to the middle top base. The *helix tilt* is a global peptide parameter; i.e., all amide I TDMs along the peptide sequence can be assumed to have the same  $\alpha$ .

- $\omega_i$ : the *rotational pitch angle* of the chromophore TDM of residue  $i$  about the peptide director. As opposed to  $\beta$ ,  $\omega_i$  is expected to be different for each residue within the peptide.  $\omega_i$  is defined arbitrarily as zero when the TDM, the peptide director and the  $z$  axis reside all in the same plane. As there are 3.6 residues per turn of a canonical  $\alpha$ -helix,  $\omega_i$  can be assumed to increment by  $100^\circ$  between each pair of consecutive residues. Additionally, assuming a canonical helix we may define a rotation angle for the complete helix, often named *helix polarity* or *azimuthal angle*, taken as the value of  $\omega_i$  for an arbitrary reference residue. In this Thesis we used the first residue in the sequence as the reference residue, and thus  $\omega_1$ , or simply  $\omega$ , reports the *helix azimuthal rotation*. In order to get information about  $\omega_i$  angles, it is necessary to use *site-specific* isotope labeled peptides, like  $1\text{-}^{13}\text{C}$  [409], Gly-D<sub>2</sub> [410], Ala-D<sub>3</sub> [411],  $1\text{-}^{13}\text{C}=^{18}\text{O}$  [410, 412]. The latter option is the most sensitive and it was the one used for this Thesis.
- $\phi$ : the rotation of the peptide director in the  $x,y$  plane (about the normal). As described above, the sample for ATR-FTIR measurements is a smectic phase, meaning that all lipids and embedded peptides are on average uniformly distributed in the  $x,y$  plane around the  $z$ -axis. i.e., the system exhibits uniaxial symmetry and the  $\phi$  angle is randomized.
- $\theta_i$ : the angle between the chromophore TDM of residue  $i$  and the smectic phase principal axis. As opposed to  $\omega$  there is no easy way to relate  $\theta$  among different residues along the sequences. However, with appropriate modeling it is possible to convert  $\theta_i$  into meaningful  $\beta$  and  $\omega$  (see SUB. 5.2.2).

For this Thesis we used mainly the the amide I vibrational mode. This has a unique absorbance frequency for  $\alpha$ -helices at  $\sim 1653\text{ cm}^{-1}$  and is sensitive to secondary structure. Upon double isotope labeling with  $^{13}\text{C}=^{18}\text{O}$  at specific sites, the absorbance frequency shifts by roughly 60 wavenumbers [412], making it easily detectable in the absorbance spectra. The TDM corresponding to the amide I mode originates on groups that belong to the peptide-bond plane: mainly the amide C=O, but also the C-N and N-H bonds. The vector that represents this vibration is tilted  $20^\circ$  from the C=O bond and crosses it at 0.0868 nm from the carbonyl carbon atom [413]. As defined above, this TDM forms the angle  $\theta$  with the  $z$ -axis, which can be easily extracted from a given structure (see SUB. 5.2.2).

**Dichroic ratios of oriented membrane peptides** The orientational information encoded within an IR spectrum can be extracted from measurements of the *dichroic ratio*,  $R$ . This is the quotient of the absorption of IR light polarized at two directions, usually parallel ( $\parallel$ ) and perpendicular ( $\perp$ ) polarized light:

$$R \equiv \frac{A_{\parallel}}{A_{\perp}} \quad (5.14)$$

The absorption of light is equal to the scalar product between the square of the axial electric field components  $\epsilon_x$ ,  $\epsilon_y$  and  $\epsilon_z$ , and the corresponding dimensionless integrated absorption coefficients  $\kappa_x$ ,  $\kappa_y$ , and  $\kappa_z$ . In the geometric configuration of ATR, the dichroic ratio is given by

$$R = \frac{\epsilon_x^2 \kappa_x + \epsilon_z^2 \kappa_z}{\epsilon_y^2 \kappa_y} \quad (5.15)$$

Given the polymeric nature of the peptide, the dichroic ratio can refer to either the average dichroic ratio of all absorbing TDMs along the molecule, denoted by  $R_{helix}$ , or the dichroic ratio corresponding to the vibrational mode of a specific amino acid residue, denoted by  $R_{site}$ . In the latter case, site specific information must be recorded, which is achieved by isotope-labeling, one by one, particular residues in the peptide sequence. For amide groups with natural isotopes, we deconvoluted the composite band in the 1800-1500  $\text{cm}^{-1}$  region, which includes the C=O stretching and the amide I and II absorption bands, into seven or eight Lorentzian-shaped bands. The Lorentzian band around 1650  $\text{cm}^{-1}$  corresponds to  $\alpha$ -helix structure and its integrated area was used to calculate  $R_{helix}^{exp}$  where the superindex *exp* refers to the experimental determination of this parameter. For specific isotope-labeled sites, an extra well-resolved absorption was observed around 1590  $\text{cm}^{-1}$ , corresponding to the displaced amide I  $^{13}\text{C}=^{18}\text{O}$  carbonyl stretching vibration [414, 415]. The area of this latter peak was used to calculate  $R_{site}^{exp}$ .

As mentioned above, the samples consisted of stacks of lipid bilayer membranes on the surface of a Ge crystal (used as the IRE). We employed the thick film approximation; i.e. we assumed that the lipid film is thicker than the penetration depth of the evanescent wave. The refractive indices of the lipid bilayer and the Ge crystal were taken as 1.43 and 4.0, respectively. Under these conditions the magnitudes of the electric field components are  $\epsilon_x = 1.399$ ,  $\epsilon_y = 1.514$ , and  $\epsilon_z = 1.621$  [416].

The integrated absorption coefficients  $\kappa_x(\alpha, \beta, \omega_i)$ ,  $\kappa_y(\alpha, \beta, \omega_i)$ , and  $\kappa_z(\alpha, \beta, \omega_i)$ , for a single chromophore TDM are used to calculate  $R_{site}$ . They are related to the square of the projection of the TDM over the axes  $x$ ,  $y$ , and  $z$ , respectively, as [414]:

$$\begin{aligned} \kappa_x(\alpha, \beta, \omega_i) = & \frac{\cos(\beta)^2 \cos(\omega_i)^2 \sin(\alpha)^2}{2} + \cos(\alpha) \cos(\beta) \cos(\omega) \sin(\alpha) \sin(\beta) + \\ & + \frac{\cos(\alpha)^2 \sin(\beta)^2}{2} + \frac{\sin(\alpha)^2 \sin(\omega_i)^2}{2} \end{aligned} \quad (5.16)$$

$$\kappa_y(\alpha, \beta, \omega_i) = \kappa_x(\alpha, \beta, \omega_i)$$

$$\begin{aligned} \kappa_z(\alpha, \beta, \omega_i) = & \cos(\alpha)^2 \cos(\beta)^2 - 2 \cos(\alpha) \cos(\beta) \cos(\omega_i) \sin(\alpha) \sin(\beta) + \\ & + \cos(\omega_i)^2 \sin(\alpha)^2 \sin(\beta)^2 \end{aligned}$$

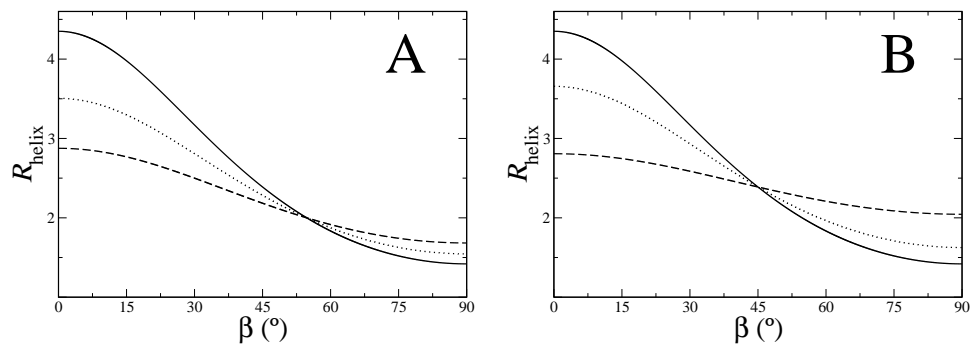


**Fig. 5.8 :** Theoretical dependence of the dichroic ratio arising from the full helix,  $R_{helix}$ , on the value of the tilt angle. A) Plot of  $R_{helix}$  as a function of  $\beta$  for different values of the fractional order parameter,  $f_\beta$  :  $f_\beta = 1$ (solid line),  $f_\beta = 0.75$  (dotted line) and  $f_\beta = 0.5$  (dashed line).  $R_{helix}$  does not depend on  $f$  for a tilt angle of  $54.7^\circ$ , i.e. at the magic angle. B) Plot of  $R_{helix}$  as a function of  $\beta$  for different values of  $\sigma_\beta$  :  $\sigma_\beta = 0^\circ$  (solid line),  $\sigma_\beta = 22.5^\circ$  (dotted line),  $\sigma_\beta = 45^\circ$  (dashed line).  $R_{helix}$  does not depend on  $\sigma$  for a tilt angle of  $45^\circ$ .

Integration through all possible pitch angles yields the dichroism for an  $\alpha$ -helix with vibrational modes rotationally distributed in a random fashion, which were used to calculate the  $R_{helix}$ :

$$\begin{aligned} \kappa_x(\alpha, \beta, \langle \omega \rangle) &= \frac{\sin(\alpha)^2}{4} + \frac{\cos(\beta)^2 \sin(\alpha)^2}{4} + \frac{\cos(\alpha)^2 \sin(\beta)^2}{2} \quad (5.17) \\ \kappa_y(\alpha, \beta, \langle \omega \rangle) &= \kappa_x(\alpha, \beta, \langle \omega \rangle) \\ \kappa_z(\alpha, \beta, \langle \omega \rangle) &= \cos(\alpha)^2 \cos(\beta)^2 + \frac{\sin(\alpha)^2 \sin(\beta)^2}{2} \end{aligned}$$

**Peptide orientations: First approximations assuming perfect order.** For cases where only  $R_{helix}$  is accessible (no isotope labeling, and thus no  $R_{site}$  possible) the assumption is made that all helices in the measured sample share the same  $\beta$  angle, which will be the only parameter that can be determined. Such a relationship is given by EQ. 5.15 and 5.16. A plot of  $R_{helix}$  as a function of  $\beta$  in a perfectly ordered sample is shown in FIG. 5.8 A and B as a solid line. The tilt obtained in this way is an upper limit value.

On the other hand, site-specific labeling allows obtaining extra experimental information, apart from  $R_{helix}$ , in the form of one value of  $R_{site}$  per each labeled residue. Therefore, it permits determining both  $\beta$  and  $\omega$  [414] and defining completely the relative orientation of the helix in the lipid bilayer. The dependence of  $R_{site}$  on the rotational angle for different tilt angles, assuming a single helix tilt and a single helix rotation (well ordered and static orientation) is shown in the first column of FIG. 5.9 A and B.

**Dealing with orientational disorder.** Above, we have assumed a single orientation of the membrane-embedded peptides (no disorder and/or dynamics) and a monomeric state

of such peptides. However, these two approximations might be unrealistic for most systems. In particular, a distribution of orientational angles of the helix, either the tilt, the rotation or both, may be considered. This is usually done to account for deviations from ideal sample order, which would correspond to perfect flat alignment of all bilayers in the stack over the plane of the Ge crystal. On the other hand, even within well ordered lipid bilayer systems we may consider spatial and time-dependent deviations of the peptide orientation from an averaged or most probable state. The spatial disorder of the peptide (different orientations that interconvert slowly) is not likely in well equilibrated homogeneous samples and in the absence of lateral domains. However, time-dependent fluctuations of peptide orientation are a likely scenario for membrane-bound peptides in a monomeric state and even for the case of small aggregates, as it has been shown by ssNMR measurements [417] and molecular dynamics simulations [54, 57]. Because the characteristic time scale of IR spectroscopy is very small (smaller than picoseconds) compared with the correlation times typical for peptide reorientation in the membrane (nano to microseconds), an IR spectrum is like an instantaneous snapshot of all peptide orientations, regardless of them originating from spatial disorder or dynamic reorientation, meaning that peptide dynamics cannot be studied using this method. Thus, for the sake of clarity we will use the terms *order* and *disorder*, instead of dynamics, when considering variations of peptide orientation. Different levels of sample disorder, as well as the possibility of peptide oligomerization are described next.

**Implicit disorder: Using order parameters.** Traditionally, the disorder has been taken into account by an *orientational order parameter*,  $S$ , using a set of nested distributions [396, 418]:

$$S_{amide I}^{exp} = S_{memb} S_{helix} S_{amide I}^{TDM} \quad (5.18)$$

where  $S_{memb}$  represents the distribution function of the lipid membrane orientation with respect to the IRE,  $S_{helix}$  describes the orientation of the peptide director with respect to the membrane, and  $S_{TDM}$  describes the TDM orientation with respect to the peptide axis. Assuming  $S_{memb} = 1$ , i.e., perfect coincidence between the membrane normal and the  $z$  axis,  $\beta$  is then calculated as follows:

$$S_{helix} = \frac{\varepsilon_x^2 - R_{helix}^{exp} \varepsilon_y^2 + \varepsilon_z^2}{\varepsilon_x^2 - R_{helix}^{exp} \varepsilon_y^2 - 2\varepsilon_z^2} \left( \frac{3\cos^2[\alpha_{amide I}] - 1}{2} \right)^{-1} \quad (5.19)$$

$$\beta = \arccos \left[ \sqrt{\frac{2S_{helix} + 1}{3}} \right] \quad (5.20)$$

$S_{helix}$  can vary between -0.5 and 1. The limiting values correspond to orientations of the molecular axis of the peptide parallel or perpendicular to the membrane plane, respectively, and  $S=0$  means either an isotropic distribution of orientations (complete disorder) or a fixed orientation at  $54.7^\circ$ , the *magic angle*. The angle  $\beta$  calculated in this way can be interpreted as the *average* angle between the helix director and the  $z$  axis.

## 5 Methods

The use of order parameters does not involve any explicit description of the underlying distribution of orientations, and thus several distributions will be valid. In the following we describe alternative strategies to model orientational disorder by assuming explicit orientational distributions.

**Modeling disorder explicitly with Gaussian distributions.** Unfortunately, the order of the sample is difficult to characterize and to model properly. A simple, first attempt was made by FRASER, who distinguished between the fraction of perfectly ordered material with a particular helix tilt,  $f_\beta$ , and a fraction  $1 - f_\beta$  with random orientation [419]. As an alternative, we will consider continuous probability distributions of the angular variables of *normal* (or Gaussian) type. These are characterized by a most probable value (the mean of the distribution) and the standard deviation, which is a measure of the *width* of the distribution. Gaussian distributions are very often used for the statistical analysis of random variables in natural sciences. In fact, they have been used before to model the orientation of helical peptides in membranes, for the analysis of ATR-FTIR [420] and ssNMR data [421, 422] and for the study of the dynamics of membrane peptides using simulation methods [57, 423].

We start considering the case where the tilt angle of a helical peptide in a membrane follows a Gaussian distribution. The probability density function giving the relative frequency of  $\beta$  values will then be [420]:

$$P(\beta) = \frac{1}{\sigma_\beta \sqrt{2\pi}} e^{-\frac{(\beta - \bar{\beta})^2}{2\sigma_\beta^2}} \quad (5.21)$$

where  $\bar{\beta}$  and  $\sigma_\beta$  are the mean and the standard deviation of the tilt angle, respectively. The following equivalencies between  $\beta$  and  $\{\bar{\beta}, \sigma_\beta\}$  apply [420]:

$$\cos(\beta)^2 = \frac{1}{2} + \frac{\cos(2\bar{\beta})}{2e^{2\sigma_\beta^2}} \quad (5.22)$$

$$\sin(\beta)^2 = \frac{1}{2} - \frac{\cos(2\bar{\beta})}{2e^{2\sigma_\beta^2}}$$

$$\cos(\beta) = \frac{\cos(\bar{\beta})}{e^{\sigma_\beta^2/2}}$$

$$\sin(\beta) = \frac{\sin(\bar{\beta})}{e^{\sigma_\beta^2/2}}$$

When substituting them in EQ. 5.16 and 5.17 one obtains the equations for the integrated absorption coefficients, both for single chromophores on a helix and rotationally averaged values, modeling the tilt disorder as a Gaussian distribution. Note that  $f_\beta$  and  $\sigma_\beta$  are inversely correlated, i.e., the larger the value of  $\sigma_\beta$ , the smaller the value of  $f_\beta$ , and *vice versa* [420].

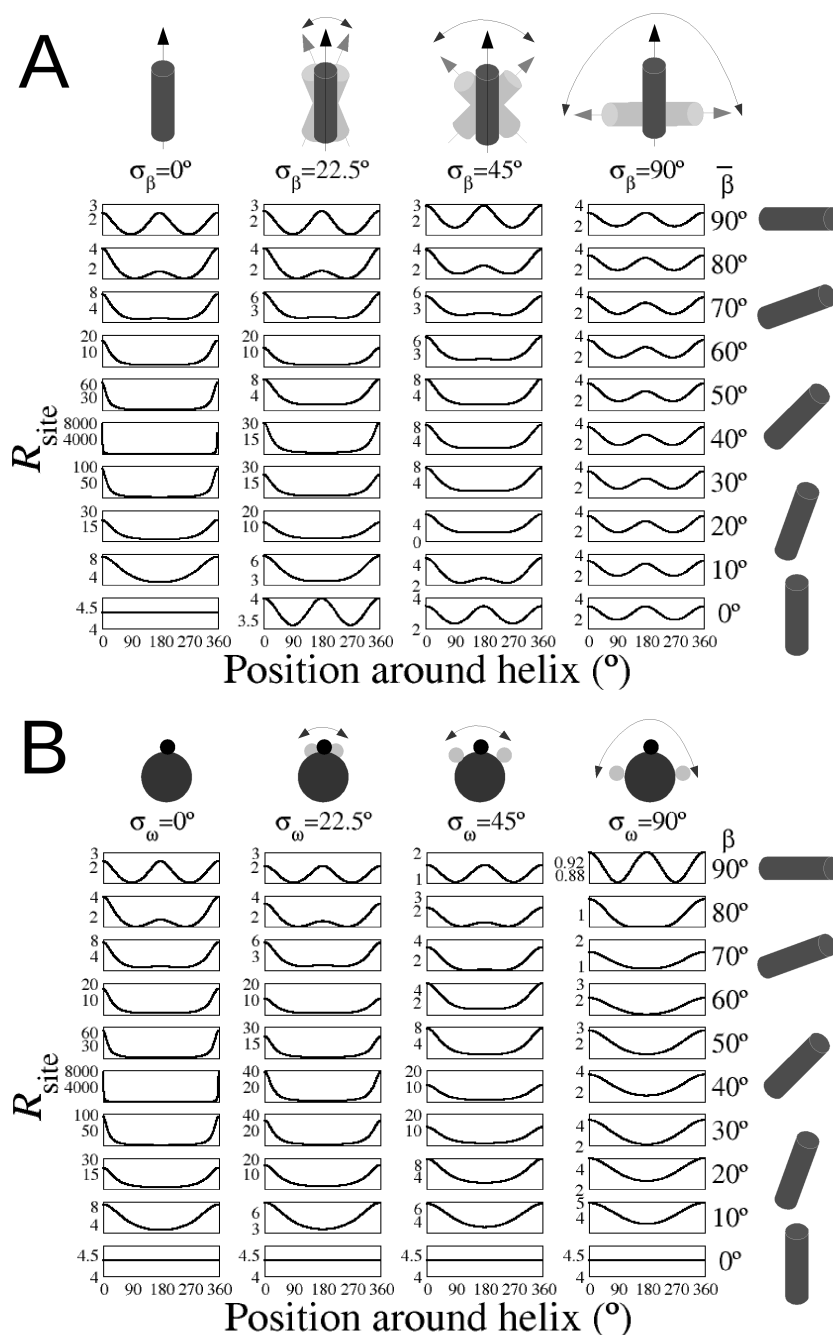


**Fig. 5.9** : Theoretical dependence of the dichroic ratio for a particular  $1\text{-}^{13}\text{C}=^{18}\text{O}$ -labeled residue ( $R_{site}$ ) as a function of the angular position of that residue,  $\omega_i$ , around the helix for different  $\beta$  angles. A) Effect of considering a Gaussian distribution of tilt angles with mean  $\bar{\beta}$  (shown on the right) and standard deviation  $\sigma_{\beta}$  (indicated above each column) and a single value of  $\omega_i$ . B) Effect of considering a Gaussian distribution of rotational angles with mean  $\bar{\omega}_i$  and standard deviation  $\sigma_{\omega_i}$  (indicated above each column) and a single value of  $\beta$  (shown on the right). In panels A and B  $\omega_1 = 0^{\circ}$  and  $\bar{\omega}_1 = 0^{\circ}$ , respectively. Other values of either  $\omega_1$  or  $\bar{\omega}_1$  simply result in horizontal shifts of the curves.

## 5 Methods

In previous work reported in the literature [386, 424], the disorder of a stack of lipid bilayers aligned over the flat IRE surface has been assessed by the orientational distribution of the bilayer normal vectors, known as *mosaicity*,  $\sigma$ . Such a parameter can be obtained from X-ray scattering (XS) experiments performed on the same samples used for the ATR-FTIR measurements [386] (see page 61). Then, assuming that  $\sigma_\beta \approx \sigma$ , the tilt angle could be calculated explicitly from this value and  $R_{helix}$  (EQ. 5.15, 5.17 and 5.22). From that  $\omega_i$  can be calculated for each  $R_{site}$  without being restricted to the canonical helical pitch (EQ. 5.15 and 5.16). However, mosaicities determined from XS are very low (usually  $\sigma < 5^\circ$ ), and appear underestimated compared to values of  $\sigma_\beta$  reported from NMR data or MD simulations [57, 422], probably because they reflect only the disorder of lipids, which should be smaller than that of the embedded peptides.

A plot of  $R_{helix}$  as a function of  $\beta$  for different levels of sample disorder, considered either as fractional order ( $f_\beta$ ) or as Gaussian distributions of  $\beta$  (of width  $\sigma_\beta$ ), is shown in FIG. 5.8. Note that for the *magic angle* ( $\beta = 54.7^\circ$ )  $R_{helix}$  does not depend on the order of the sample. A similar theoretical plot of  $R_{site}$  as a function of the position around the helix is shown in FIG. 5.9 A for different values of  $\sigma_\beta$  and for different values of  $\beta$ .

Similarly to the case of  $\beta$ , we may also consider distributions of the rotational angle  $\omega$ , modeled ideally as Gaussian probability density functions:

$$P(\omega) = \frac{1}{\sigma_\omega \sqrt{2\pi}} e^{-\frac{(\omega - \bar{\omega})^2}{2\sigma_\omega^2}} \quad (5.23)$$

where  $\bar{\omega}$  and  $\sigma_\omega$  are the mean rotational angle and the standard deviation, respectively. In analogy with the case of  $\beta$  we can write the following relationships between  $\omega$  and  $\{\bar{\omega}, \sigma_\omega\}$ :

$$\cos(\omega)^2 = \frac{1}{2} + \frac{\cos(2\bar{\omega})}{2e^{2\sigma_\omega^2}} \quad (5.24)$$

$$\sin(\omega)^2 = \frac{1}{2} - \frac{\cos(2\bar{\omega})}{2e^{2\sigma_\omega^2}}$$

$$\cos(\omega) = \frac{\cos(\bar{\omega})}{e^{\sigma_\omega^2/2}}$$

which after insertion into EQ. 5.16 allows obtaining the integrated absorption coefficients for a single chromophore modelling the rotational disorder as a Gaussian distribution.

The rotational angle distributions have no effect on  $R_{helix}$ . In FIG. 5.9 B we display a plot of  $R_{site}$  as a function of the position around the helix for different values of  $\sigma_\omega$  and for different values of  $\beta$ . The distributions of  $\beta$  and  $\omega$  may be considered separately or simultaneously.

**Selection of best-fits.** Depending on the experimental data available and the model chosen for considering sample disorder a number of different strategies can be used for

the search of the orientation angles that best describe the system. This has been often made by solving the corresponding systems of equations. For example, in previous work at least two isotope-labeled versions of the studied peptide,  $i$  and  $j$ , have been measured and analyzed, yielding four experimental parameters  $R_{helix}^i$ ,  $R_{site}^i$ ,  $R_{helix}^j$ ,  $R_{site}^j$  and the following system of four equations [420]:

$$R_{helix}^i = F\{\bar{\beta}, \sigma_\beta\} \quad (5.25)$$

$$R_{helix}^j = F\{\bar{\beta}, \sigma_\beta\}$$

$$R_{site}^i = F\{\bar{\beta}, \sigma_\beta, \omega_i\}$$

$$R_{site}^j = F\{\bar{\beta}, \sigma_\beta, \omega_i + \Delta\}$$

where  $\Delta$  is the rotational difference between two site-specific labels. As we noticed above, for a regular canonical  $\alpha$ -helix  $\Delta = n \times 100^\circ$ , where  $n$  is the difference in residue numbers between the two labeled residues under investigation. When multiple site-specific dichroisms are available, they may be studied pair-wise [415].

However, by solving a system of equations, like EQ. 5.25, we obtain just a single solution, with no information outside the calculated pair of  $\{\beta, \omega\}$  values. Alternatively, more advanced methods assisted by molecular modelling, as well as implementations with robust procedures for error analysis can also be used (explained next). These evaluate simultaneously all labeled positions and have the additional advantage of allowing consideration of best-fit states as well as other states which are close to the absolute minimum error and might also be feasible solutions.

**Selection from an implicit orientational landscape.** For this Thesis we have introduced a new method of analysis of dichroic ratios that consists on first building a complete *implicit orientational landscape* for the peptide under study, assuming a rigid canonical  $\alpha$ -helix, made of all possible combinations of  $\beta$  and  $\omega$  angles, and then selecting the  $\{\beta, \omega\}$  state which best reproduce a set of measured experimental dichroic ratios. For that, theoretical ratios,  $R_{helix}^{theo}$  and  $R_{site}^{theo}$ , are back-calculated from each  $\{\beta, \omega\}$  state in the landscape, and their values compared with the measured experimental ratios,  $R_{helix}^{exp}$  and  $R_{site}^{exp}$ . The comparison and selection of the best case can be made according to the the *root mean square deviation* (RMSD) between the theoretical and experimental values, calculated from:

$$RMSD = \sqrt{\frac{\sum_{i=1}^m (R_{helix,i}^{exp} - R_{helix,i}^{theo})^2 + \sum_{i=1}^m (R_{site,i}^{exp} - R_{site,i}^{theo})^2}{2m}} \quad (5.26)$$

where  $m$  is the total number of measured  $R_{helix}^{exp}$ , which coincides with the number of  $R_{site}^{exp}$  data, since each labeled peptide contributes one  $R_{helix}^{exp}$  and one  $R_{site}^{exp}$ .

Alternatively, a  $\chi^2$  distribution can be used:

$$\chi^2 = \sum_{i=1}^m \left( \frac{R_{helix,i}^{exp} - R_{helix,i}^{theo}}{E_i^{helix}} \right)^2 + \sum_{i=1}^m \left( \frac{R_{site,i}^{exp} - R_{site,i}^{theo}}{E_i^{site}} \right)^2 \quad (5.27)$$

where  $E_i^{helix}$  and  $E_i^{site}$  are the experimental errors in the determination of  $R_{helix}^{exp}$  and  $R_{site}^{exp}$ , respectively, which are taken as the standard deviation of the experimental values.

Using any of these methods it is easy to evaluate the best-fit  $\{\beta, \omega\}$  state and any other alternative state which although different from the absolute minimum RMSD (or  $\chi^2$ ), is close to that value and might represent a feasible solution.

The RMSD- or  $\chi^2$ -guided selection also allows considering distributions of the tilt and rotational angles around certain mean values, which can be modeled as Gaussian distributions (see above, SUB. 5.2.2). In such a case, instead of selecting single  $\{\beta, \omega\}$  states, we would select the group of states corresponding to  $\{\bar{\beta}, \sigma_\beta, \bar{\omega}, \sigma_\omega\}$  parameters. However, including such a sophistication makes sense only when the error corresponding to the evaluation of fixed angles is still higher than the experimental error; otherwise there is no margin for selection of a particular distribution compared to the case of fixed values of the orientation angles.

**Rigid body modeling.** Using the data measured in ATR-FTIR experiments it is possible to build a molecular model by applying a *rigid-body modelling* strategy, as follows [424]: An ideal helix is constructed with defined dihedral angles. This helix is aligned so that its director axis coincides with the membrane normal. The helix is then tilted and rotated. Specifically, helix tilting is made in one degree increments, from  $0^\circ$  to  $90^\circ$  and for each tilt angle it is rotated from  $0^\circ$  to  $360^\circ$  also in one degree increments. This generates 32400  $\{\beta, \omega\}$  orientation states. For each state, the local  $\theta_i^{theo}$  angles of the labeled residues is extracted, and the corresponding  $R_{site,i}^{theo}$  are calculated from EQ. 5.15 and the following integrated absorption coefficients [424]:

$$\kappa_x = \frac{1 - e^{-2\sigma_\theta^2} \cos(\bar{\theta})}{4} \quad (5.28)$$

$$\kappa_x = \kappa_y \quad (5.29)$$

$$\kappa_z = \frac{1 + e^{-2\sigma_\theta^2} \cos(\bar{\theta})}{4} \quad (5.30)$$

where  $\bar{\theta}$  and  $\sigma_\theta$  are the mean and standard deviation of a Gaussian distribution of  $\theta$ . As explained above,  $\sigma_\theta$  can also be taken as the sample mosaicity determined in the X-ray scattering experiments. Additionally, from each generated structure  $R_{helix}^{theo}$  is calculated from EQ. 5.15 and 5.17 using an average value of  $\alpha$  calculated from the structure. Finally,  $R_{site,i}^{theo}$  and  $R_{helix}^{theo}$  values are compared with the corresponding *experimental* values,  $R_{site,i}^{exp}$  and  $R_{helix}^{exp}$ . The aforementioned  $\chi^2$  error function (EQ. 5.27) is then used as a penalty for guiding the search of the best-fit model. i.e., the state with the minimum penalty is selected to represent the 3D interpretation of the IR-measured data.

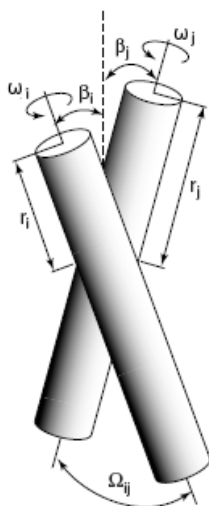


**Fig. 5.10 : Geometrical definitions in a peptide dimer.** In a bundle with  $n$   $\alpha$ -helices (helices  $i$  and  $j$  in this case),  $3n$  parameters can be used to describe the general structure, assuming that the helices are rigid: (1) the inclination of the helices with respect to the bundle axis,  $\beta$ , related to the crossing angle,  $\Omega_{ij}$ ; (2) the rotational angle about the helix director,  $\omega$ , which defines which side of each helix is facing towards the bundle core; and (3) the helix register,  $r$ , which defines the relative vertical position of the helix. Adapted from [425].

**Structural description of dimers and beyond.**  $\alpha$ -helical bundles represent a simple topology that can be described by a relatively small number of parameters: (1) helix tilt,  $\beta$ , (2) rotational position,  $\omega$ , and (3) register, which defines the relative vertical position of the helix (FIG. 5.10). Thus for any hetero-oligomer, 3 parameters are needed to describe the structure of each subunit, while for any symmetrical homo-oligomer only 2 parameters,  $\beta$  and  $\omega$ , are generally sufficient to describe the overall structure.

### 5.2.3 X-ray scattering

X-ray and neutron scattering in reflectivity geometry have been employed for a long time to investigate phospholipid membranes supported on solid surfaces and to deduce detailed structural parameters of the bilayer [426, 427]. Beyond pure lipid membranes, solid-supported membranes have further been used to study fundamental structural aspects of lipid-peptide interactions [428, 429].

FIG. 5.11 presents a diagram of an interface-sensitive scattering experiment. The incoming beam makes an angle  $\alpha_i$  with the plane of the bilayers, while the outgoing beam makes an angle  $\alpha_f$  and it can also deviate by an angle  $2\theta$  from the plane of incidence (defined by the incident beam and the bilayer normal, this latter coinciding with the  $z$  axis). For the X-ray reflectivity experiment, the reflected intensity is measured as a function of  $\alpha_i$  under specular conditions, i.e. at an exit angle  $\alpha_f = \alpha_i$  and out-of-plane angle  $2\theta = 0$ . Thus, the momentum transfer of the elastic scattering,  $q$ , is always along  $q_z$ , with the  $z$  axis parallel to the sample normal (FIG. 5.11). In contrast, moving

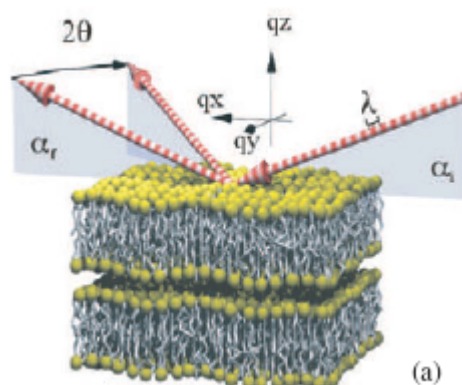


**Fig. 5.11 : Sketch of a X-ray scattering geometry.** The incidence angle  $\alpha_i$ , the reflection angle  $\alpha_f$  and the out-of-plane angle  $2\theta$  are represented. Under specular conditions,  $\alpha_i = \alpha_f$  the momentum transfer of the elastic scattering is along  $q_z$ . Therefore, information can be obtained about the vertical sample structure, i.e. the bilayer density profile. Reprinted from Journal of Physics: Condensed Matter, Volume 16 [430] ©2004 with permission from Institute of Physics.

the detector or the sample to  $\alpha_i \neq \alpha_f$  (diffuse or non-specular scattering) results in a component  $q_{\parallel}$  which is parallel to the sample surface. A reflectivity curve is a plot of the X-ray reflectivity intensity as a function of the vertical momentum transfer  $q_z$  which can be calculated as follows:

$$q_z = \frac{4\pi}{\lambda \sin(\alpha)} \quad (5.31)$$

where  $\lambda$  is the wavelength of the X-ray used. Reflectivity curves typically shows a set of sharp and intense equidistant peaks. Usually, the intensity and number of such BRAGG peaks decreases with P/L, which is indicative of peptide-induced lamellar disorder. These peaks are obtained in the diffraction pattern when scattered waves satisfy the BRAGG condition:

$$2d \sin(\alpha) = n\lambda \quad (5.32)$$

where  $d$  is the distance between the successive planes in the crystal lattice and  $n$  is an integer. In the case of multilamellar lipid membranes,  $d$  is often called the *lamellar repeat distance*.

The analysis of X-ray reflectivity requires a very low mosaicity (narrow orientational distribution of lipids) as well as a flat substrate, allowing a clear separation between the specular and non-specular components. In most published studies of oriented bilayers only the integrated BRAGG peaks of the the multilamellar samples are used for data analysis, and the one-dimensional vertical density profile  $\rho(z)$  (averaged in the  $xy$ -plane) is computed by FOURIER synthesis using a discrete set of FOURIER coefficients,  $f_n$ , according to [430]:

$$\rho(z) = \sum_{n=1}^{N_0} f_n v_n \cos \left[ \frac{2\pi n z}{d} \right] \quad (5.33)$$

where  $v_n$  are the phases. Due to mirror plane symmetry of the bilayer, the phases  $v_n = \pm 1$  are reduced to positive/negative signs only, facilitating the phase problem enormously. More problematic is the relationship between  $f_n$  and the experimental integrated intensities under the reflectivity curve,  $I_n$ . In the absence of a rigorous derivation we used the following approximation [431]:

$$f_n = I_n q z \quad (5.34)$$

## 5.3 Peptide-peptide interactions in membrane environments

Four major biophysical methods are commonly used to study transmembrane helix-helix association *in vitro*: SDS-PAGE [29], Förster resonance energy transfer (FRET) [432], sedimentation equilibrium studied by analytical ultracentrifugation [433, 434], and thiol-disulphide exchange [435]. More detailed molecular models can be obtained through the distance and orientational restraints provided by either EPR or NMR [436, 437]. A number of biological assays offer a complementary approach for addressing helix-helix interactions *in vivo* and have contributed significantly to our understanding of how membrane proteins self-associate in bilayers [438–441]. In this Thesis we have used SDS-PAGE and FRET to study the homo- and hetero-association between Bax $\alpha$ 5 and related Bcl-2 family polypeptides. SDS-PAGE was chosen because it is a fast technique which requires low sample amounts of unlabeled peptide and can thus be used as a oligomerization screening strategy. Selected peptides can be labeled and used in more detailed FRET analysis in lipid bilayers. In this section we will describe these two methods.

### 5.3.1 Electrophoretic methods: Tricine SDS-PAGE

Polyacrylamide gel electrophoresis (PAGE), which is based on the glycine-Tris buffer system, in the presence of the strongly denaturing anionic detergent sodium dodecyl sulfate (SDS) is the preferred method for the analytical separation of proteins. SDS unfolds and fully denatures proteins, essentially disregarding specific secondary structures or hydrophobic domains, and generates SDS-protein complexes that are mostly characterized by a uniform mass-to-charge ratio. This makes SDS-PAGE in general a very simple and reliable technique for protein separation and mass determination. However, glycine SDS-PAGE lacks resolving power in the low molecular weight regime, i.e., polypeptides smaller than  $\sim 10$  kDa. The use of tricine as the leading ion allows good separation efficiencies for peptides [442, 443]. However, in line with the frequent use of SDS as a mimic of the membrane environment, hydrophobic peptides and proteins can often be separated by SDS-PAGE in their native oligomeric state (monomers, dimers, etc.) [444]. In particular, the use of tricine SDS-PAGE for the determination of the oligomeric state

of transmembrane peptides is well established [445]. In general, these electrophoretic results agree well with other alternative methods, like analytical ultracentrifugation and resonance energy transfer. The tricine SDS-PAGE approach can, however, be the source of some artifacts. Molecular weight markers should be used with care since the electrophoretic mobility can be largely dependent on the primary structure especially in the case of hydrophobic sequences [446, 447]. Additionally, some amino acids are known to decrease the electrophoretic mobility, e.g. lysine residues, without causing dimerization [448]. Whenever possible, internal reference molecular weight markers should be used, i.e., sequences of known migration with a primary structure similar to that of the unknown sample.

### 5.3.2 Resonance energy transfer

When two fluorescent chromophores exhibiting overlap of their excitation and emission spectra are close to each other and at the appropriate orientation in space they may manifest an exchange of energy. This phenomenon is known as *Förster resonance energy transfer* (FRET)<sup>1</sup>, and it occurs between a donor (D) molecule in the excited state and an acceptor (A) molecule in the ground state. From an experimental point of view one observes a decrease in the fluorescence emission of the donor (i.e., quenching) and, in some cases, a concomitant increase in the fluorescence emission of the acceptor. However, this is a non-radiative process, since it does not involve emission and re-absorption of photons. Rather, the theory of FRET is based on the representation of fluorophores as oscillating dipoles which can exchange energy with one another, provided they have a similar resonance frequency. Therefore, an alternative, very common, expansion of the acronym FRET as *fluorescence resonance energy transfer* can be considered, *sensu stricto*, incorrect<sup>2</sup>.

The rate of energy transfer depends upon the extent of spectral overlap between the emission spectrum of the donor and the absorption spectrum of the acceptor, the quantum yield of the donor, the relative orientation of the donor and acceptor transition dipoles and the distance between the donor and the acceptor. Indeed, the most common biological application of FRET is the measurement of distances between donors and acceptors. Such distance measurements have resulted in the description of FRET as a “spectroscopic ruler” [450]. The distance at which FRET is 50% efficient is called the *Förster distance*,  $R_0$ , which is typically in the range of 2 to 6 nm. Energy transfer can be reliably assumed to occur whenever the donor and acceptor molecules are within the characteristic Förster distance and whenever sufficient spectral overlap occurs. The relative orientation of the donor and acceptor is also important and can modulate and even prevent energy transfer between closely spaced D/A pairs, but strong attenuation effects due to orientation are rare and can usually be neglected. Nonetheless, since we

---

1 The name refers to the German physical chemist THEODOR FÖRSTER (1910-1974), who first described this phenomenon [449].

2 Reading *fluorescence* for *F* in FRET, although widely done may be misleading, because there are cases when one of the two chromophores is not fluorescent and because, as pointed out above, the transfer of energy does actually not occur *via* fluorescence.

### 5.3 Peptide-peptide interactions in membrane environments

are going to use FRET to study helix association reactions in the membrane we will focus mainly on whether or not energy transfer occurs between D and A fluorescence labels supposedly at close proximity comparable to the Förster distance. In addition, the relative orientation between helices can be assessed, since a typical helix diameter is 1 nm. Depending on the placement of fluorescence groups with respect to the peptide ends, one can make predictions about the expected efficiency of energy transfer for parallel *versus* antiparallel associations and be able to distinguish between the two situations, for which a carefully quantitative analysis of FRET is essential.

**Theory of FRET**  $R_0$  can be expressed in terms of experimentally known values (or appropriate approximations) as follows:

$$R_0 = 0.211(\kappa^2 n^4 Q_D J(\lambda))^{1/6} \quad (5.35)$$

where  $\kappa^2$  is an orientation factor,  $n$  is the refractive index of the medium,  $Q_D$  is the quantum yield of the donor, and  $J(\lambda)$  is the spectral overlap integral. This latter is given by:

$$J(\lambda) = \frac{\int_0^\infty F_D(\lambda) \epsilon_A(\lambda) \lambda^4 d\lambda}{\int_0^\infty F_D(\lambda) d\lambda} \quad (5.36)$$

$F_D(\lambda)$  is the corrected fluorescence intensity of the donor with the total intensity (area under the curve) normalized to unity, and it is thus a dimensionless magnitude.  $\epsilon_A(\lambda)$ , typically in units of  $\text{M}^{-1}\text{cm}^{-1}$ , is the extinction coefficient of the acceptor at a characteristic wavelength  $\lambda$  (in nm). Thus,  $J(\lambda)$  is in units of  $\text{M}^{-1}\text{cm}^{-1}\text{nm}^4$  and the calculated  $R_0$  is in Å.

The efficiency of energy transfer ( $E$ ) is the fraction of photons absorbed by the donor which are transferred to the acceptor, and can be calculated from:

$$E = \frac{R_0^6}{R_0^6 + r^6} \quad (5.37)$$

which expresses the strong distance dependence around the value of  $R_0$  (FIG. 5.12). The efficiency quickly increases to 1.0 as the D/A distance ( $r$ ) decreases below  $R_0$ . Conversely, the transfer efficiency quickly decreases to zero if  $r$  is larger than  $R_0$ . Because  $E$  depends so strongly on distance, measurements are only reliable for  $r$  between  $\sim 0.5R_0$  and  $\sim 2R_0$ .

The transfer efficiency is typically measured using the relative fluorescence intensity of the donor, in the absence ( $F_D$ ) and in the presence ( $F_{DA}$ ) of acceptor:

$$E^{ss} = 1 - \frac{F_{DA}}{F_D} \quad (5.38)$$

where the term  $E^{ss}$  refers to a value of  $E$  derived from steady-state measurements. Incomplete labeling with the acceptor can be corrected as follows:

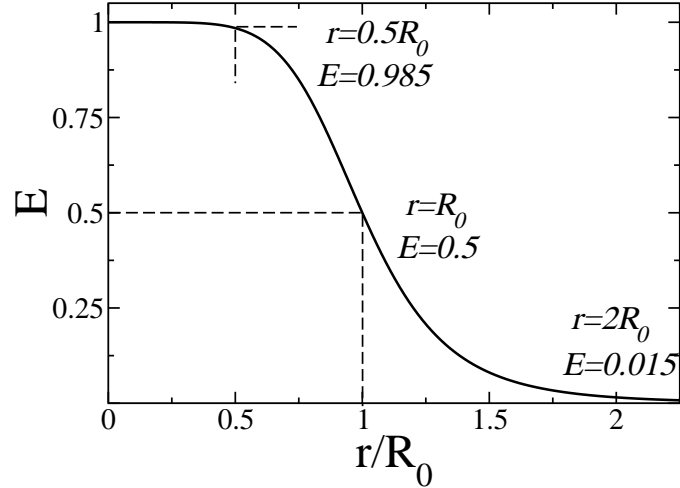


**Fig. 5.12** : Dependence of the energy transfer efficiency ( $E$ ) on distance between donor and acceptor ( $r$ ).  $R_0$  is the Förster distance. This dependence (Eq. 5.37) was first shown theoretically by FÖRSTER [449] and later verified experimentally [451].

$$E^{ss} = \left(1 - \frac{F_{DA}}{F_D}\right) \frac{1}{f_{label}} \quad (5.39)$$

where  $f_{label}$  is the fractional labeling with acceptor

The transfer efficiency can also be calculated from time-resolved experiments, denoted  $E^{tr}$ , using the amplitude-weighted lifetime of the donor in the presence,  $\langle\tau_{DA}\rangle$ , and absence,  $\langle\tau_D\rangle$ , of acceptor [452]:

$$E^{tr} = 1 - \frac{\langle\tau_{DA}\rangle}{\langle\tau_D\rangle} \quad (5.40)$$

These averages are proportional to the area under the decay curve and also to the steady state intensity and they are given by the sum of  $A_i\tau_i$  products:

$$\langle\tau\rangle = \sum_i A_i\tau_i \quad (5.41)$$

where the pre-exponential factor  $A_i$  is the amplitude of each  $i$  component at time 0, and  $\tau_i$  is the fluorescence lifetime of the  $i$  component. Both are calculated from multi-exponential fits of the fluorescence decay curves:

$$I(t) = \sum_i A_i e^{-t/\tau_i} \quad (5.42)$$

For our case we noticed that the presence of acceptors affect mainly the amplitude of the decay, with barely significant changes of the lifetime (see for example the Results in TAB. 8.6), and we reasoned that because tight dimerization should result in complete energy transfer from donor to acceptor, the quenching of the donor must be mainly *static*

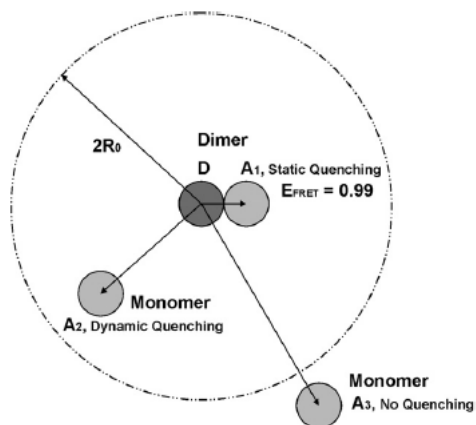


**Fig. 5.13 : Schematic illustration of the FRET-based analysis of dimer formation in membranes using lifetime measurements.** D and A denote donor- and acceptor-labeled molecules, respectively, capable of dimerization. A1 corresponds to an acceptor forming a dimeric complex with the donor, which results in total energy transfer. A2 is a diffusing acceptor which locates at a distance  $r < 2R_0$  from a donor molecule (at some moment during the donor lifetime) and thus causes dynamic-proximity FRET quenching of its fluorescence. A3 are free acceptors at a distance  $r > 2R_0$  from D monomers and thus cannot cause donor quenching. Reprinted from Analytical Biochemistry, Volume 380 [453] ©2008 with permission from Elsevier.

[453] (FIG. 5.13). In other words, a non-fluorescent ground-state complex between donor and acceptor is formed. If such a complex absorbs light, it would return immediately to the ground state without emission of a photon. Conversely, if the donor quenching is due to random proximity (case of *dynamic quenching* [453]), diffusive encounters between the donors and acceptors during the lifetime of the excited state would result in a decrease of the lifetime (FIG. 5.13). The amplitude-averaged lifetime is calculated as follows:

$$\bar{\tau} = \frac{\sum_i A_i \tau_i}{\sum_i A_i} \quad (5.43)$$

so that the dynamic contribution in a time-resolved experiment is given by:

$$E_{dynamic}^{tr} = 1 - \frac{\bar{\tau}_{DA}}{\bar{\tau}_D} \quad (5.44)$$

In a general real case, quenching would have both static and dynamic contributions, and their sum should be equivalent to the observed energy transfers in steady-state measurements:

$$E^{tr} = E_{static}^{tr} + E_{dynamic}^{tr} = E^{ss} \quad (5.45)$$

**Calculation of peptide-peptide distances in membranes** As we have just mentioned, the measured FRET efficiency,  $E^{ss}$ , of peptides in membranes is a sum of contributions due to the random colocalization of donors and acceptors ( $E_{proximity}^{ss}$ , related to

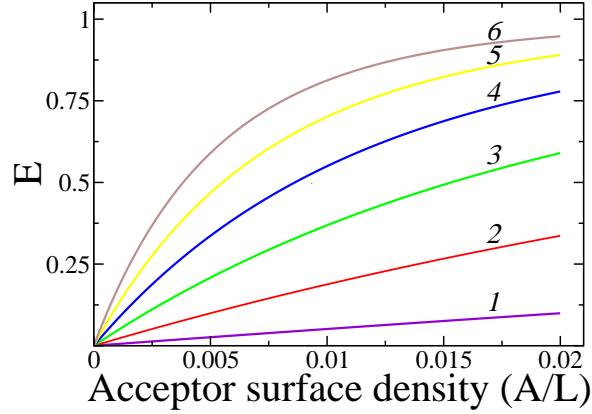


**Fig. 5.14 :** Calculated efficiencies of energy transfer for donor-acceptor pairs localized in the membrane ( $E_{proximity}^{ss}$ ). The numbers above the curves show the  $R_0$  values (in nm) used for the simulations (Eq. 5.47 [455]) The area per phospholipid was set to  $0.7 \text{ nm}^2$  (corresponding to a POPC molecule).

confinement in the limited membrane space) and due to sequence-specific interactions ( $E_{oligomer}^{ss}$ ) [454]:

$$E^{ss} = E_{proximity}^{ss} + E_{oligomer}^{ss} \quad (5.46)$$

$E_{proximity}^{ss}$  and  $E_{oligomer}^{ss}$  would be equivalent to the  $E_{dynamic}^{tr}$  and  $E_{static}^{tr}$  described above for the lifetime approach. When only steady-state information is available, FRET efficiencies due to proximity effects can be estimated computationally, as shown first by WOLBER and HUDSON [455] and later simulated by WIMLEY and WHITE [456] and by LI and co-workers [445]. FRET from randomly distributed peptides is calculated by averaging the donor quenching by acceptors in a specific configuration over a large number of acceptor configurations. The FRET efficiency of a donor by a specific acceptor configuration is given by

$$E_{proximity}^{ss} = \frac{1}{1 + \sum_i \frac{1}{(R_0/r_i)^6}} \quad (5.47)$$

where  $r_i$  is the distance between the donor and the  $i^{th}$  acceptor in the system and  $R_0$  is the Förster radius for the D/A pair. The simulation of FRET from random localization as the average of a large number of random acceptor configurations is shown in FIG. 5.14 for various  $R_0$  values and acceptor densities in the membrane (given as acceptor/lipid ratios). This nonspecific FRET is large for cases of fluorophores with large  $R_0$  values. When multibilayer vesicles are used, or for interfacially located peptides, there is also a small contribution from transbilayer FRET which was neglected in the subsequent derivations.

The FRET efficiency due to specific oligomerization can be presented as follows [457]:

$$E_{oligomer}^{ss} = f_o p_D E_o = E_{static}^{tr} \quad (5.48)$$

where  $f_o$  is the fraction of molecules in the oligomeric state,  $p_D$  is the probability for donor quenching in the oligomer and  $E_o$  is the FRET efficiency in the oligomer. For a dimer,  $E_o$  can be taken from EQ. 5.37. Additionally, any donor will be quenched if it oligomerizes with at least one acceptor, and therefore:

$$p_D = 1 - (1 - f_A)^{n-1} \quad (5.49)$$

where  $f_A$  is the fraction of acceptor-labeled molecules and  $n$  is the number of molecules in the oligomer. For the particular case of a dimer,  $f_o$  corresponds to the fraction of peptides in the dimeric state,  $f_{Di}$ , and EQ. 5.48 simplifies as follows:

$$E_{dimer}^{ss} = f_{Di} f_A \frac{R_0^6}{R_0^6 + r^6} \quad (5.50)$$

However, as  $n$  increases it becomes difficult to write out all the combinations in the expression of  $E_o$ . Approximations have been made assuming either equal energy transfer to all subunits [458, 459] or zero energy transfer to distant neighbors [460]. In a system with large subunits having dimensions comparable to, or larger than  $R_0$ , energy transfer beyond the adjacent subunit can be considered negligible. The first approximation (equal energy transfer) has been useful for distinguishing dimers from higher order oligomers, because the dimer is the only case where a plot of  $E$  vs  $f_A$  should be linear for any considered model. However, this approximation does not permit an accurate analysis of large oligomers. We follow here the approach developed by LI and co-workers [461]. For each donor-labeled subunit, energy transfer to each acceptor-labeled subunit within the oligomer is calculated explicitly, without any of the approximations discussed above. Symmetrically assembled, circular ring oligomers are assumed, for which theoretical equations (not shown here) are moderately complex. For each desired value of  $n$ , theoretical curves with  $R$  and  $f_{Mo}$  as variables, where  $R$  is the distance between dyes in neighboring subunits and  $f_{Mo}$  is the molar fraction of monomers ( $f_{Mo} = 1 - f_o$ ), are fit to the experimental pairs of  $E$  and  $f_A$ , minimizing the value of  $\chi^2$ .

## 5.4 Thermodynamic studies

### 5.4.1 Peptide-lipid interactions

The choice of an adequate conceptual framework for the study of the interaction between peptides ( $P$ ) and membrane lipids ( $L$ ) is a matter of debate [49, 462, 463]. One option is to treat this problem as a chemical equilibrium corresponding to the formation of a complex ( $PL_n$ ), of the type:



which assumes that a certain number of lipids (fixed stoichiometry) are *bound* per peptide in the complex. The *equilibrium association constant* ( $K_A$ , with units  $M^{-1}$ ) and the

## 5 Methods

number of lipids *bound* per peptide ( $n$ ) can then be calculated either using SCATCHARD plots [464] or from kinetic measurements [65]:

$$K_A = \frac{k_{on}}{k_{off}} \quad (5.52)$$

where  $k_{on}$  is the on-rate constant (binding reaction) and  $k_{off}$  is the off-rate constant (unbinding reaction).

The shortcomings of this approach have been discussed in the literature [462, 463, 465]. A major problem relates to the fluid nature of the lipid bilayer, which implies that the hydrophobic and electrostatic interactions driving the formation of peptide-membrane complexes arise from the collective properties and behavior of lipids in the bilayer ensemble. Thus, rather than considering defined groups of individual lipids bound per peptide in a particular binding site, the peptide should be better envisioned as interacting with the lipid assembly as a whole [462].

The alternative is to consider lipid bilayers and the aqueous medium as separate liquid phases. The association of peptides with membranes can then be treated as a partition between those two immiscible phases, and may be described by a characteristic *mole-fraction partition coefficient*, [24, 462, 463, 466]  $K_x$  (dimensionless), which can be approximated to:

$$K_x = \frac{[P]_b/[L]}{[P]_w/[W]} \quad (5.53)$$

with  $[P]_b$  and  $[P]_w$  being the bulk molar concentrations of the peptide attributable to the membrane and water phases, respectively,  $[L]$  is the bulk molar concentration of lipids and  $[W]$  the bulk molar concentration of water ( $[W]=55.3$  M). The partitioning framework will be the option adopted in the present Thesis. Nevertheless, for simplicity, we will often use the term *binding*, although referring generically to association with the membrane, not to individual lipids, and thus implying partitioning.

The characteristic constant  $K_x$  can be determined in dependence of  $[L]$  from the fraction  $f_p$  of the total amount of peptide partitioned into membranes, according to the following hyperbolic function:

$$f_p = \frac{K_x[L]}{[W] + K_x[L]} \quad (5.54)$$

For that, one needs to measure the amounts of peptide interacting with the membrane and peptides free in the bulk water (if the total amount of peptide is known, only either of the two is needed). This involves the use of well established methods from any of the following categories:

1. Physical separation of peptides bound to membranes (usually vesicles) from peptides free in solution, and subsequent quantitative analysis of each fraction. The separation is done using techniques like equilibrium dialysis [467], centrifugation [132] and chromatography [468], and quantification can be achieved through absorbance measurements after an HPLC run. These methods normally provide a direct measurement of  $f_p$ , from which  $K_x$  may be easily calculated. However,

the method chosen for separation must be effective and should not perturb the partitioning equilibrium.

2. Titration methods rely on the measurement of a certain property of the system, which should change upon membrane binding and be attributable specifically to the peptide in one of the two phases, with no need to separate them. In this case  $f_p$  is not obtained directly. Provided we can assume that it is proportional to the measured signal,  $K_x$  can be determined from the dependence of such a signal on  $[L]$ , according to EQ. 5.54. Spectroscopic techniques (such as fluorescence intensity or absorbance dichroism) are most often used for these measurements [463, 469], as well as other methods like titration calorimetry [466] and recordings of electrophoretic mobilities for determination of the  $\zeta$ -potential [470–472].

In the case of partitioning experiments using CD, the experiment is done by titrating a starting peptide solution with lipid vesicles which causes changes in the measured spectroscopic signal. Three parameters characterize the spectroscopic signal of a solution containing lipid at a concentration  $S(L)$ : the spectroscopic responses  $s_{min}$  and  $s_{max}$  of vesicles without peptide and fully saturated, respectively, and the partition coefficient  $K_x$ . These are related through

$$S(L) = f_p s_{max} + (1 - f_p) s_{min} \quad (5.55)$$

Because  $s_{min}$  is easily extracted from the experiment in the absence of lipids, there will be only two fitting parameters:  $K_x$  and  $s_{max}$ .

Finally, the free energy of transfer from water to bilayer is [462]:

$$\Delta G_x = -RT \ln K_x \quad (5.56)$$

FIG. 5.15 shows the thermodynamic cycle for peptide binding to the membrane interface and insertion into the bilayer. Note that according to the figure,  $\Delta G_x$  corresponds to  $\Delta G_{if}^{helix}$ .

### 5.4.2 Peptide-peptide interactions

The monomer/dimer equilibrium can be defined by the association constant  $K_{dimer}$  [445]:



$$K_{dimer} = \frac{[Di]}{[Mo]^2} \quad (5.58)$$

where  $[Di]$  is the dimer mole fraction (dimers per lipid) and  $[Mo]$  is the monomer mole fraction in the lipid vesicles (monomers per lipid) so that the total peptide concentration is  $[P] = 2[Di] + [Mo]$ . If the experiments are conducted using a fraction of donor peptide of 0.5 (and thus the fraction of acceptor peptide is also 0.5),  $E_{dimer}$  is a measure of  $[Di]/(2[Di] + [Mo])$ ; i.e., it is equal to half of the fraction of peptides in the dimeric

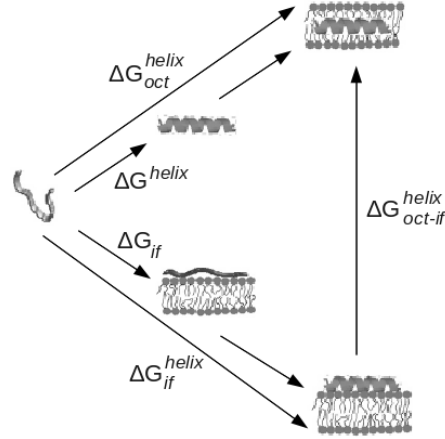


**Fig. 5.15 : Thermodynamic cycle for the transfer of a peptide from water to the bilayer interior.**

The folding equilibrium in water lies toward the unfolded state and is determined by  $\Delta G^{helix}$ , which is typically small in comparison with the other terms. The Gibbs energy of binding to the interface ( $\Delta G_{if}^{helix}$ ) includes contributions from peptide partitioning to the membrane ( $\Delta G_{if}$ ) and secondary structure formation, i.e. the partitioning-folding coupling. Transfer and folding as an  $\alpha$ -helix, from water to the bilayer interior is approximated by transfer to octanol ( $\Delta G_{oct}^{helix}$ ). The Gibbs energy of transfer from the surface to the interior of the bilayer is approximately  $\Delta G_{oct}^{helix} - \Delta G_{if}^{helix} = \Delta G_{oct-if}^{helix}$ . Adapted from Biophysical Journal, Volume 92 [473] ©2007 with permission from the Biophysical Society.

state.  $K_{dimer}$  is determined from a plot of the fraction of peptide dimeric species ( $f_{Di}$ ) versus the total peptide (per lipid) concentration:

$$f_{Di} = \frac{4K_{dimer}[P] + 1 - \sqrt{8K_{dimer}[P] + 1}}{4K_{dimer}[P]} \quad (5.59)$$

The free energy of dimerization then is given by:

$$\Delta G_{dimer} = -RT \ln K_{dimer} \quad (5.60)$$

Considering the HILL analysis formalism, Eq. 5.58 can be rewritten as follows [474]:

$$\ln \left( \frac{f_{Di}}{1 - f_{Di}} \right) = \ln(K_{dimer}) + h \ln[2Mo] \quad (5.61)$$

where  $h$  is the HILL coefficient, describing the cooperativity of “binding”:  $h=1$  (i.e. non-cooperative binding) when two monomers associate into a dimer (analogous to the binding of a ligand to a protein site) of defined structure. Anti-cooperative binding is found for  $h < 1$  which has been interpreted as heterogeneity in dimer structure.

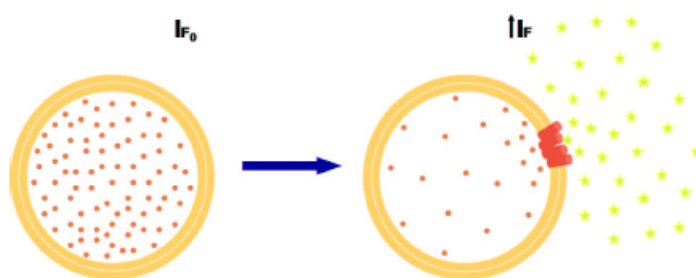


**Fig. 5.16** : Schematic representation of an experiment of contents release. The fluorescent probe is encapsulated inside vesicles. When the permeability of the bilayer is altered, the marker can exit the liposome and its fluorescence increases. Taken from [475].

## 5.5 Activity studies

### 5.5.1 Leakage experiments in ensembles of LUVs

A common experimental approach using model membranes to assess the permeability of the lipid bilayer is to load vesicles with fluorescent markers that change their intensity upon release. In order to study the leakage of water-soluble markers from liposomes, the fluorescent probe has to fulfill the following conditions: (i) it should not be capable of crossing the intact membrane, (ii) it should be highly water-soluble, with a very low solubility in organic media, i.e. it should not associate with membranes in any way, and (iii) it should be easily separated from liposomes by conventional methods.

**Self-quenching dyes.** Fluorescent dyes, like fluorescein isothiocyanate (FITC), carboxyfluorescein or calcein [476, 477], have the ability to self-quench at high concentrations (>50 mM) due to intermolecular interactions. When concentrated solutions of these water-soluble dyes are encapsulated into liposomes, they exist in the form of non-fluorescent complexes. Addition of permeabilizing agents causes dye dilution in the external medium and consequently increases the fluorescent intensity of the dye (FIG. 5.16), an event that can be conveniently monitored in a spectrofluorimeter. Leakage, given as the percentage of calcein release at any given time,  $R(t)\%$ , can be calculated as

$$R(t)\% = 100 \frac{F(t) - F_0}{F_\infty - F_0} \quad (5.62)$$

where  $F(t)$  is the measured fluorescence of protein-treated LUV at time  $t$ ,  $F_0$  is the initial fluorescence of the LUV suspension before protein addition, and  $F_\infty$  is the fluorescence value after complete LUV disruption by detergent addition. For comparison with dithionite quenching, which was taken at 250 s (see SEC. 5.5.2), release values were also taken at 250 s and are referred to as  $R_{250}^{\%}$ .

Carboxyfluorescein and its derivative calcein are the most frequently used dyes. Calcein is preferred over carboxyfluorescein because of its weaker tendency to interact with

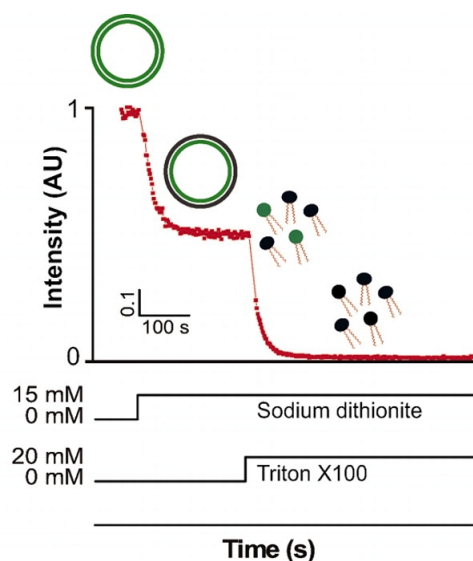


**Fig. 5.17 : NBD quenching by sodium dithionite.** Liposomes labeled symmetrically with NBD-lipids are prepared. For an intact membrane, externally added dithionite quenches NBD-lipids located in the outer membrane reducing the fluorescence intensity by approximately 50% after incubation for a few minutes. Basal fluorescence levels are determined after the addition of the detergent Triton X-100 which dissolves membranes and makes all NBD-labeled lipids accessible for quenching. Reprinted with permission from PNAS, Volume 106 [480] ©2009 National Academy of Sciences, USA.

membranes and its better photophysical properties, including a broad range of useful pH conditions. In so called fluorescein-labeled dextrans (FD), FITC is attached to dextran polysaccharides, which are complex, branched poly-glucose molecules of varying lengths used to investigate the size of the pores.

**Fluorescence quenching assay with ANTS/DPX.** This assay is based on the collisional quenching of the polyanionic fluorophore 8-aminonaphtalene-1,3,6-trisulfonate (ANTS) with the cationic quencher p-xylene-bispyridinium bromide (DPX) [478, 479]. For assays of vesicle leakage, ANTS (12.5 mM) and DPX (45 mM) can be co-encapsulated into liposomes. Upon vesicle poration, the release of the dyes in the medium surrounding the vesicles decreases their concentration. This causes an increase of the fluorescence of ANTS because quenching by DPX is diminished due to dilution. The extent of ANTS/DPX release is calculated according to Eq. 5.62. One advantage of using the ANTS/DPX pair is that the range of pH in which measurements can be performed is broader than in the case of self-quenching dyes. This property is specially useful for measuring leakage at low pH (below pH 5), where calcein fluorescence is very low.

### 5.5.2 Quenching of fluorescent lipids in ensembles of LUVs

Typical vesicle leakage assays are performed by measuring the release of encapsulated probes. However, in some cases is convenient to measure the internalization of added

reactants, since this gives a better control of the time when the assay is performed with respect to the moment of addition of the membrane porating agent. For this alternative strategy we analyze the quenching of NBD-labeled lipids from the internal monolayer by reduction in presence of sodium dithionite, added at the external solution. This method was originally developed by MCINTYRE and SLEIGHT to study lipid transbilayer asymmetry (FIG. 5.17) [481]. LUVs symmetrically labeled with NBD-lipids are prepared. Then, a membrane-active peptide is added to the vesicle suspension, and at any time one can test whether pores are open by adding the NBD-reducing agent. In an intact liposome the fluorescence intensity should drop approximately to half its initial value due to the fact that only the external (outer) leaflet will be available for quenching. If the remaining fluorescence intensity is less than 50%, it means that the quencher has gained access to internal monolayer lipids and one can interpret this as due to vesicle poration. Quenching levels ( $(Q(t)\%)$ ) were calculated according to:

$$Q(t)\% = 100 \frac{F_0 - F(t)}{F_0 - F_\infty} \quad (5.63)$$

where  $F_0$  is the initial fluorescence before quencher addition,  $F(t)$  is the fluorescence at time  $t$  and  $F_\infty$  is the fluorescence level when all lipids are accessible to the quencher and may be calculated following detergent addition as in the case of leakage experiments. However, we found that  $F_\infty$  was essentially zero under our experimental conditions. When comparing different experimental conditions (i.e. different P/L) quenching levels were taken at 250 s after dithionite addition,  $Q_{250}^\%$ . For comparison with the results of calcein release, differences between values in the presence ( $Q_{250}^{\%,pep}$ ) and absence ( $Q_{250}^{\%,mem}$ ) of peptide were calculated and expanded to a 100% scale as:

$$\Delta Q_{250}^\% = 2 \left( Q_{250}^{\%,pep} - Q_{250}^{\%,mem} \right) \quad (5.64)$$

### 5.5.3 Single vesicle experiments

**Theory of diffusion across a membrane.** For the analysis of the dye entry kinetics we consider the first FICK'S law of diffusion. This states that the rate of transport of a substance across a permeable membrane *per* area unit, or *flux*  $J_A$  (in units of  $mol\ cm^{-2}\ s^{-1}$ ) is directly proportional to the concentration gradient ( $\frac{dC}{dx}$ ), with the proportionality constant being the *diffusion* coefficient,  $D$ :

$$J_A = -D \frac{dC}{dx} \quad (5.65)$$

The integrated expression for  $x$  varying from 0 to  $m$  (the thickness of the membrane) and  $C$  varying from  $C_{out}$  to  $C_{in}$  is:

$$J_A = \frac{D}{m} (C_{out} - C_{in}) \quad (5.66)$$

where  $D/m = P$  is the *permeability* coefficient. For further developments of this theory, see SUB. 10.4.1.

**Kinetics of poration in the GUV ensemble.** The kinetics of appearance of porated GUVs ( $GUV_{pore}^{\%}$ ) can be used to estimate the rate constant of pore formation,  $k_{open}$ , as follows [85, 86]:

$$GUV_{pore}^{\%} = \Lambda \left( 1 - e^{-k_{open}(t-\Delta)} \right) \quad (5.67)$$

where  $\Lambda$  is an amplitude factor, taken as the apparent equilibrium percentage of porated GUVs (% of porated GUV after 2 h) and  $\Delta$  is the time required to start observing porated GUVs in the ensemble.

**Scanning fluorescence correlation spectroscopy (SFCS).** *Fluorescence correlation spectroscopy* (FCS) is a technique with single molecule sensitivity that analyzes the fluctuations in fluorescence intensity within a tiny volume (in the order of femtoliters) [482]. The fluorescence signal varies due to changes in the number or brightness of the fluorophores inside the detection volume, which can be due to particle motion (diffusion or transport) inside and outside the detection volume, and/or photochemical and photophysical processes. As a result, FCS can be used to measure diffusion coefficients, fluorophore concentrations, particle sizes, chemical reactions, conformational changes, and binding/unbinding processes, among others. All this makes FCS an excellent technique for the investigation of dynamic processes.

FCS is based on the time-dependent correlation analysis of the fluorescence intensity acquired for the detection volume. The auto-correlation analysis is a mathematical tool that measures the self-similarity of the signal with time (see EQ. 5.1) The correlation curve is fit with a mathematical function that takes into account the excitation profile and models the fluorescence fluctuations inside the detection volume, according to the characteristics of the system under investigation.

*Scanning FCS* (SFCS) refers to a group of FCS variants in which the detection volume is scanned through the sample. The SFCS setup was built on a confocal microscope. The detection of emitted photons was done with avalanche photo diode detectors, which have a high quantum efficiency, especially suitable for single molecule events. In the particular case of GUV samples, the detection volume is scanned perpendicularly through the equator of the membrane. We used a variant known as *two-foci cross correlation* SFCS [483]. By alternately scanning along two parallel lines at a distance  $d$  to each other, two effective foci in the membrane with a displacement  $d$  along the  $y$ -direction can be realized (FIG. 5.18 A). The intersections with the membrane gives rise to two fluorescence intensity traces,  $F_1(t)$  at focus 1 and  $F_2(t)$  at focus 2, from which the auto-correlation curve  $G_i(\tau)$  is calculated:

$$G_i(\tau) = \frac{\langle \delta F_i(t) \delta F_i(t + \tau) \rangle}{\langle F_i(t) \rangle^2} \quad (5.68)$$

where the subindex  $i$  refers to either trace 1 or 2,  $\tau$  is the correlation time and the angular brackets mean time averaging, so that  $\delta F_i(t) = F_i(t) - \langle F_i(t) \rangle$ . Additionally the spatial cross-correlation curve  $G_{12}(\tau)$ , i.e., the cross-correlation analysis of the fluorescence fluctuations in the two foci, is also extracted:

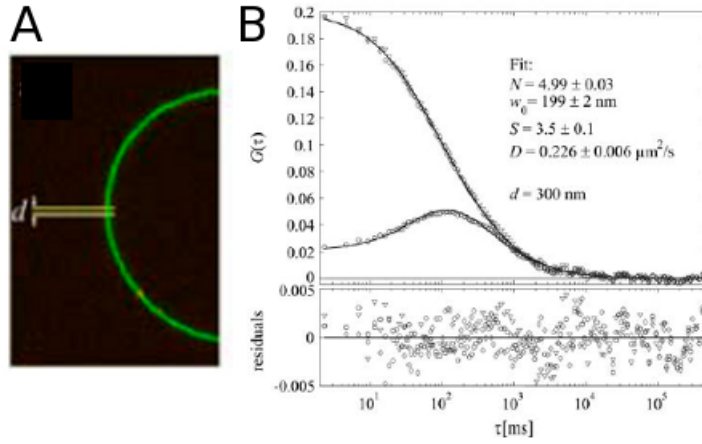


**Fig. 5.18 : The principle of two-foci scanning fluorescence correlation spectroscopy.** (A) Two lines at a distance  $d$  are repeatedly scanned through the equator of a GUV. Each intersection with the membrane gives rise to a fluorescence burst, and fluorescent bursts from all passes through the membrane are connected to an intensity trace. (B) Auto- (diamonds, triangles) and cross-correlation curves (circles) of the two fluorescence intensity traces and residuals from the global fit to Eq. 5.70 and 5.71 (solid line). Reprinted from Biophysical Journal, Volume 91 [483] ©2006 with permission from the Biophysical Society.

$$G_{12}(\tau) = \frac{\langle \delta F_1(t) \delta F_2(t + \tau) \rangle}{\langle F_1(t) \rangle \langle F_2(t) \rangle} \quad (5.69)$$

A global fit of the two auto-correlation functions and the cross-correlation function (FIG. 5.18 B) allows estimating four parameters:  $N$ , the average number of diffusing particles in the detection area ( $N = C\pi\omega_0^2 S$  where  $C$  is the particle concentration per  $\mu m^2$ );  $D$ , the diffusion coefficient of the particles;  $\omega_0$ , the waist radius of the laser focus; and  $S$ , the structure parameter describing the aspect ratio of the elliptical Gaussian area ( $S = \frac{\omega_z}{\omega_0}$ ). The auto-correlation function modeling the two-dimensional diffusion of a fluorescent labeled particle in a Gaussian elliptical detection area is given by:

$$G(\tau) = \frac{1}{N} \left(1 + \frac{4D\tau}{\omega_0^2}\right)^{-1/2} \left(1 + \frac{4D\tau}{\omega_0^2 S^2}\right)^{-1/2} \quad (5.70)$$

The cross-correlation of the intensity traces corresponding to the two intersections is described by the following correlation function:

$$G_{12}(\tau) = \frac{1}{N} \left(1 + \frac{4D\tau}{\omega_0^2}\right)^{-1/2} \left(1 + \frac{4D\tau}{\omega_0^2 S^2}\right)^{-1/2} \exp\left(-\frac{d^2}{\omega_0^2 + 4D\tau}\right) \quad (5.71)$$

## 5 *Methods*

# 6 Protocols

## 6.1 Sample preparation

### 6.1.1 Model membrane systems

#### LUVs

##### Reagents

- Lipids (POPC, DOPE, CL; Avanti Polar Lipids)
- Chloroform (VWR)
- Acetone (VWR)
- Ethanol (VWR)
- PBS1
- Liquid N<sub>2</sub> or dry ice/acetone

##### Equipment

- Glass vials
- Round-bottom glass flasks
- N<sub>2</sub> or Ar gas supply
- Vacuum desiccator
- Vortex
- Thermostated bath
- Complete mini-extruder set including two 1 mL syringes and optionally a thermal block (Avanti Polar Lipids)
- Polycarbonate membranes 13 mm 0.1  $\mu\text{m}$  (Whatman)
- Drain disc 10 mm PE (Whatman)
- LabAssay Phospholipid Kit (Wako)
- Light scattering equipment (ZetaSizer Nano ZS running *Dispersion Technology Software*; Malvern Instruments)
- UV-Vis spectrophotometer (Agilent Technologies)
- Cells (Fisher, Hellma)

## 6 Protocols

### Procedure

1. Prepare a concentrated stock solution of lipids in a glass vial. Most lipids can be conveniently dissolved in chloroform at a concentration of 50 mg/mL. For unsaturated lipids, flux Ar gas before closing to prevent oxidation by air. Keep lipids at -20°C with a desiccant.
2. Pipette the appropriate amount of lipids into a round-bottom glass flask. The flask should be washed thoroughly before use with different solvents of increasing apolarity, e.g. water<ethanol<acetone<chloroform. Plastic tips may be used. If the volume to be pipetted is very low, i.e. a few  $\mu\text{L}$ , it is better to add a small volume ( $\sim 100 \mu\text{L}$ ) of chloroform to the flask in advance in order to enhance lipid spreading over the walls.
3. Evaporate the organic solvent. It is better to remove first the bulk organic solvent by gently flushing N<sub>2</sub> or Ar gas over the sample. Then, evaporate the remaining solvent under vacuum (2 h is usually enough, although it can be left overnight).
4. Hydrate the lipid film with the buffer of choice (usually PBS1) at a temperature above the  $T_m$ . Unsaturated lipids have very low  $T_m$  and can be resuspended at room temperature. Check the  $T_m$  especially in the case of saturated lipids. In order to enhance lipid resuspension into the aqueous media, samples can be vigorously vortexed.
5. Homogenize the lipid sample by freeze/thawing. In order to accelerate this process, freezing should be done in liquid nitrogen and thawing in a thermostated bath at 37° C (always above  $T_m$ , see step 4). When high-molecular weight compounds are to be encapsulated, freeze/thawing cycles might be extended; e.g. at least 20 rounds for FD-70. At the end of this step MLVs are formed.
6. Extrude the MLVs through two stacked polycarbonate filters of the desired pore size (follow manufacturer's instructions for assembly). Most of the LUV in this Thesis have been extruded through pores of 100 nm in diameter. However, for CD experiments we used pores of 50 nm. After this step we end up with LUVs.
7. Determine the concentration of lipids in the LUV sample using the Kit of Wako according to manufacturer's instructions.
8. Check the LUV size by DLS (see FIG. 6.1). Follow *Dispersion Technology Software* (DTS) manual instructions. DTS can be downloaded from Malvern website<sup>1</sup>.
9. Store LUVs at 4° C (do not freeze!) and use them within 1 week. .

### GUV

#### Reagents

- Lipids (POPC, CL; Avanti Polar Lipids, DiD,DiO,DiI; Invitrogen Molecular Probes)
- Chloroform (VWR)
- Ethanol (VWR)
- PBS2 (Sigma)
- Sucrose (VWR)
- BSA (WWR)

---

<sup>1</sup> [http://www.malvern.com/common/software/zeta\\_nano/zeta\\_nano\\_software.htm](http://www.malvern.com/common/software/zeta_nano/zeta_nano_software.htm)

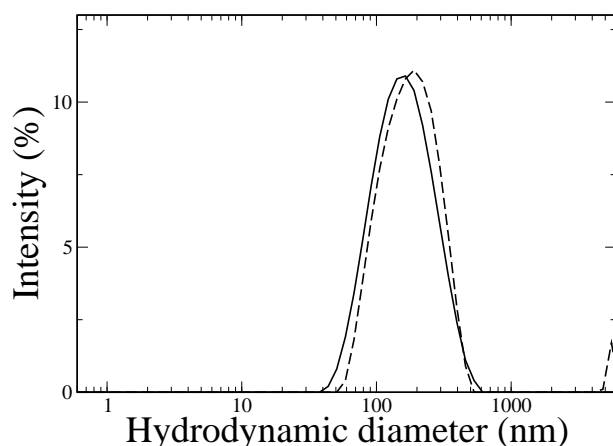


**Fig. 6.1 : Size distribution of LUVs by intensity of scattered light.** Liposomes extruded through pores of 100 nm are measured by DLS. The x axis corresponds to the size classes, and the y axis to the relative intensity of the scattered light. The size distribution is calculated from the correlation function. The solid line corresponds to LUVs alone and the dashed line to LUVs in the presence of Bax $\alpha$ 5 at a P/L=1/100.

#### Equipment

- Glass vials
- N<sub>2</sub> or Ar gas source
- A cell with Pt wires
- Function generator and electrodes (Pomoma)
- Tester
- Osmometer (Advanced Instruments Fiske 210 micro-sample osmometer; Fisher Scientific)

#### Procedure

1. Wash the wires and the cell. They can be cleaned with a variety of solvents since the materials are very resistant (teflon, Pt).
2. Make a film of the lipid composition of interest on the Pt wires. Loading 10  $\mu$ L of a lipid stock at 2 mg/mL in chloroform directly onto the wires gives good results. For visualizing the lipid membrane, a small amount of a fluorescent dye, e.g. the family of long chain dialkylcarbocyanines (DiI, DiO, DiD) can be added at 0.05 mol%.
3. Evaporate the solvent. Given the very low volume used, letting the Pt wires dry at room temperature for 5 min is enough.
4. Fill the cell with sucrose and close it. It is crucial for the sucrose solution to be isoosmolar with your buffer. If you use PBS, make a solution of sucrose at 300 mM and check the osmolarity. Minor adjustments of the osmolarity may be needed.
5. With the help of a function generator, apply 1.5 V at 10 Hz for 30 min. Check the voltage with a tester. GUVs are formed in this step.
6. Then, apply 1.5 V at 2 Hz for up to 2 hours to allow the GUVs to detach from the wires.

## 6 Protocols

7. Open the cell and pipette the GUVs out of the formation cell to the microscope observation cell, loaded with PBS2 buffer. Use micropipette tips with enlarged opening (by cutting the tip with a knife), to avoid breaking the GUV. A good ratio of volumes to make sure the GUVs sediment in the observation chamber is 50  $\mu\text{L}$  of GUVs in 450  $\mu\text{L}$  of PBS2. Be very gentle when mixing GUVs. Use the GUVs within 24h after preparation.

### 6.1.2 Peptide synthesis and purification

#### Peptide synthesis

##### Reagents

- Fmoc- and side chain-protected L-amino acids (Iris Biotech):

Amino acid*	Molecular weight (g/mol)
<i>Fmoc-L-Ala-OH</i>	311.3
<i>Fmoc-L-Cys(Trt)-OH</i>	585.7
<i>Fmoc-L-Asp(tBu)-OH</i>	411.5
<i>Fmoc-L-Glu(tBu)-OH</i>	425.5
<i>Fmoc-L-Phe-OH</i>	387.4
<i>Fmoc-Gly-OH</i>	297.3
<i>Fmoc-L-His(Trt)-OH</i>	619.7
<i>Fmoc-L-Ile-OH</i>	353.4
<i>Fmoc-L-Lys(Boc)-OH</i>	468.6
<i>Fmoc-L-Leu-OH</i>	353.4
<i>Fmoc-L-Met-OH</i>	371.5
<i>Fmoc-L-Asn(Trt)-OH</i>	597.4
<i>Fmoc-L-Pro</i>	337.4
<i>Fmoc-L-Gln(Trt)</i>	611.4
<i>Fmoc-L-Arg(Pbf)-OH</i>	648.8
<i>Fmoc-L-Ser(tBu)-OH</i>	383.4
<i>Fmoc-L-Thr(tBu)-OH</i>	397.5
<i>Fmoc-L-Val-OH</i>	339.4
<i>Fmoc-L-Trp-OH</i>	426.5
<i>Fmoc-L-Tyr(tBu)-OH</i>	459.5

\* Side-chain protecting groups are: Trt, trityl; tBu, tert-butyl; Boc, tert-butyl-oxycarbonyl; Pbf, 2,2,4,6,7-pentamethyldihydrobenzofuran-5-sulfonyl.

- RinkAmide ChemMatrix resin (Iris Biotech)
- NMP (Scharlab)

- DCM (VWR)
- Piperidine (Iris Biotech)
- Acetic anhydride (Sigma)
- HBTU (Iris Biotech)
- HOBT (Iris Biotech)
- DIEA (Iris Biotech)
- TFA (Sigma)
- Thioanisole (Sigma)
- Ethanedithiol (Sigma)
- Phenol (Sigma)
- Tert-butyl methyl ether or diethyl ether (VWR)
- Reagent K mixture: TFA:thioanisole:ethanedithiol:phenol:water (85.5:5:2.5:5:5)

#### Equipment

- ABI 433A Peptide Synthesizer, running *SynthAssist* software (Applied Biosystems)
- Consumable parts: in-line filters (Applied Biosystems); filter paper (AnaSpec); Wheaton open-top seals 13 mm rubber septum (Sigma)
- Fume hood
- Centrifuge columns 10 mL (Pierce)
- Balance
- Centrifuge (Eppendorf)
- Shaker
- Vacuum dissector (Telstar)
- Lyophilizer (Telstar)

#### Procedure

1. Weight the appropriate amount of solid resin, according to the synthesis scale and the degree of substitution of the resin, and place it in the reaction vessel. We routinely used Rink Amide ChemMatrix at loading ranges of  $\sim 0.5$  mmol/g.
2. Weight the appropriate amount of Fmoc-protected aminoacids into the cartridge according to the synthesis scale and the desired molar excess. The primary structure of the unlabeled peptides is shown in TAB. 6.1. In the case of the labeled peptides, either with fluorescent labels or  $^{13}\text{C}=^{18}\text{O}$ , please refer to CHAP. 8 and 9, respectively. We used a  $10\times$  molar excess over the resin sites for *normal* couplings and  $5\times$  for *expensive* couplings, i.e., those involving  $^{13}\text{C}=^{18}\text{O}$ -labeled amino acids.
3. Set up the peptide synthesizer according to the manufacturer's instructions. We used *FastMoc* chemistry as implemented in the *FastMoc0.1OmegaMonPrevPk* standard file provided within the *SynthAssist* software suite, with the following modifications:

**Tab. 6.1 : Aminoacid sequences of unlabeled peptides.** All peptides were acetylated at the N-terminus (Ac), amidated at the C-terminus (NH<sub>2</sub>) and the naturally occurring Cys residues (occurring at position 126 in Bax and 151 in Bcl-xL) were changed into Ser. All numbers indicate the position of the residues in the full-length proteins, either human Bax or mouse Bcl-xL. Basic residues are highlighted in blue and acidic residues are highlighted in red.

Peptide	Sequence
<i>Baxα5</i>	Ac- <sup>107</sup> WGRVVALFYFASKLVLKALSTK <sup>128</sup> -NH <sub>2</sub>
<i>Baxα5 Y115S</i>	Ac- <sup>107</sup> WGRVVALFVSFASKLVLKALSTK <sup>128</sup> -NH <sub>2</sub>
<i>Bcl-xLα5 A149K/E153K</i>	Ac- <sup>137</sup> WGRIVAFFSFGGKLSVKSVDK <sup>157</sup> -NH <sub>2</sub>
<i>Bcl-xLα5</i>	Ac- <sup>137</sup> WGRIVAFFSFGGALSVESVDK <sup>157</sup> -NH <sub>2</sub>

- a) The coupling time was extended up to 35 min
  - b) By default, double couplings were performed for each residue to be incorporated. For *difficult* residues (i.e. β-branched aminoacids like Ile and Thr) triple couplings were applied.
  - c) A capping step using acetic anhydride was added after each coupling
4. After synthesis is completed, transfer the peptide-resin from the reaction vessel to an empty column and dry it under vacuum.
  5. Weight the resin-bound peptide.
  6. Cleave the peptide off the resin with reagent K mixture for 4 h in darkness, under Ar, at room temperature and with shaking.
  7. Place ~50 mL of cold (-20°C) tert-butyl methyl ether under the column. Twist off the bottom cap of the column so that the peptide flows through it while the resin is retained.
  8. Let the peptide precipitate in ether overnight at -20°C.
  9. Pellet the peptide by centrifugation at 10000 rpm for 15 min at 4°C and resuspend in cold tert-butyl methyl ether. Repeat this washing step 6 times.
  10. Dry the peptide under vacuum by freeze-drying.

#### Synthesis of <sup>13</sup>C=<sup>18</sup>O Fmoc-amino acids<sup>1</sup>

##### Reagents

- H<sub>2</sub><sup>18</sup>O (D-chem)
- (1-<sup>13</sup>C) L-amino acids (Cambridge Isotope Laboratories)
- Dioxane (Sigma)
- CaCl<sub>2</sub> (Sigma)
- H<sub>2</sub>SO<sub>4</sub> (AppliChem)
- DIEA (Sigma)
- ACN (VWR)

<sup>1</sup> (1-<sup>13</sup>C=<sup>18</sup>O)-L-Ala and (1-<sup>13</sup>C=<sup>18</sup>O)-L-Phe were a gift from Dr. SHY ARKIN and Dr. JOSH MANOR

- Fmoc succinimidyl ester (Sigma)
- Diethyl ether (Sigma)
- Ethyl acetate (VWR)
- NaCl (Sigma)
- HCl (AppliChem)
- MgSO<sub>4</sub> (Sigma)
- DCM (VWR)
- Petroleum ether (Sigma)
- Hexane (Sigma)

### Equipment

- Ar gas source
- Compensating funnel
- Refrigerator
- Three neck flask
- Two neck flask
- Syringe
- Septum
- Tubing
- Caps, clamps and stoppers
- Two magnetic stirrers (at least one with temperature control) and stir bars.
- Silicone bath
- Separating funnel
- pH meter
- TLC aluminium plates silica gel 60 *F*<sub>254</sub> (Sigma)
- UV lamp (254 nm)

## 6 Protocols

### Procedure

1. Wash the system by flowing dry argon from the two-neck flask to the three-neck flask.
2. Put CaCl<sub>2</sub> in the three-neck flask and wash the system again with argon.
3. To the two-neck flask add the appropriate amount of the amino acid:

Amino acid	MW (g/mol)	Quantity (mmol)	Mass (g)
<i>Gly</i>	73.06	3.57	0.272
<i>Leu</i>	132.17	7.14	0.944
<i>Val</i>	118.14	3.57	0.422
<i>Phe</i>	166.18	3.57	0.593
<i>Ala</i>	90.08	3.57	0.322
<i>Ile</i>	132.18	3.57	0.472

4. Use a syringe to add (through the plastic septum) 1 ml (or 2 ml in case of Leu) of H<sub>2</sub><sup>18</sup>O and about 8-10 ml (or 16-20 in case of Leu) of dry dioxane.
5. Move the inlet argon tube to the head of the "refrigerator", and add about 20 mL of H<sub>2</sub>SO<sub>4</sub> to the separating funnel.
6. Cool the reaction mixture in an ice bath, and carefully add the H<sub>2</sub>SO<sub>4</sub> over the CaCl<sub>2</sub>.
7. Bubble the HCl(g) through the reaction mixture for about 20 min. Make sure that all the acid is dissolved.
8. Unplug the HCl tube from the three necked flask, and close the flask with a stopper.
9. Reflux the solution for about 3 hours.
10. Allow the mixture to cool down.
11. Evaporate most of the solvents using an evaporator (start at low temperature). Dry completely by lyophilization.
12. Check the degree of labeling by ESI-Q mass spectrometry. The area under the peaks is proportional to product concentration. Usually the yield of doubly labeled amino acid was 75%. Note that the degree of labeling is irrelevant as long as the signal can be detected.
13. Dissolve the <sup>13</sup>C=<sup>18</sup>O-labeled amino acid (700 mg, 1 eq) in 7 mL of milli-Q water and DIEA (609 μL, 1eq) and stir on ice for 15 min.
14. Add Fmoc-succinimidyl ester (1204 mg, 1 eq) dissolved in 7 mL of ACN dropwise over the above cold stirred mixture.
15. Make sure the pH is within the range 8.5-9.5 by adding DIEA. Once the pH is stable incubate at room temperature overnight.
16. Extract the water with ether.
17. Wash the ether with brine and combine all the water extracts.
18. Acidify the water extracts by slowly adding HCl.
19. Extract the white precipitate with ethyl acetate (AcOEt) and wash the ethyl acetate extracts with brine.
20. Check purity by thin layer chromatography (TLC), using silica gel as the solid support and a mixture of AcOEt:hexane as mobile phase. Visualize the amino acids with UV illumination.

21. Dry the organic phase using MgSO<sub>4</sub> powder, filter and evaporate.
22. Recrystallize as follows: Place the product in an erlenmeyer flask and redissolve the solute with the minimum amount of pre-warmed AcOEt (or DCM, see table) while gently stirring and heating the solution. Once fully dissolved, add a few drops of pre-warmed petroleum ether (hexane works fine also) until light turbidity under heat is observed. Add dropwise the minimum amount of heated AcOEt (or DCM) needed to fully clarify the solution. Leave the solution at room temperature till formation of crystal nuclei. Once nucleated, continue crystal growing at 4°.

<b>Fmoc-amino acid</b>	<b>Solvents of recrystallization</b>
<i>Fmoc-Gly-OH</i>	EtOAc-petroleum ether
<i>Fmoc-Leu-OH</i>	DCM-petroleum ether
<i>Fmoc-Val-OH</i>	DCM-petroleum ether
<i>Fmoc-Phe-OH</i>	EtOAc-petroleum ether
<i>Fmoc-Ala-OH</i>	EtOAc-petroleum ether
<i>Fmoc-Ile-OH</i>	DCM-petroleum ether

**Peptide labeling** *Warning:* Peptide synthesis should be run by performing a final deprotection step without acetylation. This will free the peptide N-terminus, which is necessary for the labeling reaction to proceed. Since dyes are usually expensive, before proceeding with labeling a small scale cleavage of peptide from the resin should be made in order to be sure of the success of the peptide synthesis and check peptide purity. In addition, minimize the amount of light that the labeled peptide receives. The reaction mixture and the products must be kept strictly on dark, to avoid possible photodegradation. This can be made by wrapping aluminium foil around the tubes.

#### Reagents

- Succinimidyl esters dyes (Alexa350SE, DabcylSE, Alexa647SE; Invitrogen Molecular Probes)
- DMF (Sigma)
- DCM (VWR)
- DIEA (Sigma)
- Ninhydrin test kit (Sigma)

#### Equipment

- Centrifuge columns 10 mL (Pierce)
- Shaker
- Spectrophotometer (Agilent Technologies)
- Cells (Hellma)

#### Procedure

1. Dissolve the succinimidyl ester dye at 10 mg/mL in DMF right before use.
2. In a column, place 40 mg of peptide-bound resin and add 500  $\mu$ L of DMF, 33  $\mu$ L DIEA and 250  $\mu$ L of the freshly prepared reactive dye.
3. Stir overnight at room temperature in darkness.

**Tab. 6.2 : Extinction coefficients of polypeptides and dyes used in this Thesis at the specified wavelengths, along with CF values.**

Sample	$\epsilon_{peptide}^{\lambda_{max}}$ (M <sup>-1</sup> cm <sup>-1</sup> )	$\epsilon_{dye}^{\lambda_{max}}$ (M <sup>-1</sup> cm <sup>-1</sup> )	$\lambda_{max}$ (nm)	CF
<i>Baxα5</i>	6990	-	280	-
<i>BclxLα5</i>	5500	-	280	-
<i>BclxLα5 dm</i>	5500	-	280	-
<i>BclxLΔCt</i>	41940 (43430*)	-	280	-
<i>Alexa350</i>	-	19000	346	0.19
<i>(E)EDANS</i>	-	5700	336	0
<i>(K)Dabcyl</i>	-	32000	507	0
<i>Alexa647</i>	-	239000	650	0.03

\* The value between brackets corresponds to that of the cleaved protein.

4. Wash with 3 column volumes of DMF.
5. Wash with 3 column volumes of DCM.
6. Dry under vacuum.
7. (*Optional*) Perform the ninhidrin test to check for free amino groups.
8. Proceed with the cleavage step (described in step 6 SUB. 6.1.2) and continue with the procedure.
9. After purification (SUB. 6.1.2), check the degree of labeling (DOL) by UV-Vis absorbance spectroscopy, using the following relationship:

$$DOL = \frac{A_{dye}\epsilon_{peptide}}{A_{peptide}\epsilon_{dye}} \quad (6.1)$$

where  $A_{dye}$  is the absorbance at the  $\lambda_{max}$  for the dye,  $\epsilon_{dye}$  is the extinction coefficient of the dye at its absorbance maximum,  $A_{peptide}$  is the corrected absorbance of the peptide at 280 nm and  $\epsilon_{peptide}$  is the extinction coefficient of the peptide at 280 nm calculate using the ProtParam tool on the ExPASy server<sup>1</sup> (see TAB. 6.2).  $A_{peptide}$  must be corrected for the contribution of the dye at the peptide absorption wavelength as follows:

$$A_{peptide} = A_{280} - CF A_{dye} \quad (6.2)$$

$$CF = \frac{A_{280free dye}}{A_{max free dye}} \quad (6.3)$$

**Peptide purification** *Warning:* use high quality reagents (HPLC-grade). Filter and de-gas all solutions. Samples containing harsh solvents should be filtered through especially resistant membranes, like Millex-LCR filters (Millipore).

<sup>1</sup> <http://www.expasy.org/cgi-bin/protparam>

**Reagents**

- TFA (Sigma)
- ACN HPLC grade (VWR)
- Milli-Q water
- Buffer A (water:ACN:TFA 90:10:0.1)
- Buffer B (water:ACN:TFA 10:90:0.1)

**Equipment**

- Waters Alliance 2695 separation module with a 2487 dual wavelength absorbance detector running *Mass-Lynx* software (Waters)
- XBridge 2.1x150 mm BEH300C18 5 $\mu$ m column plus 2.1x10mm BEH300C18 5 $\mu$ m precolumn (Waters).
- XBridge 10x250 mm BEH300C18 5 $\mu$ m column plus 10x10mm BEH300C18 5 $\mu$ m precolumn (Waters).

**Procedure** *Note:* These are guidelines only. Each peptide usually require fine tuning of particular conditions. Specifically, very insoluble peptides are best purified by dissolving them directly in pure TFA and eluting using gradient conditions.

1. Dissolve a small amount of crude peptide in buffer A.
2. Equilibrate the column with buffer A.
3. Make an analytical gradient run from buffer A to B. Set the detector absorbance to 214/280 nm (labeled peptides may require additional wavelengths) to monitor peptide backbone and aromatic residues respectively. Determine the gradient which gives the best resolution for the more abundant peak (which will likely be your desired peptide).
4. Reequilibrate the column with buffer A.
5. Dissolve the remaining crude peptide in the appropriate solvent.
6. Make a preparative gradient run. Follow the steps: Column equilibration-sample loading-gradient elution-column reequilibration.
7. Analyse the eluted peaks by analytical RP-HPLC and MALDI-TOF<sup>1</sup> mass spectrometry (see examples in FIG. 6.2 and 6.3). Determine peptide purity by integrating all the eluted peaks. Mass spectra can be visualized with the freeware program *moverz*<sup>2</sup>.
8. Pool the best fractions, add HCl (20  $\times$  molar excess over TFA) to remove trifluoroacetate counter-ions and lyophilize.
9. Store the peptide powder at -20°C with a desiccant.

**6.1.3 Protein expression and purification****Culture growing**

<sup>1</sup> MALDI-TOF analysis was performed at the SCSIE (Serveis Centrals de Suport a l'Investigació) facility of the University of Valencia.

<sup>2</sup> <http://bioinformatics.genomicsolutions.com/MoverZDL.html>

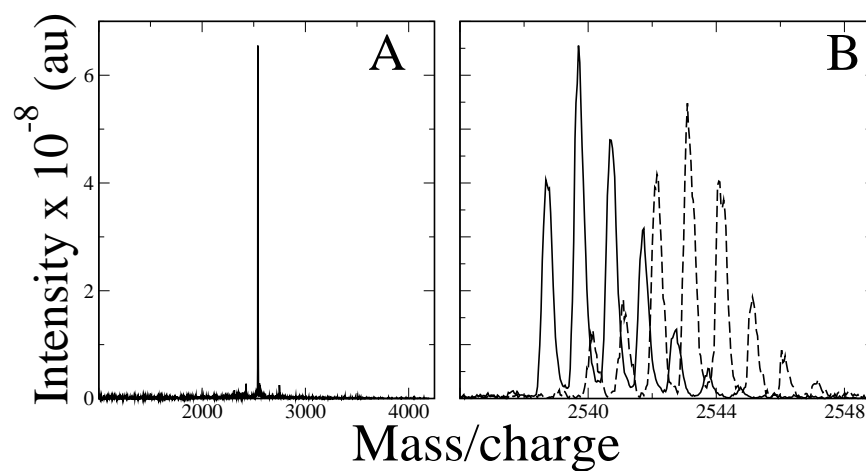


**Fig. 6.2 : Examples of mass spectra of purified Bax $\alpha$ 5.** A) MALDI-TOF spectrum of unlabeled Bax $\alpha$ 5. This technique allows semiquantitative estimation of peptide purity. B) MALDI-TOF spectra of unlabeled (solid line) and <sup>13</sup>C=<sup>18</sup>O-labeled (dotted line) Bax $\alpha$ 5, showing that even the small three dalton difference between the two peptide variants can be easily detected as a shift in the spectrum.

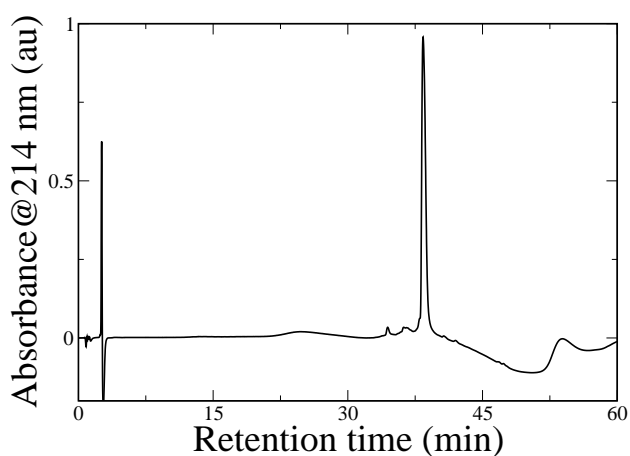


**Fig. 6.3 : Example of a HPLC chromatogram of purified Bax $\alpha$ 5.** The peptide is detected by absorbance at 214 nm, arising from the peptide bonds. The stationary phase of the column is a C18 hydrocarbon chain linked to silica beads and the mobile phase is a mixture of water:ACN plus 0.1% of TFA. Bax $\alpha$ 5 is eluted with a linear gradient from 10% to 90% of ACN.

### Host cells

- *E. coli* BL21 (DE3), transformed with a p11 plasmid which harbours the sequence of Bcl-xL $\Delta$ Ct with codons for a tag of 6 His aminoacid residues at the N-terminus followed by the cleavage site of the TEV protease.<sup>1</sup>

### Reagents

- LB (prepared in water and autoclaved; no need for pH adjustment which was typically near 7)
  - Yeast extract 0.5% w/v
  - Tryptone 1% w/v
  - NaCl 1% w/v
- Ampicillin (AppliChem). Prepare a 1000 $\times$  stock solution at 100 mg/mL in ethanol (40% v/v)
- IPTG (AppliChem). Prepare a 1000 $\times$  stock solution a 1M in water.
- Buffer 1: Lysis buffer
  - Tris-HCl 25 mM pH=8.0
  - NaCl 300 mM
  - Glycerol 10%
- Protease Inhibitors (Protease inhibitor cocktail, set III without EDTA; Novagen)
- Nuclease (Benzonase Nuclease 25 U/ $\mu$ L; Novagen)
- MgCl<sub>2</sub> (Sigma)
- Lysozyme (rLysozyme 30 KU/ $\mu$ L; Novagen)

### Equipment

- Laminar flow hood
- Autoclave
- Thermostated chamber at 37°C
- Erlenmeyer flasks (100 mL and 5 L)
- Shakers
- Spectrophotometer (Agilent technologies)
- Cells (Fisher)
- Probe-type Sonicator (Branson)
- Centrifuge (Eppendorf)

---

<sup>1</sup> *E. coli* DH5 $\alpha$  cells containing the plasmid were a gift from Dr. ANTONIO PINEDA (CIPF).

## 6 Protocols

### Procedure

1. Seed 10 mL of LB medium containing ampicillin with a few microliters of bacterial glycerol stock (transformed with the appropriate plasmid) in an Erlenmeyer flask under sterile conditions. Let it grow overnight at 37°C.
2. Next morning dilute the culture in 1L of LB with ampicillin. Grow with vigorous shaking at 37°C.
3. Monitor the optical density of the culture at 600 nm until it reaches a value of 0.6. It usually takes ~3h
4. Cool the culture down to 22°C. This low temperature improves the yield of soluble and cleavable protein.
5. Add 0.5 mM of IPTG to induce protein expression. Continue growing at 22°C until the next day.
6. Collect the cells by 25 min centrifugation at 4000 rpm and 4°C.
7. Resuspend the pellet in ~50 mL of Buffer 1
8. Freeze/thaw the cell suspension (3×cycles, always on ice).
9. Add lysozyme (1μL from stock solution) and benzonase nuclease (4 μL from stock solution) together with 1 mM MgCl<sub>2</sub>. Let the reaction proceed for 30 min on ice.
10. Briefly sonicate the sample on ice until the protein extract appears homogeneous.
11. Clarify the extract by 45 min centrifugation at 12000 rpm at 4°C.
12. (*Optional*) If the extract remains turbid pass the supernatant through 0.45 μm pore cassette filters (Milipore) to avoid column clogging in the purification steps.

### Protein purification

#### Reagents

- Buffer 1 (see SUB. 6.1.3)
- Buffer 2: Washing buffer
  - Tris-HCl 25 mM pH=8.0
  - NaCl 300 mM
  - Imidazol 5 mM
- Buffer 3: Elution buffer
  - Tris-HCl 25 mM pH=8.0
  - NaCl 100 mM
  - Imidazol 500 mM
- Buffer 4: Cleavage Buffer
  - Tris-HCl 25 mM pH=6.8
  - NaCl 50 mM
  - DTT 1mM
- Acrylamide/bisacrylamide solution 30% (Sigma)
- Tetramethylethylenediamine, (TEMED, Sigma)
- Mercaptoethanol (AppliChem)
- Ammonium persulfate (AppliChem)

- Electrophoresis buffer
- Loading buffer (protein loading buffer; Fermentas)
- Coomassie Blue (PageBlue Protein staining solution; Fermentas)
- Protein marker (PageRuler prestained protein ladder; Fermentas)

### Equipment

- Ni<sup>2+</sup>-containing column (His GraviTrap; GE)
- Vertical electrophoresis apparatus (Mini-protean 3; Bio-Rad)
- Dialysis tubing of 15 kDa cut-off (Serva). For small volumes a mini-dialysis kit (GE) is recommended.
- UV-Vis spectrophotometer (Agilent Technologies)
- 70  $\mu$ L quartz cells of 3 mm path-length (Hellma)

**Procedure** *Note:* Perform all steps at 4°C, except the electrophoresis. The column mentioned here operates by gravity flow, so there is no need for special chromatographic equipment.

1. Equilibrate the column with Buffer 1.
2. Load the supernatant.
3. Wash the column with Buffer 2
4. Elute bound proteins with Buffer 3.
5. Regenerate the column with Buffer 1.
6. Monitor the purification factor and the purification yield with SDS-PAGE and stain with Coomassie Blue (FIG. 6.4 A).
7. Pool the purest fractions and store at 4°C or proceed with the cleavage.
8. Mix Bcl-xL/TEV at a 40/1 weight ratio protein/protease.
9. Put into a dialysis bag and dialyze against Buffer 4.
10. Exchange the buffer twice.
11. Load the cleavage mixture into the column.
12. Wait 30 min to allow for protein binding
13. Wash the column with PBS1 and collect cleaved Bcl-xL.
14. Elute TEV with Buffer 3.
15. Regenerate the column with Buffer 1.
16. Store the column with ethanol 20%
17. Check the cleavage yield by SDS-PAGE using Coomassie Blue staining (FIG. 6.4 B) . Usually the Bcl-xL purity is >95%. Approximately 5 mg of pure Bcl-xL were obtained per 1L of culture.
18. Pool the purest fractions and store at 4°C. Use within 1 week to avoid protein aggregation and loss-of-function. Freezing or lyophilization usually gives bad results.

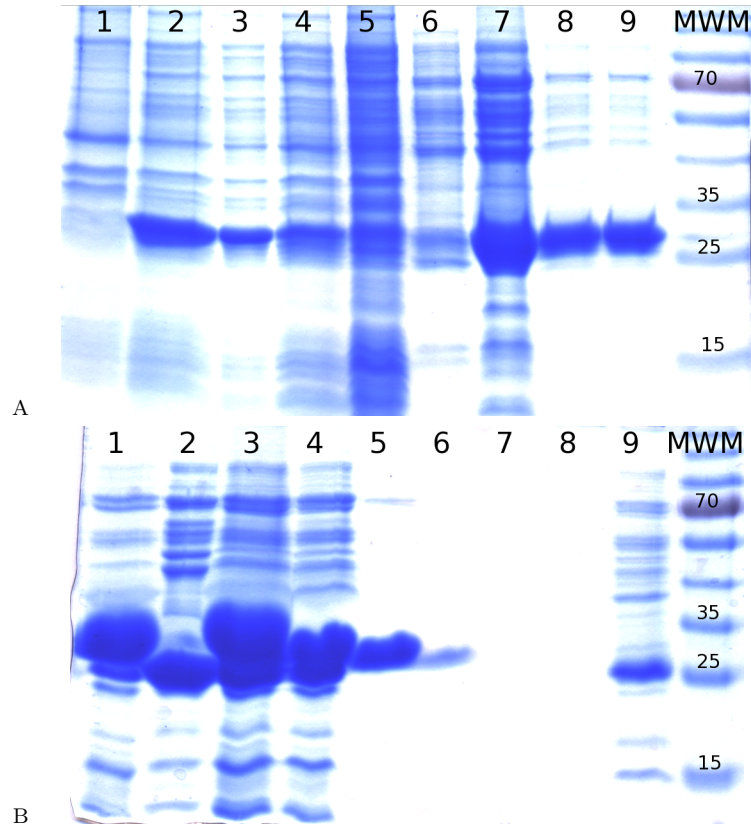


**Fig. 6.4 : Monitoring the purification of Bcl-xLΔCt by SDS-PAGE.** Samples from each purification step were run on 12% Tris-glycine SDS-PAGE and bands were visualized by Coomassie blue staining. A) Result from samples at initial steps of purification of Bcl-xLΔCt. Lane 1, uninduced culture; lane 2, induced culture; lane 3, total protein extract (after sonication); lane 4, soluble protein extract; lane 5, flow-through after Ni<sup>2+</sup> column; lane 6, 1<sup>st</sup> eluted fraction; lane 7, 2<sup>nd</sup> eluted fraction; lane 8, 3<sup>rd</sup> eluted fraction; lane 9, 4<sup>th</sup> eluted fraction. B) Cleavage and final purification of Bcl-xLΔCt. Lane 1, Bcl-xLΔCt purified by IMAC; lane 2, TEV purified by IMAC; lane 3, cleavage mixture (Bcl-xLΔCt plus TEV) at time zero; lane 4, cleavage mixture after 24 h incubation; lanes 5 - 8, 1<sup>st</sup>-4<sup>th</sup> flow-through fractions from Ni<sup>2+</sup> column; lane 9, 1<sup>st</sup> eluted fraction. MWM refers to the molecular weight markers, with numbers indicating their masses in kDa. Expected molecular masses are 26 kDa for uncleaved Bcl-xLΔCt, 24 kDa for cleaved Bcl-xLΔCt and 23 kDa for TEV.

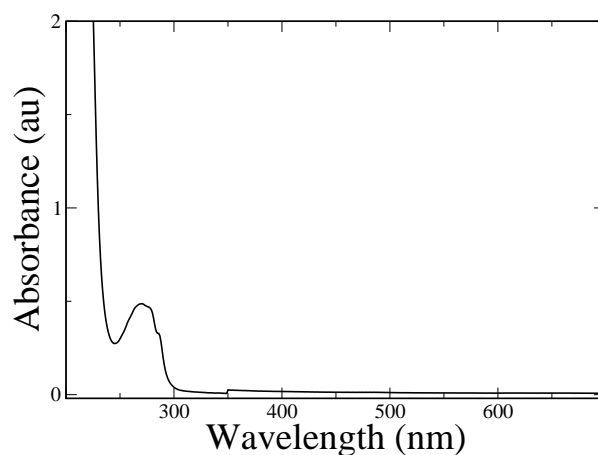


**Fig. 6.5** : Example of a UV-Vis spectrum of Bax $\alpha$ 5. The peak at 280 nm is mainly due to the single tryptophan residue in the peptide sequence (with minor contributions arising from the tyrosine and the phenylalanine residues). The peak below 230 nm corresponds to the peptide bonds. Unlabeled Bax $\alpha$ 5 does not absorb in the visible region.

### Quantification of peptides and proteins

#### Reagents

- 1,1,1,3,3,3-hexafluoroisopropanol, HFIP (Sigma)

#### Equipment

- Spectrophotometer (mod. 9648, Agilent Technologies)
- 70  $\mu$ L quartz cell of 3 mm path-length (Hellma)

#### Procedure

1. Dissolve the peptide in appropriate solvent, usually HFIP. Record a UV-Vis spectrum making the necessary dilutions if absorbance is too high (see an UV-Vis example spectrum in FIG. 6.5). Determine the concentration applying BEER-LAMBERT's law (EQ. 5.6). The concentration of peptide (or protein) should be determined immediately before use. Extinction coefficients and wavelengths used for molecules in this Thesis are shown in TAB. 6.2.

## 6.2 Structural studies

### 6.2.1 Circular dichroism spectroscopy

#### Reagents

- HFIP (Sigma)
- PBS1 or PB
- Liposomes extruded through filters of 50 nm in pore size

## 6 Protocols

### Equipment

- Jasco J-810 spectropolarimeter running *Spectra Analysis* software (Jasco)
- 100  $\mu\text{L}$  quartz cell of 1 mm path-length (Hellma)

### Procedures

1. Organic solvents (like HFIP) or detergent micelles (SDS) usually give good results. In aqueous buffers, try to reduce dissolved components at maximum. For instance, avoid using salts like NaCl, i.e. use PB instead of PBS.
2. As a guide, peptide concentration should be near 30  $\mu\text{M}$ .
3. If liposomes are required, use vesicles of  $\sim 25$  nm hydrodynamic radius and a lipid concentrations of  $\sim 4$  mM, at most. Otherwise, scattering artifacts make measurements at low wavelengths impractical.
4. Use an appropriate cell (100  $\mu\text{L}$ , 3 mm path length). The equipment must be turned on and purged with  $\text{N}_2$  gas (5 L/min) at least 15 min before measurements.
5. Record spectra using the following settings:

Parameter	Value
<i>Sensitivity</i>	Standard (100 mdeg)
<i>Wavelength range (nm)</i>	190-250
<i>Data pitch (nm)</i>	0.2
<i>Scanning mode</i>	continuous
<i>Scan rate speed (nm/min)</i>	100
<i>Response time (s)</i>	0.25
<i>Bandwidth (nm)</i>	0.5
<i>Number of accumulated scans</i>	5

6. Perform background subtraction, unit conversion (from raw  $\theta$  to  $[\theta]_{MR}$ ) and smoothing with Jasco's software.
7. Analyze the data to get the percentages of the different secondary structure components. Some useful web resources include DichroWeb<sup>1</sup> and K2D2<sup>2</sup>. Follow the instructions that appear in the web pages, with special care for choosing the appropriate algorithms and database options.

### 6.2.2 Infrared spectroscopy

#### Reagents

- Lipids (POPC, DMPC, CL, SM, Cho, DPPC, DLPC; Avanti Polar Lipids)
- HFIP (Sigma)
- $\text{D}_2\text{O}$  (99%, Sigma)

1 <http://dichroweb.cryst.bbk.ac.uk/html/home.shtml>

2 <http://www.ogic.ca/projects/k2d2/>

**Equipment**

- Magna 560 spectrometer (Nicolet), equipped with a high-sensitivity liquid nitrogen-cooled MCT/A detector. Attenuated total reflection (ATR) spectra were measured with a 25-reflection ATR accessory (Graseby Specac) and a wire grid polarizer (0.25 mM: Graseby Specac). OMNIC FTIR software is included.
- Gas source. Ideally, N<sub>2</sub> but air depleted of CO<sub>2</sub> and H<sub>2</sub>O may also be used.
- Trapezoidal Ge internal reflection element (50x2x20 mm)
- Sonicator (Sonics Vibra-cell)
- Rotaevaporator with thermostated bath

**Procedures**

1. Co-solubilize <sup>13</sup>C=<sup>18</sup>O-labeled (or unlabeled) peptide and lipid in HFIP adding the appropriate amounts to get the desired peptide-to-lipid ratio.
2. Remove the organic solvent. It can be done by rotaevaporation for 2 h at 37°C, followed by complete dessication overnight with low pressure.
3. Hydrate the lipid-peptide film in 2 mL of milli-Q water.
4. Incubate the reconstituted liposomes with incorporated peptide for 1 h at 37°C. The lipid with the highest  $T_m$  is DMPC ( $T_m \sim 23^\circ\text{C}$ ) so this temperature is appropriate for all lipids employed in this thesis.
5. Sonicate the MLV in a probe-type sonicator for 2 min at 100 W (pulses given every 2 s). This step yields SUV with embedded peptide.
6. Purge the FTIR instrument with H<sub>2</sub>O and CO<sub>2</sub>-depleted air.
7. Collect a background spectrum of the Ge crystal only. Usually 1000 interferograms were taken and averaged for every sample.
8. Spread 500  $\mu\text{L}$  of the lipid-peptide sample over the Ge crystal. It can be done in two steps of 250  $\mu\text{L}$  each.
9. Dry under a stream of H<sub>2</sub>O and CO<sub>2</sub>-depleted air for 3 h.
10. Place the resulting supported multibilayers into the spectrometer and purge for other 15 min.
11. Collect the sample spectra. Background subtraction is done automatically. Spectra were processed with 1-point zero filling HAPP-GENZEL apodization.
12. (*Optional*). For D<sub>2</sub>O exchange, add 1.5 mL of D<sub>2</sub>O to the gas stream to exchange hydrogen by deuterium in the sample. After 3h collect the spectra. Purge the system with CO<sub>2</sub> and H<sub>2</sub>O depleted air overnight to eliminate the residual D<sub>2</sub>O.
13. Correct baseline using Nicolet's OMNIC FTIR software. It can be done by choosing a linear line between the featureless area from 2500 cm<sup>-1</sup> to 1900 cm<sup>-1</sup>.
14. Integrate the peaks using Nicolet's OMNIC FTIR software. Peaks in the region 1520 to 1800 cm<sup>-1</sup> were approximated by Lorentzian and Voigt functions and integrated separately. In general, Amide I peaks were treated as Lorentzian functions and lipid related peaks as Voigt profiles. This was done to ensure maximal approximation of the 11 peaks bounded between the selected area and to avoid over-fitting of Voigt peaks addressed to the peptide-related peaks. Annotate the  $R_{helix}$  and  $R_{site}$  values.
15. Convert  $R_{helix}$  and  $R_{site}$  into peptide orientational parameters ( $\bar{\beta}$ ,  $\bar{\omega}$ ,  $\sigma_\beta$ ,  $\sigma_\omega$ ,  $\theta$ ) by applying theory described in SUB. 5.2.2. This analysis was done using *Mathematica* (Wolfram Research) code<sup>1</sup> and Fortran scripting language<sup>2</sup>.

1 Some of these programs were made available by Dr. SHY ARKIN and Dr. JOSH MANOR, both from The Hebrew University of Jerusalem, Israel.

2 Developed in collaboration with Dr. SANTI ESTEBAN-MARTÍN, Institut de Recerca Biomèdica, Barcelona.

## 6 Protocols

**Rigid-body modeling** Note: In these sections Tcl/Tk scripts <sup>1</sup> running under the *Visual Molecular Dynamics* (VMD) software<sup>2</sup> in text mode in a machine with Fedora as operating system are used.

### Monomer.

1. Generate the starting coordinate file `input.pdb`. It can be done with *SwissPdbViewer* software<sup>3</sup>. For a better control over the dihedral angles use the option `Set Phi/Psi/Omega`.
2. Set the initial tilt angle to zero. Tilt is the angle between the helix director and the z axis so that it is zero when both vectors are parallel.  
Align the structure along the z axis (This requires the Orient package<sup>4</sup>):  

```
%> vmd -dispdev text -e align.tcl -args input.pdb prot_align.pdb.
```

  
Check the tilt angle which should be near zero degrees:  

```
%> vmd -dispdev text -e helix_tilt.tcl -args prot_align.pdb
```
3. Set the initial rotation angle to zero. Rotation is the angle around the helix director and it is defined as zero when the TDM, the helix director and the z axis reside all in the same plane.  
First determine the rotational pitch angle of the first residue for a peptide with non-zero tilt (i.e. tilted in the y-z plane):  

```
%> vmd -dispdev text -e omega3.tcl -args prot_altilt.pdb.
```

  
Then, rotate the aligned structure along the z axis according to the angle so far extracted:  

```
%> vmd -dispdev text -e rotate.tcl -args prot_align.pdb
```
4. Scan tilt and rotational angle in 1 degree increments starting from `protalrot.pdb`. The tilt ranges from 0 (initial structure aligned over the z axis) and 90 degrees (helix director in the x-y plane). The peptide is being tilted over the y axis. Peptide is being rotated around the z axis so that the rotation goes from zero (initial structure) to 360°. For each of the 90x360 generated structures extract the theoretical  $R_{helix}^{theo}$  and  $R_{site,i}^{theo}$  and compare them with the experimental values by means of  $a\chi^2$  error function  

```
%> vmd -dispdev text -e temp.tcl -args protalrot.pdb > output.txt
```

### Dimer.

1. Model a theoretical Bax $\alpha$ 5 dimer based on the dimeric structure of glycoporphin A (1AFO.pdb). It can be done with *SwissPdbViewer* software. Mutate all the residues in the glycoporphin sequence by those of Bax $\alpha$ 5. Perform an energy minimization protocol. Check the helicity since some residues may have lost such definition despite possessing appropriate dihedral angles.
2. Set the initial tilt angle to zero by aligning the symmetry axis of the dimer structure over the z axis:  

```
%> vmd -dispdev text -e align. tcl -args Glycophorinintobax5afterterminmod2.pdb
```
3. Set the initial rotational angle to zero by aligning the dimer so that the symmetry axis of the dimer resides in the y-z plane
4. Scan tilt and rotational angle in 1 degree increments starting from `protalrot.pdb`. In this case, for each of the 90x360 combinations there are three tilt angles: one for the dimer, other for helix1 and the last one for helix2. Similarly, there are three rotational angles, one for the dimer, other for helix1 and the last one for helix 2.  

```
%> vmd -dispdev text -e temp.tcl -args prot_alrot.pdb > output.txt
```
5. Note that in such plots the helix tilt and helix rotation are given with respect to the axis symmetry of the dimer.

---

1 Adapted from the code made available by Dr. SHY ARKIN and Dr. JOSH MANOR, both from The Hebrew University of Jerusalem, Israel.

2 <http://www.ks.uiuc.edu/Research/vmd/>

3 <http://spdbv.vital-it.ch/>

4 [http://www.ks.uiuc.edu/Research/vmd/script\\_library/scripts/orient/](http://www.ks.uiuc.edu/Research/vmd/script_library/scripts/orient/)

**Molecular models**

1. Visualize the best fit solutions of the rigid-body modeling with VMD.
2. Render high-quality images with PovRay<sup>1</sup>.

**6.2.3 X-ray scattering****Reagents**

- For maximal consistency between FTIR and X-ray data, use the same samples prepared as just described (step 5, SUB. 6.2.2).

**Equipment**

- Bruker AXS equipped with CuK $\alpha$  X-ray tube (Made available at the Nano-characterization Institute, Hebrew University, Jerusalem, Israel)
- Platform to tilt the supported bilayers over the Ge crystal.

**Procedure 1: mosaicity**

1. Perform a specular reflectivity scan ( $\alpha_i = \alpha_f$ ) to determine the position of the first Bragg peak. Usually values of  $2\theta$  from 1 to 2.2 degrees are enough.
2.  $\chi$ -scan the sample around the axis perpendicular to the X-ray beam. Usually  $\chi$  angles vary from  $-8^\circ$  to  $8^\circ$  with  $1^\circ$  step increments.
3. Plot the intensities of the first Bragg peaks as a function of the tilt angle.
4. Fit the curve with a Gaussian function. The standard deviation of the Gaussian distribution,  $\sigma$ , is then the mosaicity.

**Procedure 2: electron density profile**

1. Perform a complete specular reflectivity scan. Under our experimental conditions  $2\theta$  ranged from 1 to 13 degrees.
2. Calculate the lamellar repeat distance,  $d$ , from Eq. 5.32.
3. Integrate the Bragg peaks in order to calculate the Fourier coefficients  $f(n)$ . Use at least four Bragg peaks.
4. Calculate the electron density profile over the  $z$  axis,  $\rho(z)$ , using the model presented in Eq. 5.33.
5. The plot of the electron density as a function of the distance from bilayer center is set on a relative  $y$ -scale and should show two peaks (the electron-rich phosphate region) and a valley (the electron-deficient hydrocarbon chains).

**6.3 Peptide-peptide interactions in membrane environments****Reagents**

- Unlabeled Bax $\alpha$ 5, Alexa350-Bax $\alpha$ 5, E(EDANS)-Bax $\alpha$ 5, K(Dabcyl)-Bax $\alpha$ 5, Dabcyl-Bax $\alpha$ 5 (prepared as described in SUB. 6.1.2)
- Lipids (POPC, CL, DOPE; Avanti Polar Lipids)
- HFIP (Sigma)
- PBS1

---

<sup>1</sup> <http://www.povray.org>

## 6 Protocols

**Equipment** See SUB. 6.5.1

### Procedure

1. Co-solubilize donor peptides, acceptor peptides and lipids in HFIP by adding the amounts needed for the desired bulk P/L and molar fraction of acceptor. Prepare a sample with the same amount of donors only or acceptors only (background control).
2. Remove the organic solvent. It can be done by gently flushing N<sub>2</sub> over the sample, followed by complete desiccation overnight at low pressure.
3. Hydrate the lipid-peptide film in PBS1. Vortex. Freeze(liquid nitrogen)/thaw (37°C) 6 times.
4. Extrude the MLVs with bound peptides through two stacked polycarbonate filters of 100 nm pore size.
5. Measure the steady-state fluorescence intensity of LUVs with bound peptides.
6. (*Optional*) Measure the fluorescence lifetime of LUVs with bound peptides.
7. Repeat steps 1-5 for different molar fractions of acceptor peptide. Plot FRET efficiency,  $E^{ss}$  for steady-state measurements or  $E^{tr}$  for time-resolved experiments, as a function of the molar fraction of acceptors.
8. Analyze the data according to the theory described in SUB. 5.3.2. This was done using *Mathematica* code.

## 6.4 Thermodynamic studies

### 6.4.1 Peptide-lipid interactions

**Reagents and Equipment** See SUB. 6.2.1

#### Procedure

1. Repeat steps 1-5 in SUB. 6.2.1 for a fixed Bax $\alpha$ 5 concentration and different lipid concentrations,  $[L]$ .
2. Plot the  $[\theta]_{MR}$  at 200 nm as a function of  $[L]$  and fit the curve with Eq. 5.54 and 5.55 to get  $K_x$ .
3. Convert  $K_x$  into  $\Delta G_x$  using Eq. 5.56
4. Estimate  $\Delta G_{if}$ ,  $\Delta G_{if}^{helix}$  and  $\Delta G_{oct}$  with the MPEx program<sup>1</sup>

### 6.4.2 Peptide-peptide interactions

#### Reagents

- Alexa350-Bax $\alpha$ 5 and K(Dabcyl)-Bax $\alpha$ 5 (prepared as described in SUB. 6.1.2)
- Lipids (POPC, DMPC; Avanti Polar Lipids)
- HFIP (Sigma)
- PBS1

**Equipment** See SEC. 6.3 and TAB. 6.3 and 6.4.

---

<sup>1</sup> <http://blanco.biomol.uci.edu/mpex/>

**Procedure**

1. Repeat steps 1-7 in SEC. 6.3 at a fix donor/acceptor molar ratio (0.5) and varying the lipid concentration.
2. Plot the steady-state FRET efficiency,  $E^{ss}$ , as a function of the lipid concentration (or acceptor mole ratio).
3. To each data point subtract the computationally determined FRET efficiency due to proximity effects,  $E_{proximity}$ .
4. Multiply the resulting FRET efficiency values due to oligomerization only,  $E_{dimer}$ , times two to get the fraction of dimeric peptide,  $f_d$ .
5. Fit a plot of  $f_d$  as a function of  $[L]$  to Eq. 5.59 to get  $K_{dimer}$ .
6. Convert  $K_{dimer}$  into  $\Delta G_x$  using Eq. 5.60.
7. Perform HILL analysis as described in page 94

**6.5 Activity studies****6.5.1 Leakage experiments in ensembles of LUVs****Equipment**

- LabAssay Phospholipid Kit (Wako)
- Light scattering equipment (ZetaSizer Nano ZS running *Dispersion Technology Software*; Malvern Instruments)
- UV-Vis spectrophotometer (mod 9648; Agilent Technologies)
- Gel filtration column (MiniTrap G-25, Sephacryl S-500 HR; GE)
- Chromatography platform (Econo system; Biorad, ÄKTA prime; GE)
- Spectrofluorimeter (Photon Technology International). For steady-state measurements a Xe arc lamp as continuous light source and a photomultiplier detection system were used. For lifetime measurements the *LaserStrobe* technique was used. The system includes a pulsed N<sub>2</sub> laser ( $\lambda=337$  nm), a dye laser (tunable over a wide spectral range from 360 to 990 nm), a frequency doubler (tunable in the deep UV region from 235 to 345 nm) and a stroboscopic detection system (which comprises a photomultiplier and controlling electronics). The dyes PLD-366 and PLD-536 were used for Alexa350-Bax $\alpha$ 5 and unlabeled Bax $\alpha$ 5 respectively.
- 1 mL quartz cells for leakage, and dithionite experiments. 50  $\mu$ L quartz cells for the FRET measurements (Hellma).

**Reagents**

- Unlabeled Bax $\alpha$ 5 (prepared as described in SUB. 6.1.2)
- Lipids (POPC, DOPE, CL; Avanti Polar Lipids)
- Chloroform (VWR)
- Acetone (VWR)
- Ethanol (VWR)
- PBS1
- Triton X-100 (AppliChem)
- Liquid N<sub>2</sub> or dry ice/acetone

**Tab. 6.3 : Steady-state fluorescence parameters.**

Sample	$\lambda_{exc}(\text{nm})$	$\lambda_{emi}(\text{nm})$
<i>Calcein/FD</i>	490	520
<i>ANTS</i>	360	530
<i>NBD-PE</i>	470	540
<i>Unlabeled Bax<math>\alpha</math>5 (Trp)</i>	280	290-550
<i>Alexa350-Bax<math>\alpha</math>5</i>	350	360-680
<i>(E)EDANS-Bax<math>\alpha</math>5</i>	336	346-650

**Tab. 6.4 : Lifetime fluorescence parameters.**

Parameter	Unlabeled Bax $\alpha$ 5 (Trp)	Alexa350-Bax $\alpha$ 5
$\lambda_{exc}(\text{nm})$	560*	360
$\lambda_{emi}(\text{nm})$	330	430
<i>Start delay (ns)</i>	158	145
<i>End delay (ns)</i>	200	220
<i>Channels</i>	300	300
<i>Integration time (<math>\mu\text{s}</math>)</i>	50	50
<i>Averages</i>	3	3
<i>Shots</i>	5	3
<i>Frequency (Hz)</i>	10	10

\* It converts into 280 nm after passing the frequency doubler

**Procedure**

1. Prepare LUVs as described in SUB. 6.1.1, but hydrate the lipid film in a buffer supplemented with the dyes, either calcein (80 mM) or ANTS/DPX (12.5 mM/45mM).
2. Remove the excess of non encapsulated dye by gel filtration chromatography. For small dyes, like calcein and ANTS/DPX, use Sephadex G-25 or G-50 as the stationary phase. For bigger dyes, like fluorescein-labeled dextrans, chromatography beds made of Sephacryl S-500 HR gives optimal results. The protocol that follows is for prepacked G-25 columns that can be operated by gravity. However, it can be conveniently scaled up using columns packed with Sephacryl S-500 HR. In this latter case an appropriate chromatography equipment is mandatory.
3. Equilibrate the column with 15 mL of buffer, isoosmolar to that used in the previous step.
4. Load 500  $\mu$ L of LUVs. If the volume is lower, add buffer after the sample has entered into the column until the void volume is completely filled (500  $\mu$ L).
5. Elute with 1 mL of equilibration buffer. For calcein, the first 250  $\mu$ L of eluted sample give the best results. For ANTS/DPX collect the first 500  $\mu$ L eluting from the column. For fluorescein-labeled dextrans, elution should be monitored by absorbance.
6. Wash the column until the excess dye has been completely removed. It may be stored for further use in 20% ethanol at 4°C.
7. Estimate the lipid concentration in the eluates with the kit of Wako following manufacturer's instructions. A colorimeter is needed in this step.
8. (*Optional*) Check LUV size by DLS.
9. Store the LUVs with entrapped dye at 4°C and use within 1 week. LUV integrity before assays can be checked by fluorescence spectroscopy as described below.
10. In a fluorescence quartz cell add the buffer and the liposomes. We used calcein-containing LUVs at 5  $\mu$ M (also valid for FD) and ANTS/DPX-containing LUVs at 50  $\mu$ M. Check baseline stability by measuring fluorescence in a spectrofluorimeter.
11. Add the appropriate amount of peptide for the desired bulk P/L.
12. Monitor the increase of fluorescence signal, wait until it stabilizes ( $\sim$ 10 min under our experimental conditions) and add Triton X-100 10% (v/v) to fully solubilize vesicles.
13. Plot the normalized fluorescence signal as a function of time from the moment of peptide addition (EQ. 5.62).

**6.5.2 Quenching of fluorescent lipids in ensembles of LUVs****Reagents**

- Unlabeled Bax $\alpha$ 5 (prepared as described in SUB. 6.1.2)
- Lipids (POPC, CL, NBD-PE; Avanti Polar Lipids)
- PBS1
- Sodium dithionite (Sigma)
- Tris (Sigma)
- HCl (AppliChem)
- Triton X-100 (AppliChem)

## 6 Protocols

### Procedure 1: *addition method*

1. Mix, in organic solvent, the lipids of choice according to desired composition plus 0.5 mol% of the fluorescent lipid NBD-PE.
2. Follow STEPS 2-9 described in SUB. 6.1.1.
3. In a quartz cell suitable for fluorescence, add the buffer and the NBD-labeled liposomes. Check baseline stability in a spectrofluorimeter.
4. Add the appropriate amount of peptide for the desired bulk P/L.
5. At any desired time, add the quencher, sodium dithionite (stock concentration 1M in Tris-HCl 1M pH=10) at a final concentration of 20 mM in the cuvette.
6. Monitor the loss in fluorescence signal and add Triton X-100 to disrupt vesicles and determine the lowest achievable level of fluorescence.
7. Plot the normalized fluorescence as a function of time since quencher addition (EQ. 5.63).

### Procedure 2: *reconstitution method*

1. Mix, in organic solvent, the lipids of choice according to the desired composition supplemented with 0.5 mol% NBD-PE lipid and the appropriate amount of peptide to get the desired bulk P/L.
2. Follow STEPS 2-9 described in SUB. 6.1.1.
3. In a cuvette add the buffer and the NBD-labeled liposomes containing peptide. Check baseline stability in a spectrofluorimeter.
4. Add sodium dithionite quencher at a final concentration of 20 mM in the cuvette.
5. Monitor the loss in fluorescence signal and add Triton X-100 to disrupt vesicles and determine the lowest achievable level of fluorescence.
6. Plot the normalized fluorescence signal as a function of time from the moment of peptide addition (EQ. 5.63).

### 6.5.3 Single GUV experiments

#### Marker diffusion across the membrane

#### Reagents

- Unlabeled Bax $\alpha$ 5, Alexa647-Bax $\alpha$ 5 (prepared as described in SUB. 6.1.2)
- GUVs (prepared as described in SUB. 6.1.1)
- BSA (Sigma)
- Fluorescent dye markers: Alexa488, Alexa555 (Invitrogen Molecular Probes); Atto655 (Atto Technology); 10 kDa fluorescein-labeled dextrans, (Sigma); and Alexa488-cytochrome c<sup>1</sup>.

---

1 A gift from Dr. ANA GARCÍA-SÁEZ, Biotec, Dresden.

**Equipment**

- LSM 510 Meta (Zeiss) using a 40x NA 1.2 C-Apochromat water immersion objective with photomultiplier tube detector. Images were recorded in multitrack mode. For the first track, the excitation light was from Ar-ion (488 nm) and He-Ne (633 nm) lasers and the emission was split into two channels and filtered by a 650 nm long-pass filter (channel colored red) and a 505–550 nm band-pass filter (channel colored green). For the second track, the sample was excited with an He-Ne laser at 543 nm and the emission light was filtered through a 560–615 nm band-pass filter (channel colored blue). Images were recorded in grayscale and pseudo-colored red, green or blue as described.
- 8-well observation chamber (LabTek)

**Procedure**

1. Prepare GUV according to the protocol described in SUB. 6.1.1. (*Alternative*) GUVs may be electroformed in the presence of peptides and this is referred to as the *reconstitution* method in the *results* PART of this Thesis. Simply add the mixture of peptides and lipids directly onto the Pt wires and proceed with the protocol. Otherwise, we talk about the *addition* approach since reagents are added sequentially.
2. Incubate the observation chamber with 500  $\mu\text{L}$  of BSA (2 mg/mL in PBS2) for 30 min. BSA binds to the walls of the observation chamber and blocks unspecific peptide adsorption.
3. Add the following components to the observation chamber: 450  $\mu\text{L}$  of PBS, the appropriate amount of dye (we will refer to this as *first* dye) to get a final concentration of 1  $\mu\text{M}$ , and the appropriate amount of peptide (labeled or unlabeled) to obtain the desired bulk P/L. Mix gently and thoroughly.
4. Add the GUVs (50  $\mu\text{L}$ ) and wait until they sediment at the bottom of the observation chamber ( $\sim 3$  min).
5. Observe the sample under the fluorescence microscope and search for a *good* area to image, with a sufficient number of well formed GUVs. There is a lag time of several minutes between peptide addition and pore formation so usually there is enough time to explore the sample before start recording data.
6. Record a video for 2 h to study the kinetics of dye entry into the GUVs. If the peptide is labeled it is possible to study the membrane binding kinetics as well. (*Alternative*) Add two dyes of different size at the same time and monitor the “leakage” kinetics.
7. Take a second image to represent the effect of peptide activity after the two hours time.
8. Carefully add a *second* dye in order not to disturb the area under observation. Do not mix. (*Alternative*) Add two dyes of different size at the same time and monitor the “leakage” kinetics.
9. Take a video in order to study the kinetics of 2nd dye entry into the GUVs.
10. Take an image at the end of the registered kinetics.
11. Carefully add a *third* dye avoiding mixing.
12. Take a video in order to study the kinetics of 3rd dye entry into the GUVs
13. Take a final image at the end of the registered kinetics.
14. Perform image analysis. We used the public domain program *Image J*<sup>1</sup>. Some image analysis can also be done with the freeware LSM Image Browser from Zeiss<sup>2</sup>. For the kinetic analysis we used the *Image J* plug-in Time Series Analyzer<sup>3</sup>

**Scanning fluorescence correlation spectroscopy**

1 <http://rsbweb.nih.gov/ij/>

2 <http://www.zeiss.de/C12567BE0045ACF1/Contents-Frame/CAA2EF638EC5F0D3C1256ADF0050E2F1>

3 <http://rsbweb.nih.gov/ij/plugins/time-series.html>

## 6 Protocols

### Reagents

- Alexa647-Bax $\alpha$ 5 (prepared as described in SUB. 6.1.2)
- GUVs (prepared as described in SUB. 6.1.1)
- BSA (Sigma)
- Fluorescent dye markers: Alexa488 (Invitrogen Molecular Probes) and Atto655 (Atto Technologies).

### Equipment

- Laser-scanning microscope LSM 510 Meta (Zeiss) using a 40x NA 1.2 UV-VIS-IR C-Apochromat water immersion objective, the 488-nm line of an Argon-ion laser (25  $\mu$ W), the 633 He-Ne laser (15 $\mu$ W) and a home-built detection unit at the fiber output channel. A bandpass filter (HQ700/75 filter; AHF Analyze Technik) was used behind a collimating achromat lens to reject residual laser and background light. Another achromat (LINOS Photonics) with a shorter focal length was used to image the internal pinhole onto the aperture of the fiber of the avalanche photo diode (APD, Perkin-Elmer). The photon arrival times were recorded in the photon mode of the hardware correlator Flex 02-01D (<http://correlator.com>, Bridgewater).
- 8-well observation chamber (LabTek)

### Procedure

1. Prepare GUVs (without fluorescent-labeled lipids) according to the protocol described in SUB. 6.1.1.
2. Treat the observation chamber with 500  $\mu$ L of BSA (2 mg/mL in PBS2) for 30 min.
3. Add the following components to the observation chamber: 450  $\mu$ L of PBS2, the amount of the Alexa488 needed for a final 1  $\mu$ M concentration, the appropriate amount of Alexa647-Bax $\alpha$ 5 for a P/L of 1/180. Mix thoroughly.
4. Add the GUVs (50  $\mu$ L) and wait 2 h to ensure complete equilibration.
5. Annotate whether each particular GUV is porated or not by looking at the presence of Alexa488 in the inside and proceed with the SFCS experiment.
6. Place a solution containing a marker of known diffusion, i.e. Atto655, in the observation chamber.
7. Remove the beam-splitter and place an appropriate filter instead.
8. In the *LSM* software set a continuous spot scan with the slowest scan speed (set laser power at 1%).
9. In the *Flex02-01* software align the optical system including:  $\{x, y\}$  position; pinhole; and correction ring.
10. Perform a 50 s run and extract the auto-correlation function. Check that the amount of signal is optimal (counts/molecule), the structure parameter  $S$  is within the limits (4-6) and that the diffusion coefficient is similar to that reported in the literature ( $D_{\text{Atto655}} = 426 \mu\text{m}^2/\text{s}$  in water at 25°C).
11. Place the GUV-Bax $\alpha$ 5 sample in the observation chamber.
12. Back in the *LSM* software set a frame scan with multiple tracking. The first forward track is done but NOT saved; check only the second back track (this is done so because only the back-scan gives parallel lines). For scanning perpendicularly to the membrane surface of the GUV, set the zoom at 12 and the rotation at 45°. Scan two parallel lines of 35 pixels each at the maximum speed in continuous mode. For ease of observation you may increase the laser power (but remember to decrease the laser power to 1% when performing the SFCS measurement to avoid APD overflowing). Note that the membrane should be at the middle of the two lines (see FIG. 5.18 A).
13. In the *Photon Stream Control Panel* software set a duration of 500 s and start measuring.

14. Construct the auto-correlation and cross-correlation curves using the *SFCS* program. The photon stream is binned in bins of  $2 \mu\text{s}$  and arranged as a matrix such that every row corresponds to one line scan. Movements of the membrane are corrected for by calculating the position of the maximum of a running average over several hundred line scans and shifting it to the same column. An average over all rows is fitted to a Gaussian so that only the elements of each row between  $-2.5\sigma$  and  $2.5\sigma$  are used to construct the intensity trace. The auto- and cross-correlation curves of the resulting intensity traces are computed with a multiple tau correlation algorithm.
15. Fit the auto- and cross-correlation curves to the analytical models described in SUB. 5.5.3 with a non linear least-squares fitting algorithm using the *FCSFit* program. It is important to exclude from further analysis irregular curves resulting from major instabilities and identified by distortions of the curves and a systematic change in the intensity trace. Both programs were written in *Matlab* (The Mathworks) code <sup>1</sup>.

## 6.6 Miscellaneous reagents

### 6.6.1 Common buffer systems

#### PBS1 (PhosphateBufferSaline1)

- Sodium dihydrogenphosphate/monohydrogenphosphate 10 mM pH=7.4
- NaCl 100 mM
- EDTA 0.1 mM

#### PBS2 (PhosphateBufferSaline2)

- Sodium dihydrogenphosphate/monohydrogenphosphate 10 mM pH=7.4
- NaCl 137 mM
- KCl 2.5 mM

#### PB (Phosphate Buffer)

- Sodium dihydrogenphosphate/monohydrogenphosphate 10mM pH=7.4

#### Acetate buffer

- Acetic acid/sodium acetate buffer 100 mM pH=4.5
- NaCl 100 mM
- EDTA 0.1 mM

### 6.6.2 Electrophoresis buffers

#### Glycine SDS-PAGE

---

<sup>1</sup> Made available by Dr. JONAS RIES, Biotec, Dresden.

**Tab. 6.5 : Glycine SDS-PAGE set up.**

	12% acrylamide	4% acrylamide
	Resolving gel ( $\mu\text{L}$ )	Stacking gel ( $\mu\text{L}$ )
<i>Solution A</i>	3200	600
<i>Solution B</i>	2000	
<i>Solution C</i>		800
<i>Water</i>	2800	1950
<i>TEMED</i>	8	10
<i>PSA 10% w/v</i>	40	9

**Running buffer**

- Tris base 25 mM pH=8.3
- Glycine 192 mM
- SDS 0.1% w/v

**Solution A<sup>1</sup>**

- Acrylamide 30% w/v
- bisacrylamide 0.8% w/v

**Solution B**

- Tris-HCl 1.5 M pH=8.8
- SDS 0.4% w/v

**Solution C**

- Tris-HCl 0.5M pH=6.8
- SDS 0.4% w/v

**Tricine SDS-PAGE****Anode buffer**

- 0.2 M Tris-HCl pH=8.9

1

This solution is also used in Tricine SDS-PAGE.

Tab. 6.6 : Tricine SDS-PAGE set up.

	16% acrylamide	10% acrylamide	4% acrylamide
	Resolving gel ( $\mu\text{L}$ )	Spacer gel ( $\mu\text{L}$ )	Stacking gel ( $\mu\text{L}$ )
<i>Solution A</i>	2750	665	265
<i>Gel buffer</i>	1660	665	500
<i>SDS 10% w/v</i>	50	20	20
<i>Glycerol 87%</i>	525		
<i>Water</i>	15	690	1220
<i>TEMED</i>	2	1	2
<i>PSA 10% w/v</i>	17	7	17

**Catode buffer**

- Tris base 0.1 M pH=8.25
- Tricine 0.1 M
- SDS 0.1% w/v

**Gel buffer**

- Tris-HCl 3M pH=8.45



## **Part III**

# **Results, Discussion and Conclusions**



# 7 Binding of Bax $\alpha$ 5 to membranes

## 7.1 Introduction

In their association with lipid membranes peptides form a very special type of supramolecular entity. First, membranes are very complex and highly dynamic, with physical properties of liquid crystals, chemical properties dominated by large gradients of polarity and a diversity of possible types of interactions. Yet, as we shortly introduce below, the interaction of peptides with membranes is dominated by the hydrophobic effect and is best studied as a partitioning equilibrium. Much like a change in solvent, the transition of a peptide to the membrane means also a dramatic change of environment which impacts the expected lowest energy structure. Like two faces of the same coin, partitioning and (re)folding come always together when peptides (and proteins in general) bind to membranes, and studies of binding of peptides to membranes should ideally be always accompanied by a structural investigation. This *partitioning-(re)folding* coupling has been considered to devise a global thermodynamic cycle which describes the binding, insertion and assembly of peptides and proteins in membranes. Thus, the membrane binding step can be split into two equilibria [462]: (i) Peptide partitioning from the water phase to the membrane phase as a random coil, and (ii) change in the peptide secondary structure in the membrane-bound state. Because free amide carbonyl and NH groups from an unstructured polypeptide backbone are highly polar, their immersion into the low-dielectric membrane environment is very unfavorable [24]. However, the free energy cost is greatly reduced when such groups participate in hydrogen bonds, which acts as a major driving force for secondary structure formation in the membrane environment [22, 24, 96, 127]. WILLIAM WIMLEY and STEPHEN WHITE have developed an experimental hydrophobicity scale based on the energetics of partitioning of unstructured small peptides to the interface of POPC membranes [22]. Since the free energy of transfer of peptides from water to the bilayer, and the accompanying gain of secondary structure, can be determined experimentally, it is possible to estimate the gain in free energy corresponding to peptide folding at the membrane interface [136]. The secondary structure of peptides in the membrane can be assessed by several spectroscopic techniques, including CD [394], FTIR [484] and NMR [485]. The first two types of measurements can provide reliable quantitative estimates of the peptide structure directly in lipid membranes and are relatively easy to perform with small amounts of sample. Therefore, they were chosen by us for this study.

**Objectives** In this chapter we analyze shortly the formation of complexes of Bax $\alpha$ 5 from both structural and thermodynamic points of view. The structural analysis, performed by simple spectroscopic methods, CD and FTIR, allows following the extent

of formation of the complex and in parallel provides the input for the thermodynamic description. A more complete structural study, which includes peptide orientation and oligomer formation, can be found in the two following chapters.

### 7.2 Secondary structure of Bax $\alpha$ 5 in vesicle membranes<sup>1</sup>

The secondary structure of Bax $\alpha$ 5 was investigated in model membranes by a combination of circular dichroism and ATR-FTIR spectroscopies<sup>2</sup>.

#### 7.2.1 CD spectra

For the CD measurements, we prepared independently several samples with Bax $\alpha$ 5 reconstituted in LUV membranes, and in all cases containing the same amount of peptide but increasing amounts of lipids. LUVs, made of POPC or POPC:CL (80:20 mol:mol), were of approximately 50 nm diameter. This is a relatively small size and was chosen to minimize scattering artifacts in the far-UV region of CD spectra. Also, since NaCl is known to increase the background CD signal, the samples were prepared in the absence of this salt (PB buffer, sodium phosphate 10 mM pH 7.4). As can be seen in FIG. 7.1 A and B, the presence of LUVs in the samples is accompanied by the development of a band with characteristic minima at 207 and 222 nm, denoting induction of  $\alpha$ -helix structure, which increases with the lipid concentration.

Quantitative determinations from CD data of secondary structure of membrane peptides in samples with LUVs is difficult mainly because of two reasons. First, light scattering due to the vesicle suspension reduces the available wavelength range in the far-UV region, which is particularly rich in structural information [486]. Second, most algorithms for spectra analysis use databases made from water soluble proteins of known structure. In a few cases, membrane proteins are also included in the database [487]. However, none of the common algorithms is optimized for membrane peptides. Nevertheless, to obtain a semi-quantitative estimation of the secondary structure of Bax $\alpha$ 5 in membranes we applied the K2D algorithm [403]. The results, shown in TAB. 7.1, agree with published data of similar amphipathic peptides [93, 118, 135, 136, 468] and with previous data from our group measured for a larger version of this Bax fragment [50, 176]. As expected, Bax $\alpha$ 5 in aqueous buffer is largely disordered, although some  $\beta$ -sheet structure appears to be present. Binding of the peptide to vesicle membranes has the effect of increasing the  $\alpha$ -helical content in a clear lipid-concentration dependent manner. For the highest POPC:CL concentration used (1.8 mM), the percentage of  $\alpha$ -helix is  $\sim$ 68%. The structure induction is clearly weaker in presence of POPC, for which one needs to increase the lipid concentration to 4.8 mM in order to reach  $\sim$ 60% helical

- 
- <sup>1</sup> The theory of CD and IR spectroscopies related to secondary structure content determination can be found in SUB. 5.2.1 and 5.2.2. Detailed protocols for CD and IR measurements can be found in SUB.6.2.1 and 6.2.2. The synthesis of labeled amino acids and peptides can be found in SUB. 6.1.2.
  - <sup>2</sup> The main peptide used in this study, Bax $\alpha$ 5, contains the segment that in the full-length, hydrosoluble structure constitutes the fifth  $\alpha$ -helix of Bax. This way of naming the fragment does not mean an *a priori* assumption of its secondary structure.

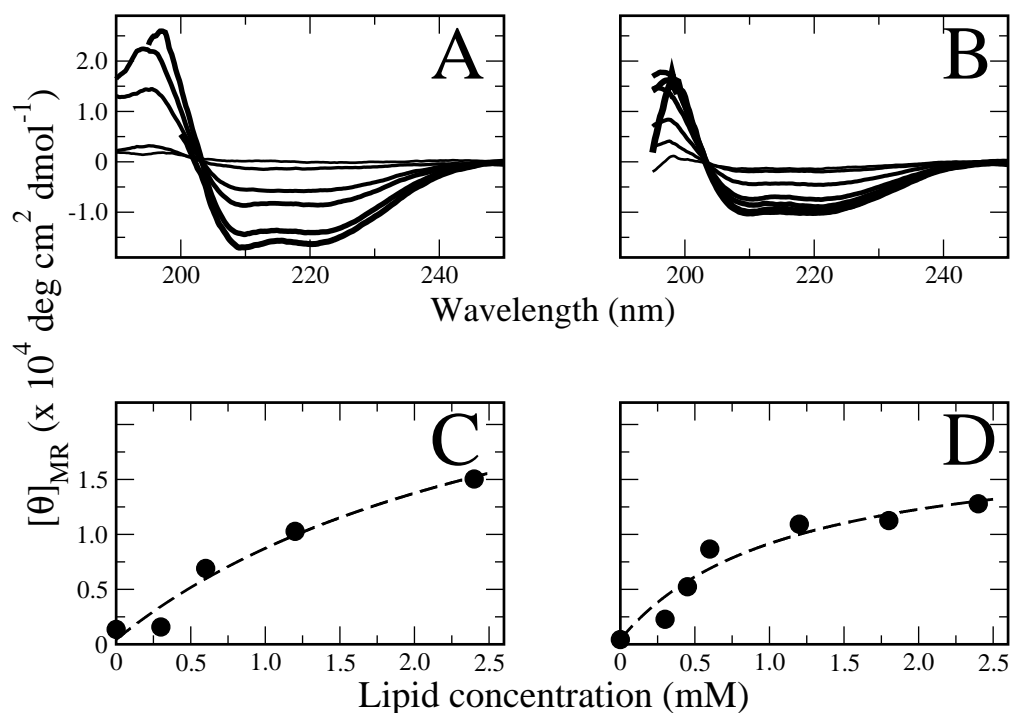


**Fig. 7.1 : Titration of Bax $\alpha$ 5 with LUVs monitored by circular dichroism spectroscopy.** The lipid compositions were POPC (left panel) or POPC:CL (80:20) (right panel). A) and B) Dependence of the mean residue ellipticity ( $[\theta]_{MR}$ ) of Bax $\alpha$ 5 on lipid concentration using peptide reconstituted in LUVs of 50 nm in diameter. While the spectra in PB (no added NaCl) is featureless, bands typical of  $\alpha$ -helix appear in presence of LUVs and the ellipticity increases with the lipid concentration. The existence of an isobestic point in the spectra suggests that the transition is taking place between two populations of Bax $\alpha$ 5: disordered Bax $\alpha$ 5, free in solution, and largely helical Bax $\alpha$ 5, bound to the membrane. C) and D) Experimental data points of the  $[\theta]_{MR}$  at 200 nm as function of lipid concentration (circles), along with the fitting curve (solid line) corresponding to the theoretical hyperbolic dependence on  $[L]$  (EQ. 5.54), from which the partition coefficient,  $K_x$ , is derived.

**Tab. 7.1 : Secondary structure of Bax $\alpha$ 5 as estimated from CD spectra.** LUVs ( $\sim$ 50 nm diameter) of two lipid compositions were used: POPC and POPC:CL (80:20), in aqueous PB buffer (absence of NaCl). Bax $\alpha$ 5 concentration was 30  $\mu$ M. P/L varied between 1/10 and  $\sim$ 1/100. Values are estimates output by the K2D algorithm with the smallest error given as the normalized RMSD between the original and the predicted values (usually below 0.15).

[Lipids] (mM)	POPC			[Lipids] (mM)	POPC:CL		
	$\alpha$ - helix (%)	$\beta$ - sheet (%)	Random coil (%)		$\alpha$ - helix (%)	$\beta$ - sheet (%)	Random coil (%)
0	4	48	48	0	10	45	45
0.3	5	47	48	0.3	11	45	44
0.6	26	25	49	0.45	29	34	37
1.2	37	13	50	0.6	59	14	27
2.4	55	11	34	1.2	67	10	23
4.8	60	7	33	1.8	68	10	22

content. Interestingly, the CD spectra show a characteristic isodichroic point, indicative of a transition between only two states, a first one of low helicity which corresponds to Bax $\alpha$ 5 in the water phase, and a membrane-bound Bax $\alpha$ 5 state characterized by high helicity [468].

## 7.2.2 FTIR spectra

For the secondary structure study we used ATR-FTIR spectra recorded with polarized light irradiation. Thus, before performing the analysis of these data, the orientational dependence of the absorbance needs to be eliminated. Polarization-independent spectra were obtained from the spectra collected at parallel and perpendicular polarizations [488]. In these measurements the sample consists of material deposited and dried on the surface of a Ge crystal and re-hydrated with humid air containing either H<sub>2</sub>O or D<sub>2</sub>O. Under these conditions, samples with lipids form ordered bilayers onto the Ge crystal, parallel to its surface. FIG. 7.2 shows spectra of Bax $\alpha$ 5 deposited from aqueous buffer (A, solid line), a HFIP solution (A, dashed), DMPC membranes (B) and POPC membranes (C). The Amide I absorption band (located between 1700 and 1600 cm<sup>-1</sup>), which corresponds mainly to the C=O stretching vibration arising from the peptide backbone, was fit with two or three Lorentzian-shaped bands (FIG. 7.2 D). Except for the spectrum of Bax $\alpha$ 5 in water, the main component of the band, centered at 1657 cm<sup>-1</sup>, can be assigned to  $\alpha$ -helix, with additional minor high- and low-frequency bands that may represent some  $\beta$ -sheet structure. The percentages of different secondary structure elements are summarized in TAB. 7.2. According to these data, Bax $\alpha$ 5 is highly  $\alpha$ -helical (about 85%) in the two types of phospholipid membranes tested (DMPC and POPC).

At a site-specific level, the observed frequency for most residues (see TAB. 7.3) is

## 7.2 Secondary structure of Bax $\alpha$ 5 in vesicle membranes

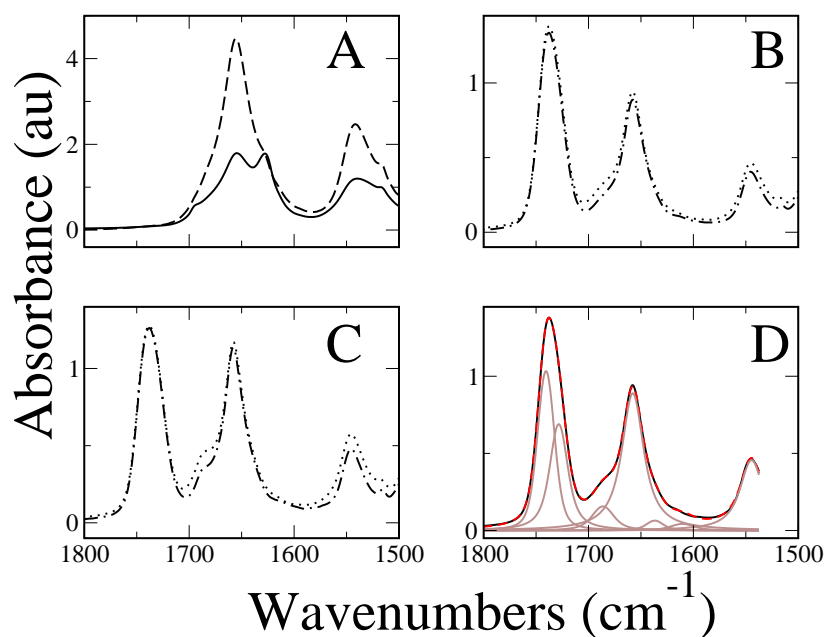


**Fig. 7.2 :** Representative Amide regions in ATR-FTIR spectra of Bax $\alpha$ 5 in different environments. A) Bax $\alpha$ 5 in water (solid line) and HFIP solvent (dashed line). B) Bax $\alpha$ 5 in DMPC membranes before (dotted line) and after (dashed dotted line) D<sub>2</sub>O exchange. C) Bax $\alpha$ 5 in POPC membranes before (dotted line) and after (dashed dotted line) D<sub>2</sub>O exchange. D) Example of deconvolution of spectrum. Original spectrum (black line), fitted spectrum (dashed red line) and individual Lorentzian-shaped bands (gray lines). Bands centered at 1750 cm<sup>-1</sup>, 1650 cm<sup>-1</sup> and 1550 cm<sup>-1</sup> correspond to lipid C=O, Amide I (mainly peptide backbone C=O) and Amide II bands (mainly peptide backbone N-H), respectively.

**Tab. 7.2 :** Secondary structure of Bax $\alpha$ 5 in water, HFIP and different lipid membranes, estimated from FTIR-ATR spectra. For the lipid samples P/L=1/50.

Medium	Secondary structure (%)			H/D exchange (%)
	1686.3±0.3 ( $\beta$ -sheet?)	1656.5±0.5 ( $\alpha$ -helix)	1618±5 ( $\beta$ -sheet?)	
<i>H<sub>2</sub>O</i>	12±9	55±10	33±8	
<i>HFIP</i>	14±7	70±8	16±9	
<i>DMPC-H<sub>2</sub>O</i>	11±3	82±6	7±3	9±7
<i>DMPC-D<sub>2</sub>O</i>	6±4	92±7	2±2	
<i>POPC-H<sub>2</sub>O</i>	12±2	85±5	4±6	22±9
<i>POPC-D<sub>2</sub>O</i>	11±4	81±6	9±5	

in agreement with the frequency shift expected taking into account the masses of the implicated isotopes (a 64  $\text{cm}^{-1}$  downshift due to  $^{13}\text{C}=^{18}\text{O}$  labeling, compared to the natural isotope frequency of  $^{12}\text{C}=^{16}\text{O}$  [410]). Nevertheless, some residues like the Leu-122 and Ala-124 do not follow this trend, which may be interpreted as due to local heterogeneities in the secondary structure with distinct  $\phi$  and  $\psi$  angles. However, both random coil and  $\alpha$ -helix display similar frequencies in samples hydrated with  $\text{H}_2\text{O}$  [489].

**Tab. 7.3 : Position of 1-  $^{13}\text{C}=^{18}\text{O}$  absorption bands of Bax $\alpha$ 5 in membranes.**

Labeled residue	Wavenumber ( $\text{cm}^{-1}$ )	
	DMPC	POPC
<i>Val-111</i>	1592.9 $\pm$ 0.9	1590.5 $\pm$ 0.5
<i>Ala-112</i>	1595.6 $\pm$ 0.7	1592.4 $\pm$ 0.1
<i>Leu-113</i>	1592.8 $\pm$ 0.3	1594.3 $\pm$ 0.1
<i>Phe-114</i>	1586.2 $\pm$ 0.3	1585.1 $\pm$ 1.3
<i>Leu-120</i>	1593.3 $\pm$ 0.2	1593.1 $\pm$ 0.3
<i>Leu-122</i>	1580.9 $\pm$ 0.6	1581.0 $\pm$ 0.4
<i>Ala-124</i>	1598.5 $\pm$ 1.1	1599.0 $\pm$ 1.0

observed that the H/D exchange was somewhat larger in POPC than in DMPC membranes, while the calculated helical content was similar in both cases, suggesting a shallower position (more exposed to water) of the peptide in POPC membranes. In summary the structure of Bax $\alpha$ 5 in membranes is mostly  $\alpha$ -helical. This conclusion is important to perform a more complete analysis of the ATR-FTIR data by assuming a rigid canonical helix model, in order to derive precisely the orientation of Bax $\alpha$ 5 in membranes (See CHAP. 9).

In conclusion, both CD and IR measurements indicate the formation of  $\alpha$ -helical secondary structure for Bax $\alpha$ 5 in membranes although to different degrees which could be related to the different types of membranes employed. For Bax $\alpha$ 5 in POPC bilayers, a  $\sim$ 85%  $\alpha$ -helical content was estimated for the IR samples, which is a 20% higher compared to the CD results (compare TAB. 7.1 and 7.2). A possible explanation could be the different hydration levels of both types of samples. For CD measurements fully hydrated small unilamellar vesicles were used while the IR measurements were made in poorly hydrated oriented multilayers. The low water content in the oriented bilayers (with an average water/lipid molar ratio of 3) could “force” Bax $\alpha$ 5 to partition into the membrane, giving rise to a higher helical content. Therefore, for the particular case of oriented multibilayers with incorporated Bax $\alpha$ 5 (like those used here and in CHAP. 9) the helical content is  $\sim$ 80%. On the other hand, when a suspension of fully hydrated vesicles has been used (like for the CD experiments reported in this chapter and also in oligomerization experiments described in CHAP. 8 and for the pore-

forming activity reported in CHAP. 10) an  $\alpha$ -helical content of 60% in POPC is the most reliable estimation. In any case, most  $\alpha$ -helical membrane-bound peptides show helicities between 50 and 90% so the helical content of Bax $\alpha$ 5 can be considered “acceptable” [65]. There is also a contribution from “random coil”, which could be attributed to the residues located near the peptide termini, and from  $\beta$ -sheet that may correspond to some fraction of the peptides being unsuccessfully reconstituted into lipid bilayer and most probably aggregated.

### 7.3 Energetics of Bax $\alpha$ 5-membrane interactions<sup>1</sup>

As explained in SUB. 5.4.1, a way to characterize partitioning is by titrating a starting solution of Bax $\alpha$ 5 with LUVs and following the change of a spectroscopic signal which is proportional to  $f_p$ , the fraction of membrane-bound peptide. We carried out such an analysis by measuring for each sample the corresponding CD spectrum, as shown in FIG. 7.1 A and B. As we noticed above (SUB. 7.2.1), the CD bands typical of  $\alpha$ -helix rise with increasing lipid concentration, in agreement with partitioning-folding coupling. Additionally, the isosbestic point seen during the titration means that there is a transition between two species, corresponding to membrane-associated (folded) and free-in-water (unfolded) peptide states. Usually, for this type of data it can be assumed that the fractional change of the measured ellipticity varies linearly with  $f_p$  [462, 468]. Then, the CD ellipticity can be expressed as a linear combination of the molar fractions of membrane-bound and free peptide, weighted by their corresponding molar spectroscopic characteristics, and the mole fraction partition coefficient,  $K_x$ , that can be determined from a fit of a hyperbolic function (EQ. 5.54). Because the signal associated to free Bax $\alpha$ 5 is known directly from the experiment in the absence of LUVs, there will be only two unknown parameters:  $K_x$  and the signal associated to membrane-bound Bax $\alpha$ 5.

Plots of molar ellipticities at 200 nm as a function of the lipid concentration for POPC and POPC:CL LUVs are shown in FIG. 7.1 C and D, respectively, together with corresponding theoretical curves. The resulting thermodynamic parameters are collected in TAB. 7.4.  $K_x$  can be converted into  $\Delta G_x$ , the free energy of transfer *from water to bilayer* (EQ. 5.56).

Alternatively, the free energy of peptide transfer from water to the interface of POPC membranes,  $\Delta G_{if}$  can be predicted using the WW-interface scale [22], including contributions of N-terminal (acetyl) and C-terminal (amide) groups [303, 490] (see FIG. 5.15). We may also include for the prediction a per-residue correction accounting for  $\alpha$ -helix structure, which will cause the partitioning free energy to be more favorable. However, this must be done with caution, since we have only an approximate value for the amount of secondary structure of the peptide, and the free energy correction that should be input is not known for certain. As the amount of  $\alpha$ -helix structure, we can get estimates from the CD and FTIR data ( $\sim$ 60–80%). With respect to the value of the correction there is no agreement in the literature, and reported values range from  $\sim$ -0.2 to -0.4

<sup>1</sup> The theory of peptide-membrane interactions can be found in SUB.5.4.1. Detailed protocols can be found in SUB. 6.4.1.

**Tab. 7.4 : Energetics of Bax $\alpha$ 5 binding to LUV membranes.<sup>a</sup>**

Lipid	$K_x$	$\Delta G_X$ (kcal/mol)	$\Delta G_{if}^{helix}$ <sup>b</sup> (kcal/mol)	$\Delta G_{if}^{helix}$ <sup>c</sup> (kcal/mol)	$\Delta G_{oct}^{helix}$ (kcal/mol)
POPC	18161	-5.8	-4.9	-7.5 – -11.9	3.4
POPC:CL	49652	-6.4			

<sup>a</sup>The meaning of these parameters is explained graphically in FIG. 5.15

<sup>b</sup>Without considering folding contribution.

<sup>c</sup>With contribution of folding (as  $\alpha$ -helix) to partitioning; using a per-residue correction between -0.2 and -0.4 kcal/mol and 60-80% helicity.

kcal/mol per residue [103, 128, 136]. Taking this into account, the predicted partition free energies to the interface of POPC bilayers for Bax $\alpha$ 5 range between -7.5 and -11.9 kcal/mol. We can also extract the free energy of helix insertion in the hydrophobic slab of the membrane,  $\Delta G_{oct-if}^{helix}$  by subtracting  $\Delta G_{if}^{helix}$  to the free energy of partitioning to octanol,  $\Delta G_{oct}^{helix}$  (see FIG. 5.15).  $\Delta G_{oct}^{helix}$  can be obtained from the whole residue octanol transfer scale [23, 303] (see TAB. 7.4). Although the octanol and the aliphatic membrane interior are not similar, it seems that the predicted values are quite reliable [65].

$\Delta G_x$  values agree well with those reported for similar amphipathic  $\alpha$ -helical peptides, which are usually in the range -5 to -10 kcal/mol [65, 462]. However, the experimentally determined  $\Delta G_x$  is lower than the conceptually equivalent  $\Delta G_{if}^{helix}$ , the free energy of transfer from water to bilayer interface as an  $\alpha$ -helix, calculated from the Wimley-White interfacial scale and supplemented with a per-residue correction [22, 136]. Both estimations could be in agreement for very low peptide helicities, less than 50%, which are incompatible with our measurements of  $\alpha$ -helix content from either CD or IR. Alternatively, the contribution of peptide bond partitioning as  $\alpha$ -helix, which are derived from a limited number of peptides [128, 136], may not be appropriate for the particular case of Bax $\alpha$ 5 for which  $\Delta G_x \sim \Delta G_{if}$  suggesting that such per-residue contribution is rather small. Finally, we have to consider that peptide partitioning to the membrane is also likely coupled with additional processes, like peptide oligomerization (CHAP. 8) or membrane reorganization. Such processes are not included in the predictions based on hydrophobicity scales which may as well explain the observed apparent disagreements.

## 7.4 Binding and pore-forming activity

ALMEIDA et al suggested that the free energy for insertion into the bilayer nonpolar interior from an initially surface-bound state of the helical peptide can be approximated as  $\Delta G_{ins} \simeq \Delta G_{oct}^{helix} - \Delta G_{if}^{helix}$  [65]. The importance of  $\Delta G_{ins}$  is that it may provide a framework for the mechanism of pore formation by peptides. Such hypothesis (recently demonstrated for some specific cases [491]) proposes that different sequences may give rise to similar dye release mechanisms as long as their thermodynamics of binding and

insertion are similar. More specifically,  $\Delta G^{ins}$  can be used to predict whether a particular peptide will follow the so-called *all-or-none* or the *graded* mechanism. Both concepts were introduced to explain the leakage of encapsulated contents from vesicle ensembles [61, 181]. In the all-or-none case, the pore lifetime is large enough to allow vesicle contents to leak out essentially all at once. This means that at any time individual vesicles are either full of dye or completely depleted. Graded release means that the pore lifetime is close to the release lifetime, so that individual vesicles show variable amounts of dye inside depending on time. It has been proposed that a value of  $\Delta G^{ins}$  near 20 kcal/mol is the threshold between these two cases [65]. Lower values correspond to peptides predicted to follow a graded mechanism, because this low free energy should facilitate peptide translocation across the bilayer. Therefore the peptide would cause efflux during this process which would eventually stop after the dissipation of mass and charge imbalance due to peptide equilibration between the two monolayers. On the other hand, for  $\Delta G^{ins} > 25$  kcal/mol, the peptide does not translocate but accumulates at the membrane interface where it induces pore opening after a certain P/L threshold. The hypothesis also tries to establish a link between the thermodynamics of binding and the dye release kinetics. It proposes that  $\Delta G^{ins}$  should be approximately equal to the activation energy for insertion into the membrane interior,  $E_a^{ins}$ . Therefore the rate constant of dye release should be larger the smaller the Gibbs energy for peptide insertion. According to the values shown in TAB. 7.4 we can estimate a  $\Delta G^{ins} \sim 13$  kcal/mol for Bax $\alpha$ 5. Within the framework of ALMEIDAS's hypothesis such a value would suggest that Bax $\alpha$ 5 permeabilizes vesicles in a graded manner. However, we will see in CHAP. 10 that this contradicts our observations for the pore activity of Bax $\alpha$ 5.

## 7.5 Conclusions

1. The  $\alpha$ -helical content of Bax $\alpha$ 5 in water is very low (random coil and  $\beta$ -structure predominate).
2. In membranes, the  $\alpha$ -helical content of Bax $\alpha$ 5 increases to different extent depending on the lipid composition and characteristics of the sample. Helicities are higher for oriented multibilayers ( $\sim 80\%$ ), compared to suspensions of lipid vesicles ( $\sim 60\%$ ). There is also slightly more  $\alpha$ -helix in POPC:CL membranes ( $\sim 68\%$ ) than in POPC bilayers ( $\sim 60\%$ ).
3. The free energy of Bax $\alpha$ 5 binding to membranes,  $\Delta G_x$ , is  $\sim -6$  kcal/mol. This value is higher than the theoretical  $\Delta G_{if}^{helix}$ , which is likely related to the fact that Bax $\alpha$ 5 interacts with membranes as a dimer, or higher order oligomer (see CHAP. 8).

## 7 *Binding of Bax $\alpha$ 5 to membranes*

## 8 Homo- and hetero-oligomers of Bax $\alpha$ 5 in membranes

### 8.1 Introduction

It is widely accepted that Bax releases to the cytoplasm pro-apoptotic factors normally sequestered in the intermembrane space of mitochondria, through the formation of proteo-lipidic pores in the MOM. However, the exact nature of the Bax *species* responsible for such function is under debate. Oligomeric states ranging from dimers to high molecular weight complexes have been proposed [257, 261, 265, 268, 275, 492–494]. In addition, Bax can bind to other proteins of the Bcl-2 family, like tBid and Bcl-xL, participating in a complicated interaction network that regulates the mitochondrial step of apoptosis and ultimately determines the cell commitment to death [269, 272]. At least two interaction surfaces have been described, which are distinguishable depending on whether they involve the BH3 domain or not. Our knowledge of BH3-dependent hetero-oligomeric interactions has increased over the last decade [175, 296, 495] and homo-oligomeric interactions, with or without participation of the BH3 domain, are being unveiled [258, 280]. Since most interactions between Bax and other Bcl-2 proteins take place in the membrane, where protein structures should change dramatically compared to structures in water, the membrane-binding helices 5 and 6 of Bax may be considered putative candidates for *in-membrane* oligomerization [279, 315].

On the other hand, the problem of oligomer formation among pore-forming polypeptides is a general one. For example, the oligomeric state of pore-forming peptides is not always clear. Similarly to what happens with Bax pores, oligomerization in the membrane is often invoked to explain the membrane disrupting activity induced by peptides [496–500]. However, only a few studies demonstrate that dimeric peptides are more active than their monomeric counterparts [501–503]. Such a confusing scenario may be at least in part due to the fact that the approaches used to study interactions of proteins free in solution are not always well suited for the case of interactions occurring in the membrane. Indeed, only four major biophysical methods are routinely used to study helix-helix association *in vitro*: SDS-PAGE [29], Förster resonance energy transfer (FRET) [432] (see SUB. 5.3.2), sedimentation equilibrium studied by analytical ultracentrifugation [433, 434] and thiol-disulphide exchange [435]. A number of biological assays offer a complementary approach for addressing helix-helix interactions *in vivo* and have contributed significantly to our understanding of how membrane proteins self-associate in bilayers [438–441]. However, most studies have focused on highly hydrophobic trans-membrane domains, and little is known about the assembly properties of amphipathic polypeptides. Intermolecular association for these latter should have special features

**Tab. 8.1 : Peptides used for the oligomerization studies.** All peptides were acetylated at the N-terminus (Ac), amidated at the C-terminus (NH<sub>2</sub>) and the naturally occurring Cys residues (occurring at position 126 in Bax and 151 in Bcl-xL) were changed into Ser (highlighted in blue) to avoid disulphide formation. All numbers indicate the position of the residues in the full-length proteins, either human Bax or mouse Bcl-xL. Fluorescence labels are highlighted in magenta. The native Trp residue at position 107 of Bax (highlighted in bold) was substituted by Glu (blue) for labeling with EDANS, and the native residue Val-129 of Bax $\alpha$ 5 (not shown) was substituted by Lys (blue) for labeling with Dabcyl. Other mutations of Bax $\alpha$ 5 and Bcl-xL $\alpha$ 5 are highlighted in red, and differences in the sequence of Bcl-xL $\alpha$ 5 peptides compared to Bax $\alpha$ 5 are highlighted in green.

Polypeptide	Sequence
<i>Bax<math>\alpha</math>5</i>	Ac- <sup>107</sup> WGRVVALFYFASKLVLKALSTK <sup>128</sup> -NH <sub>2</sub>
<i>E(EDANS)-Bax<math>\alpha</math>5</i>	Ac-E(EDANS) <sup>108</sup> GRVVALFYFASKLVLKALSTK <sup>128</sup> -NH <sub>2</sub>
<i>Alexa350-Bax<math>\alpha</math>5</i>	Alexa350- <sup>107</sup> WGRVVALFYFASKLVLKALSTK <sup>128</sup> -NH <sub>2</sub>
<i>K(Dabcyl)-Bax<math>\alpha</math>5</i>	Ac- <sup>107</sup> WGRVVALFYFASKLVLKALSTK <sup>128</sup> K(Dabcyl)-NH <sub>2</sub>
<i>Dabcyl-Bax<math>\alpha</math>5</i>	Dabcyl- <sup>107</sup> WGRVVALFYFASKLVLKALSTK <sup>128</sup> -NH <sub>2</sub>
<i>Bax<math>\alpha</math>5 Y115S</i>	Ac- <sup>107</sup> WGRVVALFSFASKLVLKALSTK <sup>128</sup> -NH <sub>2</sub>
<i>Alexa350-Bax<math>\alpha</math>5 Y115S</i>	Alexa350- <sup>107</sup> WGRVVALFSFASKLVLKALSTK <sup>128</sup> -NH <sub>2</sub>
<i>K(Dabcyl)-Bax<math>\alpha</math>5 Y115S</i>	Ac- <sup>107</sup> WGRVVALFSFASKLVLKALSTK <sup>128</sup> K(Dabcyl)-NH <sub>2</sub>
<i>Bcl-xL<math>\alpha</math>5 A149K/E153K</i>	Ac- <sup>137</sup> WGRIVAFFSFGGKLSVKSVDK <sup>157</sup> -NH <sub>2</sub>
<i>Bcl-xL<math>\alpha</math>5</i>	Ac- <sup>137</sup> WGRIVAFFSFGGALSVESVDK <sup>157</sup> -NH <sub>2</sub>

due to their higher polarity, their tendency to bind to the membrane interface and their capacity to disrupt the bilayer structure.

**Objectives** In this chapter we first wish to clarify whether Bax $\alpha$ 5 is able to form homo-oligomers. Second, we will study under which sample conditions, particularly specific lipid compositions, such interactions may occur. Third, we will explore the characteristics of the oligomers formed (number of subunits, way of association, sequence requirements). Finally we will study interactions between Bax $\alpha$ 5 and the analogous fragment from the antiapoptotic protein Bcl-xL in physiologically relevant lipids. The sequences of all peptides mentioned in this chapter are shown in TAB. 8.1.

Two approaches were used to study the self-association of Bax $\alpha$ 5 in lipids and lipid-mimetic environments: electrophoresis in polyacrylamide gels with the detergent sodium dodecyl sulfate (SDS-PAGE) and Förster resonance energy transfer, FRET, between donor and acceptor peptides (fluorescent labeled if required) in membranes.

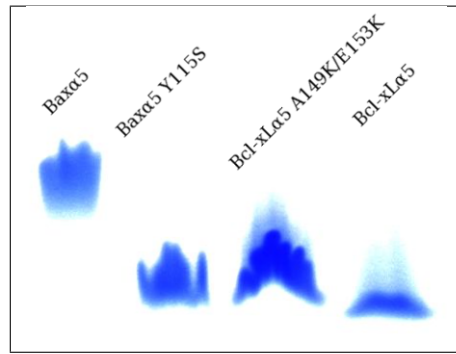


**Fig. 8.1 : Bax $\alpha$ 5 dimerization in SDS micelles.** 20 micrograms of the peptides: Bax $\alpha$ 5, Bax $\alpha$ 5 Y115S, Bcl-xL $\alpha$ 5 A149K/E153K and Bcl-xL $\alpha$ 5, were loaded onto Tris-Tricine gels. After the run, peptides were stained with Coomassie Blue. According to the electrophoretic mobility, two distinct types of bands were observed for Bcl-xL $\alpha$ 5, Bcl-xL $\alpha$ 5 A149K/E153K and Bax $\alpha$ 5 Y115S and for Bax $\alpha$ 5. The migration of the first three is very similar, in agreement with a similar molecular weight and oligomeric state. However, Bax $\alpha$ 5 moves clearly less. Because all peptides are of similar size this pattern strongly indicates the existence of monomers (near 2500 Da) in the cases of Bcl-xL $\alpha$ 5, Bcl-xL $\alpha$ 5 A149K/E153K and Bax $\alpha$ 5 Y115S, while Bax $\alpha$ 5 behaves like a dimer ( $\sim$ 5000 Da).

## 8.2 Oligomerization potential of Bax $\alpha$ 5 by SDS-PAGE<sup>1</sup>

SDS-PAGE is a widely used method for the separation of proteins according to their molecular mass. It is also used to study membrane protein interactions, since in some cases SDS preserves the quaternary structure displayed in the native membrane environment [29, 444, 445, 504]. However, it is also recognized that the highly disrupting power of SDS, compared to that of lipid membranes, may lead to inaccurate results [505]. Thus, the absence of *oligomer bands* (corresponding to  $n$  times the mass of the monomer, with  $n$  being an integer) in a SDS-PAGE gel does not necessarily mean absence of oligomerization in the membrane. Conversely, observation of bands assignable to oligomers, even if these bands are faint, will be an indication of *propensity* or *potential* for association in lipid membranes<sup>2</sup>. Furthermore, in the case of peptides care must be taken when interpreting these results, since anomalous peptide migration cannot always be discarded [446, 448, 506]. This may be especially important for membrane-interacting peptides containing a high amount of polar residues, as in the case of Bax $\alpha$ 5.

In order to make interpretations more clear and avoid potential artifacts the peptides assayed for oligomerization were run together (in the same gel) with other peptides of related sequence but different behavior, which all together help to interpret the observed migration pattern. Specifically, Bax $\alpha$ 5 was run in parallel with the single mutant Bax $\alpha$ 5 Y115S, the analogous fragment in Bcl-xL, Bcl-xL $\alpha$ 5, and a double mutant of this latter

<sup>1</sup> A detailed description of the SDS-PAGE method can be found in SUB. 5.3.1. Detailed protocols can be found in SUB. 6.6.2.

<sup>2</sup> *propensity/potential* is here defined in a non-specific way. It is a statement that depends on the observation of a band assignable to the oligomer and increases with the intensity of the band compared to the intensity of a monomer band made of the same amount of protein.

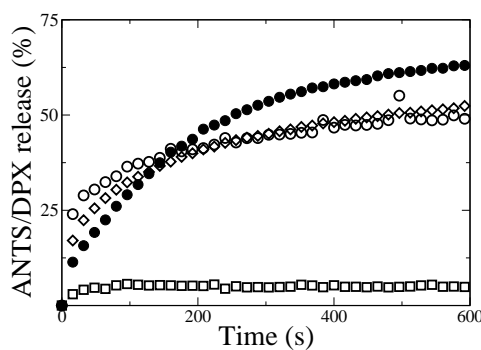


**Fig. 8.2 : Effect of mutations on the leakage activity of Bax $\alpha$ 5.** Peptides were added over POPC vesicles of 100 nm in diameter (5  $\mu$ M) at a peptide/lipid ratio of 1/800 and the release of entrapped ANTS/DPX was monitored over time as the increase in fluorescence intensity. pH was set to 4.5. The release kinetics corresponds to Bax $\alpha$ 5 (closed circles), Bax $\alpha$ 5 Y115S (diamonds), Bcl-xL $\alpha$ 5 A149K/E153K (open circles) and Bcl-xL $\alpha$ 5 (squares).

peptide, Bcl-xL $\alpha$ 5 A149K/E153K. Bax $\alpha$ 5 and Bcl-xL $\alpha$ 5 sequences partially overlap with the BH1 homology domain and thus show some sequence identity, especially at the N-terminus, and many of the differing residues have similar properties (TAB. 8.1). However, there are also a few important differences between the two peptides. Bax $\alpha$ 5 is more amphipathic and has a +4 net charge, while Bcl-xL $\alpha$ 5 has zero net charge. This is due to the existence of two extra Lys residues in Bax $\alpha$ 5, compared to Bcl-xL $\alpha$ 5, which in turn has two acidic residues absent in the former (TAB. 8.1). These details appear to be responsible for the large difference in the membrane activity observed between the two peptides (very high in the case of Bax $\alpha$ 5 and weak in the case of Bcl-xL $\alpha$ 5) [377], and in fact the Bcl-xL $\alpha$ 5 A149K/E153K double mutant, where two Lys residues are introduced resembling the Bax $\alpha$ 5 sequence, is very active in vesicle leakage experiments (FIG. 8.2).

When Bax $\alpha$ 5 and Bcl-xL $\alpha$ 5 are run in the same Tris-Tricine gel in presence of SDS, the band corresponding to the former migrates clearly less than the latter (FIG. 8.1), indicating that they form different molecular aggregates under the conditions of the assay. A Bax $\alpha$ 5 dimer and a Bcl-xL $\alpha$ 5 monomer are the most likely possibility, which is also in agreement with the FRET experiments (see below). The active double mutant A149K/E153K of Bcl-xL $\alpha$ 5 also migrates in agreement with a monomeric state (FIG. 8.1), indicating that this pair of introduced Lys residues (149/153 in Bcl-xL equivalent to 123/128 in Bax) are not involved in dimer formation. Among the other residues differentiating the sequences of Bax $\alpha$ 5 and Bcl-xL $\alpha$ 5, we focused on the ninth position in the peptide sequences. This is a Tyr in Bax $\alpha$ 5 and a Ser in Bcl-xL $\alpha$ 5, and in both peptides this residue is sandwiched between two Phe residues. Interestingly, the Bax $\alpha$ 5 Y115S single mutant has lost the ability to dimerize in presence of SDS micelles (FIG. 8.1). According to its migration in the tris-tricine gel, these data indicate that, despite the sequence similarities between Bax $\alpha$ 5 and Bcl-xL $\alpha$ 5, only the first has the requirements for high membrane activity and dimer formation (FIG. 8.1 and 8.2). Moreover, the two properties do not depend on the same residues. Thus, incorporating two Lys residues

typical of Bax $\alpha$ 5 into the sequence of Bcl-xL $\alpha$ 5 is sufficient to increase its activity<sup>1</sup> (FIG. 8.2), but not for dimerization (FIG. 8.1). Conversely, Tyr115 in Bax $\alpha$ 5 is at least one of the residues responsible for providing critical interactions stabilizing the dimer (FIG. 8.1), although it seems to have only a minor effect on membrane activity (FIG. 8.2).

## 8.3 FRET of labeled Bax $\alpha$ 5 in lipid membranes<sup>2</sup>

The SDS-PAGE experiments are not completely conclusive. It is thus convenient to use various alternative methods and, preferably, samples in lipid membranes. In this part we investigate peptide-peptide interactions using FRET. This technique has many advantages: (i) it allows studying intermolecular interactions directly in lipid membranes, (ii) helps discriminating between dimers and higher order complexes and (iii) gives information about the relative position of monomers in the complex. The latter point is very important and has to be considered initially for the design of appropriate fluorescence labeled peptides, as explained next.

### 8.3.1 Design and synthesis of labeled Bax $\alpha$ 5 peptides

For the FRET experiments, Bax $\alpha$ 5 was labeled as described in SUB. 6.1.2, which allows defining the following sets of donor/acceptor pairs (TAB. 8.1):

- Unlabeled-Bax $\alpha$ 5/E(EDANS)-Bax $\alpha$ 5<sup>3</sup>
- Alexa350-Bax $\alpha$ 5/K(Dabcyl)-Bax $\alpha$ 5
- Alexa350-Bax $\alpha$ 5/Dabcyl-Bax $\alpha$ 5

The design of labeled peptides considers the following guidelines:

1. All extrinsic labels were added at the end of the peptide, either at the N-terminus or at the C-terminus (see TAB. 8.1). This intends to minimize potential negative effects of the dyes on the structure and/or activity of Bax $\alpha$ 5. Nevertheless, the structural and functional consequences of labeling were carefully tested experimentally, as described in the next section. In addition, having alternative designs with probes at either of the two ends allowed us to investigate the relative orientation, parallel *vs* antiparallel, of peptides in the hypothetical dimers.
2. *Unlabeled-Bax $\alpha$ 5* refers to peptides without an extrinsic label, for which the naturally occurring tryptophan residue, located at the N-terminus (first residue in the sequence), was used as energy donor.

<sup>1</sup> Note that Bcl-xL $\alpha$ 5 requires both acidic pH and negatively charged lipids in order to bind efficiently to model membranes, similarly to what happens with Bcl-xL $\Delta$ Ct [284–286, 321].

<sup>2</sup> A detailed description of the FRET method can be found in SUB. 5.3.2. Protocols applying this method for can be found in SEC. 6.3. Sample preparation is described in SUB. 6.1.2.

<sup>3</sup> In this case, the donor group is the only Trp present in the natural sequence. In the acceptor peptide of this pair Trp 1 is substituted by Glu (see TAB. 8.1).

The labeling efficiency varied depending on the strategy used for the synthesis of each particular peptide version. Full labeling was attained for E(EDANS)-Bax $\alpha$ 5 and K(Dabcyl)-Bax $\alpha$ 5, for which the dyes were pre-attached to Fmoc-protected amino acids (Fmoc-Glu(EDANS) and Fmoc-Lys(Dabcyl), respectively) and introduced during the peptide synthesis. However, for Alexa350- and Dabcyl-Bax $\alpha$ 5 the dyes were introduced after the peptide synthesis and the yields were typically lower (85% and 55%, respectively). Underlabeling is not important for the case of Alexa350-Bax $\alpha$ 5, because this variant was used as an energy donor [452]. Additionally, assuming that labeling does not influence the formation of the complex, unlabeled peptides should not contribute to the fluorescence signal. However, for Dabcyl-Bax $\alpha$ 5, used as an energy acceptor, the measured “apparent” FRET efficiency must be corrected [452] to account for incomplete labeling. This correction was made as described in SUB. 5.3.2.

### 8.3.2 Effect of labeling on the structure and activity of Bax $\alpha$ 5

First we investigated the consequence of adding extrinsic fluorophores on the structure and activity of Bax $\alpha$ 5. The structural effects were analyzed qualitatively, using CD spectroscopy (FIG. 8.3 A and B). CD spectra of different Bax $\alpha$ 5 versions were recorded in HFIP and SDS. HFIP is the solvent employed routinely for the stock solutions of Bax $\alpha$ 5, and SDS is the detergent used to run PA gels (see SUB. 8.2). Although there are some differences among the various solvent media, it can be seen that the helix propensity of assayed peptides is very much preserved in all of them. Thus, labeling does not alter significantly the secondary structure of Bax $\alpha$ 5 which remains highly  $\alpha$ -helical in all lipid-mimetic environment tested.

We also monitored the leakage capacity of the different Bax $\alpha$ 5 variants. According to FIG. 8.3 C, all Bax $\alpha$ 5 versions studied induce release of contents encapsulated into POPC vesicles to a similar extent, with the exception of Alexa350-Bax $\alpha$ 5, for which the permeabilizing activity was clearly smaller. However, in this latter case the decrease of activity can be attributed to the negative charge of the fluorophore, which reduces the cationic character of the peptide and should thus affect the affinity for the LUV membrane. With these results we can conclude that labeling maintains the structure and pore-forming ability of Bax $\alpha$ 5.

### 8.3.3 Calculation of the Förster distance

FRET efficiencies are strongly dependent on the Förster distance,  $R_0$ , which is a characteristic property of the D/A pair and may also vary with the medium and other conditions of the assay. It is thus essential to get a good estimate of  $R_0$  values before attempting an accurate determination of the distance between labels,  $r$ .  $R_0$  for Trp/EDANS and Alexa350/Dabcyl pairs can be found in the literature and amount to 2.2 nm and 5.0 nm, respectively [507, 508]. However, such distances may be different for the experimental conditions used in our particular case. As described by EQ. 5.35,  $R_0$  depends upon four parameters:

- The refractive index of the medium ( $n$ )

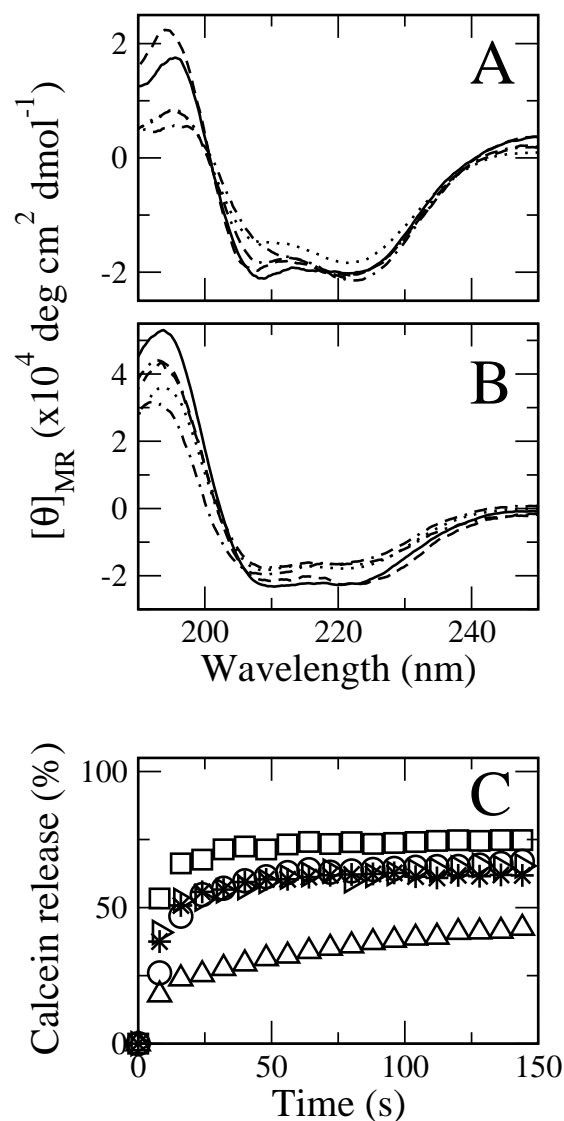


**Fig. 8.3 :** Effect of conjugation with fluorescence dyes on the secondary structure and pore-forming activity of Bax $\alpha$ 5. Circular dichroism spectra of 30  $\mu$ M Bax $\alpha$ 5 in HFIP (A) and SDS (B). In both cases the code is as follows: Unlabeled-Bax $\alpha$ 5 (solid line), E(EDANS)-Bax $\alpha$ 5 (dotted line), Alexa350-Bax $\alpha$ 5 (dashed line), K(Dabcyl)-Bax $\alpha$ 5 (dash-dot line) and Dabcyl-Bax $\alpha$ 5 (dash-dash-dot line). C) Leakage of calcein from POPC LUVs induced by unlabeled and labeled Bax $\alpha$ 5 at P/L=1/500. The reported data corresponds to unlabeled-Bax $\alpha$ 5 (open circles), E(EDANS)-Bax $\alpha$ 5 (squares), Alexa350-Bax $\alpha$ 5 (triangles up), K(Dabcyl)-Bax $\alpha$ 5 (triangles right) and Dabcyl-Bax $\alpha$ 5 (stars).

- The quantum yield of the donor ( $Q_D$ )
- The orientation factor ( $\kappa^2$ )
- The spectral overlap integral ( $J(\lambda)$ )

The refractive index was assumed to be that of water ( $n=1.33$ ). The quantum yield of the donor was obtained from the literature or assumed (see TAB. 8.2).  $\kappa^2$  was taken as 2/3, which is appropriate for dynamic random averaging of the donor and acceptor [452], i.e., donors and acceptors randomized by rotational diffusion prior to energy transfer. Given that labels are in all cases attached to the peptide termini, they are expected to be highly mobile, which renders the latter assumption reasonable. In any case, since both  $Q_D$  and  $\kappa^2$  account as the sixth root for the calculation of  $R_0$ , deviations of these values should contribute only to small errors of  $R_0$ . Finally, the integral  $J(\lambda)$ , expressing the degree of spectral overlap between the emission of the donor and the absorption of the acceptor, must be evaluated for each pair.  $J(\lambda)$  was calculated from the graphs shown in FIG. 8.4 and the data in TAB. 8.2. All excitation and emission spectra were collected using suspensions of POPC vesicles, except for peptides labeled with Dabcyl, which is not fluorescent. In those cases the excitation spectra were recorded as normal absorption spectra in a spectrophotometer and with the sample in organic solvent, because the presence of lipid vesicles impair the measurements due to scattering artifacts. The overlap in the cases with Dabcyl is smaller than values from the literature, most probably due to the attachment of this dye to Bax $\alpha$ 5, which may produce a red-shift in the excitation spectra.

In the case of the unlabeled-Bax $\alpha$ 5/E(EDANS)-Bax $\alpha$ 5 pair, the  $R_0$  values that we calculate coincide essentially with literature values for pairs of the same fluorophores (TAB. 8.3). However, for Alexa350/K(Dabcyl) and Alexa350/Dabcyl pairs our calculated values are  $\sim 20\%$  smaller than other reported values due to the aforementioned difference in the value of  $J(\lambda)$  (TAB. 8.3).

### 8.3.4 Measurements of FRET efficiency

FRET efficiencies, measured as a function of the acceptor mole ratio, give information about the proximity between acceptor and donor fluorophores and can thus be used as an indication of the presence of oligomeric structures [445, 458]. The strategy to achieve such an interpretation can be summarized as follows:

- For a monomeric peptide ( $n=1$ ) the presence of acceptor should minimally affect the fluorescent properties of the donor, and the FRET efficiency should be near zero. However, because of proximity effects (see SUB. 8.3.4) even for monomeric peptides the efficiency may not be zero, especially for a D/A pair with large  $R_0$ .
- For peptide dimers ( $n=2$ ), a plot of the FRET efficiency *vs* the acceptor mol fraction should give a straight line.

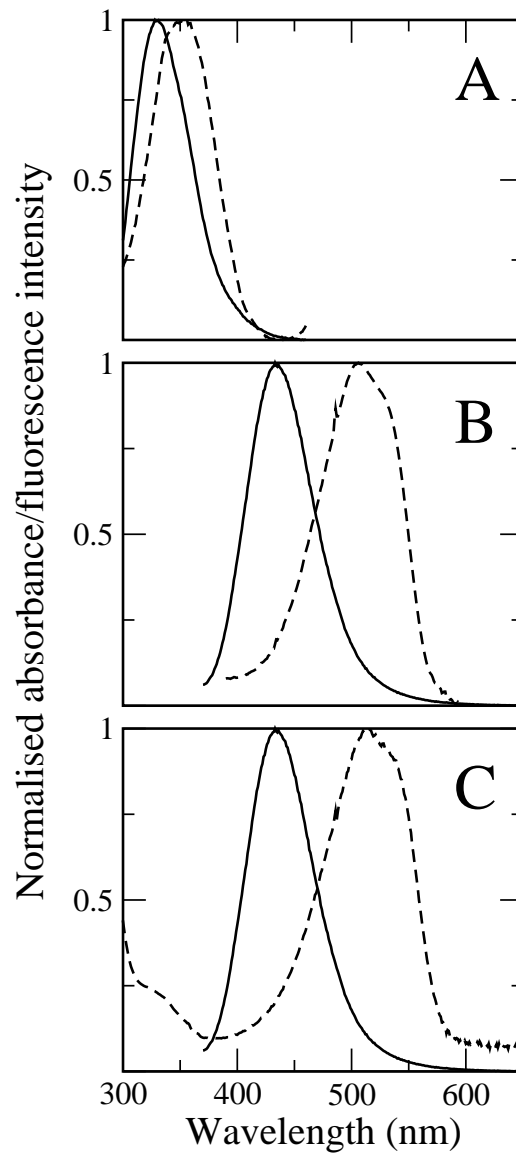


**Fig. 8.4 : Excitation and emission spectra of fluorescence labeled  $Bax\alpha 5$  peptides in various combinations (pairs).** All spectra were recorded in POPC vesicles, except for (K)Dabcyl- $Bax\alpha 5$ , recorded in HFIP. A) Unlabeled/E(EDANS)- $Bax\alpha 5$  pair. B) Alexa350/K(Dabcyl)- $Bax\alpha 5$ . C) Alexa350/Dabcyl- $Bax\alpha 5$  pair. Absorption (excitation) and emission spectra are shown as solid and dashed lines, respectively.

**Tab. 8.2 : Fluorescence parameters.**

Peptide	$\lambda_{exc}^{max}$ (nm) <sup>a</sup>	$\lambda_{emi}^{max}$ (nm) <sup>a</sup>	$\epsilon^{\lambda_{exc}^{max}}$ (M <sup>-1</sup> cm <sup>-1</sup> ) <sup>b</sup>	Quantum yield	Use
<i>Unlabeled-Bax<math>\alpha</math>5</i> (Trp)	280	330	6990	0.13 <sup>c</sup>	Donor or as Unlabeled in competition experiments
<i>E(EDANS)-Bax<math>\alpha</math>5</i>	355	430	5300	NA	Acceptor
<i>Alexa350-Bax<math>\alpha</math>5</i>	360	430	19000	0.75 <sup>d</sup>	Donor
<i>Dabcyl-Bax<math>\alpha</math>5</i> ℓ <sup>e</sup> <i>K(Dabcyl)-Bax<math>\alpha</math>5</i>	505 <sup>e</sup>	—	30000 <sup>e</sup>	NA	Acceptor

<sup>a</sup>Experimentally measured excitation and emission spectra are shown in FIG. 8.4

<sup>b</sup>Taken from [508].  $\epsilon^{\lambda_{exc}^{max}}$  was assumed to be the same as that of the free dye but at the new red-shifted wavelength (see Table note <sup>e</sup>)

<sup>c</sup>Taken from [509]

<sup>d</sup>Assumed value

<sup>e</sup> $\lambda_{exc}^{max}$  for free Dabcyl and amino acid-conjugated Dabcyl is 453 and 427 nm respectively

**Tab. 8.3 : Förster distances ( $R_0$ )**

Donor/Acceptor pair	$R_0$ (nm)	
	Literature	Calculated
<i>Unlabeled-Bax<math>\alpha</math>5/E(EDANS)-Bax<math>\alpha</math>5</i>	2.2 <sup>a</sup>	2.1
<i>Alexa350-Bax<math>\alpha</math>5/K(Dabcyl)-Bax<math>\alpha</math>5</i>	5.0 <sup>b</sup>	4.0
<i>Alexa350-Bax<math>\alpha</math>5/Dabcyl-Bax<math>\alpha</math>5</i>	5.0 <sup>b</sup>	4.0

<sup>a</sup>Taken from [507]

<sup>b</sup>Taken from [508]

- For oligomers larger than dimers ( $n > 2$ ) the dependence of the FRET efficiency on the acceptor mole fraction deviates from linearity and the determination of the stoichiometry becomes non-trivial.

For each acceptor case, three fluorescence spectra were taken:

1. Liposomes containing only donors ( $F_D$  sample)
2. Vesicles containing the same amount of donor and a variable concentration of acceptor ( $F_{DA}$  sample)
3. Liposomes containing only acceptors. ( $F_A$  sample)

**Control experiments.** There are a number of potential artifacts associated to measurements of FRET in membrane systems that should be minimized as much as possible and evaluated by adequate control experiments. First, the fluorescence intensity of labeled peptides should increase linearly with the peptide concentration. For Alexa350-Bax $\alpha$ 5 such a linear response is clear at least up to a P/L of 1/75 (FIG. 8.5 A), indicating absence of self-quenching within that P/L range. Thus, we chose to perform all experiments at  $P/L \leq 1/100$ .

Second, the measured FRET efficiencies have two contributions: one due to random localization of acceptors around donors (*proximity* effects) and the other due to sequence-specific *interactions*. Both effects can be identified in time-resolved fluorescence experiments, as explained in SUB. 8.3.4. We will describe here the proposed correction for the measured FRET efficiencies under steady-state conditions,  $E^{ss}$ .

The addition of unlabeled peptide to preformed labeled dimers should have the effect of decreasing the FRET efficiency, i.e. increasing the fluorescence signal, as demonstrated for well known cases [445, 458]. This is indeed what we observed after adding unlabeled-Bax $\alpha$ 5 to Alexa350-K(Dabcyl) samples (FIG. 8.5 B). Importantly, the mutant Bax $\alpha$ 5 Y115S was also able to compete with the Alexa350-Bax $\alpha$ 5/K(Dabcyl)-Bax $\alpha$ 5 dimers, although with less efficiency, suggesting that the mutant peptide has a reduced dimerization capacity. Thus, sequence-specific dimerization is, at least in part, responsible for the observed FRET efficiencies.

Proximity effects can be estimated by computational methods [455]. The calculated proximity contribution as a function of the acceptor/lipid molar ratio is represented in FIG. 8.5 C (solid line) for  $R_0=4$  nm. The experimental values of steady-state FRET efficiency for Bax $\alpha$ 5 in POPC (circles) and DMPC (squares for the gel phase and triangles for the liquid crystal phase), lay above this theoretical curve, confirming that both proximity effects and sequence-specific dimerization are contributing to the measured FRET. However, for the mutant Bax $\alpha$ 5 Y115S (stars) some experimental points are close or even below the theoretical curve, suggesting an important contribution of proximity effects in the measured efficiencies and thus a reduced dimerization propensity.

**Steady-state fluorescence.** Typical spectra for  $F_D$ ,  $F_{DA}$  and  $F_A$  samples taken at a total P/L of 1/200 are shown in FIG. 8.6 A, C and E. For all three pairs a clear

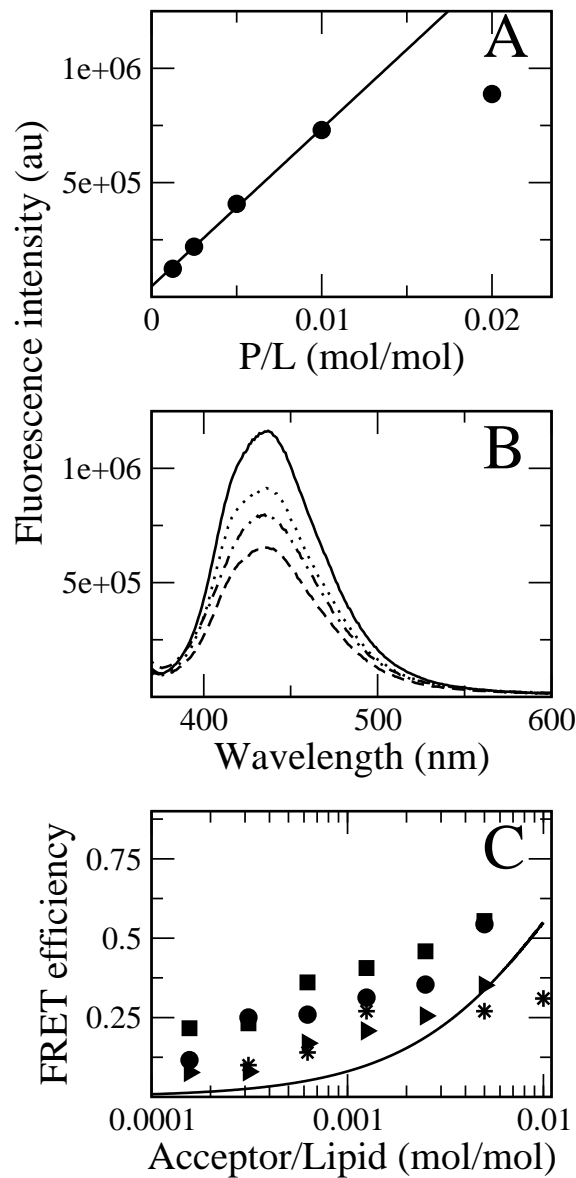


**Fig. 8.5 : Control experiments showing the absence of Alexa350-Bax $\alpha$ 5 self-quenching and the contribution of sequence-specific association and proximity effects to measured FRET in POPC vesicles.** A) Fluorescence emission of Alexa350-Bax $\alpha$ 5 as a function of P/L. B) Competition experiments with addition of unlabeled-Bax $\alpha$ 5 to Alexa350/KDabcyl-Bax $\alpha$ 5 samples. The spectra correspond to LUVs containing only donor peptides at 0.5 mol% ( $F_D$ , solid line), LUVs containing 0.5 mol% of both donor and acceptor peptides ( $F_{DA}$ , dashed line) and LUVs containing 0.33 mol% of donor, 0.33 mol% of acceptor and 0.66 mol% of unlabeled peptide ( $F_{DAU}$ , where U=unlabeled is either Bax $\alpha$ 5, dotted line or Bax $\alpha$ 5 Y115S, dashed-dotted line). C) Evaluation of effects of proximity on measured FRET efficiencies. Experimental data are shown as points, corresponding to Bax $\alpha$ 5 in POPC (circles), Y115S mutant of Bax $\alpha$ 5 in POPC (stars), Bax $\alpha$ 5 in DMPC gel phase, at 10 °C (squares) and Bax $\alpha$ 5 in DMPC LC phase, at 37 °C (triangles). The solid curve is computed according to the proximity analysis of WOLBER and HUDSON for  $R_0=4$  nm [455].

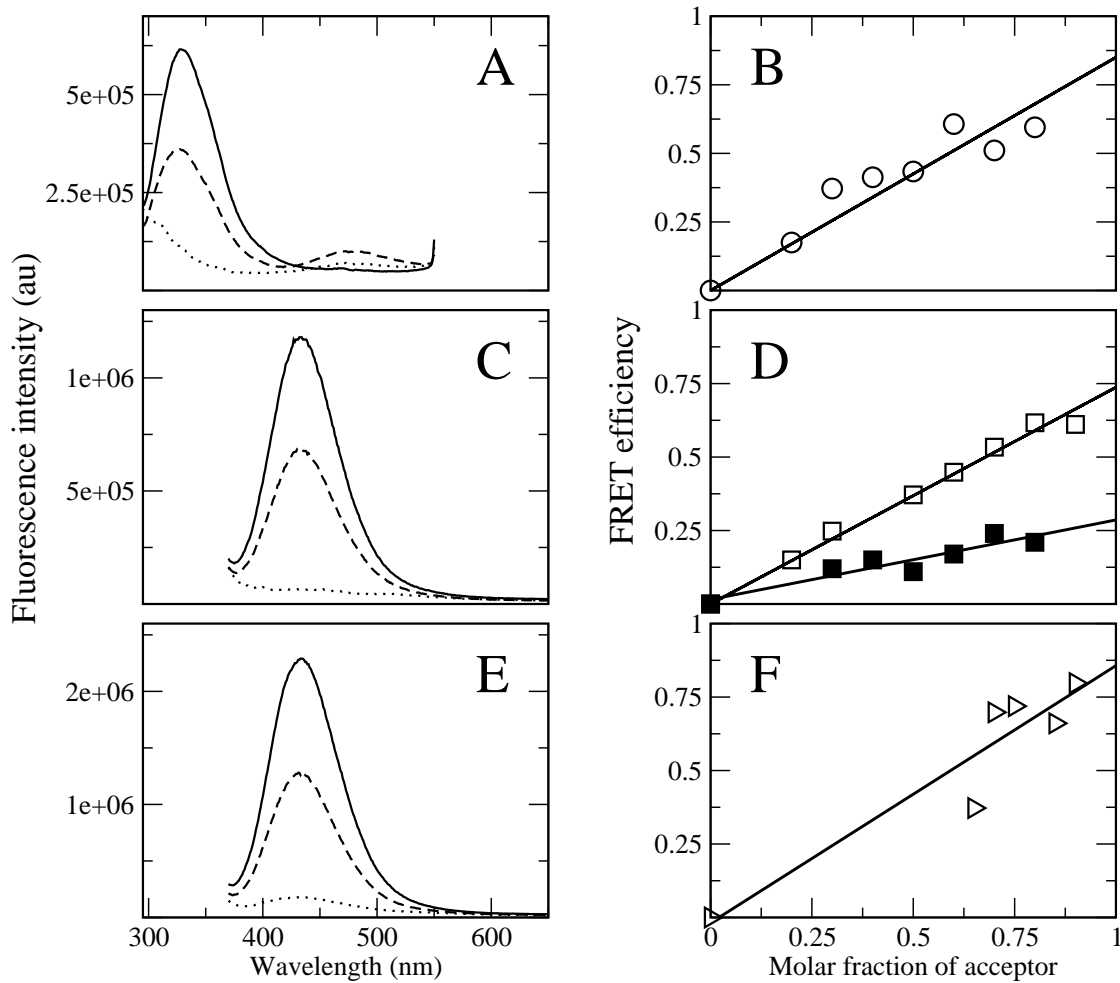


**Fig. 8.6 :** Examples of steady-state fluorescence spectra of different donor/acceptor pairs in POPC vesicles (left) along with their corresponding energy transfer efficiency,  $E^{SS}$ , as a function of acceptor molar ratio (right). The total peptide concentration was fixed at 0.05 mol %. A and B Unlabeled/E(EDANS)- $Bax\alpha 5$  pair; C and D Alexa350/K(Dabcyl)- $Bax\alpha 5$  pair (open squares) and Alexa350/K(Dabcyl)- $Bax\alpha 5$  Y115S pair (closed squares); and E and F Alexa350/Dabcyl- $Bax\alpha 5$  pair. Spectra of donor only ( $F_D$ ), acceptor only ( $F_A$ ) and donor/acceptor ( $F_{DA}$ ) are depicted as solid, dotted and dashed lines, respectively. For the data represented in A, C and E the mol fractions of acceptor were 0.5, 0.5 and 0.65, respectively. Note that Dabcyl dyes are non fluorescent. The linear fits in panels B, D, and F suggest the formation of dimers in all three cases.

Tab. 8.4 : Distance between labels calculated from steady-state and lifetime fluorescence measurements for the different D/A pairs in POPC membranes.

Donor/Acceptor pair	Steady-state					$r$ (nm) <sup>e</sup>
	$E^{ss\ a}$	$E^{ss\ proximity\ b}$	$E^{ss\ dimer\ c}$	$f_{Di}\ d$	$r$ (nm) <sup>e</sup>	
<i>Unlabeled-Bax<math>\alpha</math>5/E(EDANS)-Bax<math>\alpha</math>5</i>	0.74	0.06	0.68	0.65		$\leq 1.1$
<i>Alexa350-Bax<math>\alpha</math>5/K(Dabcyl)-Bax<math>\alpha</math>5</i>	0.74	0.19	0.55	0.65		3.0
<i>Alexa350-Bax<math>\alpha</math>5/Dabcyl-Bax<math>\alpha</math>5</i>	0.88	0.19	0.69	0.65		$\leq 2.0$
<b>Time-resolved</b>						
	$E^{tr\ f}$	$E^{tr\ dynamic\ g}$	$E^{tr\ static\ h}$	$f_{Di}\ d$		$r$ (nm) <sup>e</sup>
<i>Alexa350/K(Dabcyl)-Bax<math>\alpha</math>5</i>	0.70	0.08	0.62	0.65		2.4

- <sup>a</sup> Experimentally determined steady-state FRET efficiency (Eq. 5.38 and 5.39) at  $f_A=1$
- <sup>b</sup> Computationally determined FRET efficiency due to random proximity using the estimated  $R_0$  values shown in Tab. 8.3 and Eq. 5.47
- <sup>c</sup>  $E_{dimer}^{ss} = E^{ss} - E^{proximity}$  is the corrected FRET efficiency due to dimerization only
- <sup>d</sup> Fraction of peptides in the dimeric state estimated from the simulated curve shown in FIG. 8.8 A at P/L=1/200
- <sup>e</sup> Distance between D/A labels in the dimer calculated from Eq. 5.50
- <sup>f</sup> Experimentally determined time-resolved "total" FRET efficiency (Eq. 5.40) at  $f_A=1$
- <sup>g</sup> Experimentally determined time-resolved FRET efficiency due to dynamic quenching (Eq. 5.44) at  $f_A=1$
- <sup>h</sup>  $E_{static}^{tr} = E^{tr} - E_{dynamic}^{tr}$  is the corrected FRET efficiency due to dimerization only

decrease of donor fluorescence in  $F_{DA}$  samples, with respect to  $F_D$  samples, can be appreciated. For the unlabeled-Bax $\alpha$ 5/E(EDANS)-Bax $\alpha$ 5 pair the sensitized acceptor emission can be seen as well. Recall that Dabcyl probes are *dark quenchers*; i.e., they are not fluorescent and thus, no bands from these dyes are present in emission spectra. FRET efficiencies were calculated using EQ. 5.38, corrected for incomplete labeling if necessary (EQ. 5.39), and plotted in FIG. 8.6 B, D and F. Although with some dispersion for the case of Alexa350-Bax $\alpha$ 5/Dabcyl-Bax $\alpha$ 5, each of the data sets can be fitted with a straight line, which is indicative of the presence of dimers. A more in depth analysis may allow discriminating between a parallel (*head-to-head*) or an antiparallel (*head-to-tail*) orientations of the Bax $\alpha$ 5 peptides in the dimer.

The values of  $E^{ss}$  shown in FIG. 8.6 B, D and E, were corrected for non specific proximity effects as explained above by subtracting  $E_{proximity}^{ss}$  (EQ. 5.47) in order to obtain the contribution due exclusively to dimerization,  $E_{dimer}^{ss}$ . From EQ. 5.50 it can be seen that for a molar fraction of acceptor,  $f_A$ , equal to one (obtained from a linear fit of  $E_{dimer}^{ss}$  vs  $f_A$ ),  $E_{dimer}^{ss}$  depends only on three parameters: (i) the fraction of dimeric peptides,  $f_{Di}$  (ii) the Förster distance,  $R_0$  and (iii) the D-A distance within the dimer,  $r$ .  $f_{Di}$  depends on the P/L via the equilibrium dimerization constant,  $K_{dimer}$ , and its calculation will be explained with detail in SEC. 8.4. For P/L=1/200  $f_{Di}$  was found to be 0.65 (TAB. 8.4), which sets an upper limit for  $E_{dimer}^{ss}$ .  $R_0$  has been estimated above (SUB. 8.3.3) and the corresponding values are shown in TAB. 8.3. Therefore, we are left with  $r$  as the only unknown. For the Alexa350-Bax $\alpha$ 5/Dabcyl-Bax $\alpha$ 5 pair, with both dyes attached at the N-terminus  $E_{dimer}^{ss}$  is similar to the limiting value  $f_{Di}$  (see data in FIG. 8.6 E and F). This result means that the only prediction that can be safely made is that  $r$  should be less than  $R_0/2$ , i.e. 4 nm/2=2 nm<sup>1</sup>. The lack of sensitivity could in principle be fixed using a different D/A pair, with a smaller  $R_0$ , as for unlabeled-Bax $\alpha$ 5/E(EDANS)-Bax $\alpha$ 5. However, in this case we found also  $E_{dimer}^{ss} \simeq f_{Di}$ , again precluding an accurate determination of  $r$ , which should be  $\leq 1.05$  nm.

Thus, the FRET data from the two pairs where the probes are placed at the same peptide end, suggest a parallel dimer. Both labels are so close in space that the FRET efficiency is very high, below the range of distances that can be accurately measured. This conclusion can be supported with the data corresponding to the Alexa350/K(Dabcyl)-Bax $\alpha$ 5 pair, in which the dyes were attached at different peptide ends. The value of  $r$  calculated for this latter case is 3.0 nm. Interestingly, assuming that Bax $\alpha$ 5 adopts a canonical  $\alpha$ -helix structure from end to end, the expected peptide length is 3.3 nm (0.15 nm/residue  $\times$  22 residues). In summary, taken together these data support the conclusion that the Bax $\alpha$ 5 peptide forms dimers in POPC vesicles where peptides interact in a *head-to-head* orientation (TAB. 8.5).

Additionally, the mutant Bax $\alpha$ 5 Y115S showed impaired self-association as evidenced by the low FRET efficiencies (FIG. 8.6 D). Nevertheless, this peptide is still able dimerize since the data can be well fitted by a linear dependence.

<sup>1</sup> As a rule of thumb the range of measurable distances is between  $R_0/2$  (lower limit) for very high transfer efficiencies and  $2R_0$  (upper limit) for very low transfer efficiencies.

**Tab. 8.5 : Toward the relative orientation of the monomers in the Bax $\alpha$ 5 dimer.**

Relative orientation <sup>a</sup>	Model <sup>b</sup>	Expected distance <sup>c</sup> (nm)	Observed distance <sup>c</sup> (nm)
<i>Head-to-head</i> (“parallel”) dimer	N*  C	~3.3	3.0
	N  *C		
<i>Head-to-tail</i> (“antiparallel”) dimer	N*  C	~0	
	C*  N		

<sup>a</sup>The concepts of “parallel” and “antiparallel” should not be taken *literally* to imply a 0° degree crossing angle. Rather, they are intended to mean that both monomers have the N-terminus at the same side of the dimer or at different ends, respectively.

<sup>b</sup> For simplicity, the crossing angle has been set to 0°. See note <sup>a</sup>. The asterisks denote the position of the labels. One peptide is labeled with a *donor* dye and the other with *acceptor*.

<sup>c</sup> The expected and observed distances refer to the distance between the N-terminus of one monomer and the C-terminus of the other monomer comprising the dimer. For simplicity, the expected distance has been calculated for monomers completely  $\alpha$ -helical and crossing at a 0° angle.

**Fluorescence Lifetimes.** In parallel with the steady-state measurements we performed fluorescence lifetime experiments. In this case, instead of recording the fluorescence spectra with continuous irradiation, as in a typical steady-state experiment, we used a pulsed light source to excite the donor and analyzed how the presence of acceptor affects the relaxation process (i.e., the return to the donor ground state). For that we recorded the time dependent decay of the fluorescence of the donor, alone and in presence of varying amounts of acceptor (FIG. 8.7 A). To these data we fit multiexponential functions and extract the characteristic decay times of the different components. In general, two exponential functions were enough to achieve reasonable fits, and the results of the corresponding relaxation times ( $\tau_{D,1}$ ,  $\tau_{D,2}$ ,  $\tau_{DA,1}$ ,  $\tau_{DA,2}$ ) are listed in TAB. 8.6. In a way similar to that described for steady-state measurements, in the case of lifetime measurements we compared  $F_D$  samples and  $F_{DA}$  samples for each acceptor concentration ( $F_A$  samples were used for background subtraction only). FIG. 8.7 B and TAB. 8.6 show that the presence of acceptor Bax $\alpha$ 5 caused a marked decrease in the amplitude of the decay curves, while the lifetimes did not change much. This behavior corresponds mainly to a *static quenching* mechanism, in which tight dimerization results in a complete energy transfer from donor to acceptor (meaning small contribution of  $E_{proximity}^{ss}$  in a steady-state experiment) [453]. On the other hand, the case of a monomer acceptor in random proximity of the donor corresponds to dynamic quenching [453], which will affect mainly the lifetime of the donor excited state. In a real scenario both contributions are present, so the sum of static and dynamic contributions is what one detects in a steady-state experiment. This “total” contribution can be calculated directly from a time-resolved experiment since the area under the decay curve is proportional to the steady-state intensity, where the amplitude-weighted lifetime can be used to estimate such an area.

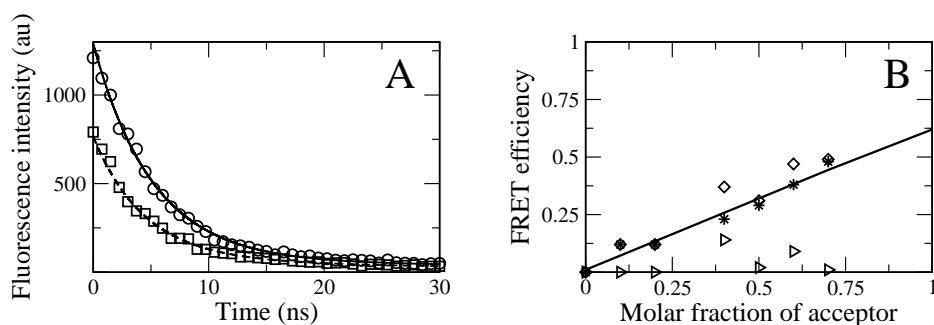


**Fig. 8.7** : Examples of fluorescence decay for Alexa350-Bax $\alpha$ 5/K(Dabcyl)-Bax $\alpha$ 5 in POPC vesicles along with the corresponding energy transfer efficiency as a function of acceptor mole ratio. The total peptide concentration was fixed at 0.05 mol%. In A the decay of fluorescence for donor-only ( $F_D$ ) and donor/acceptor samples ( $F_{DA}$ ) are shown as circles and squares, respectively. Solid and dashed lines are fits of double exponential functions to the raw data for the  $F_D$  and  $F_{DA}$  samples, respectively. B) shows the FRET efficiencies calculated from dynamic quenching contributions (triangles), static quenching contributions (total minus dynamic contribution, stars) and the sum of both contributions which is calculated from the area under the curve and is proportional to the steady state intensity (diamonds). The FRET efficiency due to oligomerization only corresponds to the static contribution and has been fit to a linear model (solid line) and used to determine the D/A distance shown in TAB. 8.4.

We thus calculated FRET efficiencies taking into account either amplitude-weighted lifetimes,  $\langle \tau \rangle$  ( $E^{tr}$ ), or amplitude-averaged lifetimes,  $\bar{\tau}$  ( $E_{dynamic}^{tr}$ ). The difference corresponds to the static contributions,  $E_{static}^{tr}$  which originate only from dimerization. These three contributions are shown in FIG. 8.7 B.  $E_{static}^{tr}$  is conceptually equivalent to  $E_{dimer}^{ss}$  and was used to calculate  $r$  (see SUB. 8.3.4) within the dimer yielding 2.4 nm (TAB. 8.4), again in agreement with a parallel orientation of Bax $\alpha$ 5 dimers.

## 8.4 Energetics of Bax $\alpha$ 5 oligomerization in membranes<sup>1</sup>

Corrected FRET efficiencies arising from oligomerization only,  $E_{dimer}^{ss}$ , have been calculated by subtracting the computationally determined proximity effect,  $E_{proximity}^{ss}$ , from the experimental steady-state FRET efficiencies  $E^{ss}$  (FIG. 8.5 C). As explained in SUB. 5.4.2,  $E_{dimer}$  is a measure of  $Di/T$  where  $Di$  is the mole fraction of dimers in the lipid vesicles (dimers per lipid) and  $T$  is total peptide concentration in the vesicles (peptides per lipid), in turn equal to  $2Di + Mo$ , where  $Mo$  is the monomer fraction in the lipid vesicles (monomers per lipid).  $Di/T$  also equals half of the fraction of peptides in the dimeric state ( $f_{Di}$ ). Knowing  $f_{Di}$  we fit the resulting curve in order to obtain the equilibrium constant for dimer formation,  $K_{dimer}$  (TAB. 8.7), following EQ. 5.59. In FIG. 8.8 A we plot the theoretical dependence of FRET efficiency vs P/L for the different fitted  $K_{dimer}$ . From the value of  $K_{dimer}$ , it is possible to derive the free energy of dimerization,  $\Delta G_{dimer}$ , which is shown in TAB. 8.7. The free energy of Bax $\alpha$ 5 dimerization in POPC

<sup>1</sup> A detailed description of the methodology used for this analysis can be found in SUB. 5.4.2. Detailed protocols are described in SUB. 6.4.2

Tab. 8.6 : Time-resolved fluorescence of Alexa350-Bax $\alpha$ 5/K(Dabcyl)-Bax $\alpha$ 5 in POPC membranes.

FD				FDA				FRET efficiencies ( $E$ )							
$f_A^a$	$\tau_{D,1}$ (ns) <sup>b</sup>	$A_{D,1}$ <sup>b</sup>	$\tau_{D,2}$ (ns) <sup>b</sup>	$A_{D,2}$ <sup>b</sup>	$f_A^a$	$\tau_{DA,1}$ (ns) <sup>c</sup>	$A_{DA,1}$ <sup>c</sup>	$\tau_{DA,2}$ (ns) <sup>c</sup>	$A_{DA,2}$ <sup>c</sup>	$E_{dynamic}^{tr,d}$	$E_{static}^{tr,d}$	$E^{tr}$	$E_{proximity}^{ss,d}$	$E_{dimer}^{ss,d}$	$E^{ss}$
0	5.1	1121	56	71	0.7	4.5	575	52	46	0.01	0.48	0.49	0.19	0.34	0.53
0	5.4	1239	55	72	0.6	4.2	692	39	70	0.09	0.38	0.47	0.19	0.26	0.45
0	5.3	1261	54	66	0.5	4.6	872	45	69	0.02	0.29	0.31	0.19	0.18	0.37
0	5.1	1096	69	75	0.4	4.7	786	47	65	0.14	0.23	0.37	0.19	NID	NID
0	5.5	1483	49	96	0.2	5.3	1318	50	87	<0.01	0.12	0.12	0.19	0	0.15
0	5.3	1511	37	149	0.1	5.3	1363	53	88	<0.01	0.12	0.12	0.19	NID	NID

<sup>a</sup>Molar fraction of acceptor

<sup>b</sup>Lifetimes ( $\tau_{D,n}$ ) and amplitudes ( $A_{D,n}$ ) of donor only samples were obtained from fittings of the experimental decay curve to Eq. 5.42 where  $n$  refers to the component, 1 or 2, of the biexponential curve.

<sup>c</sup>Lifetimes ( $\tau_{DA,n}$ ) and amplitudes ( $A_{DA,n}$ ) of donor-acceptor samples were obtained from fittings of the experimental decay curve to Eq. 5.42 where  $n$  refers to the component, 1 or 2, of the biexponential curve.

<sup>d</sup> $E_{proximity}^{ss}$ ,  $E_{dimer}^{ss}$  and  $E^{ss}$  are extracted from a steady-state experiment and are shown for comparative purposes since they are conceptually similar to  $E_{dynamic}^{tr}$ ,  $E_{static}^{tr}$ ,  $E^{tr}$ , respectively, which are extracted from a time-resolved experiment.

**Tab. 8.7 : Energetics of Alexa350/K(Dabcyl)-Bax $\alpha$ 5 dimerization in membranes.**

Sample	$K_{dimer}$	$\Delta G_{dimer}$ (Kcal/mol)	Temperature (K)
<i>Bax<math>\alpha</math>5 in POPC</i>	522 $\pm$ 380	-3.7 $\pm$ 0.6	298
<i>Bax<math>\alpha</math>5 Y115S in POPC</i>	139 $\pm$ 102	-2.9 $\pm$ 0.5	298
<i>Bax<math>\alpha</math>5 in DMPC gel phase</i>	820 $\pm$ 696	-3.6 $\pm$ 0.8	283
<i>Bax<math>\alpha</math>5 in DMPC LC phase</i>	107 $\pm$ 94	-2.5 $\pm$ 0.8	310

membranes is -3.7 kcal/mol. This value is lower than the free energy of dimerization of the well-known glycoporphin A TM domain (-7.0 kcal/mol) [434] but similar to that of other dimeric peptides, like the FGF3 TM domain (-3.0 kcal/mol) [445]. The analysis shows also that the single-point mutant Bax $\alpha$ 5 Y115S can still dimerize in POPC membranes but less efficiently compared to the peptide without this mutation. The change in the free energy of dimerization,  $\Delta\Delta G_{dimer}$ , due to the Y115S mutation is about 0.8 kcal/mol. This value is within the range of the strength of a typical hydrogen bond [510, 511] suggesting that the natural Tyr115 makes a hydrogen bond in the dimer which cannot be reproduced by the substituting Ser. However, other types of interaction like  $\pi$ -stacking between Tyr and the aromatic ring of neighboring Phe residues are also a likely possibility. Although this change of free energy may seem a modest difference, similar values have been shown to have a dramatic effect on the monomer-dimer equilibria and have even been proposed as a plausible mechanism for explaining some pathogenesis [512]. Finally, the free energy of Bax $\alpha$ 5 dimerization is similar for both POPC and DMPC gel phase membranes while for DMPC membranes in the liquid crystalline phase  $\Delta G_{dimer}$  is reduced by  $\sim$ 1 kcal/mol (TAB. 8.7) suggesting that a change in the phase state of the membrane can affect the interactions at the dimer interface.

To gain more insight into the dimer structure, a HILL plot was constructed using EQ. 5.61 (FIG. 8.8 C). A HILL coefficient,  $h$ , of 1.04 was determined, suggesting the existence of one interacting surface per Bax $\alpha$ 5 wt monomer. Values of  $h$  near one are often taken as signatures of homogeneous dimeric peptides [474] indicating that Bax $\alpha$ 5 is a good candidate for structural determination by high-resolution liquid state NMR in micelles.

## 8.5 Effect of mitochondrial lipids in Bax $\alpha$ 5 oligomerization

All experiments described so far were conducted in POPC vesicles. It has been shown recently that the oligomeric state of full-length Bax is sensitive to the lipid composition [297, 513]. To test if our reduced version of active Bax is also able to respond to lipid changes, we used different mixtures resembling the composition of mitochondrial membranes: POPC:DOPE (2:1) (MOM composition), POPC:CL (2:1) (mixture usually taken as mimicking MOM contact sites), and POPC:DOPE:CL (1:1:1) (MOM/MIM contact sites composition [378]). In all these cases the plots of FRET efficiency *vs* the mole fraction of acceptor deviated clearly from a straight line, suggesting the formation

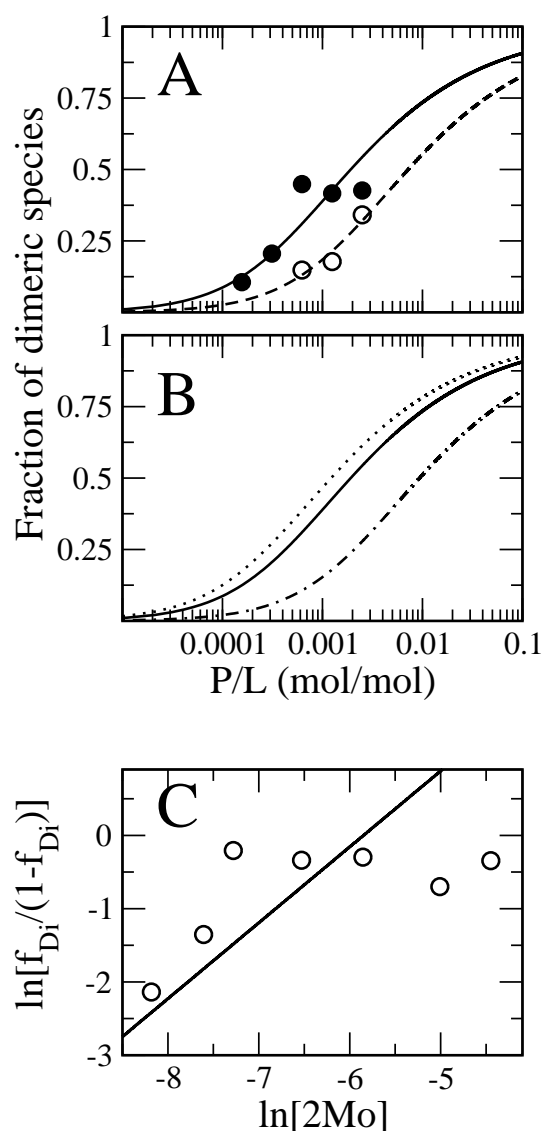


**Fig. 8.8 : Energetics of Bax $\alpha$ 5 oligomerization in vesicles.** A) Fraction of dimer species ( $f_{Di}$ ) as a function of the total peptide concentration. FRET efficiencies due to proximity are subtracted from steady-state FRET to obtain efficiencies due to oligomerization only,  $E_{dimer}^{ss}$ , which are then used to calculate  $f_{Di}$ . The experimental data points are fit to obtain  $K_{dimer}$  (TAB. 8.7). The cases of Bax $\alpha$ 5 and the mutant Bax $\alpha$ 5 Y115S correspond to solid and dashed lines, respectively. Lipid membranes were composed of POPC. B) Effect of lipid composition and phase on the fraction of dimer as a function of the total Bax $\alpha$ 5 concentration calculated as explained in A. POPC at 25°C (solid line), DMPC gel phase at 10°C (dotted line), and DMPC liquid crystal phase at 37°C (dashed dotted line). C) HILL coefficient analysis of Bax $\alpha$ 5 dimerization. Natural logarithm of  $f_{Di}/(1-f_{Di})$  vs the logarithm of  $2Mo$ , where  $f_{Di}$  is the fraction of peptides in the dimeric state and  $Mo$  is the monomer mole fraction (monomers per lipid). EQ. 5.61 was fit to the experimental data in order to obtain the HILL coefficient,  $h$ . The fit is shown as a solid line and it gives  $h=1.04$ .

**Tab. 8.8 : Results of fits of steady-state FRET of Alexa350-Bax $\alpha$ 5/K(Dabcyl)-Bax $\alpha$ 5 in different lipid membranes to different oligomeric models.** Best fits are shown in bold face.

Lipid		n <sup>a</sup>						
		2	3	4	5	6	7	8
POPC	$R$ (nm) <sup>b</sup>	<b>1.1</b>	2.1	4.1	4.1	4.1	4.1	4.1
	$f_{Mo}$ <sup>c</sup>	<b>0.26</b>	0.42	0	0	0	0	0
	$\chi^2$	<b>0.0046</b>	0.0155	0.0059	0.0060	0.0057	0.0055	0.0054
POPC:CL	$R$ (nm)	0.4	0.4	1.5	2.7	0.9	2.6	<b>2.6</b>
	$f_{Mo}$	0	0	0.08	0	0.17	0	<b>0</b>
	$\chi^2$	0.4342	0.0300	0.0267	0.0236	0.1154	0.0235	<b>0.0232</b>
POPC:DOPE	$R$ (nm)	0.4	0.5	0.3	<b>0.3</b>	0.5	0.3	1.9
	$f_{Mo}$	0	0.09	0.19	<b>0.25</b>	0.28	0.31	0.24
	$\chi^2$	0.3251	0.1405	0.0911	<b>0.0796</b>	0.0840	0.0944	0.0835
POPC:DOPE:CL	$R$ (nm)	1.7	0.2	0.4	<b>1.5</b>	2.0	2.0	1.9
	$f_{Mo}$	0.17	0.33	0.38	<b>0.41</b>	0.40	0.40	0.40
	$\chi^2$	0.1425	0.0464	0.0213	<b>0.0189</b>	0.0197	0.0200	0.0202

<sup>a</sup>Number of subunits in the oligomer<sup>b</sup>Inter-subunit distance within the oligomer<sup>c</sup>Fraction of peptide in the monomeric state

of peptide oligomers other than dimers (FIG. 8.9). To gain some insight into the possible nature of these oligomers, FRET efficiencies plotted against the molar fraction of acceptor were used to fit a model developed by LI and co-workers [461] (see page 91). This model calculates explicitly FRET between each donor-labeled subunit and each acceptor-labeled subunit within an oligomer species, assumed to be a symmetrically assembled circular ring. It allows estimating  $R$ , the distance between labels on neighboring subunits, and  $f_{Mo}$ , the molar fraction of monomers. The results of the fits for different oligomeric states are shown in TAB. 8.8. For POPC, the dimer model gave always the best fit. In contrast, the presence of DOPE, CL, or both shifted the best fits towards higher aggregation numbers. However, the errors are small and similar in most tested cases, thus precluding unambiguous assignment of a particular oligomer size.

We can conclude that mitochondrial lipids enhance the Bax $\alpha$ 5 tendency to auto-associate, suggesting the existence of at least two interacting surfaces. However, Bax $\alpha$ 5 is able to form pores in all four lipid compositions. Indeed, while DOPE has almost no effect compared with POPC alone, CL either alone or together with DOPE, dramatically decreases Bax $\alpha$ 5 activity. The Bax $\alpha$ 5 oligomerization propensity follows the series: POPC:CL $\simeq$ POPC:DOPE:CL $\simeq$ POPC:DOPE > POPC, while the Bax $\alpha$ 5 leakage activity decreases in the order: POPC $\simeq$ POPC:DOPE > POPC:CL $\simeq$ POPC:DOPE:CL.

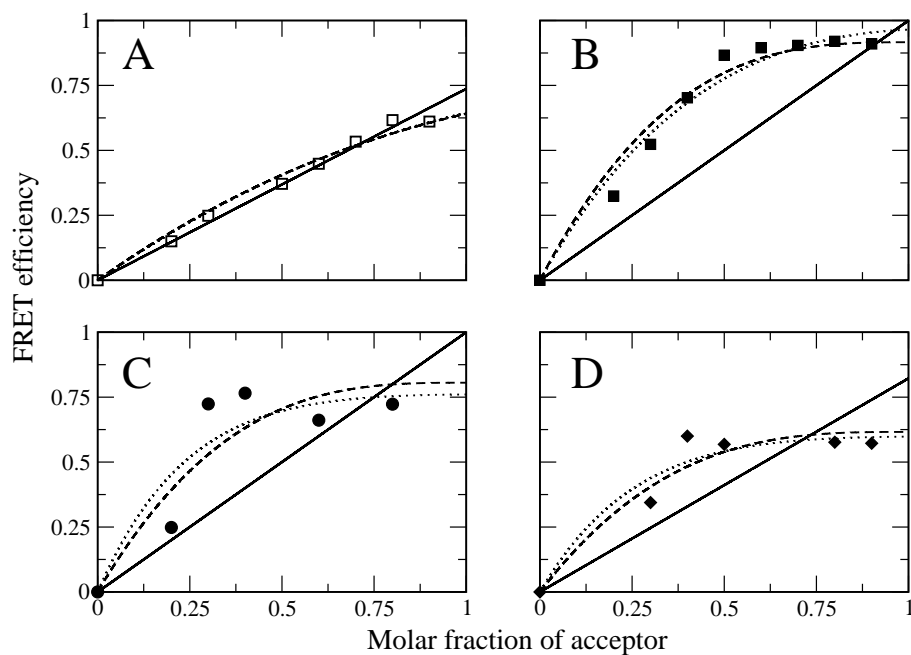


**Fig. 8.9 : Effect of lipid composition on  $Bax\alpha 5$  oligomerization.** FRET efficiencies calculated from steady-state fluorescence measurements for the Alexa350- $Bax\alpha 5$ /K(Dabcyl)- $Bax\alpha 5$  pair in different lipid environments: A) POPC, B) POPC:CL (2:1), C) POPC:DOPE (2:1) and D) POPC:DOPE:CL (1:1:1). The solid, dashed and dotted lines are best fits to the experimental data (shown as points) assuming a dimer, a tetramer and an octamer, respectively.

It seems that there is an inverse relationship between the pore-forming ability of Bax $\alpha$ 5 and its capacity to form large oligomers. Bax $\alpha$ 5 self-association is enhanced by mixtures of two or more lipids suggesting the involvement of lipid packing defects in the quaternary structure configuration. On the other hand, Bax $\alpha$ 5 activity depends on the presence of CL which displays a strong inhibitory effect, probably sequestering Bax $\alpha$ 5 due to electrostatic interactions and limiting structural and dynamical rearrangements critical for pore formation. Another possibility is that higher-order oligomers may represent unspecific aggregated peptide assemblies incompetent for membrane permeabilization. Nevertheless, the contribution of the oligomeric states to the formation of pores cannot be completely ruled out. For instance, while higher order oligomers do not cause more leakage than the dimeric species, i.e. the fraction of porated vesicles is the same in both cases, they may increase the size and/or stability of the pores formed.

Another reason to separate the processes of dimerization and leakage arise from the studies with mutant peptides. Dimerization is dependent mainly on the Tyr115 residue, as it is demonstrated by two facts, that Bax $\alpha$ 5 Y115S migrates with an apparent molecular weight corresponding to that of a monomer in SDS-PAGE gels (FIG. 8.1) and that the FRET efficiencies are clearly diminished in this mutant version (FIG. 8.2). However, Bax $\alpha$ 5 Y115S and Bax $\alpha$ 5 show similar calcein release kinetics (FIG. 8.2). On the other hand, leakage is governed mainly by Lys residues, specifically Lys at positions 119 and 123 (Bax sequence), since their introduction in equivalent positions of Bcl-xL $\alpha$ 5 converts this peptide in a Bax-like molecule with similar pore-forming capacity (FIG. 8.2). Importantly, Bcl-xL A149K/E153K cannot dimerize at least in SDS micelles (FIG. 8.1).

## 8.6 Bax $\alpha$ 5-Bcl-xL $\alpha$ 5 and Bax $\alpha$ 5-Bcl-xL $\Delta$ Ct interactions

### 8.6.1 Detection of Bax $\alpha$ 5 hetero-interactions

The same approach used to demonstrate specific Bax $\alpha$ 5-Bax $\alpha$ 5 interactions, i.e. competition experiments between labeled and unlabeled species, was used to test the potential of Bax $\alpha$ 5 to form a heterodimer with Bcl-xL $\alpha$ 5 and complete Bcl-xL. Unlabeled Bcl-xL molecules were added to  $F_{DA}$  samples containing the D/A pair Alexa350/K(Dabcyl)-Bax $\alpha$ 5 to check whether those polypeptides were able to disrupt Bax $\alpha$ 5 homo-interactions. For these experiments we used the Bcl-xL protein lacking the C-terminus, Bcl-xL $\Delta$ Ct, and a peptide derived from helix 5 of this protein, Bcl-xL $\alpha$ 5, analogous to Bax- $\alpha$ 5 in the Bcl-xL sequence (see TAB. 8.1). Both molecules were able to interact with Bax $\alpha$ 5 since the fluorescence signal  $F_{DAU}$  increased with respect to  $F_{DA}$  reaching levels similar to or even higher than in  $F_D$  samples (FIG. 8.10). The effect of Bcl-xL $\Delta$ Ct was pH-dependent, with essentially no effect at physiological pH due to its very low binding to membranes [286, 321]. The strong fluorescence enhancement of Bcl-xL $\Delta$ Ct at acidic pH can be explained as due to a change of Bax $\alpha$ 5 into a more hydrophobic environment, either because it is bound to an internal hydrophobic pocket of Bcl-xL or because Bax $\alpha$ 5 is more deeply buried into the membrane interior in the presence of Bcl-xL.

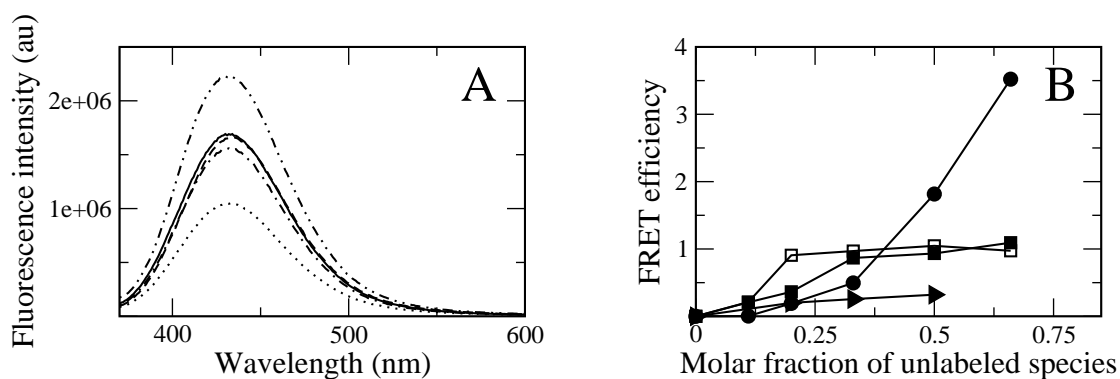


**Fig. 8.10 : Hetero-interactions between Bax $\alpha$ 5 and Bcl-xL polypeptides.** A) The presence of both Bax $\alpha$ 5 donors and acceptors ( $F_{DA}$ , dotted line) reduces the fluorescence intensity with respect to the level of a donor-only sample ( $F_D$ , solid line). The addition of unlabeled species recovers the fluorescence signal to different extents, depending on the particular case: unlabeled Bax $\alpha$ 5 control (dashed line), Bcl-xL $\alpha$ 5 (dashed-dotted line), Bcl-xL $\Delta$ Ct pH=4.5 (dashed-dotted-dotted line). Donor, acceptor and unlabeled peptides P/L are 1/300 each. B) Plot of the extent of fluorescence recovery after addition of the unlabeled species: Bax $\alpha$ 5 (open squares), Bcl-xL $\alpha$ 5 (filled squares), Bcl-xL $\Delta$ Ct pH=4.5 (circles) and Bcl-xL $\Delta$ Ct pH=7 (triangles). The total P/L was kept constant at 1/200 while varying the concentration of unlabeled species. LUVs were made of POPC:DOPE:CL at neutral pH (PBS buffer) unless otherwise state. See FOOTNOTE 1 on page 149

### 8.6.2 Effect of Bax $\alpha$ 5 heterointeractions on membrane activity

Bcl-xL is known to block the Bax-mediated permeabilization of the MOM [269]. Since Bax $\alpha$ 5 possesses also membrane permeabilizing capacity (discussed in CHAP. 10) we wished to know whether Bax $\alpha$ 5-Bcl-xL $\Delta$ Ct and Bax $\alpha$ 5-Bcl-xL $\alpha$ 5 interactions had any inhibitory effect on the Bax $\alpha$ 5 pore formation activity. In one set of experiments, Bax $\alpha$ 5 was added at a concentration that caused approximately half of the maximum leakage, thus setting the normal level of Bax $\alpha$ 5 activity. In another set of experiments either Bcl-xL $\Delta$ Ct or Bcl-xL $\alpha$ 5 were first incubated with the lipid vesicles to allow for membrane binding and then the same aliquot of Bax $\alpha$ 5 was added.

The effect of Bcl-xL $\Delta$ Ct is relatively small, with final leakage levels slightly increasing in a concentration dependent manner (FIG. 8.11 A). The effect of Bcl-xL $\alpha$ 5 on the Bax $\alpha$ 5 induced leakage is more clear and the extent of final leakage was increased with respect to that of Bax $\alpha$ 5 alone, although the leakage kinetics was slower (FIG. 8.11 B). In summary, Bcl-xL $\Delta$ Ct has a minor effect on Bax $\alpha$ 5 leakage activity while Bcl-xL $\alpha$ 5 produces a marked leakage enhancement. The absence of an inhibitory effect of Bcl-xL $\alpha$ 5 over Bax $\alpha$ 5 indicates that the two peptides are too small to mimick completely the behavior of the full-length proteins in terms of intermolecular inhibitory effects. Bax $\alpha$ 5 is able to induce the opening of membrane pores of lipidic nature [50, 176]. Apparently, it is not easy to inhibit the membrane perturbing capacity of the Bax $\alpha$ 5 peptide simply by peptide-peptide interaction (like in Bax $\alpha$ 5-Bcl-xL $\alpha$ 5 dimers), indicating that the requirements for pore formation are still fulfilled in peptidic heterodimers, where an am-

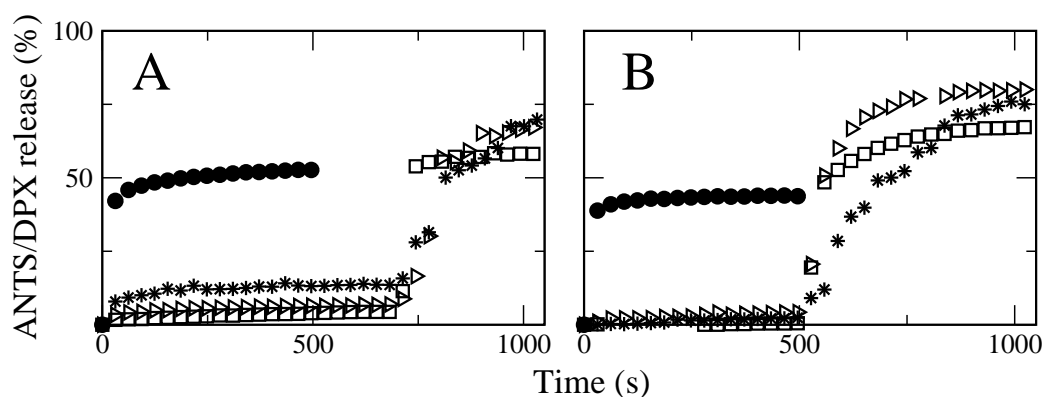


**Fig. 8.11 : Effect of Bcl-xL polypeptides on the membrane activity of Bax $\alpha$ 5.** A) Effect of Bcl-xL $\Delta$ Ct. Leakage of ANTS/DPX encapsulated into POPC:DOPE:CL LUV after the addition of Bax $\alpha$ 5 (P/L=1/100) at pH=4.5 was monitored over time (solid circles) and used as a control of the extent of leakage. In other experiments Bcl-xL $\Delta$ Ct was first added to the LUV suspension and allowed to bind. After 10 min incubation, Bax $\alpha$ 5 was then added. B) Same experiment as in A but with Bcl-xL $\alpha$ 5. P/L of Bcl-xL $\Delta$ Ct or Bcl-xL $\alpha$ 5 were 1/500 (squares), 1/250 (triangles) and 1/100 (stars). Release induced by Bax $\alpha$ 5 alone is shown as circles. Note that Bcl-xL $\Delta$ Ct and Bcl-xL $\alpha$ 5 alone have essentially no effect on membrane permeability. See FOOTNOTE 1 on page 149

phipathic interfacially-bound peptide assembly that expands the membrane is probably enough to display activity. Possible explanations of the enhancement of Bax $\alpha$ 5 activity in the presence of Bcl-xL $\Delta$ Ct and especially Bcl-xL $\alpha$ 5 are an increased partitioning of Bax $\alpha$ 5 to the membrane or an increase of the membrane tension due to polypeptide binding. Any of these effects would aid the distortion created by Bax $\alpha$ 5 and facilitate pore formation. Alternatively, a deeper insertion of Bax $\alpha$ 5 locating in a more hydrophobic environment (SUB. 8.6.1) might be responsible for the observed increase in membrane permeabilizing activity in the presence of Bcl-xL $\Delta$ Ct.

## 8.7 Discussion

### 8.7.1 Sequence determinants of Bax $\alpha$ 5 dimerization

As we have described in CHAP. 1 (SUB. 1.2.3), the interactions between helical fragments in membrane proteins follow similar patterns to those in water soluble proteins. In general, we may find parallel (head-to-head) or antiparallel (head-to-tail) orientations of the interacting helices, which normally exhibit close packing thanks to the presence of residues with small side-chains in the interacting surfaces of the helices. This gives rise to helix packing motifs abbreviated  $GAS_{Right}$  or  $GAS_{Left}$ , where  $GAS$  refers to the presence of Gly, Ala or Ser in the interface between helices and  $Right$  or  $Left$  refers to right-handed or left-handed helix packing.  $GAS_{Right}$  motifs are more common. The best known case in membrane proteins is the dimerization motif of glycophorin, with three residues flanked by two Gly, of the type GxxxG, although it can be generalized as

*Small-xxx-Small*, where *Small* refers to a residue with small side-chain.

For the case of Bax $\alpha$ 5, studied here, our results demonstrate clearly that it forms dimers, both in SDS and in POPC membranes, and higher order oligomers in membranes containing CL. Moreover, the calculated distances in POPC vesicles using FRET data indicate that the Bax $\alpha$ 5 dimers adopt a parallel orientation, which suggests the existence of specific sequence-dependent interactions. This parallel orientation of the two Bax $\alpha$ 5 helices is also in agreement with the unidirectional insertion of full-length Bax protein, when it translocates from the cytosol to the MOM [223]. If we examine carefully the sequence of Bax $\alpha$ 5 we find a putative  $GAS_{Right}$  glycoporphin-like motif:  $^{108}GxxxA^{112}$ . From FRET data we calculate  $\Delta G_{dimer} = -3.7$  kcal/mol. This is a relatively low value, compared to that of glycoporphin, which amounts to -7.0 kcal/mol [434] (see also [514] for the distributions of dimeric species of different glycoporphin variants, which can be directly compared with FIG. 8.8 A). However, a weaker dimer in our case can be due to the location of the interaction motif near the peptide end [515]. Additionally, the differences in the sequence around the core motif residues in the two cases (see below) may also be the cause of a smaller binding energy.  $GAS_{Left}$  motifs are believed to be weaker than  $GAS_{Right}$  motifs [25]. However, it is difficult to set a clear threshold between them and, in addition, Bax is not predicted to have a coiled-coil sequence so that the presence of a  $GAS_{Left}$  motif in Bax $\alpha$ 5 is unlikely. Because the putative dimerization motif is in the region of highest sequence identity with the analogous fragment Bcl-xL $\alpha$ 5 (TAB. 8.1), a very similar  $GAS_{Right}$  motif can also be found in this latter peptide:  $^{138}GxxxA^{141}$ . But, strikingly, Bcl-xL $\alpha$ 5 is unable to self-associate, at least in SDS micelles (FIG. 8.1), although the absence of a dimeric band in SDS-PAGE should be interpreted with caution, since Bcl-xL $\alpha$ 5 might form dimers in POPC membranes, but to a lesser extent (i.e. requiring higher P/L) than Bax $\alpha$ 5.

The different dimerization behavior displayed by Bax $\alpha$ 5 and Bcl-xL $\alpha$ 5 suggests that the *GxxxA* sequence may not be the only determinant of Bax $\alpha$ 5 dimerization in membranes. In fact, multiple examples show that residues surrounding the *GxxxG* sequence contribute to the stability of the dimer [516–518] and that polar motifs may complement *classical* ones [29, 519]. Hence, we compared the sequences of Bax $\alpha$ 5 and Bcl-xL $\alpha$ 5 and searched for differences outside the *GxxxA* region. Very significantly, the two extra Lys residues in Bax $\alpha$ 5 which are not present in Bcl-xL $\alpha$ 5 are critical for the peptide activity, but not for peptide dimerization (FIG. 8.1). Among the rest of the differentiating residues, Tyr115 of Bax $\alpha$ 5, replaced by Ser114 in Bcl-xL $\alpha$ 5, was selected as a plausible candidate for participating in peptide-peptide interactions and subsequently we designed the Bax $\alpha$ 5 Y115S mutant. Although this peptide behaves as a monomer in SDS-PAGE, with no appreciable dimer band, it is still able to dimerize in POPC. However, the association strength is lower by  $\sim 1$  kcal/mol with respect to the free energy of dimerization of Bax $\alpha$ 5. This effect agrees well with the loss of one hydrogen bond in the interaction region of the Bax $\alpha$ 5 Y115S dimer, compared to the dimeric Bax $\alpha$ 5. Thus, it appears that despite the presence of a hydroxyl group in both Tyr115 (from natural Bax $\alpha$ 5) and Ser115 (from the mutant), the former can make a hydrogen bond which is not possible with the latter. Although the interacting partner of Tyr115 is not clear (possible candidates are Tyr115 and Ser118 from the other peptide in the dimer). Alternatively,

the side chain of Tyr115 may be involved in interactions with any of the two Phe surrounding this residue in the partner peptide. Taken together, these results suggest that the dimerization motif of Bax $\alpha$ 5 contains at least the sequence <sup>108</sup>*GxxxAxxY*<sup>115</sup>. This basic motif can be complemented with additional residues like Trp107, Val110, Val111, Phe114, Phe116 and Ser118, which could contribute to the stability of the dimer through van der Waals, aromatic and hydrogen bond interactions [520–523].

Finally, it is interesting to compare our proposed dimerization motif with that of the BNIP3 TM domain, which is the only dimerization motif driving helix-helix association in the membrane of a Bcl-2 protein so far described. BNIP3 dimerizes through a tandem glycoporphin-like motif further stabilized by hydrogen bonding between His and Ser residues: *SHxxAxxxGxxxG* [235, 236, 524–526]. However, BNIP3 and Bax do not share the same evolutionary origin and there is no sequence homology between them [219]. Therefore, we propose that the *GxxxAxxY* motif is a novel and minimal dimerization motif driving interactions between Bax proteins and probably other phylogenetically related Bcl-2 proteins since this sequence is found in the conserved BH1 domain.

### 8.7.2 Functional importance of Bax $\alpha$ 5/Bax $\alpha$ 5 interactions

Oligomerization of Bax is often associated with MOM permeabilization, cytochrome *c* release and subsequent apoptosis induction [268, 270, 342]. As a result, Bax homo-oligomers of variable size (as well as homo-oligomers of the related protein Bak) are thought to be responsible for pore formation in the MOM. Another line of evidence supporting this hypothesis comes from the fact that the structurally similar anti-apoptotic Bcl-2 proteins can homo-dimerize but can neither engage into larger oligomers releasing cytochrome *c* nor promote apoptotic cell death efficiently [292, 295]. However, since the mechanism of Bax homo-oligomerization is poorly understood, the relationship between oligomerization and capacity to induce apoptosis remains unclear.

The simple Bax $\alpha$ 5 fragment, which in some aspects functions as a minimal version of the full length protein, may provide useful insights into the oligomerization-apoptosis issue. This peptide was first shown to release dextrans of size larger than cytochrome *c* from vesicles made of egg PC lipids [176], and more recently it has been demonstrated that it can release cytochrome *c* from mitochondria [377]. According to the results discussed in this Thesis and the composition of the lipid membranes corresponding to the previous investigations, in the first case (egg-PC LUVs) Bax $\alpha$ 5 should be dimeric, while in the second study (mitochondrial membranes) it should be oligomeric. Therefore, we may conclude that Bax $\alpha$ 5 dimers are sufficient to promote cytochrome *c* release. On the other hand, monomeric Bcl-xL $\alpha$ 5 is unable to release both high-molecular weight dextrans and cytochrome *c*. Bcl-xL $\alpha$ 5 A149K/E153K is both a monomeric peptide (at least in SDS micelles) and is able to release calcein at similar rates compared to Bax $\alpha$ 5, meaning that dimerization is not required for pore formation. Indeed, the pore formation capacity and the dimerization propensity seem to be codified separately in the peptide sequence: Lys residues placed at defined positions in Bax  $\alpha$ 5 are responsible for pore formation while the *GxxxAxxY* motif drives Bax $\alpha$ 5 dimerization. However, additional studies are needed to determine the size of pores made by monomeric Bcl-xL $\alpha$ 5

A149K/E153K. Independently from this result, the oligomerization threshold separating pro- from non-apoptotic activity would be a monomer or dimer for the peptides. On the other hand, as has been discussed before, for the full-length Bax protein this inactivity-activity threshold seems shifted toward an oligomeric species larger than a dimer.

Several evidences support the idea that *GxxxAxxY* is a key sequence for the dimerization not only of Bax $\alpha$ 5 but also the full-length Bax. The first one is the existence of a natural variant of Bax, Bax G108V, found in some hematopoietic malignancies, which eliminates mutant/mutant dimerization and also results in the loss of pro-apoptotic activity [527]. The second is that the *GxxxAxxY* motif is part of the proposed oligomerization domain of Bax. GEORGE *et al.* first identified a three-helix homo-oligomerization domain comprising helices  $\alpha$ 2 (containing the BH3 homology domain),  $\alpha$ 4 and  $\alpha$ 5 (both comprising the BH1 domain) [279]. However, the authors further suggested that helix  $\alpha$ 5 was the major determinant for homo-oligomerization. This was based on the observation that exchanging the helix  $\alpha$ 5 of Bcl-xL by that of Bax converted Bcl-xL into a Bax-like molecule, capable of homo-oligomerization and pro-apoptotic activity. Intriguingly, Bcl-xL formed low-molecular weight oligomers (most likely dimers to tetramers) and kept its anti-apoptotic function when the Bax $\alpha$ 5-derived helix contained the mutation <sup>113</sup>AAAA<sup>116</sup>, highlighting again the importance of Tyr115. Combining this information with the results of this Thesis, one would speculate that both the combination of Lys residues (which determine pore-forming activity) and the *GxxxAxxY* motif (which determine the dimerization propensity) are required for the formation of large cytochrome *c* permeable pores. Recently two interacting interfaces between Bax dimers reconstituted in micelles have been identified [280]. The first one called the “*front*” surface partially overlaps with the aforementioned three-helix homo-oligomerization domain and comprises the homology domains BH1, BH2 and BH3, including helices  $\alpha$ 2,  $\alpha$ 3,  $\alpha$ 4 (partially) and  $\alpha$ 5 (partially). In the hydrosoluble structures of Bax, the BH1-3 regions form a hydrophobic groove which has been shown to be the binding site of anti-apoptotic Bcl-2 proteins and BH3-only proteins (see below). The second interacting interface named the “*rear*” surface, is formed by helices  $\alpha$ 1 and  $\alpha$ 6 and the disordered loop between  $\alpha$ 1 and  $\alpha$ 2. Moreover, the proposed model involve *front:front* interactions to form scaffold dimers that would be then linked together by *rear:rear* interactions. However, this model assumes that Bax-Bax interactions take place in the tail-anchored conformation before extensive membrane insertion, which contrasts with previous results showing membrane insertion before oligomerization [257]. Thus, some of the mapped contacts may be lost in the membrane-inserted conformation of Bax, which may also be the origin of new interaction surfaces. Our proposed *GxxxAxxY* motif is located within the *front* pocket, in agreement with the above model. Nevertheless, another study with Bax protein reconstituted in lipid bilayers suggested also close proximity between BH3 domains (helices  $\alpha$ 2 and  $\alpha$ 3), but apparently no interaction between  $\alpha$ 5 helices [258]. It seems clear that the introduction of the Y115S mutation in the full-length protein is mandatory to check whether Bax-Bax interactions in the membrane are driven at least partially by the proposed motif.

### 8.7.3 Functional importance of Bax $\alpha$ 5/Bcl-xL $\alpha$ 5 interactions

Bcl-xL and Bcl-2 inhibit MOM permeabilization by Bax at three different levels: (i) through binding to tBid, and thus blocking Bax translocation to mitochondria, (ii) through binding tail-anchored Bax, and thus preventing further Bax insertion into the MOM, and (iii) *via* binding to Bax in the membrane, and thus inhibiting Bax oligomerization [269]. Interestingly, two point mutations of Bcl-xL, Bcl-xL G138A and G148E, reduce its heterodimerization with Bax and also its inhibition of apoptosis, suggesting the involvement of the BH1 domain, including part of helix  $\alpha$ 5 [528]. Conversely, mutations in the BH3 domain of Bax (and other pro-apoptotic Bcl-2 proteins) abolished its binding with either Bcl-2 or Bcl-xL [529, 530]. Structures of Bcl-2-like proteins in complex with BH3 peptides or BH3-only proteins provided explanations for the mutagenesis results [238, 239, 531, 532]. Thus, the main paradigm explaining Bax/Bcl-xL hetero-oligomers has been the interaction between the BH3 domain of Bax and the BH1-3 hydrophobic groove of Bcl-xL. The Bax/Bcl-2 binding interface has been recently mapped [293]. Within the Bax sequence, residues Ala-112, Lys-123 and Lys-128 on helix  $\alpha$ 5 were in close proximity ( $<1.2$  nm) to Bcl-2 in the heterodimers, while in Bcl-2 Arg-146 (equivalent to Arg-139 in Bcl-xL) and Lys-164 (equivalent to Lys-157 in Bcl-xL) in helix  $\alpha$ 5 were near Bax. This study proposed also a second interacting interface formed by the BH4 domain of Bcl-2 and the helix  $\alpha$ 6 of Bax. However, these experiments were performed in Triton X-100 and it is unclear which is the effect of the detergent on the protein conformation, especially because insertion of helices  $\alpha$ 5 and  $\alpha$ 6 in both Bax and Bcl-xL might not be compatible with the preservation of the two interacting surfaces.

Our results suggest that both Bcl-xL $\Delta$ Ct and Bcl-xL $\alpha$ 5 are able to hetero-oligomerize with Bax $\alpha$ 5 in membranes. However, it is still unclear whether the same dimerization motif, *GxxxAxxY* in Bax $\alpha$ 5, is also responsible for interactions with Bcl-xL. Competition experiments between Bax $\alpha$ 5 and Bax $\alpha$ 5 Y115S suggest that one single intact motif could be enough to drive helix-helix association. Nevertheless, Bax $\alpha$ 5-Bcl-xL $\alpha$ 5 and Bax $\alpha$ 5-Bcl-xL $\Delta$ Ct interactions do not lead to appreciable inhibition of Bax $\alpha$ 5 pore-forming activity. However, Bcl-xL $\alpha$ 5 and Bcl-xL $\Delta$ Ct are not expected to inhibit Bax $\alpha$ 5 by any of the three mechanisms proposed above, for the case of interactions between full-length proteins. This is because Bax $\alpha$ 5 is expected to target quickly the membrane where it may form pores independently of its interaction partner, since large oligomers as well as monomers may all induce the appearance of pores. It would however be interesting to study the size and other properties of pores formed by Bax $\alpha$ 5 in presence of its interaction partners. On the other hand, the fact that inhibiting of the pore-forming activity of the peptide Bax $\alpha$ 5 appears to be a difficult task, which cannot be easily performed by the physiological apoptosis inhibitors of mitochondrial poration, reinforces the potential therapeutic use of peptides of this type to trigger cell death in malignant cells, where the complex apoptotic regulatory network could be bypassed.

## 8.8 Conclusions

1. Bax $\alpha$ 5 forms at least dimers in lipidic and lipid-like environments. The Bax $\alpha$ 5-Bax $\alpha$ 5 interactions can be studied in both SDS micelles and lipid vesicles.
2. The oligomerization state of Bax $\alpha$ 5 depends on the lipid composition. It forms dimers in POPC and higher order oligomers in mixtures of POPC with DOPE and/or CL. The dimerization also depends on the phase state of the membrane, with the self-association being higher in gel phase DMPC membranes than in the LC phase.
3. Tyr115 is one of the key residues comprising the dimerization motif of Bax $\alpha$ 5 and it is probably involved in hydrogen bond formation. Additionally, there is a putative glycophorin-like dimerization motif in this Bax fragment, all together comprising a *GxxxArxY* motif.
4. Although Tyr115 is important for dimerization, it does not affect significantly the pore formation activity.
5. Lys residues of Bax, absent in similar positions of Bcl-xL, are important for the pore formation activity, all together comprising a *KxxxKxxx(x)K* motif. However, they do not seem to participate in dimerization.
6. Bax $\alpha$ 5-Bcl-xL $\Delta$ Ct and Bax $\alpha$ 5-Bcl-xL $\alpha$ 5 interactions can be detected in POPC:DOPE:CL membranes, but such interactions are not accompanied by an inhibitory effect of Bax $\alpha$ 5-induced membrane leakage.
7. Points 4, 5 and 6 suggest that dimerization is not a requirement for the pore formation activity of Bax $\alpha$ 5. They also mean that the sequence determinants for pore formation and dimerization are well separated, despite the small length of the peptide.

# 9 Structure of complexes of Bax $\alpha$ 5 with membranes

## 9.1 Introduction

**The structure problem in membrane-protein systems.** Elucidating the structure of proteins bound to membranes remains a major challenge in Biology. Difficulties in preparing and handling hydrophobic proteins at the required amounts and purity for structural studies slow down these investigations dramatically, compared to water-soluble proteins. Membrane proteins are not easy to crystallize, which is a requirement for X-ray diffraction studies, and are also difficult to reconstitute in lipid-mimicking environments, as it is needed for high resolution liquid-state NMR, all together explaining the slow progress in this field and the small number of solved membrane protein structures. These facts have impeded the use of alternative approaches, which although usually rendering a limited amount of structural information (a few distances or orientational restraints), provide realistic pictures of proteins or peptides directly in their *natural* membrane-bound state and give as well access to information about the dynamics of the protein-membrane complex.

On the other hand, when dealing with membrane-interacting peptides, the *odyssey* of complete determination of their structure at atomic resolution may be in part bypassed: In the majority of cases, the structure of a membrane-bound peptide can be appropriately described by a qualitative, or semi-quantitative description of the secondary structure content plus the orientation of the peptide with respect to the membrane normal and the depth of penetration in the lipid bilayer. Additionally, a model for the dynamics of the peptide can be also obtained from the structural analysis. This level of structural organization, reporting the orientation and location of membrane-bound peptides with respect to the membrane, has been referred to as *quinary* structure [533]. There are a number of spectroscopic techniques which allow performing such a structural analysis of peptides and proteins in lipid bilayer environments (see SEC. 5.2 to 5.3 for a discussion of those used in this Thesis). IR spectroscopy [396, 405], and ssNMR [534, 535] have acquired an important level of sophistication during the last decades and are most often used. Other spectroscopic methods, like OCD [536, 537], EPR [538] and fluorescence spectroscopy [539, 540], although in a more limited or indirect manner, provide also useful structural information. Additionally, the use of numerical simulations [541, 542], specially MD, is experiencing an important expansion. These latter methods are very important for the investigation of the dynamics of membrane systems and may be used as well as auxiliary methods for the interpretation of experimental results.

**The peptide-membrane complex.** Another important characteristic of the *structure problem* in membrane proteins and peptides is the role of the surrounding medium, namely the lipid bilayer membrane. For the particular case of membrane-active peptides, it is clear that both the peptide and the lipid bilayer, affect the structure of each other, and thus, they should be best considered as a whole, i.e., it is the structure of the peptide-lipid supramolecular complex that matters. For example, the active structures for the case of pore forming peptides (we may argue similarly for pore-forming proteins), from the mechanism of formation to their final configuration, are shaped by both peptides and lipid molecules. Infrared spectroscopy is a particularly suitable technique which allows simultaneous access to structural parameters from peptides and lipids [396, 405]. This method was chosen for this work, and results of its application to samples of Bax $\alpha$ 5 in supported bilayers will be presented and discussed here.

### 9.1.1 Objectives

In this Chapter we study the structure of complexes of Bax $\alpha$ 5 in oriented synthetic lipid membranes. We will first focus on the orientation of the peptide relative to the membrane normal using *site-specific infrared dichroism* (SSID). For that, we will measure dichroic ratios of normal and *isotope-displaced* amide I bands for a set of peptides, each labeled at a different sequence position with the probe 1- $^{13}\text{C}=^{18}\text{O}$ , introduced in place of normal peptide-bond carbonyls (TAB. 9.1). The structural characteristics of the lipidic components due to the presence of the peptide, including the orientation of lipid molecules and the phase properties of the bilayer, will also be addressed from the IR data. These studies will be complemented with X-ray scattering experiments, which will allow evaluating changes of the bilayer thickness. Finally, with the structural data here obtained, together with data from the oligomerization study of Bax  $\alpha$ 5 in vesicles (CHAP. 8), we will construct a molecular model of Bax $\alpha$ 5 in a lipid bilayer. The relationships between structure and pore-forming activity will then be addressed.

## 9.2 Molecular orientation within the peptide-membrane complexes<sup>1</sup>

Our structural study of Bax $\alpha$ 5-membrane complexes is based on the detailed characterization of the molecular orientation of the peptide with respect to the lipid bilayer. For that we used mainly ATR-FTIR measurements and the SSID strategy. SSID is based on the fact that the measured dichroic ratio of a TDM (we are going to use particularly the peptidic C=O stretching mode), is a function of its spatial orientation. As we explained in SUB. 5.2.2, the orientation of a TDM is defined by an angle  $\theta$ , with respect to the axis of orientation of the system (for us, the membrane normal). This angle, in turn, can be related to the orientation of the molecule where the TDM is placed, which for an  $\alpha$ -helical peptide is defined by the *tilt angle* of the helix axis,  $\beta$ , and the *rotational*

<sup>1</sup> The theory for orientation determination by FTIR can be found in SEC. 5.2.2. Detailed protocols are described in SUB. 6.2.2. For details about sample preparation please refer to SUB. 6.1.2.

**Tab. 9.1 : Peptides used for the structural study.** All peptides were acetylated at the N-terminus (Ac) and amidated at the C-terminus (NH<sub>2</sub>). We underline for each case the residue where the double isotope-labeled probe  $1\text{-}^{13}\text{C}=^{18}\text{O}$  was introduced. Numbering corresponds to the sequence of full-length Bax.

Polypeptide	Sequence
Unlabeled-Bax $\alpha$ 5	Ac-WGRVVALFYFASKLVLKALSTK-NH <sub>2</sub>
Bax $\alpha$ 5 Val111	Ac-WGRV <u>V</u> ALFYFASKLVLKALSTK-NH <sub>2</sub>
Bax $\alpha$ 5 Ala112	Ac-WGRV <u>V</u> <u>A</u> LFYFASKLVLKALSTK-NH <sub>2</sub>
Bax $\alpha$ 5 Leu113	Ac-WGRV <u>V</u> <u>A</u> <u>L</u> FYFASKLVLKALSTK-NH <sub>2</sub>
Bax $\alpha$ 5 Phe114	Ac-WGRV <u>V</u> ALFY <u>F</u> ASKLVLKALSTK-NH <sub>2</sub>
Bax $\alpha$ 5 Leu120	Ac-WGRVVALFYFASK <u>L</u> VLKALSTK-NH <sub>2</sub>
Bax $\alpha$ 5 Leu122	Ac-WGRVVALFYFASKLVL <u>K</u> ALSTK-NH <sub>2</sub>
Bax $\alpha$ 5 Ala124	Ac-WGRVVALFYFASKLVLK <u>A</u> LSTK-NH <sub>2</sub>

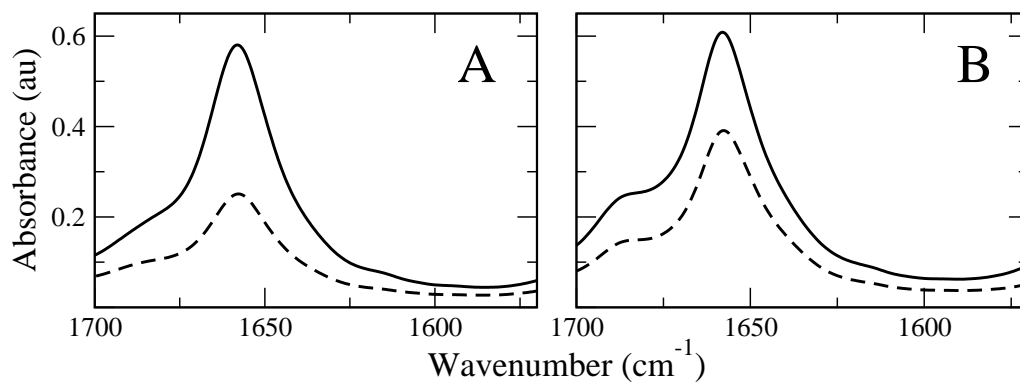


**Fig. 9.1 : Representative ATR-FTIR spectra of the amide I region of unlabeled groups of Bax $\alpha$ 5 in lipid membranes.** Spectra collected with parallel and perpendicular polarizations of incident light are represented by solid and dashed lines, respectively. A) Bax $\alpha$ 5 in DMPC membranes. B) Bax $\alpha$ 5 in POPC membranes. The values of  $R_{helix,i}^{exp}$  collected in TAB. 9.2 and 9.3 were calculated from the analysis of spectra of this type.

angle of the residue around that axis,  $\omega_i$ . The latter is a pitch angle for each site along the peptide sequence. It is defined arbitrarily as  $0^\circ$  when the TDM of the site under consideration, the helix director and the  $z$  axis reside in the same plane [414]. Assuming a canonical  $\alpha$ -helix, with 3.6 residues per turn, there will be only one unknown rotational angle for a set of site-specific labeled peptides. For example, for two consecutive residues the difference in  $\omega$  angle will be  $100^\circ$ . In practice, we made all calculations and molecular representations with reference to the first residue of the peptide sequence, and the value of  $\omega_1$ , or simply  $\omega$ , was taken as the helix azimuthal rotation.

Dichroic ratios were calculated as the ratio between the integrated absorptions of spectra collected with parallel and perpendicular polarized light. For unlabeled peptides, from each peptide-lipid combination, we may access only the value of  $R_{helix}^{exp}$ . For labeled peptides, each one with the isotopic mark in a different position  $i$ , two different dichroic ratios are determined:  $R_{helix,i}^{exp}$  and  $R_{site,i}^{exp}$  [414].  $R_{helix}^{exp}$  or  $R_{helix,i}^{exp}$ , as composite dichroism values from all unlabeled amide C=O bonds in the helical structure, depend solely on the tilt angle (they do not depend on  $\omega$ ). On the other hand, each  $R_{site,i}^{exp}$  is measured for a specific labeled residue, and depends on both  $\beta$  and  $\omega_i$ . Additionally, both dichroic ratios also depend on the order/dynamics of the system (see SUB. 5.2.2).

FIG. 9.1 shows IR spectra collected on oriented peptide-membrane systems with polarized light. The  $R_{helix,i}^{exp}$  values that follow from spectra of this type, for all cases studied, are listed in TAB. 9.2 and 9.3. Similarly, typical spectra of the labeled peptides focusing on the  $1-^{13}C =^{18}O$  absorption band are shown in FIG. 9.2 and the full list of  $R_{site,i}^{exp}$  values are collected in TAB. 9.2 and 9.3.

The orientation angles can be determined using a number of alternative strategies, as described in SUB. 5.2.2. Following we describe a step-by-step comparative analysis using various strategies.

### 9.2.1 Determining peptide orientations from dichroic ratios

In principle, only one labeled site is enough to solve the corresponding equations (EQ. 5.15, 5.16 and 5.25). However, in practice at least two labeled sites are required to get an accurate description of the system [414, 415, 543]. On the other hand, the same theory can be used to back-calculate expected values of dichroic ratios,  $R_{helix,i}^{theo}$  and  $R_{site,i}^{theo}$ , given a particular orientation defined by a pair of angles  $\{\beta, \omega\}$ . Thus, starting from complete sets of possible orientational states of the peptide (*implicit orientational landscape*, see explanation on page 81), the corresponding complete space of theoretical dichroic ratios can be obtained, which may then be compared with the experimental values.

Based on such a comparison, a best-fit analysis consists on finding the minimum of a *penalty* (or *error*) function. Two penalty functions are commonly used (described in SUB. 5.2.2), called *root mean square deviation* (*rmsd*) and *chi-square* ( $\chi^2$ ) (EQ. 5.26 and 5.27, respectively). As the name indicates, *rmsd* gives the square root of the average of the squared differences between the experimental and predicted data. It is therefore measured in the same units as the observed quantity, being dimensionless in the present case. The second common penalty function,  $\chi^2$ , is a squared deviation between experimental and predicted data normalized to the experimental error of each data point,

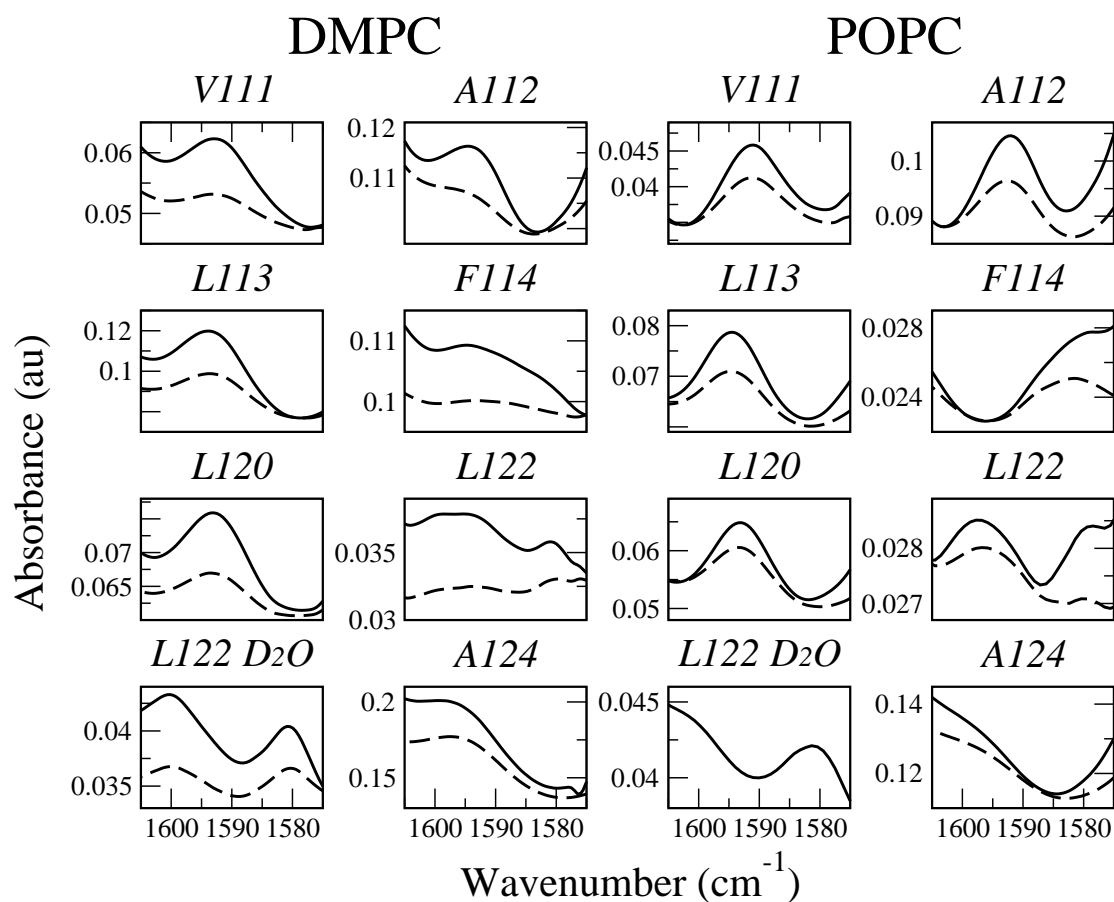


**Fig. 9.2** : Representative isotope-shifted amide I bands of  $1\text{-}^{13}\text{C}=^{18}\text{O}$  labeled  $\text{Bax}\alpha 5$  in lipid membranes. The two columns on the left are data in DMPC membranes and the two columns on the right correspond to POPC membranes. Spectra collected with parallel and perpendicular polarizations of incident light are represented by solid and dashed lines, respectively. Labeled residues were Val111, Ala112, Leu113, Phe114, Leu120, Leu122 and Ala124. Also shown are spectra in  $\text{D}_2\text{O}$  for the case of Leu120-labeled  $\text{Bax}\alpha 5$ . The values of  $R_{site,i}^{exp}$  given in TAB. 9.2 and 9.3 were calculated from the analysis of the bands represented here.

9 Structure of complexes of Bax $\alpha$ 5 with membranes

**Tab. 9.2 : Dichroic ratios of Bax $\alpha$ 5 in DMPC at P/L=1/50 calculated from the amide I bands corresponding to unlabeled ( $R_{helix,i}^{exp}$ ) and  $1-^{13}C=^{18}O$  labeled ( $R_{site,i}^{exp}$ ) sites.**

Bax $\alpha$ 5 <sup>a</sup>	$R_{helix}^{exp}$ <sup>b</sup>	$R_{site,i}^{exp}$ <sup>b</sup>						
		Val111	Ala112	Leu113	Phe114	Leu120	Leu122	Ala124
<i>Unlabeled</i>	2.54 (2.16)							
<i>Val111-1</i>	2.37 (2.37)	3.07 (3.20)						
<i>Val111-2</i>	2.29	2.67						
<i>Val111-3</i>	2.23	1.80						
<i>Val111-4</i>	2.32	1.83						
<i>Ala112-1</i>	2.00		1.92					
<i>Ala112-2</i>	2.21		2.03					
<i>Leu113-1</i>	2.38			1.79				
<i>Leu113-2</i>	2.37			1.89				
<i>Leu113-3</i>	2.46			2.83				
<i>Leu113-4</i>	2.52			2.43				
<i>Phe114-1</i>	2.76				2.01			
<i>Phe114-2</i>	2.63				1.92			
<i>Phe114-3</i>	2.39				1.63			
<i>Leu120-1</i>	2.43					2.75		
<i>Leu120-2</i>	2.45					2.67		
<i>Leu120-3</i>	2.39					2.16		
<i>Leu122-1</i>	2.63						2.18	
<i>Leu122-2</i>	2.44						1.68	
<i>Ala124-1</i>	2.26							2.05
<i>Ala124-2</i>	2.04							1.91
<i>Average<math>\pm</math>SD</i>	<i>2.39<math>\pm</math>0.17</i>	<i>2.3<math>\pm</math>0.6</i>	<i>2.0<math>\pm</math>0.1</i>	<i>2.2<math>\pm</math>0.5</i>	<i>1.9<math>\pm</math>0.2</i>	<i>2.5<math>\pm</math>0.3</i>	<i>2.0<math>\pm</math>0.5</i>	<i>2.0<math>\pm</math>0.1</i>

<sup>a</sup>1, 2, etc. refer to different independent repetitions of the corresponding spectrum, each one with a different sample prepared using the same batch of the peptide. These repetitions were used to calculate average $\pm$ SD values.

<sup>b</sup>Values between brackets correspond to measurements in D<sub>2</sub>O.

9.2 Molecular orientation within the peptide-membrane complexes

**Tab. 9.3 : Dichroic ratios of Bax $\alpha$ 5 in POPC at P/L=1/50 calculated from the amide I bands of unlabeled ( $R_{helix,i}^{exp}$ ) and  $1-^{13}\text{C}=^{18}\text{O}$  labeled ( $R_{site,i}^{exp}$ ) peptides.**

Bax $\alpha$ 5 <sup>a</sup>	$R_{helix}^{exp}$ <sup>b</sup>	$R_{site,i}^{exp}$ <sup>b</sup>						
		Val111	Ala112	Leu113	Phe114	Leu120	Leu122	Ala124
Unlabeled-(1)	1.66 (1.63)							
Unlabeled-(2)	1.53							
Val111-1	1.62	1.83						
Val111-2	1.72 (1.74)	1.55 (1.60)						
Val111-3	1.63	2.17						
Val111-4	1.74	2.17						
Ala112-1	1.68		1.86					
Ala112-2	1.67		1.84					
Leu113-1	1.66			2.31				
Leu113-2	1.66			1.76				
Leu113-3	1.78			2.83				
Leu113-4	1.77			1.91				
Phe114-1	1.71				1.85			
Phe114-2	1.51				1.24			
Phe114-3	1.67				1.45			
Leu120-1	1.60					1.94		
Leu120-2	1.65					1.37		
Leu120-3	1.63					2.48		
Leu122-1	1.52						2.01	
Leu122-2	1.62						2.66	
Leu122-3	1.65						2.17	
Leu122-4	1.54						1.18	
Leu122-5	1.62						1.83	
Ala124-1	1.71							1.58
Ala124-2	1.73							1.56
Average $\pm$ SD	1.65 $\pm$ 0.07	1.9 $\pm$ 0.3	1.9 $\pm$ 0.1	2.2 $\pm$ 0.5	1.6 $\pm$ 0.3	2.0 $\pm$ 0.6	2.0 $\pm$ 0.6	1.6 $\pm$ 0.1

<sup>a</sup>1, 2, etc. refer to different independent repetitions of the corresponding case, each one with a different sample prepared using the same batch of the peptide.

<sup>b</sup>Values between brackets correspond to measurements in D<sub>2</sub>O.

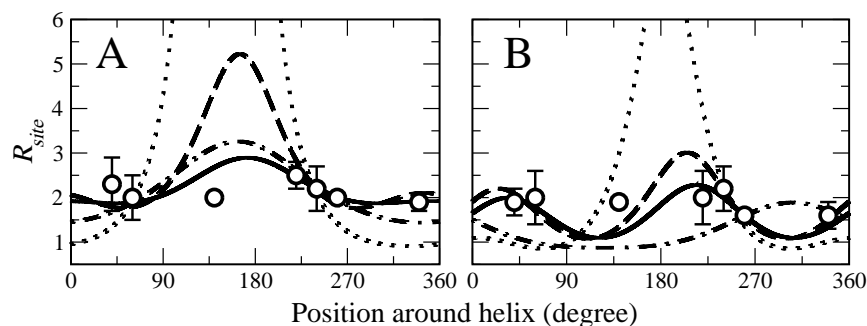


**Fig. 9.3** : Helical wave plots of  $R_{site,i}^{exp}$  and  $R_{site}^{theo}$  as a function of the residue angular position around the helix. Graphs A are for Bax $\alpha$ 5 in DMPC and B are for Bax $\alpha$ 5 in POPC. The first residue is set arbitrarily at zero degrees to allow easy comparison, i.e., independently of the  $\omega = \omega_1$  value. The position of the remaining residues are calculated considering a monotonous canonical  $\alpha$ -helix, for which consecutive residues are separated by  $100^\circ$  rotation. Each  $R_{site}^{theo}$  curve was calculated using one of four alternative models and their associated best-fit parameters (TAB. 9.5: The dotted lines correspond to models assuming *fixed orientation*; dashed lines are for models including a *distribution of  $\beta$* ; dashed-dotted lines refer to a *distribution of  $\omega$* ; and solid lines are for models that include *distributions of both  $\beta$  and  $\omega$* . The measured  $R_{site,i}^{exp}$  values are shown as circles, with error bars corresponding to  $\pm SD$ .

becoming unitless. A value of  $\chi^2$  smaller than the number of data points indicates coincidence between experimental and model-predicted data within the experimental error. Any minimum of the  $\chi^2$  function will give one important piece of information [544]: it will show (from its value) whether the solution found is acceptable, i.e. whether the corresponding fit explains the data within experimental error. If the quality of the fit is acceptable, then the corresponding values of the parameters may be used in model building. In our case, each acceptable minimum will give a pair of angles  $\{\beta, \omega\}$  (and depending on the model considered, also a measure of the width of their distribution, see SUB. 5.2.2), that may be interpreted in structural terms. Importantly, since  $\chi^2$  is normalized to the experimental error, values calculated for different dichroic ratios,  $R_{helix}$  and  $R_{site}$ , each one with a different error (see TAB. 9.2 and 9.3, bottom line), can be compared and even added (EQ. 5.27). Thus, we have chosen to use  $\chi^2$  for the analysis of experimental data.

As an alternative method to derive the peptide orientation, in some instances we applied the *rigid-body modeling* strategy reported by ARKIN and coworkers [424]. For that, the orientational landscape was constructed explicitly, by making an atomic detail molecular model of the peptide, considered a rigid canonical  $\alpha$ -helix, for each possible  $\{\beta, \omega\}$  state (explained below in SUB. 9.2.4). Then, for each peptide orientational state, the internal structural angles  $\theta_i^{theo}$  of peptides labeled at position  $i$  are extracted from the model, and used to calculate  $R_{site,i}^{theo}$  and  $R_{helix,i}^{theo}$ , which are collectively compared with values determined from experiments. Again, the  $\chi^2$  error function expressed by EQ. 5.27 was used to evaluate such comparison and select best-fit cases.

The quality of all fits made by including values of  $R_{site}$  can be checked with the help of *helical wave* plots (see FIG. 9.3 below). In these graphs, we represent experimental

**Tab. 9.4 : Tilt angle of Bax $\alpha$ 5 in different lipid membranes.** The values correspond to the use of  $R_{helix}$  data only.

Lipid	$S_{helix}$	$\beta(^{\circ})^a$
DMPC	0.23 $\pm$ 0.12	46 $\pm$ 5
POPC	-0.30 $\pm$ 0.14	69 $\pm$ 7
DOPC	-0.27 $\pm$ 0.13	68 $\pm$ 7
DOPC:CL	-0.33 $\pm$ 0.04	70 $\pm$ 3
DLPC	-0.02 $\pm$ 0.06	55 $\pm$ 3
DOPC:SM:CHOL	-0.20 $\pm$ 0.10	64 $\pm$ 5
DPPC	-0.13 $\pm$ 0.05	60 $\pm$ 3

<sup>a</sup>Peptide tilt corresponding to  $S_{memb}=1$ , according to EQ. 5.19 and 5.20.

data points for each labeled site as a function of its angular position around the helix (as in an Edmundson's *helical wheel* [545]) together with the theoretical curve calculated using best-fit parameters. This analysis is also useful to evaluate the behavior of each individual site with respect to the rest. Thus, major errors for one particular site may indicate deviations from the assumed structure (implicitly considered an ideal  $\alpha$ -helix in the model used for calculations, SUB. 5.2.2) with impact on  $R_{site}$ . For example, we noticed that Ala112 tends to be an outlier compared to the trend corresponding to the other residues, and in fact, excluding  $R_{site}$  from this residue improved the fits significantly.

### 9.2.2 Calculations using order parameters

As a first approximation, we start with determining the peptide orientation for the different conditions assayed in this study, using initially only data of  $R_{helix}$  and solving EQ. 5.19 and 5.20 (SUB. 5.2.2 on page 77). This is the simplest method possible, proper for unlabeled peptides. It allows only for an estimation of the upper limit of the tilt, with no information about  $\omega$ , through the use of an *order parameter* [396] ( $S_{helix}$ , see page 77).

In order to better understand the orientation of Bax $\alpha$ 5 in the membrane and to be able to relate such an orientation with a model explaining pore formation, it is useful to study Bax $\alpha$ 5 in different membrane systems. For that we chose lipids with different properties, like charge, chain length and phase-transition temperature ( $T_m$ ). The calculated peptide tilt,  $\beta$ , estimated via  $S_{helix}$  is shown in TAB. 9.4. We can classify the data into two groups. The first cluster includes unsaturated lipids POPC, DOPC, DOPC:CL and DOPC:SM:CHOL, where peptide tilts tend to be close to parallel to the bilayer surface ( $\sim 70^{\circ}$ ). The second includes saturated lipids: DMPC, DLPC and DPPC, where Bax $\alpha$ 5 is tilted away from the flat portion in the membrane ( $\beta = 46$ -60 $^{\circ}$ ). The possible reason for such variations will be explained below SEC. 201.

The orientations of the two extreme cases, i.e Bax $\alpha$ 5/DMPC and Bax $\alpha$ 5/POPC were

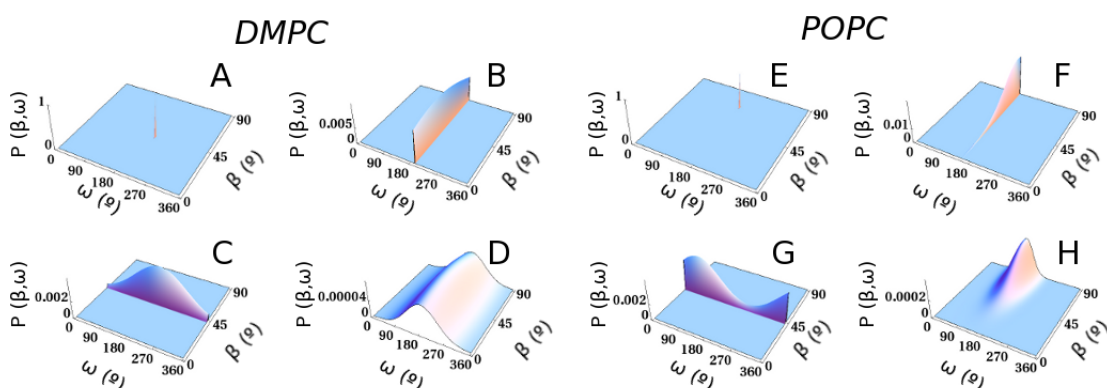


**Fig. 9.4 : Visualization of the orientational distribution for the best fit solutions arising from the four proposed models.** The graphs correspond to Bax $\alpha$ 5 in DMPC membranes (A-D) and POPC membranes (E-H). We plot the probability of finding a particular peptide orientation,  $P(\beta, \omega)$ , as a function of the helix tilt,  $\beta$ , and the helix rotation,  $\omega$ . A) and E) are for models assuming a *fixed orientation*; B) and F) assume a *distribution of  $\beta$* ; C) and G) assume a *distribution of  $\omega$* ; D) and H) assume *distributions of both  $\beta$  and  $\omega$* .

studied further by SSID [414]. For that, we used a set of peptides labeled with  $1-^{13}\text{C} =^{18}\text{O}$  probes at seven specific positions (see spectra in FIG. 9.2 and values of  $R_{helix,i}^{exp}$  and  $R_{site,i}^{exp}$  in TAB. 9.2 and 9.3), which allows obtaining information also on the value of the azimuthal rotation angle. *Best-fit* values of  $\beta$  and  $\omega$  were determined as explained above and on page 81, by first back-calculating expected theoretical dichroic ratios  $R_{helix,i}^{theo}$  and  $R_{site,i}^{theo}$  for a complete set of possible  $\{\beta, \omega\}$  pairs and selecting lowest-error cases after comparison with experimental values using the  $\chi^2$  penalty function (Eq. 5.27). In a first step both angles were considered invariable (static and perfectly ordered system) (FIG. 9.4 A,E). However, as for the case of the analysis with only  $R_{helix}$ , we also performed more realistic interpretations by way of accounting for space- and/or time-dependent orientational disorder. Such implementations are explained next

### 9.2.3 Including distributions of the orientation angles

In the analysis described above, disorder is only considered implicitly by inputting an order parameter. This was calculated from  $S_{helix}$  and only reflects variations of  $\beta$ . However, we can also use explicit models to account for disorder, like *via* introduction of Gaussian distribution functions of  $\beta$  and  $\omega$ , which reflect spacial variations and time dependent fluctuations of these parameters. In such a case the peptide orientation is defined by the mean values of tilt and rotation:  $\bar{\beta}$  and  $\bar{\omega}$ , and standard deviations of the distributions of these angles:  $\sigma_{\beta}$  and  $\sigma_{\omega}$ . This model has already been used with success for the analysis of IR data to take into account disorder of the tilt angle [420]. We now propose to generalize it also for changes of the helix azimuthal rotation. On

**Tab. 9.5 : Best-fit parameters describing the orientation of Bax $\alpha$ 5 in multibilayer stacks.** The peptide is depicted as a cylinder and the black sphere shows the position of the tryptophan residue, which defines  $\omega$ . Arrows are proportional to  $\sigma_\beta$  and  $\sigma_\omega$ .

Model	DMPC				POPC					
	Error ( $\chi^2$ )	$\beta$ or $\bar{\beta}$ ( $^\circ$ )	$\sigma_\beta$ ( $^\circ$ )	$\omega$ or $\bar{\omega}$ ( $^\circ$ )	$\sigma_\omega$ ( $^\circ$ )	Error ( $\chi^2$ )	$\beta$ or $\bar{\beta}$ ( $^\circ$ )	$\sigma_\beta$ ( $^\circ$ )	$\omega$ or $\bar{\omega}$ ( $^\circ$ )	$\sigma_\omega$ ( $^\circ$ )
<i>Fixed orientation</i>	76	42	0	208	0	35	69	0	175	0
<i>Tilt distribution</i>	6	34	60	195	0	3	86	24	155	0
<i>Rotation distribution</i>	7	44	0	197	90	15	67	0	54	80
<i>Tilt and rotation distributions</i>	0.6	42	68	188	56	1.3	88	24	146	28

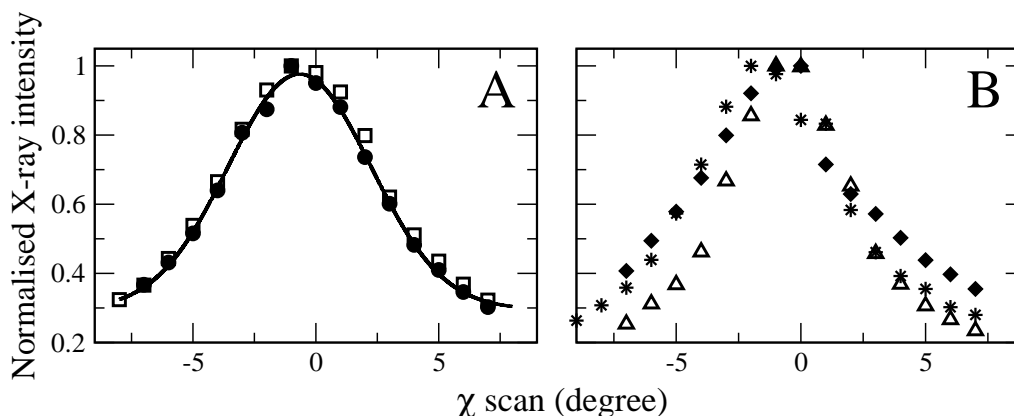


**Fig. 9.5 : Estimating the mosaicity by a  $\chi$ -scan on the first Bragg peak.** A) DMPC alone (filled circles) and in presence of Bax $\alpha$ 5 at a  $P/L=1/50$  (squares), along with a fitted Gaussian distribution (solid line). The fit yields  $\sigma=3^\circ$ , which relates to the probability distribution of local membrane normal vectors. B) POPC alone (diamonds), and in presence of Bax $\alpha$ 5 in POPC at  $P/L=1/50$ : “phase 2” (triangles) and “phase 1” (stars).

the other hand, Gaussian distributions have been found to be appropriate to describe the dynamic behavior of membrane bound peptides studied in MD simulations [57]. In fact, an implementation similar to the one that we are testing here has been proved to be adequate for the analysis of  $^2\text{H}$ -ssNMR data [422]. Other probability distribution functions either disagree with the MD data or are too complex mathematically for easy implementation [57, 546, 547].

In order to best understand the effect of introducing distributions, we will carry out our analysis considering an increasing level of disorder, from an absolutely ordered system to a case with distributions of both  $\beta$  and  $\omega$ .<sup>1</sup>

**Static and completely ordered system.** Although physically unlikely, this simplest case is useful because it serves as a reference for comparison with the other cases. Here the orientation is just represented by one  $\{\beta, \omega\}$  pair of angles. The best tilt values are very similar to those calculated above using an order parameter, and they are represented in FIG. 9.4 A and E.

**Mosaicity.** This may be considered a particular case of the next model, but with interesting conceptual and experimental characteristics. We assume that the standard deviation of the tilt distribution can be equaled to the mosaicity ( $\sigma$ ) of the oriented bilayer sample; i.e., the distribution of normal bilayer vectors [386]. Mosaicities of the same ordered lipid membranes used for the IR studies can be estimated from X-ray scattering measurements (see *mosaicity* in SEC. 5.1.1). Thus, this approach has the

<sup>1</sup> We follow a rationale similar to the one used to introduce fluctuations of tilt and azimuthal rotation for the analysis of  $^2\text{H}$ -ssNMR data [422].

advantage that the input disorder is based on a parameter that is accessible experimentally. Fitting a Gaussian distribution to  $\chi$ -scan X-ray scattering intensities (EQ. 5.5) allows the determination of  $\sigma$ . Results of this analysis are shown in FIG. 9.5 A and B for DMPC and POPC, respectively (the two phases found in POPC will be explained below). We obtain  $\sigma=3^\circ$ , which is comparable to other reported values ( $\sigma \leq 5^\circ$ ) [386]. With this value we calculate the peptide tilt angles, which are the same as those corresponding to the fixed-tilt case. However, such estimates of disorder can be considered *small* if used to account for the amplitude of peptide tilt distributions in membranes. For example, from analysis of  $^2\text{H}$ -ssNMR data  $\sigma_\beta$  is estimated to be in the order of  $15^\circ$  or higher [422]. Thus, because mosaicities correspond to the background disorder of the lipid bilayer, they likely represent a lower limit of the peptide tilt disorder and would underestimate the real width of the tilt distribution.

**A normal distribution of tilts.** Next, we move on to search for a Gaussian distribution of  $\beta$  that accounts for its total disorder. For this we apply EQ. 5.27 systematically, and compare jointly the  $6 \times \{R_{helix,i}^{exp}, R_{site,i}^{exp}\}$  pairs measured for each Bax $\alpha$ 5/lipid system with theoretical dichroic ratios corresponding to distributions of  $\beta$  states over a range of  $\sigma_\beta$  values. Best-fit  $\{\bar{\beta}, \omega\}$  pairs are collected in TAB. 9.5. Similarly to what happens for the commonly used fractional order,  $f_\beta$  (SUB. 5.2.2), the introduction of a distribution of tilts has the effect of decreasing  $\bar{\beta}$ , compared to  $\beta$ , when these angles are below the *magic angle* ( $54.7^\circ$ ), or increasing  $\bar{\beta}$ , for the case of tilts above the *magic angle*. Thus, for POPC the tilt increases from  $\beta=69^\circ$  to  $\bar{\beta}=86^\circ$ , while for DMPC it decreases from  $\beta=42^\circ$  to  $\bar{\beta}=34^\circ$ . No significant changes were found in the values of  $\omega$  (see TAB. 9.5).

With respect to the standard deviation of the distributions,  $\sigma_\beta$ , the best fit corresponds to  $24^\circ$  for Bax $\alpha$ 5 in POPC membranes and  $60^\circ$  for Bax $\alpha$ 5 in DMPC. While the first value can be acceptable, the second appears much too large, as it would indicate that the peptide can sample all possible tilt configurations (FIG. 9.4 B and F). Nevertheless, theoretical considerations (FIG. 5.8) suggest that the order of the sample is ill-defined for tilt angles near  $45^\circ$ , which is the case for DMPC samples. i.e. we can get similar quality of fits with multiple distributions, including a uniform distribution of  $45^\circ$ , or with a completely random peptide orientation, meaning that there is large ambiguity in the determination of  $\beta$  for this peptide orientation.

**A normal distribution of peptide rotation.** We consider now a Gaussian distribution of  $\omega$ , with mean  $\bar{\omega}$  and standard deviation  $\sigma_\omega$ , while fixing the value of  $\beta$ . The results of fits for all Bax $\alpha$ 5/lipid systems studied, using a range of  $\sigma_\omega$  values, are presented in TAB. 9.5. The best fit is achieved with *large* values of  $\sigma_\omega$  for Bax $\alpha$ 5 in either of the two lipid systems ( $90^\circ$  and  $80^\circ$  in DMPC and POPC respectively, FIG. 9.4 C and G). Similar values have been found in  $^2\text{H}$ -ssNMR studies of the dynamics of hydrophobic transmembrane peptides, but not for amphipathic interface-bound peptides (like Bax $\alpha$ 5 in POPC), where such fluctuations may be considered unlikely as they would imply the unfavorable exposure of the polar face of the helix to the hydrophobic interior [422]. Additionally, for this latter case the value of  $\bar{\omega}$  decreases by more than  $100^\circ$  compared

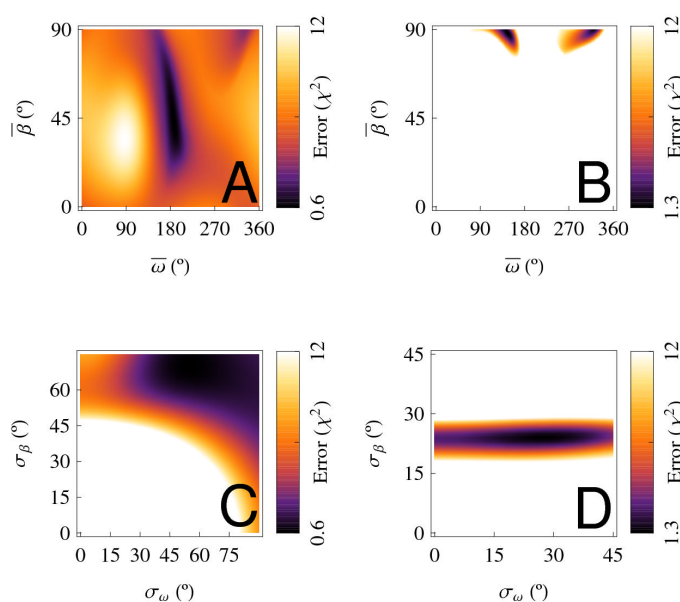


**Fig. 9.6** :  $\chi^2$  error analysis for different combinations of parameters in fits of IR data considering distributions of  $\beta$  and  $\omega$ . Represented are  $\{\beta, \omega\}$  for Bax $\alpha$ 5 in DMPC (A) or POPC (B), and  $\{\sigma_\beta, \sigma_\omega\}$  for Bax $\alpha$ 5 in DMPC (C) or POPC (D). Best fit values are shown in TAB. 9.5.

to  $\omega$ . On the other hand, we have again to be cautious with the best fit  $\sigma_\omega$  of Bax $\alpha$ 5 in DMPC, as this may be blurred due to the particular orientation (near  $45^\circ$  tilt, see above) of the peptide in this lipid system.

Nevertheless, it seems that allowing for a distribution of  $\omega$  affects only weakly  $\beta$  and  $\bar{\omega}$ , at least for Bax $\alpha$ 5/DMPC (TAB. 9.5). This suggests that orientations determined using the SSID method are only weakly sensitive to disorder and/or dynamics of the peptide azimuthal rotation, which may then be safely ignored for the analysis.

**Normal distributions of peptide tilt and rotation.** Finally we consider the case of using simultaneously Gaussian tilt and rotational angle distributions. Two-dimensional graphs of  $\{\bar{\beta}, \bar{\omega}\}$  and  $\{\sigma_\beta, \sigma_\omega\}$  pairs mapped to their corresponding  $\chi^2$  value, are shown in FIG. 9.6 and the best fit values are shown in TAB. 9.5. For the two lipid systems studied the reduction of  $\chi^2$  is larger than in fits where only one of the two distributions was considered. For Bax $\alpha$ 5 in POPC the helix maintains a similar orientation as when including only a tilt distribution, being almost parallel to the bilayer surface:  $\bar{\beta} \sim 88^\circ$ , and with  $\bar{\omega} \sim 146^\circ$ . On the other hand, in DMPC membranes Bax $\alpha$ 5 maintains an *averaged* orientation similar to that found with other models, although with very large values of  $\sigma_\beta$  and  $\sigma_\omega$ , which means that it would sample a large part of the possible orientational space (FIG. 9.4 D, H). However, as suggested before, such large widths of the distributions are probably unrealistic and may be due to a limitation of the method

for cases where the tilt angle is near  $45^\circ$ .

All in all, it appears clear that including distributions, either of the tilt angle, the rotational angle or both, has the effect of reducing the error of the fits. However, the tilt distributions are responsible for the main part of the improvement of the fits and have the largest impact on the peptide orientation results, suggesting as well that the two types of peptide disorder have independent effects. Nevertheless, the fact that including  $\omega$  distributions lowers significantly  $\chi^2$  indicates that disorder/dynamics of  $\omega$  is indeed present in the samples, although the values of  $\sigma_\omega$  determined here might be overestimated. A question arising is the reason for the smaller impact on peptide orientation of rotational disorder compared to tilt disorder. This may be due to the fact that only  $R_{site}$  (not  $R_{helix}$ ) depends on  $\omega$ , while both,  $R_{site}$  and  $R_{helix}$  depend on  $\beta$ , which means that there is more experimental information available to define the peptide tilt (including the tilt distribution) than the peptide rotation. Additionally, the experimental error associated to  $R_{site}$  is larger and thus this parameter has smaller weight in the analysis.

It is also interesting to notice that the effects of tilt and azimuthal rotation distributions on the orientations determined by  $^2\text{H}$ -ssNMR are opposite to the ones just described for SSID. Thus, the tilt of membrane peptides determined by  $^2\text{H}$ -ssNMR is mainly affected by distributions of the azimuthal rotation [422], while for studies made by SSID it is mainly affected by tilt distributions. Although the analysis in both types of experiments is conceptually different, since the case of NMR considers specifically peptide dynamics while the distributions for the IR method include all kinds of disorder, we may conclude that the two alternative methods are complementary for the study of peptide orientation.

#### 9.2.4 Orientation refinement assisted by rigid body modeling

All mathematical models used up to now to determine angular restraints from IR dichroic ratios are derived from a geometry that corresponds to an implicit ideal  $\alpha$ -helix, which is considered rigid and homogeneous along its complete extension. However, with the help of relatively simple molecular modeling tools it is possible to handle efficiently *explicit* representations of the peptide structures, which can then be positioned at specific orientations with respect to an external reference axis and from which we can “measure” directly angular magnitudes like  $\alpha$  and  $\theta$  (see definitions in SUB. 5.2.2). An obvious advantage of the use of explicit molecular representations of the peptide is then that each state considered within the explored orientational landscape has an immediate and direct meaning.

Another useful advantage is that this strategy allows for an easy consideration of any starting structure, i.e. it is not bound to the use of a canonical homogeneous helix, and it allows, for example, considering dimeric arrangements of the peptide. The rationale of including a dimer in the analysis and the corresponding results will be explained below. We start by considering the simple case of a monomeric rigid canonical  $\alpha$ -helix (with  $\phi=-60^\circ$  and  $\psi=-45^\circ$  [548, 549]). Even for this case, there are small sequence dependent structural variations between residues that affect the local values of  $\alpha$  and  $\theta$ . This is

9 Structure of complexes of Bax $\alpha$ 5 with membranes

**Tab. 9.6 :** Values of  $\theta_i^{exp}$  for Bax $\alpha$ 5 in DMPC obtained from  $R_{site,i}^{exp}$ , setting  $\sigma=3^\circ$ .

Sample	$\theta_i^{exp}$ ( $^\circ$ ), for the indicated labeled residue						
	Val111	Ala112	Leu113	Phe114	Leu120	Leu122	Ala124
Val111-1	45.5						
Val111-2	48.4						
Val111-3	57.4						
Val111-4	56.9						
Ala112-1		55.8					
Ala112-2		54.4					
Leu113-1			57.5				
Leu113-2			56.2				
Le113-3			47.1				
Leu113-4			50.4				
Phe114-1				54.7			
Phe114-2				55.8			
Phe114-3				59.9			
Leu120-1					47.7		
Leu20-2					48.4		
Leu120-3					53		
Leu122-1						52.8	
Leu122-2						59.1	
Ala124-1							54.2
Ala124-2							55.9
Average $\pm$ SD	52 $\pm$ 6	55 $\pm$ 1	53 $\pm$ 5	57 $\pm$ 3	50 $\pm$ 3	56 $\pm$ 4	55 $\pm$ 1

<sup>a</sup>1, 2, *etc.* refer to different independent repetitions of the corresponding case, each one with a different sample prepared using the same batch of the peptide. These repetitions were used to calculate average $\pm$ SD values.

9.2 Molecular orientation within the peptide-membrane complexes

**Tab. 9.7 :** Values of  $\theta_i^{exp}$  for Bax $\alpha$ 5 in POPC obtained from  $R_{site,i}^{exp}$ , setting  $\sigma=3^\circ$ .

Sample	$\theta_i^{exp}$ ( $^\circ$ ), for the indicated labeled residue						
	Val111	Ala112	Leu113	Phe114	Leu120	Leu122	Ala124
<b>Bax<math>\alpha</math>5 in POPC</b>							
Val111-1	56.9						
Val111-2	61.2						
Val111-3	52.9						
Val111-4	52.9						
Ala112-1		56.6					
Ala112-2		56.8					
Leu113-1			51.5				
Leu113-2			57.9				
Leu113-3			47.1				
Leu113-4			55.9				
Phe114-1				56.7			
Phe114-2				67.8			
Phe114-3				63.1			
Phe114-4				55.5			
Leu120-1					64.7		
Leu120-2					49.9		
Leu120-3					54.7		
Leu122-1						48.4	
Leu122-2						52.9	
Leu122-3						69.5	
Leu123-4						56.9	
Ala124-1							60.7
Ala124-2							61.0
Average $\pm$ SD	56 $\pm$ 4	57 $\pm$ 1	53 $\pm$ 5	61 $\pm$ 6	56 $\pm$ 8	57 $\pm$ 9	61 $\pm$ 1

<sup>a</sup>(1), (2), *etc.* refer to different independent repetitions of the corresponding case, each one with a different sample prepared using the same batch of the peptide. These repetitions were used to calculate average $\pm$ SD values.

due to the fact that the angles and distances within each residue in the peptide are not exactly the same, as it is (implicitly) assumed for the *implicit*<sup>1</sup> model. Thus, the exact values of  $\alpha$  and  $\theta$ , which define the orientation of the relevant TDM for our case, depend on the modeling program used to construct the starting  $\alpha$ -helix structure. This has also an impact on the values of the pitch angle between consecutive residues ( $\Delta$ ), which in the implicit model is assumed constant and equal to 100°, while in the explicit model varies depending on the residue and on the reference point in the structure used to follow it (see TAB. 9.8 on page 194). Our  $\alpha$ -helix model was built using standard tools of the Swiss-PDB<sup>2</sup> package, which employs the GROMOS96<sup>3</sup> force-field for energy minimization.

This approach has been introduced recently by ARKIN and coworkers, who named it *rigid body refinement* [424]. In order to apply it the model peptide structure is first aligned with the z axis of coordinates and then tilted and rotated, 1 degree at a time, sampling from 0° to 90° for tilt and from 0° to 360° for azimuthal rotation. For each of the 90×360 generated structures, the values of the  $\theta$  angle corresponding to each labeled residue in the model,  $\theta_i^{theo}$ , are computed and used to calculate  $R_{site,i}^{theo}$  and  $R_{helix}^{theo}$ . These are then compared with experimental values,  $R_{site,i}^{exp}$  and  $R_{helix}^{exp}$ , both measured by ATR-FTIR, and  $\sigma$ , measured by X-ray scattering (EQ. 5.28). We used the  $\chi^2$  error function to guide the selection of “best fit” values (EQ. 5.27).

In FIG. 9.7 we have plotted all possible combinations of  $\beta$  and  $\omega$  for a rigid model of Bax $\alpha$ 5, along with penalty values corresponding to measurements in DMPC (A,C) and POPC membranes (B,D). The best-fit values of the orientation angles are shown in TAB. 9.10. In the case of complexes of Bax $\alpha$ 5 with DMPC membranes, assuming a monomeric peptide, the lowest penalty was 81, which corresponds to  $\beta=46^\circ$  and  $\omega=311^\circ$ , respectively. Similarly, for POPC the best solution has a penalty of 29 and is found for  $\beta=65^\circ$  and  $\omega=266^\circ$ . Such orientations are similar to those obtained using the alternative models described above. The small differences are probably due to the geometry differences between the implicit and explicit helices. In any case, the associated errors are very large, in agreement with the lack of consideration of disorder.

### 9.2.5 Monomers vs dimers.

One important conclusion from the results described so far is that the quality of the fits improves largely by including disorder of the orientation angles. However, the width of  $\beta$  and  $\omega$  distributions appear in general unrealistically large. There is even one case where the results of best fits including  $\{\beta, \omega\}$  distributions can be clearly considered unreliable (Bax $\alpha$ 5 in DMPC). We should then consider the possibility that orientational disorder is associated with a structural organization of the peptide which is different from just a

1 And thereby our distinction between implicit and explicit representations of the helix. Although in both cases the declared assumption is a canonical  $\alpha$ -helix defined by the same given pair of  $\phi$  and  $\psi$  rotamers, the implicit model considers exactly the same geometry for all residues in the sequence, while the explicit model uses specific geometry details that depend on the sequence and are included by the modeling algorithm used to generate the starting rigid  $\alpha$ -helix structure.

2 <http://spdbv.vital-it.ch/>

3 <http://www.igc.ethz.ch/GROMOS/>

normal distribution of orientations. The obvious possibilities are an equilibrium between (at least) two coexisting orientational states and a peptide dimer which is placed in the membrane in a way which makes each peptide unit orientationally different from the other.

As we have pointed out, the rigid body refinement method has the advantage of permitting an easy and intuitive implementation of any starting structure, including oligomeric arrangements of the peptide, apart from the simplest consideration as a monomer. We have shown that dimers are the prevailing assemblies in both DMPC and POPC. It is thus instructive to test the hypothesis of the dimer using the available IR data. In order to do that, all we need is a reasonable starting structure for the Bax $\alpha$ 5 dimer and then repeating the strategy used for the case of a monomer.

In order to build a dimer model, we hypothesized that the *GxxxA* sequence of Bax $\alpha$ 5 represents a dimerization motif (SEC. 8.7), which is then essentially analogous to that of the TM domain of glycoporphin A. Moreover, as in the case of this latter protein, our most likely hypothesis, considering the FRET study, is that Bax $\alpha$ 5 forms a parallel dimer (at least in POPC, see SEC. 8.7). Thus, using the experimental structure of glycoporphin as a framework (PDB ID: 1AFO) we modeled a hypothetical Bax $\alpha$ 5 dimer using the Swiss-PDB platform. Such a Bax $\alpha$ 5 dimer has a crossing angle of 40° and a register of 1.6 nm.

Best fit values of the rigid body modeling approach using a dimeric starting structure are shown in TAB. 9.10. The most remarkable fact is that  $\chi^2$  diminishes up to the point that we can find an acceptable solution in POPC ( $\chi^2 < 12$ ). The minimization of the error function is an expected result, since the use of two peptide tilts and two peptide rotations creates extra degrees of freedom, in a way similar to considering Gaussian distributions. For Bax $\alpha$ 5/DMPC,  $\chi^2$  is slightly above the experimental error, which supports the best fit found. Taking into account that Bax $\alpha$ 5 dimerizes both in DMPC and in POPC (see SUB. 8.4) the structural model obtained by the rigid body modeling approach is the most appropriate. Therefore, Bax $\alpha$ 5 can be modeled as an asymmetric dimer with  $\{\beta, \omega\}$  pairs of  $\{74^\circ, 157^\circ\}$  and  $\{60^\circ, 20^\circ\}$  for each monomer. Similarly, the best fit for the case of Bax $\alpha$ 5/DMPC is also an asymmetric dimer with distinct pairs,  $\{59^\circ, 157^\circ\}$  and  $\{51^\circ, 10^\circ\}$  for each subunit.

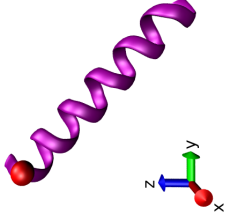
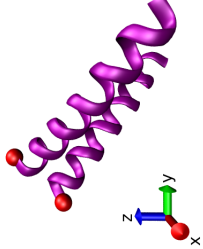
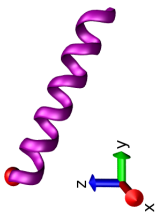
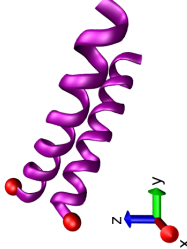
### 9.3 Effect of the peptide on the membrane phase properties

Apart from the structure and orientation of Bax $\alpha$ 5 in the lipid environment, the influence of the peptide in the bilayer structure is also of interest. This is particularly important to understand functions like pore formation, for which the lipids arguably play starring roles [550]. We addressed this issue by investigating the capacity of the peptide to affect the phase properties of the bilayer, through a combination of ATR-FTIR and X-ray reflectivity experiments. At the low hydration conditions used for the IR experiments the main phase transition is expected to occur at considerably higher temperatures than under excess of water. Thus DMPC, with a normal  $T_m$  of 23°C at excess hydration, is expected to be in the  $L_\beta$  gel phase under our sample conditions. On the other hand,

**Tab. 9.8 : Bax $\alpha$ 5 helix geometry in the *explicit* model used for rigid body refinement.** The model corresponds to a canonical  $\alpha$ -helix with the sequence of Bax $\alpha$ 5 modeled using the Swiss-PDB package with  $\phi=-60^\circ$  and  $\psi=-45^\circ$ . The angles  $\alpha$  and  $\theta$  have been defined in SUB. 5.2.2 on page 73.  $\Delta$  is the angle between two consecutive residues around the helix and can be calculated considering either radial vectors going from the helix axis to the  $C_\alpha$ ,  $\Delta_{C_\alpha}$ , as it is usually done for helical wheel projections, or vectors corresponding to the amide I TDM,  $\Delta_{TDM}$ , as it is defined from the geometry of an ATR-FTIR set-up (FIG. 5.7 on page 73). For comparison, we give the values corresponding to the *implicit* model, where  $\alpha=39^\circ$  and  $\Delta_{TDM}=100^\circ$  for all residues. The angle  $\theta$  depends on the residue and the orientation of the peptide. As an example, we give here the values corresponding to the best fit orientation for Bax $\alpha$ 5/DMPC and Bax $\alpha$ 5/POPC systems (TAB. 9.10).

Residue	$\alpha$ ( $^\circ$ )	$\Delta_{C_\alpha}$ ( $^\circ$ )	$\Delta_{TDM}$ ( $^\circ$ )	$\theta_i^{DMPC}$ ( $^\circ$ )	$\theta_i^{POPC}$ ( $^\circ$ )
1	33.8	-	-	5.0	60.8
2	33.6	99.0	99.5	45.9	69.4
3	36.4	98.0	117.5	63.5	68.1
4	36.5	100.7	99.6	33.7	61.6
5	33.7	100.8	81.7	18.3	78.3
6	33.6	98.0	99.6	58.5	56.6
7	36.5	98.9	117.4	56.4	88.9
8	36.5	101.4	99.6	14.3	56.5
9	33.6	99.6	81.7	37.3	79.8
10	36.4	97.8	117.4	64.0	60.2
11	36.5	100.1	99.6	42.6	70.0
12	33.8	101.2	81.6	8.3	68.1
13	33.6	98.5	99.5	52.8	61.5
14	36.5	98.3	117.5	61.1	77.7
15	36.5	101.0	99.6	24.4	56.9
16	33.7	100.3	81.6	27.9	88.9
17	33.7	97.9	99.6	62.2	56.1
18	36.5	99.3	117.5	50.4	80.3
19	36.4	101.4	99.5	5.4	60.4
20	33.6	99.2	81.7	45.4	69.9
21	36.4	97.9	117.5	63.6	67.6
22	36.5	100.5	99.6	40.1	69.0
Average $\pm$ SD	35.2 $\pm$ 1.4	99.5 $\pm$ 1.3	100 $\pm$ 13	40 $\pm$ 21	69 $\pm$ 11

**Tab. 9.10 : Results from the rigid body modeling.** Best fit tilt and azimuthal rotation of the explicit  $\alpha$ -helix model using the  $\chi^2$  error function as guide. Bax $\alpha$ 5 is shown as a ribbon representation and the red sphere shows the position of the tryptophan residue, which defines  $\omega$ . The z axis is parallel to the membrane normal.

Monomer				Dimer <sup>a</sup>						
Lipid	Error ( $\chi^2$ )	$\beta$ ( $^\circ$ )	$\omega$ ( $^\circ$ )	Model	Error ( $\chi^2$ )	$\beta_A$ ( $^\circ$ )	$\beta_B$ ( $^\circ$ )	$\omega^A$ ( $^\circ$ )	$\omega^B$ ( $^\circ$ )	Model
<i>DMPC</i>	81	46	311		12.4	59	51	157	10	
<i>POPC</i>	29	65	266		7.8	74	60	157	20	

<sup>a</sup>  $\beta$  and  $\omega$  angles are given for each helix comprising the dimer here named A and B

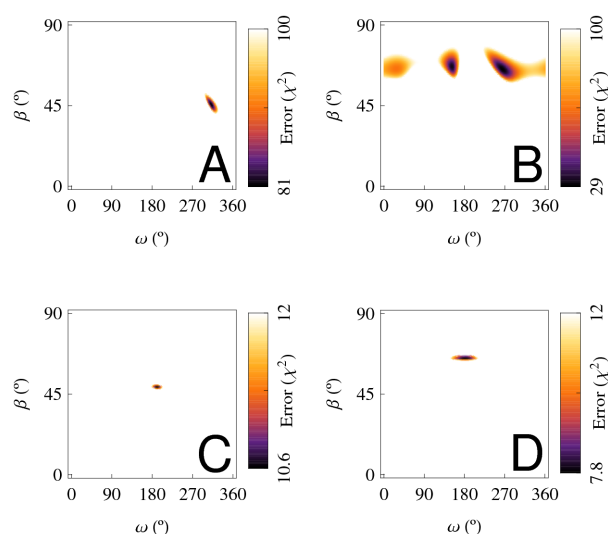


**Fig. 9.7 : Rigid body modeling of the orientation of Bax $\alpha$ 5.** A) Monomer peptide in DMPC, B) Monomer peptide in POPC. C) Bax $\alpha$ 5 dimer modeled after the structure of glycoprotein A in DMPC, D) Same Bax $\alpha$ 5 dimer structure as in C, in POPC membranes. Each point in the graphs represents a particular combination of tilt and rotation angles for a canonical  $\alpha$ -helix. The color scale shows the difference between the modeled structure and the system measured by SSID expressed as the values of the  $\chi^2$  error function.

POPC and DOPC have a much lower characteristic  $T_m$  ( $-3$  and  $-21^\circ\text{C}$ , respectively) and the liquid crystalline  $L_\alpha$  phase should be easier to achieve in these cases.

### 9.3.1 Insights from ATR-FTIR

In IR experiments the phase of the membrane can be assessed by measuring both the symmetric and antisymmetric  $\text{CH}_2$  lipid stretching modes, since the energy of this vibration is known to increase from the gel to the liquid crystalline phase [400]. In DMPC samples the symmetric and antisymmetric modes are found near  $2850$  and  $2918\text{ cm}^{-1}$ , respectively, and do not change with the presence of Bax $\alpha$ 5 (FIG. 9.8). These values can be interpreted as corresponding to gel phase DMPC membranes, both in absence and presence of Bax $\alpha$ 5. However, in the case of POPC bilayers, lipid-only membranes appear to be in the gel phase but the addition of increasing amounts of Bax $\alpha$ 5 is accompanied by a systematic increase in the frequency of both lipid vibration modes, suggesting a transition from gel to liquid crystal phase. Finally, in DOPC the vibration frequency is kept constant at  $2924\text{ cm}^{-1}$ , independently of the presence of peptide addition, indicating a fluid state. Thus, DMPC and DOPC can be used as a reference for gel phase and liquid crystal phase, respectively, while POPC would be a system where phase transition and phase coexistence possibly occur in the presence of Bax $\alpha$ 5 and under our experimental conditions.

In addition, the phase state of the membrane can also be followed from the tilt angle

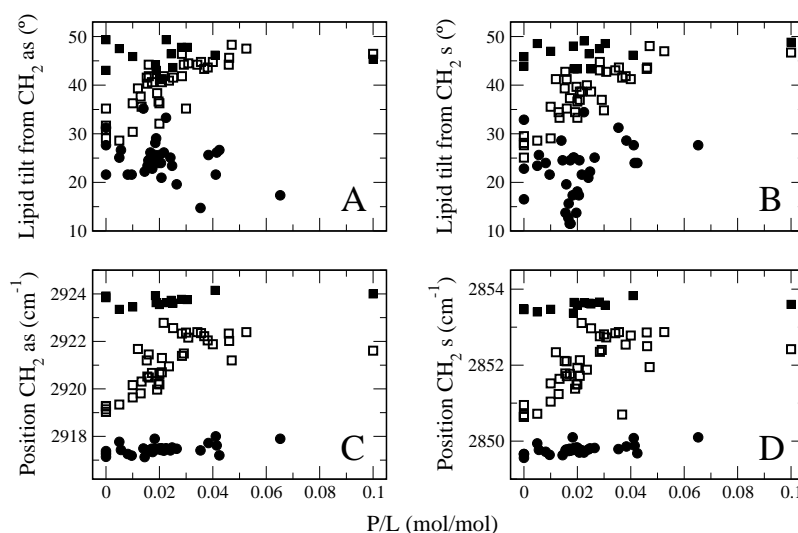


**Fig. 9.8** : Effect of Bax $\alpha$ 5 on the lipid order as determined from ATR-FTIR spectra. The lipid tilts derived from dichroic ratios of the lipid CH<sub>2</sub> asymmetric and symmetric stretchings are represented vs *P/L* molar ratios in graphs A and B, respectively. C and D show the frequencies of lipid CH<sub>2</sub> asymmetric and symmetric stretching, respectively, as a function of *P/L*. DMPC (filled circles), POPC (open squares) and DOPC (filled squares).

of the molecular axis of lipids, which can be calculated from the dichroic ratios of either the CH<sub>2</sub> symmetric or asymmetric stretching [396]. In the absence of peptide, both DMPC and POPC show a tilt of 30° (FIG. 9.8). The tilt of DMPC lipids decreases slightly after addition of Bax $\alpha$ 5, while that of POPC increases in the presence of Bax $\alpha$ 5, up to ~50°. The latter high tilt values were in turn found for DOPC and DOPC/Bax $\alpha$ 5 complexes. We must emphasize that these tilts are upper limit values, but are enough for comparative purposes.

In conclusion, Bax $\alpha$ 5 appears to have a small ordering effect on DMPC membranes, a clear disordering or fluidizing effects on POPC membranes and almost no effect on the already fluid DOPC membranes. For all these effects, there is consistency between the behaviors of vibrational frequencies and lipid tilts.

### 9.3.2 Insights from X-ray scattering

X-ray scattering (XS) can be the source of a detailed structural characterization of multilamellar lipid samples by means of electron density profiles along the *z* axis [429]. From these profiles one can calculate *peak-to-peak*, *PtP*, distances, which refer to the two maxima of the profile and are often assumed to correspond to distances between the averaged position of the phosphate groups across the bilayer [431, 551]. *PtP* distances are more reliable than lamellar repeat distances, *d*, extracted from the position of the Bragg peaks, since the latter depend strongly on hydration levels. Because gel and liquid crystalline phases exhibit clearly different thicknesses, the *PtP* values derived from X-ray

measurements, performed on the same samples used for the ATR-FTIR studies, should help to characterize unambiguously the phases present in such samples.

For the DMPC and DOPC samples only one set of Bragg peaks was observed, even in the presence of Bax $\alpha$ 5 (FIG. 9.9). However, in POPC we observed one set of Bragg peaks in pure lipid samples but two sets of peaks in samples containing Bax $\alpha$ 5 above a certain threshold concentration (FIG. 9.9). For comparison, we used a lipid mixture consisting on DOPC:SM:Cho, which is known to separate into Cho-rich liquid ordered and Cho-poor liquid disordered phases. Such phases of different thickness can be clearly seen as two Bragg peaks in the X-ray scattering curve (FIG. 9.9). Indeed, only in DOPC:SM:Chol and POPC membranes, we were able to detect two Bragg peaks. However, in the first case such peaks were present independently of Bax $\alpha$ 5, i.e., they are an intrinsic property of these membranes. On the other hand, in POPC bilayers the two peaks were induced by a certain Bax $\alpha$ 5 concentration. These results suggest that in the POPC/Bax $\alpha$ 5 complexes there is coexistence of two lipid phases of different thickness which most likely correspond to gel and liquid crystal phases. Because such a phase coexistence occurs as a consequence of the presence of the peptide, we may interpret this as a preference of the peptide for any of the two lipid phases (which would then be peptide-rich and lipid-rich phases). Alternatively, there may be a preference of the peptide for the phase boundary of lipids. The preference for defect-rich phase boundaries has indeed been proposed for Bax $\alpha$ 5 and equinatoxin [179, 197].

Importantly, for POPC membranes with Bax $\alpha$ 5 at low P/L ratios, the only phase present exhibits a distance  $d$  which tends to be smaller than in the absence of peptide. When  $P/L$  reaches the threshold level of 1/50, two phases of different thickness start to distinguish. The first set of Bragg peaks (named *phase-1* in TAB. 9.11) corresponds to a slightly higher  $d$  than for POPC alone, while the second set (*phase-2* in TAB. 9.11) corresponds to a smaller  $d$ . Additionally, the presence of Bax $\alpha$ 5 is accompanied by a reduction in the number of resolved Bragg peaks, which indicates an increase of membrane fluidity.

The different lipid phases can be further characterized through measurements of PtP distances. Some of the calculated electron density profiles from which PtP distances were derived are shown in FIG. 9.10, and the PtP values are listed in (TAB. 9.11). The PtP distances determined here for DMPC, in absence and presence Bax $\alpha$ 5, and for POPC alone, are similar to those reported in the literature for a gel phase of the same lipids [552, 553]. The electron density profiles were calculated only for cases showing at least four Bragg peaks. When the data were of enough quality, a value of 3.8 nm was obtained, consistent with a POPC bilayer in the liquid crystalline phase [554].

Taken together, both IR and XS data indicate that incorporation of Bax $\alpha$ 5 into POPC membrane gives rise to two types of domain: thicker domains composed of POPC in the gel phase, and thinner domains composed of POPC in the liquid crystalline phase. Although the location of the peptide with respect to these two phases is unknown, it is reasonable to assume that Bax $\alpha$ 5 locates preferentially in the fluid phase or at the boundaries between the two phases [555]. In contrast, DMPC and DOPC multilayers are always in the gel and liquid crystal phase, respectively, regardless of the presence of Bax $\alpha$ 5. At this point, it is interesting to remind that the orientation of the peptide is

### 9.3 Effect of the peptide on the membrane phase properties

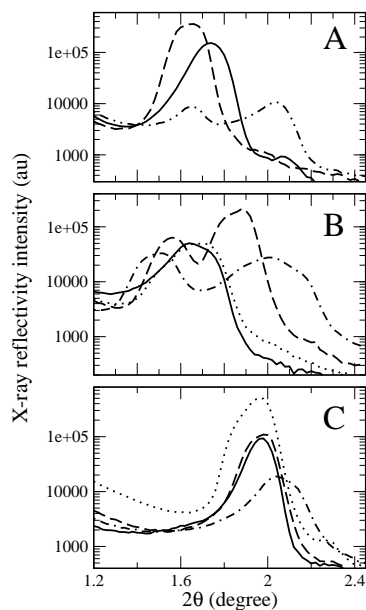


**Fig. 9.9 : Effect of Bax $\alpha$ 5 on the bilayer thickness determined from XS data.** X-ray reflectivity curves as a function of  $2\theta$  for DMPC (A), POPC(B) and DOPC (C). Bare lipids are represented with a solid line, membranes in presence of Bax $\alpha$ 5 at  $P/L=1/100$  correspond to the dotted line, the dashed line is for  $P/L=1/50$  and the dashed-dotted line corresponds to  $P/L=1/10$ . In A we show also the results of bare DOPC:SM:Chol membranes (dashed-dotted-dotted line).

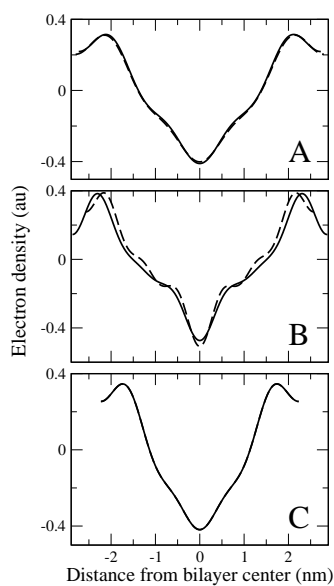


**Fig. 9.10 : Electron density profiles of oriented lipid multilayers in presence of Bax $\alpha$ 5.** A) DMPC, B) POPC and C) DOPC. For data of membranes with only lipids a solid line is used, and complexes of Bax $\alpha$ 5 with lipids at  $P/L=1/50$  correspond to the dotted line. Distances between the peak maxima in these plots are used to calculate the PtP values shown in TAB. 9.11.

**Tab. 9.11 : Structural characterization of multilamellar membrane stacks by XS.** Lamellar repeat distances (*d-spacing*) and PtP distances derived from the specular reflectivity curves. ND means that the reflectivity curve did not contain enough peaks for an accurate measurement of PtP. Typical SD were  $\pm 0.2$  nm.

Sample		$d_{phase1}$ (nm)	$d_{phase2}$ (nm)	$PtP_{phase1}$ (nm)	$PtP_{phase2}$ (nm)
DMPC	<i>Lipid only</i>	5.3	-	4.2	-
	<i>Bax<math>\alpha</math>5 1/50</i>	5.4	-	4.3	-
POPC	<i>Lipid only</i>	5.5	-	4.6	-
	<i>Bax<math>\alpha</math>5 1/200</i>	5.3	-	ND	-
	<i>Bax<math>\alpha</math>5 1/100</i>	5.2	-	4.2	-
	<i>Bax<math>\alpha</math>5 1/75</i>	5.0	-	4.0	-
	<i>Bax<math>\alpha</math>5 1/50</i>	5.7	4.7	4.7	3.8
	<i>Bax<math>\alpha</math>5 1/25</i>	6.1	4.9	ND	3.9
DOPC	<i>Bax<math>\alpha</math>5 1/10</i>	5.8	4.4	ND	ND
	<i>Lipid only</i>	4.5	-	3.7	-
	<i>Bax<math>\alpha</math>5 1/200</i>	4.6	-	3.7	-
	<i>Bax<math>\alpha</math>5 1/100</i>	4.5	-	3.6	-
	<i>Bax<math>\alpha</math>5 1/50</i>	4.4	-	3.6	-
DOPC:SM:CHOL	<i>Bax<math>\alpha</math>5 1/10</i>	4.3	-	ND	-
	<i>Lipid only</i>	5.4	4.3	ND	3.2

different in these lipid systems. Thus, in the DMPC membranes Bax $\alpha$ 5 is on average more *inclined* and inserted than in POPC and DOPC membranes where it tends to be *flat* in the membrane plane and likely bound at the membrane-water interface<sup>1</sup>. Additionally, these results are in agreement with recent DSC investigations performed in our group (D. GIMÉNEZ, unpublished results), which show that Bax $\alpha$ 5 facilitates the gel-to-liquid crystal phase transition by reducing the associated change of enthalpy.

## 9.4 Orientation and pore-forming activity

One interesting question is why does Bax $\alpha$ 5 orient differently in DMPC than in POPC or DOPC membranes? The tilts of hydrophobic peptides in membranes are generally dependent on the hydrophobic thickness of the lipid bilayer, according to the mattress model and the concept known as *hydrophobic matching* [56, 556, 557]. This simple model proposes that peptides tilt to an angle such that there is maximum overlap between their hydrophobic length and the hydrophobic thickness of the bilayer. For instance, such model predicts that for a given hydrophobic length of the peptide, the larger the hydrophobic thickness of the membrane (considering the acyl chain region) the smaller the peptide tilt. Some elaborated extensions of these ideas have recently been employed to search within configurational energy landscapes for the relative position in the bilayer and the expected orientation of membrane proteins [558–561]. However for an accurate orientational description one needs to take into account not only tilt angles and penetration depth but also rotational angles [562]. This view, which puts rotational angles into play as important factors in determining peptide orientation especially for amphipathic interface-bound peptides, complements the concept of hydrophobic mismatch with what may be named *interfacial tuning* (S. ESTEBAN-MARTÍN, unpublished results).

The lipid compositions used in this study differ at least in two properties: fluidity and acyl chain length. As we have just shown, DMPC is in the gel phase under our experimental conditions, while POPC is at least partially fluid in the presence of the peptide. In addition, DMPC lipids are shorter than POPC lipids. We have shown that in the gel phase and short chain combination (DMPC) Bax $\alpha$ 5 is less tilted (and the rotation angle is different) than in the fluid phase and long chain combination. As can be seen from FIG. 9.11 B, the general tendency is that the smaller tilts are observed for longer lamellar repeat distances in agreement with the hydrophobic matching concept. In FIG. 9.11 C and D, Bax $\alpha$ 5 tilt is plotted against lipid fluidity. The latter parameter can be estimated, as discussed in SEC. 9.3.1, by the vibration frequency of both  $CH_2$  symmetric and asymmetric stretching modes. We find also a correlation between peptide tilt and lipid fluidity since larger peptide tilts are found for more fluid membranes. This result is unexpected since a larger fluidity should facilitate peptide insertion while a gel-like membrane tend to expel the peptide. A possible explanation could be the presence

<sup>1</sup> Notice that none of the structural measurements performed here gives a direct measure of the depth of peptide insertion in the membrane. Thus, the insertion position is deduced as the most likely one, considering the measured orientation, the properties (amphipathicity) of the peptide and the general structure of the lipid bilayer.

of defects in gel phase through which the peptide could squeeze. Finally, peptide tilts and lipid tilts also show a positive correlation (FIG. 9.11 E and F) suggesting that there is a some mechanism of mutual adaptation between both. These results show clearly that Bax $\alpha$ 5 tilt depends on physical properties of the lipid bilayer, such as membrane thickness, lipid fluidity and lipid tilt, which the peptide in turn is able to influence.

However, the peptide orientation does not depend exclusively on the lipid background. For a given lipid composition a number of antimicrobial peptides have been reported to change their tilt from *large* to *small* values upon surpassing a threshold concentration [536, 563–565]. The large tilt (near 90°) corresponds to a surface bound state, often named *S*, which is a favorable expected state for amphipathic  $\alpha$ -helices. On the other hand, the small tilt means an state that approaches alignment with the membrane normal, termed *I* state, which most often involves the assumption of deep (transmembrane) peptide insertion across the membrane. It is also most generally considered that this change of tilt occurs as a transition between two states [141]. This framework has implications for the mechanism of action of the peptides, since the *S*-state found at low P/L is taken to be *inactive* for membrane leakage while the *I*-state found at high P/L is assumed to be associated with an *active* pore [564, 566]. The tilt angles of Bax $\alpha$ 5 (determined via the use of the order parameter) for P/L in the range 1/200 to 1/10 are represented in FIG. 9.11 A. There is essentially no change of  $\beta$  with P/L, for any of the three lipid compositions studied. This is in contrast with studies of a different variant of Bax $\alpha$ 5 that encompasses from residue 102 to 135, i.e., slightly longer than the version used here, measured by OCD, which reported an orientation essentially *parallel* to the plane of the membranes at P/L=1/100, but with  $\sim$ 30% of the helical components oriented *perpendicular* to the plane of the bilayer at P/L=1/30 [183]. However, the terms *parallel* and *perpendicular* used in the referred work should be taken as approximate qualitative definitions, since a accurate measurement of the orientation angle cannot be easily extracted from the OCD method. Moreover, the P/L dependent changes of OCD spectra may as well be interpreted using alternative combinations of peptide orientations, apart from the two extreme cases normal to each other. Nevertheless, variations in both the lipid and the peptide version used for each study may also explain different orientations. Additionally, the longer Bax $\alpha$ 5 peptide was also measured by ATR-FTIR and it was concluded that there were two distinct helices with tilts of  $\sim$ 0° and  $\sim$ 90° in egg PC (which is composed mainly of POPC) for the so-called regular  $\alpha$ -helix  $\alpha$ 1 and distorted  $\alpha$ -helix  $\alpha$ 2 [50]. This results suggest that our tilt of 90° for the shorter Bax $\alpha$ 5 may correspond to the helix  $\alpha$ 2.

Amphipathic pore-forming peptides like magainin bind to the bilayer interface and decrease the bilayer thickness up to a threshold P/L\* which corresponds to the appearance of pores [319]. If the concentration is above the P/L\* membrane thickness keeps constant. This effect appears to be an essential step of their mechanism of action, leading to bilayer distortion and membrane poration through an increase in the surface tension. A similar mechanism can be envisioned for the Bax $\alpha$ 5 fragment. Membrane thickness, estimated as the PtP distance, as a function of Bax $\alpha$ 5 concentration was measured in POPC and DOPC membranes. Bax $\alpha$ 5 seems to reduce the membrane thickness in both lipid compositions used. As discussed previously, in POPC multilayers, such a decrease

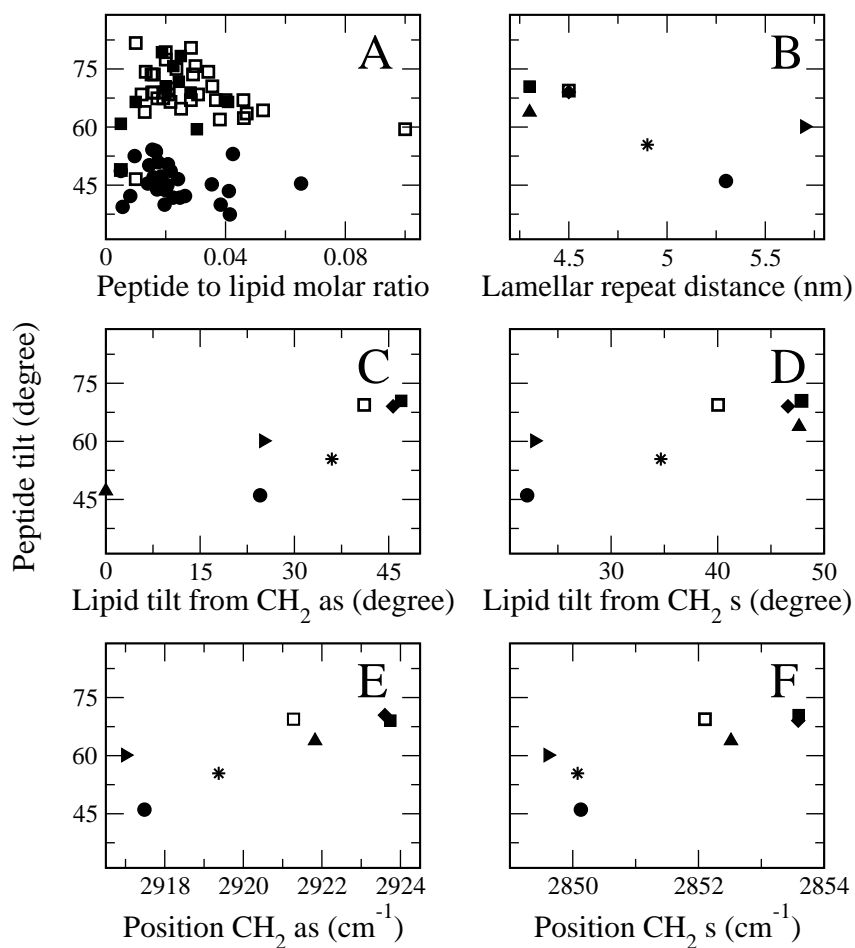


**Fig. 9.11 : Dependence of Bax $\alpha$ 5 tilt angle on several parameters.** A) Peptide tilt vs P/L molar ratio, B) Peptide tilt vs lamellar repeat distance (d), C) Peptide tilt vs lipid tilt derived from CH<sub>2</sub> antisymmetric stretching. D) Peptide tilt vs lipid tilt derived from CH<sub>2</sub> symmetric stretching, E) Peptide tilt vs CH<sub>2</sub> antisymmetric stretching frequency, and F) Peptide tilts vs CH<sub>2</sub> symmetric stretching. DMPC (circles), POPC (open squares), DOPC (closed squares), DOPC:CL (diamonds), DOPC:SM:CHOL (triangles up), DPPC (triangles right) and DLPC (stars). Peptide tilts were calculated using order parameters (see TAB. 9.4). In graphs B-F, P/L ratios were 1/50. All measurements were done at room temperature.

in hydrophobic thickness is most likely due to a phase transition from gel to liquid crystalline, and not to the appearance of pores. On the contrary, in fluid phase DOPC, a small reduction of 0.1 nm is found (TAB. 9.11) which is similar in magnitude to other peptide-lipid systems [567, 568]. However, this value is within the experimental error, meaning that the difference in thickness between pure bilayers and membranes with embedded Bax $\alpha$ 5 is not significant.

## 9.5 Conclusions

1. An accurate description of the orientation of peptides in membranes can be provided by two complementary methods: the implicit landscape analysis, which uses theoretical equations with an implicit structure, and the rigid body modeling, that uses an explicit structural model. In both cases the search for minimum is best achieved via a  $\chi^2$  error function. The implicit landscape method is especially useful when the order of the sample should be taken into account. The rigid body modeling is most suited when dealing with oligomeric peptide assemblies or structures that deviate from monomeric ideal helices. For the particular case studied here, Bax $\alpha$ 5 in DMPC and POPC membranes, rigid body modeling provided a better structural description of both systems.
2. In DMPC membranes, the structure and orientation of Bax $\alpha$ 5 can be best modeled as a dimer with  $\{\beta, \omega\}$  pairs of  $\{59^\circ, 157^\circ\}$  and  $\{51^\circ, 10^\circ\}$  for each subunit. In POPC membranes Bax $\alpha$ 5 can be modeled also as a dimer with  $\{\beta, \omega\}$  pairs of  $\{74^\circ, 157^\circ\}$  and  $\{60^\circ, 20^\circ\}$  for each monomer.
3. The orientation displayed by Bax $\alpha$ 5 depends on lipid properties, such as lipid fluidity (direct correlation), lipid tilt (direct correlation) and hydrophobic thickness (inverse correlation).
4. In turn, Bax $\alpha$ 5 seems to affect the properties of the surrounding lipid matrix. Under our experimental conditions Bax $\alpha$ 5 has a “fluidizing” effect, facilitating the gel to liquid crystalline phase transition in POPC membranes, but not in DMPC or DOPC. The fluidizing effect of Bax $\alpha$ 5 may be related with a stabilization of phase boundaries which would facilitate the formation of pores.

# 10 Pore formation by Bax $\alpha$ 5

## 10.1 Introduction

**Vesicle leakage experiments for the study of pore formation mechanisms.** Experiments of vesicle leakage induced by peptides are a standard assay for the investigation of peptide/membrane interactions which provide a direct measure of their potential toxicity. Since membranes are impermeable to most solutes, leakage may be investigated with appropriate reporter molecules placed inside, or outside, of vesicles, which will diffuse down their concentration gradient if the membrane is significantly perturbed. For these studies one can use either natural membranes (e.g. red blood cells, as it is done in hemolysis experiments) or, more commonly, synthetic lipid vesicles.

In experiments with suspensions of vesicles (SUB. 5.5.1), membrane permeabilization can be monitored by recording the efflux of an initially entrapped dye using fluorescence spectroscopy. Self-quenching fluorophores, like carboxyfluorescein or calcein, which tend to form non-fluorescent dimers [476], or fluorophore/quencher pairs, such as ANTS/DPX [479], are most often used. These dyes are entrapped in large unilamellar vesicles (LUVs). For single vesicle experiments the liposomes must be of the giant type (GUVs). Pore formation in single GUVs is monitored by measuring the changes in the fluorescence intensity of appropriate dyes when they are let to either leak-into the vesicle from the outside solution [179] or leak-out from the vesicle interior [569]. In any of these cases the recorded kinetics results from multiple overlapping equilibration processes, like peptide diffusion, binding to the membrane, structural reorganization of the complex, pore formation and finally the release of the probe. Then, understanding pore formation and describing the pore formation mechanism consists on disentangling the different steps through detailed kinetic and thermodynamic studies. For example, it has been argued that the structural rearrangement leading to the appearance of pores is the slowest of the chain of processes involved and dominates the observed kinetics [62, 65, 85, 86]. However, an alternative view has proposed that the rate-limiting step of peptide induced leakage relates to the discrete nature of vesicle suspensions, and fluctuations over time in the number of peptide molecules bound to each vesicle [570]. These, like many of the principal aspects of the pore formation mechanism by membrane active peptides and proteins, continue being a matter of debate and intense investigation, despite many years of work. Although the action modes may in some cases be diverse, due to diversity of the peptide/membrane systems, a *framework agreement* for the different mechanisms should also be expected. Yet, what is most often found is a proliferation of *models* [83, 191, 500, 564] which are not always justified sufficiently with data. We have noticed that one of the problems arises from differences in the type of experiments used as the basis to propose a mechanism. Namely, typical kinetic studies allow the investigation of

pore formation events in systems far from equilibrium, at short times after arrangement of the peptide/membrane complex. On the other hand, structural studies measure well equilibrated systems.

**Kinetic vs structural models.** The pore formation mechanisms that can be described from common vesicle leakage experiments are closely connected to the equilibration of the peptide/vesicle complexes [87]. A plethora of studies over the years have given rise to a number of activity-based or kinetic models [65, 109, 191, 570, 571], where a peculiar feature of the observed leakage processes is their apparent transient nature. In experiments made with LUV suspensions, after an initial burst of release of contents, there is generally a drastic slowing down of efflux which often leaves the depletion of the total marker pool incomplete. As a consequence, these *short-time pores* are naturally viewed as *transient* structures, linked to the relaxation of the membrane after a peptide attack [62, 83, 87, 116, 572]. However, for most cases studied pores are sufficiently long-lived to allow for complete release of vesicle entrapped dyes, and are thus said to follow an *all-or-none* release mechanism [62, 65, 84, 85, 116, 496]. Beyond the point of dye release the pore activity is not registered, but the vesicle is often assumed to relax finally into a non porated state [62, 65, 85].

Even though natural peptide-induced pores in cells seem to occur as kinetic processes [573, 574], *long-term* and/or *equilibrium* pores<sup>1</sup> may also be physiologically relevant [575]. Moreover, such equilibrium structures can be important in case of pores made by proteins, like Bcl-2 family members and bacterial toxins [110], which although related to peptide-induced pores, are more complex and highly regulated phenomena and might function as stable assemblies. In addition, from practical reasons it is convenient to investigate pores at equilibrium, since molecular models cannot be easily deduced only from the kinetic studies [65, 86, 114, 576]. Structural investigations of peptide-membrane systems have been performed on supported multibilayer stacks made by equilibrated peptide/lipid mixtures. Oriented circular dichroism [536] and NMR [565] allow observing a change in the orientation of peptide helices from a flat, *S*, to a tilted/inserted, *I*, alignment, passed a threshold peptide/lipid molar ratio,  $P/L^*$  ([88, 141]). This has been used to propose a structure-based mechanism where pore formation is linked to the change of orientation of the peptide and the *I* state is assigned to be the pore state. However, little has been done so far to relate kinetic and structure-based (or equilibrium) models [319, 577]. Here we will tackle this task through an extensive study of the pore formation mechanism at short times and long times after peptide-vesicle mixing and in

---

<sup>1</sup> Throughout this work, we use the term *long-term* pores to refer to pores detected a minimum of 1.5 h after mixing the peptide with vesicles, as opposed to pores formed at *short term* (minutes) after mixing the peptide with vesicles. The short-term (first-instance) case corresponds to typical leakage studies, both with LUVs and GUVs, while in this work we devised specific methods to investigate leakage at long-term (for LUVs and GUVs). On the other hand *equilibrium* pores are structures formed in systems reconstituted from homogeneous peptide/lipid mixtures. Although without clear definition and knowledge of the equilibration process(es) and corresponding equilibration time(s), under the different conditions used, we cannot strictly distinguish long-term and equilibrium pores, our work indicates that initial pores relax relatively fast (within minutes). Thus, for simplicity, we will treat in most cases long-term and equilibrium pores as equivalent.

reconstituted systems, by using classical (LUV suspensions) and advanced (single GUVs) experiments.

**Objectives.** In this chapter we will carry out an ample investigation of the pore formation mechanism by Bax $\alpha$ 5 which includes short-time, long-time and true equilibrium regimes. For that, we will use common (dye release) and specially tailored methods, and will study peptide-induced pore formation in both ensembles of vesicles (of the LUV type, using fluorescence spectroscopy) and single vesicles (of the GUV type, using confocal fluorescence microscopy). The kinetic traces will be analyzed in detail using theoretical models, from which we will describe and compare the types of pore found for each case. Finally, we will propose a global model accounting for pore formation in vesicles by Bax $\alpha$ 5.

## 10.2 Experiments in ensembles of LUVs<sup>1</sup>

### 10.2.1 Bax $\alpha$ 5-dependent dye efflux in LUVs

**Peptide-membrane binding and vesicle leakage.** Vesicle leakage was measured as a function of the concentration of Bax $\alpha$ 5 on synthetic vesicles of two compositions: POPC and POPC:CL (80:20). The use of CL in the vesicle membranes was motivated by the reported functional significance of this lipid for the activity of Bax [300, 309, 379]. We have observed previously that CL reduces the leakage induced by Bax fragments in LUVs [50]. This occurs also in presence of other negatively charged lipids, and was interpreted as due to a strong electrostatic interaction which would keep the peptide adsorbed to the membrane interface in a non-productive state [50].

At constant lipid concentration, the extent of calcein leakage increases with the bulk peptide concentration (see FIG. 10.1 A,C for POPC and B,D for POPC:CL). The point of saturation of the release of the probe is taken at the plateau of the fluorescence signal, observed usually within 10 min after peptide addition (FIG. 10.1 A, B). This is given as a percentage value, indicated as  $R\%$  and calculated according to Eq. 5.62. *Dose/response* graphs, where the release of the probe is plotted *vs* the amount of Bax $\alpha$ 5 causing such an effect are represented in FIG. 10.1 C,D. In the figures, the  $P/L$  ratios correspond to the total amounts of lipids and Bax $\alpha$ 5 initially added to the cuvette (*bulk*  $P/L$ , filled symbols) or just the membrane-bound peptide (open symbols), according to the water to membrane partition coefficient (see SEC. 7.3). These graphs have a shape typical of a saturation process, since the membrane acts as a finite binding platform for the active peptide. Thus, the dose/response behavior can be modeled with a function of the type:

$$R\% = \frac{(P/L)^h}{(P/L_{50})^h + (P/L)^h} * 100 \quad (10.1)$$

<sup>1</sup> The preparation of LUVs is described in detail in SUB. 6.1.1. The synthesis and purification of the peptide has been explained in SUB. 6.1.2. The method for measuring and analyzing the kinetics of dye release is described in SUB. 5.5.1. Quenching of NBD by dithionite is explained in SEC. 5.5.2. Detailed protocols are described in SUB. 6.5.1 and 6.5.2.

where  $P/L_{50}$  is the value of  $P/L$  giving 50% leakage and  $h$  is a phenomenological coefficient related to the cooperativity of the system<sup>1</sup>. From fits of this curve to experimental data (FIG. 10.1 C,D), and considering membrane-bound peptide, we obtain  $P/L_{50}=1/14500$  for POPC and  $P/L_{50}=1/800$  for POPC:CL. These values allow to estimate the approximate number of peptide molecules, bound directly to each LUV membrane and needed to porate individual LUVs. Each LUV with diameter of  $\sim 100$  nm, as it is the case here, can be estimated to be made of  $\sim 10^5$  lipids<sup>2</sup>. Thus, for POPC vesicles the porated state is achieved with an average of  $\sim 7$  Bax $\alpha$ 5 molecules bound per LUV. However, each POPC:CL vesicle needs to bind  $\sim 125$  Bax $\alpha$ 5 molecules to become porated. It has been shown that most antimicrobial peptides are active against vesicles at about 100-2000 peptides per vesicles [62]. The “best” pore-forming peptides found so far can permeabilize vesicles with as few as 4-10 peptides bound per vesicle [496, 572]. Thus, our results illustrate the potent pore forming activity of Bax $\alpha$ 5 in POPC membranes and also the protecting effect of CL, as already reported for other versions of Bax $\alpha$ 5 [50]. In addition, some important considerations about the mechanism of action of the peptide can be derived. For example, in the case of the peptaibol trichogin GA IV, recent theoretical models based on the stochastic nature of pore formation propose that fluctuations in the number of bound peptides determine the peptide kinetics and are responsible of the rate-limiting step [570]. For this model to apply, the number of peptides bound to each vesicle in the porated state must be small. Therefore, although it might be an adequate model to explain the observed leakage kinetics in POPC LUVs, it does not appear valid for POPC:CL. Finally, the vesicle surface coverage by Bax $\alpha$ 5 is small suggesting that models that rely on high numbers of peptides bounds per lipid, like the carpet model [109, 191], do not explain the leakage in this case.

With respect to  $h$ , its value is related to the minimal number of peptide molecules,  $n$ , involved in the process of leakage and/or configuring the active structure. For peptides acting as monomers  $h=n=1$ . For involvement of  $n$  peptide molecules and in case of *positive cooperativity*  $n > h > 1^3$ . For Bax $\alpha$ 5 in POPC membranes  $h=1.58$ , which is consistent with a dimeric active species, but the value in POPC:CL ( $h=2.14$ ) indicates at least a trimer. These results are in good agreement with results from the FRET analysis (CHAP. 8) and suggest a role for the oligomers in the leakage process.

### 10.2.2 Capturing long-term and equilibrium pores in ensembles of LUVs

As we have seen, standard assays of peptide induced pores are made in vesicle suspensions by recording the release of entrapped dyes only for a few minutes after peptide addition. In order to capture the activity of pores a long time after peptide/vesicle mixing, we first chose an indirect approach based on the quenching of a fluorescent lipid (0.5% NBD-PE), equally distributed in the two monolayers of vesicle membranes, as it is reduced

1 This equation is in fact analogous to the HILL equation, used for the study of cooperativity in protein-ligand interactions, and  $h$  represents the *Hill coefficient*.

2 Assuming an area per lipid of  $0.68 \text{ nm}^2$  [554]

3 Other possible cases are *supercooperativity*, with  $h=n$ , and *negative cooperativity*, for which  $0 < h < 1$ , although neither of the two are common in biological systems.

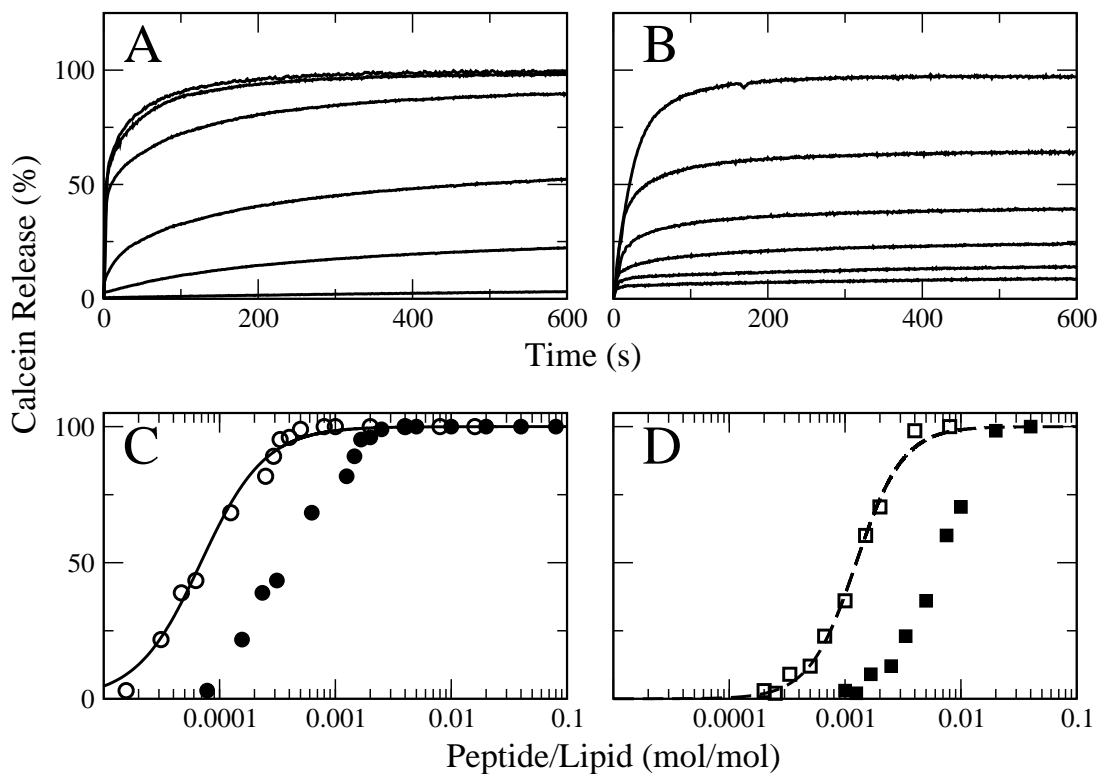


**Fig. 10.1 : Vesicle leakage as a function of peptide-to-lipid molar ratio.** The lipid concentration was constant at  $5 \mu\text{M}$  while the peptide concentration was increased. The graphs on the left show results with LUVs of POPC and the graphs on the right correspond to LUVs of POPC:CL (80:20). Bulk peptide concentrations ranged from 0.58-25 nM in POPC and 12.5-100 nM in POPC:CL. In A and B the percentage of calcein release (EQ. 5.62) is plotted over time for different bulk  $P/L$  ratios (increasing from bottom to top). C and D show the percentage of calcein release at the plateau of the kinetic curves (A and B) (for all cases we took values 10 min after peptide addition), plotted against values of the bulk  $P/L$  (filled symbols) or the  $P/L$  corresponding to vesicle-bound peptide (open symbols). This latter  $P/L$  was calculated considering the water to membrane partition coefficient (SEC. 7.3). The curves fit over the open symbols are from a theoretical dose-response model, expressed as EQ. 10.1.

by sodium dithionite [481]. In the absence of pores or membrane defects, this reactant permeates slowly through phospholipid membranes and quenching affects mainly the external monolayer reaching  $\sim 50\%$  (FIG. 10.2 A,B). But for leaky membranes the inner monolayer becomes also accessible to dithionite, yielding higher levels of quenching.

The assay must be performed and interpreted with care, since apart from pores, membrane defects and lipid flip-flop may also contribute to increase quenching, and such effects can intensify when amphipathic peptides bind to the membrane interface. Another reason for caution is that the quenching kinetics is dominated by the dithionite reaction, which is slower than the rate of vesicle leakage (see FIG. 10.2 C). However, the rate constant for dithionite reduction may be assumed independent on the presence of the peptide, and for a given time after dithionite addition the increase of quenching with respect to the absence of peptide would be proportional to the increased accessibility of NBD-PE.

The increments of normalized NBD-PE quenching, 250 s after dithionite addition ( $\Delta Q_{250}^{\%}$ , Eq. 5.64) in LUVs preincubated with Bax $\alpha$ 5 are presented in FIG. 10.2 D for two  $P/L$  ratios. When Bax $\alpha$ 5 and dithionite were added simultaneously to POPC:CL:NBD-PE 79.5:20:0.5 (FIG. 10.2 D, white bars), there was an increment of quenching ( $\Delta Q_{250}^{\%} > 0$ ) compared to LUVs in the absence of peptide, indicating that NBD-PE from the internal monolayer was accessible to dithionite. The extent of  $\Delta Q_{250}^{\%}$  was comparable, within errors, to the calcein release measured under analogous conditions and at 250 s ( $R_{250}^{\%}$ , see on page 95) and, importantly, the  $P/L$  dependence was very similar for the two types of experiments (FIG. 10.2 D, gray bars). All together these data support that under our conditions the extra accessibility of dithionite to internal monolayer lipids in the presence of Bax $\alpha$ 5 is due to peptide-induced membrane permeability and/or phenomena closely coupled to the presence of pores.

The NBD-PE quenching experiment on vesicles previously incubated with Bax $\alpha$ 5 allowed registering the vesicle permeability at any stage of an evolved peptide/membrane system. The results in FIG. 10.2 D (striped bars) show that the vesicle leaky state was still present at least 24 h after the addition of the peptide. Because the relaxation of initial pores states might be slow, the experiments were repeated using vesicles reconstituted with Bax $\alpha$ 5 (FIG. 10.2 B,D, dotted bars). Again, the values of  $\Delta Q_{250}^{\%}$  suggest that pores exist also in this truly equilibrated system. The quenching levels are similar for long-term incubated and reconstituted Bax $\alpha$ 5/LUVs, and they are larger than the values obtained without preincubation of Bax $\alpha$ 5, but these and other small differences may not be significant, considering the error of the experiments. The dose-response and lipid composition effects of long-term and equilibrium activities are basically maintained as described above, suggesting that they are due to peptide-induced pores. In the next section we demonstrate the existence of such pores in single GUVs by direct visualization of leakage using fluorescence microscopy.

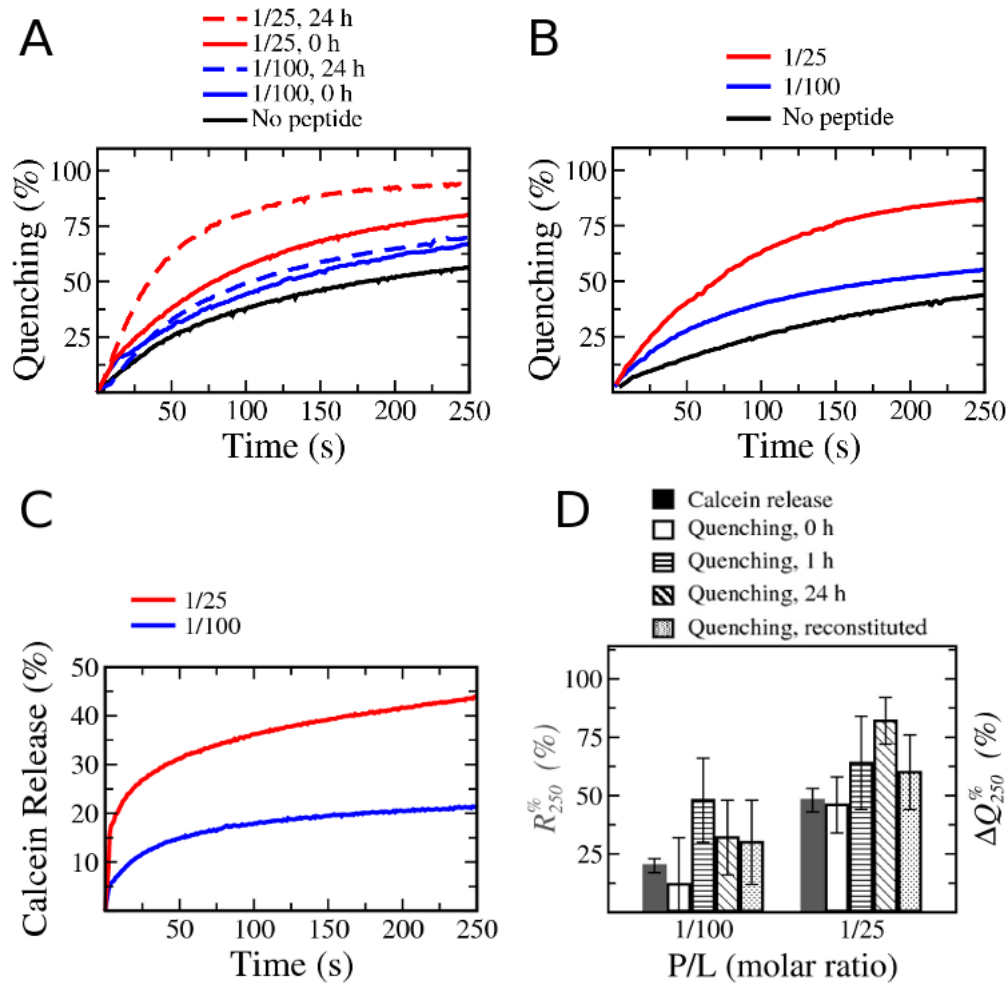


**Fig. 10.2 : Short-term, long-term and equilibrium pore activities in ensembles of LUVs.** A) NBD-PE quenching kinetics in suspensions of symmetrically labeled POPC:CL:NBD-PE (79.5:20:0.5) LUVs, in the absence of Bax $\alpha$ 5 (control, black line) or in the presence of this peptide added at bulk  $P/L$  ratios indicated in the legends. The kinetics were recorded immediately after peptide addition (solid lines) or after 24 hours incubation with the peptide (dashed lines). B) NBD-PE quenching kinetics for POPC:CL:NBD-PE (79.5:20:0.5) LUVs prepared in the presence of Bax $\alpha$ 5 at bulk  $P/L$  ratios indicated in the legends. C) Calcein leakage from POPC:CL (80:20) LUVs. The kinetics of dye efflux were recorded immediately after addition of Bax $\alpha$ 5 at the bulk  $P/L$  values indicated by the legends. The pore activity is expressed as a percentage of calcein release. D) Normalized differences (with-peptide, minus without-peptide) of percentages of quenching of NBD-PE 250 s after addition of dithionite,  $\Delta Q_{250}^{\%}$ . Bax $\alpha$ 5 was either added simultaneously with dithionite (0 h), or preincubated with LUVs for 1 h or 24 h. Alternatively LUVs were prepared in the presence of the peptide (*reconstituted*). Percentages of calcein release from LUVs 250 s after peptide addition,  $R_{250}^{\%}$  (gray), are also shown for comparison. Values are averages of three repetitions  $\pm$ SD.

## 10.3 Single vesicle experiments with GUVs<sup>1</sup>

### 10.3.1 Successive leakage events in single GUVs

The mechanism of pore formation by peptides and proteins can be followed through the direct visualization of the behavior of individual GUVs using fluorescence microscopy [69, 85, 179, 569]. This method, by recording the internalization of fluorescent dyes from the external solution to the inside of selected single GUVs [179], allows monitoring multiple leakage events at specific moments on the same set of lipid vesicles. The time between successive leakage events is limited to the order of minutes by the time required for dye addition and proper mixing, and each GUV is monitored for a maximum of a few hours to avoid problems due to unspecific vesicle rupture. The vesicle integrity is controlled continuously by the fluorescence of the inert lipophilic dye DiD, present in the membrane [578].

In a typical series of experiments (FIG. 10.3) a suspension of GUVs labeled with DiD (red) is added to the observation chamber containing a *first* dye (Alexa555, blue; FIG. 10.3 A) and Bax $\alpha$ 5. Then, vesicle poration begins in a stochastic way, similar to that reported also with single GUVs for the kinetics of dye release in presence of magainin 2 [85, 86], for dye entrance in presence of the protein equinatoxin II [179], and for the kinetics of area/volume vesicle expansion induced by melittin [69]. The onset of Bax $\alpha$ 5-dependent dye entrance occurs at a variable time, mostly between 20 min and 1 h, for each GUV. However, as soon as leakage starts, the dye concentration reaches near complete equilibration with the outside pool in about two minutes. A few examples of entrance kinetics for some individual vesicles are shown in FIG. 10.3 E, bottom graph. It has been described before that the kinetics of accumulating leaky vesicles registered for large ensembles of GUVs from the moment of peptide addition is similar to the kinetics of contents release from LUV suspensions [85, 86, 179]. In both types of ensembles the kinetics corresponds to the onset of pores in the complete vesicle pool, which at the end point affects a number of vesicles dependent on the  $P/L$  ratio.

2 hours after peptide addition (FIG. 10.3 B) all vesicles appear intact, but some are completely filled with Alexa555 (marked with an arrow in the image of the red channel) while others are empty of fluorescence probe. In most filled vesicles the exchange of contents was complete, and is thus clear that they followed an *all-or-none* poration mechanism [65, 181, 496]. However, a few vesicles refilled only partially with dye, because the rate of entrance was very slow and eventually stopped. Such a behavior corresponds to the so called *graded* mechanism of leakage [65, 473, 496]. Recall from SEC. 7.4 that it has been hypothesized that the release behavior of a peptide can be predicted on the basis of  $\Delta G_{ins}$ . Since  $\Delta G_{ins} = -13$  kcal/mol for Bax $\alpha$ 5, less than the proposed threshold value (20 kcal/mol, [65]), this peptide would be predicted to porate vesicles in a graded manner. Due to the limited number of predictions tested experimentally we cannot conclude whether the behavior of Bax $\alpha$ 5 constitutes an exception or whether the

<sup>1</sup> The method for studying vesicle poration at the single vesicle level, including details for quantitative image observation by fluorescence microscopy and data analysis, was described in SEC. 5.1.1 and 5.5.3. Detailed protocols for this method can be found in SEC. 6.1.1 and 6.5.3.

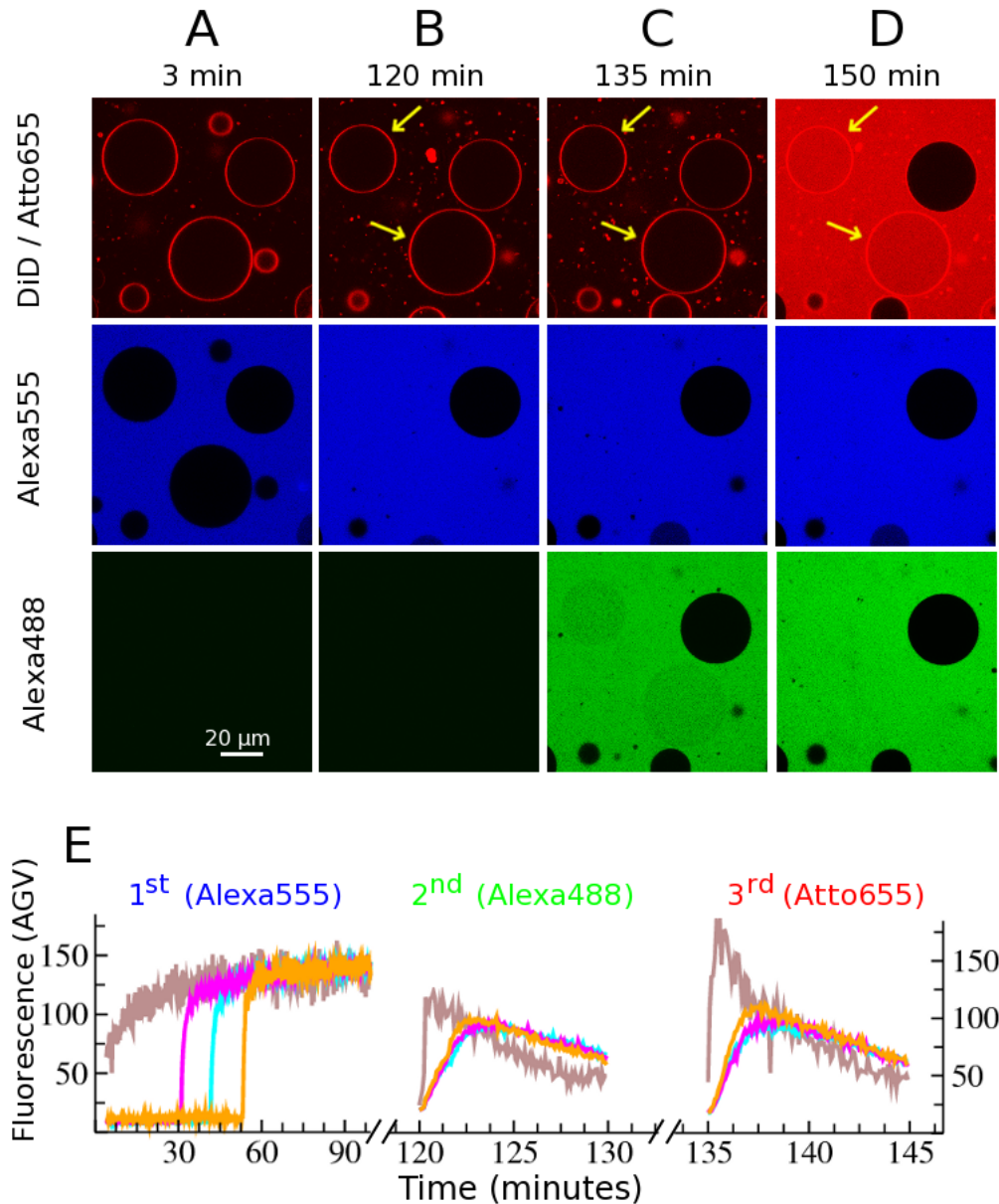


**Fig. 10.3 : Successive leak-in of serially added dyes for individual GUVs showing all-or-none release.** Bax $\alpha$ 5 and a first dye (Alexa555, blue) are initially present in the observation chamber, where GUVs labeled with DiD (red) are added to  $P/L=1/90$  (time=0). A) Fluorescence images start being recorded from minute 3 in three channels. Eventually, some GUVs become permeable stochastically and the dye internalized rapidly. B) Two hours later all GUVs maintained their integrity (red), but some (marked with arrows) have allowed complete entrance of the first dye. Immediately after, a second dye (Alexa488, green) is added. C) Images after second dye entrance: the leaky vesicles for this dye (green) are the same as those for the first dye (blue), marked in the image of the red channel. Immediately after, a third dye (Atto655, red) is added. D) Images taken at 150 min show that the porated vesicles are still the same as for the first and second dyes. E) Examples of recorded changes in the fluorescence inside three selected single GUVs (different colors) for 1<sup>st</sup>, 2<sup>nd</sup> and 3<sup>rd</sup> dye entrance (left to right). Changes in the external concentration of the dye are also represented (gray traces).

proposed hypothesis fails.

After 120 min of peptide/vesicle equilibration a *second* dye was added (Alexa488, green), whose leak-in is shown in pictures taken 15 min later (FIG. 10.3 C). Finally, at  $\sim$ 135 min we added a *third* dye (Atto655, red) and the response can be seen in pictures taken again 15 min later (FIG. 10.3 D). During this time (150 min in total) we registered the fluorescence from the same set of GUVs. We observed two clear and most remarkable facts:

i) For all observed leaky vesicles, the entrance of the second and third dyes started with no significant delay from the moment they were added. These shows that all porated vesicles were already in that state at the moment of addition of dyes.

ii) Such porated vesicles were indeed all individual vesicles which were completely permeable to the first dye. Additionally, all vesicles initially not permeable to the first dye, remained sealed also for the second and third dyes, and the few vesicles which exhibited partial first dye entrance showed insignificant entrance of successive dyes (FIG. 10.4).

As mentioned above, there is a small fraction of vesicles showing partial or graded first-dye exchange ( $\sim$ 22% of all porated vesicles for  $P/L=1/720$ ), mainly due to a very low entrance rate and eventually pore closure; i.e., graded leakage appears to be a kinetic mechanism, linked to peptide/membrane equilibration. On the other hand, the fact that graded and all-or-none filling coexist during the equilibration process shows that both mechanisms can occur simultaneously for a given peptide/lipid system, as already suggested [579]. It should also be noticed that the vesicle pool presents an intrinsic small percentage of porated vesicles in the absence of peptide, which exhibit both all-or-none and graded filling (FIG. 10.5 B), indicating that at least for the present lipid composition the coexistence of both types of mechanism is a characteristic of purely lipidic pores. Curiously, the percentage of vesicles showing graded filling decreases in the presence of the peptide, in favor of all-or-none filling.

We have also analyzed the dependence of the proportion of Bax $\alpha$ 5 porated GUVs with the  $P/L$  ratio. The kinetics of appearance of porated vesicles (for first dye leak-in) is shown in FIG. 10.5 A. Increasing  $P/L$  while keeping the GUV concentration constant causes both, a faster poration rate and a larger number of porated GUVs. The fraction of porated GUVs increases with time until a constant (maximum) level is achieved, usually before 1.5 h. A dose/response plot using all porated vesicles for the leak-in of the first dye up to the first two hours is shown in FIG. 10.5 B (black circles). This graph is similar to the dose/response measured in calcein-release assays using LUV suspensions (see for example FIG. 10.1 C, a detailed comparison will be addressed in SEC. 10.6). Because a few vesicles (those exhibiting graded filling) did not remain in the porated state for long time, the plots for successive dye entrances are slightly different (FIG. 10.5 C, blue circles). In turn, the number of partially (transiently) porated vesicles depends on  $P/L$ . Thus, from the data of the first leakage event we can plot also percentages of stably porated vesicles, relative to the total number of porated vesicles (stable and transient), which reaches 100% near  $P/L$  of 1/100 (FIG. 10.5 B, red squares). The latter  $P/L$  value appears reminiscent of threshold  $P/L$  values reported in different studies for other systems [69, 86, 183], being also of a similar magnitude.

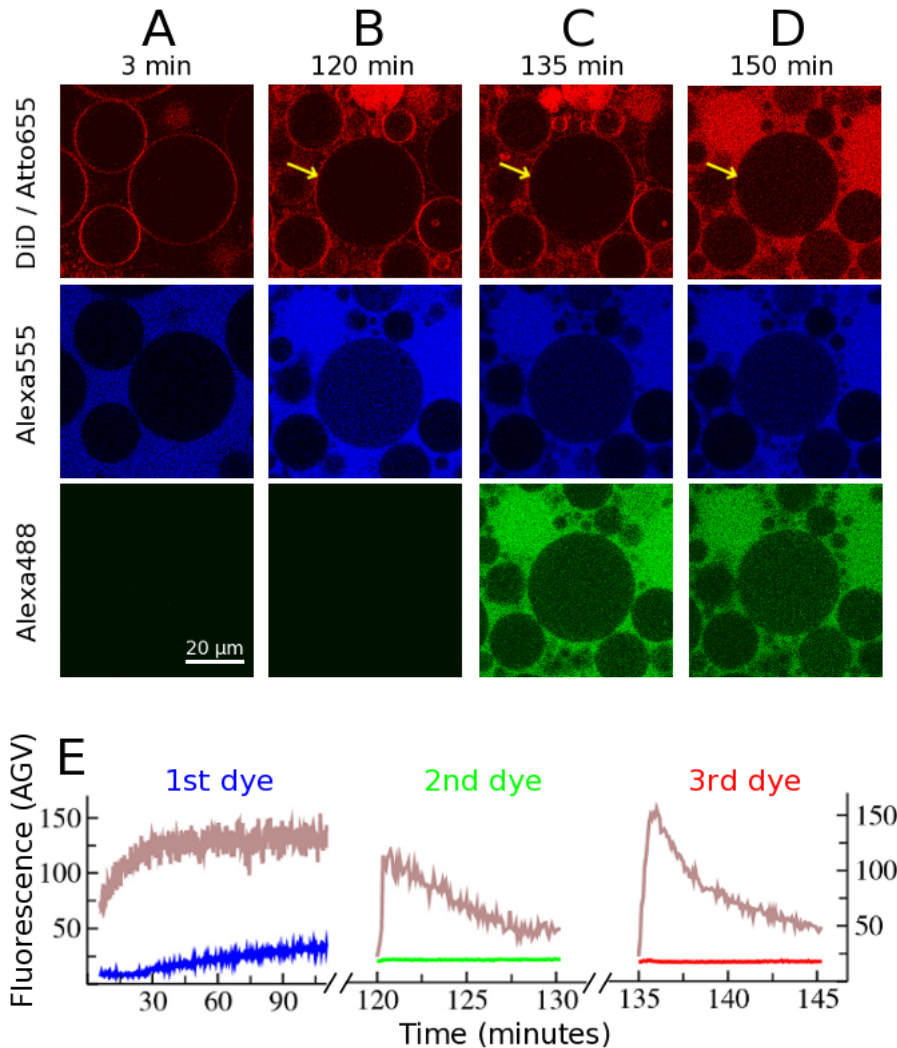


**Fig. 10.4 : Successive leak-in kinetics of serially added dyes at short and long times, showing partial refilling of GUVs and eventually pore closure.**  $Bax\alpha 5$  and a first dye (Alexa555, blue) are initially present in the observation chamber, where GUVs labeled with DiD (red) are added to  $P/L=1/90$  (time=0). A) After 3 min the GUVs have sunk and fluorescence images start being recorded in three channels. Most of the GUVs are rapidly refilled with dye, but some exhibit a graded refilling (slow and eventually stopped). B) Pictures taken two hours later show that GUVs kept their integrity (red), but one (marked with an arrow) has filled refilled partially with the first dye. Immediately after, a second dye (Alexa488, green) is added. The same GUV as before is now not permeable to the second dye (bottom graph). C). Immediately after, a third dye (Atto655, red) is added, but the same GUV as before keeps impermeable (bottom graph). D) Images taken  $\sim 15$  min after third dye addition. E) Example of the recorded change in the fluorescence inside a selected single GUVs together with the changes in the external dye concentration (gray trace), showing graded refilling for the first dye and no entrance of successive dyes.

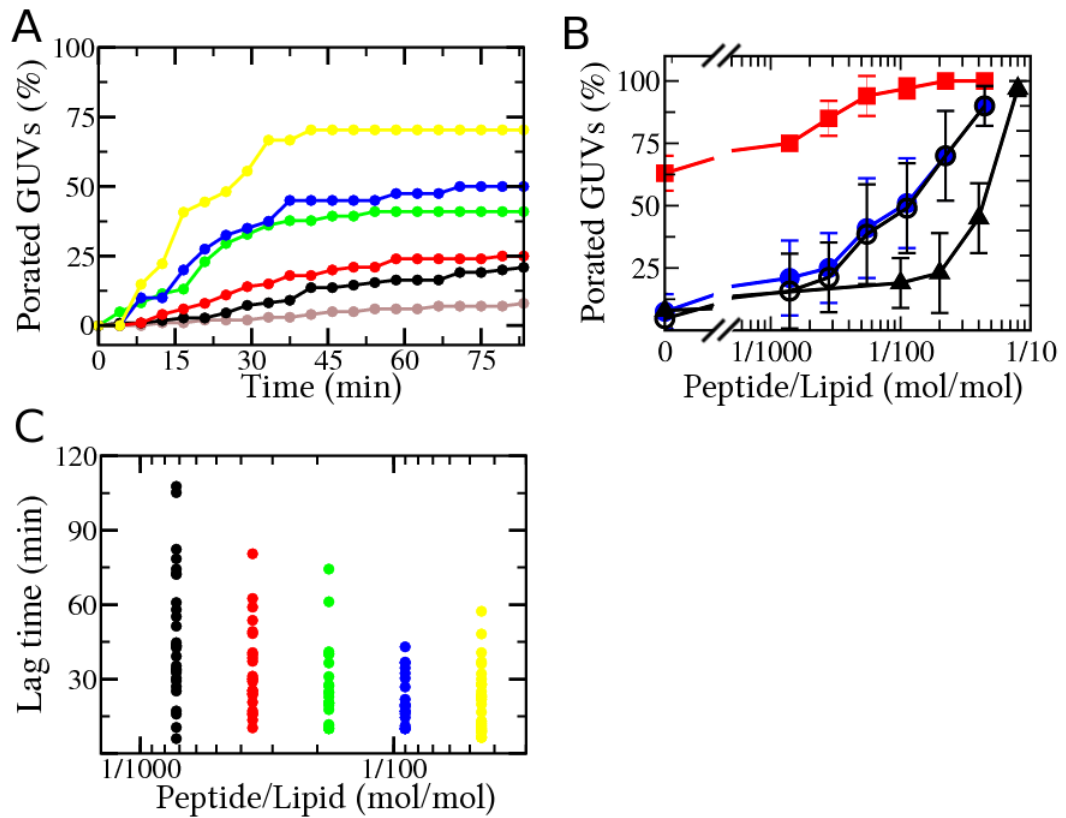


**Fig. 10.5 : Effect of the relative amount of Bax $\alpha$ 5 on GUV poration.** A) Kinetics of appearance of filled GUVs for different bulk  $P/L$  (leak-in of first dye). B) Dose/response graphs for the leak-in of externally added dyes. The black circles are percentages of GUVs which were permeable to a first dye (Alexa488) during the first two hours after they are in contact with Bax $\alpha$ 5 (including completely and partially filled GUVs); the dose/response curve for any successive dye entrance is slightly different (blue circles). The percentage of completely permeable GUVs in the first leak-in event, relative to the total permeable GUVs (including partially porated) is represented with red squares. Triangles are data for the entrance of external Alexa488 at equilibrium, measured with GUVs prepared in the presence of Alexa647-labeled Bax $\alpha$ 5. C) Lag time needed for the appearance of pores in single GUVs as a function of the bulk  $P/L$ . Each dot in the plot corresponds to the observation made on an individual GUV.

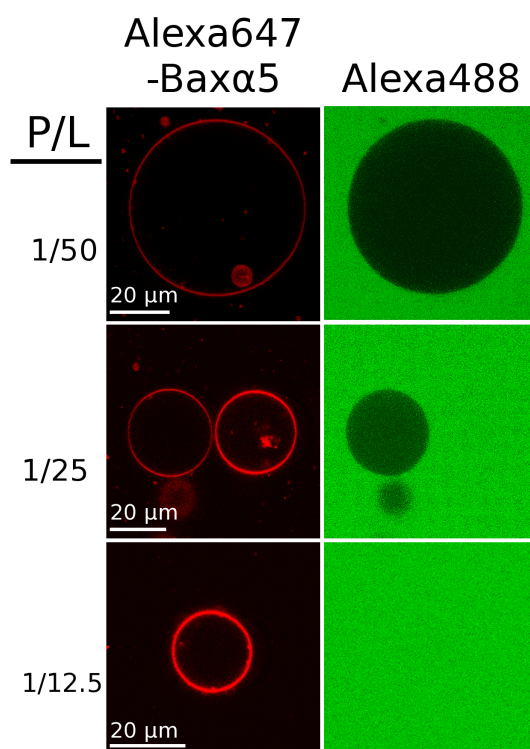


**Fig. 10.6 : Bax $\alpha$ 5 binding and activity in reconstituted vesicles.** Images of GUVs prepared in the presence of Alexa647-Bax $\alpha$ 5 at different  $P/L$  ratios, demonstrating accumulation of the peptide in the membrane (left, red fluorescence) and peptide-induced leak-in of Alexa488 (right, green fluorescence).

### 10.3.2 Pores in reconstituted GUVs

A difference between LUVs and GUVs is that the second type of vesicles, of much larger size, tend to be more fragile. Thus, to avoid possible artifacts due to vesicle instability, successive leakage events were not registered for very long times. Instead, as we also did with LUVs, equilibrated systems were prepared by reconstituting GUVs in presence of Bax $\alpha$ 5. Additionally, this time we used a fluorescence-labeled version of the peptide (Alexa647-Bax $\alpha$ 5) which allowed us testing directly membrane binding. The increased fluorescence of the membrane in presence of Alexa647-Bax $\alpha$ 5 (FIG. 10.6) shows clearly that Alexa647-Bax $\alpha$ 5 accumulates readily in the vesicle membrane. Nevertheless, the yield of GUV formation in the presence of Alexa647-Bax $\alpha$ 5 was low and the distribution of the peptide among individual vesicles within the same batch was found to be inhomogeneous. After addition of Alexa488 to the observation chamber, internalization of the dye was observed for a fraction of the vesicles which increased with the bulk  $P/L$  (FIG. 10.5 B, triangles and 10.6). Such leakage was always of the all-or-none type, again supporting that graded leakage is not found at equilibrium. The dose/response plot for bulk  $P/L$  values suggests a threshold  $P/L$  for the onset of equilibrium pores near

1/25, which is larger than the one extracted from the trend of peptide-added systems ( $\sim 1/100$ ). We recall that the activity registered in reconstituted LUVs also tends to be smaller than the one measured after a few hours in presence of peptide (FIG. 10.2 D). This might indicate that the latter systems were still not equilibrated after two hours incubation with the peptide. However, we are cautious with this comparison because of the differences between the two types of samples.

Up to this point, more than individual *pores* we are characterizing *leaky-* or *pore-states* of vesicles. We may by now conclude that the vesicle pore-state acquired through equilibration either keeps or transforms into a long-term, and eventually stable (equilibrium) pore state. There also seems to be a threshold P/L value for the onset of both types of pores, which is probably larger at equilibrium; but below saturation, porated and non porated vesicles coexist and keep in stable or metastable states which do not exchange appreciably among each other.

## 10.4 The two types of pores differ at least in their size

An important question is whether the initial pores (short-time or pre-equilibrium pores) are similar in their properties to pores observed at long-term or at equilibrium. Although this is difficult to answer, in the following we address it through a careful analysis of the kinetics of dye entry, which will allow an indirect approximation to the pore size. On the other hand, we will also evaluate the size of pores directly, by testing the entry of dyes with different sizes.

### 10.4.1 Leak-in kinetics of pre-equilibrium pores

**Mono-exponential kinetics.** As we have shown, the kinetics of entry of external fluorescent dyes can be monitored through the changes of the fluorescence intensity inside individual GUVs. This is measured as the average gray value (AGV) from within each GUV, which is proportional to the fluorophore concentration, as a function of time. For the first dye, the kinetics was recorded as described above. Briefly, GUVs were added and allowed to diffuse to the bottom of the observation chamber, which already contained a homogeneous solution of Bax $\alpha$ 5 and Alexa555 in PBS. After  $\sim 5$  min most vesicles had sunk, while Bax $\alpha$ 5 has begun adsorbing in the GUV membranes. As soon as a pore opens in a particular GUV, fluorescence starts brightening inside that GUV, increasing with time until it equilibrates with the fluorescence in the outside solution (FIG. 10.7 A). Any possible variation of the outside concentration of the dye with respect to the equilibrium concentration, like a slight dilution at short times after vesicle sinking (gray trace in FIG. 10.3 E, left), is taken into account to correct the value of inside signal (Fig. 10.3 E, left, color traces). For that, the fluorescence inside a GUV at any given time ( $F(t)_{in}$ ) was normalized ( $F(t)_{in}^N$ ) with respect to the fluorescence at time 0 ( $F_{0,in}$ ) and to the almost constant outside fluorescence ( $F(t)_{out}$ ), according to:

$$F(t)_{in}^N = \frac{F(t)_{in} - F_{0,in}}{F(t)_{out} - F_{0,in}} \quad (10.2)$$

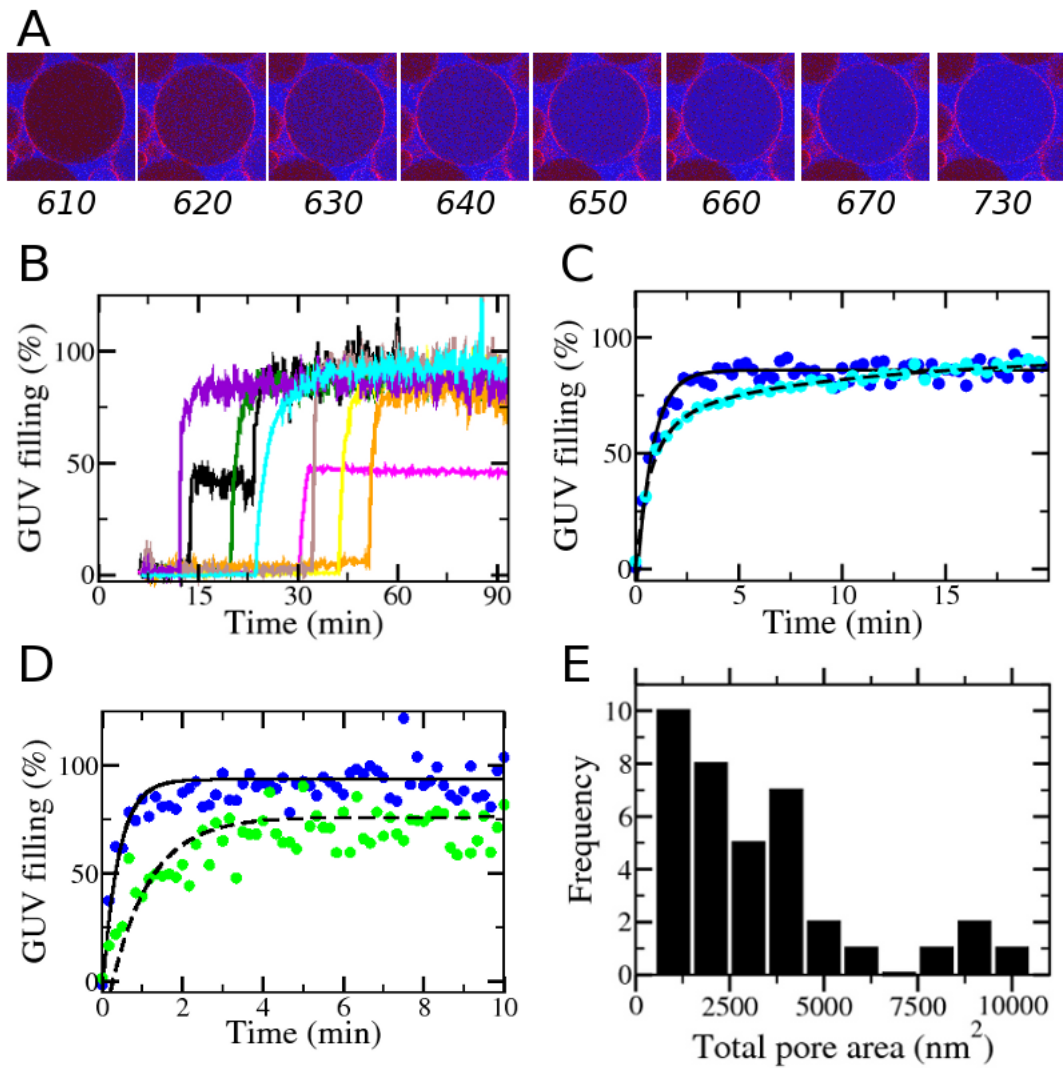


**Fig. 10.7 : Kinetic analysis of short-term pores.** A) Time series of Alexa555 (*first dye*) filling kinetics. The numbers under the figures are the time in seconds after mixing of Bax $\alpha$ 5 with GUVs (labeled with DiD, red) and Alexa555 (blue). B) Catalog of Alex555 filling kinetics (normalized inside fluorescence, EQ. 10.2). In general, exponential all-or-none release is observed, and graded release (pink) is seldom detected. Occasionally, complex kinetics are found where an initial fast permeabilization is followed by a resealing phase and eventually continuation of the exponential leak-in up to completion (black). Note the broad distribution of pore opening times. C) Examples of fits of Alexa555 entry into single GUVs (adjusted, for clarity, to the same onset time) for a case following a mono-exponential function (EQ. 10.4, blue points) and a case following a bi-exponential function that accounts for pore shrinkage (EQ. 10.8, cyan points). From the fits the total pore area was extracted. D) Examples of kinetics for co-addition of dyes with different size: Alexa555 (blue circles) and cytochrome *c* (green circles) along with the corresponding fits. E) Histogram showing the distribution of calculated non equilibrium pore areas ( $A_0$ ) for  $P/L=1/45$ . Averaged  $A_0$  values corresponding to other  $P/L$  ratios are given in TAB. 10.1.

A collection of kinetic curves (using normalized fluorescence) for several individual vesicles is plotted in FIG. 10.7 B. In order to analyze these data, we considered the first FICK'S law of diffusion (SUB. 5.5.3), which integrated with respect to distance gives the flux of dye transport across the membrane as a function of the difference in concentration between the vesicle inside,  $C_{in}$  and outside,  $C_{out}$  (see EQ. 5.66). For permeation through a pore of area  $A_0$  the flux can be written as the rate of change of the inside concentration as follows:

$$\frac{V}{A_0} \frac{dC_{in}}{dt} = P(C_{out} - C_{in})$$

where  $P$  is the *permeability* coefficient of the pore which equals  $D/m$ , with  $D$  being the *diffusion* coefficient and  $m$  the effective length of the pore, and  $V$  is the vesicle volume. This expression can be integrated between time 0 and  $t$  and the concentration inside the vesicle between 0 and  $C_{in}$  [61, 570]:

$$C_{in}(t) = C_{out}(1 - e^{-t/\tau_{flux}}) \quad (10.3)$$

which gives the exponential increase of the dye concentration inside the GUV up to equilibration with the outside concentration. Although we do not know the concentration values, these are proportional to the measured fluorescence of the probe. Thus, the latter equation can be re-written considering the time variation of the inside fluorescence normalized with respect to the outside fluorescence ( $F(t)_{in}^N$ , EQ. 10.2) and thus ranging between 0 and 1:

$$F(t)_{in}^N = 1 - e^{-t/\tau_{flux}} \quad (10.4)$$

The time constant  $\tau_{flux}$  equates to:

$$\tau_{flux} = \frac{V}{A_0 \cdot P} = \frac{V}{A_0 \cdot D/m} \quad (10.5)$$

and allows easy calculation of the pore area<sup>1</sup>, which is denoted  $A_0$  to indicate that it corresponds to *initial* (short-term) pores. For that, we assume that  $D$  is constant within the pore and approximates to the diffusion coefficient of the dye free in solution, which can be taken from the literature [482]. The value of  $m$  (pore length) is taken as the membrane thickness. Although there are no data in the literature for our exact lipid composition, we take the thickness of POPC bilayers [554] as a good approximation. On the other hand,  $V$  is calculated as  $\frac{4}{3}\pi r_g^3$ , which assumes perfect spherical GUVs of radius  $r_g$  measured directly under the fluorescence microscope<sup>2</sup>.

Before going ahead with the use of this theory it is interesting to revise other implicit assumptions involved. First, the outside and inside marker concentrations should

1 Assuming a cylindrical pore geometry, the pore area can be further converted into pore radius, which would be in fact an *equivalent* pore radius (see below).

2 In a previous publication, analysis of leak-in kinetics has been done using the volume flux through the membrane,  $J_V$  [179]. It can be shown that  $\tau_{flux} = r_g/3J_V$ .

reequilibrate fast compared to the rate of transport across the membrane, which ordinarily holds true [571]. Second, EQ.10.3 and 10.4 apply when one pore is open continuously at least during the time needed for complete entry of the dye. Several pore openings can also be in agreement with the formulation, but in this case they must be essentially simultaneous. In other words, it is the total permeating area that matters. It is then not possible to distinguish between cases of a single large pore or the sum of two or more simultaneous pores (equal or different among each other). We will thus refer to *total* or *equivalent* pore area. And third, for comparison of leakage of different dyes (see below), the concentration gradient must be the same in all cases considered (we used always an external dye concentration of 1  $\mu\text{M}$ ).

Some simple calculations using EQ. 10.5 illustrate the relationship between the pore size and the time needed for complete equilibration of the vesicle inside with the external solution. For a LUV ( $\sim 100$  nm size) with a pore of 6 nm radius the reequilibration time,  $\tau_{flux}$ , would be just 37  $\mu\text{s}$ ; i.e., the leakage for individual LUVs is expected to be essentially instantaneous. Thus, the retarded kinetics (to the order of minutes, see for example FIG. 10.1 A) observed for LUV ensembles should correspond to the kinetics of pore onset in the complete vesicle population. However, for a single 25  $\mu\text{m}$  GUV with one pore of 6 nm radius the leakage time increases up to  $\sim 10$  min. This theoretical time scale corresponds well with the leak-in kinetics that we measured for single GUVs.

Fits of EQ. 10.4 to normalized fluorescence data (FIG. 10.7 C) yield values of the pore area (from EQ. 10.5). Averaged values of total pore area obtained from the fits, in cases of clear mono-exponential kinetics (see below), are listed in TAB. 10.1 for different  $P/L$  values (column named  $A_0$ ). The corresponding frequency distributions are plotted in FIG. 10.7 E. The meaning of these values will be discussed with more detail below.

**Multi-exponential kinetics: Pore shrinkage.** Through the analysis of first dye leakage we noticed that the data of some GUVs could not be well fitted with a single exponential model, since a first fast phase is followed by a significantly slower phase.

Interestingly, there have been several attempts to account for slowing down of the leakage rates in LUV suspensions. For example, SCHWARZ and coworkers suggested a pore deactivation process [572, 580]. ALMEIDA and coworkers claimed that since the ratio of full vesicles decreases with time, the probability for a peptide to find a fresh vesicle to porate (full of dye in their experiments) also decreases with time [84, 116]. On the other hand, STELLA and coworkers have proposed recently that the slow leakage kinetics at long times is due to fluctuations in the number of bound-peptides per LUV, with some vesicles “loosing” peptide molecules and other “gaining” them [570]. None of these proposed models seem to apply to our Bax $\alpha$ 5:GUV system. Pore deactivation does not explain our observations at single vesicle level, since, as we have seen in the previous section, once each individual vesicle porates, its pore-state is maintained over time. ALMEIDA’s claim cannot be applied to slowing down kinetics of single GUVs. On the other hand, fluctuations in the number of membrane-inserted peptides (STELLA’s proposition) should not have a significant effect on GUVs, given the large number of lipids and peptides in a single vesicle of this size. In fact, as we will show in SUB.

10.5, the amount of Bax $\alpha$ 5 bound to any observed single GUV always increases up to a constant value (variable for different GUVs), but we have never observed net unbinding.

One alternative explanation for our observations is that there can be a reduction of the pore size (and/or number of pores; i.e., a reduction of the equivalent pore area) during the time sampled by the kinetic traces. Furthermore, since we have concluded above that the long-term pores exhibit significantly slower rate than short-term pores, the cases of multi-exponential kinetics could be reporting the *relaxation* of non-equilibrium pores into equilibrium ones. Then, the idea is that as soon as a GUV *first* porates (after the encounter with Bax $\alpha$ 5), the *first* dye starts entering quickly because the equivalent pore area at this stage is relatively large. However, as the peptide/GUV system equilibrates the pore area reduces. It may happen that in some cases such a pore relaxation (size reduction) overlaps with the dye entrance process, thus slowing down the entrance kinetics. We therefore implemented a time-dependent reduction of the total pore area in the theoretical model described above (EQ. 10.3-10.4). The change of pore size was modeled as an exponential decay from a state corresponding to an initially *large* area ( $A_0$ ) into one of *smaller* area ( $A_\infty$ ), with relaxation time  $\tau_{relax}$ :

$$A(t) = A_\infty + (A_0 - A_\infty) e^{-t/\tau_{relax}} \quad (10.6)$$

This, in turn, means that the characteristic flux time of dye leak-in is in fact time dependent, and EQ. 10.5 converts into:

$$\tau_{flux}(t) = \frac{V}{A(t) \cdot D/m} \quad (10.7)$$

which can now be included in EQ. 10.4 to account for the pore-shrinking kinetics:

$$F(t)_{in}^N = 1 - e^{-t/\tau_{flux}(t)} \quad (10.8)$$

The corresponding fits then yield values of  $A_0$ ,  $A_\infty$  and  $\tau_{relax}$ . We remind that because the areas here refer to total pore area (or the area of a pore equivalent to the sum of all pores present), a reduction of  $A_\infty$  with respect to  $A_0$  can be interpreted, without distinction, as a reduction of the number of pores, a reduction of the size of individual pores, or a combination of both effects.

Averaged total initial pore area,  $A_0$  for different  $P/L$  ratios are shown in TAB. 10.1, where the values obtained from single exponential kinetics are kept apart from those of multi-exponential kinetics, despite the fact that, at least conceptually, both correspond to pre-equilibrium pores. Similarly, we may argue that the values of  $A_\infty$  from the multi-exponential fits of first dye leakage correspond to equilibrium pores, as it will be discussed in the next SEC. The frequency distributions of total pore areas can be seen in FIG. 10.8 A, represented for each  $P/L$  ratio and as frequency distributions of values accumulated from all  $P/L$  conditions, showing that, within each group, the smaller total sizes are always more probable. However, such frequency distributions of pore area are in all cases very broad, since they include a large range of sizes. Therefore, although the highest  $P/L$  (1/45) shows the largest pore area on average, this difference should not be considered significant when the SD of the values is taken into account.

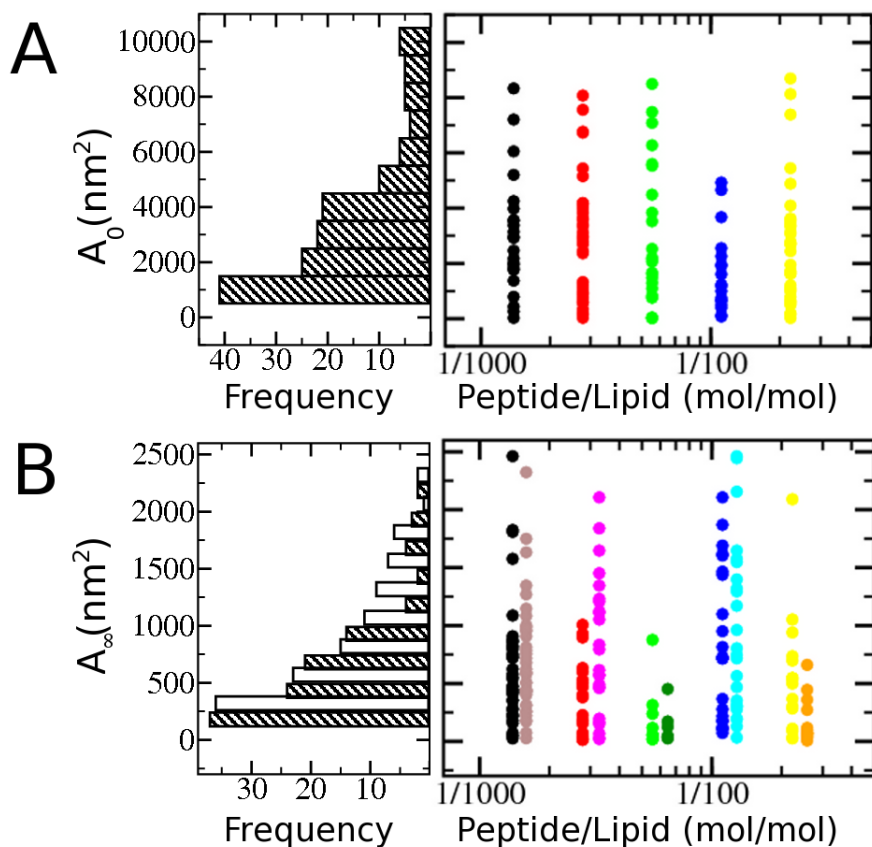


**Fig. 10.8 :** Distributions of total pore area per vesicle for pre-equilibrium and equilibrium pores. Graphs on the left are accumulated distributions, with total size corresponding to any of the assayed  $P/L$  ratios for pre-equilibrium ( $A_0$ ) pores using a *first* dye (A) or equilibrium ( $A_\infty$ ) pores using *second* and *third* dyes (B). The corresponding total areas from each of the analyzed GUVs are represented on the right for each  $P/L$  ratio, color-coded as follows: 1/720 (black), 1/360 (red), 1/180 (light green) 1/90 (blue) and 1/45 (yellow). In the case of the *third* dye addition the P/L are the same as above but have been shifted for an ease of visualization: 1/720 (gray), 1/360 (pink), 1/180 (dark green) 1/90 (cyan) and 1/45 (orange).

Tab. 10.1 : Effect of the bulk  $P/L$  ratio on the size of pores induced by Bax $\alpha$ 5 in POPC:CL GUVs.

$P/L$	Pre-equilibrium pores			Equilibrium pores			$T_{relax}$ (min) <sup>e</sup>
	$A_0$ , constant size (nm <sup>2</sup> ) <sup>a</sup>	$A_0$ , shrinking size (nm <sup>2</sup> ) <sup>b</sup>	$A_0^{Alexa}/A_0^{Gyt}$ , constant size <sup>c</sup>	$A_\infty$ , shrinking size (nm <sup>2</sup> ) <sup>b</sup>	$A_\infty$ , 2 <sup>nd</sup> dye (nm <sup>2</sup> ) <sup>d</sup>	$A_\infty$ , 3 <sup>rd</sup> dye (nm <sup>2</sup> ) <sup>d</sup>	
1/45	3247±3716	6184±5158	0.88±0.14	182±242	900±1142	146±175	5±4
1/90	1121±770	2777±1949	0.85±0.14	407±314	953±884	934±735	3±5
1/180	2114±2171	4690±2734	0.9±0.3	682±854	212±289	117±145	3±2
1/360	1403±1091	3499±3873	1.0±0.3	219±356	476±758	815±598	2±3
1/720	1504±3314	3357±2142	1.05±0.05	137±178	333±409	476±466	4±3

<sup>a</sup>Total pore area per GUV (average of values from a total of 99 GUVs) calculated from fits of the entry kinetics of Alexa555 (1<sup>st</sup> dye) with a mono-exponential function (constant pore area, Eq. 10.4).

<sup>b</sup>Total pore areas per GUV (average of values from a total of 48 GUVs) calculated from fits of the entry kinetics of Alexa555 (1<sup>st</sup> dye) with a theoretical model (Eq. 10.8) that considers a shrinking pore with an area decaying exponentially from  $A_0$  to  $A_\infty$ , according to Eq. 10.6.

<sup>c</sup>Ratio of equivalent pore area estimated from fits of the entry kinetics of Alexa555 and cytochrome  $c$  (both as 1<sup>st</sup> dyes, present initially in the observation chamber). A ratio close to 1 indicates that both dyes leak into the vesicles at a similar rate.

<sup>d</sup>Total pore area per GUV (average of values from a total of 117 GUVs) calculated from fits (Eq. 10.10) of the entry kinetics of Alexa488 (2<sup>nd</sup> dye) or Atto655 (3<sup>rd</sup> dye), added 2 h (or 2.5 h) after incubating GUVs with Bax $\alpha$ 5.

<sup>e</sup>Relaxation time of pore shrinking. Note that  $\tau_{relax}$  is the reciprocal of the kinetic constant of pore shrinking,  $k_{relax}$  (Eq. 10.6).

### 10.4.2 Leak-in kinetics of equilibrium pores

What we here call *equilibrium* pores refers to studies made after sufficient time to ensure stationary levels of peptide bound to GUVs (therefore, also named *long-term* pores, see also FOOTNOTE 1 on page 206). This time was estimated from the type of experiments shown in FIG. 10.11, see SUB. 10.5), which demonstrated peptide accumulation at the membrane of single GUVs up to 1.5 h after addition of vesicles. Similarly, no further GUV poration events were found beyond the first 1.5 h after getting in contact with Bax $\alpha$ 5 (FIG. 10.5 A). Therefore, we decided to set the equilibration time as 2 h. Only then *subsequent* dyes (*second* and *third*)<sup>1</sup> were added and their kinetics of entry recorded in the way described above (SUB. 10.3.1). Such successive dyes then report on the presence of equilibrium pores. On the other hand, because for recording the successive leak-in events the dye was added to already porated GUVs, we have to deal with the fact that the kinetics of dye entrance occurs in parallel with its equilibration of the pool outside GUVs. This means that, although we can still apply Fick's law to analyze the kinetics, the flux registered for each GUV is driven by a variable concentration gradient. Moreover, the complex dependence on time and space of such a gradient makes any simple normalization of inside fluorescence values, with respect to (measured) outside fluorescence, unfeasible. Nevertheless, we noticed that, on average<sup>2</sup>, the kinetics of the diffusive dilution of the second and third dyes in the outside pool can be modeled as an exponential decay from an initial high value,  $F_{0,out}$ , into an equilibrium value,  $F_{\infty,out}$ , with rate  $k$ :

$$F(t)_{out'} = F_{\infty,out'} + (F_{0,out'} - F_{\infty,out'}) e^{-kt} \quad (10.9)$$

where  $F(t)_{out'}$  represents the time-dependent outside fluorescence in the immediate surroundings of the vesicle. This expression was included in the integrated Fick's law (EQ. 10.3) to obtain the corresponding exponential change of inside fluorescence, this time using unnormalized data (FIG. 10.3 E, middle and right):

$$F(t)_{in} = F_{0,in} + (F(t)_{out'} - F_{0,in}) (1 - e^{-t/\tau_{flux}}) \quad (10.10)$$

Thus, fits of this function yield values of  $\tau_{flux}$ , which as defined above are used to calculate equivalent pore areas (EQ. 10.5), giving as well values of  $k$ ,  $F_{0,out'}$  and  $F_{\infty,out'}$ . The  $F(t)_{out'}$  values from the fits were used to normalize the kinetics of second and third dyes (FIG. 10.9 C and D). Notice also that this model does not consider a variable pore area within the time of monitored dye entry (i.e.  $\tau_{flux}$  is not time dependent). Including pore size variation in these cases does not appear justified by the data and may easily result in over-fitting. On the other hand, the fact that the pore areas calculated in this way keep within similar ranges, considering the large dispersion of values, for second and

1 Subsequent dyes are named *second* and *third* just to distinguish them from the *first* dye which was present from the beginning of the experiment. Notice then that *in principle* we give no importance to the type of molecule that is used as first, second or third dye (the specific names may be found, for example, in the caption of FIG. 10.3), since we consider that the small differences between their size and other potentially relevant properties (like charge and polarity) are not important for the differences that we observed in their leak-in kinetics.

2 From multiple measurements in the volume surrounding the GUVs

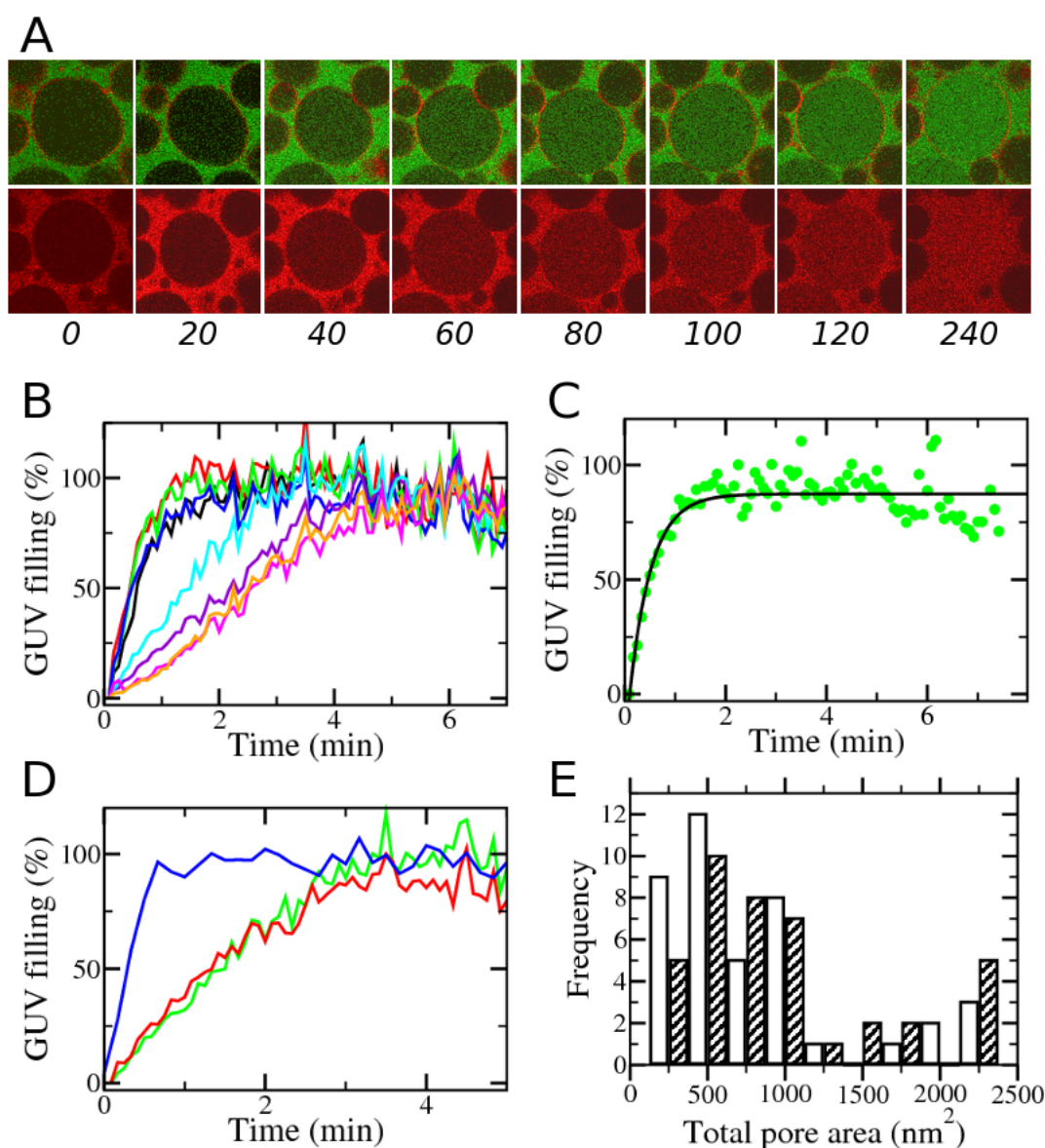


**Fig. 10.9 : Kinetic analysis of long-term pores.** Dyes were added after first incubating Bax $\alpha$ 5 with GUVs (labeled with DiD, red) for 2 h. A) Time series of the filling kinetics for Alexa488 (top) and Atto655 (bottom); *second* and *third* dye, respectively. The numbers under the images are the time in seconds after dye addition. B) Kinetic traces for Alexa488 filling (similar kinetics were recorded for Atto655). Note the absence of a lag time. C) Example of curve fitting for leak-in data of Alexa488 using Eq. 10.10. D) Comparison of the entry kinetics of the three successive dyes on the same GUV. The first dye (Alexa555, blue) was present from the beginning, and the second (Alexa488, green) and third dyes (Atto655, red) were added 2 h and 2.5 h later, respectively. For better comparison, the onset time for GUV filling was set to 0 in the three cases. E) Histograms showing the distributions of calculated equilibrium pore sizes for second dye (white bars) or third dye (striped bars) entry, in both cases corresponding to  $P/L = 1/45$ .

third successive dyes (see below), indicates that at this stage we are dealing with stable pores.

As mentioned above (SUB. 10.3.1), a prominent feature of the entry kinetics at long-term (equilibrium) conditions is that the second and third dye leak into the same GUVs (and not any other) which were completely refilled with the first dye (FIG. 10.3 and 10.9 A). Additionally, for these cases there is no appreciable lag time, i.e., the second and third dyes begin entering into GUVs immediately after they are added. The corresponding kinetic traces (see examples in FIG. 10.9 B) for various  $P/L$  ratios were analyzed quantitatively using fits of EQ. 10.10, and averaged values of equivalent pore area are shown also in TAB. 10.1. Again, one can appreciate from the large standard deviations that for each  $P/L$  the areas make very broad distributions. However, considering this large dispersion of values, within each  $P/L$  the total *per* vesicle pore areas are comparable for the leak-in of second and third dyes. Interestingly these values are also comparable with the areas of the relaxed pores obtained from multiexponential kinetic traces of leakage of first dye (also shown in TAB. 10.1). It appears that in both cases the size corresponds to equilibrium pores, and thus both are labeled as  $A_\infty$ . On the other hand, in contrast to what happened with the pre-equilibrium pores, the long-term pores show a less clear dependence on the  $P/L$  ratio (see TAB. 10.1). However, the distributions of total size values are complex (FIG. 10.8 B), and their large dispersion does not allow drawing clear conclusions from the averages.

### 10.4.3 Estimating the size of individual pores

A way to evaluate the size of individual pores is by studying the leakage of big and small markers. For example, previous experiments of release of high molecular weight dextran from LUVs, using a different version of Bax $\alpha$ 5, suggest that the pore size increases with  $P/L$  [176], and similar conclusions have been drawn for other pore-forming peptides [576, 581]. For experiments with single GUVs, we may predict that if two dyes of different size are transported across the same pores, and these pores are large compared to the size of the largest dye, the leakage of both dyes should occur simultaneously and the ratio of total pore areas determined for the two dyes should be close to 1. On the other hand, as the pore size approximates the size of the biggest dye, its permeability should be greatly restricted compared to that of the smaller dye.

In a first set of these experiments, we used Alexa or Atto dyes as small markers and cytochrome *c* labeled with Alexa488 as the big marker, both present simultaneously in the observation chamber together with Bax $\alpha$ 5 when GUVs were added (case of short-term kinetics for the two markers). Additionally, in order to have better chances of finding a restrictive pore size, the experiments were performed at different bulk  $P/L$  ratios. Any significant increase in the size ratio  $A_0^{Alexa}/A_0^{cyl}$  with decreasing  $P/L$  would show that the size of individual pores get smaller at smaller  $P/L$ . We found that the two dyes leak into single GUVs at similar rates (FIG. 10.7 D). Moreover, although the average total pore area decreases with the  $P/L$  (as discussed above, 10.1) individual pores are still large compared to the size of cytochrome *c* ( $\sim 9$  nm<sup>2</sup> cross-sectional area), as we can conclude from  $A_0^{Alexa}/A_0^{cyl} \sim 1$  irrespective of  $P/L$  (TAB. 10.1). We also noticed that

cytochrome *c* alone could permeabilize GUVs, and although this background activity is of low efficiency compared to that of Bax $\alpha$ 5, it makes the interpretation of results difficult.

In a second set of experiments we compared the entrance in GUVs of Alexa555 (1.25 kDa) and a  $\sim$ 10 kDa fluorescein-labeled dextran (FD10). FD10 has a hydrodynamic radius of 2.3 nm. This size is slightly larger than the 1.7 nm of the physiologically relevant cytochrome *c*, but compared to it, FD10 is completely inert as far as vesicle poration is concerned. Two hours after mixing gently a suspension of GUVs with both dyes and Bax $\alpha$ 5, we saw that any chosen individual GUV which was permeable for the Alexa dye (FIG. 10.10 A, blue) had also allowed entry of FD10 (FIG. 10.10 A, green). As explained above, for a given vesicle the onset of the porated state is normally delayed and stochastic. A recording of the kinetics (FIG. 10.10 B) shows that both fluorescence molecules start entering to the same vesicles simultaneously and initially with a similar rate. However, while the entry of Alexa proceeds smoothly up to complete equilibration with the external pool, the entry of FD10 starts to be slowed down near the end point of the kinetics (compare blue and green traces in FIG. 10.10 B). This suggests again that although the pores were initially sufficiently large to allow entry of the FD10, they relax to a smaller size in a few minutes. In fact, we observed that continuous irradiation for two minutes bleached the fluorescence of FD10 only from the inside of the GUV (FIG. 10.10 C), indicating that FD10 had become entrapped and could no longer re-equilibrate with the outside pool. In order to confirm the smaller size of long-term pores, in an independent experiment we monitored entry of Alexa555 and FD10 added simultaneously to a GUV suspension which had been previously incubated with Bax $\alpha$ 5 for two hours. Initially porated GUVs, distinguishable by the complete entrance of Atto655 (present in the external solution from the beginning), allowed immediate and complete entry of added Alexa555 (FIG. 10.10 D, blue). However, the same GUVs were very weakly permeable to FD10, which was found to penetrate only to about 12%, even 30 min after addition (FIG. 10.10 D, green). Considering the approximate size of FD10, we can estimate that each of the initial pores should, individually, have an area  $A_0$  which is clearly larger than 17 nm<sup>2</sup> (the approximate cross-sectional area of FD10). These pores shrink as they relax to an individual area  $A_\infty$  smaller than (but probably not far from)  $\sim$ 17 nm<sup>2</sup>. Initial pores of  $A_0 \gg 17$  nm<sup>2</sup> is what can be also concluded from the fact that  $A_0^{Alexa}/A_0^{cyt}$  values were close to 1 and from the very large  $A_0$  values, even for the smallest  $P/L$  (TAB. 10.1). On the other hand,  $A_\infty \sim 17$  nm<sup>2</sup>, suggests that most leaky GUVs should contain more than one pore.

These experiments, thus, unambiguously demonstrate that the decrease of total pore area from  $A_0$  to  $A_\infty$ , described above, is at least due to a net reduction of the size of individual pores from  $\gg 17$  nm<sup>2</sup> to  $\sim 17$  nm<sup>2</sup>. However, changes in the number of pores, accompanying the pore size reduction, can not be excluded. A reduction of size after an initial burst has been observed for purely lipidic pores induced by tension, which typically relaxed to complete closure [72]. However, although Bax $\alpha$ 5-induced pores start reducing size quickly after forming, the peptide avoids complete pore closure and seems to stabilize the pore at a certain radius. Based on a kinetic analysis, it has also been suggested that the pores formed by other amphiphatic peptides like melittin

10.4 The two types of pores differ at least in their size

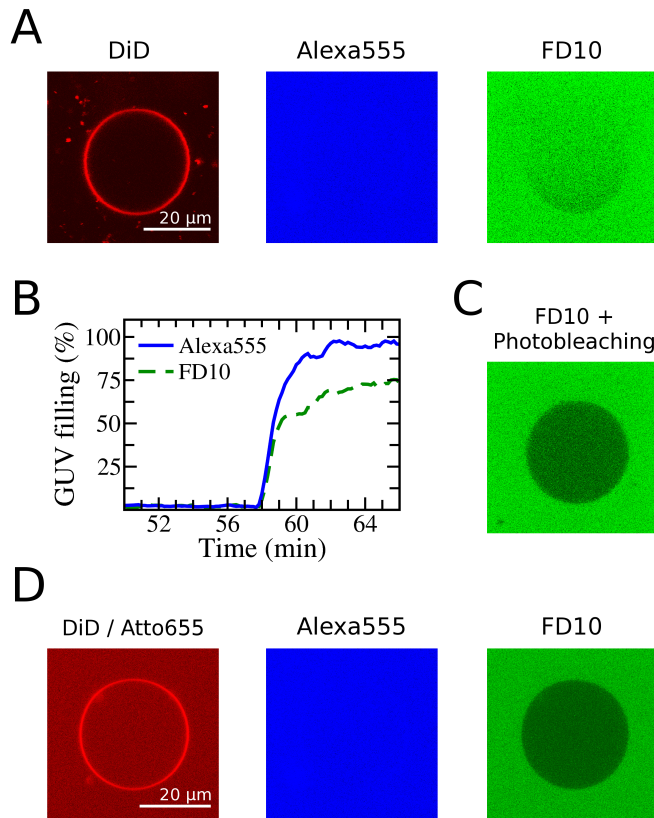


**Fig. 10.10 : Pores shrink with equilibration.** A) Example GUV (labeled with DiD, red) 2 hours after mixing in a solution containing Bax $\alpha$ 5, Alexa555 (blue) and fluorescent-dextran FD10 (green). B) Both dyes leak into the vesicle, starting simultaneously and proceeding at similar rates. However, for FD10 (green) the communication with the external pool slowed down at some time and eventually stopped before complete filling. C) Continuing irradiation at 488 nm for 2 min bleached the FD10 fluorescence only from the inside of the GUV. D) In an additional experiment DiD-labeled GUVs were first put in a solution with Bax $\alpha$ 5 and Atto655 to identify GUVs porated at short time. Two hours later, Alexa555 and FD10 were added together and the vesicles were observed. Vesicles which were initially completely permeable to Atto655 (like the example shown), were subsequently also fully permeable to Alexa555, but not to FD10. The experiments correspond to a bulk P/L of 1/22.5.

and magainin shrink with equilibration [576, 582]. Such observations can be related to a general role of amphipathic peptides for the stabilization of lipidic pores, which has been proposed previously based on theoretical arguments [76] and on single vesicle experiments [69].

#### 10.4.4 Non-equilibrium vs equilibrium pores

Our data in the case of Bax $\alpha$ 5 further evidences that pre-equilibrium and equilibrium pores, although likely related, are not identical. Pre-equilibrium pores can be seen as a response of the membrane to peptide adsorption in the accessible monolayer. A molecular mechanism for such a situation has been provided by MD simulations for the cases of melittin and magainin 2 [82, 83]. The increased interfacial area creates a tension which makes the membrane rupture. In principle, this should happen simply above a certain limit of tension, related to a limit area stress and a limit of bound peptide per unit area. However, in an asymmetrically expanded bilayer the packing of the compressed monolayer is expected to increase significantly the activation energy for membrane rupture [583]. In such a strained metastable state, pores initiate stochastically in points of nucleation of defects. On the other hand, the pore formation can generally be assisted by molecules perturbing the packing of the lipids [162, 583], for which membrane-adsorbing peptides should also play a role. The onset of peptide induced pores must be accompanied by a reorganization of the peptide/membrane complex. In turn, the pre-equilibrium pores themselves help equilibration of the peptide across the bilayer, as observed for other cases [576]. But as mass imbalance dissipates, the pores of the all-or-none type do not close as is frequently assumed. Instead, they seem to relax into stable structures which are at least smaller than the pre-equilibrium pores. It is reasonable to speculate that the stable pores would also be more organized structures.

Finally, an interesting question is the relevance of equilibrium pores vs kinetic or pre-equilibrium pores. Other peptides that follow an all-or-none mechanism, like magainin [84] and cecropin [116], may also form stable pores at equilibrium. On the other hand, peptides displaying a graded kinetics of leakage [473] can be expected to form mainly transient pores [584]. From a practical point of view the structure of transient pre-equilibrium pores is difficult, if not impossible, to characterize. Not surprisingly, the structural information normally available corresponds to equilibrated peptide/membrane complexes. Additionally, from a physiological point of view it is likely that the function of membrane active peptides occurs mainly through pre-equilibrium pores. The fact that the action of antimicrobial peptides on individual bacteria appears to be delayed and stochastic [573], in a way similar to the action over single vesicles, supports this hypothesis. This would be less clear for the case of pore forming proteins, where the process is mechanistically more complex and regulated, and may need to extend to longer times or involve different steps. In this sense, despite the simplicity of the Bax $\alpha$ 5 fragment, the stable pores reported here may well be mechanistically relevant for the function of the full length protein [258, 309]. Although still not well characterized, the pores formed by the protein Bax are likely stable and organized structures [258, 318], and this work shows that the short sequence of the  $\alpha$ 5 fragment codifies the necessary

information to induce and stabilize pores. This would be an specific property of this domain of Bax, compared to equivalent fragments of other Bcl-2 proteins of a different type, which has been selected through evolution to contribute to the function of Bax.

## 10.5 Membrane binding and leakage

### 10.5.1 The lag time of vesicle poration depends on $P/L$

One of the intriguing characteristics of single vesicle poration is the broad distribution of the lag time before the appearance of first pores, i.e. the time required for the onset of pore formation in each particular GUV (see SUB. 10.3.1 on page 212). We find that such a lag time is inversely dependent on the bulk  $P/L$  ratio (FIG. 10.5 C and TAB. 10.2). This suggests that a minimum peptide concentration in the membrane is required to drive pore formation, which is achieved faster the larger  $P/L$ .

The above uncertainties regarding the effects of the peptide may be due, at least in part, to the use of bulk  $P/L$  values, which assumes that the *bound*-peptide to lipid ratio is the same for all vesicles. However, such an assumption may not be necessarily true, and we may ask, for example, if the relatively wide distribution of pore sizes for a particular  $P/L$  could be due to an inhomogeneous peptide distribution among the vesicle population. Indeed, in the case of reconstituted peptide/GUV complexes (SUB. 10.3.2), despite the fact that they were prepared from homogeneous peptide-lipid mixtures, the peptide is found to bind rather inhomogeneously to different vesicles. Although we do not know the reasons for that observation, and conditions are very different for formation of Bax $\alpha$ 5/GUV complexes using the *addition* method (SUB. 10.3.1) we set out to study the binding of Bax $\alpha$ 5 to single GUVs and the effects of bound peptide on vesicle poration. For that we used the fluorescent labeled version of Bax $\alpha$ 5, Alexa647-Bax $\alpha$ 5 and performed fluorescence microscopy measurements at short and long times after peptide/vesicle mixing, monitoring both peptide binding and GUV leakage.

### 10.5.2 Peptide binding and pre-equilibrium GUV leakage

**Simultaneous kinetics of peptide binding and GUV leakage.** Using Alexa647-labeled Bax $\alpha$ 5 it is easy to follow peptide accumulation in the membrane of single GUVs, by measuring the fluorescence intensity at the rim of focused vesicles under the fluorescence microscope. Moreover, the leak-in kinetics of a dye present initially outside (Alexa488) can also be monitored simultaneously (see an example in FIG. 10.11 A,B).

When several GUVs are followed over time, it becomes apparent that binding and leakage are separate events (FIG. 10.11 D,E). The binding of Bax $\alpha$ 5 is preceded by a certain delay, which varies between different GUVs but is smaller than the delay for pore opening. On the other hand, in general, pores appear before the amount of Bax $\alpha$ 5 reaches a steady-state value. Instead, poration initiates at an apparently random moment during the process of Bax $\alpha$ 5 partitioning to the GUV membrane. As we already described (SUB. 10.3.1), once pore opening takes place (delayed and in an stochastic way), GUV filling is fast and complete within a few minutes. However, Bax $\alpha$ 5 binding

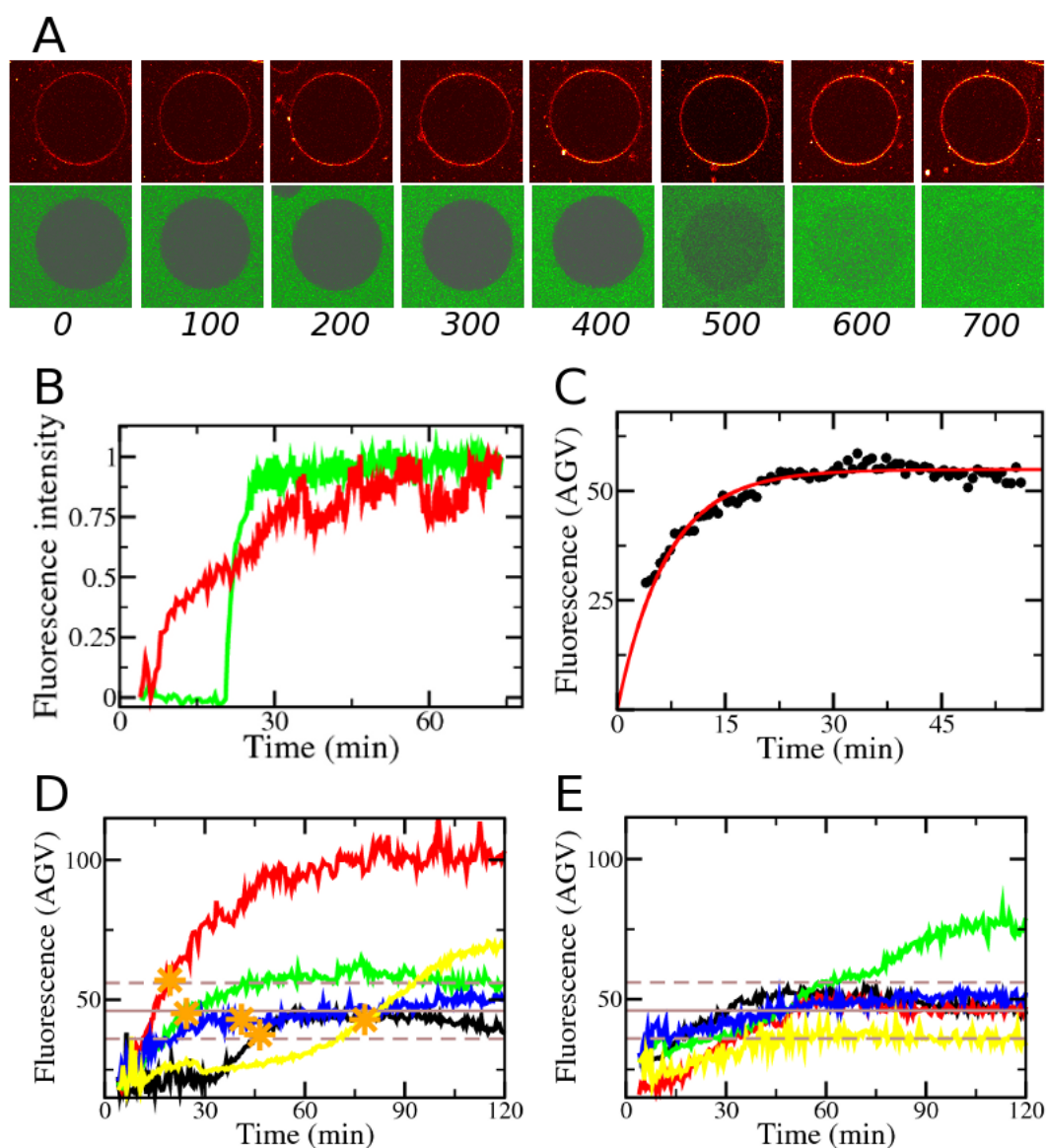


**Fig. 10.11 : Simultaneous monitoring of binding of Bax $\alpha$ 5 and permeabilization on single GUVs.** A) Time series of Alexa647-Bax $\alpha$ 5 GUV binding (top row, red color) and Alexa488 leak-in, (bottom row, green). The numbers under the figures are times after adding an aliquot of GUVs over the a well mixed solution containing Alexa647-Bax $\alpha$ 5 and Alexa488. B) Plot of the binding kinetics of Alexa647-Bax $\alpha$ 5 (red) and the leak-in kinetics of Alexa488 (green) both referring to the same single GUV. The data are normalized with respect to the maximum fluorescence signal on each case. Note the apparent uncoupling between the two events. C) Example fit of the kinetics of Alexa647-Bax $\alpha$ 5 binding to a single GUV using EQ. 10.11. D) Different individual GUVs display different binding kinetics, but membrane permeabilization mainly occurs when the amounts of Bax $\alpha$ 5 in the bilayer (marked with asterisks) fall within a certain range. E) Same as D) but for non-porated GUVs (during 2 h of observation).

**Tab. 10.2 : Effect of the P/L on the kinetics of peptide binding and pore formation.**

P/L <sup>a</sup>	Binding		$C_{open}$ (AGV) <sup>d</sup>	Poration	
	$\delta_{on}$ (min) <sup>b</sup>	$\tau_{on}^{app}$ (min) <sup>c</sup>		lag-time (min) <sup>e</sup>	$k_{open}$ (min <sup>-1</sup> ) <sup>f</sup>
1/90	3.7±0.8	21±3	43±9	22±10	0.051±0.011
1/180	7±3	15±6	43±8	27±16	0.045±0.006
1/360	5±2	15±6	46±9	34±18	0.035±0.006
1/720	6±2	15±12	49±12	47±26	0.025±0.004
Average±SD			45±10		

<sup>a</sup>Bulk peptide-to-lipid molar ratio.

<sup>b</sup>Time needed to observe a measurable fluorescence signal arising from Alexa647-Bax $\alpha$ 5 on the GUV membrane. The threshold was set to 16 (AGV units).

<sup>c</sup>Apparent time constant for the binding of Alexa647-Bax $\alpha$ 5 to the GUV membrane.  $\tau_{on}^{app}$  is the reciprocal of  $k_{on}^{app}$  (see reaction scheme in SUB. 5.4.1). It is an “apparent” value since it includes the effect of  $k_{off}$  and the lipid concentration.

<sup>d</sup>Averaged values (over the total number of GUVs analyzed for each P/L) of the critical amount of Alexa647-Bax $\alpha$ 5 in the membrane at the onset of pore formation  $\pm$  SD.

<sup>e</sup>Elapsed time from the moment of GUV addition until the onset of pore formation.

<sup>f</sup>Rate constant for the appearance of porated GUV.

to membranes continues, even while leakage is complete, and eventually stabilizes. The recorded binding kinetics for GUVs that eventually become porated (FIG. 10.11 D) does not differ appreciably from those of GUVs that remain intact (FIG. 10.11 E), although on average non-porated vesicles have lower amounts of bound Bax $\alpha$ 5. We were able to analyze some binding kinetics using a single exponential function involving an apparent binding time constant,  $\tau_{on}^{app}$ , shifted by a binding delay time,  $\delta_{on}$ , which took into account the time needed to get a measurable signal (an example is shown in FIG. 10.11 C):

$$F_{Bax\alpha 5}(t) = \Gamma \left( 1 - e^{-(t-\delta_{on})/\tau_{on}^{app}} \right) \quad (10.11)$$

where  $\Gamma$  is an amplitude factor, since we are using unnormalized AGV units,  $\delta_{on}$  is the lag time for the onset of observable peptide binding and  $\tau_{on}^{app}$  is the characteristic time constant for the kinetics of peptide binding. After fitting this function to binding kinetic traces, we obtained values of  $\delta_{on}$  and  $\tau_{on}^{app}$  shown in TAB. 10.2. As it can be expected,  $\delta_{on}$  decreases with increasing the bulk P/L; however,  $\tau_{on}^{app}$  appears invariable between P/L=1/720 and P/L=1/180, but increases slightly for P/L=1/90. We also give values of the fluorescence of labeled Bax $\alpha$ 5 at the onset of leakage and the corresponding lag time corresponding to the leaky state (TAB. 10.2). The first ones represent the *critical amount* of membrane-bound Bax $\alpha$ 5,  $C_{open}$ . According to FIG. 10.12 A, although  $C_{open}$  is variable for individual GUVs, the distributions for different bulk P/L are similar. In fact, the averaged values,  $\overline{C}_{open}$ , are very close for all assayed P/L ratios (TAB. 10.2). Moreover, the accumulated distribution approximates to a Gaussian shape (FIG. 10.12 B) where the global critical value,  $\overline{C}_{open} = 45$  AGV, stands as a characteristic

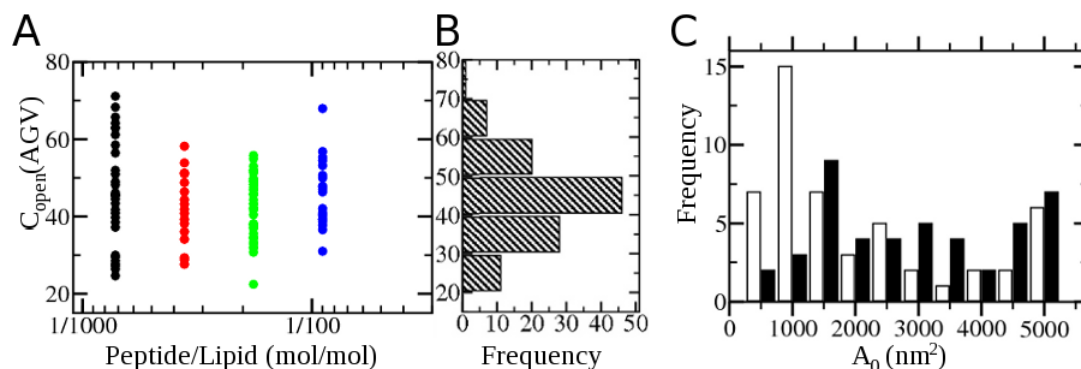


**Fig. 10.12 : Effect of the amount of Bax $\alpha$ 5 bound to the GUV membrane on vesicle poration.** A) Plot of the amount of Alexa647-Bax $\alpha$ 5 bound to the membrane (AGV units) at the onset of pore formation (critical amount of Bax,  $C_{open}$ ) as a function of the bulk P/L: 1/720 (black), 1/360 (red), 1/180 (green) and 1/90 (blue). B) Histogram showing the cumulative distribution of the individual points in graph A. C) Histogram depicting the distributions of total pore size for vesicles that became porated with Alexa647-Bax $\alpha$ 5 amounts above (black bars) and below (white bars) the average  $\bar{C}_{open}$  value (45 AGV units) corresponding to the distribution in B.

parameter of the system. Interestingly, apart from *controlling* the pore onset,  $\bar{C}_{open}$  appears to determine the total pore size. Thus, if we split the frequency distribution of total per-vesicle pore size for pre-equilibrium pores, in sub-distributions corresponding to GUVs with  $C_{open} < \bar{C}_{open}$  and GUVs with  $C_{open} > \bar{C}_{open}$  (FIG. 10.12 C), we find clearly smaller averaged equivalent pores ( $\bar{A}_0 \sim 2000 \text{ nm}^2$ ) for GUVs porated at smaller critical amounts of bound Bax $\alpha$ 5 compared to those porated at high peptide densities ( $\bar{A}_0 \sim 3000 \text{ nm}^2$ ).

**Kinetics of poration in the GUV ensemble.** Although it is clear from the discussion above that a critical density of membrane-bound peptide is required for pore opening, other factors must also influence pore induction since not all GUVs with an amount of bound Bax $\alpha$ 5 above the value of  $\bar{C}_{open}$  become leaky, at least during the time of observation (FIG. 10.11 E). The kinetics of appearance of porated GUVs can be used to estimate the rate constant of pore formation,  $k_{open}$  (EQ. 5.67). As expected,  $k_{open}$  increases with the bulk P/L, indicating that higher total peptide concentration, relative to the lipid concentration, increases the probability of opening pores in vesicles.

### 10.5.3 Peptide binding and pores at equilibrium

The absolute concentration of Bax $\alpha$ 5 in the membrane was analyzed by two-foci scanning fluorescence correlation spectroscopy, SFCS (see SUB. 5.5.3)<sup>1</sup>. This novel technique

<sup>1</sup> SFCS has some inherent limitations that must be considered: First, measurements can be performed only for constant total fluorescence, i.e., the method is useful only for equilibrium or steady-state concentrations. In addition, the measurement time is relatively large: in the order of 10 min. Both factors

gives access simultaneously to values of number ( $N$ , in particles per  $\mu\text{m}^2$ ) and diffusion coefficient ( $D$ , in  $\mu\text{m}^2/\text{s}$ ) of fluorescent particles [483] (see TAB. 10.3). This allows extracting the number of diffusing particles per unit area, which, given a value of the area per lipid [554, 585], can be used to calculate the in-membrane  $P/L$  molar ratio.

As we have described above (SUB. 10.3.2), the distribution of Alexa647-Bax $\alpha$ 5 among vesicles in samples prepared by reconstitution is rather inhomogeneous. The peptide accumulates more in some GUVs, without any apparent reason, and does not seem to re-equilibrate after the vesicles are formed. We measured the diffusion coefficient of Alexa647-Bax $\alpha$ 5 annotating whether the observed GUV was, or was not porated (FIG. 10.13 B). In general, diffusion coefficients are lower in the case of porated GUV, suggesting the presence of peptide aggregates. To test this hypothesis, we estimated the hydrodynamic radius of the diffusing particles as described in [586] (TAB. 10.3). The size of Bax $\alpha$ 5 particles in non porated GUV was 0.5 nm on average, which is compatible with the presence of a monomeric peptide. However, in porated GUVs the averaged hydrodynamic radius of Bax $\alpha$ 5 particles increases up to 2.2 nm. This value suggests the presence of oligomers in the membrane, although the molecular mass of the molecules involved in the aggregates cannot be readily determined. It seems clear, however, that Bax $\alpha$ 5 oligomerization (smaller  $D$ ) is connected to pore formation (FIG. 10.13 C) and this result gives functional relevance to our previous finding of Bax $\alpha$ 5 self-assembly (CHAP. 8)

After determining the  $P/L$  ratios corresponding to Bax $\alpha$ 5 bound to GUVs, we can analyze pore formation with respect to the real peptide density in the membrane. At first sight we observed an apparent weak relationship between the amount of bound peptide and vesicle leakage (FIG. 10.13 A), with porated or non porated GUVs being observed irrespectively of the value of  $P/L$ . However, a careful examination showed that the porated state was more frequent at increasing  $P/L$  (FIG. 10.13 B). The probabilities of finding a porated GUV, calculated as ratios between porated and non porated vesicles, plotted against the *bound*- $P/L$  ratio FIG. 10.13 D look similar to a typical dose-response trend (FIG. 10.14). Such probabilities are displaced with respect to the analogous plot corresponding to bulk  $P/L$  ratios, which appears shifted to higher  $P/L$  values (FIG. 10.13 D). The shift may be understood as corresponding to the equilibrium of partition of the peptide between the membrane and the water solution and the corresponding equilibrium association constant can be extracted (see TAB. 10.3). This  $K_A$  value is similar to those found for the association between other pore-forming peptides and negatively charged vesicles [65].

---

contribute to make these measurements impractical for studying Bax $\alpha$ 5 concentration for the case of pre-equilibrium pores. Second, this is a single molecule technique that makes use of high sensitivity photon detectors. Thus, high particle concentrations cannot be easily measured. One possible solution is using mixtures of labeled and unlabeled Bax $\alpha$ 5. However, both peptide variants may behave differently and our experimental conditions are far from ideal mixing. Thus, we have always used the same stock of Alexa647-labeled Bax $\alpha$ 5 at the same bulk concentration.

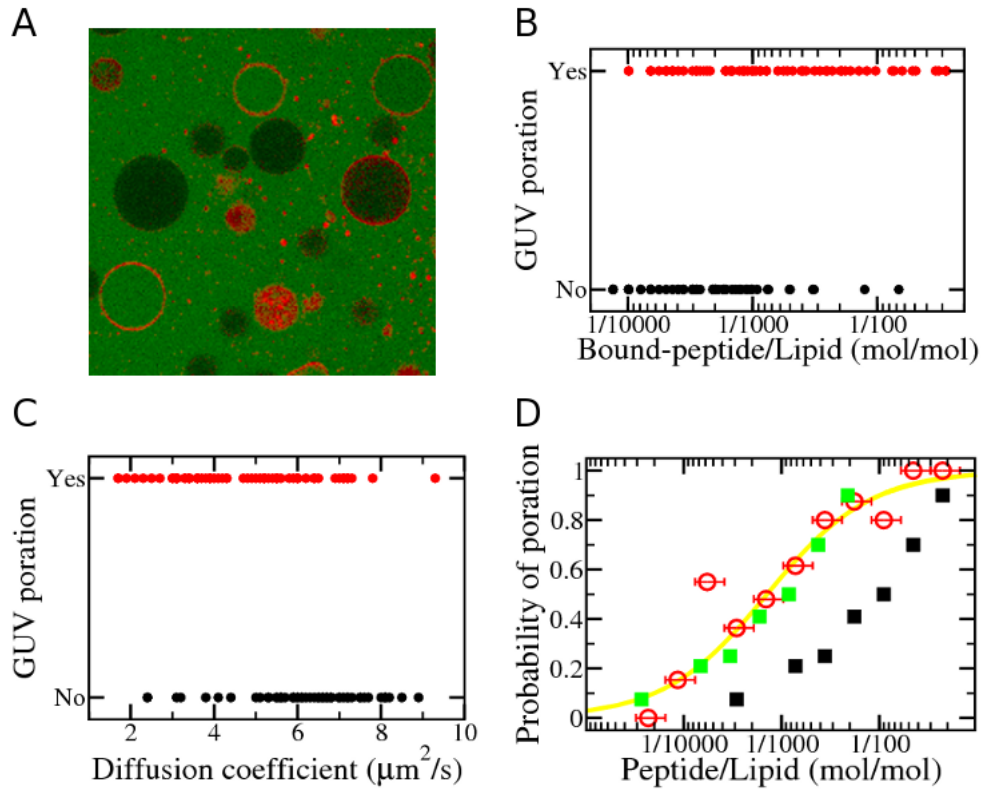


**Fig. 10.13 : Vesicle poration at equilibrium depending on Bax $\alpha$ 5 bound to the membrane.** A) Image showing the heterogeneous distribution of Alexa647-Bax $\alpha$ 5 in GUVs after 2h incubation. The entrance of Alexa488 from the outside solution allows distinguishing porated from non porated GUVs. B)  $P/L$  ratio corresponding to membrane-bound Alexa647-Bax $\alpha$ 5 measured by SFCS in porated (red circles) and non porated (black squares) GUVs. C) Diffusion coefficient of Alexa647-Bax $\alpha$ 5 in porated (red circles) and non porated (black squares) GUVs. F) Probability of finding a porated GUV at equilibrium conditions, depending on either the  $P/L$  ratio corresponding to membrane-bound Alexa647-Bax $\alpha$ 5 (red circles) or the bulk  $P/L$  ratio (black squares). The line is the best fit of experimental data to a dose-response model (see the text). The green squares show the expected peptide(membrane-bound)/lipid ratio calculated from the bulk peptide/lipid given a  $K_A = 20000 \text{ M}^{-1}$ .

**Tab. 10.3 : Parameters derived from the SFCS analysis of Alexa647-Bax $\alpha$ 5/GUV complexes.**

GUV	$N^a$	$D$ ( $\mu\text{m}^2/\text{s}$ ) <sup>a</sup>	$R_H$ (nm) <sup>b</sup>	$K_A$ ( $M^{-1}$ ) <sup>c</sup>
<i>Porated</i>	189 $\pm$ 337	4.7 $\pm$ 1.7	2.2	20000 $\pm$ 1000
<i>Non porated</i>	39 $\pm$ 88	6.3 $\pm$ 1.6	0.5	

<sup>a</sup>Raw data from the SFCS experiment.  $N$  is the number of particles in the focal area and  $D$  is the particle diffusion coefficient.

<sup>b</sup>Average hydrodynamic radius, estimated from the diffusion coefficient as described in [586].

<sup>c</sup>Equilibrium association constant estimated by comparison of the dosis-response curves plotted as a function of the bulk Bax $\alpha$ 5 concentration and the membrane-bound Bax $\alpha$ 5 concentration. The shift between the two curves is due to the equilibrium between free and membrane-bound Bax $\alpha$ 5.

## 10.6 Comparing leakage in GUVs and LUVs

Finally, it is interesting to compare the release of contents from LUVs with the leakage studied with single GUVs. In FIG. 10.5 A we saw that the variation in the percentage of filled GUVs over time increases gradually until a steady-state, approximately 1.5 h after peptide addition. A similar stabilization is also observed for the kinetics of peptide binding (FIG. 10.11 D and E). Although the first observation refers to the complete ensemble of GUVs and the second to the equilibration of single GUVs, it is tempting to speculate with a possible relationship between the two. Thus, we suggest that the opening of pores in the membrane is closely connected to the process of equilibration of the peptide/vesicle complexes. On the other hand, as we pointed out before the dosis-response behavior is similar for suspensions of LUVs and GUVs (FIG. 10.14), with the small discrepancies between the two being perhaps due to the apparently poor statistics of the GUV data (where about 100 vesicles were assayed, compared to millions present in a typical LUV sample).

## 10.7 Conclusions

1. Bax $\alpha$ 5 induces and stabilizes long lived pores that exist at equilibrium in both suspensions of LUVs and ensembles of GUVs. These appear to be mechanistically related to pre-equilibrium pores, as the long-term ones are formed in the same vesicles after relaxation of the short-term pores.
2. The kinetics of short-term, long-term and equilibrium pores can be well fitted with a model derived from the Fick's law of diffusion which allows estimation of an equivalent (total) pore area per vesicle. Some kinetics are best fit with a model considering a constant pore area, while others necessitate a shrinking pore model.
3. Individual equilibrium pores stabilized by Bax $\alpha$ 5 have a smaller size ( $\sim$ 2.3 nm in

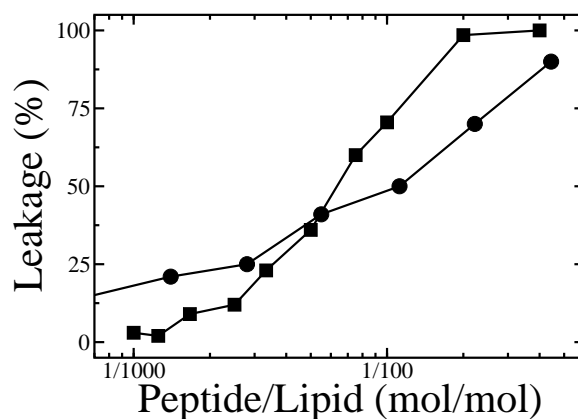


**Fig. 10.14 : Single GUV vs ensemble LUV.** Dose-response curves for the GUV approach (circles) and the LUV approach (squares). P/L ratios are nominal. The lipid composition is POPC:CL (80:20).

radius) than individual pre-equilibrium pores. Changes in the number of individual pores cannot be easily determined.

4. Bax $\alpha$ 5 permeabilizes vesicles mainly in an all-or-none fashion: at any time individual vesicles are either completely full of dye or completely empty.
5. A critical concentration of membrane-bound Bax $\alpha$ 5 is necessary, but not sufficient, to trigger pore formation. The probability of finding a porated vesicle increases with  $P/L$  but for any given bound-peptide/lipid ratio a vesicle may or may not become porated. Therefore both the membrane-bound concentration of Bax $\alpha$ 5 and stochastic factors contribute to the opening of pores.

# 11 General discussion, perspectives and conclusions

Throughout the previous Chapters the results of this Thesis have been described, analyzed and discussed in detail. Here is a more general discussion, which integrates the most important aspects treated in different results Chapters, followed by perspectives and a summary of the main conclusions

## 11.1 General discussion

### 11.1.1 Energetics of Bax $\alpha$ 5-membrane interactions

We have seen that the action mechanism of pore-forming peptides can be conceptualized in distinct steps: (i) peptide partition/binding to the membrane, (ii) peptide insertion and folding to form independently stable helices at the lipid bilayer, (iii) helix association to form a helix bundle intermediate, and (iv) further rearrangements leading to the opening of peptide-lipid toroidal pores. All these processes are accompanied by a release of energy, so thermodynamic studies can provide insights regarding pore formation. The first three steps are common to other membrane-interacting peptides [24, 587] so that pore-forming peptides are unique in their ability to promote pore formation and stabilization.

The peptide binding to POPC membranes was monitored by CD spectroscopy by measuring the increase in ellipticity upon peptide partitioning-folding as a function of the lipid concentration, and the free energy of water-bilayer partitioning,  $\Delta G_x$ , was found to be  $\sim -6$  kcal/mol (CHAP. 7). Similar values have been reported for other amphipathic peptides [65]. Note that this value includes the free energies of peptide-membrane binding and peptide folding. The free energy of dimerization,  $\Delta G_{dimer}$ , calculated from the fraction of dimeric peptide (taken from the corrected FRET efficiencies) as a function of  $P/L$  was  $\sim -4$  kcal/mol (CHAP. 8), which is less than the dimerization strength of glycoporphin [434] but similar to that found for other transmembrane helix dimers [445]. However, our peptide is not a classical TM peptide, since it binds to the lipid bilayer interface, and there are no similar cases studied for comparison. The free energy of pore formation,  $\Delta G_{pore}$ , has not been determined.

Since pore-forming peptides accelerate the leakage of vesicles, the peptide action can be formulated as a *catalysis-like* effect, depicted graphically in FIG. 11.1 as the free energy along the reaction coordinate. Starting from peptide and membrane free species, an initial membrane-peptide complex is formed favorably ( $\Delta G_x < 0$ ), with peptides adsorbed at the interface. Then peptides self-assemble into dimeric species ( $\Delta G_{dimer} <$

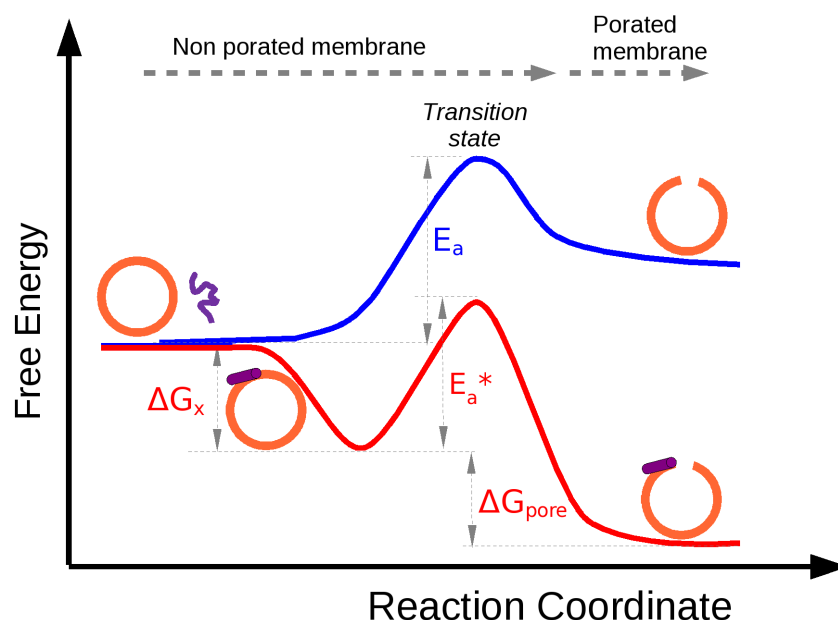


**Fig. 11.1 : The action of Bax $\alpha$ 5 understood as a catalysis-like effect.** The blue line shows the free energy as a function of the reaction coordinate (pore formation) for vesicles porated in the absence of peptides. Such free energy is positive in agreement with the fact that the spontaneous formation of pores has very low probability. The red line shows the change in the free energy profile of a vesicle with a pore-forming peptide bound to it. Amphipathic peptides bind spontaneously to the bilayer interface ( $\Delta G_x < 0$ ). The vesicle-peptide complex has then a lower free energy level than free vesicle and peptide molecules. On the other hand, peptides are postulated to bind more strongly in zones of bilayer defects, which would correspond to a *transition state* in the way to pore formation. In such a state lipids reorient before a lipidic pores appear, which involves an activation free energy  $E_a$ . The peptide, bound to the membrane at a certain threshold density, reduces such an activation energy ( $E_a^* < E_a$ ). Additionally, after the pore is formed, binding of the peptide near the pore rim stabilizes it via reduction of the line tension ( $\Delta G_{pore} < 0$ ). Notice that the first part of the transformation resembles a catalyzed reaction. The scheme is general, and would be valid for monomeric and dimeric (or oligomeric) active peptides. The free energy of dimerization ( $\Delta G_{dimer} < 0$ ) has not been included in the diagram, for the sake of clarity.

0, not shown in the figure for the sake of simplicity). As peptides accumulate, the lipid bilayer is stretched asymmetrically causing thinning and increase of fluctuations. Peptides are postulated to bind more strongly in zones of bilayer defects [113, 555], which would likely correspond to the the *transition state* towards pore formation. We postulate a catalysis-like action of the peptide which consists of a reduction of the activation free energy ( $E_{a^*} < E_a$ ) for lipid reorientation and lipidic pore formation. The  $E_{a^*}$  energy barrier is expected to decrease with increasing the density of the membrane-bound peptide. Additionally, after the pore is formed, binding of the peptide near the pore rim stabilizes the pore, i.e.  $\Delta G_{pore} < 0$  via reduction of the line tension due to peptide action [555].

### 11.1.2 Kinetics of Bax $\alpha$ 5-membrane interactions

In this Thesis we have investigated thoroughly the kinetics of leakage of encapsulated dyes induced by Bax $\alpha$ 5 (CHAP. 10). For single GUVs, most kinetics traces can be well fitted taking into account the first Fick's law of diffusion [61]. According to this law, the time needed for leakage through individual pores increases with the vesicle volume and the length of the pore (which corresponds basically to the thickness of the membrane). On the other hand, large diffusion coefficients (dyes of small size) and large pore sizes reduce the release time. However, this law assumes a constant pore size over time and we have shown that pores shrink on a time range of a few minutes. Pore shrinkage within the release time window could be observed in a few cases, where the leak-in kinetics displayed a fast initial phase followed by a slow one. This could be well fitted by considering a relaxation of the total pore area per vesicle from an initially large value ( $A_0$ ) to a final stable smaller value ( $A_\infty$ ). Alternatively  $A_\infty$  can be estimated adding a *second* dye after steady-state conditions are achieved<sup>1</sup> ( $\sim 2$ h in the present case). Therefore, the analysis allows extracting information about an *equivalent* pore size from the leakage kinetics of individual GUVs. However, these size values include information about the area of individual pores and the number of pores, which cannot be easily separated.

In order to probe individual pore sizes we used a large fluorescent dextran, FD10, which confirmed the shrinkage of Bax $\alpha$ 5-induced pores from  $>2.3$  nm in radius at short term to  $\sim 2.3$  nm at long term. Thus, our results show unambiguously that the reduction of the total pore area upon equilibration is at least partially due to a reduction of the size of individual pores, although changes in the number of pores cannot be discarded.

Regarding the interpretation of the kinetics from LUV samples, the situation is much more complex because other factors, apart from those related to the release itself (pore size and relaxation time) must be taken into account. For example, processes that eventually lead to pore opening, like peptide binding, secondary structure acquisition, oligomerization, configuration of the active pore structure, etc must also be considered. In particular, attention should be paid to the rate-limiting step which will dominate the observed kinetics, as it has been thoroughly discussed in the literature. Peptide binding and aggregation are usually very fast compared to the time scale of leakage and

<sup>1</sup> Steady-state (ideally equilibrium) conditions are achieved when neither the vesicle-bound peptide density nor the number of porated vesicles changes over time.

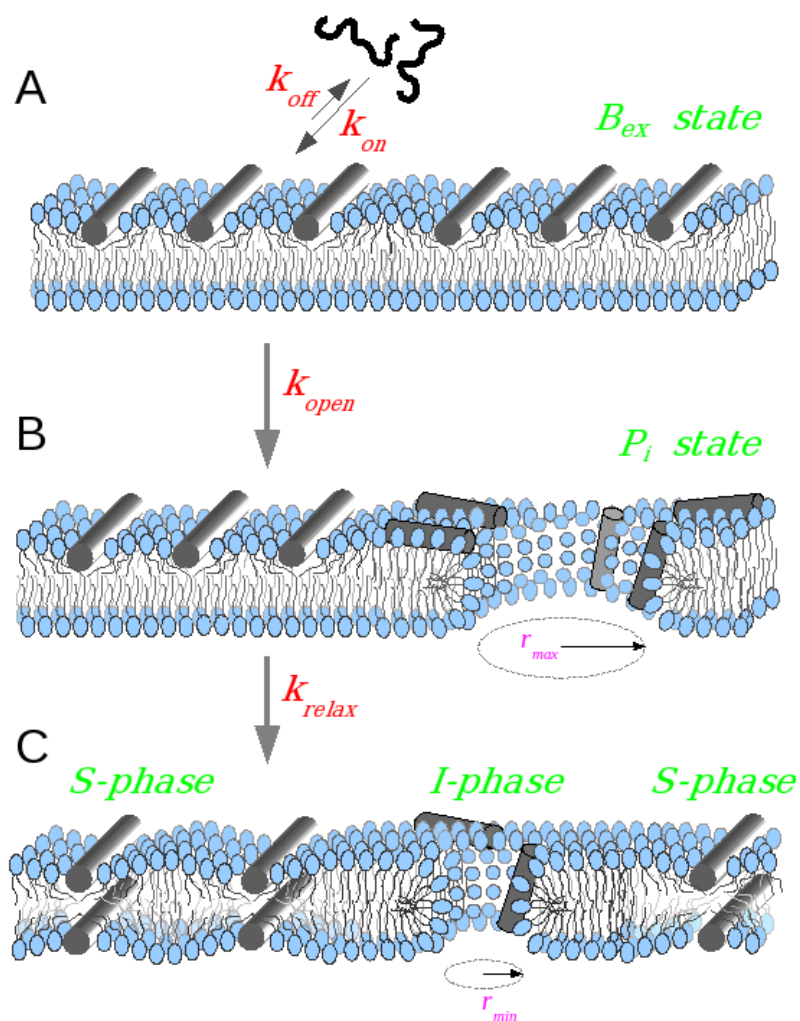


**Fig. 11.2 : Kinetic model for pore induction by amphipathic cationic peptides.** A) Pore active peptides bind avidly to the accessible interface of lipid bilayers, and peptide binding is coupled to folding (in this case as an  $\alpha$ -helix, represented by a cylinder). The volume of the bound peptides corresponds mainly to the interfacial region, thus causing asymmetric area stretching and membrane thinning. In the so called  $B_{ex}$  state [85], membrane perturbation increases with the amount of bound peptides. B) Eventually, the membrane yields and a pore is formed (so called  $P_i$  state [85]). The initial pore is large ( $r_{max}$ ). C) The peptides bind near the pore rim and reduce the line tension, until an equilibrium is reached with a smaller ( $r_{min}$ ) but stable pore. The appearance of pores can be understood like a phase transition, and in the equilibrium state two phases coexist [114, 141]: namely  $S$ , with peptides bound essentially parallel to the membrane and lamellar bilayer lipids, and  $I$ , with peptides exhibiting a certain tilt near the rim of pores and the pore wall formed by non-bilayer lipids.

thus they are usually ignored [570]. Pore deactivation [580], the competition between empty and full vesicles, especially at long times [84, 116], and slow fluctuations in the number of bound peptides per vesicle [570] have all been suggested as possible reasons for slowing down the leakage kinetics. Our results with GUVs, like others using different peptide and proteins systems, show that the onset of pores is delayed and stochastic. Additionally, there is a small, but not negligible, percentage of vesicles whose pores shrink in a relatively small time scale (see values of  $\tau_{relax} = 1/k_{relax}$  in TAB. 10.1) therefore, increasing the time for complete marker release. As a result we propose that the major determinant of the initial leakage rate in LUV suspensions is the relatively low probability for opening a pore, related to the rate constant  $k_{open}$  (see TAB. 10.2). This is expected to be smaller in GUV experiments due to the absence of stirring and larger surface area per vesicle. Also, at long times the release rate may be slowed down due to the presence of a small population of fast relaxing vesicles with pores of small size, and therefore reduced permeability.

In summary, Bax $\alpha$ 5, and probably other pore-forming peptides, porate vesicles according to the following kinetic mechanism (see FIG. 11.2): (i) peptides bind to the bilayer interface with a rate constant  $k_{on}$  (see values of  $\tau_{on}^{app} = 1/k_{on}^{app}$  in TAB. 10.2) causing area stretching and membrane thinning. This state may correspond to the kinetic  $B_{ex}$  state proposed by TAMBA and YAMAZAKI [85, 86]. (ii) A pore opens stochastically with a rate constant  $k_{open}$  partially depending on the peptide concentration. Such *initial* pores are big (corresponding to a big equivalent pore radius,  $r_{max}$ ). This may correspond to the  $P_i$  state proposed by TAMBA and YAMAZAKI [85, 86]. (iii) The peptide/vesicle complexes equilibrate with a rate constant  $k_{relax}$ . This involves equilibration of the peptide molecules across the initial pores and reduction of the line tension, which stabilizes the pores to a smaller size (corresponding to a small equivalent pore radius,  $r_{min}$ ). The final equilibrium state may correspond to the co-existence of the  $I$ - and  $S$ -phases, described on the bases of structural measurements by HUANG in reconstituted peptide-lipid systems [114, 141].

### 11.1.3 Structure of Bax $\alpha$ 5/membrane complexes

We emphasized in CHAP. 9 that in order to understand the function of membrane-interacting peptides it is necessary to study them in complex with lipid bilayers. Regarding the peptide, we have described the secondary, quaternary and quinary structures of Bax $\alpha$ 5. Bax $\alpha$ 5 was found to be mostly  $\alpha$ -helical (60-80%), with some dependence on the membrane preparation and method used (SEC. 7.2)

We have shown in CHAP. 8 that Bax $\alpha$ 5 is able to self-assemble in bilayers and lipid-mimetic media. For instance Bax $\alpha$ 5 forms dimers in the presence of the detergent SDS (as seen by SDS-PAGE, SEC. 8.2) or in POPC liposomes (as seen by FRET measurements, SEC. 8.3). It was further concluded that the two monomers in the Bax $\alpha$ 5 dimer arrange in a parallel orientation. However, the relatively small free energy of dimerization (compared with other well-known transmembrane helix dimers [434]) suggests that the monomers and dimers are in equilibrium in the membrane-bound active state. Moreover, the use of lipid mixtures including mitochondrial lipids, like CL,

induced the appearance of larger oligomeric states, although it is difficult to determine the number of subunits involved (SEC. 8.5).

In support for an active role of such oligomers in pore formation we can cite two pieces of evidence. On the one hand, the small diffusion coefficient of Bax $\alpha$ 5 in POPC:CL GUVs estimated by SFCS (SUB. 10.5) supports the presence of large aggregates in this phospholipid composition. The fact that the oligomers increase in porated vesicles provides a correlation, not necessarily causality, between aggregation and pore formation. On the other hand, the HILL coefficient larger than one in POPC and two in POPC:CL, respectively, also suggest that at least dimers are involved in the induction of leakage from LUVs (SEC. 10.2.1). Nevertheless, the combined role of lipid composition and peptide assembly is difficult to evaluate, since CL has an inhibitory effect on pore formation.

Additionally, we showed that Bax $\alpha$ 5 is able to interact with other Bcl-2 family polypeptides like Bcl-xL $\Delta$ Ct and Bcl-xL $\alpha$ 5. The importance of Bax $\alpha$ 5 hetero-interactions was further evaluated. One of the mechanisms by which Bcl-xL counteracts Bax function is by heterodimerization, which gives rise to pore-incompetent Bax molecules [269]. However, no effect on Bax $\alpha$ 5 leakage activity was observed upon interaction with either Bcl-xL $\Delta$ Ct or Bcl-xL $\alpha$ 5. Thus, Bax $\alpha$ 5, as a minimal active domain, seems able to escape to the tight inhibitory regulation of apoptosis via antiapoptotic proteins, and this could be useful for the design of therapeutic applications of this peptide.

With respect to the peptide orientation in the membrane, the Bax $\alpha$ 5 helix director was found to be almost perpendicular to the bilayer normal of POPC membranes suggesting an interfacial binding mode of interaction (FIG. 11.3 B). On the other hand, in DMPC membranes Bax $\alpha$ 5 was more tilted (FIG. 11.3 A). In order to understand the sensitivity of Bax $\alpha$ 5 to the lipid composition we studied systematically different lipid parameters such as acyl chain length and fluidity. The peptide tilt was shown to decrease with increasing bilayer thickness. Finally, a greater membrane fluidity was associated with a larger tilt. Clearly, the orientation of Bax $\alpha$ 5 in membranes depends on the background physical chemistry of lipids, which in turn the peptide is also able to affect.

Perhaps the most surprising fact was the absence of a clear change in the tilt angle as a function of  $P/L$ . According to the two-state hypothesis the tilt angle subtended by a peptide is one of the critical factors that tell us whether the peptide is in an inactive or active (pore) state, since peptides in the pre-pore state are supposed to be surface-bound while peptides in the pore state would be essentially transmembrane [141]. From the GUV experiments we know that the vesicle pore state is stable over time. Therefore, we also expect that some pores will be present in the IR samples. Thus, if pores would be associated with peptides aligned at a small angle with respect to the membrane normal, one possible explanation of the orientation found would be that only a small fraction of the peptide population is actually in the pore state. Indeed, some calculations suggests a number of active peptides per vesicle close to one [570, 572]. Thus the relation between the peptide-tilt state and pore activity seems to be less direct than previously thought, at least when we are looking at the complete peptide population. Indeed, the orientation of Bax $\alpha$ 5 is similar in POPC and DOPC:CL membranes while the leakage activity is clearly weaker in the presence of CL. The establishment of orientation-activity relationships is also hampered by the fact that it is not easy to study the leakage kinetics

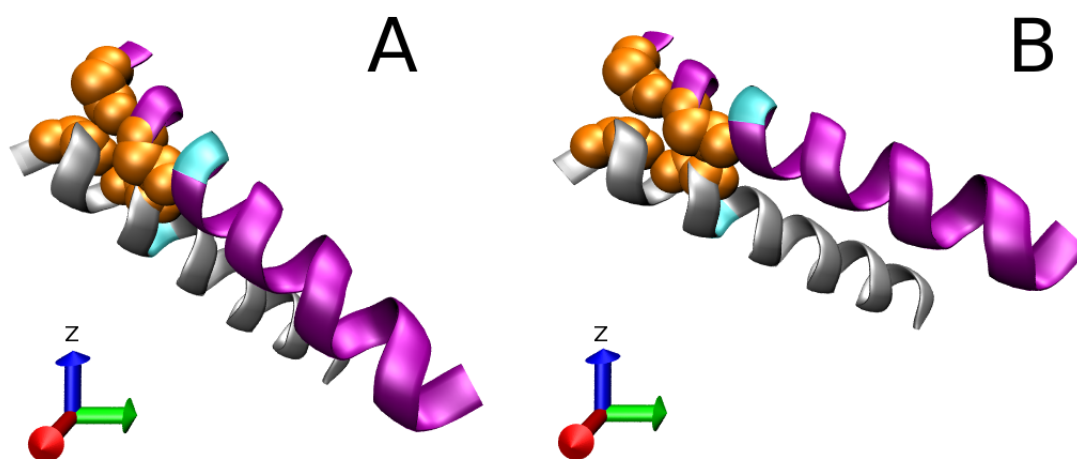


**Fig. 11.3 : Molecular models of Bax $\alpha$ 5 orientation in lipid bilayers.** The pictures show the result of applying rigid body modeling with selection based on a  $\chi^2$  error function and a starting structure assumed similar to the glycophorin A dimer. A) The best fit orientation of Bax $\alpha$ 5 in DMPC was found for the following  $\{\beta, \omega\}$  pairs:  $\{59^\circ, 157^\circ\}$  and  $\{51^\circ, 10^\circ\}$  for each monomer. B) In POPC, the best fit orientation of the Bax $\alpha$ 5 dimer was found for the following  $\{\beta, \omega\}$  pairs:  $\{74^\circ, 157^\circ\}$  and  $\{60^\circ, 20^\circ\}$  for each monomer (asymmetric dimer). The *small* Gly108 and Ala112 residues are depicted as VAN DER WAALS spheres and the critical Tyr115 residues are shown in cyan.

in DMPC vesicles due to the strong background release of entrapped dyes for this lipid composition. It would be interesting, although very difficult, to monitor the orientational of single peptides during the process of pore formation.

On the other hand, the exact values of the orientational parameters, i.e. tilt and rotational angle, are dependent on whether disorder and/or oligomerization is taken into account. Most structural descriptions of membrane-embedded peptides have been based on static models described by theoretical equations (in this Thesis referred to as the implicit landscape analysis) which neglect fluctuations of their position and orientation. However, the NMR community is beginning to accept the importance of taking into account peptide dynamics, in order to describe correctly their structure in membranes [421, 422]. The work done in CHAP. 9 goes beyond previous considerations of disorder for the case of IR measurements [386, 420]. Disorder can be accounted for by introducing Gaussian distributions of the tilt and rotational angle. In addition, the SSID data analysis has been performed so far by directly resolving the theoretical equations for each of two label pairs, making it difficult to evaluate the goodness of solutions [415]. Comparing theoretical and experimental data can be better performed using error functions like *rmsd* or  $\chi^2$ . In this manner, the complete orientational landscape is probed and the goodness of the solution can be easily checked by plotting the results which are below the experimental error. We have also shown the utility of the rigid body modeling strategies where the complete orientational landscape of the peptide is first generated explicitly [424]. This approach is especially useful for the modeling of helix bundles

since different oligomeric structures can be generated first and then checked against the experimental constraints. One main advantage is that we can challenge starting structural models other than ideal canonical  $\alpha$ -helices in a monomeric state. For example, we found that experimental data are reasonably well represented by dimeric models of Bax $\alpha$ 5 constructed using the structure of glycoporphin A as a scaffold. Although more specific structural information is needed, this solution seems a good model for Bax $\alpha$ 5 in membranes.

We also investigated the structure of the phospholipid bilayer by XS and IR. Bax $\alpha$ 5 provoked a measurable decrease in the bilayer thickness. Such behavior has been observed for antimicrobial peptides and interpreted as a consequence of the peptide being at the membrane interface, i.e., stretching the membrane area and concomitantly decreasing membrane thickness due to the low volume compressibility of lipids [319, 588]. However, under our experimental conditions, we interpret that such effect is coupled with a transition from a thicker gel phase POPC membranes, present in the absence of peptide, to a thinner liquid crystalline phase at increasing amounts of membrane-bound Bax $\alpha$ 5. This increase in fluidity had also its hallmark in the infrared spectra, where it induced a shift in the vibration frequency of some lipid moieties and an increase in lipid tilt.

### 11.1.4 The Bax $\alpha$ 5 code

This Thesis has also unveiled some of the sequence requirements for pore formation and dimerization by Bax $\alpha$ 5. Interestingly, the residues responsible for such functionalities appear to be different.

Pore formation depends on the presence of lysine residues in specific positions, since the introduction of two Lys in the sequence of the leakage-defective Bcl-xL $\alpha$ 5 converts it in a Bax $\alpha$ 5-like molecule. However, Bcl-xL $\alpha$ 5 A149K/E153K, like Bcl-xL $\alpha$ 5, is not able to dimerize in SDS micelles. Therefore, we propose the following pore formation motif: *KxxxKxxx(x)K*.

The sequence requirements for dimerization was also evaluated and Tyr115 was found to be a key residue for driving Bax $\alpha$ 5 self-interaction, since its substitution by Ser abolished dimer formation in SDS micelles. However, Bax $\alpha$ 5 Y115S displayed a leakage rate similar to that of Bax $\alpha$ 5. Although we do not have complete evidence yet, data from the literature [527] and preliminary results from our laboratory suggest that the Bax $\alpha$ 5 sequence based on small-size residues *GxxxA* is also important for dimerization. Therefore, we propose a glycoporphin-like dimerization motif in Bax $\alpha$ 5: *GxxxAxxY*. Indeed, aromatic residues have been shown to complement the classical *Small-xxx-Small* motif [31, 521]. We may also conclude that dimerization is not essential for induction of pre-equilibrium pores, although it might be useful for configuring a large short-term pore or stabilizing a long-term pore.

### 11.1.5 Bax $\alpha$ 5 as a minimal active domain of Bax

We can safely conclude that our Bax $\alpha$ 5 fragment is a minimal active version of full-length Bax, at least in synthetic vesicles. It is informative to compare the two molecules with some detail:

1. Random coil Bax $\alpha$ 5 in solution can independently target lipid membranes and then fold as an  $\alpha$ -helix, like similar amphiphatic peptides. The protein Bax, on the other hand, has a stable hydrosoluble fold hiding the  $\alpha$ 5 fragment into its interior, and needs the aid of other Bcl-2 proteins, like Bid, in order to bind effectively to the MOM [272].
2. The orientation and dynamics of  $\alpha$ -helical Bax $\alpha$ 5 is strongly dependent on the background physical chemistry of lipids. In the physiologically relevant fluid phase, it adopts an interface-bound state essentially perpendicular to the bilayer normal. However, helix-5 of active-Bax (pore-competent Bax, usually also oligomeric Bax) has been suggested to arrange into a transmembrane configuration spanning the lipid bilayer [257].
3. Bax $\alpha$ 5 forms oligomeric assemblies ranging from dimers to higher-order oligomers depending on the lipid composition. Membrane-bound Bax is known to self-assemble into large aggregates [280].
4. Bax $\alpha$ 5 induces the opening of toroidal pores which then relax into smaller stable pores. Bax forms large toroidal pore openings in membranes that most probably also keep open for a long time [258, 309].

## 11.2 Perspectives

While this Thesis has clarified important aspects about the structure of Bax $\alpha$ 5 and also the properties of induced pores, it has led to new questions. In particular, the complete dimerization motif should be deciphered. By comparing the sequence of Bax $\alpha$ 5 with that of other Bcl-2 proteins, putative important residues may be identified and according to this information mutant peptides could be carefully designed. Tricine SDS-PAGE could be used as a rapid screening platform and selected mutants could be further characterized by FRET. Importantly, since Bax $\alpha$ 5 also forms large aggregates, a second interacting surface should also be searched for. The relevance of these findings in the context of the full-length Bax should be tested. Bax mutants will tell us whether these residues (Tyr115, Gly108, Ala112) are only important for Bax $\alpha$ 5 or if their role is transferable to the full-length protein. Additionally, the high resolution structure of dimeric Bax $\alpha$ 5 in micelles could be addressed by liquid state NMR spectroscopy which would unveil some of the principles behind interfacial peptide dimerization.

The binding of Bax $\alpha$ 5 to membranes has been only superficially studied here. A complete thermodynamic description of Bax $\alpha$ 5-lipid interactions should include a careful analysis of the forces (electrostatics, hydrophobic interactions) involved.

The orientation and dynamics of Bax $\alpha$ 5 in membranes should be complemented by other approaches. SSID has intrinsic limitations in terms of choice of labeled residues, relatively low signal-to-noise ratio, a very fast timescale, low sample hydration, etc., which are not always easy to overcome and can notably influence peptide orientation. On the other hand, solid state NMR seems a good alternative technique and could provide further structural insights. Furthermore, the interpretation of the infrared data could be extended to include other possible situations. So far, we have attempted to improve the quality of the fits by introducing disorder and dimers. Another interesting possibility could be the inclusion of two orientations, in agreement with the well-known two-state transition. Oligomers could be modeled using well-developed strategies, like global search molecular dynamics simulations as implemented in the CHI (CNS searching of Helix Interactions) package [425, 589].

The presence of stable openings induced by peptides that follow the so-called all-or-none mechanism should be investigated. This would tell us whether our kinetic model reflects only the particularities of Bax $\alpha$ 5 or if it is of general validity. However, we can foresee that pores of the all-or-none type do not close. The structure of such equilibrium pores will be a challenge for the structural biology community. Most of the published work have focused on kinetic pores and this Thesis suggests the feasibility of studying long-term and equilibrium pores made by Bax $\alpha$ 5, although such an investigation may be hampered by the low abundance of the pores. The first issue to check would be the general outline of the pore. While the lipidic outline of equilibrium pores has been characterized [183, 187], the position occupied by the peptides with respect to the pore wall is still unknown. Most likely we will have to wait some time before a high resolution structure of a supramolecular peptide-lipid pore complex becomes available.

Finally, the usefulness of Bax $\alpha$ 5 in a biomedical context, for instance as a pro-death anticancer drug, should also be seriously considered. We have shown that Bax $\alpha$ 5 can induce cytochrome *c* release in isolated mitochondria [377] and also can induce apoptosis in full cellular environments [590], i.e., Bax $\alpha$ 5 can bypass the complex regulatory network of interactions with other Bcl-2 proteins: it targets mitochondrial membranes without the help of any other cellular partner and once in the MOM it induces the formation of long-lived pores large enough to allow the escape of cytochrome *c*, ending up with an apoptotic phenotype. Bio-availability, reduced toxicity to healthy cells and selective targeting of Bax $\alpha$ 5 to the desired cells will be the next challenges.

### 11.3 Conclusions

The conclusions of this Thesis can be summarized in the following points:

1. Disordered Bax $\alpha$ 5 in solution binds spontaneously to lipid membranes folding as an  $\alpha$ -helix. The secondary structure content depends on the lipid composition, being lower in POPC ( $\sim$ 60%) than in the presence of CL ( $\sim$ 68%).
2. In the membrane bound state, Bax $\alpha$ 5 is able to oligomerize. The self-assembled species depend on the lipid composition, varying from parallel dimers in POPC

and probably also in DMPC to higher order oligomers in the presence of CL. The proposed dimerization motif of Bax $\alpha$ 5 is *GxxxAxxY*.

3. Bax $\alpha$ 5-Bcl-xL $\Delta$ Ct and Bax $\alpha$ 5-Bcl-xL $\alpha$ 5 interactions can be detected in POPC:DOPE:CL membranes, but they do not have an inhibitory effect on Bax $\alpha$ 5-induced membrane leakage.
4. The SSID method allows determination of the orientation of peptides in membranes using various alternative strategies for considering peptide disorder. A search within an explicit orientational landscape, guided by  $\chi^2$  error analysis, is the best option for finding acceptable solutions, including oriented peptide dimers.
5. The orientation of Bax $\alpha$ 5 depends on the lipid composition. In DMPC membranes, the structure and orientation of Bax $\alpha$ 5 can be modeled as a dimer with  $\{\beta, \omega\}$  pairs of  $\{59^\circ, 157^\circ\}$  and  $\{51^\circ, 10^\circ\}$  for each subunit. In POPC membranes Bax $\alpha$ 5 can be modeled also as dimer with  $\{\beta, \omega\}$  pairs of  $\{74^\circ, 157^\circ\}$  and  $\{60^\circ, 20^\circ\}$  for each subunit.
6. The leakage activity of Bax $\alpha$ 5 depends on the lipid composition, with CL strongly inhibiting pore formation.
7. The leakage activity of Bax $\alpha$ 5 depends on the presence and location of Lys residues within the primary structure. The proposed pore-forming motif of Bax $\alpha$ 5 is *KxxxKxxx(x)K*.
8. Bax $\alpha$ 5 induces the opening of kinetic, short-term pores before equilibration, which then relax into stable long-term equilibrium structures.
9. Individual equilibrium pores are different from the kinetic pores at least in size, having a radius of  $\sim 2.3$  nm.
10. A critical concentration of membrane-bound Bax $\alpha$ 5 is necessary, but not sufficient, to trigger pore formation. Both the membrane-bound concentration of Bax $\alpha$ 5 and stochastic factors contribute to the opening of pores.

## *11 General discussion, perspectives and conclusions*

## **Part IV**

# **Versión Resumida en Español**



# 12 Introducción

## 12.1 Membranas biológicas

Las *membranas biológicas* o *biomembranas* forman capas delgadas que rodean a la célula o a sus orgánulos. Las membranas poseen una permeabilidad selectiva y controlan el intercambio de sustancias y el flujo de información entre diferentes compartimentos subcelulares, o bien entre las células y su entorno. Como fundamento para su comprensión estudiaremos primero la composición química de las membranas para después describir los modelos que tratan de explicar su estructura. Finalmente veremos cómo las aproximaciones reduccionistas pueden constituir una estrategia útil a la hora de estudiar las biomembranas.

### 12.1.1 Composición de las biomembranas

**Lípidos.** Son un conjunto de sustancias químicamente heterogéneas que se caracterizan por su baja solubilidad en agua. Sólo un grupo reducido entra a formar parte en la composición de las biomembranas, entre ellos los *fosfolípidos*, los *esfingolípidos* y los *esteroles*. De todos estos, sólo los fosfolípidos han sido utilizados en esta Tesis y se describen a continuación.

Los fosfolípidos son los principales componentes lipídicos de las biomembranas. Químicamente son fosfoglicéridos, es decir, están formados por una molécula de glicerol esterificado con dos ácidos grasos de cadena larga (normalmente entre 16 y 20 carbonos de longitud, usualmente uno de ellos es insaturado). El tercer hidroxilo del glicerol está esterificado con un fosfato. Si el fosfato se une a otros radicales, el fosfolípido correspondiente se denomina de acuerdo con el nombre de este radical. Entre los principales fosfolípidos se encuentran los unidos a: colina (*fosfatidilcolina*) o a otra molécula de glicerol (*fosfatidilglicerol*). Los fosfolípidos comúnmente empleados en esta Tesis han sido palmitiloleilfosfatidilcolina (POPC) y cardiolipina (CL). La cardiolipina es un lípido atípico, resultante de la unión de dos moléculas de fosfatidilglicerol, que se localiza en la mitocondria [378], lugar de acción de la proteína Bax, objeto de estudio de esta Tesis. La estructura de ambos lípidos se representa en la FIG. 12.1.

Los fosfolípidos se caracterizan por ser marcadamente *anfipáticos*; es decir, poseen un parte polar (“cabeza”) constituida por el glicerol, el fosfato y la colina (u otro grupo según los casos), y otra apolar (“cola”) formada por las cadenas hidrocarbonadas. Esta propiedad hace que, en presencia de agua, tiendan a interaccionar entre ellos para reducir el elevado coste energético de la exposición de cadenas alifáticas al medio polar. Dicho *efecto hidrofóbico* es la principal fuerza que dirige el *auto-ensamblaje* de los fosfolípidos en medio acuoso. Como resultado de esta interacción y dependiendo de la forma de los

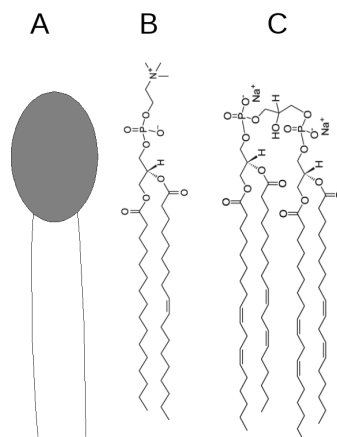


**Fig. 12.1 : Principales lípidos usados en esta Tesis.** (A) Representación esquemática de un lípido anfipático con un grupo de cabeza polar y una cola hidrofóbica constituida por dos cadenas hidrocarbonadas. B) Palmitoleilfofatidilcolina (POPC). C) Cardiolipina (CL). Las estructuras lipídicas se descargaron de <http://avantilipids.com/>.

lípidos, estos pueden formar diversas estructuras [5, 8]. Los lípidos con forma cilíndrica tienden a formar *bicapas lipídicas*, las cuales poseen un núcleo interno hidrofóbico formado por las colas apolares y dos *interfases* hidrofílicas constituidas por las cabezas polares. Las bicapas pueden cerrarse sobre sí mismas formando *vesículas lipídicas* o *liposomas* esféricos de tamaño variable. Un tipo común de vesículas son las llamadas vesículas unilamelares grandes (LUV) las cuales contienen una única bicapa lipídica y su tamaño varía entre 50 y 200 nm. Otro tipo importante son las vesículas unilamelares gigantes (GUV) de tamaño superior a un micrómetro. LUVs y GUVs constituyen modelos útiles para estudiar la estructura y función de las membranas. Por otra parte, si los lípidos se depositan sobre un sustrato sólido se pueden obtener *multicapas orientadas*, las cuales son especialmente útiles para el estudio de la orientación de péptidos y lípidos con respecto al plano de la membrana.

**Proteínas.** Las proteínas de membrana se asocian con las membranas de diferentes formas. Las proteínas *integrales* de membrana interactúan extensamente con el interior hidrofóbico de las membranas, mientras que las proteínas *periféricas* se unen a las membranas directamente a través de interacciones superficiales o bien indirectamente a través de proteínas integrales. La mayoría de las proteínas de membrana se incorpora a la bicapa y se pliega en ella mientras son sintetizadas, a través de la maquinaria del complejo denominado translocón. Sin embargo, otras proteínas se insertan en las membranas post-traduccionalmente y sin la ayuda del translocón. Entre ellas cabe destacar las proteínas formadoras de poros en membrana, objeto de estudio en la presente Tesis [19]. También es importante destacar en este punto que muchos péptidos pueden insertarse y plegarse en las membranas espontáneamente.

Debido al particular entorno proporcionado por las membranas, la estructura primaria

de las proteínas de membrana presenta algunas particularidades con respecto a las proteínas hidrosolubles. Especialmente, las secuencias de proteínas de membrana contienen una elevada proporción de residuos hidrofóbicos que se acomodan bien en el interior apolar de la membrana. No obstante, las proteínas de membrana también presentan residuos polares y cargados, normalmente ubicados en la zona de interfase de la membrana. Las proteínas de membrana adoptan estructuras secundarias mayoritariamente en forma de hélices- $\alpha$  y hojas- $\beta$ , las cuales sirven de base para la formación de fardos de hélices- $\alpha$  y barriles- $\beta$ , respectivamente, que son los dos tipos de conformaciones más comunes. Además, las proteínas de membrana pueden asociarse mediante fuerzas de VAN DER WAALS e interacciones polares para formar oligómeros [25].

### 12.1.2 Modelos estructurales de biomembranas

SINGER y NICOLSON (1972) propusieron el modelo del *mosaico fluido* para explicar la organización general de las membranas biológicas [51]. Según este modelo, las proteínas transmembrana (TM) se parecen a icebergs flotando en un mar lipídico bidimensional y difunden rápidamente en el plano de la membrana (difusión lateral) a menos que estén ancladas a otros componentes celulares. Aunque este modelo todavía constituye el paradigma central en la ciencia de membranas, ahora se reconoce que la distribución de los componentes de la membrana es heterogénea, con presencia de dominios, balsas lipídicas (“rafts”) y compartimentos [52, 591].

Una visión alternativa considera las membranas como *complejos supra-moleculares* donde tanto los lípidos como las proteínas determinan la estructura y dinámica del conjunto y que a su vez definen las propiedades necesarias para su función [550]. Los lípidos imponen una ordenación tipo cristal líquido, lo que condiciona la estructura, orientación y dinámica de la membrana. A su vez, las proteínas modifican el contexto lipídico donde están embebidas lo cual afecta a la organización molecular del complejo. En definitiva, muchos procesos dinámicos que suceden en membranas resultan de la adaptación mutua entre proteínas y lípidos. La formación de poros en membranas, objeto de estudio de la presente Tesis, constituye un ejemplo de dichos procesos.

### 12.1.3 Estudio de las biomembranas bajo una aproximación reduccionista

La complejidad de las membranas biológicas dificulta su estudio directo *in vivo*. Sin embargo, con el objetivo de aumentar nuestro conocimiento sobre las mismas, es posible utilizar sistemas modelo simplificados. Por lo que respecta a la composición lipídica, ésta puede ser convenientemente controlada mediante el uso de lípidos definidos. La mencionada propiedad del auto-ensamblaje de los lípidos permite reconstituir fácilmente en el laboratorio diferentes tipos de agregados lipídicos. En cuanto al componente proteico, el problema es más complejo. Las proteínas de membrana presentan problemas asociados a su expresión y purificación, lo que dificulta la obtención de cantidades suficientes. Por otro lado, no siempre es fácil reconstituir proteínas de membrana en conformaciones activas. Una alternativa que está ganando popularidad es el uso de péptidos correspondientes a las regiones de dichas proteínas que interaccionan con las membranas [48, 49].

La síntesis química de dichos péptidos no está exenta de dificultades, pero las estrategias de obtención disponibles así como la posibilidad de incorporar sondas son mayores comparadas con las existentes para las proteínas. Un dominio proteico se define a nivel estructural como un segmento capaz de plegarse independientemente del resto de la proteína. Desde este punto de vista, una región de interacción con membrana de unos ~20 aminoácidos de longitud constituye no sólo el dominio proteico más pequeño sino además el más sencillo donde las estructuras secundaria y terciaria son una [45].

### 12.2 Poros inducidos por polipéptidos: una visión lipocéntrica

En los estudios funcionales de biomoléculas, los claros protagonistas son los péptidos y las proteínas (polipéptidos en general). Tal es el caso de las membranas biológicas, donde los polipéptidos ocupan una posición predominante en términos de función. En este trabajo se propone una visión alternativa en la que tanto lípidos como proteínas se asocian en complejos supramoleculares dinámicos, donde los lípidos desempeñan un papel activo incluso en funciones normalmente asignadas a proteínas. A continuación pretendemos discutir la formación de poros en biomembranas con especial énfasis en el papel desempeñado por los lípidos.

De acuerdo a SCHWARZ, se define *poro* como cualquier perturbación local de la membrana que permite el flujo pasivo de sustancias hasta un cierto tamaño [61]. Según esta definición, pueden existir poros en membranas puramente lipídicas aunque con baja probabilidad o asociados a procesos de estrés, por ejemplo mecánico o eléctrico. La aparición de poros puede inducirse por *polipéptidos formadores de poros* (PFPPs). Se pretende incluir en esta categoría tanto a proteínas como a péptidos dado que la actividad de membrana de proteínas formadoras de poros puede ser reproducida en muchos casos por fragmentos peptídicos [50]. El proceso completo de formación de poros puede ser dividido en cuatro etapas:

1. Interacción entre el PFPP y la membrana lipídica
2. Cambio en la conformación del PFPP.
3. Cambio en el estado de asociación del PFPP
4. Reorganización del complejo PFPP-membrana con la consiguiente apertura de poros.

Los lípidos pueden ejercer su papel a estos cuatro niveles, como se verá enseguida.

#### 12.2.1 Las membranas lipídicas como receptores de PFPPs

La mayoría de PFPPs están constituidas por residuos hidrofílicos e hidrofóbicos que se organizan en estructuras anfipáticas [81, 93]. La interfase de la membrana constituye una región idónea para la unión de los PFPPs ya que sus propiedades fisicoquímicas complementan la anfipaticidad de los PFPPs. [24, 95]. Los residuos polares y los cargados tienden a localizarse en la región de interfase, formada por las “cabezas” hidratadas de los lípidos, mientras que los residuos apolares tienden a residir en el interior hidrofóbico de las membranas [95, 98]. Semejante adaptación de polipéptidos anfipáticos para unirse

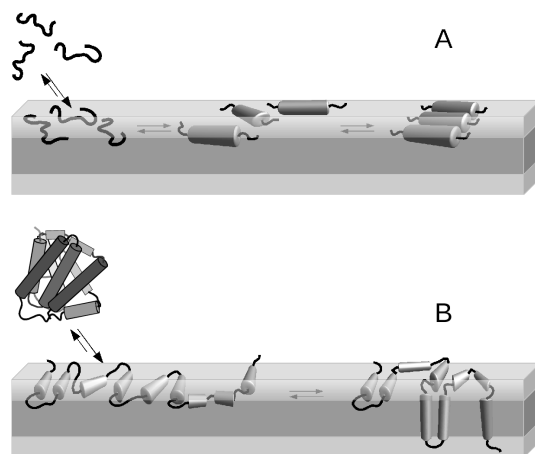


**Fig. 12.2 : El papel activo de las membranas en la formación de poros mediada por PFPPs.** Las bicapas lipídicas controlan la estructura de los polipéptidos que particionan en ella. A) Acoplamiento-partición-plegamiento de péptidos en la interfase de la membrana. Muchos péptidos están desplegados en agua pero tras su unión a la superficie de la membrana, la interfase promueve la aparición de estructura secundaria. B) Partición-replegamiento de proteínas globulares formadoras de poros al unirse a la membrana. En todos los casos, reorganizaciones moleculares dan lugar a poros transmembrana (no mostrado) que dependiendo del caso pueden involucrar asociaciones inter-moleculares (ilustrado en A).

a la región interfacial de las membranas ha sido denominada *acoplamiento-partición-plegamiento*, en donde la partición a la membrana desencadena la adquisición de estructura secundaria con la consiguiente estabilización del complejo polipéptido-membrana [94]. Una característica de las interacciones PFPP-membrana es su baja especificidad, es decir, los PFPPs suelen ser activos frente a membranas lipídicas de composición variada [62, 108]. No obstante, dicha unión no específica a interfases lipídicas puede superponerse a interacciones adicionales de especificidad variable, desde interacciones electrostáticas a sofisticados mecanismos de unión a través de receptores lipídicos o proteicos [115]. Dado que muchos PFPPs tienen carácter catiónico, su interacción con membranas se ve incrementada en presencia de lípidos cargados negativamente [116].

### 12.2.2 Las membranas lipídicas como carabinas de los PFPPs

Dado que la partición del esqueleto peptídico a medios hidrofóbicos es energéticamente desfavorable, existe una tendencia acusada a la formación de estructuras secundarias [24, 96, 127]. Más aún, dicho plegamiento acentúa el carácter anfipático de los PFPPs, lo que incrementa la estabilidad del polipéptido en la interfase [95, 103]. La transición ovillo-hélice- $\alpha$  dependiente de membrana se conoce como *acoplamiento-partición-plegamiento* [24] (FIG. 12.2 A). La adquisición de estructura secundaria en forma de lámina- $\beta$  también es posible pero menos frecuente. Las proteínas formadoras de poros también reorganizan su estructura tras unirse a las membranas, lo que se puede llamar *partición-replegamiento* dado que dichas proteínas ya poseen un plegamiento estable en agua (FIG. 12.2 B). En este punto es importante destacar otra propiedad de las membranas: la *anisotropía*, que

restringe el número posible de organizaciones moleculares. Dicha propiedad selecciona preferentemente una orientación de polipéptidos anfipáticos con el eje peptídico principal esencialmente paralelo al plano de la membrana, de tal forma que la cara hidrofóbica se sumerja en la región apolar de la membrana, mientras que la cara hidrofílica permanezca en la región hidratada de las cabezas polares. De hecho, ésta es la configuración más usual para PFPPs [140]. No obstante, también se han observado cambios hacia una orientación perpendicular con respecto al plano de la membrana a partir de un valor límite de concentración peptídica o asociados a cambios de temperatura [141, 142, 565].

### 12.2.3 Las membranas lipídicas controlan la asociación entre PFPPs

Las interfases lipídicas también pueden promover homo-asociaciones proteína-proteína. De hecho, la oligomerización de PFPPs es, en muchos casos, un paso característico de su mecanismo de activación. Además, los estados hidrosolubles suelen ser monoméricos y la formación de oligómeros es dependiente de su interacción con membranas. Las membranas controlan la asociación entre proteínas configurando nuevas superficies de interacción o aumentando la accesibilidad de sitios de unión. En el caso de los péptidos, la presencia e importancia de los oligómeros no siempre está clara.

### 12.2.4 Las membranas lipídicas tienen un papel activo en la formación y estabilización de poros

Los poros se pueden formar en membranas puramente lipídicas independientemente de la presencia de péptidos y proteínas, aunque con baja probabilidad debido a la elevada barrera energética de la transición membrana no porada  $\leftrightarrow$  membrana porada [73, 75, 150]. Sin embargo, fluctuaciones en la bicapa lipídica pueden dar lugar a alteraciones en la estructura de equilibrio de la membrana, las cuales permiten explicar procesos tales como la formación de poros, la difusión transbicapa de los lípidos (“flip-flop”) y la permeabilidad basal de las membranas [73, 126, 150]. Por tanto, la acción de los PFPPs solapa parcialmente con la capacidad intrínseca de formación de poros de las bicapas lipídicas. A continuación pasaremos a describir los diferentes modelos de formación de poros por péptidos con el objeto de extraer las ideas comunes a todos ellos.

MATSUZAKI propuso un *complejo supramolecular péptido-lípido dinámico* para explicar la difusión transbicapa simultánea de magainina y lípidos, acoplada a la cinética de liberación de contenidos de vesículas lipídicas [592]. Dicho modelo es similar al *poro toroidal “agujero de gusano”* propuesto por HUANG [88]. La visión de éste se basa en la observación de la disminución del espesor de la membrana al unirse péptidos anfipáticos en la superficie en condiciones de equilibrio (*fase-S*, FIG. 12.3 B). Pasado un determinado umbral, los péptidos se reorientan insertándose perpendicularmente al plano de la membrana y manteniendo constante el espesor de la bicapa (*fase-I*, FIG. 12.3 B) [185, 186]. A partir de una misma fase-S el modelo propone dos fases-I que se corresponden con el poro de *barril de hélices* y el *poro toroidal* [564]. En el primer caso los péptidos TM delimitan el borde de un poro de pequeño tamaño [187]. En el caso del poro toroidal las dos monocapas se fusionan en el borde del poro (FIG. [183]. La

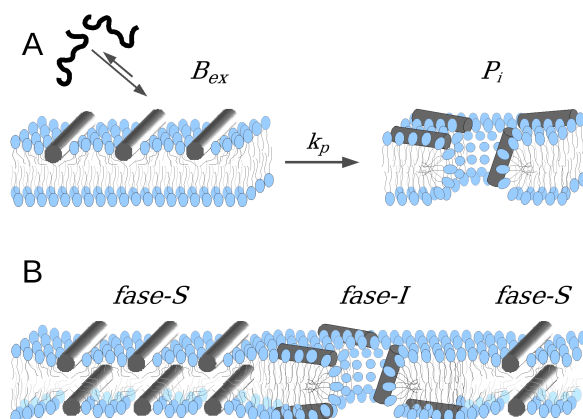


**Fig. 12.3 :** Representación esquemática de dos modelos de formación de poros. A) Modelo cinético de dos estados ( $B_{ex} \rightarrow P_i$ ). La unión-replegamiento inicial de péptidos anfipáticos en la interfase de la membrana ( $B_{ex}$ ) da lugar a la transición al estado poro ( $P_i$ ) [85, 86]. B) Modelo de equilibrio donde el péptido está unido en la interfase de ambas monocapas (*fase S*) [114]. A partir de un umbral de P/L dicha fase coexiste con otra (*fase I*) en la que se observan poros toroidales. La organización de los péptidos se desconoce (la elegida para este dibujo es arbitraria).

estructura de la parte lipídica de ambos tipos de poros ha sido caracterizada [183, 187]. La rotura de la bicapa también es el ingrediente principal del llamado *modelo alfombra*, que a concentraciones grandes de péptido se corresponde con el modelo *tipo detergente* propuesto por SHAI, así como de otros modelos similares [109, 116, 189, 191]. Todos ellos coinciden en que la membrana se recubre extensamente por péptidos hasta que finalmente se desintegra. En estos casos, se asume que el poro toroidal es un estado transitorio previo a la ruptura de la membrana y la formación de micelas mixtas. Si no se tiene en cuenta dicha micelización, los estudios cinéticos de actividad liberadora de contenidos de vesículas realizados por MATSUZAKI y SHAI coinciden en que la formación de poros se debe al “ataque” asimétrico de la membrana por parte del péptido, debido a su unión con la monocapa externa dado que es la única inicialmente accesible (el llamado estado  $B_{ex}$  por TAMBA y YAMAZAKI [85, 86], FIG. 12.3 A). Puede inferirse que los poros serán transitorios desapareciendo tan pronto como dicho desequilibrio se disipe gracias a la apertura de los poros (el llamado estado  $P_i$  por TAMBA y YAMAZAKI [85, 86], FIG. 12.3 A). Por el contrario, HUANG asume que dicho “ataque” se produce simétricamente (en ambas monocapas) y, de acuerdo con sus estudios estructurales en multicapas péptido-lípido equilibradas, los poros corresponden a un mínimo de energía siendo por lo tanto estables [319]. Sin embargo, la relación entre los poros cinéticos y los de equilibrio no está clara. De la misma manera, la relación entre la transición  $B_{ex} \rightarrow P_i$  y el modelo de dos fases *S/I* no han sido aún definidas.

En resumen, el consenso emergente es el siguiente: la rotura de la membrana debido a la unión interfacial es el mecanismo principal de los PFPPs. Dicha rotura procede a través de un transición estocástica entre dos estados o fases modulada por las propiedades de la membrana.

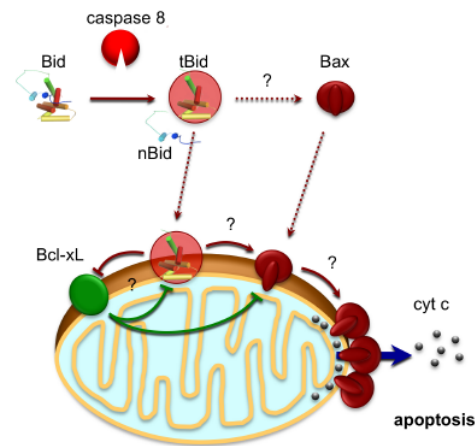


**Fig. 12.4 : Permeabilización de la membrana mitocondrial externa por proteínas de la familia Bcl-2.** El corte proteolítico de Bid al inicio de la apoptosis da lugar a la forma activa tBid. Una vez tBid se transloca a la MOM, promueve a su vez la translocación e inserción de Bax, el cual oligomeriza, forma poros y libera factores pro-apoptóticos tales como el citocromo c. Los miembros anti-apoptóticos de la familia Bcl-2, como Bcl-xL, bloquean la translocación, inserción y oligomerización de Bax.

## 12.3 Papel de los poros en mecanismos de muerte celular mediada por mitocondrias

Independientemente de las características morfológicas que presentan las células en procesos de muerte apoptótica, la permeabilización de las membranas mitocondriales (MMP) es frecuentemente un evento clave que delimita la vida de la muerte. Dicha permeabilización se da fundamentalmente a nivel de la membrana mitocondrial externa (MOM). La MMP depende principalmente de la actividad de proteínas de la familia Bcl-2 así como de los lípidos mitocondriales.

### 12.3.1 MMP en apoptosis

La apoptosis es un tipo de muerte celular programada caracterizada por la condensación de la cromatina, fragmentación nuclear y encogimiento celular. Es un proceso natural que elimina células innecesarias, dañadas o mutadas. El programa apoptótico se puede llevar a cabo mediante diferentes rutas moleculares. En la llamada ruta *intrínseca*, diferentes señales intracelulares convergen a nivel de la mitocondria causando la liberación de factores apoptogénicos secuestrados normalmente en el espacio intermembrana. Una vez en el citosol, dichos factores, cuyo principal representante es el citocromo c, promueven la activación de las caspasas. Las caspasas son una familia de proteasas que degradan selectivamente los diferentes componentes intracelulares provocando eventualmente la muerte celular.

### 12.3.2 Proteínas de la familia Bcl-2

Las proteínas de la familia Bcl-2 son reguladores clave de la apoptosis a través del control de la MMP.

**Estructura.** Dependiendo de la presencia de hasta cuatro *dominios de homología Bcl-2* (BH), las proteínas de la familia Bcl-2 se pueden clasificar en: (i) Bcl-2 anti-apoptóticas (prototipos: Bcl-xL y Bcl-2), que poseen los cuatro dominios BH e inhiben la MMP; (ii) Bcl-2 pro-apoptóticas (prototipos: Bax y Bak), que poseen los dominios BH1, BH2 y BH3 y facilitan la MMP; (iii) “BH3-sólo” (prototipos: Bid y Bad) que, como su nombre indica, poseen únicamente el dominio BH3 y son como sensores que detectan los diferentes estímulos apoptóticos facilitando la MMP indirectamente.

Las proteínas de la familia Bcl-2, al igual que las toxinas bacterianas formadoras de poros, presentan al menos dos conformaciones: una en solución acuosa y otra en la membrana. Sin embargo, con la única excepción de la proteína BH3-sólo BNIP3 [235], sólo se conoce la estructura de alta resolución de formas hidrosolubles. La mayoría de proteínas Bcl-2 presenta una plegamiento similar en ambiente acuoso consistente en una horquilla central de hélices- $\alpha$  rodeada de varias hélices [226–230]. Exceptuando la presencia de una región hidrofóbica en algunas proteínas Bcl-2, que les sirve para anclarse a la MOM, la mencionada horquilla presenta una mayor hidrofobicidad que el resto de la proteína, manteniendo el carácter anfipático. Una característica importante de la estructura de las proteínas Bcl-2 es que los dominios BH1-3 forman un surco hidrofóbico en la superficie. Se ha visto que dicho surco constituye el sitio de unión para el dominio BH3 de otras proteínas Bcl-2. El plegamiento global de las proteínas Bcl-2 es semejante al de proteínas formadoras de poros, tales como las colicinas y la toxina de la difteria.

Aunque no se conoce con detalle la estructura de las proteínas Bcl-2 insertada en membranas, se tienen indicios acerca de cómo podría ser dicha estructura. Por ejemplo, modelos recientes de Bax sugieren que las dos hélices de la horquilla central ( $\alpha 5$  y  $\alpha 6$ ) junto con la hélice hidrofóbica  $\alpha 9$  se encontrarían insertadas TM mientras que el resto de hélices yacería en la superficie de la membrana [257]. De forma similar, para Bcl-xL se ha propuesto que únicamente las hélices  $\alpha 5$ ,  $\alpha 6$  y el dominio hidrofóbico C-terminal se insertarían en la membrana [256, 283].

Otra característica importante de las proteínas Bcl-2 es su capacidad para formar homo- y hetero-oligómeros [229, 288, 292, 528]. La homo-oligomerización de Bax se encuentra asociada a la permeabilización de la MOM, liberación de citocromo c e inducción de apoptosis [268, 270, 342]. Por tanto, los oligómeros de Bax se cree que son los causantes de la formación de poros en la MOM. No obstante, no se conoce con detalle la estructura de homo-oligómeros de Bax. Se ha propuesto la existencia de dos superficies de interacción que regulan la formación de oligómeros de Bax: la primera coincide con las regiones que forman el surco hidrofóbico (dominios BH1-3) [258, 279, 280], mientras que la segunda está formada por las hélices  $\alpha 1$ ,  $\alpha 6$  y el lazo entre  $\alpha 1$  y  $\alpha 2$  [280].

**Actividad formadora de poros.** Muchas proteínas Bcl-2, independientemente de su función pro-vida o pro-muerte, son capaces de formar poros tanto en membranas modelo

como en la MOM [195, 295, 329]. En concreto, Bax es capaz de formar poros toroidales parcialmente lipídicos [196]. Se ha demostrado que la región de la proteína responsable de la formación de poros es la horquilla central de hélices  $\alpha 5$  y  $\alpha 6$  [311, 312]. Más aún, se ha visto que fragmentos peptídicos correspondientes a cada una de dichas hélices son capaces de porar membranas de forma similar a como lo hace la proteína entera [50, 176]. De hecho, se conoce la estructura de la parte lipídica de los poros inducidos por un péptido derivado de la hélice  $\alpha 5$  de Bax [183], similar al utilizado en esta Tesis.

**Regulación de la apoptosis.** Un modelo ampliamente aceptado de regulación de la apoptosis por proteínas de la familia Bcl-2 se detalla a continuación [353] (FIG. 12.4). En presencia de un estímulo apoptótico, las proteínas BH3-sólo se activan en primera instancia. Por ejemplo, Bid se convierte en tBid (Bid truncado). Una vez activadas se translocan espontáneamente a la MOM donde interactúan con otras Bcl-2 para inducir MMP. En función de la capacidad de las proteínas BH3-sólo para interactuar con Bax/Bak se clasifican como “activadores directos” o “sensibilizadores/de-represores”. Estas últimas no se unen directamente a Bax/Bak sino que interactúan fuertemente con las proteínas pro-apoptóticas liberando los “activadores directos” que son los que “reclutan” a Bax acercándolo a la membrana y facilitando la adquisición de su conformación “activa”. Como se ha discutido, dicha conformación, responsable de la formación de poros, implica una inserción profunda de la proteína en la MOM, así como la asociación entre varios monómeros de Bax.

Las proteínas anti-apoptóticas como Bcl-xL inhiben la activación de Bax/Bak a dos niveles distintos [269, 272]: (i) interactuando con las proteínas BH3-sólo unidas a membrana y por tanto “secuestrándolas” impidiendo que recluten a Bax/Bak, (ii) interactuando con Bax/Bak en la membrana bloqueando su activación, o bien impidiendo la inserción en la membrana, o bien impidiendo la formación de oligómeros.

### 12.3.3 Importancia de la apoptosis

Las alteraciones de la MMP han sido descritas en varias enfermedades humanas tales como isquemia/reperfusión, intoxicación con xenobióticos, infecciones víricas, enfermedades neurodegenerativas y cáncer [211]. Por tanto, la manipulación de la MMP constituye una diana biomédica importante. Por un lado, se han desarrollado antagonistas de Bcl-2 para iniciar la MMP con el objetivo de utilizarse para sensibilizar células tumorales a los tratamientos de quimioterapia, o incluso como agentes únicos. Por otro lado, se ha demostrado que varios péptidos, no relacionados con secuencias de proteínas Bcl-2, son capaces de desencadenar la apoptosis a través de la inducción de la MMP [375]. El trabajo desarrollado en esta Tesis podría ser utilizado como base para el diseño de poro-péptidos mitocondrio-tóxicos [590].

## 12.4 Objetivo de este trabajo

Dado que hélices- $\alpha$  de proteínas de membrana pueden considerarse dominios proteicos, esto es, unidades de plegado independiente, en el proceso de su ensamblaje funcional,

el desafío de expresar y purificar proteínas de membrana completas, puede ser evitado mediante una aproximación tipo “divide y vencerás”: péptidos individuales derivados de secuencias únicas de inserción en membrana pueden ser usados para evaluar experimentalmente los fundamentos de los procesos de unión-estructuración-poración. Así, varios fragmentos activos en membranas derivados de proteínas Bcl-2 prototípicas, tales como Bax, Bcl-xL y Bid están siendo estudiados en nuestro grupo de investigación.

En esta Tesis nos hemos centrado principalmente en un fragmento derivado de la proteína pro-apoptótica Bax llamado Bax $\alpha$ 5. Desde un punto de vista de conocimiento fundamental hemos tratado de entender el mecanismo biofísico de formación de poros de Bax $\alpha$ 5, con énfasis en el papel desempeñado por los lípidos, el cual podría ser de utilidad general para otras proteínas y péptidos formadores de poros. Nos hemos propuesto los siguientes objetivos concretos:

1. Caracterización del acoplamiento unión-plegamiento de Bax $\alpha$ 5 con membranas lipídicas (SEC. 14.1).
2. Caracterización de la estructura de complejos Bax $\alpha$ 5-membrana, incluyendo la orientación de Bax $\alpha$ 5 (SEC. 14.3)
3. Caracterización de interacciones Bax $\alpha$ 5-Bax $\alpha$ 5 (SEC. 14.2).
4. Caracterización de la actividad formadora de poros de Bax $\alpha$ 5 combinando estudios “clásicos” en conjuntos de vesículas lipídicas con estudios con vesículas individuales (SEC. 14.4).



# 13 Materiales y métodos

## 13.1 Preparación de muestras

### 13.1.1 Membranas modelo

Debido al fenómeno del auto-ensamblaje descrito en la SUB. 12.1.1, la preparación de bicapas lipídicas modelo se simplifica notablemente. Basta con disolver los lípidos en un disolvente orgánico adecuado (normalmente cloroformo). Esta solución madre se puede conservar a  $-20^{\circ}\text{C}$  durante meses. De aquí se toma el volumen pertinente en función de la cantidad deseada y posteriormente se evapora a vacío. La capa lipídica resultante se hidrata en el tampón deseado y como resultado se forman MLVs. Éstos se extruden a través de filtros con el tamaño de poro deseado (en esta Tesis se han usado principalmente poros de 100 nm de diámetro) con el objetivo de formar LUVs. Si se desean multicapas orientadas, la suspensión de MLVs se somete a sonicación con el objetivo de formar SUVs las cuales se depositan sobre la superficie deseada y el exceso de disolvente se elimina mediante corriente de  $\text{N}_2$  (en esta Tesis se ha usado un cristal de Ge como soporte sólido para llevar a cabo las medidas de IR).

En cuanto a la composición lipídica, se ha usado principalmente POPC y POPC:CL (Avanti Polar Lipids) a una relación 80:20, con el objetivo de estudiar el papel específico de la CL, cuya relevancia fisiológica en apoptosis está documentada [379].

La concentración de lípidos en la muestra se determinó mediante un kit comercial (Wako Chemicals). El método se basa en la generación de un producto coloreado a partir del grupo colina. La cuantificación se realiza mediante una curva de calibrado usando un patrón de concentración conocida y midiendo la absorbancia con un colorímetro.

### 13.1.2 Síntesis y purificación de péptidos

Todos los péptidos se obtuvieron mediante *síntesis química en fase sólida* (SPPS) en un sintetizador automático de péptidos (Applied Biosystems). Tras la síntesis, los péptidos fueron cortados de la resina, precipitados y secados. Los péptidos presentan el extremo N-terminal acetilado y el C-terminal amidado, excepto los que fueron marcados mediante sondas fluorescentes en el grupo amino terminal, el cual debe estar libre para que la reacción tenga lugar. El principal péptido sintetizado fue el correspondiente a la hélice quinta de Bax por lo que se ha llamado Bax $\alpha$ 5: WGRVVALFYFASKLVLKALSTK. No obstante, se sintetizaron variantes de esta secuencia incluyendo sondas apropiadas para su análisis estructural (ver SUB. 13.2.2 y 13.3.2).

Los péptidos se purificaron mediante *cromatografía líquida de alta resolución* (HPLC) en fase reversa, usando como fase estacionaria sílica-C18 empaquetada en una columna

(Waters) y como eluyente una mezcla de agua y acetonitrilo con 1 % de TFA. La pureza e identidad de los péptidos se comprobó mediante HPLC analítico (Waters) y espectrometría de masas MALDI-TOF (SCSIE). Las fracciones más puras (>85 % de pureza) se guardaron liofilizadas.

Los péptidos se midieron en un espectrofotómetro UV-vis (Agilent Technologies) y se cuantificaron mediante la ley de LAMBERT-BEER.

## 13.2 Estudios estructurales

### 13.2.1 Dicroísmo circular (CD)

CD es un método espectroscópico que permite obtener datos estructurales a baja resolución de péptidos y proteínas en solución, así como en entornos que mimetizan las membranas biológicas (detergentes, liposomas, etc.) [394]. La luz linealmente polarizada puede ser entendida como la suma de dos componentes de luz circularmente polarizada de igual magnitud, uno girando en el sentido de las agujas del reloj (dextrógiro, D) y otro en el sentido opuesto (levógiro, L). Si se produce una absorción diferencial de estos dos componentes se producirá el efecto conocido como dicroísmo circular. En este caso la radiación resultante variará el plano de polarización con el tiempo dado que el vector resultante de la suma de D y L (ahora de magnitud diferente) ya no permanece constante. Cuando esto ocurre se dice que la luz se encuentra elípticamente polarizada.

Los espectros de CD fueron tomados en un espectropolarímetro J-810 (Jasco)

Los polipéptidos presentan al menos dos cromóforos de interés, la cadena lateral de los aminoácidos aromáticos (absorción entre 260 y 320 nm) y el enlace peptídico (absorción por debajo de 240 nm). Este último cromóforo se encuentra en todas los polipéptidos. Los diferentes tipos de estructura secundaria polipeptídica presentan unos espectros de CD característicos. Existen diferentes algoritmos que estiman la composición de estructura secundaria a partir del espectro de CD en el ultravioleta lejano, algunos de los cuales se pueden encontrar en la plataforma DichroWeb [403]. La mayoría de estos programas emplea bases de datos de proteínas con estructura conocida. Sin embargo, el uso de vesículas lipídicas dificulta la adquisición de espectros a longitudes de onda bajas, impidiendo el uso de algunos programas. La excepción es el algoritmo K2D, que no se basa una serie de proteínas como referencia sino que usa redes neurales, y puede emplearse en el rango de 200-250 nm.

### 13.2.2 Espectroscopia infrarroja (IR)

La radiación infrarroja se corresponde con energías que se solapan con las transiciones vibracionales. Las proteínas dan lugar a diferentes bandas de absorción, siendo la más útil para nuestro estudio la llamada amida I que corresponde fundamentalmente a la vibración del grupo C=O del esqueleto peptídico [397]. En concreto hemos usado una variante de espectroscopia infrarroja conocida como *reflexión total atenuada* (ATR) [396]. El rayo infrarrojo es reflejado totalmente dentro del llamado *elemento de reflexión interna* (IRE), en nuestro caso un cristal de Ge. En cada reflexión se produce una *onda*

*evanescente* que penetra una cierta distancia en el medio existente más allá del IRE, en nuestro caso multicapas lipídicas con péptido incorporado. Dicha configuración nos va a permitir estudiar la orientación de péptidos y lípidos con respecto a la normal de la bicapa (perpendicular al cristal de Ge). Los espectros se midieron en un espectrofotómetro Magna 560 (Nicolet)

Todo *momento dipolar de transición* (TDM) del cromóforo (en nuestro caso se trata de la banda amida I, es decir, el grupo C=O) puede ser localizado en el espacio y con respecto a la estructura molecular mediante cinco ángulos [414]:

- $\alpha$ , ángulo entre el TDM y el eje director de la hélice- $\alpha$ . Dicho valor es conocido para estructuras canónicas [408].
- $\beta$ , inclinación del péptido o ángulo entre el eje director de la hélice y el eje z. Se trata de un parámetro global que define la inclinación de toda la hélice.
- $\omega$ , ángulo de rotación azimutal alrededor del eje director de la hélice. Por convenio, dicho ángulo equivale a cero cuando el TDM, el eje director de la hélice y el eje z son coplanares. Los valores de  $\omega$  entre residuos consecutivos de una hélice- $\alpha$  canónica se diferencian en  $100^\circ$ . En esta Tesis los valores de  $\omega$  se han calculado respecto al primer residuo de la secuencia de forma que  $\omega = \omega_1$ .
- $\phi$ , la rotación el eje director de la hélice en el plano x,y (alrededor de la normal). Debido a la simetría uniaxial dicho ángulo no interviene en los cálculos.
- $\theta$ , ángulo entre el TDM y el eje z.

La información concerniente a la orientación de una molécula está contenida en un parámetro conocido como *razón dicroica*, que es el cociente de la absorbancia de luz polarizada en dos direcciones, normalmente paralela y perpendicular ( $R \equiv \frac{A_{\parallel}}{A_{\perp}}$ ). Por un lado,  $R$  puede referirse a la relación dicroica promedio de todos los TDM de la hélice, donde se denota  $R_{helix}$ , y depende sólo de  $\alpha$  y  $\beta$ .  $R$  también puede hacer referencia a la relación dicroica correspondiente a un residuo concreto donde se designa como  $R_{site}$  que depende de  $\alpha$ ,  $\beta$  y  $\omega$ . Para la obtención de la  $R_{site}$  se precisa de marcaje isotópico [593]. Hemos usados la sonda  $1-^{13}C=^{18}O$  para marcar el péptido Bax $\alpha$ 5 en siete residuos diferentes [410]. A partir del espectro IR de cada uno de dichos péptidos se obtienen dos parámetros experimentales,  $R_{helix}$  y  $R_{site}$ .

Proponemos un nuevo método para la extracción de los ángulos de orientación de la hélice,  $\{\beta, \omega\}$ , basado en la función de error  $\chi^2$ :

$$\chi^2 = \sum_{i=1}^n \left( \frac{R_{helix,i}^{exp} - R_{helix,i}^{theo}}{Er_i} \right)^2 + \sum_{i=1}^n \left( \frac{R_{site,i}^{exp} - R_{site,i}^{theo}}{Er_j} \right)^2 \quad (13.1)$$

donde los superíndice *exp* y *theo* hacen referencia a mediciones experimentales y determinaciones teóricas, respectivamente, y *Er* se refiere al error experimental asociado a cada medida.

Por un lado los datos se pueden analizar mediante el método del *paisaje de orientaciones implícito*. Este método permite generar todas las soluciones teóricas posibles

de  $R_{helix}$  y  $R_{site}$  para cada el espacio completo de pares  $\{\beta, \omega\}$ , que son posteriormente comparadas con los valores experimentales ponderados por su error.

Por otro lado, el método de modelado de cuerpo rígido utiliza representaciones *explícitas* de las estructuras peptídicas. Dichas estructuras se usan para generar el paisaje de orientaciones variando el par  $\{\beta, \omega\}$ . A partir de cada orientación se calculan los valores teóricos  $R_{helix}^{theo}$  y  $R_{site}^{theo}$ , los cuales son comparados con los valores experimentales. El mejor ajuste viene dado por el mínimo en la función de error  $\chi^2$ . Una ventaja inmediata derivada del uso de estructuras explícitas es que cada estado del paisaje de orientaciones tiene un significado directo e inmediato. Por el contrario, la mayoría de modelos usados hasta la fecha utilizan una descripción implícita de la estructura la cual es modelada mediante consideraciones geométricas simplificadas. Otra ventaja importante es que se puede escoger la estructura de partida que mejor representa al sistema de estudio.

## 13.3 Interacciones péptido-péptido

### 13.3.1 Método electroforético: Tricina SDS-PAGE

Las proteínas se pueden separar en función de su peso molecular mediante *electroforesis en gel de poliacrilamida* en presencia de SDS (SDS-PAGE) con glicina como ión conductor. Dado que el SDS es un agente lípido-mimético, la estructura cuaternaria nativa de las proteínas es normalmente preservada [444]. En muchos casos, es posible observar bandas correspondientes a pesos moleculares aparentes de monómeros, dímeros, trímeros, etc. No obstante, se deben tomar precauciones para su correcta interpretación [446–448]. Sin embargo, el poder de resolución es bajo para péptidos y proteínas de bajo peso molecular (menos de 10 kDa). En estos casos es conveniente sustituir la glicina por tricina [442].

### 13.3.2 Transferencia de energía por resonancia

Cuando el espectro de emisión fluorescente de un compuesto (“dador”) solapa con el espectro de absorción de otro (“aceptor”) y ambos se encuentran próximos en el espacio y con la orientación adecuada, se produce una transferencia de la energía del dador al aceptor por resonancia, fenómeno que se conoce como *transferencia de energía por resonancia de Förster* (FRET) [452]. La distancia para la cual la eficiencia en la transferencia es del 50% se conoce como *distancia de Förster* ( $R_0$ ), la cual suele encontrarse en el rango de 2-6 nm. Este hecho hace que se pueda considerar la técnica de FRET como una “regla espectroscópica” para medir distancias a nivel molecular [451]. En experimentos de estado estacionario, la eficiencia de la transferencia ( $E^{ss}$ ) se estima a partir de la intensidad de fluorescencia del dador en presencia ( $F_{DA}$ ) y ausencia ( $F_D$ ) del aceptor:

$$E^{ss} = 1 - \frac{F_{DA}}{F_D} \quad (13.2)$$

La obtención de una línea recta en un gráfico de  $E^{ss}$  en función de la fracción molar de aceptor ( $f_A$ ) es indicativa de la presencia de dímeros [458]. En membranas,  $E^{ss}$  tiene dos contribuciones: una debida a la proximidad aleatoria dador-aceptor, debido al espacio

limitado de la membrana ( $E^{proximity}$ ) y otra debida a la dimerización propiamente dicha ( $E^{dimer}$ ) [445].  $E^{proximity}$  puede estimarse por métodos computacionales y sustraerse de  $E^{ss}$  para obtener  $E^{dimer}$ . La distancia dador/aceptor ( $r$ ) se obtiene a partir de la siguiente relación:

$$E^{dimer} = f_A f_{Di} \frac{R_0^6}{R_0^6 + r^6} \quad (13.3)$$

donde  $f_{Di}$  es la fracción de dímeros en la muestra.

En algunos casos también se estudió la capacidad de interaccionar midiendo la fluorescencia de vesículas conteniendo péptidos dadores, aceptores y no marcados ( $F_{DAU}$ )

Todos los espectros de fluorescencia se midieron en un espectrofluorímetro (Photon Technology International)

## 13.4 Estudios termodinámicos

### 13.4.1 Interacciones péptido-lípido

Partiendo de un equilibrio de partición del péptido entre las fases acuosa y de membranas, la fracción de péptido en la fase membranosa ( $f_p$ ) depende del coeficiente de partición ( $K_x$ ), a través de [462]:

$$f_p = \frac{K_x[L]}{[W] + K_x[L]} \quad (13.4)$$

donde  $[W]$  y  $[L]$  son las concentraciones molares de agua y lípido, respectivamente. En nuestro caso se midió la variación de la señal de CD, proporcional a  $f_p$ , en función de  $[L]$ . La energía libre de partición agua-membrana ( $\Delta G_x$ ) viene dada por:

$$\Delta G_x = -RT \ln K_x \quad (13.5)$$

### 13.4.2 Interacciones péptido-péptido

La energética de las interacciones péptido-péptido puede estudiarse partiendo de las medidas de  $E^{dimer}$ . La fracción de dímeros ( $f_{Di} = 2E^{dimer}$ ) depende de la constante de dimerización ( $K_{dimer}$ ) a través de [46]:

$$f_{Di} = \frac{4K_{dimer}[P] + 1 - \sqrt{8K_{dimer}[P] + 1}}{4K_{dimer}[P]} \quad (13.6)$$

donde  $[P]$  es la concentración total de péptido en la muestra (dador más acepto). La energía libre de dimerización viene dada por:

$$\Delta G_{dimer} = -RT \ln K_{dimer} \quad (13.7)$$

## 13.5 Estudios de actividad

### 13.5.1 Experimentos con poblaciones de vesículas lipídicas

Se prepararon LUVs de  $\sim 100$  nm de diámetro hidrodinámico conteniendo la sonda fluorescente calceína (Sigma) en su interior. La elevada concentración (80 mM) de dicha sonda mientras se encuentra encapsulada en el interior del liposoma hace que la intensidad de fluorescencia inicial sea baja [476]. Sin embargo, si la sonda se libera al exterior, la fluorescencia aumenta debido a su dilución y la consiguiente disminución de la auto-extinción. El porcentaje de liberación de calceína se calculó a partir de:

$$\text{Liberación (\%)} = 100 \frac{F(t) - F_0}{F_\infty - F_0} \quad (13.8)$$

donde  $F(t)$  es la fluorescencia medida a tiempo  $t$  tras la adición del péptido,  $F_0$  es la fluorescencia inicial y  $F_\infty$  es la fluorescencia final obtenida tras la desintegración total de las vesículas mediante el detergente Triton X-100.

### 13.5.2 Experimentos con vesículas lipídicas individuales

Las imágenes se obtuvieron mediante microscopía confocal de fluorescencia con un equipo LSM 510 (Zeiss) [179]. A la cámara de observación del microscopio se añadieron la sonda fluorescente Alexa555 (Molecular Probes) y el péptido Bax $\alpha$ 5. Posteriormente se añadieron vesículas unilamelares gigantes (GUVs), de  $\sim 25$   $\mu\text{m}$  de diámetro, marcadas con la sonda lipofílica DiD (Molecular Probes). La cinética de entrada de las sondas externas se registró midiendo la fluorescencia en el interior de GUVs individuales a lo largo del tiempo. Para comprobar si los poros permanecen abiertos a tiempos largos, se añadieron un segundo (Alexa488, Molecular Probes) y un tercer (Atto655, AttoTec) colorante a los 120 y 135 min, respectivamente.

# 14 Resultados, discusión y conclusiones

## 14.1 Unión de Bax $\alpha$ 5 a membranas

### 14.1.1 Estructura secundaria de Bax $\alpha$ 5 en membranas

La estructura secundaria de Bax $\alpha$ 5 en membranas se estudió principalmente mediante espectroscopia de CD. Para ello se prepararon varias muestras con la misma cantidad de Bax $\alpha$ 5 y diferentes cantidades de lípidos. Las composiciones lipídicas usadas fueron POPC y POPC:CL (80:20). Los complejos reconstituidos Bax $\alpha$ 5-membranas se extrudieron para obtener liposomas de 50 nm de tamaño. Los espectros de CD se muestran en la FIG. 14.1 A y B. Puede apreciarse cómo la elipticidad media por residuo ( $[\theta]_{MR}$ ) se incrementa al aumentar la concentración lipídica, lo que es indicativo de la adquisición de estructura secundaria. Dicha estructura secundaria se cuantificó mediante el algoritmo K2D [403] y los resultados se muestran en la TAB. 14.1. En tampón acuoso en ausencia de lípidos, el contenido en hélice- $\alpha$  de Bax $\alpha$ 5 es bajo, predominando estructuras desordenadas (“ovillo aleatorio”) y hoja- $\beta$ . En cambio, en presencia de liposomas la proporción de hélice- $\alpha$  aumenta, aunque en un grado distinto dependiendo de la composición lipídica: hasta un 60 % en POPC y hasta un 68 % en POPC:CL. Estas pequeñas diferencias pueden deberse a la carga negativa de la CL, que puede favorecer la interacción electrostática con Bax $\alpha$ 5, el cual posee carga positiva.

### 14.1.2 Energética de las interacciones Bax $\alpha$ 5-membrana

El coeficiente de partición agua-membrana,  $K_x$ , se determinó a partir del ajuste de la variación de  $[\theta]_{MR}$  a 200 nm en función de la concentración lipídica (FIG. 14.1 C y D) [462]. Dicho coeficiente es mayor para interacciones Bax $\alpha$ 5-POPC:CL que para Bax $\alpha$ 5-POPC, lo que indica una mayor atracción entre Bax $\alpha$ 5 y POPC:CL. A partir de  $K_x$  se calculó la energía libre de partición agua-membrana,  $\Delta G_x$ , obteniéndose valores en torno a las -6 kcal/mol para ambos lípidos, algo mayores en membranas compuestas de POPC:CL.

## 14.2 Auto-ensamblaje de Bax $\alpha$ 5 en membranas

### 14.2.1 Oligomerización de Bax $\alpha$ 5 usando micelas de SDS

Para facilitar la interpretación del patrón de migración electroforético, se corrieron varios péptidos en el mismo gel (FIG. 14.2). En concreto, se usaron cuatro péptidos: Bax $\alpha$ 5, Bax $\alpha$ 5 Y115S, Bcl-xL $\alpha$ 5 A149/E153K y Bcl-xL $\alpha$ 5. Estos péptidos se diseñaron a partir de la comparación de secuencias entre Bax $\alpha$ 5 y su análogo Bcl-xL $\alpha$ 5. Existen ciertas

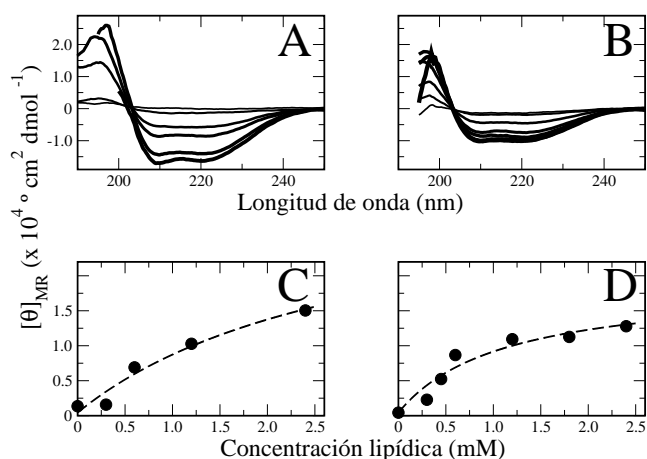


**Fig. 14.1 :** Estructura secundaria de Bax $\alpha$ 5 analizada mediante espectroscopia de dicroísmo circular. A) y B) Dependencia de la elipticidad media por residuo ( $[\theta]_{MR}$ ) de Bax $\alpha$ 5 con la concentración lipídica para muestras de péptido reconstituido en LUVs de 50 nm. C) y D) Datos experimentales de  $[\theta]_{MR}$  a 200 nm en función de la concentración lipídica (círculos). El ajuste teórico (línea punteada) se realizó usando la EC. 13.4, obteniéndose el coeficiente de partición  $K_x$ . La composición lipídica fue POPC (panel izquierdo) o POPC:CL (80:20) (panel derecho).

**Tab. 14.1 :** Estructura secundaria de Bax $\alpha$ 5 estimada a partir de los espectros de CD. Se usaron LUVs ( $\sim$ 50 nm diámetro) de dos composiciones lipídicas: POPC y POPC:CL (80:20), en tampón acuoso PB (ausencia de NaCl). La concentración de Bax $\alpha$ 5 fue 30  $\mu$ M. La relación P/L osciló entre 1/10 y  $\sim$ 1/100. Los valores corresponden a la estimación del algoritmo K2D con el mínimo error dado como la desviación cuadrática media normalizada entre los valores medidos y teóricos.

[Lípido] (mM)	POPC			[Lípido] (mM)	POPC:CL		
	Hélice- $\alpha$ (%)	Hoja- $\beta$ (%)	Ovillo aleato- rio (%)		Hélice- $\alpha$ (%)	Hoja- $\beta$ (%)	Ovillo aleato- rio (%)
0	4	48	48	0	10	45	45
0.3	5	47	48	0.3	11	45	44
0.6	26	25	49	0.45	29	34	37
1.2	37	13	50	0.6	59	14	27
2.4	55	11	34	1.2	67	10	23
4.8	60	7	33	1.8	68	10	22

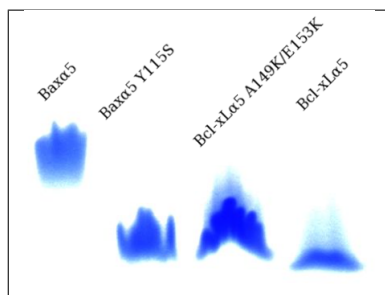


**Fig. 14.2 : Dimerización de Bax $\alpha$ 5 en micelas de SDS.** Se analizaron mediante electroforesis en gels de Tris-Tricina, 20  $\mu$ g de cada uno de los péptidos: Bax $\alpha$ 5, Bax $\alpha$ 5 Y115S, Bcl-xL $\alpha$ 5 A149K/E153K y Bcl-xL $\alpha$ 5. Una vez separados, los péptidos se tiñeron con azul de Coomassie. Se observaron dos tipos de bandas de acuerdo a su migración electroforética: uno correspondiente a Bcl-xL $\alpha$ 5, Bcl-xL $\alpha$ 5 A149K/E153K y Bax $\alpha$ 5 Y115S; y un segundo, de menor movilidad, correspondiente a Bax $\alpha$ 5. Dado que todos los péptidos son de tamaño similar, este patrón indica la existencia de monómeros (en torno a los 2500 Da) para Bcl-xL $\alpha$ 5, Bcl-xL $\alpha$ 5 A149K/E153K y Bax $\alpha$ 5 Y115S, mientras que Bax $\alpha$ 5 se comporta como un dímero ( $\sim$ 5000 Da).

diferencias entre las estructuras primarias de ambos péptidos. El doble mutante Bcl-xL $\alpha$ 5 A149K/E153K, acerca la secuencia de Bcl-xL $\alpha$ 5 a la de su homólogo de Bax, de manera que presenta cuatro residuos con carga positiva en las mismas posiciones que Bax $\alpha$ 5. Por otro lado, otra diferencia importante es la presencia en la posición 115 de una Tyr en Bax y una Ser en Bcl-xL. La movilidad electroforética de Bax $\alpha$ 5 es menor que la de los otros tres péptidos, lo que sugiere la presencia de un complejo de mayor peso molecular en ese caso. Aunque en este tipo de ensayos es difícil saber a qué estado oligomérico corresponden dichas bandas, la interpretación más probable, sustentada también por los estudios de FRET, es la presencia de dímeros de Bax $\alpha$ 5 y monómeros en el resto de los casos. Además, también podemos concluir que los residuos de Lys mencionados no son indispensables para la dimerización. Sin embargo, Tyr 115 de Bax $\alpha$ 5 sí es un residuo crítico para su dimerización.

### 14.2.2 Oligomerización de Bax $\alpha$ 5 en membranas por FRET

Se usaron los dos pares de péptidos, Bax $\alpha$ 5 y Bax $\alpha$ 5 Y115S, marcados con la sonda fluorescente Alexa350 como “dador” y el cromóforo Dabcyl como “aceptor”. Se midieron los espectros de fluorescencia en presencia,  $F_{DA}$ , y ausencia de acepto,  $F_D$  (FIG. 14.3 A y B) para varias fracciones molares de acepto. Para determinar la capacidad de Bax $\alpha$ 5 para formar dímeros en membranas se representó la eficiencia en la transferencia de energía calculada a partir de la Ec. 13.2 en función de la fracción de acepto (FIG. 14.3 C y D). En el caso de membranas compuestas por POPC se obtiene un buen ajuste lineal para ambos pares dador/acepto, no siendo así para POPC:CL. Este resultado indica la formación específica de dímeros en POPC y la presencia de oligómeros mayores en membranas de POPC:CL, lo que puede interpretarse como que la CL promueve la asociación de Bax $\alpha$ 5. Los dímeros de Bax $\alpha$ 5 en POPC se estudiaron con más detalle. En concreto, se estimó la distancia dador/acepto. En el caso de la sonda dadora presente en

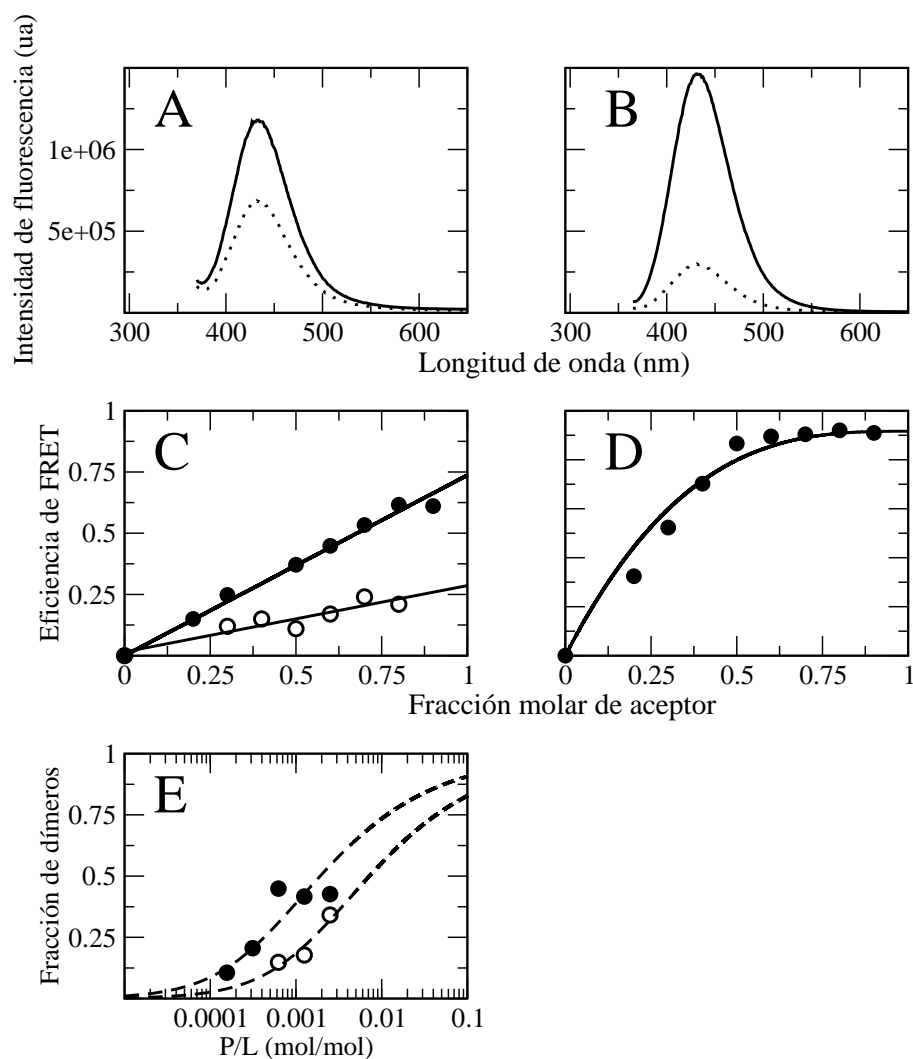


**Fig. 14.3 : Dimerización de Bax $\alpha$ 5 en membranas usando FRET en estado estacionario.** Se usaron dos parejas dador/aceptor: Alexa350-Bax $\alpha$ 5/K(DabcyI)-Bax $\alpha$ 5 (círculos cerrados) y Alexa350-Bax $\alpha$ 5 Y115S/K(DabcyI)-Bax $\alpha$ 5 Y115S (círculos abiertos). La relación P/L total fue 1/200. En A) y B) se muestran espectros de emisión de fluorescencia del dador sólo ( $F_D$ , línea continua) y del par dador/aceptor ( $F_{DA}$ , línea punteada). La fracción molar de aceptor ( $f_A$ ) usada fue 0.5. La sonda DabcyI no es fluorescente. En C) y D) se muestra la eficiencia en la transferencia de energía ( $E^{ss}$ ) en función de la fracción molar de aceptor. El ajuste lineal (línea continua) en C) ilustra la formación exclusiva de dímeros. En D) se usó un modelo tetramérico para ajustar los datos experimentales [461]. En E) se presenta la fracción de dímeros (obtenida a partir de la eficiencia en la transferencia de energía debida únicamente a dimerización,  $E^{dimer}$ ) en función de la relación P/L y el correspondiente ajuste usado para obtener  $K_{dimer}$  (línea discontinua). La composición lipídica fue POPC (panel izquierdo) o POPC:CL (80:20) (panel derecho).

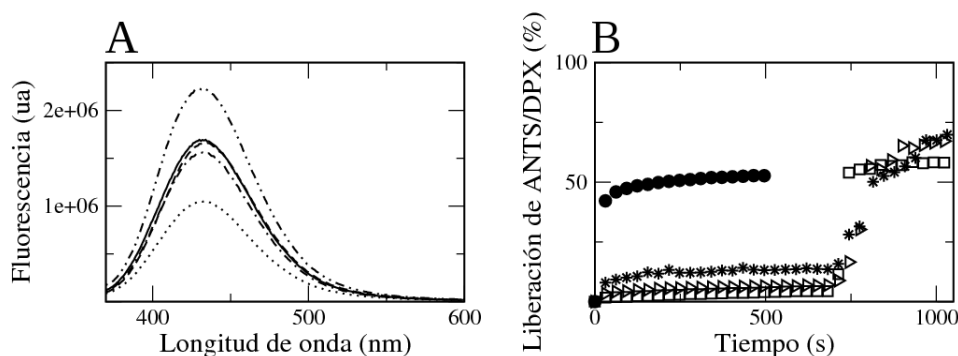


**Fig. 14.4 : Interacción entre Bax $\alpha$ 5 y otros polipéptidos derivados de Bcl-xL.** A) La presencia de dadores y aceptores en la misma preparación reduce la intensidad de fluorescencia (línea punteada,  $F_{DA}$ ) con respecto al nivel mostrado por muestras que contienen únicamente dador (línea continua,  $F_D$ ). La adición de especies no marcadas permite recuperar parcialmente los niveles originales de fluorescencia dependiendo del caso ( $F_{DAU}$ ): Bax $\alpha$ 5 (línea discontinua), Bcl-xL $\alpha$ 5 (línea discontinua y punteada), Bcl-xL $\Delta$ Ct pH=4.5 (línea discontinua y punto doble). Cada especie (dador, aceptor y no marcado) se usó a una relación P/L de 1/300. B) Efecto de Bcl-xL $\Delta$ Ct sobre la liberación de ANTS/DPX inducida por Bax $\alpha$ 5. Los LUVs fueron incubados durante  $\sim$ 10 min con Bcl-xL $\Delta$ Ct (pH=4.5) a diferentes relaciones P/L: 1/500 (cuadrados), 1/250 (triángulos) y 1/100 (estrellas). A continuación se añadió Bax $\alpha$ 5 a una relación P/L=1/500. Los círculos muestran el comportamiento de Bax $\alpha$ 5 en ausencia de Bcl-xL $\Delta$ Ct.

el extremo N-terminal y la aceptora en el extremo C-terminal, la distancia obtenida fue 3.0 nm, similar a la distancia entre extremos en un péptido completamente helicoidal (3.3 nm), lo cual sugiere una orientación cabeza-cabeza (“paralela”) de las unidades peptídicas que forman en el dímero. Es importante destacar que la mutación Y115S causó una notable disminución en la eficiencia de la transferencia de energía, sugiriendo de nuevo una capacidad de dimerización disminuida en el caso de Bax $\alpha$ 5 Y115S.

### 14.2.3 Energética de la interacción Bax $\alpha$ 5-Bax $\alpha$ 5

La EC. 13.6 se usó para ajustar la fracción de dímeros en función de la relación molar péptido-lípido (P/L) con el objetivo de obtener la constante de equilibrio de dimerización,  $K_{dimer}$  (FIG. 14.3 E). A partir de dicha constante se calculó la energía libre de dimerización,  $\Delta G_{dimer}$ , obteniéndose un valor de -3.7 kcal/mol.

### 14.2.4 Interacciones Bax $\alpha$ 5 y otros polipéptidos derivados de Bcl-xL

La posible interacción entre Bax $\alpha$ 5 y Bcl-xL $\Delta$ Ct se evaluó mediante experimentos de competición. A muestras con Alexa350-Bax $\alpha$ 5 como dador y K(Dabcyl)-Bax $\alpha$ 5 como aceptor se les añadió una especie no marcada (FIG. 14.4 A). Tanto el propio Bax $\alpha$ 5 como Bcl-xL $\alpha$ 5 y Bcl-xL $\Delta$ Ct, este último a pH=4.5, son capaces de interactuar con Alexa350-Bax $\alpha$ 5 desplazando a K(Dabcyl)-Bax $\alpha$ 5, por lo que la fluorescencia retorna a niveles similares a muestras que contienen sólo dador. Este hecho sugiere que todos estos polipéptidos son capaces de interactuar con Bax $\alpha$ 5 en membranas. Posteriormente se

estudió el posible efecto inhibitorio de dichas interacciones sobre la capacidad formadora de poros de Bax $\alpha$ 5. Para ello liposomas con ANTS/DPX encapsulado fueron incubados con Bcl-xL $\Delta$ Ct a pH=4.5 para facilitar su unión (FIG. 14.4 B). Posteriormente se añadió Bax $\alpha$ 5, comprobándose que los niveles de liberación de contenidos son iguales o incluso superiores a los presentados por Bax $\alpha$ 5 sin incubación previa con Bcl-xL $\Delta$ Ct. Este hecho sugiere que el complejo Bax $\alpha$ 5-Bcl-xL $\Delta$ Ct es competente para la formación de poros en membranas. Resultados similares se obtuvieron con Bcl-xL $\alpha$ 5.

## 14.3 Estructura de complejos Bax $\alpha$ 5-membranas

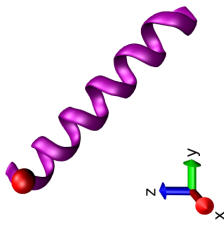
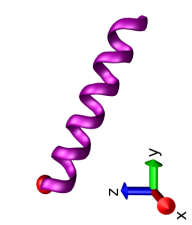
### 14.3.1 Orientación de Bax $\alpha$ 5 en la membrana

La técnica de *dicroísmo de infrarrojos con especificidad de sitio* (SSID) se basa en el hecho de que la razón dicroica de un TDM (en esta Tesis se ha usado específicamente la banda amida I correspondiente a la vibración del grupo C=O) depende de su orientación espacial, definida por los ángulos  $\beta$  y  $\omega$  [414]. Se sintetizaron diferentes versiones de Bax $\alpha$ 5 marcadas cada una de ellas con la sonda  $1-^{13}C-^{18}O$ . De esta forma, la señal que procede específicamente de la sonda aparece resuelta en un región espectral diferente, en torno a  $1590\text{ cm}^{-1}$ , separada del resto de la banda de absorción amida I, localizada entre  $1700$  y  $1600\text{ cm}^{-1}$ . Por tanto, a partir de la medición de la razón dicroica se obtienen dos parámetros experimentales,  $R_{helix}$ , que es el dicroísmo promedio de todos los grupos C=O peptídicos y depende sólo de  $\beta$ ; y  $R_{site}$ , dicroísmo procedente exclusivamente de la marca isotópica y cuya magnitud depende de  $\beta$  y  $\omega$ . En esta Tesis se propone una nueva forma para analizar los datos de SSID que se basa en el uso de la función de error  $\chi^2$  (EC. 13.1). El valor mínimo de  $\chi^2$  proporciona dos tipos de información. En primer lugar, su valor informa sobre la bondad de la solución encontrada, es decir, si el error se encuentra dentro del error experimental. En nuestro caso, dado que se han utilizado en total 14 restricciones experimentales (7  $R_{helix}$  y 7  $R_{site}$ ) los valores de  $\chi^2$  por debajo de 14 se consideran “aceptables”<sup>1</sup>. En segundo lugar, si el valor mínimo encontrado es aceptable, los parámetros correspondientes  $\{\beta, \omega\}$  pueden ser interpretados en términos moleculares.

En nuestro caso decidimos utilizar modelos de monómero y dímero como punto de partida para el modelado de cuerpo rígido (ver SEC. 14.2). En la TAB. 14.2 se presenta el resultado de dicho modelado para multicapas orientadas de DMPC y POPC<sup>2</sup>. Puede verse que cuando se usan monómeros los valores de  $\chi^2$  obtenidos son no aceptables ( $\chi^2 > 12$ ) ni en POPC ni en DMPC. Por el contrario, si se modela Bax $\alpha$ 5 como un dímero los errores disminuyen drásticamente tanto en DMPC como en POPC. La mejor solución en DMPC se encuentra para un dímero asimétrico, con respecto a la orientación de la membrana, con pares de valores  $\{\beta, \omega\}$  de  $\{59^\circ, 157^\circ\}$  y  $\{51^\circ, 10^\circ\}$  para cada monómero.

- 
- 1 En la práctica, sólo se utilizaron 12 restricciones experimentales dado que un residuo se excluyó por dar sistemáticamente valores anómalos.
  - 2 Los valores de  $R_{helix}$  fueron similares entre POPC, DOPC y POPC:CL concluyéndose que la presencia de CL no afecta a la orientación de Bax $\alpha$ 5. Sin embargo, se observó una diferencia importante entre DMPC y POPC lo cual motivó su posterior estudio.

**Tab. 14.2 : Resultados del modelado mediante cuerpo rígido.** Se muestran los mejores ajustes de ángulos de inclinación y de rotación del modelo explícito de hélice- $\alpha$  de Bax $\alpha$ 5 usando la función de error  $\chi^2$  como guía. La esfera roja marca la posición del residuo de triptófano y sirve para definir el valor de  $\omega$ . El eje z es paralelo a la normal de la membrana.

Lípido	Monómero			Dímero					
	Error	$\beta(^{\circ})$	$\omega(^{\circ})$	Error	$\beta_A(^{\circ})^a$	$\omega_A(^{\circ})^a$	$\omega_B(^{\circ})^a$	Modelo	
<i>DMPC</i>	81	46	311	12.4	59	51	157	10	
<i>POPC</i>	29	65	266	7.8	74	60	157	20	

<sup>a</sup> Los ángulos  $\beta$  y  $\omega$  están dados para cada hélice individual, A y B, del dímero

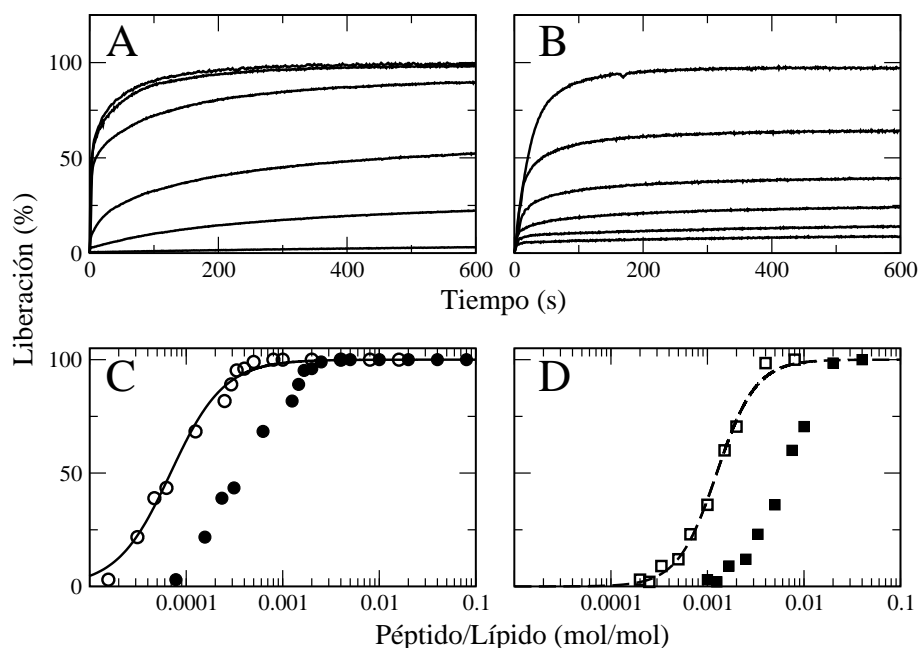


**Fig. 14.5 :** Estudio de la liberación de contenidos encapsulados en LUVs en función de la relación molar  $Bax\alpha 5$ /lípidio. La concentración lipídica se mantuvo constante en  $5 \mu M$  mientras que la concentración peptídica se varió. En A) y B) se han representado las cinéticas de liberación para varias P/L que crecen de abajo arriba. En C) y D) se ha representado el porcentaje de liberación en el equilibrio (transcurridos  $\sim 10$  min tras la adición del péptido) en función de la relación P/L teniendo en cuenta todo el péptido añadido (puntos cerrados) o sólo el péptido unido a membrana (puntos abiertos) a través de  $K_x$ . La composición lipídica fue POPC (panel izquierdo) o POPC:CL (80:20) (panel derecho).

En POPC, el mejor ajuste se obtiene también para un dímero asimétrico pero con los siguientes valores angulares para cada subunidad:  $\{74^\circ, 157^\circ\}$  y  $\{60^\circ, 20^\circ\}$ .

## 14.4 Formación de poros por $Bax\alpha 5$

### 14.4.1 Experimentos en LUVs

La cinética de liberación de contenidos encapsulados en LUVs se estudió en función de la relación P/L para dos composiciones distintas: POPC y POPC:CL. Podemos observar que cantidades crecientes de péptido provocan una mayor liberación, hasta tal punto que a partir de cierta P/L todas las vesículas se encuentran poradas (FIG. 14.5 A y B). Dado que la relación P/L que importa no es la correspondiente al péptido total sino más bien la derivada de la cantidad de péptido unido a la membrana, es necesario tener en cuenta el coeficiente de partición agua-membrana. Se utilizó el modelo dosis-respuesta para ajustar la dependencia del porcentaje de liberación con respecto a la relación P/L (FIG. 14.5 C y D). La relación P/L para la cual se produce el 50% de liberación es mayor en POPC:CL (1/160) que en POPC (1/2800). Este hecho sugiere que la CL tiene

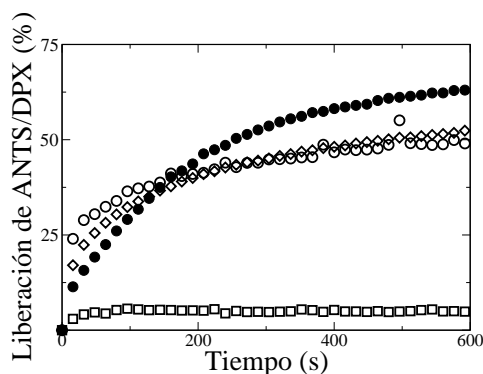


**Fig. 14.6 :** Efecto de las mutación de residuos de Bax $\alpha$ 5 en la liberación de contenidos encapsulados en LUVs mediada por los péptidos correspondientes. La relación molar péptido/lípido se mantuvo constante (1/800) en todos los casos. Bax $\alpha$ 5 (círculos cerrados), Bax $\alpha$ 5 Y115S (diamantes), Bcl-xL $\alpha$ 5 A149K/E153K (círculos abiertos) y Bcl-xL $\alpha$ 5 (cuadrados). El pH fue 4.5 con el objeto de facilitar la unión de Bcl-xL $\alpha$ 5.

un efecto inhibitor de la formación de poros por Bax $\alpha$ 5.

Por otro lado, con el objeto de estudiar los determinantes de secuencia implicados en la formación de poros se estudió la liberación de contenidos de vesículas por parte de varias versiones de Bax $\alpha$ 5 (FIG. 14.6). Bcl-xL $\alpha$ 5 presentó una actividad de membrana prácticamente nula mientras que los mutantes Bax $\alpha$ 5 Y115S y Bcl-xL $\alpha$ 5 A149K/E153K mostraron cinéticas de liberación similares a la de Bax $\alpha$ 5. Este resultado sugiere que son las Lys y no la Tyr los residuos importantes responsables de la formación de poros. Al mismo tiempo este resultado sugiere que la dimerización no es indispensable para la formación de poros.

La principal dificultad de los experimentos de liberación de calceína es que no informan sobre lo que ocurre a tiempos largos, es decir, ¿siguen los poros abiertos cuando la señal de fluorescencia llega al estado estacionario? Para responder a esta pregunta, se utilizó una estrategia distinta, consistente en la visualización directa de las vesículas lipídicas.

#### 14.4.2 Experimentos con GUVs

La ventaja del estudio con GUVs es que se puede analizar el comportamiento individual de cada vesícula mediante microscopía de fluorescencia. En este caso la investigación se realiza mediante la adición de sondas fluorescentes desde el exterior y en tiempos definidos a GUVs marcados con el análogo lipídico DiD (fluorescencia roja), lo cual permite el estudio de la entrada sucesiva de sondas. En la FIG. 14.7 se muestran imágenes de GUVs antes y después de la adición consecutiva de tres sondas en los tiempos indicados. La primera sonda (Alexa555, azul) comienza su entrada a un tiempo variable para cada vesícula, normalmente entre los 30 y 90 min, reflejando la naturaleza estocástica del proceso de formación de poros. A los 120 min se tomó otra imagen donde puede verse que algunos GUVs están completamente llenos de sonda mientras que otros están

completamente vacíos. Este hecho demuestra que Bax $\alpha$ 5 sigue el mecanismo conocido como “todo o nada” [181]. En cambio, la segunda sonda (Alexa488, verde) se añadió a los 120 min y entró inmediatamente sólo en aquellos GUVs que habían sido porados previamente. Finalmente, la tercera sonda (Atto655, rojo) muestra un comportamiento similar a la segunda. Estos resultados sugieren que aquellas vesículas que fueron inicialmente poradas mantienen dicho estado de poración a lo largo del tiempo. Al mismo tiempo, existe una población de GUVs que permanecen inalterados (sin poros) durante todo el tiempo de observación. Téngase en cuenta que este experimento informa sólo de estados porados y no de poros individuales.

Una cuestión importante es si los poros observados *a tiempos cortos* (poros *cinéticos* o de *pre-equilibrio*) presentan propiedades similares a aquellos observados *a tiempos largos* o *en equilibrio*. Aunque esta pregunta es difícil de responder, nos hemos centrado en el tamaño de los poros, que puede ser estudiado mediante el uso de sondas fluorescentes de distinto tamaño. En concreto, se usaron sondas “pequeñas” de  $\sim 0.5$  nm de radio hidrodinámico (de la serie Alexa y Atto) y “grandes”  $\sim 2.3$  nm de radio hidrodinámico (dextrano fluorescente de 10 kDa). Cuando las dos sondas, pequeña y grande, son añadidas desde el principio junto con Bax $\alpha$ 5, ambas pueden entrar en los GUVs (FIG. 14.8 A-C). El análisis de las cinéticas de entrada de ambas demuestra que la sonda pequeña es capaz de entrar completamente, mientras que la grande experimenta una desaceleración en su entrada antes de llegar a equilibrarse con su concentración exterior. Este hecho sugiere que los poros iniciales son de tamaño grande pero se relajan en cuestión de minutos a poros más pequeños que no permite el paso del dextrano. De hecho, si los GUVs se incuban en presencia de Bax $\alpha$ 5 y a los 120 min se añaden las dos sondas, sólo la pequeña es capaz de entrar (FIG. 14.8 D). Por tanto, los poros iniciales, o de tipo cinético, son de mayor tamaño (más de 2.3 nm de radio) que los poros de equilibrio ( $\sim 2.3$  nm de radio). Por otro lado, una análisis cuantitativo detallado de las cinéticas de entrada de sonda en un gran número de GUVs individuales también muestra que el tamaño efectivo de los poros presentes en cada GUV se reduce a los pocos minutos de comenzar el proceso de formación.

Finalmente, se estudió el efecto de la concentración de Bax $\alpha$ 5 sobre la formación de poros. Para ello se sintetizó un derivado de Bax $\alpha$ 5 conteniendo la sonda fluorescente Alexa647. Así, es posible monitorizar simultáneamente la cinética de unión del péptido a la membrana y la cinética de entrada de contenidos. En primer lugar se midió la cantidad de Alexa647-Bax $\alpha$ 5 en el momento de abrirse los poros,  $C_{open}$ . Los resultados, mostrados en la FIG. 14.9 A y B, demuestran que independientemente de la relación molar péptido/lípido empleada, las vesículas se poran con una cantidad similar de Alexa647-Bax $\alpha$ 5 en la membrana. Este hecho sugiere que se precisa de una cierta concentración umbral de péptido para la formación de poros. No obstante, este análisis no tiene en cuenta el hecho observable de que existen GUVs con cantidades similares de Bax $\alpha$ 5 unido y que, sin embargo, no se poran. Por otro lado, las cantidades de Bax $\alpha$ 5 están expresadas en unidades relativas idealmente proporcionales a la concentración. Para evitar estos problemas, la cantidad absoluta de Alexa647-Bax $\alpha$ 5 en la membrana de los GUVs, tanto porados como no porados, se estimó mediante SFCS de doble foco (FIG. 14.9 C). Puede verse cómo la probabilidad de encontrar GUVs porados aumenta con la relación

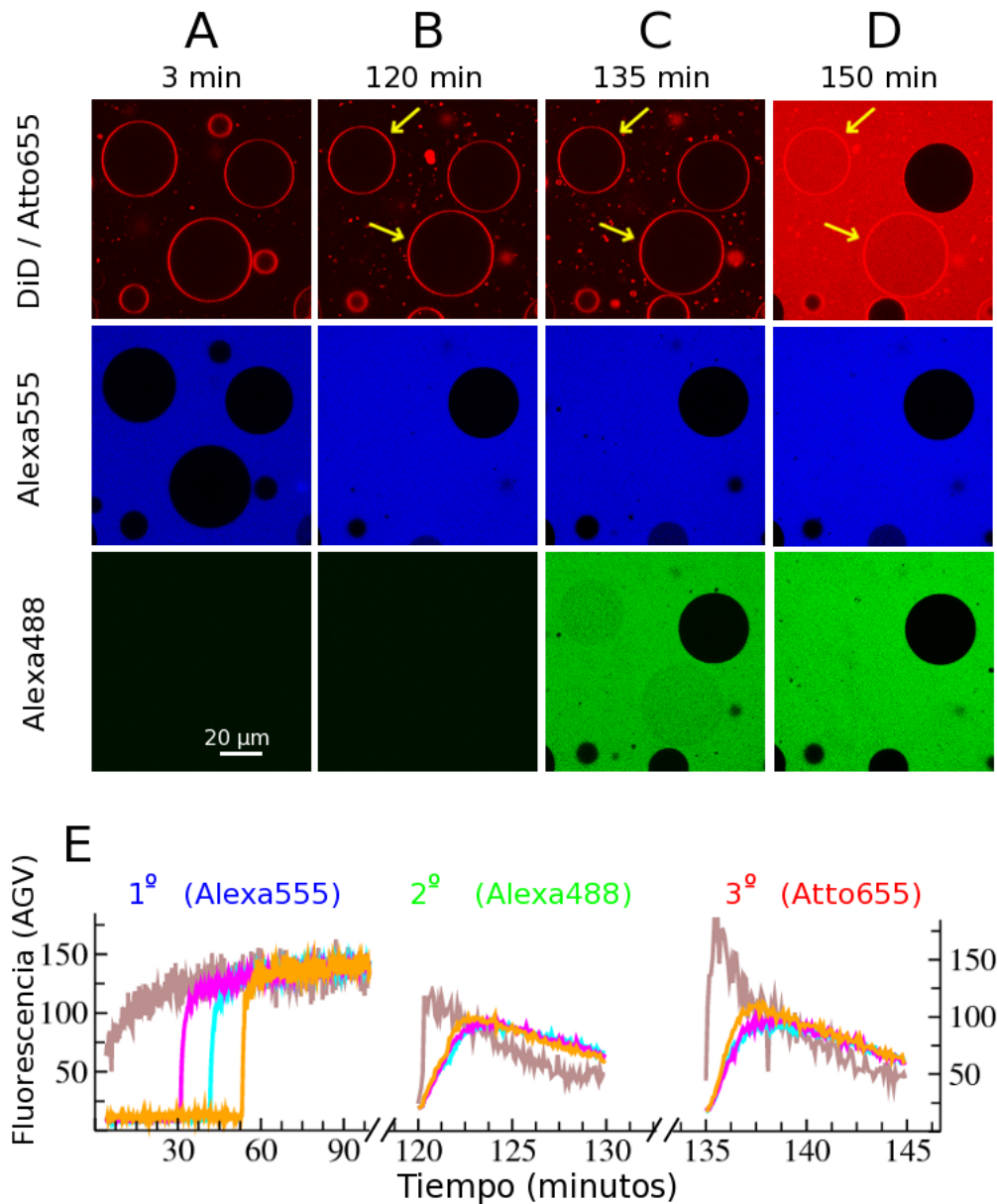


**Fig. 14.7 : Entrada sucesiva de sondas fluorescentes en GUVs individuales mostrando el comportamiento “todo o nada”.** Bax $\alpha$ 5 y el primer colorante (Alexa555, azul) están presentes desde el inicio en la cámara de observación del microscopio. Los GUVs marcados fluorescentemente con la sonda lipofílica DiD (rojo) se añaden hasta conseguir una P/L=1/90 (tiempo=0). A) Se empieza a registrar imágenes de fluorescencia en tres canales desde el minuto 3. Eventualmente algunos GUVs se permeabilizan de forma estocástica y el colorante entra rápidamente. B) Dos horas después, todos los GUVs mantienen su integridad (rojo), pero en algunos (marcados con flechas) la sonda ha entrado completamente. Inmediatamente después, se añadió un segundo colorante (Alexa488, verde). C) Imágenes tomadas tras la entrada del segundo colorante; las vesículas poradas para este colorante (verde) son las mismas que para el primero (azul) y se han marcado en la imagen del canal rojo. Inmediatamente después, se añadió un tercer colorante (Atto655, rojo). D) Imágenes tomadas a los 150 min muestran que todas las vesículas poradas son las mismas que para el primero y segundo. E) Ejemplos de cinéticas de entrada de contenidos en tres GUVs distintos para el primer, segundo y tercer colorante (de izquierda a derecha).

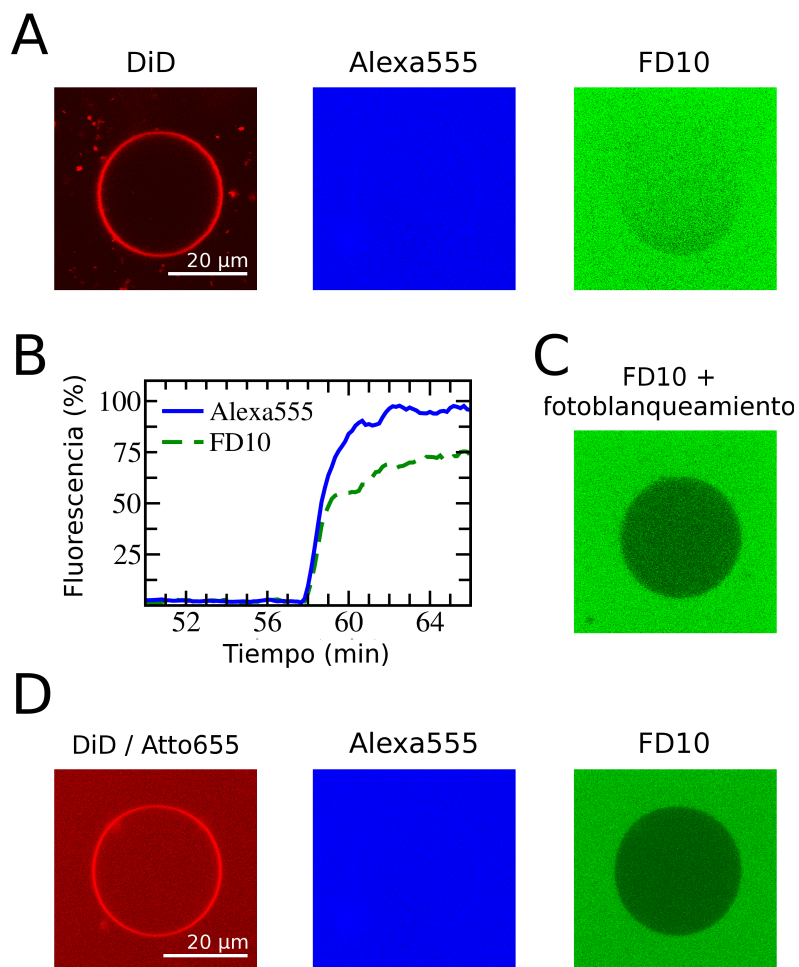


**Fig. 14.8 : Los poros formados por Bax $\alpha$ 5 encogen con el tiempo.** A) Ejemplo de GUV (marcado con DiD, rojo) tras 2 horas de incubación con Bax $\alpha$ 5 en presencia de Alexa555 (azul) y un dextrano fluorescente de 10 kDa (FD10, verde). B) Ambos colorantes empiezan a entrar simultáneamente en el mismo GUV, inicialmente a la misma velocidad aunque la entrada se frena antes de completarse para FD10 (línea discontinua). C) La irradiación continua a 488 nm durante 2 min blanqueó la fluorescencia de aquellas moléculas de FD10 localizadas en el interior del GUV. D) En un experimento adicional los GUVs (marcados con DiD, rojo) se incubaron con Bax $\alpha$ 5 y Atto655 para identificar los GUVs porados a tiempos cortos. GUVs completamente permeables a Atto655 (rojo) al inicio, eran después también permeables a Alexa 555 (azul) pero no a FD10 (verde) ambos añadidos a las 2 h. Los experimentos corresponden a P/L=1/22.5.

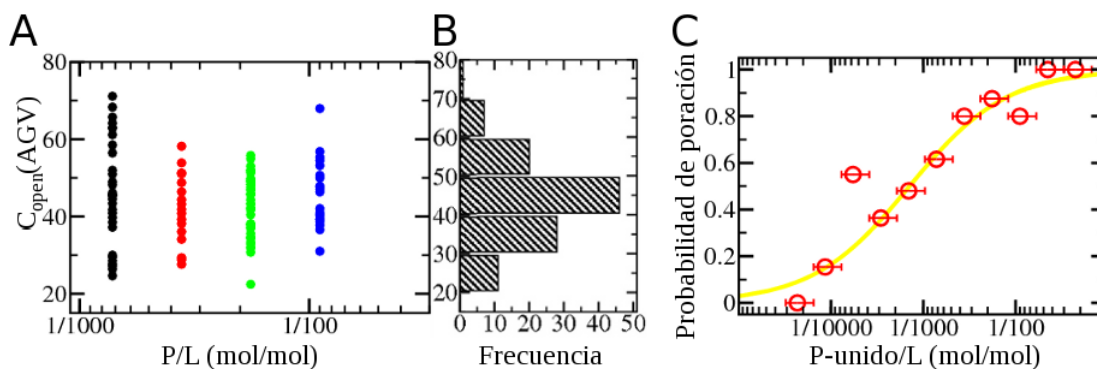


**Fig. 14.9 :** Efecto de la concentración de Alexa647-Bax $\alpha$ 5 sobre sobre la formación de poros. A) Cantidad de Alexa647-Bax $\alpha$ 5 en el momento de abrirse los poros,  $C_{open}$ , en función de la relación péptido/lípido total: 1/720 (negro), 1/360 (rojo), 1/180 (verde) y 1/90 (azul). B) Histograma acumulado para las diferentes P/L.  $\bar{C}_{open} = 45$ . C) Probabilidad de encontrar GUVs con poros, expresada como el cociente entre el número GUVs porados y no porados, en función de la relación molar entre Alexa647-Bax $\alpha$ 5 unido a la membrana y lípidos. La línea muestra el mejor ajuste de los datos a un modelo dosis-respuesta.

molar péptido-unido/lípido. Este resultado indica que la formación de poros en membranas depende no sólo de la concentración de Bax $\alpha$ 5 sino también de otros factores, probablemente relacionados con la naturaleza estocástica del proceso.

## 14.5 Discusión general

### 14.5.1 Energética de las interacciones Bax $\alpha$ 5-Bax $\alpha$ 5 y Bax $\alpha$ 5-membrana

Los resultados obtenidos en las SUB. 14.1.2, 14.2.3 y 14.5 permiten asimilar la actividad formadora de poros de Bax $\alpha$ 5 y péptidos formadores de poros en general a un efecto *tipo catálisis*, representado esquemáticamente en la FIG.14.10 A. (i) Empezando con péptido y membrana libres se forma favorablemente un complejo péptido-membrana ( $\Delta G_x < 0$ ) con los péptidos adsorbidos en interfase<sup>1</sup>. (ii) Se ha postulado que los péptidos se unen mejor en aquellas zonas de la membrana que presentan defectos, lo que constituiría el estado de transición para la formación de poros. Este hecho rebajaría la energía de activación correspondiente a la formación de poros lipídicos con respecto a la ausencia de péptidos ( $E_a^* < E_a$ ). (iii) Adicionalmente, la unión de los péptidos en el borde del poro contribuye a su estabilización ( $\Delta G_{pore} < 0$ ) mediante la reducción en la tensión lineal [197].

<sup>1</sup> La estabilidad del complejo péptido-membrana puede aumentar si el péptido es capaz de ensamblarse generando especies oligoméricas. En el caso de Bax $\alpha$ 5  $\Delta G_{dimer} < 0$ . Dicho proceso no se ha representado en la figura.

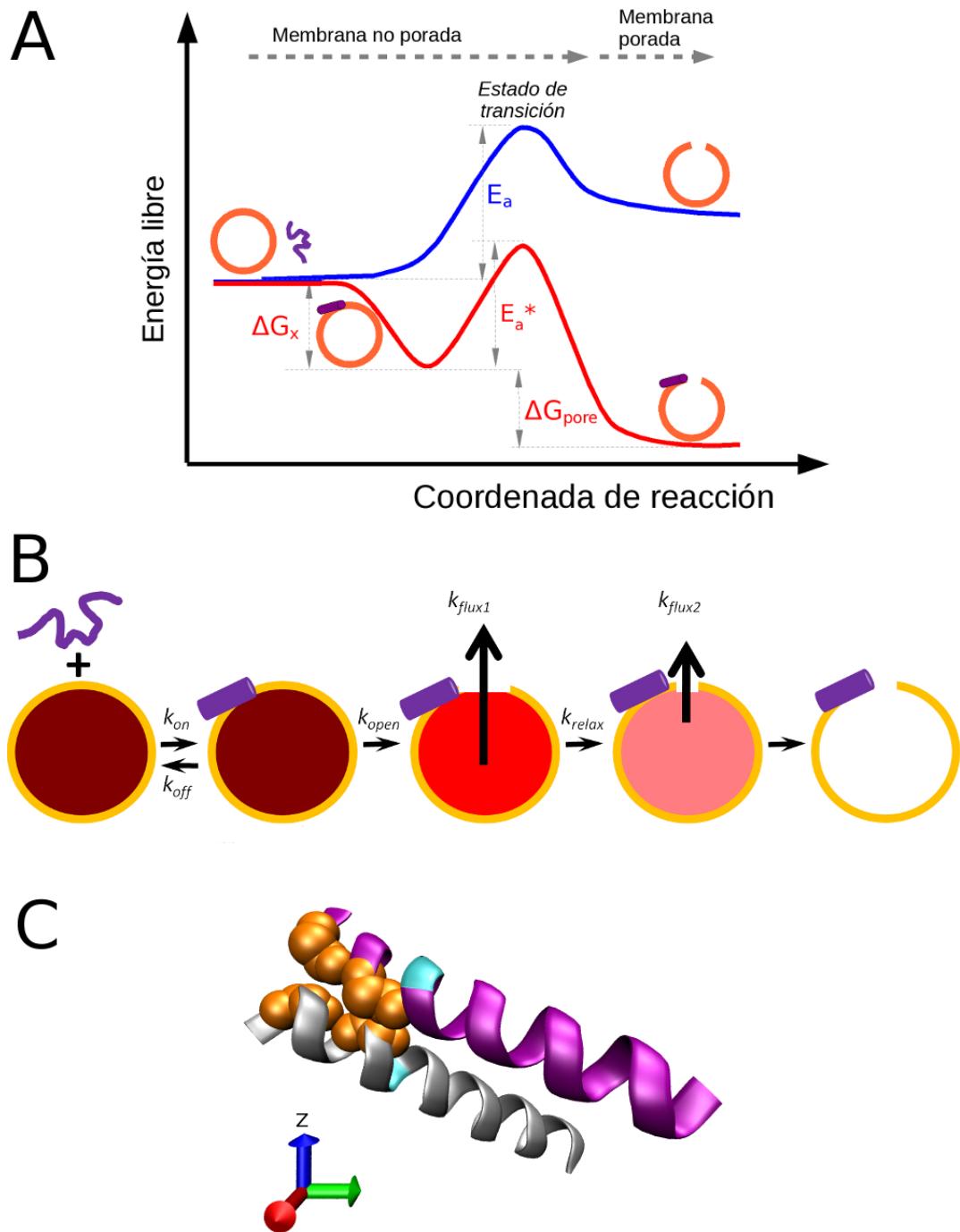


**Fig. 14.10 :** Modelos que se derivan de los resultados obtenidos en esta Tesis. A) Modelo termodinámico, B) Modelo cinético, C) Modelo molecular. Ver texto principal para una explicación detallada.

### 14.5.2 Cinética de las interacciones Bax $\alpha$ 5-membrana

Los resultados presentados en la SEC. 14.4 permiten formular el siguiente modelo cinético (FIG. 14.10 B). (i) Los péptidos, inicialmente en solución acuosa, se unen a las vesículas lipídicas con una constante cinética  $k_{on}$ . También pueden disociarse de ellas con una constante cinética  $k_{off}$ . La adsorción de péptidos en la interfase de la membrana causa un aumento del área y una disminución del espesor de la misma. Esta situación se puede corresponder al llamado estado  $B_{ex}$  [85, 86]. (ii) Los poros se abren estocásticamente con una constante de velocidad  $k_{open}$ , que depende de la composición lipídica siendo menor en presencia de CL. Este estado puede corresponder al llamado estado  $P_i$  [85, 86] La sonda encapsulada inicialmente en el interior de la vesícula sale con una constante cinética  $k_{flux1}$ . (iii) Los poros iniciales relajan a poros “de equilibrio” con una constante cinética  $k_{relax}$ . Los poros a tiempo corto se diferencian de los poros a tiempo largo al menos en su tamaño presentando estos últimos un radio aproximado de 2.3 nm. El estado final puede corresponderse a la coexistencia de las fases  $S$  e  $I$  [114] donde coexisten poros relajados y péptidos en interfase. Desde este estado la sonda puede liberarse con una constante  $k_{flux2}$  ( $k_{flux2} < k_{flux1}$ ).

### 14.5.3 Estructura de complejos Bax $\alpha$ 5-membrana y formación de poros

Los resultados de la SEC. 14.2 demuestran que Bax $\alpha$ 5 es capaz de dimerizar tanto en micelas de SDS como en membranas de POPC. En presencia de CL, Bax $\alpha$ 5 es capaz de formar complejos mayores. La estructura de Bax $\alpha$ 5 en membranas de POPC se estudió con detalle mediante SSID, técnica que permite estimar la orientación de péptidos con respecto a la membrana en forma de ángulos de inclinación ( $\beta$ ) y rotación azimutal ( $\omega$ ). El análisis de los datos experimentales se realizó usando el método de modelado de cuerpo rígido. La búsqueda del mejor ajuste mediante la función de error  $\chi^2$  sugiere también que Bax $\alpha$ 5 se encuentra en forma dimerica en su estado unido a membrana, donde los pares de valores  $\{\beta, \omega\}$  de las correspondientes unidades del dímero serían  $\{74^\circ, 157^\circ\}$  y  $\{60^\circ, 20^\circ\}$  en membranas de POPC (FIG. 14.10 C).

### 14.5.4 El código de Bax $\alpha$ 5

En esta Tesis hemos desvelado también parte de los requerimientos de secuencia para los procesos de dimerización y formación de poros. La formación de poros depende de la presencia de Lys en posiciones específicas dado que la introducción de estas en la secuencia de Bcl-xL $\alpha$ 5, que presenta actividad permeabilizadora baja, hace que el péptido resultante tenga una capacidad liberadora de contenidos mayor, casi tan alta como la de Bax $\alpha$ 5 (FIG. 14.6). Sin embargo, Bcl-xL $\alpha$ 5 A149K/E153K, al igual que Bcl-xL $\alpha$ 5, no es capaz de dimerizar, al menos en micelas de SDS (FIG. 14.2). En consecuencia, proponemos que el motivo responsable de la formación de poros en Bax $\alpha$ 5 es el siguiente:  $KxxxKxxx(x)K$ . Tal motivo no interviene en la formación de dímeros.

Por otro lado el potencial de oligomerización depende al menos del residuo Tyr115, ya que el mutante de Bax $\alpha$ 5 Y115S presenta una tendencia a dimerizar mucho menor (FIG. 14.2). No obstante, la actividad formadora de poros de Bax $\alpha$ 5 Y115S es similar a

la de Bax $\alpha$ 5 (FIG. 14.6). Adicionalmente, la secuencia de Bax $\alpha$ 5 presenta un motivo de dimerización similar al de glicoforina [27], *GxxxA* y se ha reportado que la mutación de dicha glicina genera especies de Bax incapaces de dimerizar [527]. Por tanto proponemos que el motivo de dimerización en membranas de Bax $\alpha$ 5 es el siguiente: *GxxxAxxY*. Tal motivo no es responsable de la liberación de contenidos.

#### 14.5.5 Bax $\alpha$ 5 es un dominio activo mínimo de Bax

La comparación entre Bax y Bax $\alpha$ 5 permite concluir lo siguiente: (i) Bax $\alpha$ 5 se une a membranas lipídicas espontáneamente mientras que Bax necesita la ayuda de otras proteínas [269]. (ii) Bax $\alpha$ 5 se orienta de forma casi paralela a la superficie de la membrana mientras que se ha propuesto que la correspondiente hélice en Bax se inserta de forma transmembrana [257]. (iii) Bax $\alpha$ 5 es capaz de ensamblarse en oligómeros, al menos dímeros, aunque Bax es capaz de formar agregados aparentemente mayores [265, 268]. (iv) Bax $\alpha$ 5 induce la apertura de grandes poros lipídicos que relejan a poros estables más pequeños, mientras que Bax forma poros de tamaños mayores cuya estabilidad a tiempos largos se desconoce.

### 14.6 Conclusiones

Las conclusiones de esta Tesis se pueden resumir en los siguientes puntos:

1. Bax $\alpha$ 5 se une espontáneamente a membranas lipídicas plegándose en forma de hélice- $\alpha$ . El contenido en hélice- $\alpha$  depende de la composición lipídica, siendo menor en POPC (~60 %) que en presencia de CL (~68 %).
2. Bax $\alpha$ 5 es capaz de oligomerizar en el estado unido a membrana. La especie agregada depende de la composición lipídica, variando desde dímeros paralelos en POPC y probablemente también en DMPC a oligómeros de mayor tamaño en presencia de CL. Se propone el siguiente motivo de dimerización para Bax $\alpha$ 5: *GxxxAxxY*.
3. Se pueden detectar interacciones Bax $\alpha$ 5-Bcl-xL $\Delta$ Ct y Bax $\alpha$ 5-Bcl-xL $\alpha$ 5 en membranas compuestas por POPC:DOPE:CL, pero no se observa inhibición de la actividad liberadora de contenidos de vesículas de Bax $\alpha$ 5 con motivo de tal interacción.
4. La búsqueda de la mejor orientación de Bax $\alpha$ 5 en membranas puede realizarse mediante la generación explícita de modelos estructurales y guiada por la función de error  $\chi^2$ .
5. La orientación de Bax $\alpha$ 5 en membranas depende de la composición lipídica. En DMPC, Bax $\alpha$ 5 puede ser modelado como un dímero con pares  $\{\beta, \omega\}$  de  $\{59^\circ, 157^\circ\}$  y  $\{51^\circ, 10^\circ\}$ . En POPC, Bax $\alpha$ 5 puede ser modelado como un dímero con pares  $\{\beta, \omega\}$  de  $\{74^\circ, 157^\circ\}$  y  $\{60^\circ, 20^\circ\}$ .
6. La actividad liberadora de contenidos de vesículas lipídicas de Bax $\alpha$ 5 depende de la composición lipídica, presentando la CL un efecto inhibitor fuerte sobre la formación de poros.

7. Dicha actividad depende de la presencia de Lys en posiciones específicas de la estructura primaria. Se propone el siguiente motivo de formación de poros para Bax $\alpha$ 5:  $KxxxKxxx(x)K$ .
8. Bax $\alpha$ 5 induce la apertura de poros cinéticos a tiempos cortos que posteriormente relajan a estructuras estables de equilibrio a tiempos largos.
9. A nivel individual, los poros de equilibrio inducidos por Bax $\alpha$ 5 son diferentes de los poros cinéticos, al menos en tamaño, presentando un radio de  $\sim 2.3$  nm.
10. Una concentración crítica de Bax $\alpha$ 5 unido a membrana es condición necesaria, pero no suficiente, para la formación de poros. Tanto dicha concentración como factores estocásticos contribuyen a la apertura de los poros.



# Bibliografía

- [1] Berg, J. M., J. L. Tymoczko, and L. Stryer, 2010. *Biochemistry*. W.H. Freeman & Company.
- [2] Fernandez, M. G., L. Troiano, L. Moretti, M. Nasi, M. Pinti, S. Salvioli, J. Dobrucki, and A. Cossarizza, 2002. Early changes in intramitochondrial cardiolipin distribution during apoptosis. *Cell Growth Differ* 13:449–455.
- [3] Degroote, S., J. Wolthoorn, and G. van Meer, 2004. The cell biology of glycosphingolipids. *Semin Cell Dev Biol* 15:375–387.
- [4] Mouritsen, O. G., and M. J. Zuckermann, 2004. What's so special about cholesterol? *Lipids* 39:1101–1113.
- [5] Mouritsen, O. G., 2004. *Life as a Matter of Fat: The Emerging Science of Lipidomics*. Springer, 1st ed. 2004. corr. 2nd printing edition.
- [6] Helfrich, W., 1973. Elastic properties of lipid bilayers: theory and possible experiments. *Z Naturforsch C* 28:693–703.
- [7] Marsh, D., 1996. Intrinsic curvature in normal and inverted lipid structures and in membranes. *Biophys J* 70:2248–2255.
- [8] Seddon, J. M., and R. H. Templer, 1995. Structure and Dynamics of Membranes, Generic and Specific Interaction, *Handbook of Biological Physics*, Elsevier, Amsterdam, chapter Polymorphism of Lipid-Water Systems in Structure and Dynamics of Membranes. From Cells to Vesicles, 97–160.
- [9] de Kruijff, B., 1997. Lipid polymorphism and biomembrane function. *Curr Opin Chem Biol* 1:564–569.
- [10] Epanand, R. M., 1998. Lipid polymorphism and protein-lipid interactions. *Biochim Biophys Acta* 1376:353–368.
- [11] van den Brink-van der Laan, E., J. A. Killian, and B. de Kruijff, 2004. Nonbilayer lipids affect peripheral and integral membrane proteins via changes in the lateral pressure profile. *Biochim Biophys Acta* 1666:275–288.
- [12] Hickel, A., S. Danner-Pongratz, H. Amenitsch, G. Degovics, M. Rappolt, K. Lohner, and G. Pabst, 2008. Influence of antimicrobial peptides on the formation of nonlamellar lipid mesophases. *Biochim Biophys Acta* 1778:2325–2333.
- [13] Joanne, P., C. Galanth, N. Goasdoué, P. Nicolas, S. Sagan, S. Lavielle, G. Chassaing, C. E. Amri, and I. D. Alves, 2009. Lipid reorganization induced by membrane-active peptides probed using differential scanning calorimetry. *Biochim Biophys Acta* 1788:1772–1781.
- [14] Prenner, E. J., R. N. Lewis, K. C. Neuman, S. M. Gruner, L. H. Kondejewski, R. S. Hodges, and R. N. McElhaney, 1997. Nonlamellar phases induced by the interaction of gramicidin S with lipid bilayers. A possible relationship to membrane-disrupting activity. *Biochemistry* 36:7906–7916.
- [15] Lipowsky, R., and E. Sackmann, 1995. *Structure and Dynamics of Membranes: I. From Cells to Vesicles / II. Generic and Specific Interactions: From Cells to Vesicles AND Vol 1*. North Holland.
- [16] White, S. H., and G. von Heijne, 2008. How translocons select transmembrane helices. *Annual Review of Biophysics* 37:23–42.
- [17] Johnson, A. E., 2009. The structural and functional coupling of two molecular machines, the ribosome and the translocon. *J Cell Biol* 185:765–767.
- [18] Johnson, J. E., and R. B. Cornell, 1999. Amphitropic proteins: regulation by reversible membrane interactions (review). *Mol Membr Biol* 16:217–235.

## Bibliografía

- [19] Lesieur, C., B. Vecsey-Semjen, L. Abrami, M. Fivaz, and F. G. van der Goot, 1997. Membrane insertion: The strategies of toxins (review). *Mol Membr Biol* 14:45–64.
- [20] Rabu, C., V. Schmid, B. Schwappach, and S. High, 2009. Biogenesis of tail-anchored proteins: the beginning for the end? *J Cell Sci* 122:3605–3612.
- [21] Kyte, J., and R. F. Doolittle, 1982. A simple method for displaying the hydropathic character of a protein. *J Mol Biol* 157:105–132.
- [22] Wimley, W. C., and S. H. White, 1996. Experimentally determined hydrophobicity scale for proteins at membrane interfaces. *Nat Struct Biol* 3:842–848.
- [23] Wimley, W. C., T. P. Creamer, and S. H. White, 1996. Solvation energies of amino acid side chains and backbone in a family of host-guest pentapeptides. *Biochemistry* 35:5109–5124.
- [24] White, S. H., and W. C. Wimley, 1999. Membrane protein folding and stability: physical principles. *Annu Rev Biophys Biomol Struct* 28:319–365.
- [25] Moore, D. T., B. W. Berger, and W. F. DeGrado, 2008. Protein-protein interactions in the membrane: sequence, structural, and biological motifs. *Structure* 16:991–1001.
- [26] Walters, R. F. S., and W. F. DeGrado, 2006. Helix-packing motifs in membrane proteins. *Proc Natl Acad Sci U S A* 103:13658–13663.
- [27] MacKenzie, K. R., J. H. Prestegard, and D. M. Engelman, 1997. A transmembrane helix dimer: structure and implications. *Science* 276:131–133.
- [28] Smith, S. O., D. Song, S. Shekar, M. Groesbeek, M. Ziliox, and S. Aimoto, 2001. Structure of the transmembrane dimer interface of glycophorin A in membrane bilayers. *Biochemistry* 40:6553–6558.
- [29] Lemmon, M. A., J. M. Flanagan, H. R. Treutlein, J. Zhang, and D. M. Engelman, 1992. Sequence specificity in the dimerization of transmembrane alpha-helices. *Biochemistry* 31:12719–12725.
- [30] Senes, A., M. Gerstein, and D. M. Engelman, 2000. Statistical analysis of amino acid patterns in transmembrane helices: the GxxxG motif occurs frequently and in association with beta-branched residues at neighboring positions. *J Mol Biol* 296:921–936.
- [31] Senes, A., D. E. Engel, and W. F. DeGrado, 2004. Folding of helical membrane proteins: the role of polar, GxxxG-like and proline motifs. *Curr Opin Struct Biol* 14:465–479.
- [32] Arbely, E., Z. Granot, I. Kass, J. Orly, and I. T. Arkin, 2006. A trimerizing GxxxG motif is uniquely inserted in the severe acute respiratory syndrome (SARS) coronavirus spike protein transmembrane domain. *Biochemistry* 45:11349–11356.
- [33] Bocharov, E. V., K. S. Mineev, P. E. Volynsky, Y. S. Ermolyuk, E. N. Tkach, A. G. Sobol, V. V. Chupin, M. P. Kirpichnikov, R. G. Efremov, and A. S. Arseniev, 2008. Spatial structure of the dimeric transmembrane domain of the growth factor receptor ErbB2 presumably corresponding to the receptor active state. *J Biol Chem* 283:6950–6956.
- [34] Wu, Y., S. C. C. Shih, and N. K. Goto, 2007. Probing the structure of the Ff bacteriophage major coat protein transmembrane helix dimer by solution NMR. *Biochim Biophys Acta* 1768:3206–3215.
- [35] Kleiger, G., R. Grothe, P. Mallick, and D. Eisenberg, 2002. GXXXG and AXXXA: common alpha-helical interaction motifs in proteins, particularly in extremophiles. *Biochemistry* 41:5990–5997.
- [36] Engelman, D. M., Y. Chen, C.-N. Chin, A. R. Curran, A. M. Dixon, A. D. Dupuy, A. S. Lee, U. Lehnert, E. E. Matthews, Y. K. Reshetnyak, A. Senes, and J.-L. Popot, 2003. Membrane protein folding: beyond the two stage model. *FEBS Lett* 555:122–125.
- [37] Kim, S., T.-J. Jeon, A. Oberai, D. Yang, J. J. Schmidt, and J. U. Bowie, 2005. Transmembrane glycine zippers: physiological and pathological roles in membrane proteins. *Proc Natl Acad Sci U S A* 102:14278–14283.

- [38] Cosson, P., and J. S. Bonifacino, 1992. Role of transmembrane domain interactions in the assembly of class II MHC molecules. *Science* 258:659–662.
- [39] Senes, A., I. Ubarretxena-Belandia, and D. M. Engelman, 2001. The Calpha —H...O hydrogen bond: a determinant of stability and specificity in transmembrane helix interactions. *Proc Natl Acad Sci U S A* 98:9056–9061.
- [40] Gratkowski, H., J. D. Lear, and W. F. DeGrado, 2001. Polar side chains drive the association of model transmembrane peptides. *Proc Natl Acad Sci U S A* 98:880–885.
- [41] Zhou, F. X., H. J. Merianos, A. T. Brunger, and D. M. Engelman, 2001. Polar residues drive association of poly-leucine transmembrane helices. *Proc Natl Acad Sci U S A* 98:2250–2255.
- [42] O’Shea, E. K., J. D. Klemm, P. S. Kim, and T. Alber, 1991. X-ray structure of the GCN4 leucine zipper, a two-stranded, parallel coiled coil. *Science* 254:539–544.
- [43] Harbury, P. B., T. Zhang, P. S. Kim, and T. Alber, 1993. A switch between two-, three-, and four-stranded coiled coils in GCN4 leucine zipper mutants. *Science* 262:1401–1407.
- [44] Sengupta, D., and S. J. Marrink, 2010. Lipid-mediated interactions tune the association of glycoporphin A helix and its disruptive mutants in membranes. *Phys Chem Chem Phys* 12:12987–12996.
- [45] Arkin, I. T., 2002. Structural aspects of oligomerization taking place between the transmembrane alpha-helices of bitopic membrane proteins. *Biochim Biophys Acta* 1565:347–363.
- [46] Yano, Y., and K. Matsuzaki, 2006. Measurement of thermodynamic parameters for hydrophobic mismatch 1: self-association of a transmembrane helix. *Biochemistry* 45:3370–3378.
- [47] Sparr, E., W. L. Ash, P. V. Nazarov, D. T. S. Rijkers, M. A. Hemminga, D. P. Tieleman, and J. A. Killian, 2005. Self-association of transmembrane alpha-helices in model membranes: importance of helix orientation and role of hydrophobic mismatch. *J Biol Chem* 280:39324–39331.
- [48] Killian, J. A., and T. K. M. Nyholm, 2006. Peptides in lipid bilayers: the power of simple models. *Curr Opin Struct Biol* 16:473–479.
- [49] Bordag, N., and S. Keller, 2010. Alpha-helical transmembrane peptides: a "divide and conquer" approach to membrane proteins. *Chem Phys Lipids* 163:1–26.
- [50] García-Sáez, A. J., M. Coraiola, M. D. Serra, I. Mingarro, G. Menestrina, and J. Salgado, 2005. Peptides derived from apoptotic Bax and Bid reproduce the poration activity of the parent full-length proteins. *Biophys J* 88:3976–3990.
- [51] Singer, S. J., and G. L. Nicolson, 1972. The fluid mosaic model of the structure of cell membranes. *Science* 175:720–731.
- [52] Vereb, G., J. Szöllosi, J. Matkó, P. Nagy, T. Farkas, L. Vigh, L. Mátyus, T. A. Waldmann, and S. Damjanovich, 2003. Dynamic, yet structured: The cell membrane three decades after the Singer-Nicolson model. *Proc Natl Acad Sci U S A* 100:8053–8058.
- [53] Simons, K., and W. L. C. Vaz, 2004. Model systems, lipid rafts, and cell membranes. *Annu Rev Biophys Biomol Struct* 33:269–295.
- [54] Esteban-Martín, S., and J. Salgado, 2007. Self-assembling of peptide/membrane complexes by atomistic molecular dynamics simulations. *Biophys J* 92:903–912.
- [55] Nyholm, T. K. M., S. Ozdirekcan, and J. A. Killian, 2007. How protein transmembrane segments sense the lipid environment. *Biochemistry* 46:1457–1465.
- [56] Kandasamy, S. K., and R. G. Larson, 2006. Molecular dynamics simulations of model trans-membrane peptides in lipid bilayers: a systematic investigation of hydrophobic mismatch. *Biophys J* 90:2326–2343.
- [57] Esteban-Martín, S., and J. Salgado, 2007. The dynamic orientation of membrane-bound peptides: bridging simulations and experiments. *Biophys J* 93:4278–4288.

## Bibliografía

- [58] Khandelia, H., J. H. Ipsen, and O. G. Mouritsen, 2008. The impact of peptides on lipid membranes. *Biochim Biophys Acta* 1778:1528–1536.
- [59] Andersen, O. S., and R. E. Koeppe, 2007. Bilayer thickness and membrane protein function: an energetic perspective. *Annu Rev Biophys Biomol Struct* 36:107–130.
- [60] Tribet, C., and F. Vial, 2008. Flexible macromolecules attached to lipid bilayers: impact on fluidity, curvature, permeability and stability of the membranes. *Soft Matter* 4:68–81.
- [61] Schwarz, G., and C. H. Robert, 1992. Kinetics of pore-mediated release of marker molecules from liposomes or cells. *Biophys Chem* 42:291–296.
- [62] Rathinakumar, R., W. F. Walkenhorst, and W. C. Wimley, 2009. Broad-spectrum antimicrobial peptides by rational combinatorial design and high-throughput screening: the importance of interfacial activity. *J Am Chem Soc* 131:7609–7617.
- [63] Wimley, W. C., 2010. Describing the mechanism of antimicrobial Peptide action with the interfacial activity model. *ACS Chem Biol* 5:905–917.
- [64] Brasseur, R., and G. Divita, 2010. Happy birthday cell penetrating peptides: already 20 years. *Biochim Biophys Acta* 1798:2177–2181.
- [65] Almeida, P. F., and A. Pokorny, 2009. Mechanisms of antimicrobial, cytolytic, and cell-penetrating peptides: from kinetics to thermodynamics. *Biochemistry* 48:8083–8093.
- [66] Matsuzaki, K., A. Nakamura, O. Murase, K. Sugishita, N. Fujii, and K. Miyajima, 1997. Modulation of magainin 2-lipid bilayer interactions by peptide charge. *Biochemistry* 36:2104–2111.
- [67] Basanez, G., 2002. Membrane fusion: the process and its energy suppliers. *Cell Mol Life Sci* 59:1478–1490.
- [68] Nir, S., and J. L. Nieva, 2000. Interactions of peptides with liposomes: pore formation and fusion. *Prog Lipid Res* 39:181–206.
- [69] Lee, M., W. Hung, F. Chen, and H. W. Huang, 2008. Mechanism and kinetics of pore formation in membranes by water-soluble amphipathic peptides. *Proc Natl Acad Sci U S A* 105:5087–5092.
- [70] Brustovetsky, N., and M. Klingenberg, 1996. Mitochondrial ADP/ATP carrier can be reversibly converted into a large channel by  $\text{Ca}^{2+}$ . *Biochemistry* 35:8483–8488.
- [71] González-Barroso, M. M., C. Fleury, C. Levi-Meyrueis, P. Zaragoza, F. Bouillaud, and E. Rial, 1997. Deletion of amino acids 261–269 in the brown fat uncoupling protein converts the carrier into a pore. *Biochemistry* 36:10930–10935.
- [72] Sandre, O., L. Moreaux, and F. Brochard-Wyart, 1999. Dynamics of transient pores in stretched vesicles. *Proc Natl Acad Sci U S A* 96:10591–10596.
- [73] Evans, E., V. Heinrich, F. Ludwig, and W. Rawicz, 2003. Dynamic tension spectroscopy and strength of biomembranes. *Biophys J* 85:2342–2350.
- [74] Tieleman, D. P., H. Leontiadou, A. E. Mark, and S. Marrink, 2003. Simulation of pore formation in lipid bilayers by mechanical stress and electric fields. *J Am Chem Soc* 125:6382–6383.
- [75] Tieleman, D. P., and S. Marrink, 2006. Lipids out of equilibrium: energetics of desorption and pore mediated flip-flop. *J Am Chem Soc* 128:12462–12467.
- [76] Huang, H. W., F. Chen, and M. Lee, 2004. Molecular mechanism of Peptide-induced pores in membranes. *Phys Rev Lett* 92:198304.
- [77] Zakharov, S. D., E. A. Kotova, Y. N. Antonenko, and W. A. Cramer, 2004. On the role of lipid in colicin pore formation. *Biochim Biophys Acta* 1666:239–249.
- [78] Matsuzaki, K., 1999. Why and how are peptide-lipid interactions utilized for self-defense? Magainins and tachyplesins as archetypes. *Biochim Biophys Acta* 1462:1–10.

- [79] Lins, L., K. E. Kirat, B. Charlotheaux, C. Flore, V. Stroobant, A. Thomas, Y. Dufrene, and R. Brasseur, 2007. Lipid-destabilizing properties of the hydrophobic helices H8 and H9 from colicin E1. *Mol Membr Biol* 24:419–430.
- [80] Gerber, D., and Y. Shai, 2000. Insertion and organization within membranes of the delta-endotoxin pore-forming domain, helix 4-loop-helix 5, and inhibition of its activity by a mutant helix 4 peptide. *J Biol Chem* 275:23602–23607.
- [81] Zasloff, M., 2002. Antimicrobial peptides of multicellular organisms. *Nature* 415:389–395.
- [82] Leontiadou, H., A. E. Mark, and S. J. Marrink, 2006. Antimicrobial peptides in action. *J Am Chem Soc* 128:12156–12161.
- [83] Sengupta, D., H. Leontiadou, A. E. Mark, and S. Marrink, 2008. Toroidal pores formed by antimicrobial peptides show significant disorder. *Biochim Biophys Acta* 1778:2308–2317.
- [84] Gregory, S. M., A. Pokorny, and P. F. F. Almeida, 2009. Magainin 2 revisited: a test of the quantitative model for the all-or-none permeabilization of phospholipid vesicles. *Biophys J* 96:116–131.
- [85] Tamba, Y., and M. Yamazaki, 2005. Single giant unilamellar vesicle method reveals effect of antimicrobial peptide magainin 2 on membrane permeability. *Biochemistry* 44:15823–15833.
- [86] Tamba, Y., and M. Yamazaki, 2009. Magainin 2-induced pore formation in the lipid membranes depends on its concentration in the membrane interface. *J Phys Chem B* 113:4846–4852.
- [87] Matsuzaki, K., O. Murase, N. Fujii, and K. Miyajima, 1996. An antimicrobial peptide, magainin 2, induced rapid flip-flop of phospholipids coupled with pore formation and peptide translocation. *Biochemistry* 35:11361–11368.
- [88] Ludtke, S. J., K. He, W. T. Heller, T. A. Harroun, L. Yang, and H. W. Huang, 1996. Membrane pores induced by magainin. *Biochemistry* 35:13723–13728.
- [89] Nieva, J. L., and A. Agirre, 2003. Are fusion peptides a good model to study viral cell fusion? *Biochim Biophys Acta* 1614:104–115.
- [90] Longo, M. L., A. J. Waring, and D. A. Hammer, 1997. Interaction of the influenza hemagglutinin fusion peptide with lipid bilayers: area expansion and permeation. *Biophys J* 73:1430–1439.
- [91] Deshayes, S., T. Plénat, P. Charnet, G. Divita, G. Molle, and F. Heitz, 2006. Formation of transmembrane ionic channels of primary amphipathic cell-penetrating peptides. Consequences on the mechanism of cell penetration. *Biochim Biophys Acta* 1758:1846–1851.
- [92] Yang, L., and H. W. Huang, 2002. Observation of a membrane fusion intermediate structure. *Science* 297:1877–1879.
- [93] Dathe, M., and T. Wieprecht, 1999. Structural features of helical antimicrobial peptides: their potential to modulate activity on model membranes and biological cells. *Biochim Biophys Acta* 1462:71–87.
- [94] White, S. H., and W. C. Wimley, 1998. Hydrophobic interactions of peptides with membrane interfaces. *Biochim Biophys Acta* 1376:339–352.
- [95] Fernández-Vidal, M., S. Jayasinghe, A. S. Ladokhin, and S. H. White, 2007. Folding amphipathic helices into membranes: amphiphilicity trumps hydrophobicity. *J Mol Biol* 370:459–470.
- [96] Seelig, J., 2004. Thermodynamics of lipid-peptide interactions. *Biochim Biophys Acta* 1666:40–50.
- [97] Hristova, K., C. E. Dempsey, and S. H. White, 2001. Structure, location, and lipid perturbations of melittin at the membrane interface. *Biophys J* 80:801–811.
- [98] Aliste, M. P., J. L. MacCallum, and D. P. Tieleman, 2003. Molecular dynamics simulations of pentapeptides at interfaces: salt bridge and cation- $\pi$  interactions. *Biochemistry* 42:8976–8987.
- [99] Killian, J. A., and G. von Heijne, 2000. How proteins adapt to a membrane-water interface. *Trends Biochem Sci* 25:429–434.

## Bibliografía

- [100] Kandasamy, S. K., and R. G. Larson, 2004. Binding and insertion of alpha-helical anti-microbial peptides in POPC bilayers studied by molecular dynamics simulations. *Chem Phys Lipids* 132:113–132.
- [101] Johnston, J. M., G. A. Cook, J. M. Tomich, and M. S. P. Sansom, 2006. Conformation and environment of channel-forming peptides: a simulation study. *Biophys J* 90:1855–1864.
- [102] Uematsu, N., and K. Matsuzaki, 2000. Polar angle as a determinant of amphipathic alpha-helix-lipid interactions: a model peptide study. *Biophys J* 79:2075–2083.
- [103] Klocek, G., T. Schulthess, Y. Shai, and J. Seelig, 2009. Thermodynamics of melittin binding to lipid bilayers. Aggregation and pore formation. *Biochemistry* 48:2586–2596.
- [104] Tang, J., R. S. Signarvic, W. F. DeGrado, and F. Gai, 2007. Role of helix nucleation in the kinetics of binding of mastoparan X to phospholipid bilayers. *Biochemistry* 46:13856–13863.
- [105] Meier, M., and J. Seelig, 2007. Thermodynamics of the coil  $\rightleftharpoons$  beta-sheet transition in a membrane environment. *J Mol Biol* 369:277–289.
- [106] Ladokhin, A. S., R. Legmann, R. J. Collier, and S. H. White, 2004. Reversible refolding of the diphtheria toxin T-domain on lipid membranes. *Biochemistry* 43:7451–7458.
- [107] Wade, D., A. Boman, B. W. hlin, C. M. Drain, D. Andreu, H. G. Boman, and R. B. Merrifield, 1990. All-D amino acid-containing channel-forming antibiotic peptides. *Proc Natl Acad Sci U S A* 87:4761–4765.
- [108] Hilpert, K., M. R. Elliott, R. Volkmer-Engert, P. Henklein, O. Donini, Q. Zhou, D. F. H. Winkler, and R. E. W. Hancock, 2006. Sequence requirements and an optimization strategy for short antimicrobial peptides. *Chem Biol* 13:1101–1107.
- [109] Shai, Y., 1999. Mechanism of the binding, insertion and destabilization of phospholipid bilayer membranes by alpha-helical antimicrobial and cell non-selective membrane-lytic peptides. *Biochim Biophys Acta* 1462:55–70.
- [110] Anderluh, G., and J. H. Lakey, 2008. Disparate proteins use similar architectures to damage membranes. *Trends Biochem Sci* 33:482–490.
- [111] Parker, M. W., and S. C. Feil, 2005. Pore-forming protein toxins: from structure to function. *Prog Biophys Mol Biol* 88:91–142.
- [112] Magzoub, M., L. E. G. Eriksson, and A. Gräslund, 2003. Comparison of the interaction, positioning, structure induction and membrane perturbation of cell-penetrating peptides and non-translocating variants with phospholipid vesicles. *Biophys Chem* 103:271–288.
- [113] Shaw, J. E., R. F. Epan, J. C. Y. Hsu, G. C. H. Mo, R. M. Epan, and C. M. Yip, 2008. Cationic peptide-induced remodelling of model membranes: direct visualization by in situ atomic force microscopy. *J Struct Biol* 162:121–138.
- [114] Huang, H. W., 2009. Free energies of molecular bound states in lipid bilayers: lethal concentrations of antimicrobial peptides. *Biophys J* 96:3263–3272.
- [115] Valeva, A., N. Hellmann, I. Walev, D. Strand, M. Plate, F. Boukhallouk, A. Brack, K. Hanada, H. Decker, and S. Bhakdi, 2006. Evidence that clustered phosphocholine head groups serve as sites for binding and assembly of an oligomeric protein pore. *J Biol Chem* 281:26014–26021.
- [116] Gregory, S. M., A. Cavanaugh, V. Journigan, A. Pokorny, and P. F. F. Almeida, 2008. A quantitative model for the all-or-none permeabilization of phospholipid vesicles by the antimicrobial peptide cecropin A. *Biophys J* 94:1667–1680.
- [117] McLaughlin, S., 1989. The electrostatic properties of membranes. *Annu Rev Biophys Biophys Chem* 18:113–136.
- [118] Wieprecht, Apostolov, and Seelig, 2000. Binding of the antibacterial peptide magainin 2 amide to small and large unilamellar vesicles. *Biophys Chem* 85:187–198.

- [119] Wieprecht, T., O. Apostolov, M. Beyermann, and J. Seelig, 2000. Membrane binding and pore formation of the antibacterial peptide PGLa: thermodynamic and mechanistic aspects. *Biochemistry* 39:442–452.
- [120] van Meer, G., D. R. Voelker, and G. W. Feigenson, 2008. Membrane lipids: where they are and how they behave. *Nat Rev Mol Cell Biol* 9:112–124.
- [121] Allende, D., S. A. Simon, and T. J. McIntosh, 2005. Melittin-induced bilayer leakage depends on lipid material properties: evidence for toroidal pores. *Biophys J* 88:1828–1837.
- [122] Mani, R., S. D. Cady, M. Tang, A. J. Waring, R. I. Lehrer, and M. Hong, 2006. Membrane-dependent oligomeric structure and pore formation of a beta-hairpin antimicrobial peptide in lipid bilayers from solid-state NMR. *Proc Natl Acad Sci U S A* 103:16242–16247.
- [123] Wessman, P., A. A. Strömstedt, M. Malmsten, and K. Edwards, 2008. Melittin-lipid bilayer interactions and the role of cholesterol. *Biophys J* 95:4324–4336.
- [124] Zakharov, S. D., J. B. Heymann, Y. L. Zhang, and W. A. Cramer, 1996. Membrane binding of the colicin E1 channel: activity requires an electrostatic interaction of intermediate magnitude. *Biophys J* 70:2774–2783.
- [125] Valcarcel, C. A., M. D. Serra, C. Potrich, I. Bernhart, M. Tejuca, D. Martinez, F. Pazos, M. E. Lanio, and G. Menestrina, 2001. Effects of lipid composition on membrane permeabilization by sticholysin I and II, two cytolytins of the sea anemone *Stichodactyla helianthus*. *Biophys J* 80:2761–2774.
- [126] Tilley, S. J., and H. R. Saibil, 2006. The mechanism of pore formation by bacterial toxins. *Curr Opin Struct Biol* 16:230–236.
- [127] Wimley, W. C., and S. H. White, 2004. Reversible unfolding of beta-sheets in membranes: a calorimetric study. *J Mol Biol* 342:703–711.
- [128] Wieprecht, T., O. Apostolov, M. Beyermann, and J. Seelig, 1999. Thermodynamics of the alpha-helix-coil transition of amphipathic peptides in a membrane environment: implications for the peptide-membrane binding equilibrium. *J Mol Biol* 294:785–794.
- [129] Li, Y., X. Han, and L. K. Tamm, 2003. Thermodynamics of fusion peptide-membrane interactions. *Biochemistry* 42:7245–7251.
- [130] Im, W., and C. L. Brooks, 2005. Interfacial folding and membrane insertion of designed peptides studied by molecular dynamics simulations. *Proc Natl Acad Sci U S A* 102:6771–6776.
- [131] Marrink, S. J., A. H. de Vries, and D. P. Tieleman, 2009. Lipids on the move: simulations of membrane pores, domains, stalks and curves. *Biochim Biophys Acta* 1788:149–168.
- [132] Wimley, W. C., K. Hristova, A. S. Ladokhin, L. Silvestro, P. H. Axelsen, and S. H. White, 1998. Folding of beta-sheet membrane proteins: a hydrophobic hexapeptide model. *J Mol Biol* 277:1091–1110.
- [133] Meier, M., and J. Seelig, 2008. Length dependence of the coil  $\leftrightarrow$  beta-sheet transition in a membrane environment. *J Am Chem Soc* 130:1017–1024.
- [134] Tucker, M. J., J. Tang, and F. Gai, 2006. Probing the kinetics of membrane-mediated helix folding. *J Phys Chem B* 110:8105–8109.
- [135] Silvestro, L., and P. H. Axelsen, 2000. Membrane-induced folding of cecropin A. *Biophys J* 79:1465–1477.
- [136] Ladokhin, A. S., and S. H. White, 1999. Folding of amphipathic alpha-helices on membranes: energetics of helix formation by melittin. *J Mol Biol* 285:1363–1369.
- [137] Perier, A., A. Chassaing, S. Raffestin, S. Pichard, M. Masella, A. Ménez, V. Forge, A. Chenal, and D. Gillet, 2007. Concerted protonation of key histidines triggers membrane interaction of the diphtheria toxin T domain. *J Biol Chem* 282:24239–24245.
- [138] Zakharov, S. D., M. Lindeberg, Y. Griko, Z. Salamon, G. Tollin, F. G. Prendergast, and W. A. Cramer, 1998. Membrane-bound state of the colicin E1 channel domain as an extended two-dimensional helical array. *Proc Natl Acad Sci U S A* 95:4282–4287.

## Bibliografía

- [139] Oh, K. J., H. Zhan, C. Cui, K. Hideg, R. J. Collier, and W. L. Hubbell, 1996. Organization of diphtheria toxin T domain in bilayers: a site-directed spin labeling study. *Science* 273:810–812.
- [140] Bechinger, B., 1999. The structure, dynamics and orientation of antimicrobial peptides in membranes by multidimensional solid-state NMR spectroscopy. *Biochim Biophys Acta* 1462:157–183.
- [141] Huang, H. W., 2000. Action of antimicrobial peptides: two-state model. *Biochemistry* 39:8347–8352.
- [142] Afonin, S., S. L. Grage, M. Ieronimo, P. Wadhvani, and A. S. Ulrich, 2008. Temperature-dependent transmembrane insertion of the amphiphilic peptide PGLa in lipid bilayers observed by solid state <sup>19</sup>F NMR spectroscopy. *J Am Chem Soc* 130:16512–16514.
- [143] Luo, W., X. Yao, and M. Hong, 2005. Large structure rearrangement of colicin ia channel domain after membrane binding from 2D <sup>13</sup>C spin diffusion NMR. *J Am Chem Soc* 127:6402–6408.
- [144] Lindeberg, M., S. D. Zakharov, and W. A. Cramer, 2000. Unfolding pathway of the colicin E1 channel protein on a membrane surface. *J Mol Biol* 295:679–692.
- [145] Aisenbrey, C., U. S. Sudheendra, H. Ridley, P. Bertani, A. Marquette, S. Nedelkina, J. H. Lakey, and B. Bechinger, 2007. Helix orientations in membrane-associated Bcl-X(L) determined by <sup>15</sup>N-solid-state NMR spectroscopy. *Eur Biophys J* 37:71–80.
- [146] Gong, X., J. Choi, C. M. Franzin, D. Zhai, J. C. Reed, and F. M. Marassi, 2004. Conformation of membrane-associated proapoptotic tBid. *J Biol Chem* 279:28954–28960.
- [147] Oh, K. J., S. Barbuto, N. Meyer, R. Kim, R. J. Collier, and S. J. Korsmeyer, 2005. Conformational changes in BID, a pro-apoptotic BCL-2 family member, upon membrane binding. A site-directed spin labeling study. *J Biol Chem* 280:753–767.
- [148] Tilley, S. J., E. V. Orlova, R. J. C. Gilbert, P. W. Andrew, and H. R. Saibil, 2005. Structural basis of pore formation by the bacterial toxin pneumolysin. *Cell* 121:247–256.
- [149] Abrami, L., and F. G. van Der Goot, 1999. Plasma membrane microdomains act as concentration platforms to facilitate intoxication by aerolysin. *J Cell Biol* 147:175–184.
- [150] Farago, O., and C. D. Santangelo, 2005. Pore formation in fluctuating membranes. *J Chem Phys* 122:44901.
- [151] Gurtovenko, A. A., and I. Vattulainen, 2005. Pore formation coupled to ion transport through lipid membranes as induced by transmembrane ionic charge imbalance: atomistic molecular dynamics study. *J Am Chem Soc* 127:17570–17571.
- [152] de Vries, A. H., A. E. Mark, and S. J. Marrink, 2004. Molecular dynamics simulation of the spontaneous formation of a small DPPC vesicle in water in atomistic detail. *J Am Chem Soc* 126:4488–4489.
- [153] Wang, Z., and D. Frenkel, 2005. Pore nucleation in mechanically stretched bilayer membranes. *J Chem Phys* 123:154701.
- [154] Tolpekina, T. V., W. K. den Otter, and W. J. Briels, 2004. Nucleation free energy of pore formation in an amphiphilic bilayer studied by molecular dynamics simulations. *J Chem Phys* 121:12060–12066.
- [155] Marrink, S. J., E. Lindahl, O. Edholm, and A. E. Mark, 2001. Simulation of the spontaneous aggregation of phospholipids into bilayers. *J Am Chem Soc* 123:8638–8639.
- [156] Daleke, D. L., 2007. Phospholipid flippases. *J Biol Chem* 282:821–825.
- [157] Kornberg, R. D., and H. M. McConnell, 1971. Inside-outside transitions of phospholipids in vesicle membranes. *Biochemistry* 10:1111–1120.
- [158] Wimley, W. C., and T. E. Thompson, 1990. Exchange and flip-flop of dimyristoylphosphatidylcholine in liquid-crystalline, gel, and two-component, two-phase large unilamellar vesicles. *Biochemistry* 29:1296–1303.
- [159] Kruijff, B. D., and E. J. V. Zoelen, 1978. Effect of the phase transition on the transbilayer movement of dimyristoyl phosphatidylcholine in unilamellar vesicles. *Biochim Biophys Acta* 511:105–115.

- [160] Nakano, M., M. Fukuda, T. Kudo, M. Miyazaki, Y. Wada, N. Matsuzaki, H. Endo, and T. Handa, 2009. Static and dynamic properties of phospholipid bilayer nanodiscs. *J Am Chem Soc* 131:8308–8312.
- [161] Wimley, W. C., and T. E. Thompson, 1991. Transbilayer and interbilayer phospholipid exchange in dimyristoylphosphatidylcholine/dimyristoylphosphatidylethanolamine large unilamellar vesicles. *Biochemistry* 30:1702–1709.
- [162] Karatekin, E., O. Sandre, H. Guitouni, N. Borghi, P. Puech, and F. Brochard-Wyart, 2003. Cascades of transient pores in giant vesicles: line tension and transport. *Biophys J* 84:1734–1749.
- [163] Rodriguez, N., S. Cribier, and F. Pincet, 2006. Transition from long- to short-lived transient pores in giant vesicles in an aqueous medium. *Phys Rev E Stat Nonlin Soft Matter Phys* 74:061902.
- [164] Bramhall, J., J. Hofmann, R. DeGuzman, S. Montestruque, and R. Schell, 1987. Temperature dependence of membrane ion conductance analyzed by using the amphiphilic anion 5/6-carboxyfluorescein. *Biochemistry* 26:6330–6340.
- [165] Clerc, S. G., and T. E. Thompson, 1995. Permeability of dimyristoyl phosphatidylcholine/dipalmitoyl phosphatidylcholine bilayer membranes with coexisting gel and liquid-crystalline phases. *Biophys J* 68:2333–2341.
- [166] Bennett, W. F. D., J. L. MacCallum, and D. P. Tieleman, 2009. Thermodynamic analysis of the effect of cholesterol on dipalmitoylphosphatidylcholine lipid membranes. *J Am Chem Soc* 131:1972–1978.
- [167] Ruiz-Argüello, M. B., G. Basañez, F. M. Goñi, and A. Alonso, 1996. Different effects of enzyme-generated ceramides and diacylglycerols in phospholipid membrane fusion and leakage. *J Biol Chem* 271:26616–26621.
- [168] Siskind, L. J., and M. Colombini, 2000. The lipids C2- and C16-ceramide form large stable channels. Implications for apoptosis. *J Biol Chem* 275:38640–38644.
- [169] Contreras, F., G. Basañez, A. Alonso, A. Herrmann, and F. M. Goñi, 2005. Asymmetric addition of ceramides but not dihydroceramides promotes transbilayer (flip-flop) lipid motion in membranes. *Biophys J* 88:348–359.
- [170] Goñi, F. M., and A. Alonso, 2009. Effects of ceramide and other simple sphingolipids on membrane lateral structure. *Biochim Biophys Acta* 1788:169–177.
- [171] Anishkin, A., S. Sukharev, and M. Colombini, 2006. Searching for the molecular arrangement of transmembrane ceramide channels. *Biophys J* 90:2414–2426.
- [172] Kol, M. A., A. I. de Kroon, D. T. Rijkers, J. A. Killian, and B. de Kruijff, 2001. Membrane-spanning peptides induce phospholipid flop: a model for phospholipid translocation across the inner membrane of *E. coli*. *Biochemistry* 40:10500–10506.
- [173] de Kruijff, B., E. J. van Zoelen, and L. L. van Deenen, 1978. Glycophorin facilitates the transbilayer movement of phosphatidylcholine in vesicles. *Biochim Biophys Acta* 509:537–542.
- [174] Fattal, E., S. Nir, R. A. Parente, and F. C. Szoka, 1994. Pore-forming peptides induce rapid phospholipid flip-flop in membranes. *Biochemistry* 33:6721–6731.
- [175] Terrones, O., B. Antonsson, H. Yamaguchi, H. Wang, J. Liu, R. M. Lee, A. Herrmann, and G. Basañez, 2004. Lipidic pore formation by the concerted action of proapoptotic BAX and tBID. *J Biol Chem* 279:30081–30091.
- [176] García-Sáez, A. J., M. Coraiola, M. D. Serra, I. Mingarro, P. Müller, and J. Salgado, 2006. Peptides corresponding to helices 5 and 6 of Bax can independently form large lipid pores. *FEBS J* 273:971–981.
- [177] Sobko, A. A., E. A. Kotova, Y. N. Antonenko, S. D. Zakharov, and W. A. Cramer, 2006. Lipid dependence of the channel properties of a colicin E1-lipid toroidal pore. *J Biol Chem* 281:14408–14416.
- [178] Müller, P., S. Schiller, T. Wieprecht, M. Dathe, and A. Herrmann, 2000. Continuous measurement of rapid transbilayer movement of a pyrene-labeled phospholipid analogue. *Chem Phys Lipids* 106:89–99.

## Bibliografía

- [179] Schön, P., A. J. García-Sáez, P. Malovrh, K. Bacia, G. Anderluh, and P. Schwille, 2008. Equinatoxin II permeabilizing activity depends on the presence of sphingomyelin and lipid phase coexistence. *Biophys J* 95:691–698.
- [180] Polozov, I. V., G. M. Anantharamaiah, J. P. Segrest, and R. M. Epand, 2001. Osmotically induced membrane tension modulates membrane permeabilization by class L amphipathic helical peptides: nucleation model of defect formation. *Biophys J* 81:949–959.
- [181] Weinstein, J. N., R. D. Klausner, T. Innerarity, E. Ralston, and R. Blumenthal, 1981. Phase transition release, a new approach to the interaction of proteins with lipid vesicles. Application to lipoproteins. *Biochim Biophys Acta* 647:270–284.
- [182] Malev, V. V., L. V. Schagina, P. A. Gurnev, J. Y. Takemoto, E. M. Nestorovich, and S. M. Bezrukov, 2002. Syringomycin E channel: a lipidic pore stabilized by lipopeptide? *Biophys J* 82:1985–1994.
- [183] Qian, S., W. Wang, L. Yang, and H. W. Huang, 2008. Structure of transmembrane pore induced by Bax-derived peptide: evidence for lipidic pores. *Proc Natl Acad Sci U S A* 105:17379–17383.
- [184] Cruciani, R. A., J. L. Barker, S. R. Durell, G. Raghunathan, H. R. Guy, M. Zasloff, and E. F. Stanley, 1992. Magainin 2, a natural antibiotic from frog skin, forms ion channels in lipid bilayer membranes. *Eur J Pharmacol* 226:287–296.
- [185] Ludtke, S. J., K. He, Y. Wu, and H. W. Huang, 1994. Cooperative membrane insertion of magainin correlated with its cytolytic activity. *Biochim Biophys Acta* 1190:181–184.
- [186] Chen, F., M. Lee, and H. W. Huang, 2002. Sigmoidal concentration dependence of antimicrobial peptide activities: a case study on alamethicin. *Biophys J* 82:908–914.
- [187] Qian, S., W. Wang, L. Yang, and H. W. Huang, 2008. Structure of the alamethicin pore reconstructed by x-ray diffraction analysis. *Biophys J* 94:3512–3522.
- [188] Lee, M., F. Chen, and H. W. Huang, 2004. Energetics of pore formation induced by membrane active peptides. *Biochemistry* 43:3590–3599.
- [189] Pokorny, A., T. H. Birkbeck, and P. F. F. Almeida, 2002. Mechanism and kinetics of delta-lysin interaction with phospholipid vesicles. *Biochemistry* 41:11044–11056.
- [190] Dufourc, E. J., J. M. Bonmatin, and J. Dufourcq, 1989. Membrane structure and dynamics by 2H- and 31P-NMR. Effects of amphipathic peptidic toxins on phospholipid and biological membranes. *Biochimie* 71:117–123.
- [191] Bechinger, B., and K. Lohner, 2006. Detergent-like actions of linear amphipathic cationic antimicrobial peptides. *Biochim Biophys Acta* 1758:1529–1539.
- [192] Pott, T., and E. J. Dufourc, 1995. Action of melittin on the DPPC-cholesterol liquid-ordered phase: a solid state 2H-and 31P-NMR study. *Biophys J* 68:965–977.
- [193] Latorre, R., and O. Alvarez, 1981. Voltage-dependent channels in planar lipid bilayer membranes. *Physiol Rev* 61:77–150.
- [194] Anderluh, G., M. D. Serra, G. Viero, G. Guella, P. Macek, and G. Menestrina, 2003. Pore formation by equinatoxin II, a eukaryotic protein toxin, occurs by induction of nonlamellar lipid structures. *J Biol Chem* 278:45216–45223.
- [195] Basanez, G., A. Nechushtan, O. Drozhinin, A. Chanturiya, E. Choe, S. Tutt, K. A. Wood, Y. Hsu, J. Zimmerberg, and R. J. Youle, 1999. Bax, but not Bcl-xL, decreases the lifetime of planar phospholipid bilayer membranes at subnanomolar concentrations. *Proc Natl Acad Sci U S A* 96:5492–5497.
- [196] Basañez, G., J. C. Sharpe, J. Galanis, T. B. Brandt, J. M. Hardwick, and J. Zimmerberg, 2002. Bax-type apoptotic proteins porate pure lipid bilayers through a mechanism sensitive to intrinsic monolayer curvature. *J Biol Chem* 277:49360–49365.
- [197] García-Sáez, A. J., S. Chiantia, J. Salgado, and P. Schwille, 2007. Pore formation by a Bax-derived peptide: effect on the line tension of the membrane probed by AFM. *Biophys J* 93:103–112.

- [198] Glaser, R. W., S. L. Leikin, L. V. Chernomordik, V. F. Pastushenko, and A. I. Sokirko, 1988. Reversible electrical breakdown of lipid bilayers: formation and evolution of pores. *Biochim Biophys Acta* 940:275–287.
- [199] Puech, P., N. Borghi, E. Karatekin, and F. Brochard-Wyart, 2003. Line thermodynamics: adsorption at a membrane edge. *Phys Rev Lett* 90:128304.
- [200] Lee, M., W. Hung, F. Chen, and H. W. Huang, 2005. Many-body effect of antimicrobial peptides: on the correlation between lipid's spontaneous curvature and pore formation. *Biophys J* 89:4006–4016.
- [201] Huang, H. W., 1986. Deformation free energy of bilayer membrane and its effect on gramicidin channel lifetime. *Biophys J* 50:1061–1070.
- [202] Nielsen, C., M. Goulian, and O. S. Andersen, 1998. Energetics of inclusion-induced bilayer deformations. *Biophys J* 74:1966–1983.
- [203] Cullis, P. R., M. J. Hope, and C. P. Tilcock, 1986. Lipid polymorphism and the roles of lipids in membranes. *Chem Phys Lipids* 40:127–144.
- [204] Matsuzaki, K., K. Sugishita, N. Ishibe, M. Ueha, S. Nakata, K. Miyajima, and R. M. Epand, 1998. Relationship of membrane curvature to the formation of pores by magainin 2. *Biochemistry* 37:11856–11863.
- [205] Sobko, A. A., E. A. Kotova, Y. N. Antonenko, S. D. Zakharov, and W. A. Cramer, 2004. Effect of lipids with different spontaneous curvature on the channel activity of colicin E1: evidence in favor of a toroidal pore. *FEBS Lett* 576:205–210.
- [206] Fosnarič, M., V. Kralj-Iglič, K. Bohinc, A. Iglič, and S. May, 2003. Stabilization of Pores in Lipid Bilayers by Anisotropic Inclusions. *J Phys Chem B* 107:12519–12526.
- [207] Kerr, J. F., A. H. Wyllie, and A. R. Currie, 1972. Apoptosis: a basic biological phenomenon with wide-ranging implications in tissue kinetics. *Br J Cancer* 26:239–257.
- [208] Kroemer, G., W. S. El-Deiry, P. Golstein, M. E. Peter, D. Vaux, P. Vandenabeele, B. Zhivotovsky, M. V. Blagosklonny, W. Malorni, R. A. Knight, M. Piacentini, S. Nagata, and G. Melino, 2005. Classification of cell death: recommendations of the Nomenclature Committee on Cell Death. *Cell Death Differ* 12 Suppl 2:1463–1467.
- [209] Reed, J. C., 2002. Apoptosis-based therapies. *Nat Rev Drug Discov* 1:111–121.
- [210] Thompson, C. B., 1995. Apoptosis in the pathogenesis and treatment of disease. *Science* 267:1456–1462.
- [211] Kroemer, G., L. Galluzzi, and C. Brenner, 2007. Mitochondrial membrane permeabilization in cell death. *Physiol Rev* 87:99–163.
- [212] Malladi, S., M. Challa-Malladi, H. O. Fearnhead, and S. B. Bratton, 2009. The Apaf-1\*procaspase-9 apoptosome complex functions as a proteolytic-based molecular timer. *EMBO J* 28:1916–1925.
- [213] Green, D. R., and G. Kroemer, 2004. The pathophysiology of mitochondrial cell death. *Science* 305:626–629.
- [214] Chipuk, J. E., and D. R. Green, 2005. Do inducers of apoptosis trigger caspase-independent cell death? *Nat Rev Mol Cell Biol* 6:268–275.
- [215] Kroemer, G., and S. J. Martin, 2005. Caspase-independent cell death. *Nat Med* 11:725–730.
- [216] Green, D., and G. Kroemer, 1998. The central executioners of apoptosis: caspases or mitochondria? *Trends Cell Biol* 8:267–271.
- [217] Kumarswamy, R., and S. Chandna, 2009. Putative partners in Bax mediated cytochrome-c release: ANT, CypD, VDAC or none of them? *Mitochondrion* 9:1–8.
- [218] Tsujimoto, Y., J. Cossman, E. Jaffe, and C. M. Croce, 1985. Involvement of the bcl-2 gene in human follicular lymphoma. *Science* 228:1440–1443.
- [219] Aouacheria, A., F. Brunet, and M. Gouy, 2005. Phylogenomics of life-or-death switches in multicellular animals: Bcl-2, BH3-Only, and BNip families of apoptotic regulators. *Mol Biol Evol* 22:2395–2416.

## Bibliografía

- [220] Blaineau, S. V., and A. Aouacheria, 2009. BCL2DB: moving 'helix-bundled' BCL-2 family members to their database. *Apoptosis* 14:923–925.
- [221] Hockenbery, D., G. Nuñez, C. Milliman, R. D. Schreiber, and S. J. Korsmeyer, 1990. Bcl-2 is an inner mitochondrial membrane protein that blocks programmed cell death. *Nature* 348:334–336.
- [222] Gross, A., X. M. Yin, K. Wang, M. C. Wei, J. Jockel, C. Milliman, H. Erdjument-Bromage, P. Tempst, and S. J. Korsmeyer, 1999. Caspase cleaved BID targets mitochondria and is required for cytochrome c release, while BCL-XL prevents this release but not tumor necrosis factor-R1/Fas death. *J Biol Chem* 274:1156–1163.
- [223] Hsu, Y. T., K. G. Wolter, and R. J. Youle, 1997. Cytosol-to-membrane redistribution of Bax and Bcl-X(L) during apoptosis. *Proc Natl Acad Sci U S A* 94:3668–3672.
- [224] Wolter, K. G., Y. T. Hsu, C. L. Smith, A. Nechushtan, X. G. Xi, and R. J. Youle, 1997. Movement of Bax from the cytosol to mitochondria during apoptosis. *J Cell Biol* 139:1281–1292.
- [225] Zha, J., S. Weiler, K. J. Oh, M. C. Wei, and S. J. Korsmeyer, 2000. Posttranslational N-myristoylation of BID as a molecular switch for targeting mitochondria and apoptosis. *Science* 290:1761–1765.
- [226] Muchmore, S. W., M. Sattler, H. Liang, R. P. Meadows, J. E. Harlan, H. S. Yoon, D. Nettlesheim, B. S. Chang, C. B. Thompson, S. L. Wong, S. L. Ng, and S. W. Fesik, 1996. X-ray and NMR structure of human Bcl-xL, an inhibitor of programmed cell death. *Nature* 381:335–341.
- [227] Chou, J. J., H. Li, G. S. Salvesen, J. Yuan, and G. Wagner, 1999. Solution structure of BID, an intracellular amplifier of apoptotic signaling. *Cell* 96:615–624.
- [228] McDonnell, J. M., D. Fushman, C. L. Milliman, S. J. Korsmeyer, and D. Cowburn, 1999. Solution structure of the proapoptotic molecule BID: a structural basis for apoptotic agonists and antagonists. *Cell* 96:625–634.
- [229] Suzuki, M., R. J. Youle, and N. Tjandra, 2000. Structure of Bax: coregulation of dimer formation and intracellular localization. *Cell* 103:645–654.
- [230] Petros, A. M., A. Medek, D. G. Nettlesheim, D. H. Kim, H. S. Yoon, K. Swift, E. D. Matayoshi, T. Oltersdorf, and S. W. Fesik, 2001. Solution structure of the antiapoptotic protein bcl-2. *Proc Natl Acad Sci U S A* 98:3012–3017.
- [231] Hinds, M. G., M. Lackmann, G. L. Skea, P. J. Harrison, D. C. S. Huang, and C. L. Day, 2003. The structure of Bcl-w reveals a role for the C-terminal residues in modulating biological activity. *EMBO J* 22:1497–1507.
- [232] Denisov, A. Y., M. S. R. Madiraju, G. Chen, A. Khadir, P. Beauparlant, G. Attardo, G. C. Shore, and K. Gehring, 2003. Solution structure of human BCL-w: modulation of ligand binding by the C-terminal helix. *J Biol Chem* 278:21124–21128.
- [233] Day, C. L., L. Chen, S. J. Richardson, P. J. Harrison, D. C. S. Huang, and M. G. Hinds, 2005. Solution structure of prosurvival Mcl-1 and characterization of its binding by proapoptotic BH3-only ligands. *J Biol Chem* 280:4738–4744.
- [234] Moldoveanu, T., Q. Liu, A. Tocilj, M. Watson, G. Shore, and K. Gehring, 2006. The X-ray structure of a BAK homodimer reveals an inhibitory zinc binding site. *Mol Cell* 24:677–688.
- [235] Bocharov, E. V., Y. E. Pustovalova, K. V. Pavlov, P. E. Volynsky, M. V. Goncharuk, Y. S. Ermolyuk, D. V. Karpunin, A. A. Schulga, M. P. Kirpichnikov, R. G. Efremov, I. V. Maslennikov, and A. S. Arseniev, 2007. Unique dimeric structure of BNIP3 transmembrane domain suggests membrane permeabilization as a cell death trigger. *J Biol Chem* 282:16256–16266.
- [236] Sulistijo, E. S., and K. R. Mackenzie, 2009. Structural basis for dimerization of the BNIP3 transmembrane domain. *Biochemistry* 48:5106–5120.
- [237] Petros, A. M., E. T. Olejniczak, and S. W. Fesik, 2004. Structural biology of the Bcl-2 family of proteins. *Biochim Biophys Acta* 1644:83–94.

- [238] Petros, A. M., D. G. Nettlesheim, Y. Wang, E. T. Olejniczak, R. P. Meadows, J. Mack, K. Swift, E. D. Matayoshi, H. Zhang, C. B. Thompson, and S. W. Fesik, 2000. Rationale for Bcl-xL/Bad peptide complex formation from structure, mutagenesis, and biophysical studies. *Protein Sci* 9:2528–2534.
- [239] Sattler, M., H. Liang, D. Nettlesheim, R. P. Meadows, J. E. Harlan, M. Eberstadt, H. S. Yoon, S. B. Shuker, B. S. Chang, A. J. Minn, C. B. Thompson, and S. W. Fesik, 1997. Structure of Bcl-xL-Bak peptide complex: recognition between regulators of apoptosis. *Science* 275:983–986.
- [240] Gavathiotis, E., M. Suzuki, M. L. Davis, K. Pitter, G. H. Bird, S. G. Katz, H. Tu, H. Kim, E. H. Cheng, N. Tjandra, and L. D. Walensky, 2008. BAX activation is initiated at a novel interaction site. *Nature* 455:1076–1081.
- [241] Lazebnik, Y., 2001. Why do regulators of apoptosis look like bacterial toxins? *Curr Biol* 11:R767–768.
- [242] Hinds, M. G., C. Smits, R. Fredericks-Short, J. M. Risk, M. Bailey, D. C. S. Huang, and C. L. Day, 2007. Bim, Bad and Bmf: intrinsically unstructured BH3-only proteins that undergo a localized conformational change upon binding to prosurvival Bcl-2 targets. *Cell Death Differ* 14:128–136.
- [243] Chang, B. S., A. J. Minn, S. W. Muchmore, S. W. Fesik, and C. B. Thompson, 1997. Identification of a novel regulatory domain in Bcl-X(L) and Bcl-2. *EMBO J* 16:968–977.
- [244] Cheng, E. H., D. G. Kirsch, R. J. Clem, R. Ravi, M. B. Kastan, A. Bedi, K. Ueno, and J. M. Hardwick, 1997. Conversion of Bcl-2 to a Bax-like death effector by caspases. *Science* 278:1966–1968.
- [245] Rautureau, G. J. P., C. L. Day, and M. G. Hinds, 2010. Intrinsically disordered proteins in bcl-2 regulated apoptosis. *Int J Mol Sci* 11:1808–1824.
- [246] García-Sáez, A. J., G. Fuertes, J. Suckale, and J. Salgado, 2010. Permeabilization of the outer mitochondrial membrane by Bcl-2 proteins. *Adv Exp Med Biol* 677:91–105.
- [247] Nguyen, M., D. G. Millar, V. W. Yong, S. J. Korsmeyer, and G. C. Shore, 1993. Targeting of Bcl-2 to the mitochondrial outer membrane by a COOH-terminal signal anchor sequence. *J Biol Chem* 268:25265–25268.
- [248] Priault, M., N. Camougrand, B. Chaudhuri, and S. Manon, 1999. Role of the C-terminal domain of Bax and Bcl-XL in their localization and function in yeast cells. *FEBS Lett* 443:225–228.
- [249] Nechushtan, A., C. L. Smith, Y. T. Hsu, and R. J. Youle, 1999. Conformation of the Bax C-terminus regulates subcellular location and cell death. *EMBO J* 18:2330–2341.
- [250] Cartron, P., C. Moreau, L. Oliver, E. Mayat, K. Meflah, and F. M. Vallette, 2002. Involvement of the N-terminus of Bax in its intracellular localization and function. *FEBS Lett* 512:95–100.
- [251] Ausili, A., A. Torrecillas, M. M. Martínez-Senac, S. Corbalán-García, and J. C. Gómez-Fernández, 2008. The interaction of the Bax C-terminal domain with negatively charged lipids modifies the secondary structure and changes its way of insertion into membranes. *J Struct Biol* 164:146–152.
- [252] Hsu, Y. T., and R. J. Youle, 1998. Bax in murine thymus is a soluble monomeric protein that displays differential detergent-induced conformations. *J Biol Chem* 273:10777–10783.
- [253] Desagher, S., A. Osen-Sand, A. Nichols, R. Eskes, S. Montessuit, S. Lauper, K. Maundrell, B. Antonsson, and J. C. Martinou, 1999. Bid-induced conformational change of Bax is responsible for mitochondrial cytochrome c release during apoptosis. *J Cell Biol* 144:891–901.
- [254] Peyerl, F. W., S. Dai, G. A. Murphy, F. Crawford, J. White, P. Marrack, and J. W. Kappler, 2007. Elucidation of some Bax conformational changes through crystallization of an antibody-peptide complex. *Cell Death Differ* 14:447–452.
- [255] Dewson, G., and R. M. Kluck, 2009. Mechanisms by which Bak and Bax permeabilise mitochondria during apoptosis. *J Cell Sci* 122:2801–2808.
- [256] García-Sáez, A. J., I. Mingarro, E. Pérez-Payá, and J. Salgado, 2004. Membrane-insertion fragments of Bcl-xL, Bax, and Bid. *Biochemistry* 43:10930–10943.

## Bibliografía

- [257] Annis, M. G., E. L. Soucie, P. J. Dlugosz, J. A. Cruz-Aguado, L. Z. Penn, B. Leber, and D. W. Andrews, 2005. Bax forms multispansing monomers that oligomerize to permeabilize membranes during apoptosis. *EMBO J* 24:2096–2103.
- [258] Bleicken, S., M. Classen, P. V. L. Padmavathi, T. Ishikawa, K. Zeth, H. Steinhoff, and E. Bordignon, 2010. Molecular details of Bax activation, oligomerization, and membrane insertion. *J Biol Chem* 285:6636–6647.
- [259] George, N. M., N. Targy, J. J. D. Evans, L. Zhang, and X. Luo, 2010. Bax contains two functional mitochondrial targeting sequences and translocates to mitochondria in a conformational change- and homo-oligomerization-driven process. *J Biol Chem* 285:1384–1392.
- [260] Sani, M., E. J. Dufourc, and G. Gröbner, 2009. How does the Bax-alpha1 targeting sequence interact with mitochondrial membranes? The role of cardiolipin. *Biochim Biophys Acta* 1788:623–631.
- [261] Eskes, R., S. Desagher, B. Antonsson, and J. C. Martinou, 2000. Bid induces the oligomerization and insertion of Bax into the outer mitochondrial membrane. *Mol Cell Biol* 20:929–935.
- [262] Korsmeyer, S. J., M. C. Wei, M. Saito, S. Weiler, K. J. Oh, and P. H. Schlesinger, 2000. Pro-apoptotic cascade activates BID, which oligomerizes BAK or BAX into pores that result in the release of cytochrome c. *Cell Death Differ* 7:1166–1173.
- [263] Ruffolo, S. C., D. G. Breckenridge, M. Nguyen, I. S. Goping, A. Gross, S. J. Korsmeyer, H. Li, J. Yuan, and G. C. Shore, 2000. BID-dependent and BID-independent pathways for BAX insertion into mitochondria. *Cell Death Differ* 7:1101–1108.
- [264] Wei, M. C., W. X. Zong, E. H. Cheng, T. Lindsten, V. Panoutsakopoulou, A. J. Ross, K. A. Roth, G. R. MacGregor, C. B. Thompson, and S. J. Korsmeyer, 2001. Proapoptotic BAX and BAK: a requisite gateway to mitochondrial dysfunction and death. *Science* 292:727–730.
- [265] Antonsson, B., S. Montessuit, S. Lauper, R. Eskes, and J. C. Martinou, 2000. Bax oligomerization is required for channel-forming activity in liposomes and to trigger cytochrome c release from mitochondria. *Biochem J* 345 Pt 2:271–278.
- [266] Pagliari, L. J., T. Kuwana, C. Bonzon, D. D. Newmeyer, S. Tu, H. M. Beere, and D. R. Green, 2005. The multidomain proapoptotic molecules Bax and Bak are directly activated by heat. *Proc Natl Acad Sci U S A* 102:17975–17980.
- [267] Tan, C., P. J. Dlugosz, J. Peng, Z. Zhang, S. M. Lapolla, S. M. Plafker, D. W. Andrews, and J. Lin, 2006. Auto-activation of the apoptosis protein Bax increases mitochondrial membrane permeability and is inhibited by Bcl-2. *J Biol Chem* 281:14764–14775.
- [268] Antonsson, B., S. Montessuit, B. Sanchez, and J. C. Martinou, 2001. Bax is present as a high molecular weight oligomer/complex in the mitochondrial membrane of apoptotic cells. *J Biol Chem* 276:11615–11623.
- [269] Billen, L. P., C. L. Kokoski, J. F. Lovell, B. Leber, and D. W. Andrews, 2008. Bcl-XL inhibits membrane permeabilization by competing with Bax. *PLoS Biology* 6:e147.
- [270] Gross, A., J. Jockel, M. C. Wei, and S. J. Korsmeyer, 1998. Enforced dimerization of BAX results in its translocation, mitochondrial dysfunction and apoptosis. *EMBO J* 17:3878–3885.
- [271] Hardwick, J. M., and B. M. Polster, 2002. Bax, along with lipid conspirators, allows cytochrome c to escape mitochondria. *Mol Cell* 10:963–965.
- [272] Lovell, J. F., L. P. Billen, S. Bindner, A. Shamas-Din, C. Fradin, B. Leber, and D. W. Andrews, 2008. Membrane binding by tBid initiates an ordered series of events culminating in membrane permeabilization by Bax. *Cell* 135:1074–1084.
- [273] Mikhailov, V., M. Mikhailova, D. J. Pulkrabek, Z. Dong, M. A. Venkatachalam, and P. Saikumar, 2001. Bcl-2 prevents Bax oligomerization in the mitochondrial outer membrane. *J Biol Chem* 276:18361–18374.
- [274] Roucou, X., S. Montessuit, B. Antonsson, and J. Martinou, 2002. Bax oligomerization in mitochondrial membranes requires tBid (caspase-8-cleaved Bid) and a mitochondrial protein. *Biochem J* 368:915–921.

- [275] Saito, M., S. J. Korsmeyer, and P. H. Schlesinger, 2000. BAX-dependent transport of cytochrome c reconstituted in pure liposomes. *Nat Cell Biol* 2:553–555.
- [276] Valentijn, A. J., J. Upton, and A. P. Gilmore, 2008. Analysis of endogenous Bax complexes during apoptosis using blue native PAGE: implications for Bax activation and oligomerization. *Biochem J* 412:347–357.
- [277] Zhou, L., and D. C. Chang, 2008. Dynamics and structure of the Bax-Bak complex responsible for releasing mitochondrial proteins during apoptosis. *J Cell Sci* 121:2186–2196.
- [278] Brustovetsky, T., T. Li, Y. Yang, J.-T. Zhang, B. Antonsson, and N. Brustovetsky, 2010. BAX insertion, oligomerization, and outer membrane permeabilization in brain mitochondria: role of permeability transition and SH-redox regulation. *Biochim Biophys Acta* 1797:1795–1806.
- [279] George, N. M., J. J. D. Evans, and X. Luo, 2007. A three-helix homo-oligomerization domain containing BH3 and BH1 is responsible for the apoptotic activity of Bax. *Genes Dev* 21:1937–1948.
- [280] Zhang, Z., W. Zhu, S. M. Lapolla, Y. Miao, Y. Shao, M. Falcone, D. Boreham, N. McFarlane, J. Ding, A. E. Johnson, X. C. Zhang, D. W. Andrews, and J. Lin, 2010. Bax forms an oligomer via separate, yet interdependent, surfaces. *J Biol Chem* .
- [281] Dussmann, H., M. Rehm, C. G. Concannon, S. Anguissola, M. Wurstle, S. Kacmar, P. Voller, H. J. Huber, and J. H. M. Prehn, 2010. Single-cell quantification of Bax activation and mathematical modelling suggest pore formation on minimal mitochondrial Bax accumulation. *Cell Death Differ* 17:278–290.
- [282] Dlugosz, P. J., L. P. Billen, M. G. Annis, W. Zhu, Z. Zhang, J. Lin, B. Leber, and D. W. Andrews, 2006. Bcl-2 changes conformation to inhibit Bax oligomerization. *EMBO J* 25:2287–2296.
- [283] Kim, P. K., M. G. Annis, P. J. Dlugosz, B. Leber, and D. W. Andrews, 2004. During apoptosis bcl-2 changes membrane topology at both the endoplasmic reticulum and mitochondria. *Mol Cell* 14:523–529.
- [284] Thuduppathy, G. R., and R. B. Hill, 2006. Acid destabilization of the solution conformation of Bcl-xL does not drive its pH-dependent insertion into membranes. *Protein Sci* 15:248–257.
- [285] Thuduppathy, G. R., J. W. Craig, V. Kholodenko, A. Schon, and R. B. Hill, 2006. Evidence that membrane insertion of the cytosolic domain of Bcl-xL is governed by an electrostatic mechanism. *J Mol Biol* 359:1045–1058.
- [286] Thuduppathy, G. R., O. Terrones, J. W. Craig, G. Basañez, and R. B. Hill, 2006. The N-terminal domain of Bcl-xL reversibly binds membranes in a pH-dependent manner. *Biochemistry* 45:14533–14542.
- [287] Losonczi, J. A., E. T. Olejniczak, S. F. Betz, J. E. Harlan, J. Mack, and S. W. Fesik, 2000. NMR studies of the anti-apoptotic protein Bcl-xL in micelles. *Biochemistry* 39:11024–11033.
- [288] Jeong, S., B. Gaume, Y. Lee, Y. Hsu, S. Ryu, S. Yoon, and R. J. Youle, 2004. Bcl-x(L) sequesters its C-terminal membrane anchor in soluble, cytosolic homodimers. *EMBO J* 23:2146–2155.
- [289] O'Neill, J. W., M. K. Manion, B. Maguire, and D. M. Hockenbery, 2006. BCL-XL dimerization by three-dimensional domain swapping. *J Mol Biol* 356:367–381.
- [290] Denisov, A. Y., T. Sprules, J. Fraser, G. Kozlov, and K. Gehring, 2007. Heat-induced dimerization of BCL-xL through alpha-helix swapping. *Biochemistry* 46:734–740.
- [291] Feng, Y., Z. Lin, X. Shen, K. Chen, H. Jiang, and D. Liu, 2008. Bcl-xL forms two distinct homodimers at non-ionic detergents: implications in the dimerization of Bcl-2 family proteins. *J Biochem* 143:243–252.
- [292] Zhang, Z., S. M. Lapolla, M. G. Annis, M. Truscott, G. J. Roberts, Y. Miao, Y. Shao, C. Tan, J. Peng, A. E. Johnson, X. C. Zhang, D. W. Andrews, and J. Lin, 2004. Bcl-2 homodimerization involves two distinct binding surfaces, a topographic arrangement that provides an effective mechanism for Bcl-2 to capture activated Bax. *J Biol Chem* 279:43920–43928.
- [293] Ding, J., Z. Zhang, G. J. Roberts, M. Falcone, Y. Miao, Y. Shao, X. C. Zhang, D. W. Andrews, and J. Lin, 2010. Bcl-2 and Bax interact via the BH1-3 groove-BH3 motif interface and a novel interface involving the BH4 motif. *J Biol Chem* 285:28749–28763.

## Bibliografía

- [294] Peng, J., S. M. Lapolla, Z. Zhang, and J. Lin, 2009. The cytosolic domain of Bcl-2 oligomerizes to form pores in model mitochondrial outer membrane at acidic pH. *J Biomed Eng* 26:631–637.
- [295] Peng, J., J. Ding, C. Tan, B. Baggenstoss, Z. Zhang, S. M. Lapolla, and J. Lin, 2009. Oligomerization of membrane-bound Bcl-2 is involved in its pore formation induced by tBid. *Apoptosis* 14:1145–1153.
- [296] Kuwana, T., M. R. Mackey, G. Perkins, M. H. Ellisman, M. Latterich, R. Schneider, D. R. Green, and D. D. Newmeyer, 2002. Bid, Bax, and lipids cooperate to form supramolecular openings in the outer mitochondrial membrane. *Cell* 111:331–342.
- [297] Lucken-Ardjomande, S., S. Montessuit, and J.-C. Martinou, 2008. Contributions to Bax insertion and oligomerization of lipids of the mitochondrial outer membrane. *Cell Death Differ* 15:929–937.
- [298] Lutter, M., M. Fang, X. Luo, M. Nishijima, X. Xie, and X. Wang, 2000. Cardiolipin provides specificity for targeting of tBid to mitochondria. *Nat Cell Biol* 2:754–761.
- [299] Gonzalez, F., F. Pariselli, P. Dupaigne, I. Budihardjo, M. Lutter, B. Antonsson, P. Dirolez, S. Manon, J. Martinou, M. Goubern, X. Wang, S. Bernard, and P. X. Petit, 2005. tBid interaction with cardiolipin primarily orchestrates mitochondrial dysfunctions and subsequently activates Bax and Bak. *Cell Death Differ* 12:614–626.
- [300] Lucken-Ardjomande, S., S. Montessuit, and J. Martinou, 2008. Contributions to Bax insertion and oligomerization of lipids of the mitochondrial outer membrane. *Cell Death Differ* 15:929–937.
- [301] Lucken-Ardjomande, S., S. Montessuit, and J. Martinou, 2008. Bax activation and stress-induced apoptosis delayed by the accumulation of cholesterol in mitochondrial membranes. *Cell Death Differ* 15:484–493.
- [302] Christenson, E., S. Merlin, M. Saito, and P. Schlesinger, 2008. Cholesterol effects on BAX pore activation. *J Mol Biol* 381:1168–1183.
- [303] Snider, C., S. Jayasinghe, K. Hristova, and S. H. White, 2009. MPEX: a tool for exploring membrane proteins. *Protein Sci* 18:2624–2628.
- [304] Schendel, S. L., M. Montal, and J. C. Reed, 1998. Bcl-2 family proteins as ion-channels. *Cell Death Differ* 5:372–380.
- [305] Schlesinger, P. H., A. Gross, X. M. Yin, K. Yamamoto, M. Saito, G. Waksman, and S. J. Korsmeyer, 1997. Comparison of the ion channel characteristics of proapoptotic BAX and antiapoptotic BCL-2. *Proc Natl Acad Sci U S A* 94:11357–11362.
- [306] Epand, R. F., J. Martinou, S. Montessuit, and R. M. Epand, 2003. Transbilayer lipid diffusion promoted by Bax: implications for apoptosis. *Biochemistry* 42:14576–14582.
- [307] Martinez-Caballero, S., L. M. Dejean, M. S. Kinnally, K. J. Oh, C. A. Mannella, and K. W. Kinnally, 2009. Assembly of the mitochondrial apoptosis-induced channel, MAC. *J Biol Chem* 284:12235–12245.
- [308] Jürgensmeier, J. M., Z. Xie, Q. Deveraux, L. Ellerby, D. Bredesen, and J. C. Reed, 1998. Bax directly induces release of cytochrome c from isolated mitochondria. *Proc Natl Acad Sci U S A* 95:4997–5002.
- [309] Schafer, B., J. Quispe, V. Choudhary, J. E. Chipuk, T. G. Ajero, H. Du, R. Schneider, and T. Kuwana, 2009. Mitochondrial outer membrane proteins assist Bid in Bax-mediated lipidic pore formation. *Mol Biol Cell* 20:2276–2285.
- [310] Zha, H., H. A. Fisk, M. P. Yaffe, N. Mahajan, B. Herman, and J. C. Reed, 1996. Structure-function comparisons of the proapoptotic protein Bax in yeast and mammalian cells. *Mol Cell Biol* 16:6494–6508.
- [311] Heimlich, G., A. D. McKinnon, K. Bernardo, D. Brdiczka, J. C. Reed, R. Kain, M. Krönke, and J. M. Jürgensmeier, 2004. Bax-induced cytochrome c release from mitochondria depends on alpha-helices-5 and -6. *Biochem J* 378:247–255.
- [312] Matsuyama, S., S. L. Schendel, Z. Xie, and J. C. Reed, 1998. Cytoprotection by Bcl-2 requires the pore-forming alpha5 and alpha6 helices. *J Biol Chem* 273:30995–31001.

- [313] Asoh, S., T. Ohtsu, and S. Ohta, 2000. The super anti-apoptotic factor Bcl-xFNK constructed by disturbing intramolecular polar interactions in rat Bcl-xL. *J Biol Chem* 275:37240–37245.
- [314] Nouraini, S., E. Six, S. Matsuyama, S. Krajewski, and J. C. Reed, 2000. The putative pore-forming domain of Bax regulates mitochondrial localization and interaction with Bcl-X(L). *Mol Cell Biol* 20:1604–1615.
- [315] Parikh, N., C. Koshy, V. Dhayabaran, L. R. Perumalsamy, R. Sowdhamini, and A. Sarin, 2007. The N-terminus and alpha-5, alpha-6 helices of the pro-apoptotic protein Bax, modulate functional interactions with the anti-apoptotic protein Bcl-xL. *BMC Cell Biol* 8:16.
- [316] Marchi, U. D., S. Campello, I. Szabò, F. Tombola, J. Martinou, and M. Zoratti, 2004. Bax does not directly participate in the Ca(2+)-induced permeability transition of isolated mitochondria. *J Biol Chem* 279:37415–37422.
- [317] Majewski, N., V. Nogueira, P. Bhaskar, P. E. Coy, J. E. Skeen, K. Gottlob, N. S. Chandel, C. B. Thompson, R. B. Robey, and N. Hay, 2004. Hexokinase-mitochondria interaction mediated by Akt is required to inhibit apoptosis in the presence or absence of Bax and Bak. *Mol Cell* 16:819–830.
- [318] Epand, R. F., J. Martinou, S. Montessuit, R. M. Epand, and C. M. Yip, 2002. Direct evidence for membrane pore formation by the apoptotic protein Bax. *Biochem Biophys Res Commun* 298:744–749.
- [319] Lee, M.-T., W.-C. Hung, F.-Y. Chen, and H. W. Huang, 2008. Mechanism and kinetics of pore formation in membranes by water-soluble amphipathic peptides. *Proc Natl Acad Sci U S A* 105:5087–5092.
- [320] Minn, A. J., P. Véléz, S. L. Schendel, H. Liang, S. W. Muchmore, S. W. Fesik, M. Fill, and C. B. Thompson, 1997. Bcl-x(L) forms an ion channel in synthetic lipid membranes. *Nature* 385:353–357.
- [321] García-Sáez, A. J., J. Ries, M. Orzáez, E. Pérez-Payà, and P. Schwille, 2009. Membrane promotes tBID interaction with BCL(XL). *Nat Struct Mol Biol* 16:1178–1185.
- [322] Basañez, G., J. Zhang, B. N. Chau, G. I. Makshev, V. A. Frolov, T. A. Brandt, J. Burch, J. M. Hardwick, and J. Zimmerberg, 2001. Pro-apoptotic cleavage products of Bcl-xL form cytochrome c-conducting pores in pure lipid membranes. *J Biol Chem* 276:31083–31091.
- [323] Lin, B., S. K. Kolluri, F. Lin, W. Liu, Y. Han, X. Cao, M. I. Dawson, J. C. Reed, and X. kun Zhang, 2004. Conversion of Bcl-2 from protector to killer by interaction with nuclear orphan receptor Nur77/TR3. *Cell* 116:527–540.
- [324] Wei, M. C., W. X. Zong, E. H. Cheng, T. Lindsten, V. Panoutsakopoulou, A. J. Ross, K. A. Roth, G. R. MacGregor, C. B. Thompson, and S. J. Korsmeyer, 2001. Proapoptotic BAX and BAK: a requisite gateway to mitochondrial dysfunction and death. *Science* 292:727–730.
- [325] Zong, W.-X., C. Li, G. Hatzivassiliou, T. Lindsten, Q.-C. Yu, J. Yuan, and C. B. Thompson, 2003. Bax and Bak can localize to the endoplasmic reticulum to initiate apoptosis. *J Cell Biol* 162:59–69.
- [326] Kudla, G., S. Montessuit, R. Eskes, C. Berrier, J. C. Martinou, A. Ghazi, and B. Antonsson, 2000. The destabilization of lipid membranes induced by the C-terminal fragment of caspase 8-cleaved bid is inhibited by the N-terminal fragment. *J Biol Chem* 275:22713–22718.
- [327] Schendel, S. L., R. Azimov, K. Pawlowski, A. Godzik, B. L. Kagan, and J. C. Reed, 1999. Ion channel activity of the BH3 only Bcl-2 family member, BID. *J Biol Chem* 274:21932–21936.
- [328] Yan, L., Q. Miao, Y. Sun, and F. Yang, 2003. tBid forms a pore in the liposome membrane. *FEBS Lett* 555:545–550.
- [329] Epand, R. F., J.-C. Martinou, M. Fornallaz-Mulhauser, D. W. Hughes, and R. M. Epand, 2002. The apoptotic protein tBid promotes leakage by altering membrane curvature. *J Biol Chem* 277:32632–32639.
- [330] Esposti, M. D., J. T. Erler, J. A. Hickman, and C. Dive, 2001. Bid, a widely expressed proapoptotic protein of the Bcl-2 family, displays lipid transfer activity. *Mol Cell Biol* 21:7268–7276.
- [331] Grad, J. M., X. R. Zeng, and L. H. Boise, 2000. Regulation of Bcl-xL: a little bit of this and a little bit of STAT. *Curr Opin Oncol* 12:543–549.

## Bibliografía

- [332] Youle, R. J., and A. Strasser, 2008. The BCL-2 protein family: opposing activities that mediate cell death. *Nat Rev Mol Cell Biol* 9:47–59.
- [333] Gardai, S. J., D. A. Hildeman, S. K. Frankel, B. B. Whitlock, S. C. Frasch, N. Borregaard, P. Murrack, D. L. Bratton, and P. M. Henson, 2004. Phosphorylation of Bax Ser184 by Akt regulates its activity and apoptosis in neutrophils. *J Biol Chem* 279:21085–21095.
- [334] Kim, B., S. Ryu, and B. Song, 2006. JNK- and p38 kinase-mediated phosphorylation of Bax leads to its activation and mitochondrial translocation and to apoptosis of human hepatoma HepG2 cells. *J Biol Chem* 281:21256–21265.
- [335] Linseman, D. A., B. D. Butts, T. A. Pecht, R. A. Phelps, S. S. Le, T. A. Laessig, R. J. Bouchard, M. L. Florez-McClure, and K. A. Heidenreich, 2004. Glycogen synthase kinase-3 $\beta$  phosphorylates Bax and promotes its mitochondrial localization during neuronal apoptosis. *J Neurosci* 24:9993–10002.
- [336] Akiyama, T., P. Bouillet, T. Miyazaki, Y. Kadono, H. Chikuda, U. Chung, A. Fukuda, A. Hikita, H. Seto, T. Okada, T. Inaba, A. Sanjay, R. Baron, H. Kawaguchi, H. Oda, K. Nakamura, A. Strasser, and S. Tanaka, 2003. Regulation of osteoclast apoptosis by ubiquitylation of proapoptotic BH3-only Bcl-2 family member Bim. *EMBO J* 22:6653–6664.
- [337] Tran, S. E. F., A. Meinander, and J. E. Eriksson, 2004. Instant decisions: transcription-independent control of death-receptor-mediated apoptosis. *Trends Biochem Sci* 29:601–608.
- [338] Dijkers, P. F., R. H. Medema, J. W. Lammers, L. Koenderman, and P. J. Coffey, 2000. Expression of the pro-apoptotic Bcl-2 family member Bim is regulated by the forkhead transcription factor FKHR-L1. *Curr Biol* 10:1201–1204.
- [339] Li, H., H. Zhu, C. J. Xu, and J. Yuan, 1998. Cleavage of BID by caspase 8 mediates the mitochondrial damage in the Fas pathway of apoptosis. *Cell* 94:491–501.
- [340] Goping, I. S., A. Gross, J. N. Lavoie, M. Nguyen, R. Jemmerson, K. Roth, S. J. Korsmeyer, and G. C. Shore, 1998. Regulated targeting of BAX to mitochondria. *J Cell Biol* 143:207–215.
- [341] Yethon, J. A., R. F. Epand, B. Leber, R. M. Epand, and D. W. Andrews, 2003. Interaction with a membrane surface triggers a reversible conformational change in Bax normally associated with induction of apoptosis. *J Biol Chem* 278:48935–48941.
- [342] Mikhailov, V., M. Mikhailova, K. Degenhardt, M. A. Venkatachalam, E. White, and P. Saikumar, 2003. Association of Bax and Bak homo-oligomers in mitochondria. Bax requirement for Bak reorganization and cytochrome c release. *J Biol Chem* 278:5367–5376.
- [343] Sawada, M., P. Hayes, and S. Matsuyama, 2003. Cytoprotective membrane-permeable peptides designed from the Bax-binding domain of Ku70. *Nat Cell Biol* 5:352–357.
- [344] Willis, S. N., J. I. Fletcher, T. Kaufmann, M. F. van Delft, L. Chen, P. E. Czabotar, H. Ierino, E. F. Lee, W. D. Fairlie, P. Bouillet, A. Strasser, R. M. Kluck, J. M. Adams, and D. C. S. Huang, 2007. Apoptosis initiated when BH3 ligands engage multiple Bcl-2 homologs, not Bax or Bak. *Science* 315:856–859.
- [345] Oltvai, Z. N., C. L. Millman, and S. J. Korsmeyer, 1993. Bcl-2 heterodimerizes in vivo with a conserved homolog, Bax, that accelerates programmed cell death. *Cell* 74:609–619.
- [346] Korsmeyer, S. J., J. R. Shutter, D. J. Veis, D. E. Merry, and Z. N. Oltvai, 1993. Bcl-2/Bax: a rheostat that regulates an anti-oxidant pathway and cell death. *Semin Cancer Biol* 4:327–332.
- [347] Veis, D. J., C. M. Sorenson, J. R. Shutter, and S. J. Korsmeyer, 1993. Bcl-2-deficient mice demonstrate fulminant lymphoid apoptosis, polycystic kidneys, and hypopigmented hair. *Cell* 75:229–240.
- [348] Motoyama, N., F. Wang, K. A. Roth, H. Sawa, K. Nakayama, K. Nakayama, I. Negishi, S. Senju, Q. Zhang, and S. Fujii, 1995. Massive cell death of immature hematopoietic cells and neurons in Bcl-x-deficient mice. *Science* 267:1506–1510.
- [349] Shindler, K. S., C. B. Latham, and K. A. Roth, 1997. Bax deficiency prevents the increased cell death of immature neurons in bcl-x-deficient mice. *J Neurosci* 17:3112–3119.

- [350] Chen, L., S. N. Willis, A. Wei, B. J. Smith, J. I. Fletcher, M. G. Hinds, P. M. Colman, C. L. Day, J. M. Adams, and D. C. S. Huang, 2005. Differential targeting of prosurvival Bcl-2 proteins by their BH3-only ligands allows complementary apoptotic function. *Mol Cell* 17:393–403.
- [351] Peng, J., C. Tan, G. J. Roberts, O. Nikolaeva, Z. Zhang, S. M. Lapolla, S. Primorac, D. W. Andrews, and J. Lin, 2006. tBid elicits a conformational alteration in membrane-bound Bcl-2 such that it inhibits Bax pore formation. *J Biol Chem* 281:35802–35811.
- [352] Wilson-Annan, J., L. A. O'Reilly, S. A. Crawford, G. Hausmann, J. G. Beaumont, L. P. Parma, L. Chen, M. Lackmann, T. Lithgow, M. G. Hinds, C. L. Day, J. M. Adams, and D. C. S. Huang, 2003. Proapoptotic BH3-only proteins trigger membrane integration of prosurvival Bcl-w and neutralize its activity. *J Cell Biol* 162:877–887.
- [353] Leber, B., J. Lin, and D. W. Andrews, 2007. Embedded together: the life and death consequences of interaction of the Bcl-2 family with membranes. *Apoptosis* 12:897–911.
- [354] Friberg, H., and T. Wieloch, 2002. Mitochondrial permeability transition in acute neurodegeneration. *Biochimie* 84:241–250.
- [355] Niizuma, K., H. Yoshioka, H. Chen, G. S. Kim, J. E. Jung, M. Katsu, N. Okami, and P. H. Chan, 2010. Mitochondrial and apoptotic neuronal death signaling pathways in cerebral ischemia. *Biochim Biophys Acta* 1802:92–99.
- [356] Cao, G., M. Minami, W. Pei, C. Yan, D. Chen, C. O'Horo, S. H. Graham, and J. Chen, 2001. Intracellular Bax translocation after transient cerebral ischemia: implications for a role of the mitochondrial apoptotic signaling pathway in ischemic neuronal death. *J Cerebr Blood F Met* 21:321–333.
- [357] Mattson, M. P., and G. Kroemer, 2003. Mitochondria in cell death: novel targets for neuroprotection and cardioprotection. *Trends Mol Med* 9:196–205.
- [358] Cao, Y., T. Shibata, and N. G. Rainov, 2002. Liposome-mediated transfer of the bcl-2 gene results in neuroprotection after in vivo transient focal cerebral ischemia in an animal model. *Gene Ther* 9:415–419.
- [359] Sullivan, P. G., A. G. Rabchevsky, P. C. Waldmeier, and J. E. Springer, 2005. Mitochondrial permeability transition in CNS trauma: cause or effect of neuronal cell death? *J Neurosci Res* 79:231–239.
- [360] Lee, S. I., B. G. Kim, D. H. Hwang, H. M. Kim, and S. U. Kim, 2009. Overexpression of Bcl-XL in human neural stem cells promotes graft survival and functional recovery following transplantation in spinal cord injury. *J Neurosci Res* 87:3186–3197.
- [361] Irusta, P. M., Y. bei Chen, and J. M. Hardwick, 2003. Viral modulators of cell death provide new links to old pathways. *Curr Opin Cell Biol* 15:700–705.
- [362] Galluzzi, L., C. Brenner, E. Morselli, Z. Touat, and G. Kroemer, 2008. Viral control of mitochondrial apoptosis. *PLoS Pathog* 4:e1000018.
- [363] Hanahan, D., and R. A. Weinberg, 2000. The hallmarks of cancer. *Cell* 100:57–70.
- [364] Gascoyne, R. D., M. Krajewska, S. Krajewski, J. M. Connors, and J. C. Reed, 1997. Prognostic significance of Bax protein expression in diffuse aggressive non-Hodgkin's lymphoma. *Blood* 90:3173–3178.
- [365] Kitada, S., I. M. Pedersen, A. D. Schimmer, and J. C. Reed, 2002. Dysregulation of apoptosis genes in hematopoietic malignancies. *Oncogene* 21:3459–3474.
- [366] Aouacheria, A., 2009. Novel genetic and peptide-based strategies targeting the Bcl-2 family, an update. *Recent Pat DNA Gene Seq* 3:123–129.
- [367] Cheng, E. H., B. Levine, L. H. Boise, C. B. Thompson, and J. M. Hardwick, 1996. Bax-independent inhibition of apoptosis by Bcl-XL. *Nature* 379:554–556.
- [368] Cheng, E. H., M. C. Wei, S. Weiler, R. A. Flavell, T. W. Mak, T. Lindsten, and S. J. Korsmeyer, 2001. BCL-2, BCL-X(L) sequester BH3 domain-only molecules preventing BAX- and BAK-mediated mitochondrial apoptosis. *Mol Cell* 8:705–711.

## Bibliografía

- [369] Shimizu, S., M. Narita, and Y. Tsujimoto, 1999. Bcl-2 family proteins regulate the release of apoptogenic cytochrome c by the mitochondrial channel VDAC. *Nature* 399:483–487.
- [370] Marzo, I., C. Brenner, N. Zamzami, J. M. Jürgensmeier, S. A. Susin, H. L. Vieira, M. C. Prévost, Z. Xie, S. Matsuyama, J. C. Reed, and G. Kroemer, 1998. Bax and adenine nucleotide translocator cooperate in the mitochondrial control of apoptosis. *Science* 281:2027–2031.
- [371] Wang, J. L., D. Liu, Z. J. Zhang, S. Shan, X. Han, S. M. Srinivasula, C. M. Croce, E. S. Alnemri, and Z. Huang, 2000. Structure-based discovery of an organic compound that binds Bcl-2 protein and induces apoptosis of tumor cells. *Proc Natl Acad Sci U S A* 97:7124–7129.
- [372] Degtarev, A., A. Lugovskoy, M. Cardone, B. Mulley, G. Wagner, T. Mitchison, and J. Yuan, 2001. Identification of small-molecule inhibitors of interaction between the BH3 domain and Bcl-xL. *Nat Cell Biol* 3:173–182.
- [373] Oltersdorf, T., S. W. Elmore, A. R. Shoemaker, R. C. Armstrong, D. J. Augeri, B. A. Belli, M. Bruncko, T. L. Deckwerth, J. Dinges, P. J. Hajduk, M. K. Joseph, S. Kitada, S. J. Korsmeyer, A. R. Kunzer, A. Letai, C. Li, M. J. Mitten, D. G. Nettesheim, S. Ng, P. M. Nimmer, J. M. O'Connor, A. Oleksijew, A. M. Petros, J. C. Reed, W. Shen, S. K. Tahir, C. B. Thompson, K. J. Tomaselli, B. Wang, M. D. Wendt, H. Zhang, S. W. Fesik, and S. H. Rosenberg, 2005. An inhibitor of Bcl-2 family proteins induces regression of solid tumours. *Nature* 435:677–681.
- [374] Walensky, L. D., A. L. Kung, I. Escher, T. J. Malia, S. Barbuto, R. D. Wright, G. Wagner, G. L. Verdine, and S. J. Korsmeyer, 2004. Activation of apoptosis in vivo by a hydrocarbon-stapled BH3 helix. *Science* 305:1466–1470.
- [375] Jacotot, E., A. Deniaud, A. Borgne-Sanchez, Z. Touat, J. Briand, M. L. Bras, and C. Brenner, 2006. Therapeutic peptides: Targeting the mitochondrion to modulate apoptosis. *Biochim Biophys Acta* 1757:1312–1323.
- [376] Ellerby, H. M., W. Arap, L. M. Ellerby, R. Kain, R. Andrusiak, G. D. Rio, S. Krajewski, C. R. Lombardo, R. Rao, E. Ruoslahti, D. E. Bredesen, and R. Pasqualini, 1999. Anti-cancer activity of targeted pro-apoptotic peptides. *Nat Med* 5:1032–1038.
- [377] Guillemin, Y., J. Lopez, D. Gimenez, G. Fuertes, J. G. Valero, L. Blum, P. Gonzalo, J. Salgado, A. Girard-Egrot, and A. Aouacheria, 2010. Active fragments from pro- and antiapoptotic BCL-2 proteins have distinct membrane behavior reflecting their functional divergence. *PLoS One* 5:e9066.
- [378] Ardail, D., J. P. Privat, M. Egret-Charlier, C. Levrat, F. Lerme, and P. Louisot, 1990. Mitochondrial contact sites. Lipid composition and dynamics. *J Biol Chem* 265:18797–18802.
- [379] Schug, Z. T., and E. Gottlieb, 2009. Cardiolipin acts as a mitochondrial signalling platform to launch apoptosis. *Biochim Biophys Acta* 1788:2022–2031.
- [380] Mayer, L. D., M. J. Hope, and P. R. Cullis, 1986. Vesicles of variable sizes produced by a rapid extrusion procedure. *Biochim Biophys Acta* 858:161–168.
- [381] Dimitrov, D., and M. Angelova, 1988. Lipid swelling and liposome formation mediated by electric fields. *Bioelectroch Bioener* 19:323–336.
- [382] Silvestro, L., and P. H. Axelsen, 1998. Infrared spectroscopy of supported lipid monolayer, bilayer, and multibilayer membranes. *Chem Phys Lipids* 96:69–80.
- [383] Naito, A., 2009. Structure elucidation of membrane-associated peptides and proteins in oriented bilayers by solid-state NMR spectroscopy. *Solid State Nucl Magn Reson* 36:67–76.
- [384] Santos, N. C., and M. A. Castanho, 1996. Teaching light scattering spectroscopy: the dimension and shape of tobacco mosaic virus. *Biophys J* 71:1641–1650.
- [385] Domingues, M. M., P. S. Santiago, M. A. R. B. Castanho, and N. C. Santos, 2008. What can light scattering spectroscopy do for membrane-active peptide studies? *J Pept Sci* 14:394–400.
- [386] Manor, J., Z. Khattari, T. Salditt, and I. T. Arkin, 2005. Disorder influence on linear dichroism analyses of smectic phases. *Biophys J* 89:563–571.

- [387] Wellings, D. A., and E. Atherton, 1997. Standard Fmoc protocols. *Methods Enzymol* 289:44–67.
- [388] García-Martín, F., M. Quintanar-Audelo, Y. García-Ramos, L. J. Cruz, C. Gravel, R. Furic, S. Čížek, J. Tulla-Puche, and F. Albericio, 2006. ChemMatrix, a poly(ethylene glycol)-based support for the solid-phase synthesis of complex peptides. *J Comb Chem* 8:213–220.
- [389] Albericio, F., and L. A. Carpino, 1997. Coupling reagents and activation. *Methods Enzymol* 289:104–126.
- [390] Guy, C. A., and G. B. Fields, 1997. Trifluoroacetic acid cleavage and deprotection of resin-bound peptides following synthesis by Fmoc chemistry. *Methods Enzymol* 289:67–83.
- [391] Mant, C. T., L. H. Kondejewski, P. J. Cachia, O. D. Monera, and R. S. Hodges, 1997. Analysis of synthetic peptides by high-performance liquid chromatography. *Methods Enzymol* 289:426–469.
- [392] Chen, Y., C. T. Mant, and R. S. Hodges, 2007. Preparative reversed-phase high-performance liquid chromatography collection efficiency for an antimicrobial peptide on columns of varying diameters (1 mm to 9.4 mm I.D.). *J Chromatogr A* 1140:112–120.
- [393] Moore, W. T., 1997. Laser desorption mass spectrometry. *Methods Enzymol* 289:520–542.
- [394] Kelly, S. M., T. J. Jess, and N. C. Price, 2005. How to study proteins by circular dichroism. *Biochim Biophys Acta* 1751:119–139.
- [395] Bulheller, B. M., A. Rodger, and J. D. Hirst, 2007. Circular and linear dichroism of proteins. *Phys Chem Chem Phys* 9:2020–2035.
- [396] Goormaghtigh, E., V. Raussens, and J. M. Ruyschaert, 1999. Attenuated total reflection infrared spectroscopy of proteins and lipids in biological membranes. *Biochim Biophys Acta* 1422:105–185.
- [397] Tamm, L. K., and S. A. Tatulian, 1997. Infrared spectroscopy of proteins and peptides in lipid bilayers. *Q Rev Biophys* 30:365–429.
- [398] Inbaraj, J. J., T. B. Cardon, M. Laryukhin, S. M. Grosser, and G. A. Lorigan, 2006. Determining the topology of integral membrane peptides using EPR spectroscopy. *J Am Chem Soc* 128:9549–9554.
- [399] Pabst, G., N. Kucerka, M.-P. Nieh, M. C. Rheinstädter, and J. Katsaras, 2010. Applications of neutron and X-ray scattering to the study of biologically relevant model membranes. *Chem Phys Lipids* 163:460–479.
- [400] Mantsch, H. H., and R. N. McElhaney, 1991. Phospholipid phase transitions in model and biological membranes as studied by infrared spectroscopy. *Chem Phys Lipids* 57:213–226.
- [401] Grelard, A., A. Couvreur, C. Loudet, and E. J. Dufourc, 2009. Solution and solid-state NMR of lipids. *Methods Mol Biol* 462:111–133.
- [402] Sreerama, N., and R. W. Woody, 2004. On the analysis of membrane protein circular dichroism spectra. *Protein Sci* 13:100–112.
- [403] Whitmore, L., and B. A. Wallace, 2004. DICHROWEB, an online server for protein secondary structure analyses from circular dichroism spectroscopic data. *Nucleic Acids Res* 32:W668–W673.
- [404] Bierzynski, A., 2001. Methods of peptide conformation studies. *Acta Biochim Pol* 48:1091–1099.
- [405] Tatulian, S. A., 2003. Attenuated total reflection Fourier transform infrared spectroscopy: a method of choice for studying membrane proteins and lipids. *Biochemistry* 42:11898–11907.
- [406] Arbely, E., I. Kass, and I. T. Arkin, 2003. Site-specific dichroism analysis utilizing transmission FTIR. *Biophys J* 85:2476–2483.
- [407] Tsuboi, M., 1962. Infrared dichroism and molecular conformation of alpha-form poly-gamma-benzyl-L-glutamate. *J Polym Sci* 59:139–153.
- [408] Marsh, D., M. Müller, and F. J. Schmitt, 2000. Orientation of the infrared transition moments for an alpha-helix. *Biophys J* 78:2499–2510.

## Bibliografía

- [409] Ludlam, C. F., I. T. Arkin, X. M. Liu, M. S. Rothman, P. Rath, S. Aimoto, S. O. Smith, D. M. Engelman, and K. J. Rothschild, 1996. Fourier transform infrared spectroscopy and site-directed isotope labeling as a probe of local secondary structure in the transmembrane domain of phospholamban. *Biophys J* 70:1728–1736.
- [410] Torres, J., P. D. Adams, and I. T. Arkin, 2000. Use of a new label,  $(^{13}\text{C})\text{C}=\text{C}(^{18}\text{O})$ , in the determination of a structural model of phospholamban in a lipid bilayer. Spatial restraints resolve the ambiguity arising from interpretations of mutagenesis data. *J Mol Biol* 300:677–685.
- [411] Torres, J., and I. T. Arkin, 2002. C-deuterated alanine: a new label to study membrane protein structure using site-specific infrared dichroism. *Biophys J* 82:1068–1075.
- [412] Torres, J., A. Kukol, J. M. Goodman, and I. T. Arkin, 2001. Site-specific examination of secondary structure and orientation determination in membrane proteins: the peptidic  $(^{13}\text{C})\text{C}=\text{C}(^{18}\text{O})$  group as a novel infrared probe. *Biopolymers* 59:396–401.
- [413] Torii, H., and M. Tasumi, 1992. Model calculations on the amide-I infrared bands of globular proteins. *J Chem Phys* 96:3379–3387.
- [414] Arkin, I. T., K. R. MacKenzie, and A. T. Brünger, 1997. Site-Directed Dichroism As a Method for Obtaining Rotational and Orientational Constraints for Oriented Polymers. *J Am Chem Soc* 119:8973–8980.
- [415] Torres, J., J. A. G. Briggs, and I. T. Arkin, 2002. Multiple site-specific infrared dichroism of CD3-zeta, a transmembrane helix bundle. *J Mol Biol* 316:365–374.
- [416] Harrick, N., 1967. *Internal Reflection Spectroscopy*. John Wiley & Sons Inc.
- [417] Davis, J. H., M. Auger, and R. S. Hodges, 1995. High resolution  $^1\text{H}$  nuclear magnetic resonance of a transmembrane peptide. *Biophys J* 69:1917–1932.
- [418] Axelsen, P. H., and M. J. Citra, 1996. Orientational order determination by internal reflection infrared spectroscopy. *Prog Biophys Mol Biol* 66:227–253.
- [419] Fraser, R. D. B., 1956. Interpretation of Infrared Dichroism in Fibrous Proteins. *J Chem Phys* 24:89.
- [420] Kass, I., E. Arbely, and I. T. Arkin, 2004. Modeling sample disorder in site-specific dichroism studies of uniaxial systems. *Biophys J* 86:2502–2507.
- [421] Esteban-Martín, S., E. Strandberg, G. Fuertes, A. S. Ulrich, and J. Salgado, 2009. Influence of whole-body dynamics on  $^{15}\text{N}$  PISEMA NMR spectra of membrane proteins: a theoretical analysis. *Biophys J* 96:3233–3241.
- [422] Strandberg, E., S. Esteban-Martín, J. Salgado, and A. S. Ulrich, 2009. Orientation and dynamics of peptides in membranes calculated from  $^2\text{H}$ -NMR data. *Biophys J* 96:3223–3232.
- [423] Monticelli, L., D. P. Tieleman, and P. F. J. Fuchs, 2010. Interpretation of  $^2\text{H}$ -NMR experiments on the orientation of the transmembrane helix WALP23 by computer simulations. *Biophys J* 99:1455–1464.
- [424] Manor, J., P. Mukherjee, Y. Lin, H. Leonov, J. L. Skinner, M. T. Zanni, and I. T. Arkin, 2009. Gating mechanism of the influenza A M2 channel revealed by 1D and 2D IR spectroscopies. *Structure* 17:247–254.
- [425] Kochva, U., H. Leonov, I. T. Arkin, and P. D. Adams, 2004. Modeling membrane proteins utilizing information from silent amino acid substitutions. *Curr Protoc Bioinformatics* Chapter 5:Unit5.3.
- [426] Wang, W., D. Pan, Y. Song, W. Liu, L. Yang, and H. W. Huang, 2006. Method of x-ray anomalous diffraction for lipid structures. *Biophys J* 91:736–743.
- [427] Wiener, M. C., and S. H. White, 1992. Structure of a fluid dioleoylphosphatidylcholine bilayer determined by joint refinement of x-ray and neutron diffraction data. III. Complete structure. *Biophys J* 61:434–447.
- [428] Salditt, T., C. Li, and A. Spaar, 2006. Structure of antimicrobial peptides and lipid membranes probed by interface-sensitive X-ray scattering. *Biochim Biophys Acta* 1758:1483–1498.

- [429] Giahi, A., M. E. A. Faris, P. Bassereau, and T. Salditt, 2007. Active membranes studied by X-ray scattering. *Eur Phys J E Soft Matter* 23:431–437.
- [430] Li, C., D. Constantin, and T. Salditt, 2004. Biomimetic membranes of lipid-peptide model systems prepared on solid support. *J Phys : Condens Matter* 16:S2439–S2453.
- [431] Khattari, Z., E. Arbely, I. T. Arkin, and T. Salditt, 2006. Viral ion channel proteins in model membranes: a comparative study by X-ray reflectivity. *Eur Biophys J* 36:45–55.
- [432] Merzlyakov, M., and K. Hristova, 2008. Forster resonance energy transfer measurements of transmembrane helix dimerization energetics. *Methods Enzymol* 450:107–127.
- [433] Reynolds, J. A., and C. Tanford, 1976. Determination of molecular weight of the protein moiety in protein-detergent complexes without direct knowledge of detergent binding. *Proc Natl Acad Sci U S A* 73:4467–4470.
- [434] Fleming, K. G., 2002. Standardizing the free energy change of transmembrane helix-helix interactions. *J Mol Biol* 323:563–571.
- [435] Cristian, L., J. D. Lear, and W. F. DeGrado, 2003. Use of thiol-disulfide equilibria to measure the energetics of assembly of transmembrane helices in phospholipid bilayers. *Proc Natl Acad Sci U S A* 100:14772–14777.
- [436] Hilger, D., H. Jung, E. Padan, C. Wegener, K.-P. Vogel, H.-J. Steinhoff, and G. Jeschke, 2005. Assessing oligomerization of membrane proteins by four-pulse DEER: pH-dependent dimerization of NhaA Na<sup>+</sup>/H<sup>+</sup> antiporter of *E. coli*. *Biophys J* 89:1328–1338.
- [437] Toke, O., R. D. O'Connor, T. K. Weldeghiorghis, W. L. Maloy, R. W. Glaser, A. S. Ulrich, and J. Schaefer, 2004. Structure of (KIAGKIA)<sub>3</sub> aggregates in phospholipid bilayers by solid-state NMR. *Biophys J* 87:675–687.
- [438] Langosch, D., B. Brosig, H. Kolmar, and H. J. Fritz, 1996. Dimerisation of the glycoporphin A transmembrane segment in membranes probed with the ToxR transcription activator. *J Mol Biol* 263:525–530.
- [439] Russ, W. P., and D. M. Engelman, 1999. TOXCAT: a measure of transmembrane helix association in a biological membrane. *Proc Natl Acad Sci U S A* 96:863–868.
- [440] Schneider, D., and D. M. Engelman, 2003. GALLEX, a measurement of heterologous association of transmembrane helices in a biological membrane. *J Biol Chem* 278:3105–3111.
- [441] Chen, L., L. Novicky, M. Merzlyakov, T. Hristov, and K. Hristova, 2010. Measuring the energetics of membrane protein dimerization in mammalian membranes. *J Am Chem Soc* 132:3628–3635.
- [442] Schagger, H., and G. von Jagow, 1987. Tricine-sodium dodecyl sulfate-polyacrylamide gel electrophoresis for the separation of proteins in the range from 1 to 100 kDa. *Anal Biochem* 166:368–379.
- [443] Schagger, H., 2006. Tricine-SDS-PAGE. *Nat Protoc* 1:16–22.
- [444] Melnyk, R. A., A. W. Partridge, and C. M. Deber, 2001. Retention of native-like oligomerization states in transmembrane segment peptides: application to the *Escherichia coli* aspartate receptor. *Biochemistry* 40:11106–11113.
- [445] Li, E., M. You, and K. Hristova, 2005. Sodium dodecyl sulfate-polyacrylamide gel electrophoresis and forster resonance energy transfer suggest weak interactions between fibroblast growth factor receptor 3 (FGFR3) transmembrane domains in the absence of extracellular domains and ligands. *Biochemistry* 44:352–360.
- [446] Rath, A., M. Glibowicka, V. G. Nadeau, G. Chen, and C. M. Deber, 2009. Detergent binding explains anomalous SDS-PAGE migration of membrane proteins. *Proc Natl Acad Sci U S A* 106:1760–1765.
- [447] Rath, A., V. G. Nadeau, B. E. Poulsen, D. P. Ng, and C. M. Deber, 2010. Novel Hydrophobic Standards for Membrane Protein Molecular Weight Determinations via Sodium Dodecyl Sulfate-Polyacrylamide Gel Electrophoresis. *Biochemistry* 49:10589–10591.
- [448] Walkenhorst, W. F., M. Merzlyakov, K. Hristova, and W. C. Wimley, 2009. Polar residues in transmembrane helices can decrease electrophoretic mobility in polyacrylamide gels without causing helix dimerization. *Biochim Biophys Acta* 1788:1321–1331.

## Bibliografía

- [449] Förster, T., 1948. Zwischenmolekulare Energiewanderung und Fluoreszenz. *Ann. Phys.* 437:55–75 [English Translated version "Intermolecular energy migration and fluorescence" by RS Knox, Department of Physics and Astronomy, University of Rochester, Rochester, NY 14627].
- [450] Stryer, L., 1978. Fluorescence energy transfer as a spectroscopic ruler. *Annu Rev Biochem* 47:819–846.
- [451] Stryer, L., and R. P. Haugland, 1967. Energy transfer: a spectroscopic ruler. *Proc Natl Acad Sci U S A* 58:719–726.
- [452] Lakowicz, J. R., 2006. Principles of Fluorescence Spectroscopy. Springer-Verlag New York Inc., 3Rev ed edition.
- [453] Posokhov, Y. O., M. Merzlyakov, K. Hristova, and A. S. Ladokhin, 2008. A simple "proximity correction for Förster resonance energy transfer efficiency determination in membranes using lifetime measurements. *Anal Biochem* 380:134–136.
- [454] You, M., E. Li, W. C. Wimley, and K. Hristova, 2005. Förster resonance energy transfer in liposomes: measurements of transmembrane helix dimerization in the native bilayer environment. *Anal Biochem* 340:154–164.
- [455] Wolber, P. K., and B. S. Hudson, 1979. An analytic solution to the Förster energy transfer problem in two dimensions. *Biophys J* 28:197–210.
- [456] Wimley, W. C., and S. H. White, 2000. Determining the membrane topology of peptides by fluorescence quenching. *Biochemistry* 39:161–170.
- [457] Merzlyakov, M., L. Chen, and K. Hristova, 2007. Studies of receptor tyrosine kinase transmembrane domain interactions: the EmEx-FRET method. *J Membr Biol* 215:93–103.
- [458] Adair, B. D., and D. M. Engelman, 1994. Glycophorin A helical transmembrane domains dimerize in phospholipid bilayers: a resonance energy transfer study. *Biochemistry* 33:5539–5544.
- [459] Fung, B. K., and L. Stryer, 1978. Surface density determination in membranes by fluorescence energy transfer. *Biochemistry* 17:5241–5248.
- [460] Moens, P. D., D. J. Yee, and C. G. dos Remedios, 1994. Determination of the radial coordinate of Cys-374 in F-actin using fluorescence resonance energy transfer spectroscopy: effect of phalloidin on polymer assembly. *Biochemistry* 33:13102–13108.
- [461] Li, M., L. G. Reddy, R. Bennett, N. D. Silva, L. R. Jones, and D. D. Thomas, 1999. A fluorescence energy transfer method for analyzing protein oligomeric structure: application to phospholamban. *Biophys J* 76:2587–2599.
- [462] White, S. H., W. C. Wimley, A. S. Ladokhin, and K. Hristova, 1998. Protein folding in membranes: determining energetics of peptide-bilayer interactions. *Methods Enzymol* 295:62–87.
- [463] Santos, N. C., M. Prieto, and M. A. R. B. Castanho, 2003. Quantifying molecular partition into model systems of biomembranes: an emphasis on optical spectroscopic methods. *Biochim Biophys Acta* 1612:123–135.
- [464] Reshetnyak, Y. K., O. A. Andreev, M. Segala, V. S. Markin, and D. M. Engelman, 2008. Energetics of peptide (pHLIP) binding to and folding across a lipid bilayer membrane. *Proc Natl Acad Sci U S A* 105:15340–15345.
- [465] Seelig, A., and P. M. Macdonald, 1989. Binding of a neuropeptide, substance P, to neutral and negatively charged lipids. *Biochemistry* 28:2490–2496.
- [466] Seelig, J., 1997. Titration calorimetry of lipid-peptide interactions. *Biochim Biophys Acta* 1331:103–116.
- [467] Wimley, W. C., and S. H. White, 1993. Quantitation of electrostatic and hydrophobic membrane interactions by equilibrium dialysis and reverse-phase HPLC. *Anal Biochem* 213:213–217.
- [468] Vogel, H., 1981. Incorporation of melittin into phosphatidylcholine bilayers. Study of binding and conformational changes. *FEBS Lett* 134:37–42.

- [469] Ladokhin, A. S., S. Jayasinghe, and S. H. White, 2000. How to measure and analyze tryptophan fluorescence in membranes properly, and why bother? *Anal Biochem* 285:235–245.
- [470] McLaughlin, S., and H. Harary, 1976. The hydrophobic adsorption of charged molecules to bilayer membranes: a test of the applicability of the stern equation. *Biochemistry* 15:1941–1948.
- [471] Kim, J., M. Mosior, L. A. Chung, H. Wu, and S. McLaughlin, 1991. Binding of peptides with basic residues to membranes containing acidic phospholipids. *Biophys J* 60:135–148.
- [472] Peitzsch, R. M., and S. McLaughlin, 1993. Binding of acylated peptides and fatty acids to phospholipid vesicles: pertinence to myristoylated proteins. *Biochemistry* 32:10436–10443.
- [473] Yandek, L. E., A. Pokorny, A. Florén, K. Knoelke, U. Langel, and P. F. F. Almeida, 2007. Mechanism of the cell-penetrating peptide transportan 10 permeation of lipid bilayers. *Biophys J* 92:2434–2444.
- [474] Soong, R., M. Merzlyakov, and K. Hristova, 2009. Hill coefficient analysis of transmembrane helix dimerization. *J Membr Biol* 230:49–55.
- [475] García-Sáez, A. J., 2005. Characterising the interaction of fragments derived from Bax, Bcl-xL and Bid with lipid membranes. Ph.D. thesis, Universitat de València.
- [476] Weinstein, J. N., S. Yoshikami, P. Henkart, R. Blumenthal, and W. A. Hagins, 1977. Liposome-cell interaction: transfer and intracellular release of a trapped fluorescent marker. *Science* 195:489–492.
- [477] Allen, T. M., and L. G. Cleland, 1980. Serum-induced leakage of liposome contents. *Biochim Biophys Acta* 597:418–426.
- [478] Duzgunes, N., R. M. Straubinger, P. A. Baldwin, D. S. Friend, and D. Papahadjopoulos, 1985. Proton-induced fusion of oleic acid-phosphatidylethanolamine liposomes. *Biochemistry* 24:3091–3098.
- [479] Ellens, H., J. Bentz, and F. C. Szoka, 1985. H<sup>+</sup>- and Ca<sup>2+</sup>-induced fusion and destabilization of liposomes. *Biochemistry* 24:3099–3106.
- [480] Kamal, M. M., D. Mills, M. Grzybek, and J. Howard, 2009. Measurement of the membrane curvature preference of phospholipids reveals only weak coupling between lipid shape and leaflet curvature. *Proc Natl Acad Sci U S A* 106:22245–22250.
- [481] McIntyre, J. C., and R. G. Sleight, 1991. Fluorescence assay for phospholipid membrane asymmetry. *Biochemistry* 30:11819–11827.
- [482] García-Sáez, A. J., and P. Schuille, 2008. Fluorescence correlation spectroscopy for the study of membrane dynamics and protein/lipid interactions. *Methods* 46:116–122.
- [483] Ries, J., and P. Schuille, 2006. Studying slow membrane dynamics with continuous wave scanning fluorescence correlation spectroscopy. *Biophys J* 91:1915–1924.
- [484] Vigano, C., L. Manciu, F. Buyse, E. Goormaghtigh, and J. M. Ruysschaert, 2000. Attenuated total reflection IR spectroscopy as a tool to investigate the structure, orientation and tertiary structure changes in peptides and membrane proteins. *Biopolymers* 55:373–380.
- [485] Bechinger, B., R. Kinder, M. Helmle, T. C. Vogt, U. Harzer, and S. Schinzel, 1999. Peptide structural analysis by solid-state NMR spectroscopy. *Biopolymers* 51:174–190.
- [486] Miles, A. J., and B. A. Wallace, 2006. Synchrotron radiation circular dichroism spectroscopy of proteins and applications in structural and functional genomics. *Chem Soc Rev* 35:39–51.
- [487] Whitmore, L., and B. A. Wallace, 2008. Protein secondary structure analyses from circular dichroism spectroscopy: methods and reference databases. *Biopolymers* 89:392–400.
- [488] Marsh, 1999. Quantitation of secondary structure in ATR infrared spectroscopy. *Biophys J* 77:2630–2637.
- [489] Tamm, L. K., and S. A. Tatulian, 1997. Infrared spectroscopy of proteins and peptides in lipid bilayers. *Q Rev Biophys* 30:365–429.

## Bibliografía

- [490] Hristova, K., and S. H. White, 2005. An experiment-based algorithm for predicting the partitioning of unfolded peptides into phosphatidylcholine bilayer interfaces. *Biochemistry* 44:12614–12619.
- [491] McKeown, A. N., J. L. Naro, L. J. Huskins, and P. F. Almeida, 2011. A thermodynamic approach to the mechanism of cell-penetrating peptides in model membranes. *Biochemistry* 50:654–662.
- [492] Nechushtan, A., C. L. Smith, I. Lamensdorf, S. H. Yoon, and R. J. Youle, 2001. Bax and Bak coalesce into novel mitochondria-associated clusters during apoptosis. *J Cell Biol* 153:1265–1276.
- [493] Bleicken, S., and K. Zeth, 2009. Conformational changes and protein stability of the pro-apoptotic protein Bax. *J Bioenerg Biomembr* 41:29–40.
- [494] Ivashyna, O., A. J. García-Sáez, J. Ries, E. T. Christenson, P. Schwille, and P. H. Schlesinger, 2009. Detergent-activated BAX protein is a monomer. *J Biol Chem* 284:23935–23946.
- [495] Oh, K. J., S. Barbuto, K. Pitter, J. Morash, L. D. Walensky, and S. J. Korsmeyer, 2006. A membrane-targeted BID BCL-2 homology 3 peptide is sufficient for high potency activation of BAX in vitro. *J Biol Chem* 281:36999–37008.
- [496] Parente, R. A., S. Nir, and F. C. Szoka, 1990. Mechanism of leakage of phospholipid vesicle contents induced by the peptide GALA. *Biochemistry* 29:8720–8728.
- [497] Schwarz, G., R. T. Zong, and T. Popescu, 1992. Kinetics of melittin induced pore formation in the membrane of lipid vesicles. *Biochim Biophys Acta* 1110:97–104.
- [498] Matsuzaki, K., O. Murase, and K. Miyajima, 1995. Kinetics of pore formation by an antimicrobial peptide, magainin 2, in phospholipid bilayers. *Biochemistry* 34:12553–12559.
- [499] Chen, F.-Y., M.-T. Lee, and H. W. Huang, 2002. Sigmoidal concentration dependence of antimicrobial peptide activities: a case study on alamethicin. *Biophys J* 82:908–914.
- [500] Pokorny, A., and P. F. F. Almeida, 2004. Kinetics of dye efflux and lipid flip-flop induced by delta-lysin in phosphatidylcholine vesicles and the mechanism of graded release by amphipathic, alpha-helical peptides. *Biochemistry* 43:8846–8857.
- [501] Hara, T., H. Kodama, M. Kondo, K. Wakamatsu, A. Takeda, T. Tachi, and K. Matsuzaki, 2001. Effects of peptide dimerization on pore formation: Antiparallel disulfide-dimerized magainin 2 analogue. *Biopolymers* 58:437–446.
- [502] Mukai, Y., Y. Matsushita, T. Niidome, T. Hatekeyama, and H. Aoyag, 2002. Parallel and antiparallel dimers of magainin 2: their interaction with phospholipid membrane and antibacterial activity. *J Pept Sci* 8:570–577.
- [503] Dempsey, C. E., S. Ueno, and M. B. Avison, 2003. Enhanced membrane permeabilization and antibacterial activity of a disulfide-dimerized magainin analogue. *Biochemistry* 42:402–409.
- [504] Lemmon, M. A., J. M. Flanagan, J. F. Hunt, B. D. Adair, B. J. Bormann, C. E. Dempsey, and D. M. Engelman, 1992. Glycophorin A dimerization is driven by specific interactions between transmembrane alpha-helices. *J Biol Chem* 267:7683–7689.
- [505] Ramjeesingh, M., L. J. Huan, E. Garami, and C. E. Bear, 1999. Novel method for evaluation of the oligomeric structure of membrane proteins. *Biochem J* 342 ( Pt 1):119–123.
- [506] Therien, A. G., F. E. Grant, and C. M. Deber, 2001. Interhelical hydrogen bonds in the CFTR membrane domain. *Nat Struct Biol* 8:597–601.
- [507] Wu, P., and L. Brand, 1994. Resonance energy transfer: methods and applications. *Anal Biochem* 218:1–13.
- [508] 2010. Molecular Probes Handbook, A Guide to Fluorescent Probes and Labeling Technologies, 11th Edition. Molecular Probes, Invitrogen.
- [509] Demchenko, A. P., 1988. Ultraviolet spectroscopy of proteins A P Demchenko. Springer-Verlag, Berlin. *Biochem. Educ.* 16:112–112.

- [510] Fersht, A. R., J. P. Shi, J. Knill-Jones, D. M. Lowe, A. J. Wilkinson, D. M. Blow, P. Brick, P. Carter, M. M. Waye, and G. Winter, 1985. Hydrogen bonding and biological specificity analysed by protein engineering. *Nature* 314:235–238.
- [511] Pace, C. N., B. A. Shirley, M. McNutt, and K. Gajiwala, 1996. Forces contributing to the conformational stability of proteins. *FASEB J* 10:75–83.
- [512] Li, E., M. You, and K. Hristova, 2006. FGFR3 dimer stabilization due to a single amino acid pathogenic mutation. *J Mol Biol* 356:600–612.
- [513] Lucken-Ardjomande, S., S. Montessuit, and J.-C. Martinou, 2008. Bax activation and stress-induced apoptosis delayed by the accumulation of cholesterol in mitochondrial membranes. *Cell Death Differ* 15:484–493.
- [514] MacKenzie, K. R., and K. G. Fleming, 2008. Association energetics of membrane spanning alpha-helices. *Curr Opin Struct Biol* 18:412–419.
- [515] Johnson, R. M., A. Rath, and C. M. Deber, 2006. The position of the Gly-xxx-Gly motif in transmembrane segments modulates dimer affinity. *Biochem Cell Biol* 84:1006–1012.
- [516] Melnyk, R. A., S. Kim, A. R. Curran, D. M. Engelman, J. U. Bowie, and C. M. Deber, 2004. The affinity of GXXXG motifs in transmembrane helix-helix interactions is modulated by long-range communication. *J Biol Chem* 279:16591–16597.
- [517] Doura, A. K., F. J. Kobus, L. Dubrovsky, E. Hibbard, and K. G. Fleming, 2004. Sequence context modulates the stability of a GxxxG-mediated transmembrane helix-helix dimer. *J Mol Biol* 341:991–998.
- [518] Zhang, J., and T. Lazaridis, 2009. Transmembrane helix association affinity can be modulated by flanking and noninterfacial residues. *Biophys J* 96:4418–4427.
- [519] Duong, M. T., T. M. Jaszewski, K. G. Fleming, and K. R. MacKenzie, 2007. Changes in apparent free energy of helix-helix dimerization in a biological membrane due to point mutations. *J Mol Biol* 371:422–434.
- [520] Cunningham, F., B. E. Poulsen, W. Ip, and C. M. Deber, 2010. Beta-branched residues adjacent to GG4 motifs promote the efficient association of glycophorin A transmembrane helices. *Biopolymers* .
- [521] Unterreitmeier, S., A. Fuchs, T. Schäffler, R. G. Heym, D. Frishman, and D. Langosch, 2007. Phenylalanine promotes interaction of transmembrane domains via GxxxG motifs. *J Mol Biol* 374:705–718.
- [522] Johnson, R. M., K. Hecht, and C. M. Deber, 2007. Aromatic and cation-pi interactions enhance helix-helix association in a membrane environment. *Biochemistry* 46:9208–9214.
- [523] Smith, S. O., M. Eilers, D. Song, E. Crocker, W. Ying, M. Groesbeek, G. Metz, M. Ziliox, and S. Aimoto, 2002. Implications of threonine hydrogen bonding in the glycophorin A transmembrane helix dimer. *Biophys J* 82:2476–2486.
- [524] Sulistijo, E. S., T. M. Jaszewski, and K. R. MacKenzie, 2003. Sequence-specific dimerization of the transmembrane domain of the "BH3-only" protein BNIP3 in membranes and detergent. *J Biol Chem* 278:51950–51956.
- [525] Sulistijo, E. S., and K. R. MacKenzie, 2006. Sequence dependence of BNIP3 transmembrane domain dimerization implicates side-chain hydrogen bonding and a tandem GxxxG motif in specific helix-helix interactions. *J Mol Biol* 364:974–990.
- [526] Lawrie, C. M., E. S. Sulistijo, and K. R. MacKenzie, 2010. Intermonomer hydrogen bonds enhance GxxxG-driven dimerization of the BNIP3 transmembrane domain: roles for sequence context in helix-helix association in membranes. *J Mol Biol* 396:924–936.
- [527] Meijerink, J. P., E. J. Mensink, K. Wang, T. W. Sedlak, A. W. Slöetjes, T. de Witte, G. Waksman, and S. J. Korsmeyer, 1998. Hematopoietic malignancies demonstrate loss-of-function mutations of BAX. *Blood* 91:2991–2997.
- [528] Sedlak, T. W., Z. N. Oltvai, E. Yang, K. Wang, L. H. Boise, C. B. Thompson, and S. J. Korsmeyer, 1995. Multiple Bcl-2 family members demonstrate selective dimerizations with Bax. *Proc Natl Acad Sci U S A* 92:7834–7838.

## Bibliografía

- [529] Zha, H., C. Aimé-Sempé, T. Sato, and J. C. Reed, 1996. Proapoptotic protein Bax heterodimerizes with Bcl-2 and homodimerizes with Bax via a novel domain (BH3) distinct from BH1 and BH2. *J Biol Chem* 271:7440–7444.
- [530] Wang, K., A. Gross, G. Waksman, and S. J. Korsmeyer, 1998. Mutagenesis of the BH3 domain of BAX identifies residues critical for dimerization and killing. *Mol Cell Biol* 18:6083–6089.
- [531] Czabotar, P. E., E. F. Lee, M. F. van Delft, C. L. Day, B. J. Smith, D. C. S. Huang, W. D. Fairlie, M. G. Hinds, and P. M. Colman, 2007. Structural insights into the degradation of Mcl-1 induced by BH3 domains. *Proc Natl Acad Sci U S A* 104:6217–6222.
- [532] Smits, C., P. E. Czabotar, M. G. Hinds, and C. L. Day, 2008. Structural plasticity underpins promiscuous binding of the prosurvival protein A1. *Structure* 16:818–829.
- [533] Tatulian, S. A., S. Qin, A. H. Pande, and X. He, 2005. Positioning membrane proteins by novel protein engineering and biophysical approaches. *J Mol Biol* 351:939–947.
- [534] Bechinger, B., C. Aisenbrey, and P. Bertani, 2004. The alignment, structure and dynamics of membrane-associated polypeptides by solid-state NMR spectroscopy. *Biochim Biophys Acta* 1666:190–204.
- [535] Esteban-Martín, S., E. Strandberg, J. Salgado, and A. S. Ulrich, 2010. Solid state NMR analysis of peptides in membranes: Influence of dynamics and labeling scheme. *Biochim Biophys Acta* 1798:252–257.
- [536] Wu, Y., H. W. Huang, and G. A. Olah, 1990. Method of oriented circular dichroism. *Biophys J* 57:797–806.
- [537] Bürck, J., S. Roth, P. Wadhvani, S. Afonin, N. Kanithasen, E. Strandberg, and A. S. Ulrich, 2008. Conformation and membrane orientation of amphiphilic helical peptides by oriented circular dichroism. *Biophys J* 95:3872–3881.
- [538] Rufener, E., A. A. Frazier, C. M. Wieser, A. Hinderliter, and D. S. Cafiso, 2005. Membrane-bound orientation and position of the synaptotagmin C2B domain determined by site-directed spin labeling. *Biochemistry* 44:18–28.
- [539] Nazarov, P. V., R. B. M. Koehorst, W. L. Vos, V. V. Apanasovich, and M. A. Hemminga, 2007. FRET study of membrane proteins: determination of the tilt and orientation of the N-terminal domain of M13 major coat protein. *Biophys J* 92:1296–1305.
- [540] Holt, A., R. B. M. Koehorst, T. Rutters-Meijneke, M. H. Gelb, D. T. S. Rijkers, M. A. Hemminga, and J. A. Killian, 2009. Tilt and rotation angles of a transmembrane model peptide as studied by fluorescence spectroscopy. *Biophys J* 97:2258–2266.
- [541] Basyn, F., B. Charloteaux, A. Thomas, and R. Brasseur, 2001. Prediction of membrane protein orientation in lipid bilayers: a theoretical approach. *J Mol Graphics Modell* 20:235–244.
- [542] Ash, W. L., M. R. Zlomislic, E. O. Oloo, and D. P. Tieleman, 2004. Computer simulations of membrane proteins. *Biochim Biophys Acta* 1666:158–189.
- [543] Torres, J., K. Parthasarathy, X. Lin, R. Saravanan, A. Kukol, and D. X. Liu, 2006. Model of a putative pore: the pentameric alpha-helical bundle of SARS coronavirus E protein in lipid bilayers. *Biophys J* 91:938–947.
- [544] Dürr, U., 2005. Solid-state  $^{19}\text{F}$ -NMR studies on fluorine-labeled model compounds and biomolecules. Ph.D. thesis, Universität Karlsruhe (TH). Fakultät für Chemie und Biowissenschaften.
- [545] Schiffer, M., 1967. Use of Helical Wheels to Represent the Structures of Proteins and to Identify Segments with Helical Potential. *Biophys J* 7:121–135.
- [546] Ozdirekcan, S., C. Etchebest, J. A. Killian, and P. F. J. Fuchs, 2007. On the orientation of a designed transmembrane peptide: toward the right tilt angle? *J Am Chem Soc* 129:15174–15181.
- [547] Im, W., and C. L. Brooks, 2005. Interfacial folding and membrane insertion of designed peptides studied by molecular dynamics simulations. *Proc Natl Acad Sci U S A* 102:6771–6776.
- [548] Kim, S., and T. A. Cross, 2002. Uniformity, ideality, and hydrogen bonds in transmembrane alpha-helices. *Biophys J* 83:2084–2095.

- [549] Page, R. C., S. Kim, and T. A. Cross, 2008. Transmembrane helix uniformity examined by spectral mapping of torsion angles. *Structure* 16:787–797.
- [550] Fuertes, G., D. Giménez, S. Esteban-Martin, A. Garcia-Sáez, O. Sánchez, and J. Salgado, 2010. Role of membrane lipids for the activity of pore forming peptides and proteins. *Adv Exp Med Biol* 677:31–55.
- [551] Khattari, Z., G. Brotons, M. Akkawi, E. Arbely, I. T. Arkin, and T. Salditt, 2006. SARS coronavirus E protein in phospholipid bilayers: an x-ray study. *Biophys J* 90:2038–2050.
- [552] Tristram-Nagle, S., Y. Liu, J. Legleiter, and J. F. Nagle, 2002. Structure of gel phase DMPC determined by X-ray diffraction. *Biophys J* 83:3324–3335.
- [553] Leekumjorn, S., and A. K. Sum, 2007. Molecular characterization of gel and liquid-crystalline structures of fully hydrated POPC and POPE bilayers. *J Phys Chem B* 111:6026–6033.
- [554] Kucerka, N., S. Tristram-Nagle, and J. F. Nagle, 2005. Structure of fully hydrated fluid phase lipid bilayers with monounsaturated chains. *J Membr Biol* 208:193–202.
- [555] García-Sáez, A. J., S. Chiantia, and P. Schwille, 2007. Effect of line tension on the lateral organization of lipid membranes. *J Biol Chem* 282:33537–33544.
- [556] Mouritsen, O. G., and M. Bloom, 1984. Mattress model of lipid-protein interactions in membranes. *Biophys J* 46:141–153.
- [557] de Planque, M. R. R., and J. A. Killian, 2003. Protein-lipid interactions studied with designed transmembrane peptides: role of hydrophobic matching and interfacial anchoring. *Mol Membr Biol* 20:271–284.
- [558] Sengupta, D., L. Meinhold, D. Langosch, G. M. Ullmann, and J. C. Smith, 2005. Understanding the energetics of helical peptide orientation in membranes. *Proteins* 58:913–922.
- [559] Ulmschneider, M. B., M. S. P. Sansom, and A. D. Nola, 2006. Evaluating tilt angles of membrane-associated helices: comparison of computational and NMR techniques. *Biophys J* 90:1650–1660.
- [560] Lomize, A. L., I. D. Pogozheva, M. A. Lomize, and H. I. Mosberg, 2006. Positioning of proteins in membranes: a computational approach. *Protein Sci* 15:1318–1333.
- [561] Senes, A., D. C. Chadi, P. B. Law, R. F. S. Walters, V. Nanda, and W. F. Degrado, 2007.  $E(z)$ , a depth-dependent potential for assessing the energies of insertion of amino acid side-chains into membranes: derivation and applications to determining the orientation of transmembrane and interfacial helices. *J Mol Biol* 366:436–448.
- [562] Esteban-Martín, S., D. Giménez, G. Fuertes, and J. Salgado, 2009. Orientational landscapes of peptides in membranes: prediction of  $(2)H$  NMR couplings in a dynamic context. *Biochemistry* 48:11441–11448.
- [563] Heller, W. T., A. J. Waring, R. I. Lehrer, and H. W. Huang, 1998. Multiple states of beta-sheet peptide protegrin in lipid bilayers. *Biochemistry* 37:17331–17338.
- [564] Yang, L., T. A. Harroun, T. M. Weiss, L. Ding, and H. W. Huang, 2001. Barrel-stave model or toroidal model? A case study on melittin pores. *Biophys J* 81:1475–1485.
- [565] Glaser, R. W., C. Sachse, U. H. N. Dürr, P. Wadhvani, S. Afonin, E. Strandberg, and A. S. Ulrich, 2005. Concentration-dependent realignment of the antimicrobial peptide PGLa in lipid membranes observed by solid-state  $^{19}F$ -NMR. *Biophys J* 88:3392–3397.
- [566] Lee, M.-T., F.-Y. Chen, and H. W. Huang, 2004. Energetics of pore formation induced by membrane active peptides. *Biochemistry* 43:3590–3599.
- [567] Wu, Y., K. He, S. J. Ludtke, and H. W. Huang, 1995. X-ray diffraction study of lipid bilayer membranes interacting with amphiphilic helical peptides: diphytanoyl phosphatidylcholine with alamethicin at low concentrations. *Biophys J* 68:2361–2369.
- [568] Heller, W. T., A. J. Waring, R. I. Lehrer, T. A. Harroun, T. M. Weiss, L. Yang, and H. W. Huang, 2000. Membrane thinning effect of the beta-sheet antimicrobial protegrin. *Biochemistry* 39:139–145.

## Bibliografía

- [569] Ambroggio, E. E., F. Separovic, J. H. Bowie, G. D. Fidelio, and L. A. Bagatolli, 2005. Direct visualization of membrane leakage induced by the antibiotic peptides: maculatin, citropin, and aurein. *Biophys J* 89:1874–1881.
- [570] Mazzuca, C., B. Orioni, M. Coletta, F. Formaggio, C. Toniolo, G. Maulucci, M. D. Spirito, B. Pispisa, M. Venanzi, and L. Stella, 2010. Fluctuations and the rate-limiting step of peptide-induced membrane leakage. *Biophys J* 99:1791–1800.
- [571] Schwarz, G., and C. H. Robert, 1990. Pore formation kinetics in membranes, determined from the release of marker molecules out of liposomes or cells. *Biophys J* 58:577–583.
- [572] Rex, S., and G. Schwarz, 1998. Quantitative studies on the melittin-induced leakage mechanism of lipid vesicles. *Biochemistry* 37:2336–2345.
- [573] Fantner, G. E., R. J. Barbero, D. S. Gray, and A. M. Belcher, 2010. Kinetics of antimicrobial peptide activity measured on individual bacterial cells using high-speed atomic force microscopy. *Nat Nanotechnol* 5:280–285.
- [574] Imura, Y., N. Choda, and K. Matsuzaki, 2008. Magainin 2 in action: distinct modes of membrane permeabilization in living bacterial and mammalian cells. *Biophys J* 95:5757–5765.
- [575] Mangoni, M. L., N. Papo, D. Barra, M. Simmaco, A. Bozzi, A. D. Giulio, and A. C. Rinaldi, 2004. Effects of the antimicrobial peptide temporin L on cell morphology, membrane permeability and viability of *Escherichia coli*. *Biochem J* 380:859–865.
- [576] Matsuzaki, K., S. Yoneyama, and K. Miyajima, 1997. Pore formation and translocation of melittin. *Biophys J* 73:831–838.
- [577] Han, M., Y. Mei, H. Khant, and S. J. Ludtke, 2009. Characterization of antibiotic peptide pores using cryo-EM and comparison to neutron scattering. *Biophys J* 97:164–172.
- [578] Kahya, N., D. Scherfeld, K. Bacia, and P. Schwille, 2004. Lipid domain formation and dynamics in giant unilamellar vesicles explored by fluorescence correlation spectroscopy. *J Struct Biol* 147:77–89.
- [579] Ladokhin, A. S., W. C. Wimley, and S. H. White, 1995. Leakage of membrane vesicle contents: determination of mechanism using fluorescence reequenching. *Biophys J* 69:1964–1971.
- [580] Arbuzova, A., and G. Schwarz, 1999. Pore-forming action of mastoparan peptides on liposomes: a quantitative analysis. *Biochim Biophys Acta* 1420:139–152.
- [581] Sharpe, J. C., and E. London, 1999. Diphtheria toxin forms pores of different sizes depending on its concentration in membranes: probable relationship to oligomerization. *J Membr Biol* 171:209–221.
- [582] Tamba, Y., H. Ariyama, V. Levadny, and M. Yamazaki, 2010. Kinetic pathway of antimicrobial peptide magainin 2-induced pore formation in lipid membranes. *J Phys Chem B* 114:12018–12026.
- [583] Esteban-Martín, S., H. J. Risselada, J. Salgado, and S. J. Marrink, 2009. Stability of asymmetric lipid bilayers assessed by molecular dynamics simulations. *J Am Chem Soc* 131:15194–15202.
- [584] Apellániz, B., J. L. Nieva, P. Schwille, and A. J. García-Sáez, 2010. All-or-none versus graded: single-vesicle analysis reveals lipid composition effects on membrane permeabilization. *Biophys J* 99:3619–3628.
- [585] Dahlberg, M., and A. Maliniak, 2008. Molecular dynamics simulations of cardiolipin bilayers. *J Phys Chem B* 112:11655–11663.
- [586] Ramadurai, S., A. Holt, V. Krasnikov, G. van den Bogaart, J. A. Killian, and B. Poolman, 2009. Lateral diffusion of membrane proteins. *J Am Chem Soc* 131:12650–12656.
- [587] Popot, J. L., and D. M. Engelman, 1990. Membrane protein folding and oligomerization: the two-stage model. *Biochemistry* 29:4031–4037.
- [588] He, K., S. J. Ludtke, W. T. Heller, and H. W. Huang, 1996. Mechanism of alamethicin insertion into lipid bilayers. *Biophys J* 71:2669–2679.

- [589] Brünger, A. T., P. D. Adams, G. M. Clore, W. L. DeLano, P. Gros, R. W. Grosse-Kunstleve, J. S. Jiang, J. Kuszewski, M. Nilges, N. S. Pannu, R. J. Read, L. M. Rice, T. Simonson, and G. L. Warren, 1998. Crystallography & NMR system: A new software suite for macromolecular structure determination. *Acta Crystallogr D Biol Crystallogr* 54:905–921.
- [590] Valero, J. G., L. Sancey, J. Kucharczak, Y. Guillemain, D. Gimenez, J. Prudent, G. Gillet, J. Salgado, J.-L. Coll, and A. Aouacheria, 2011. Bax-derived membrane-active peptides act as potent and direct inducers of apoptosis in cancer cells. *J Cell Sci* 124:556–564.
- [591] Simons, K., and M. J. Gerl, 2010. Revitalizing membrane rafts: new tools and insights. *Nat Rev Mol Cell Biol* 11:688–699.
- [592] Matsuzaki, K., S. Yoneyama, O. Murase, and K. Miyajima, 1996. Transbilayer transport of ions and lipids coupled with mastoparan X translocation. *Biochemistry* 35:8450–8456.
- [593] Arkin, I. T., 2006. Isotope-edited IR spectroscopy for the study of membrane proteins. *Curr Opin Chem Biol* 10:394–401.